Probing the impact of metallicity on the dust properties in galaxies

Aurélie Rémy-Ruyer

UNIVERSITÉ PARIS SUD

Comprendre le monde, construire l'avenir®

AIM

Université Paris-Sud

Ecole Doctorale d'Astronomie et Astrophysique d'Ile de France
Laboratoire AIM, CEA Saclay

Discipline : Astronomie et Astrophysique

Thèse de doctorat

Soutenue le 13 Décembre 2013 par

Aurélie Rémy-Ruyer

Probing the impact of metallicity on the dust properties in galaxies

Directrice de thèse :	Dr. Suzanne Madden	(AIM, CEA Saclay)
Composition du jury :		
Président du jury :	Pr. Guillaume Pineau des Forêts	(Institut d'Astrophysique Spatiale)
Rapporteurs :	Pr. Daniel Dale	(University of Wyoming)
	Pr. François-Xavier Désert	(Institut de Planétologie et d'Astrophysique de Grenoble)
Examinateurs :	Pr. Maarten Baes	(Sterrenkundig Observatorium, Universiteit Gent)
	Pr. Jonathan Davies	(Cardiff University)
Invitée :	Dr. Caroline Bot	(Observatoire de Strasbourg)

Acknowledgements

J'ai effectué cette thèse au CEA à Saclay au Laboratoire AIM (ou Service d'Astrophysique) au sein de l'IRFU, grâce à une bourse CFR. Je tenais donc à remercier le chef de service Pierre-Olivier Lagage de m'avoir accueillie au sein du service et de m'avoir donné les moyens techniques, financiers et humains nécessaires à la réalisation de mon travail. Plus particulièrement je voulais le remercier de m'avoir accordé trois mois de plus pour finaliser ma thèse sans quoi la fin de cette troisième année aurait été beaucoup moins drôle... Merci aussi à Marie Gay et Nicolas Pailley pour avoir su gérer avec patience mes petits soucis informatiques au quotidien, à Dominique Monvoisin et Christine Toutain pour leur efficacité, et à Marylise et Angélique qui régulièrement viennent égayer le bureau.

Plus proche de moi je voudrais aussi évidemment remercier tous mes collaborateurs directs au SAp, Suzanne, bien sûr, Fred, Sacha, Vianney, Ronin, Marc, les nouvelles arrivées de l'année : Min et Mélanie et les dejà parties depuis quelque temps : Diane et Maud. Merci à toi Suzanne pour ces trois années. J'ai vraiment appris beaucoup et notamment la gestion de situations de dernière minute... grâce à ta conception si particulière de l'écoulement du temps ("What ? Is it February already ? Where did January go ???"). Merci de m'avoir laissé une grande liberté pour mon projet, tout en gardant un oeil sur la direction générale des travaux. Merci encore pour m'avoir donné l'opportunité d'aller observer au Chili sur APEX, cette expérience restera à coup sûr gravée dans ma mémoire. Merci également d'avoir fait en sorte que notre relation soit plus qu'une simple relation d'étudiante à directrice, pour ces quelques diners chez toi et ces fameuses lasagnes végétariennes. Merci à toi Sacha de m'avoir épaulée en tout début de thèse quand IDL n'était encore qu'un obscur language de programmation pour moi, d'avoir eu la patience de m'apprendre ce qu'il fallait effectivement que je mette dans mon code pour que ça marche. Merci à toi Fred, l'expert des SEDs. Merci pour ton aide précieuse, tes explications toujours très détaillées, ta patience et ta disponibilité. Je n'oublie pas bien sûr Vianney et son aide précieuse sur les spectres IRS. Merci à vous tous de la Suzanne's team pour avoir fait en sorte que ces trois années se passent aussi bien tant sur le plan scientifique que sur le plan personnel en gardant toujours une bonne ambiance entre nous.

Ces trois années ont été riches en voyages et en rencontres. Merci à Ilse, Oskar, Phil, Jeremy, Lynn (qui a partagé pendant quelques semaines notre bureau) et George pour leur aide/amitié qui m'ont beaucoup enrichie. Merci à toi Maud, pour m'avoir aidée à garder mon calme et ma patience pour les images 3 couleurs du DGS et le fameux poster ! On ne s'est croisées que brièvement à la fin de ta thèse et au début de la mienne, mais tes visites régulières au SAp et nos matinées passées à discuter (de science, entre autres...) nous ont permis de développer une réelle amitié. J'espère pouvoir garder contact avec vous tous et de pouvoir (continuer à) collaborer de manière fructueuse à l'avenir. Merci aussi à Ant de m'accueillir à l'IAS pour cette année qui commence.

Ces trois années n'auraient pas été les mêmes s'il n'y avait pas eu tous les autres étudiants (pardon, doctorants...) et post docs, j'ai nommé : Long, Kevin, Alexis, Camille, Lionel, Corentin, Lucie, Laurie, Nicolas, Pierre-Emmanuel, Jérémy, Erwann, Thomas, Esther, Julien, Carine, Amandine, l'autre Kévin, Pascuale, Doris, Vera, Fadia... et tant d'autres que j'oublier certainement. Ainsi qu'à tous les "permanants" avec qui j'ai eu l'occasion de discuter science (ou pas) : Roland,

Sandrine, Michel, Sébastien, Cécile, Jérôme, Koryo. Merci pour tous ces bons moments passés ensemble à table le midi, lors de diners chez l'un ou l'autre le soir, le matin autour d'un café ou d'un thé, pendant les (trop rares) pique-niques ou lors des p'tit déjs étudiants/post docs. Merci à toi Ronin, ma co-bureau, pour avoir partagé avec moi mes espoirs et mes déceptions, mes réussites ou mes frustrations, pour ces innombrables heures passées à papoter et pour cette belle semaine d'été en Provence. Un grand merci tout spécialement à Sacha et Diane venus exprès de Heidelberg, Ronin, Vianney, Sue, Ant et les filles Elianna et Marissa, à Long et ses magnifiques photos, Kévin et Alexis pour avoir partagé le premier grand jour de cette année 2013 avec moi, jour que j'ai passé habillée d'une belle robe blanche...

Un grand merci à tous mes amis "hors CEA" qui ont suivi de près ou de loin cette thèse et notamment à Charlène, Emilia et Valentin, Etienne et Aymeric. Merci à Charlène, l'avocate, de s'être dévouée pour lire un chapitre de ma thèse dans lequel elle a découvert "de nouvelles lettres". Merci à Aymeric pour avoir lu un autre chapitre quand mes yeux fatigués ne pouvaient décidemment pas le relire une nouvelle fois. Merci à toi Etienne pour tous ces bons moments passés à échanger sur nos thèses respectives, pour ton écoute et tes conseils. Merci à vous Emilia et Valentin pour m'avoir accueillie à Cambridge et pour votre amitié et votre soutien. A toi maintenant Valentin de finir et la boucle sera bouclée.

Merci tout particulièrement à ma famille qui a su patiemment m'écouter parler de galaxies ou d'étoiles ou de poussière et qui m'a soutenue de près ou de loin pendant ces trois ans. Je tiens à remercier tout particulièrement mes parents, mon frère, ma soeur, mon oncle Dominique et ma tante Andrée-Lise pour être venus assister à ma soutenance un vendredi après-midi de Décembre dans le fin fond du sud de la banlieue parisienne.

Et enfin "merci" me semble bien faible pour exprimer ma gratitude envers toi, Charles, ma moitié depuis bientôt 6 ans, et maintenant officiellement depuis huit mois. Merci pour ta patience, pour ton soutien sans failles, pour avoir tout pris en charge pendant ce dernier mois de rédaction et pour avoir relu un bout de ma thèse également. J'espère être en mesure de faire de même cette année pour toi.

Merci pour tout !

Abstract

The aim of this work is to study dust in the interstellar medium (ISM) of nearby galaxies and especially how the metallicity impacts the physical properties of the dust. Local dwarf galaxies, characterised by a low metallicity, are thus the ideal targets for such a study. Indeed previous works have shown that the spectral energy distribution (SED) of these galaxies was different from those of more metal-rich environments. However these studies were limited to the warmer dust emitting at wavelengths shorter than 200 μm and were done only on a limited number of dwarf galaxies. Thanks to its increased sensitivity and resolution in the far-infrared (FIR), *Herschel* gives us a new view on the cold dust properties in galaxies and enables us to study the lowest metallicity galaxies in a systematic way. Our work is focused on a sample of 48 low-metallicity local dwarf galaxies from one of the *Herschel* key programs: the Dwarf Galaxy Survey (DGS). We complete the DGS with another *Herschel* sample : Key Insights on Nearby Galaxies : a Far-Infrared Survey with *Herschel* (KINGFISH), probing more metal-rich environments.

We adopt a multi-wavelength approach, first focusing on the cold dust probed by *Herschel* in the FIR and second by probing the observed SED over the whole infrared range (using ancillary data from 2MASS, *Spitzer*, *WISE*, *IRAS* and ground-based facilities), that we model with a semi-empirical dust model. We find that a good wavelength coverage of the peak of the SED and a realistic dust model is crucial to properly determine the dust properties, especially the dust mass. We find that dust masses estimated using a modified blackbody model are *systematically underestimated* by a factor of ~ 1.8 compared to dust masses from a full dust SED model. We find that dwarf galaxies harbour on average warmer dust than their metal-rich counterparts (about 1.5 times warmer), due to the harder interstellar radiation field interacting with the porous ISM of dwarf galaxies.

Previous observations of some low-metallicity dwarf galaxies also led to the detection of an emission in the submillimeter (submm) that current models cannot explain: the so-called "submm excess". In our sample of 110 galaxies we confirm the presence of a submm excess in half of the sample, and not necessarily metal-poor objects. We find that submm colours are a good empirical tool to detect or predict the appearance of the submm excess. Another dust composition, using more emissive grains, is able to explain the excess for half of the galaxies. However another mechanism is needed to account for the strongest excesses.

We finally look at the variation of the gas-to-dust mass ratios (G/D) in our sample with metallicity as it is a good tracer of the chemical evolution stage of a galaxy. In the past, the G/D has been seen to correlate linearily with metallicity down to metallicities of $\sim 1/5\ Z_{\odot}$. We add another sample to the DGS and KINGFISH samples, totalling 126 galaxies, spanning a 2 dex metallicity range, from $\sim 1/40\ Z_{\odot}$ to $\sim 2\ Z_{\odot}$. Our study shows that this linear dependance does not hold at low metallicities and that the relation between G/D and metallicity is steeper. We provide an empirical relation, via a broken power-law fit to the observed G/D values, to estimate the G/D at low metallicities from a metallicity value. However, the scatter in the observed G/D vs metallicity relation is large, due to the variety of environments that we probe, showing that metallicity is not the only parameter driving the relation. We find that the star-formation histories of the galaxies and dust grain growth in the ISM are both important in the evolution of the G/D with metallicity.

Contents

List of Figures

List of Tables

Introduction

The work presented in this manuscript is incorporated within the vast and general framework of evolution of galaxies. The processes by which galaxies evolve, from the very first galaxies of the primordial Universe to the present-day systems, are still widely debated. The seeds of this evolution lay in the star-formation histories of the galaxies. How are stars formed and at what rate? What controls the efficiency at which the stars are formed? How does this efficiency vary over time? How does this impact the galaxy?

Galaxies are composed primarily of stars and of an interstellar medium (ISM) of gas and dust. The continuous interplay between stars and the ISM is one of the major drivers of galaxy evolution. The ISM plays a key role in this evolution, being the repository of stellar ejecta and the site of stellar birth. It thus contains the imprint of the astrophysical processes occurring in a galaxy. These astrophysical processes can be studied with observations of ISM in galaxies at various wavelengths throughout the spectral energy distribution (SED). The SED is a powerful tool to probe the current physical and chemical state of a galaxy with this historical information integrated over the lifetime of the galaxy.

Interstellar dust is present in most phases of the ISM, from warm ionized regions around young stars to the cores of dense molecular clouds. Because dust is mainly formed from the available metals in the ISM, the dust content traces its internal evolution through metal enrichment. Metallicity is thus a key parameter in studying the evolution of galaxies and is at the heart of this work. Dust influences the subsequent star formation and has a significant impact on the total SED of a galaxy: the absorbed stellar light by dust in the ultraviolet (UV) and visible wavelengths is re-emitted in the infrared (IR) domain by the dust grains. In our Galaxy, dust reprocesses about 30% of the stellar power, and it can be as large as $\sim$ 99% in a starburst galaxy. Studying the IR emission of galaxies thus provides valuable information on the dust properties of the galaxies and on their overall star-formation activity.

With the advent of infrared space missions, such as *ISO*, *IRAS*, *Spitzer*, *AKARI*, and more recently *Herschel*, much progress has been made in characterizing the dust properties of galaxies. For a few decades now, IR astronomy has revolutionized our understanding of the dust properties in galaxies. Dust is no longer viewed only as the culprit in obscuring starlight, but also as a powerful tracer of the star-formation activity and of the evolutionary stage of the galaxy. Our Galaxy, as well as other well studied local Universe galaxies, provide various observational benchmarks to calibrate the physical dust properties around solar metallicity. However, for galaxies of the high-redshift Universe, dust properties are still poorly known, and evolution of the dust properties with galactic properties, such as metallicity, star-formation activity, morphology, etc. is unclear. Because of their low metal abundance and active star formation, dwarf galaxies of the local Universe are ideal laboratories for studying star formation and its feedback on the ISM in conditions that may be representative of different stages in early Universe environments.

However due to their low luminosities, and to the lack of full wavelength coverage from the mid-IR to submillimetre (submm) wavelengths, only a handful of dwarf galaxies had been studied until recently, and large uncertainties existed on their dust properties, even on one as fundamental

as the dust mass. An excess emission in the submm has also been observed in several dwarf galaxies and low-metallicity spirals, unexplained by current dust models. With the new wavelength range covered by *Herschel* in the far-IR (FIR) and submm domains and its unprecedented sensitivity, we are now able to study the detailed dust properties more accurately, and probe dust in systems of extremely low metallicities ($\sim 1/40\ Z_{\odot}$).

My research focus on the following questions: How do the dust properties (such as mass, temperature, luminosity, etc.) vary with metallicity? In which environments does the submm excess preferentially appear? How do the proportions of metals in the gas and dust phases relate to each other? How do the gas-to-dust mass ratios (G/D) evolve as a function of metallicity?

In this work, I carry out a study of the dust properties in dwarf galaxies and compare with more metal rich environments, in order to address the question of the impact of metallicity on the dust properties. The novelty of this work lays in the fact that dwarf galaxies are studied here in a systematic way, enabling us to derive and quantify the general properties that are representative of these systems. This study is conducted over the full IR-to-submm range, using new FIR/submm *Herschel* observations, along with *Spitzer*, *WISE*, *IRAS* and 2MASS data. We complete this set of data with longer submm measurements from ground-based facilities such as *APEX* and *JCMT* to study the presence and characteristics of the submm excess in my sample of galaxies. I also collect HI and CO data to access the gas properties of the galaxies and study the evolution of the G/D with metallicity.

This manuscript is composed of three parts. The first part is dedicated to a general description of the ISM in galaxies (Chapter 1) and of low-metallicity systems and their peculiarities (Chapter 2). In these first two Chapters, we also present the main motivations for this work. The second part of my work is dedicated to the study of the cold dust component uncovered by *Herschel* in low-metallicity environments. *Herschel* and the two samples that are considered for this study (a sample of dwarf galaxies and a sample probing more metal-rich environments) are presented in Chapter 3. Chapter 4 presents the new *Herschel* data obtained for our objects, that we interpret with the aid of a modified blackbody model (Chapter 5). The third part of my work (Chapters 6 to 9) broadens our view of dust in these low-metallicity systems by looking at the total dust component across the whole IR-to-submm range (data presented in Chatper 6). The SEDs are modelled with a semi-empirical dust model, presented in Chapter 7 and the results are then analysed and discussed in Chapter 8. We especially focus on the variation of the dust properties with metallicity and address the submm excess issue in this Chapter. The last chapter of this thesis (Chapter 9) incorporates the gas into our dust picture and presents a study of the variations of G/D of galaxies with metallicity. Results are discussed and interpreted with the aid of three chemical evolution models.

Part I

The ISM of low-metallicity galaxies

Chapter 1

Structure and physics of the interstellar medium

Contents

This Chapter aims to give a brief overview of our current understanding of the structure and the physics of the interstellar medium (ISM) of galaxies and especially our Galaxy for which most details are known. Our current view of the ISM has been shaped by the observations at various wavelengths available to astronomers. Thus we start this Chapter with a description of the physical properties that can be probed by observations at different wavelengths (Section 1.1), and introduce the main components of a galaxy. Then, detailed properties of the dust and gas, the two main components of the ISM, are presented and discussed in Sections 1.2 and 1.3 for the case of our Galaxy. We especially focus on linking the observations of the ISM with a theoretical description of the physical processes at stake responsible for what we see. In the last Section 1.4 we describe the main tools at our disposal to probe the ISM emission of a galaxy, and describe how this emission can vary according to the different types of galaxies.

1.1 A multi-wavelength picture of a galaxy

In the most general view, a galaxy is composed of stars evolving in an interstellar medium (ISM) and surrounded by a dark matter halo. The ISM contains all of the matter that fills in the vast empty space between the stars in a galaxy: for example, in the solar neighbourhood, stars are separated by ~ 2 pc. The ISM can be decomposed into a gaseous component: interstellar gas; and a solid component: interstellar dust. Gas structures the ISM in a large variety of phases depending on its local physical conditions (mainly density and temperature): from ionized to molecular phase, where "ionized" and "molecular" refer to the state of the hydrogen element. Dust, however, is present throughout the ISM.

The only way to access information about a galaxy, such as its composition or its physical and chemical states, is through the light we receive from space. Galaxies emit over the whole electromagnetic spectrum and the light at a given energy brings its own piece of information: i.e., having access to a large range of wavelengths is crucial to build the most complete picture of a given galaxy. Fig. 1.1 shows, as an example, the Whirlpool galaxy, M51, seen with five different instruments[1].

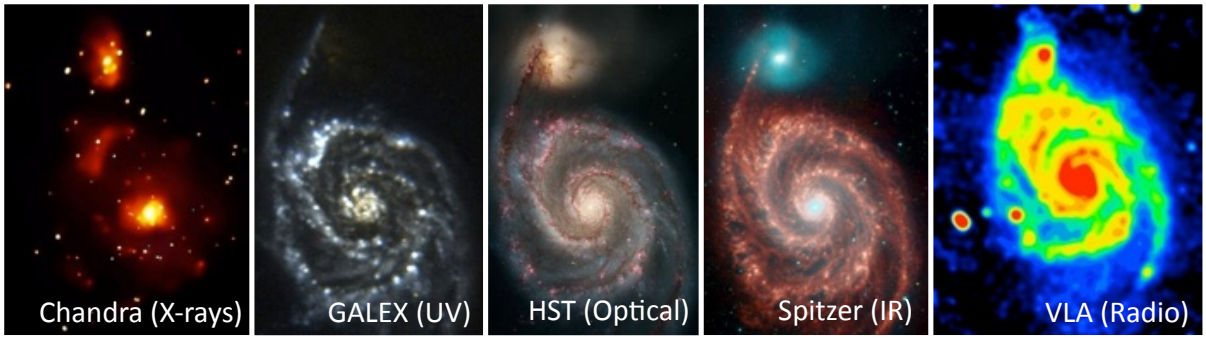

Fig. 1.1. M51 seen by *Chandra* (hot gas), *GALEX* (young stars), *HST* (old stars), *Spitzer* (dust) and VLA (atomic gas) telescopes.

We clearly see differences between the various wavelengths: for example the spiral structure of the galaxy is visible at all the wavelengths observed here except in the X-rays; or the northern companion of M51 is not visible with *GALEX*. We can deduce the presence of all of the components in the galaxy with these observations: for example, stars are visible with *GALEX* and *HST*. If there are stars, then gas must also be present as can be seen with *Chandra* and the VLA. And finally the

[1]Images from http://www.sedfitting.org/SED08/Welcome.html

black lanes obscuring the *HST* image can be attributed to micro-particles obscuring the light from the galaxy, that were generically called dust.

The distribution of the amount of total energy emitted by a galaxy over a given wavelength or frequency range is called a spectral energy distribution (SED). The SED is a precious tool for the astronomers as it gives an instantaneous multiwavelength snapshot of a galaxy. Figure 1.2 shows an example of UV-to-mm SED for a galaxy. The black points and red spectrum represent direct observations from the galaxy. The challenge for astronomers is to find a realistic model (i.e., the blue curve of Fig. 1.2) that will take into account all of the physical processes occurring in the galaxy, in order to disentangle the emission from the different components and then access information about the galaxy. Here for example, the model tells us that this galaxy is forming stars at a rate of 9.5 $M_{\odot}\,yr^{-1}$.

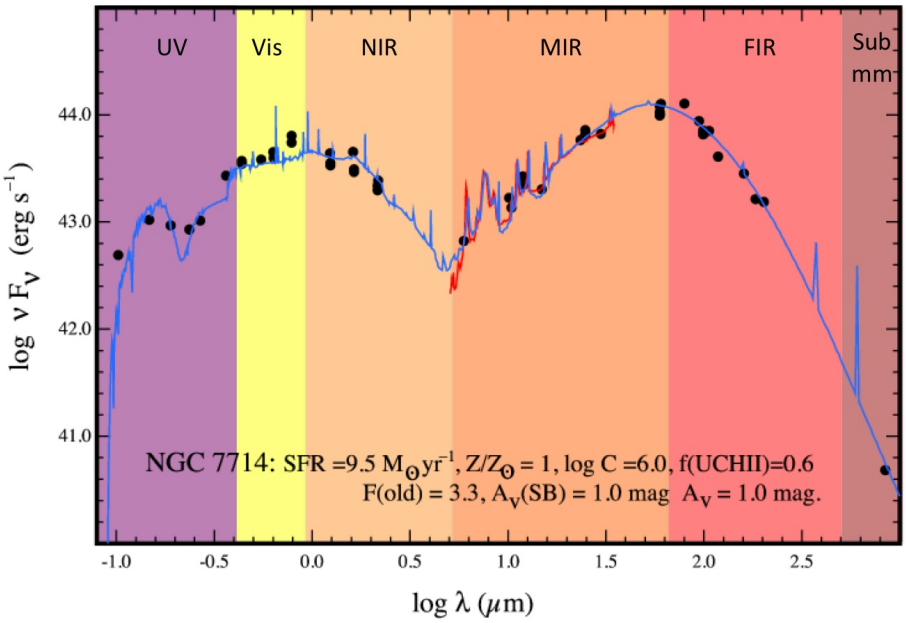

Fig. 1.2. Example of a UV-to-mm SED for a galaxy, here NGC7714 from Groves et al. (2008).The black points and red spectrum are observational constraints. A realistic model (blue curve from Groves et al. 2008) reproduces the emission from the galaxy and enables us to access physical properties of the galaxy. *Note:* We define the acronyms for the wavelength ranges we use throughout this manuscript: ultra-violet (UV) from 0.1 to 0.4 μm, visible from 0.4 to 0.8 μm, near-infrared (NIR) from 0.8 to $\sim$ 5 μm, mid-infrared (MIR) from $\sim$ 5 to $\sim$ 50 μm, far-infrared (FIR) from $\sim$ 60 to $\sim$ 600-700 μm and sub-millimetre (submm) from $\sim$ 500 to 1000 μm.

Indeed the various components of a galaxy all dominate the total emission in a specific wavelength domain:

Stars: Stars dominate in the UV to NIR range: young stars (ages of a few Myr) have a peak of emission around 0.1 μm in the UV and older stars (ages of 0.1 - 1 Gyr) have their emission peaking in the visible around 0.5 μm. Thus in Fig. 1.2, stars are responsible for the UV-to-NIR peak of the SED.

Dust: Dust absorbs the stellar radiation and re-emits the bulk of its energy in the IR. Emission by dust will be discussed in Section 1.2.4 and will be the main topic of Chapter 7. The broad IR peak of the SED in Fig. 1.2 is due to dust in NGC7714.

Gas: Gas emits over the whole electromagnetic spectrum and is visible in the total SED of a galaxy through spectral lines and a continuum in emission or in absorption. These spectral lines come from a change in the state of the gas (excitation) and are powerful tracers of the physical state of the gas in the galaxy (see Section 1.3). Atomic hydrogen gas emission can dominate the SED of a galaxy in radio wavelengths.

We note in Fig. 1.2 a sudden and important drop in the energy emitted at far-UV (FUV) wavelengths around 0.1 μm. This is because, at wavelengths below the Lyman edge at 912 Å, a small amount of hydrogen present in the ISM is capable of absorbing nearly all radiation. This sharp transition at 912 Å is often used by cosmologists to determine the redshift of a galaxy: knowing the wavelength of this transition in the observed spectrum of a distant galaxy and comparing to 912 Å indicates its redshift. At shorter wavelengths in the X-ray emission domain, the total emission of a galaxy is dominated by emission from hot plasmas: coronal gas in the halo of the galaxy and in supernovae remnants.

The relative importance of all of these components (stars, gas and dust) to the total SED is not the same for different galaxies. Indeed these differences depend on numerous physical characteristics of the galaxies such as morphological type or stellar activity for example (see Section 1.4). To be able to disentangle the different components, we need to know more about how they interact with each other, about the physical processes occurring in the galaxy and the theory governing them. This will be the object of Sections 1.2 and 1.3.

Let us now focus more in details on the ISM of our Galaxy. Table 1.1 gives a view of the repartition of mass and luminosity between the different components of the Galaxy, and provides useful reference values for comparison with other galaxies. The total baryonic mass is dominated by the mass of stars and the ISM represents about 2.5 % of the baryonic mass (Tielens 2005), but it accounts for about 30% of the total luminosity.

Table 1.1. Masses and luminosities in the Milky Way (adapted from Table 3 of Tielens 2005).

Component	Mass $[M_\odot]$	Luminosity $[L_\odot]$
Stars	1.8×10^{11}	$\sim 4.8 \times 10^{10}$
Gas	4.5×10^{9}	$\sim 2 \times 10^{8}$
Dust	$\sim 4.5 \times 10^{7}$	$\sim 1.7 \times 10^{10}$
Total	$\sim 2 \times 10^{11,a}$ - $\geq 10^{12,b}$	$\sim 6.5 \times 10^{10}$

[a]: visible matter only.
[b]: including dark matter.

1.2 Dust in the ISM

1.2.1 Observational evidence of dust in the ISM

The first evidence of the presence of dust in the ISM was through the obscuration of some parts of the sky in the optical wavelengths that were first accessible to astronomers (Fig. 1.3[2]). The light coming from the stars is extinguished by dust present along the line-of-sight between the stars and the observer. Comparing the light arriving from a non-obscured star and that from an obscured star, i.e., measuring extinction (see Section 1.2.2), provides valuable information on the nature of dust present along the line-of-sight.

[2] Image from http://www.astro.ucla.edu/ ghezgroup/gc/journey/wave.shtml

Fig. 1.3. Optical image of the Galactic Center. Dust present in between the observer and the center of the Milky Way causes the light coming from the inner parts of the Galaxy to be heavily extinguished.

The physical processes responsible for the extinction of stellar light are absorption and scattering of the light by dust grains, which strongly depend on the intrinsic properties of the dust grain, mainly its chemical composition and size. We observe extinction of starlight along a wide range of wavelengths indicating that grains of different natures and sizes are present in the ISM. A dust model can be defined as an ensemble of dust properties (see Section 1.2.5) needed to reproduce a set of observational constraints. That is why the very first dust models (e.g., Mathis et al. 1977) were derived using the mean interstellar extinction in our Galaxy to constrain the dust size distribution and chemical composition.

As the dust grain absorbs energy, it also radiates this energy away at IR wavelengths. Thus we can also obtain constraints on the nature of the dust by looking at emission of the ISM in the IR domain. This was only possible after the advent of space astronomy in the early 80's with the first IR space telescope: the InfraRed Astronomy Satellite (*IRAS*). Indeed the Earth atmosphere absorbs IR radiation from space and obliges the astronomers to explore this wavelength range from space. The availability of these new constraints, from dust emission, revolutionized the study of ISM dust, as astronomers started to incorpore them into their models (e.g., Desert et al. 1990).

Dust grains are made from the available elements in the ISM, the most abundant being carbon and oxygen. A fraction of them being locked up in the solid phase of the ISM, these elements are depleted from the gas phase. Informations about the chemical composition of the dust can thus be deduced from what is called "elemental depletions", i.e., what is *not* seen in the gas phase (as in the modelling of Zubko et al. 2004).

Other constraints can be used to determine the nature of the dust grains such as X-ray scattering by dust (Smith & Dwek 1998), bringing information on the abundance and composition of the biggest grains; polarisation of the starlight by dust providing information on the geometry of the medium and on the grain elongation; reflection nebulae constraining the grain albedo[3]; or spectral features to access the grain composition.

[3]The albedo of a dust grain describes the relative importance of scattering compared to absorption by the dust grain.

1.2.2 Extinction by dust grains

Dust has thus a major impact on the propagation of starlight throughout the galaxy as it absorbs radiation from the stars. The amount of extinction suffered from a starlight radiation after passing through a cloud of dust is related to the optical depth of the cloud $\tau(\lambda)$, which is, in turn, related to the dust column density, i.e., the quantity of dust along a given line-of-sight. Historically, the extinction is expressed as $A(\lambda)$, in magnitudes (see Eq. 1.2).

The monochromatic specific intensity received by the observer, I_λ, after passing through a cloud of dust with an optical depth $\tau(\lambda)$, is related to the source intensity, I^0_λ, by:

$$I_\lambda = I^0_\lambda \times e^{-\tau(\lambda)} = I^0_\lambda \times 10^{-A(\lambda)/2.5} \tag{1.1}$$

From Eq. 1.1 we can relate $\tau(\lambda)$ and $A(\lambda)$:

$$A(\lambda) = 1.086 \times \tau(\lambda) \tag{1.2}$$

Figure 1.4 shows the extinction curve of the diffuse Galactic ISM from UV to mm wavelengths. Note the two absorption features at 9.7 and 18 μm and the "UV-bump" at 2175 Å, that will be attributed, respectively, to silicates, and small graphitic grains and large molecules (see Section 1.2.5). We see that the extinction is most important in the UV and optical wavelengths and drops at longer wavelengths.

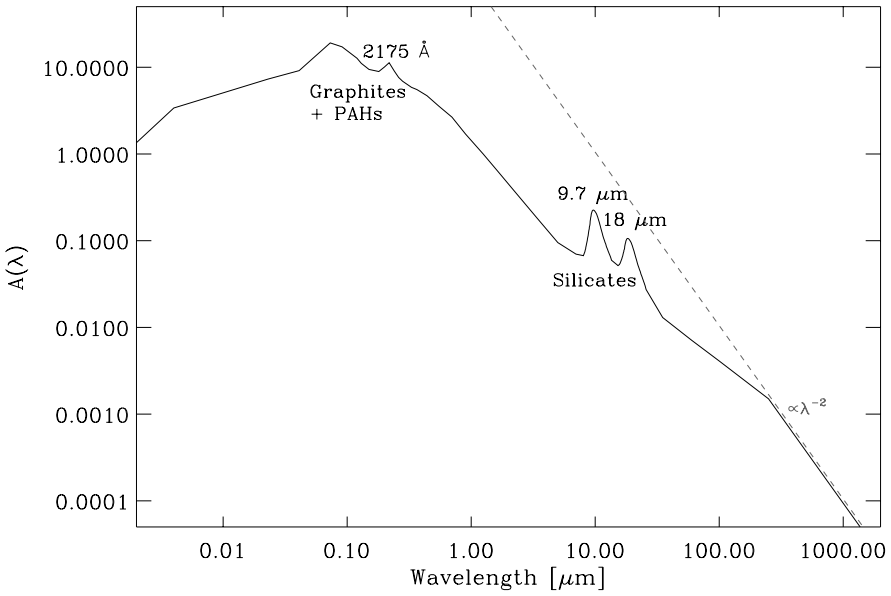

Fig. 1.4. Extinction curve for the diffuse Galactic ISM, from Mathis (1990) with the silicate features from Dudley & Wynn-Williams (1997). The λ^{-2} dependence in the IR is indicated with the grey dashed line (see Section 1.2.3).

By definition $A(\lambda)$ depends on where the observer is looking in the sky: the form of the extinction curve is dictated by the grain properties and this can differ depending on the local environment. Thus the extinction curve can vary across the Galaxy and from one galaxy to another (see Chapter 2).

Extinction determination

The most common way of estimating *A(λ)* is via the "pair-method". It consists in comparing the SEDs of two stars of the same spectral type and luminosity class, i.e., two stars with the same absolute magnitude, *Mag*. The "reference" star is assumed to be unaffected by extinction and the other star is located behind the absorbing material for which we want to know *A(λ)*. At a given wavelength their apparent magnitudes, *mag*, are given by:

$$\begin{cases} mag(\lambda) &= Mag(\lambda) + 5 \times log(d) + A(\lambda) \\ mag_{ref}(\lambda) &= Mag_{ref}(\lambda) + 5 \times log(d_{ref}) \end{cases} \tag{1.3}$$

where d and d_{ref} are the distances to the star and to the "reference" star respectively. Given that $Mag(\lambda) = Mag_{ref}(\lambda)$, we can access $A(\lambda)$ by comparing the apparent magnitudes at two different wavelengths, λ and λ_0. By taking the difference of the apparent magnitudes, we remove the unknown distance parameter:

$$A(\lambda) - A(\lambda_0) = [mag(\lambda) - mag_{ref}(\lambda)] - [mag(\lambda_0) - mag_{ref}(\lambda_0)] \tag{1.4}$$

or:

$$A(\lambda) - A(\lambda_0) = \Delta mag(\lambda) - \Delta mag(\lambda_0) \tag{1.5}$$

The colour excess between two wavelengths, $E(\lambda - \lambda_0)$, is defined by $\Delta mag(\lambda) - \Delta mag(\lambda_0)$ and usually the extinction is expressed in terms of $E(\lambda - V)$ and normalised by $E(B\text{-}V) = A_B - A_V$, where B and V refer to the optical bands at 440 and 560 nm. An important parameter can be extracted from the extinction curve in Fig. 1.4: $R_V = A_V \,/\, E(B\text{-}V)$. This parameter describes the ratio of the total-to-selective extinction and can be estimated from the IR slope of the extinction curve. In the diffuse Galactic ISM, the mean value of R_V is 3.05 ± 0.15 (Whittet 2003). The value of R_V depends on the nature and on the size distribution of the dust grains along the line-of-sight. For example, in denser regions, where bigger grains can be formed by coagulation, R_V is higher (~ 5).

1.2.3 Dust physics: absorption and scattering processes

As we saw in Section 1.2.1, dust extinguishes stellar light. The physical processes responsible for this extinction are absorption and scattering of the light by dust grains. These processes depend strongly on the intrinsic properties of the dust grains, as described in this Section.

Useful definitions and notations

Let us now consider a homogeneous cloud of spherical dust grains of radius a. The dust optical depth, $\tau(\lambda)$, through a dust cloud of size l, is related to the dust properties via:

$$\tau(\lambda) = n_d C_{ext}(a, \lambda) l \tag{1.6}$$

where n_d is the dust number density, C_{ext} is the dust extinction cross-section at wavelength λ for a grain radius a.

For a dust grain, C_{ext} is given by:

$$C_{ext}(a, \lambda) = Q_{ext}(a, \lambda) \times \pi a^2 \tag{1.7}$$

where πa^2 represents the geometric cross-section of the dust grain and Q_{ext} is the extinction efficiency. As extinction is due to absorption and scattering, C_{ext} can be decomposed into:

$$C_{ext} = C_{abs} + C_{sca} \tag{1.8}$$

with:

$$\begin{cases} C_{abs}(a,\lambda) &= Q_{abs}(a,\lambda) \times \pi a^2 \\ C_{sca}(a,\lambda) &= Q_{sca}(a,\lambda) \times \pi a^2 \end{cases} \tag{1.9}$$

where Q_{abs} and Q_{sca} are the absorption and scattering efficiencies respectively.

We can define the "absorption coefficient", $\alpha(\lambda)$, of the dust cloud by:

$$\alpha(\lambda) = n_d C_{abs}(a,\lambda) \tag{1.10}$$

Often, $\alpha(\lambda)$ is written as $\alpha(\lambda) = \rho_{ISM}\ \kappa_{abs}(\lambda)$, with ρ_{ISM} the cloud mass density and $\kappa_{abs}(\lambda)$ is called the "opacity" or "mass absorption coefficient". $\kappa_{abs}(\lambda)$ is given by:

$$\kappa_{abs}(\lambda) = \frac{n_d \pi a^2 Q_{abs}(a,\lambda)}{\rho_{ISM}} \tag{1.11}$$

We have:

$$\frac{n_d}{\rho_{ISM}} = \frac{N_g}{V_{ISM}} \frac{V_{ISM}}{M_g} = \frac{1}{m_g} \tag{1.12}$$

where N_g is the number of dust grains along the line-of-sight within the beam, M_g is the total mass of the grains, and m_g is the mass of a single dust grain: $m_g = \frac{4}{3}\pi a^3 \rho$, where ρ is the dust material mass density. Injecting Eq. 1.12 into Eq. 1.11 yields:

$$\kappa_{abs}(\lambda) = \frac{\pi a^2 Q_{abs}(a,\lambda)}{m_g} = \frac{3 Q_{abs}(a,\lambda)}{4 a \rho} \tag{1.13}$$

Accessing the dust properties: absorption and scattering efficiencies

The quantities Q_{abs} and Q_{sca} contain all of the dust grain information: its chemical components, its porosity and the spectral dependence of its dielectric properties. They represent an *intrinsic* property of the dust grain. These quantities can be measured in the laboratory or theoretically derived by solving Maxwell's equations of propagation of an electromagnetic wave through the dust grain with the appropriate boundary conditions. In this theoretical framework, the dust grain is made of a material with complex refractory index, m, related to the dielectric constant, e_{diel}, of the material via $e_{diel} = m^2$. The Mie theory provides numerical solutions for absorption and scattering in the case of a spherical and homogeneous dust grain. This theory has also been extended to more general cases of non-spherical dust grains. For example, realistic dielectric functions for graphite and silicates have been derived by Draine & Lee (1984) (see Section 1.2.5 for reasons to consider these specific materials in the interpretation of observations).

In the case of spherical dust grains, the absorption and scattering efficiencies can be expressed as series expansions of the "size parameter", $x = 2\pi a/\lambda$. We can distinguish two limiting regimes:

The grey extinction: x $\gg$ 1 i.e., the wavelength is very small compared to the grain size and the grain behaves as an opaque screen. We have:

$$\begin{cases} Q_{abs}(a,\lambda) &\sim 1 \\ Q_{sca}(a,\lambda) &\sim 1 \end{cases} \tag{1.14}$$

The Rayleigh limit: x $\ll$ 1 i.e., the grain size is very small compared to the wavelength, as it is the

case in the IR. In this domain, only the first term of the series dominates and we have:

$$Q_{abs}(a,\lambda) = 4x\ Im\left[\frac{m^2-1}{m^2+2}\right] \tag{1.15}$$

where Im denotes the imaginary part of the bracketed expression, and:

$$Q_{sca}(a,\lambda) = \frac{8}{3}x^4\left|\frac{m^2-1}{m^2+2}\right| \tag{1.16}$$

Often, Q_{abs} is approximated in the IR domain by a power-law with index β:

$$Q_{abs}(a,\lambda) = Q_0\left(\frac{\lambda_0}{\lambda}\right)^{\beta} \text{ for } \lambda > \lambda_0 \tag{1.17}$$

where β is called the "emissivity index", and Q_0 is such that $Q_{abs}(a,\lambda_0) = Q_0$. Typically, values of β between 1 and 2 are considered. Here we develop why that is.

Let us assume that we can model a dust grain by a system of harmonic oscillators, representing the plasma of free electrons tied to the lattice of the crystal, and that this dust grain is interacting with a plane electromagnetic wave with electric field $E = E_0 e^{i\omega t}$, where ω is the pulsation ($\omega = 2\pi\nu$). After solving the equations of motion for a harmonic oscillator we can derive a dispersion relation and obtain an expression of the dielectric function, e_{diel}, as a function of the pulsation, ω:

$$e_{diel} = 1 + \frac{\omega_p^2(\omega_0^2-\omega^2)}{(\omega_0^2-\omega^2)^2+\gamma_0^2\omega^2} + i\frac{\omega\omega_p^2\gamma_0}{(\omega_0^2-\omega^2)^2+\gamma_0^2\omega^2} \tag{1.18}$$

where ω_0 and γ_0 are the resonant frequency and the damping constant, respectively, of the oscillator; and ω_p is the plasma pulsation: $\omega_p = \sqrt{\frac{4\pi N e^2}{m_e}}$, where N is the number density of free electrons.

In the ISM, we can assume that the electromagnetic field interacting with the grain is slowly varying. In this approximation: $\omega \ll \omega_0$, and the expression for e_{diel} becomes:

$$e_{diel} = 1 + \frac{\omega_p^2}{\omega_0^2} + i\frac{\gamma_0\omega_p^2}{\omega_0^4}\omega \tag{1.19}$$

Using $e_{diel} = m^2$ and writing $e_{diel} = e_1 + \mathrm{i}\ e_2$, we can transform Eq. 1.15 in:

$$Q_{abs}(a,\lambda) = \frac{8\pi a}{\lambda}\frac{3e_2}{|e_{diel}+2|^2} \tag{1.20}$$

Injecting Eq. 1.19 in Eq 1.20 gives:

$$Q_{abs}(a,\lambda) = \frac{48\pi^2 ac}{\lambda^2}\frac{\gamma_0\omega_p^2}{\omega_0^4\left(3+\frac{\omega_p^2}{\omega_0^2}\right)^2} \tag{1.21}$$

Thus for an idealised dust grain made of harmonic oscillators, in the slowly varying field approximation and Rayleigh limit we have:

$$Q_{abs}(a,\lambda) \sim \lambda^{-2} \tag{1.22}$$

Thus for a crystalline grain we have $\beta = 2$. In a more general case, materials can show a range of β values depending on their temperature.

Following the same method for the scattering efficiency we also get:

$$Q_{sca}(a,\lambda) = \frac{8}{3}\left(\frac{2\pi a}{\lambda}\right)^4 \frac{\omega_p^2}{\omega_0^2\left(3+\frac{\omega_p^2}{\omega_0^2}\right)} \tag{1.23}$$

i.e.,

$$Q_{sca}(a,\lambda) \sim \lambda^{-4} \tag{1.24}$$

From Eqs. 1.22 and 1.24, we see that at IR wavelengths, absorption dominates over scattering.

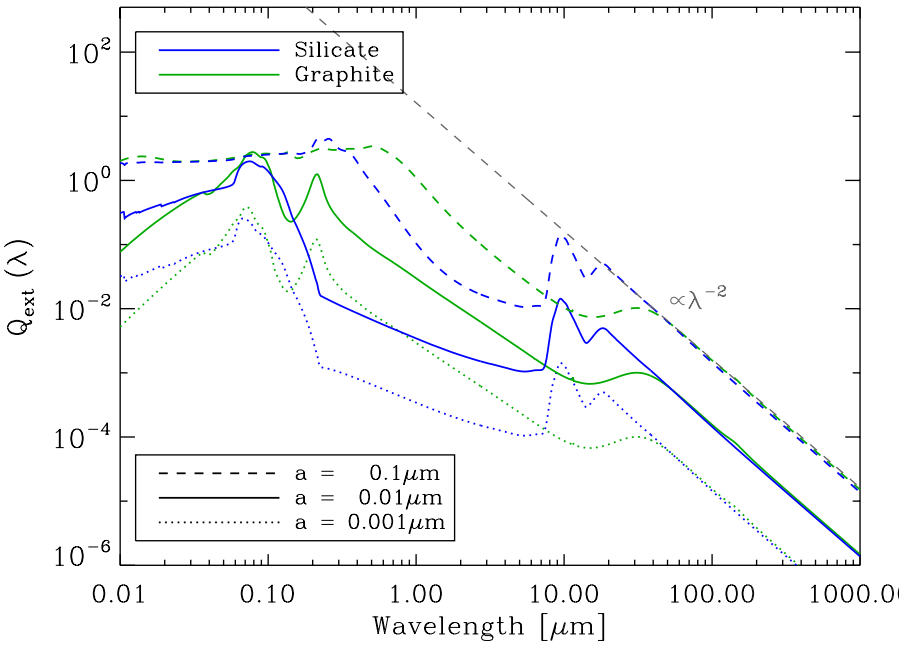

Fig. 1.5. Extinction efficiencies, $Q_{ext} = Q_{abs} + Q_{sca}$, from 0.01 to 1000 μm, for silicate grains (in blue, from Weingartner & Draine 2001) and graphite grains (in green, from Laor & Draine 1993) of different radiuses: $a = 0.001$ μm (dotted lines), 0.01 μm (plain lines) and 0.1 μm (dashed lines). The λ^{-2} dependence in the IR is indicated with the grey dashed line.

Figure 1.5 shows the extinction efficiency, Q_{ext}, for different grains of different sizes. We see that for big grains the extinction efficiency is constant at short wavelengths (UV - visible): we are in the "grey extinction" limit (Eq. 1.14). In the IR domain, the grain size is small compared to the wavelength and $Q_{ext} \sim Q_{abs} \sim \lambda^{-2}$ (Rayleigh limit, Eq. 1.15 and 1.22). As Q_{ext} is directly linked to A(λ) through Eqs. 1.2, 1.6, and 1.7, we find the same λ^{-2} dependency in the FIR for the extinction curve, as presented in Fig. 1.4. We also note that, for a given grain size, in the UV - visible the graphite extinction efficiency is greater than the silicate extinction efficiency. The opposite is true in the MIR. Both types are equivalent in the FIR. We clearly see here the influence of the nature of the grain on the observed dust properties.

1.2.4 Emission by dust grains

After absorbing stellar light, the dust grains re-emit the absorbed energy and this emission depends on the nature of the grains and on the strength and hardness of the incident radiation field.

The interstellar radiation field

The ISM of a galaxy bathes in the interstellar radiation field (ISRF) created by every source of radiation in the galaxy. Three sources of radiation can be identified:
Stars: They are the main source of radiation in the ISM, and play a prominent role in determining the thermal balance of the dust grains.
Gas and Dust: Gas and dust are not *a priori* radiation sources. They radiate away the energy absorbed from stars, in the IR range for the dust and over a large part of the electromagnetic spectrum for the gas.
Extragalactic component: It is mainly composed of the cosmic microwave background (CMB) radiation in the millimetre (mm) wavelength range. The CMB is a radiation of cosmological origin with the spectral shape of a $T_{CMB} = 2.73$ K blackbody (Mather et al. 1994). This is the only radiation, along with cosmic rays, that can penetrate into deeply embedded regions. This means that everywhere in the ISM, even in this deeply embedded regions, dust grains have a minimal temperature equal to T_{CMB}.

Technically all of the three sources of radiation contribute to dust heating. However, only the stellar component provides photons energetic enough to sensibly affect the internal energy of the grains and to induce a significant change in temperature (except in the deepest embedded regions where the CMB and cosmic rays also contribute to the dust heating). Thus we will only focus on the UV-to-NIR part of the ISRF.

In the solar neighbourhood, the ISRF has been empirically determined by Mathis et al. (1983), and is composed of: a UV component to model the young stars; three blackbodies with different temperatures $T_{\{1,2,3\}} = \{7500, 4000, 3000\}$ K, to model the main disk stellar populations and old stars; and the CMB radiation. A zoom on the UV-to-NIR part of the Mathis et al. (1983) ISRF is shown in Fig. 1.6.

Grains in thermal equilibrium

Inside the dust cloud, a dust grain large enough and bathing in a given interstellar radiation field acquires an equilibrium temperature, T_d. This temperature is determined by the condition that the dust grain absorbs the same amount of energy as it emits per unit time: i.e., the power absorbed is the same as the power emitted.

The power (or luminosity) absorbed by the dust cloud is given by:

$$\Gamma_{abs} = \int 4\pi\alpha(\lambda)J_\lambda(\lambda)\,\mathrm{d}\lambda = \int 4\pi \times n_d\pi a^2 Q_{abs}(a,\lambda)J_\lambda(\lambda)\,\mathrm{d}\lambda \tag{1.25}$$

where J_λ is the mean intensity of the interstellar radiation field, and $\alpha(\lambda)$ is the absorption coefficient from Eq. 1.10.

The power (or luminosity) emitted by the dust cloud is given by:

$$\Gamma_{em} = \int 4\pi j_\lambda(\lambda)\,\mathrm{d}\lambda \tag{1.26}$$

where j_λ is the emission coefficient, in units of W m^{-3} sr^{-1} μm^{-1}.

Kirchhoff's law for thermal emission tells us that $j_\lambda = \alpha(\lambda) \times B_\lambda(\lambda, T_d)$ where $B_\lambda(\lambda, T)$ is the Planck function. Injecting in Eq. 1.26, we have:

$$\Gamma_{em} = \int 4\pi \times n_d\pi a^2 Q_{abs}(a,\lambda)B_\lambda(\lambda,T_d)\,\mathrm{d}\lambda \tag{1.27}$$

At thermal equilibrium we have $\Gamma_{abs} = \Gamma_{em}$, leading to:

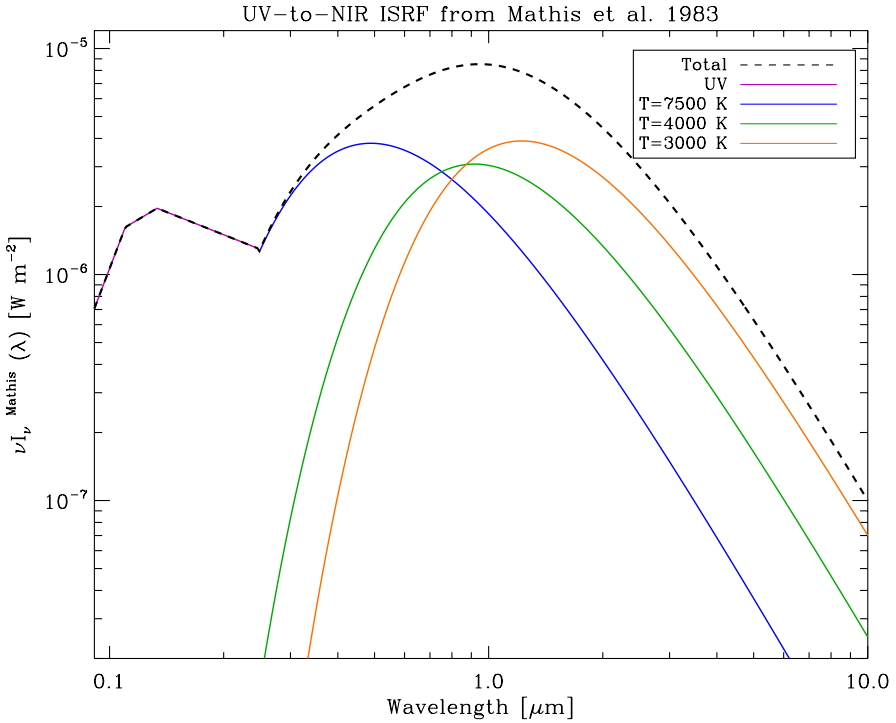

Fig. 1.6. Zoom on the UV-to-NIR part of the Mathis et al. (1983) ISRF. The UV component is shown in purple, and the three effective stellar sources in blue, green and orange. The total ISRF is shown with the black dashed line.

$$\int Q_{abs}(a,\lambda) J_\lambda(\lambda)\,\mathrm{d}\lambda = \int Q_{abs}(a,\lambda) B_\lambda(\lambda, T_d)\,\mathrm{d}\lambda \tag{1.28}$$

The dust equilibrium temperature T_d can be deduced from Eq. 1.28.

T_d and Stefan's law In the case of grains in thermal equilibrium, and assuming Eq. 1.17 for the absorption efficiency in the IR, Stefan's law tells us that the energy density[4] of the radiation emitted by the dust grains is $\propto {T_d}^{4+\beta}$. With β usually ranging from 1 to 2 for typical interstellar grains, we see that a relatively small increase of the dust grain temperature results in a large increase of the emitted power of the grain (up to orders of magnitude). In other words, hot grains emit *much* more than cold grains. Moreover, as the grains are in thermal equilibrium with the interstellar radiation field, we have:

$$u_{ISRF} \propto T_d^{4+\beta} \tag{1.29}$$

where u_{ISRF} is the energy density of the interstellar radiation field integrated over the wavelength. Thus knowing the strength of the interstellar radiation field, one can get a rough estimate of the dust grains temperature. Using the equilibrium temperature value from the diffuse Galactic ISM: $T_{d,\odot} = 17.5$ K (Boulanger et al. 1996), we estimate:

$$T_d = T_{d,\odot} \left(\frac{u_{ISRF}}{u_{ISRF,\odot}} \right)^{1/(4+\beta)} \tag{1.30}$$

[4]The energy density is related to the mean intensity of a given radiation by: $u_\lambda = \frac{4\pi}{c} \times J_\lambda$

where $u_{ISRF,\odot}$ is the energy density of the diffuse Galactic ISRF, given by Mathis et al. (1983).

T_d and Wien's law Another interesting property of the emission of dust grains in thermal equilibrium is that we can have a useful information on the shape of the SED, the position of the peak of emission (in a νL_ν representation), using Wien Displacement's law:

$$\lambda_{max} T_d \sim 3000 \ \mu\text{m K} \tag{1.31}$$

i.e., for hotter grains, the peak of the SED is moved to shorter wavelengths. For example, using the value of Boulanger et al. (1996), we can deduce that the peak of dust emission for the diffuse Galactic ISM is around 170 μm, in the FIR.

T_d and a The dust temperature T_d also depends on the grain size a. Intuitively we can understand that the larger the grains the colder they are. This also means that the bulk of the dust mass resides in cold grains. Using Eq. 1.31 we see that large, cold grains emit at longer wavelengths than small, hot grains.

We emphasize that these relations are only approximations that are only useful to get a *rough* idea of the dust emission properties. In the ISM, the dust grains are distributed in sizes and thus in temperatures.

Stochastic heating

When the grains are very small, their temperature fluctuates and we say that they undergo "stochastic heating". For small grains, the internal energy of the grain is comparable to the energy of a single incident photon and thus will be considerably affected by the absorption of a single photon, resulting in a sudden rise in temperature. The grain then cools down to its equilibrium temperature until it absorbs another photon, giving a "spiky" temperature profile (see Fig. 1.7). Inversely, for a big grain, the internal energy is large compared to the energy of an incident photon. Consequently its absorption does not affect the temperature of the grain: big grains are then in thermal equilibrium with a constant temperature profile. Fig. 1.7 illustrates this point for carbonaceous grains heated by the Galactic ISRF.

To compute the emission of a stochastically heated grain, we then need to know its thermal properties in addition to its optical properties, i.e., its specific heat. The specific heat of a dust grain brings information on how much energy is needed to raise the temperature of the dust grain by 1 K. This enables us to compute the temperature of the grain after absorption of a photon of energy $\epsilon_\gamma(a) = \text{h}\nu$ via:

$$\epsilon_\gamma(a) = \frac{4}{3}\pi a^3 \int_{T_i}^{T_f} C(T)\,\text{d}T \tag{1.32}$$

where $C(T)$ is the specific heat per unit volume of the grain, T_i and T_f are the grain temperatures before and after the absorption of a photon of energy $\epsilon_\gamma(a)$.

Let us now define $P(a,T)dT$ the probability that a grain of radius a has a temperature between $[T, T+dT]$, with $P(a,T)$ the temperature probability distribution, verifying:

$$\int_0^\infty P(a,T)\,\text{d}T = 1 \tag{1.33}$$

We assume that radiation from a stochastically heated grain obeys Kirchhoff's law at any time, and the emission coefficient now can be expressed as:

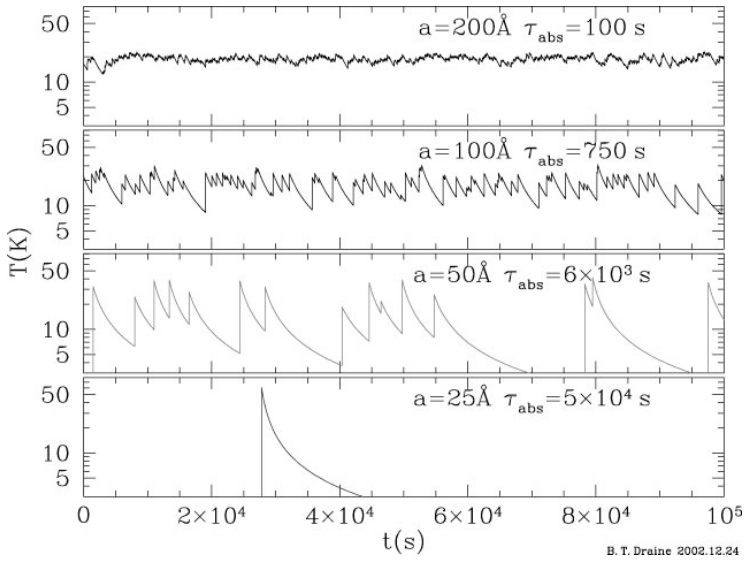

Fig. 1.7. Illustration of stochastic heating of small grains: carbonaceous grains heated by the Galactic ISRF (figure from Draine 2003). a is the radius of the grain and τ_{abs} the mean time between photon absorptions. The plotted time range corresponds approximately to a day.

$$j_\lambda(a,\lambda) = \alpha(a,\lambda) \times \int_0^\infty B_\lambda(\lambda,T)P(a,T)\,\mathrm{d}T \tag{1.34}$$

For a big grain, the temperature only oscillates a little around the equilibrium temperature T_d and *P(a,T)* can be approximated by a δ-function δ(T-T$_d$): we arrive back at Kirchhoff's law which we used for big grains in thermal equilibrium: $j_\lambda = \alpha(\lambda) \times B_\lambda(\lambda, T_d)$.

We refer to Guhathakurta & Draine (1989) for details on the calculation of the temperature probability distribution.

Grain size distribution

So far we have considered the case of a cloud of dust grains, all with the same radius a, absorbing stellar radiation over a large range of wavelengths. In the ISM dust grains exist in a distribution of sizes so let us now consider a dust specie spanning a range in sizes between a_{min} and a_{max}, the minimum and maximum grain sizes. We define *n(a)da* the number density of grains with sizes between [*a*,*a*+*da*], and *n(a)* is the size distribution of the dust specie. The dust column density, N_d, is the number of grains over a given line of sight of length l and is given by:

$$N_d = l\int_{a_{min}}^{a_{max}} n(a)\,\mathrm{d}a \tag{1.35}$$

Following Eq. 1.6, the optical depth, $\tau(\lambda)$, for this dust specie is given by:

$$\tau(\lambda) = l\int_{a_{min}}^{a_{max}} C_{ext}(a,\lambda)n(a)\,\mathrm{d}a \tag{1.36}$$

Following Eqs 1.26 and 1.34, the IR luminosity, L_λ, emitted by this dust specie is given by:

$$L_\lambda(\lambda) = l\int_{a_{min}}^{a_{max}} 4\pi^2 a^2 Q_{abs}(a,\lambda)\left(\int_0^\infty B_\lambda(\lambda,T)P(a,T)\,\mathrm{d}T\right)n(a)\,\mathrm{d}a \tag{1.37}$$

We now have all the necessary tools to interpret the observations and access the nature of the dust grains present in the ISM.

1.2.5 The nature of dust grains unveiled

Now that we know how the physical processes responsible for dust extinction and emission depend on the nature of the dust grain, we can access the chemical composition and size distribution of the dust in the ISM from a well-chosen set of observational constraints.

Chemical composition

Dust grains are built from the available elements in the ISM, and those are then depleted from the gas phase. The difference between what is expected to be ejected from stars, i.e., the total element abundances, and what is actually observed in the ISM in the gas phase, is called the elemental depletions. Elemental depletion measurements can be used to estimate which metals, i.e., elements heavier than Helium, are locked up into dust and to what fraction. Figure 1.8 shows the elemental depletions for several elements as a function of their condensation temperature, i.e., the ease at which a given element is incorporated into dust. The C, O, Si, Mg and Fe elements, are among the main constituents of dust grains and are indeed depleted from the gas phase.

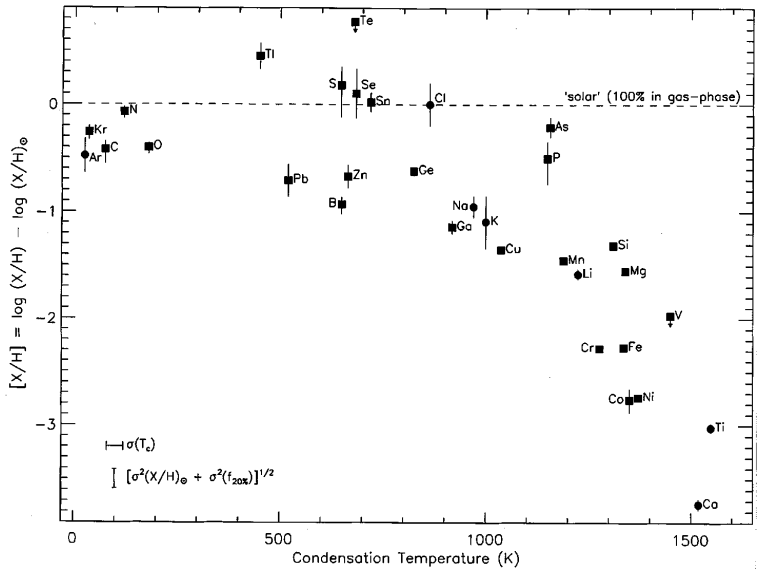

Fig. 1.8. Interstellar elemental depletions for a variety of metals as a function of the condensation temperature (from Savage & Sembach 1996).

As stated throughout this Section, observations of the ISM (such as UV extinction, IR emission, elemental depletion, etc.) provided several clues to determine what kind of grains are present in the ISM. Several types of dust grains have been identified: silicate grains, carbon grains and polycyclic aromatic hydrocarbons (PAHs). Of course, the composition of interstellar dust has been widely debated but these three families are considered to be the most important dust components.

Silicates: The broad band absorption features at 9.7 and 18 μm observed in the interstellar extinction curve (Fig. 1.4) have been attributed to silicate-based material. They are made from SiO blocks and present a wide variety of composition: $MgSiO_3$, $(Mg,Fe)SiO_4$, Mg_2SiO_4, $(Mg,Fe)_2SiO_4$, etc. The absence of a sub-feature in the 9.7 μm, contrary to what laboratory measurements of

absorption profiles show for crystalline silicates, may be the sign that these grains are mostly amorphous in the ISM (except in circumstellar environments) (Kemper et al. 2004). The features at 9.7 and 18 μm are usually attributed to the Si-O stretching and O-Si-O bending modes respectively.

Carbons: Small graphitic grains are required to explain the 2175 Å feature of the observed interstellar extinction curve. Indeed graphite has a strong resonance at $\sim$ 2000 Å due to $\pi \rightarrow \pi^{\star}$ transition associated with its aromatic bond. The position and profile of this band is determined by several parameters such as grain size, grain shape and grain optical properties. Graphite can evolve into amorphous carbon grains if the physical conditions of their environment are suitable.

Polycyclic Aromatic Hydrocarbons (PAHs): Observations in the 1970s and 1980s have shown that the MIR spectra of bright sources with associated dust and gas are dominated by broad emission features, that could not be explained by the silicate or carbon grains. Spectroscopic studies with *ISO* have revealed that these broad emission features were dominating the NIR spectrum of a wide variety of objects: from planetary nebulae to (nearby) galaxies (with the exception of asymptotic giant branch stars and deeply embedded young stellar objects). These broad emission features are observed primarily at 3.3, 6.2, 7.7, 8.6 and 11.3 μm as well as other wavelengths, and were long called the "unidentified infrared bands" (UIB).

Duley & Williams (1981) showed that the 3.3 and 11.3 μm features could correspond to vibrational modes of C-H groups in aromatic materials. A few years later, Leger & Puget (1984) proposed large planar molecules made of aromatic cycles to explain these NIR broad emission features.

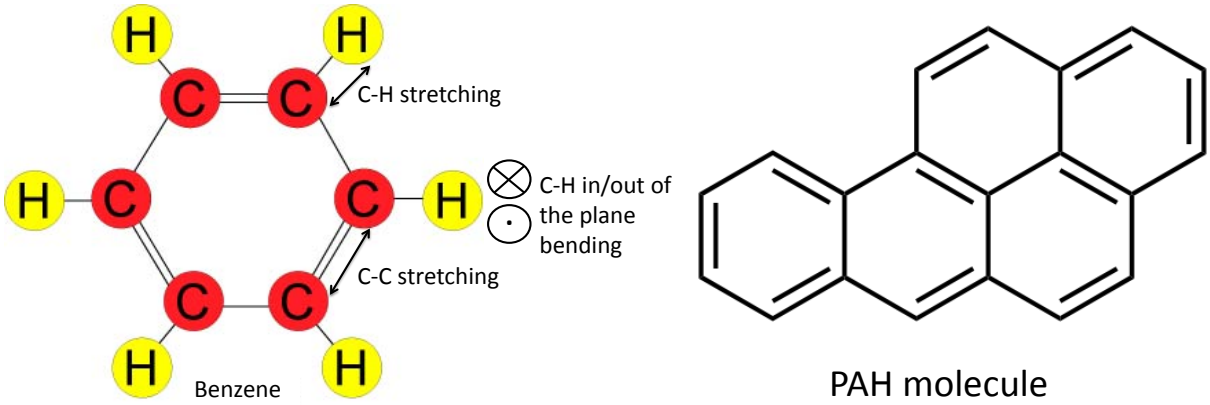

Fig. 1.9. *(left)* Structure of a benzene molecule with the principal vibration modes indicated. *(right)* Example of a PAH molecule, here benzo(a)pyrene $C_{20}H_{12}$.

An example of a PAH molecule is shown in Fig. 1.9, together with the typical vibration modes of benzene: C-H and C-C stretching modes, C-H in/out of the plane bending modes. PAHs typically possess between 50 and 1000 atoms. The main vibration modes give rise to the NIR emission features. Figure 1.10 shows an example of a PAH spectrum in the Orion Bar and we can identify the different bands: the 3.3 μm feature from C-H stretching mode, the 6.2 μm feature from C-C stretching mode, the 7.7 μm feature which is a combination of C-C stretching and C-H in-the-plane bending modes, the 8.6 μm feature from C-H in-the-plane bending mode and the 11.3 μm feature from C-H out-of-the-plane bending mode. The central wavelength of the observed features can vary depending on the structure of the molecules, and the relative intensity of the bands depends on the ionisation degree of the PAHs in the ISM.

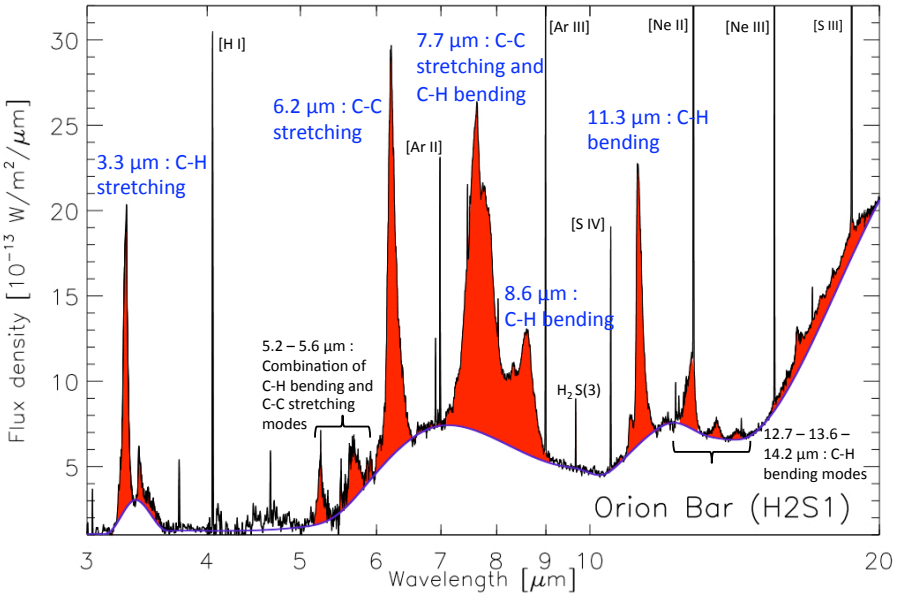

Fig. 1.10. Example of a PAH spectrum from the Orion Bar (from Peeters et al. 2002). The main PAH features are indicated in red along with the vibration mode they originate from. Several ionic fine-structure lines have been identified too.

Size distribution

Since dust is responsible for extinction from UV to visible wavelengths, and the extinction cross-section depends on the grain radius a, dust grains must span a range of sizes. Mathis et al. (1977) was the first to propose a size distribution for spherical silicate and carbon grains (hereafter called "MRN" model) that was able to reproduce the interstellar extinction curve in the Galaxy between 0.11 and 1 μm. This size distribution was a simple power-law distribution for grain sizes between 5 and 250 nm:

$$n(a) \propto a^{-3.5} \tag{1.38}$$

where $n(a)$ is the size distribution and $n(a)da$ is the number of particles with radius between [a, a+da]. The MRN model did not include PAHs and indeed, *IRAS* observations at 12 and 25 μm revealed that the MRN model could not reproduce the observations of the IR emission from the diffuse Galactic medium. The first model that was able to reproduce both the extinction and emission of the diffuse Galactic ISM was the Desert et al. (1990) model that took into account PAHs, with sizes between 0.4 and 0.12 nm, on top of the silicate and carbon grain populations. To explain the observations, the Desert et al. (1990) model requires dust grains spanning a wide range in grain sizes ($\sim$ 3 orders of magnitude) from sub-nanometre grains to grains of a fraction of a micron. The PAHs are the smallest grains, with sub-nanometre to nanometre sizes. These grains are transiently heated by the absorption of a single photon (see Section 1.2.4) and cool down by emitting MIR photons in vibrational modes representative of their aromatic structure, producing the broad emission features described previously. Another component, very small grains (VSG), is also required to explain the continuum emission in the MIR in the Desert et al. (1990) model. These nanometre grains also undergo significant temperature fluctuations in the ISM. They can be made from either carbonaceous or silicate material. The third component of the dust model is the big grain (BG) component, with sizes $\geq$ 10 nm to $\sim$ 400 nm, necessary to account for the FIR emission. The BG component usually dominates the total dust mass, and is mostly composed of

silicate grains. Depending on their sizes, these bigger grains can be either in thermal equilibrium with the stellar radiation field or stochastically heated by the ISRF.

The grain size distribution we will consider for our study is that presented by Zubko et al. (2004), who simultaneously fit the extinction, emission and also elemental abundances of the diffuse Galactic ISM. The difference with the Desert et al. (1990) model is that Zubko et al. (2004) use both PAHs and graphite grains, and not only graphite, to explain the 2175 Å feature and the FUV continuum of the interstellar extinction curve. We refer to Chapter 7 for a complete description of this grain size distribution and its determination.

1.2.6 Life and death of a dust grain in the ISM

As we mentioned in Section 1.2.1, dust is formed from the metals produced by the stars. The main stardust factories are circumstellar shells around evolved stars that provide the necessary high densities and temperatures to produce the dust grains. Two main categories in these dust sources can be distinguished: low-mass stars that undergo quiescent mass-loss and return dust to the ISM via stellar winds; and high-mass stars with violent death that return their ejecta to the ISM via supernova explosions:

- *Mass-loss through stellar winds:* These stellar sources can be low-mass stars ($M \lesssim 8\ M_{\odot}$) in the red giant phase of their evolution (e.g., M giants, carbon stars, radio luminous OH/IR stars), but dust also forms in the circumstellar shells around supergiants, planetary nebulae and Wolf-Rayet stars. Those sources are either C-rich or O-rich. Depending on their C/O abundance ratio, the type of dust produced will differ. For C-rich stars (C/O >1), all of the oxygen is tied up in CO, and no oxygen is available for the dust. Thus the dust grains are carbon rich (C and SiC types). For O-rich stars (C/O<1), the remaining oxygen can combine with other elements, and especially Si to form silicate type material (based on the SiO block). Dust grains are supposed to survive the injection phase in the ISM.

- *Explosive mass-loss:* ($M \geq 8\ M_{\odot}$) Novae, Type Ia and Type II supernovae (SN) are sites of dust production, Type II SN being the most important one. However, most of the dust grains are thought to be immediately destroyed by SN shocks when injected into the ISM.

The main dust production sites are summarised in Table 1.2.

Table 1.2. Summary of the dust production sites and their contribution in the ISM, for the Galaxy (adapted from Jones et al. 1997).

Source	Type of dust	Contribution [$10^{-6}\ M_{\odot}\mathrm{kpc}^{-2}\ \mathrm{yr}^{-1}$]
M giants	Silicate	3
Radio Loud OH/IR stars	Silicate	2
Carbon stars	SiC - Carbon - PAHs	2
Supergiants	Silicate	0.2
Planetary Nebulae	Carbon - PAHs	0.03
Wolf Rayet stars	Carbon - PAHs	0.03
Type II SN	Silicate - Carbon	0.15 - 14
Type Ia SN	Silicate - Carbon	0.03 - 2.3
Novae	Silicate - SiC - Carbon - PAHs	0.003 - 0.2

After formation, dust is submitted to various evolution processes either constructive (i.e., accretion - coagulation) or destructive processes (such as sputtering, erosion, vaporisation and shattering). These evolution processes result from supernovae shocks that can induce grain-grain collisions or impacts with atoms from the hot gas. This various processes can thus affect the grain size distribution.

Collisions with atoms from the hot gas provoke thermal and chemical sputtering and erosion of the dust grain, transferring grain material back to the gas phase.

Grain-grain collisions have different consequences depending on the velocity of the shock. For high-velocity shocks ($v \geq 20$ km.s^{-1}, Tielens et al. 1994), the grains are vaporised and grain material is returned to the gas phase. The destruction of dust grains by SN shocks is the dominant process of recycling dust into gas in the ISM. Intermediate velocity shocks ($v \sim 2$ km.s^{-1}, Jones et al. 1996) lead to shattering of the dust grains and transfer mass from big grains to small grains. At low velocities, ($v \lesssim 0.1$ - 1 km.s^{-1}, Jones 2004) grain-grain collisions lead to grain sticking and coagulation. This impacts the grain size distribution in the opposite way, by increasing the mean grain size. Coagulation mainly occurs in dense regions such as molecular clouds and circumstellar shells.

The typical timescale for dust formation is $\sim 3 \times 10^9$ yr (Jones & Tielens 1994) whereas the typical timescale for dust destruction is $\sim 5 \times 10^8$ yr (Jones et al. 1996). Because we still observe dust in the ISM, we need re-accretion processes in the ISM to maintain equilibrium between formation and destruction of the dust grains. Dwek (1998) included re-accretion in the ISM in their model for dust evolution in the Galaxy and indeed found that dust formation and re-accretion can be in equilibrium. How dust is preserved for re-accretion is still a debated question.

1.2.7 Dust: a fundamental component of the ISM

Even though dust represents only $\sim 1\%$ in mass in the ISM, it plays a major role in the total emission of a galaxy: in our Galaxy, dust reprocesses about 30% of the stellar power, and it can be as high as $\sim 99\%$ in a starburst galaxy (i.e., a galaxy undergoing a burst of star formation). Through the absorption of stellar light, dust is the main source of opacity in the ISM for non-ionising photons.

Dust also impacts the chemical evolution of the ISM by locking up a significant fraction of the heavy elements available in the ISM.

Figure 1.11 illustrates the role of interstellar dust in the lifecycle of the ISM. Stars are born in molecular clouds, form elements in their cores, and re-inject them into the ISM as they evolve and die. Low-mass stars inject elements into the ISM through stellar winds and massive stars through stellar winds and supernovae explosions (Section 1.2.6). Dust grains form from the available elements in the ISM and thus regulate the abundance of elements in the different ISM phases: metals are depleted from the gas phase, when used to form a dust grain. As we saw in Section 1.2.6, through constructive processes (accretion or coagulation) more metals will be locked up in the solid phase of the ISM, while through destructive processes (erosion and sputtering), metals are released once again into the gas phase and are available for the next generation of stars.

As we will see in Section 1.3, dust grains participate actively in the heating and cooling of the ISM: they cool the ISM by absorbing stellar photons and heat the ISM by re-emitting the absorbed power. The main heating process in the neutral ISM is indeed the photoelectric effect on dust grains. FUV photons are absorbed by the dust grain and this generates a diffusion of electrons in the grain. These electrons loose energy through collisions while they diffuse in the grain and eventually escape into the gas phase, thus heating it. The major actors of the photoelectric effect are the smallest grains or very large molecules (PAHs).

Dust also has a double effect on star formation. Indeed to form stars we need cold molecular clouds and thus enough shielding from interstellar radiation to be able to form the molecules and cool the gas. Dust absorbs the stellar radiation that would otherwise dissociate the H_2 molecules, and

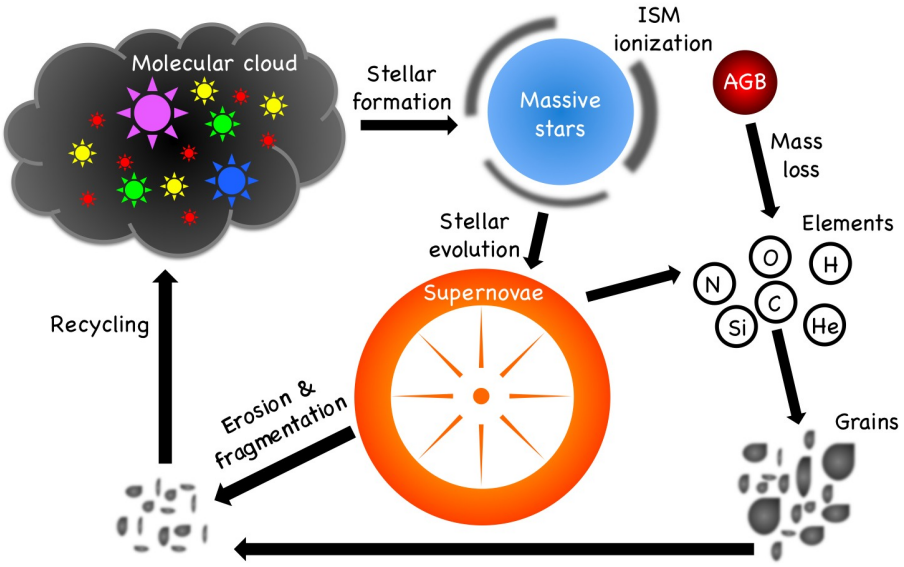

Fig. 1.11. Schematic view of the processes of matter recycling in the ISM. Credits: F. Galliano.

thus participates actively in the cooling of the ISM. It is also a catalyser of H_2 molecule formation by providing a surface where two H atoms can accrete, meet and react. Indeed the presence of dust grains can increase the H_2 formation rate by about two orders of magnitudes compared to H_2 formation without dust (Tielens 2005), thus activating star formation. Hence dust is an important agent of galaxy evolution.

1.3 Gas phases of the ISM

The gas is the other major component of the ISM and is the main fuel for star formation. It represents 99% of the ISM mass, the majority of which is in the form of hydrogen gas ($\sim$ 71.5%). The rest of the gas reservoir consists of Helium ($\sim$ 27%) and gaseous metals ($\sim$ 1.5%) (values from Asplund et al. 2009). It is convenient to describe the different gas phases of the ISM by the physical state of hydrogen: ionised in the form of H^+, neutral in the form of H atoms, molecular in the form of H_2. For the different phases, we follow the description of Tielens (2005).

1.3.1 Ionised phase

The ionised phase in the ISM is composed of three different regions: the Hot Ionised Medium (HIM), HII regions and the Warm Ionised Medium (WIM).

The Hot Ionised Medium - hot and diffuse

Typical temperature $\sim 10^5$ - 10^6 *K - Typical density* $\sim 3 \times 10^{-3}$ cm^{-3}

The HIM consists of very hot coronal gas originating from SN ejected material. It is a very hot but diffuse component of the ionised gas phase of the ISM. This gas is heated and ionised by shock waves generated from supernovae explosions and stellar winds of dying stars. It cools down via thermal X-ray continuum emission and line emission from highly ionised species, such as CIV, SIV, NV, OVI or even OVII and OVIII. In such hot plasmas, several radiation processes can occur: Bremsstrahlung continuum emission (also called "free-free", transition of a free electron between two states), discrete line emission (transition between two levels of the ion), radiative recombination

continuum emission (capture of an electron into a bound state), dielectronic recombination line emission (capture of a free electron into a doubly excited ion state) or two-photon continuum emission (simultaneous emission of two photons) (see Ehle 2005 for a review).

Fig. 1.12. *(left)* Example of HIM: Supernovae remnants Simeis 147 in the Taurus constellation. The image is a colour composite of 66 colour band images from the Palomar Observatory. *(right)* Example of an HII region: the Orion Nebula M42 in the Orion constellation. The image is a colour composite of hydrogen, oxygen and sulfur gas emission (source: APOD).

HII regions - hot and dense

Typical temperature $\sim$ 10^4 *K - Typical density* $\sim$ *1 -* 10^5 cm^{-3}

HII regions are regions around massive O and B stars or OB associations and are thus directly linked to star formation. These stars ionise their immediate surrounding medium creating an ionisation front in the ISM which delineates the HII region. They span a wide range of densities: from 1 cm^{-3} for the most diffuse nebulae to 10^3 - 10^4 cm^{-3} for compact HII regions and up to 10^5 cm^{-3} for the densest regions. Their temperature is directly linked to the gas density but also to the amount of metals in the region, and they are thus extensively used to determine the quantity of metals in the ISM of a galaxy (see Section 2.1, Pilyugin & Thuan 2005; Izotov et al. 2006). The main heating sources of these regions are photoionising photons (i.e., photons with $h\nu \geq 13.6$ eV) from the OB stars, and dust grains through photoelectric heating. HII regions cool down over the whole electromagnetic spectrum from UV to radio wavelengths. They are strong sources of thermal radio emission (free-free emission), Hα recombination line emission in the visible or forbidden fine-structure line emission in the FIR (such as OIII). The dust present in these regions also absorbs and scatters stellar light (reflection nebulae) and sometimes can completely obscure the HII region at visible wavelengths. This absorption results in bright MIR continuum emission observed in these regions arising from the heated dust grains.

Figure 1.12 shows an example of the hot ionised phase as viewed from optical emission lines.

The Warm Ionised Medium - warm and diffuse

Typical temperature $\sim$ *8000 K - Typical density* $\sim$ *0.1* cm^{-3}

The WIM represents 90% of the ionised gas phase and is a wide-spread, diffuse medium across galaxies. It is heated by ionising photons that escape HII regions and/or by UV radiation from isolated hot stars. The cooling processes are the same as in an HII region but the dominant emission

used to probe the WIM is free-free radio emission or Hα recombination line emission. The spectra of diffuse HII regions differ from those of dense HII regions by showing strong emission from low stages of ionisation (NII, SII) and weak emission from higher stages of ionisation (OIII). In a dense HII region, on the other hand, we would rather see the opposite.

1.3.2 Atomic phase

The atomic phase is defined as the phase of the ISM where photons have energies lower than 13.6 eV (i.e., non-ionising photons) and where molecules do not exist. In this phase we thus find neutral atomic species (HI, CI, OI) as well as ionised species with ionisation potentials lower than that of hydrogen (i.e., CII, SII, SiII). It is composed of the Warm Neutral Medium (WNM) and the Cold Neutral Medium (CNM): the atomic phase can be seen as an ensemble of cold and dense clouds (CNM) bathing in a more diffuse and warmer intercloud phase (WNM).
WNM: Typical temperature $\sim$ 8000 K - Typical density $\sim$ 0.5 cm^{-3}
CNM: Typical temperature $\sim$ 80 K - Typical density $\sim$ 50 cm^{-3}

The neutral gas is usually mapped through the HI line at 21 cm, arising from the transition between two hyperfine structure levels of the ground state of atomic hydrogen.

The major sources of heating for the WNM are photoelectric heating by dust grains, FUV pumping of H_2 (see below), cosmic rays and X-rays. The WNM mainly cools through the optical Hα recombination line.

Photodissociation Regions (PDRs)

We can define a transition phase that separates the ionised medium from the molecular cloud cores, the photodissociation regions (PDRs), where FUV photons with 6 eV $<$ hν $<$ 13.6 eV control the physics and chemistry of the gas. PDRs contain part of the atomic (the dense and cold neutral medium) and part of the molecular phases of the gaseous ISM, and are directly associated with star formation (to be distinguished from diffuse neutral gas). Dust is associated with these regions and plays an important role in heating up the gas and absorbing the incoming stellar radiation.

Fig. 1.13 shows a schematic representation of a PDR. FUV photons penetrate the cloud and ionise the gas creating an ionisation front at the outer edge of the PDR. Then photons with energies $<$ 13.6 eV penetrate deeper into the cloud ionising other species such as carbon and oxygen, and photodissociating the molecules. This creates an HI/CII region. Once the flux of dissociating H_2 photons is sufficiently attenuated (usually around $A_V \sim 2$ mag), H_2 molecules form in a layer of H_2/CII. Beyond this layer ($A_V \sim 4$ mag), carbon-ionising photons are also attenuated and there is a quick transition from CII to CI and then to CO. The transition from atomic to molecular oxygen marks the inner edge of the PDR: where the molecular core is shielded from photodissociating photons.

Two major processes dominate the heating of the gas in PDRs: photoelectric heating by the dust grains and FUV pumping of H_2. As explained in Section 1.2.7, for the photoelectric effect, an electron is ejected from the dust grain and then heats the gas through collisions. This process is less efficient in PDRs than in HII regions, as the incoming photons are less energetic. The photoelectric heating efficiency also depends on the grain size and charge. The major actors of photoelectric heating are thus the smallest grains of the ISM, which are often the most numerous, and provide the largest cumulative surface: PAHs and small graphitic grains, emitting in the MIR range. The charge of the dust grain is controlled by the balance between photoionisation and recombination with an electron. This depends on the intensity of the incident radiation field, the temperature of the gas and the density of electrons (through the ionisation parameter $\gamma = G_0 T_e^{0.5}/n_e$ where G_0 is the intensity of the radiation field expressed in Habing units[5], and n_e is the electron density in the

[5] 1 Habing = 1.6×10^{-3} erg cm^{-2} s^{-1}

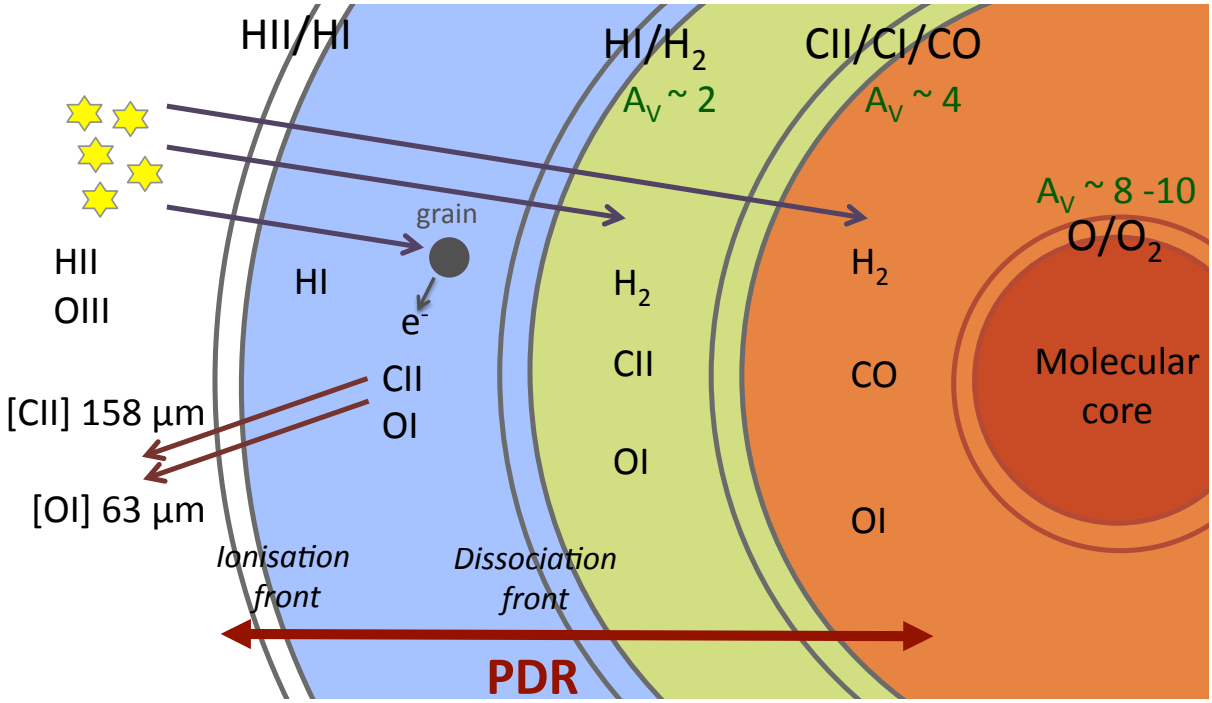

Fig. 1.13. Schematic view of a PDR.

PDR, usually $\sim 10^{-4}$ cm^{-3}).

FUV photopumping of H_2 occurs through photons with energies > 11.2 and 12.3 eV (Lyman-Werner electronic transitions). Absorption of these FUV photons brings the H_2 molecule to a bound excited electronic state. The molecule then cascades back to ground vibrational states releasing energy into the gas. In 10 to 15 % of the cases it also leads to H_2 dissociation. Other heating sources in PDRs are ionisation of carbon (releasing an electron into the gas), formation of H_2 and H_2 photodissociation. In denser regions, the contribution of grain-grain collisions to the heating of the gas may become important.

Cooling of the PDR occurs mostly through FIR fine structure line emission of abundant ionic and atomic species i.e., [CII] λ158 μm or [OI] λ63, 146 μm. PDRs are thus bright in the IR: MIR-FIR continuum emission, MIR PAH emission features and FIR fine structure line emission. PDRs are also sources of rotational lines from molecular species, mostly CO, but also CO^+, CN, C_2, and rotational-vibrational transitions of warm H_2.

1.3.3 Molecular phase

Typical temperature $\sim$ *10 K - Typical density* $\geq$ *200 cm*$^{-3}$

The molecular phase is the densest and coldest phase of the gaseous ISM and is defined by every locations where there is molecular hydrogen, which is the most important and abundant molecule in the ISM. Other molecules can also be found deeper into the molecular cloud such as CO, CS, HCN, O_2, CH+, OH, H_2O, etc, if there is enough shielding from stellar radiation. Molecules can survive in these dense clouds because radiation is weakly penetrating the molecular cores. Today, about 200 molecules have been identified in the ISM (Tielens 2005). The molecular phase is in the form of discrete clumps of sizes of the order of tens of parsecs and masses of 10^3 - 10^6 $M_\odot$, that are gravitationally-bound rather than in pressure equilibrium with the other phases. They are considered to be the stellar nurseries where stars form by fragmentation processes and gravitational

collapse of the clouds. Figure 1.14 shows a well-known example of a molecular cloud: the Horsehead nebula, from the Orion giant molecular cloud.

Fig. 1.14. Example of a molecular cloud: the famous HorseHead Nebula illuminated from behind by IC434 (source APOD).

H_2 molecules, as well as other molecules, are most easily formed on the surface of dust grains at cold temperatures. They can be destroyed by UV photons but are efficient at self-shielding. Molecular gas is mainly heated by cosmic rays that are able to penetrate the clouds. Molecules are excited by collisions or shocks. Molecular clouds mainly cool through vibrational and rotational molecular transitions, CO being the dominant coolant. Dust is cold in molecular clouds and mostly emits in the FIR-to-submm wavelengths.

H_2 is a symmetric molecule and does not have dipolar momentum, rendering it very difficult to observe directly through its rotational lines. Some electronic transitions can be observed along the line of sight towards hot stars. NIR rotational vibrational transitions of H_2 are indicative of warm ($\sim$ 1000 K) and dense ($\sim 10^4$ cm^{-3}) gas in shocks. This warm H_2 represents a small mass fraction of the total molecular gas mass. Cold H_2 gas is indirectly observed, through CO rotational transitions in the submm: CO(1-0) at 2.6 mm, CO(2-1) at 1.3 mm, CO(3-2) at 870 μm, etc., as CO is the most abundant molecule after H_2.

Converting the observed CO intensity into a molecular gas mass is usually done via a conversion factor, X_{CO}, defined by:

$$X_{CO} = N(H_2)/I_{CO} \tag{1.39}$$

where $N(H_2)$ is the column density of H_2 we want to determine, and I_{CO} is the CO intensity measured from one given transition. X_{CO} was first determined from CO(1-0) observations in the Galaxy, calibrated from cold clouds assumed to be virialised. The Galactic conversion factor, $X_{CO,MW}$, has been estimated to be 2.0 $\times$ 10^{20} cm^{-2} (K km s^{-1})$^{-1}$ (Ackermann et al. 2011). Sometimes the conversion factor is written in terms of mass surface density: α_{CO}, with:

$$\alpha_{CO} = M(H_2)/L_{CO} \tag{1.40}$$

where L_{CO} is the CO luminosity and $M(H_2)$ is the molecular gas mass. α_{CO} is related to X_{CO} via:

$$\alpha_{CO} = X_{CO} \times m_{H_2} \times \frac{\Omega}{4\pi D^2} \tag{1.41}$$

where m_{H_2} is the mass of one H_2 molecule in $M_\odot$, Ω is the source solid angle and D is the distance to the source. α_{CO} is expressed in units of $M_\odot$(K km s^{-1} pc^2)$^{-1}$, and the Galatic value is 3.8 $M_\odot$(K km s^{-1} pc^2)$^{-1}$.

This conversion between CO intensity and molecular gas mass is still under investigation as X_{CO} strongly depends on various parameters such as the radiation field intensity, metallicity, gas density and velocities, etc. (Shetty et al. 2011; Feldmann et al. 2012). The impact of metallicity on the X_{CO} conversion factor is discussed in Chapter 2. For a review on X_{CO}, see Bolatto et al. (2013).

Table 1.3 summarises the main characteristics of the various gas phases in the Galaxy.

Table 1.3. Characteristics of the phases of the ISM in the Galaxy (adapted from Tielens 2005). For each phase, a typical temperature and density are given, along with its total mass in the Galaxy and the local surface density in the solar neighbourhood. Means of detection of each phase are given in the last column.

Phase	T^a [K]	n^b [cm^{-3}]	M^c [10^9 $M_\odot$]	Σ^d [$M_\odot$pc^{-2}]	Observation
Hot Ionised Medium	10^5 - 10^6	0.003	-	0.3	Thermal X-ray emission Ionised metals absorption/emission lines Thermal radio emission
HII regions	10^4	1 - 10^5	0.05	0.05	Thermal radio emission Hα recombination line FIR fine-structure lines Bright MIR continuum emission from dust
Warm Ionised Medium	8000	0.1	1.0	1.1	Hα recombination line Thermal radio emission
Warm Neutral Medium	8000	0.5	2.8	1.5	HI 21 cm absorption/emission line
Cold Neutral Medium	80	50	2.2	2.3	HI 21 cm emission line
Molecular clouds	10	$\geq$ 200	1.3	1.0	CO rotational lines

[a] Typical temperature.
[b] Typical density.
[c] Representative mass in the Milky Way.
[d] Mass surface density in the solar neighbourhood.

1.4 Probing the ISM of galaxies

1.4.1 Disentangling the different components

Sections 1.2 and 1.3 give us means to interpret the SED of a galaxy and we can now disentangle the various physical components and processes at the origin of what is observed in galaxies: i.e., decompose the blue profile in Fig. 1.2.

Fig. 1.15 shows the detailed decomposition of the total SED of a galaxy in the different contributions from stars, dust and gas[6]. The observational constraints are indicated in black and are broad-band photometry from space or ground-based telescopes, spectrum (in the MIR) and emission lines. The total modelled emission of the galaxy that best reproduces the observational constraints is shown with the dashed grey curve. This total emission can be decomposed into the contributions of the various physical components in the galaxy. The most massive stars (in cyan) ionise the gas and heat the dust surrounding them. The emission from this gas is shown in yellow: note all of the emission lines, due to the ionised species in the gas. The emission from this dust is shown in blue: note the peak emission in the MIR, around 30 μm, indicative of a hot dust component with high equilibrium temperatures and the absence of PAH features in this particular case (PAHs have been photodissociated by the hard and intense FUV photons in these regions). These combined emission profiles correspond primarily to the emission from HII regions in the galaxy.

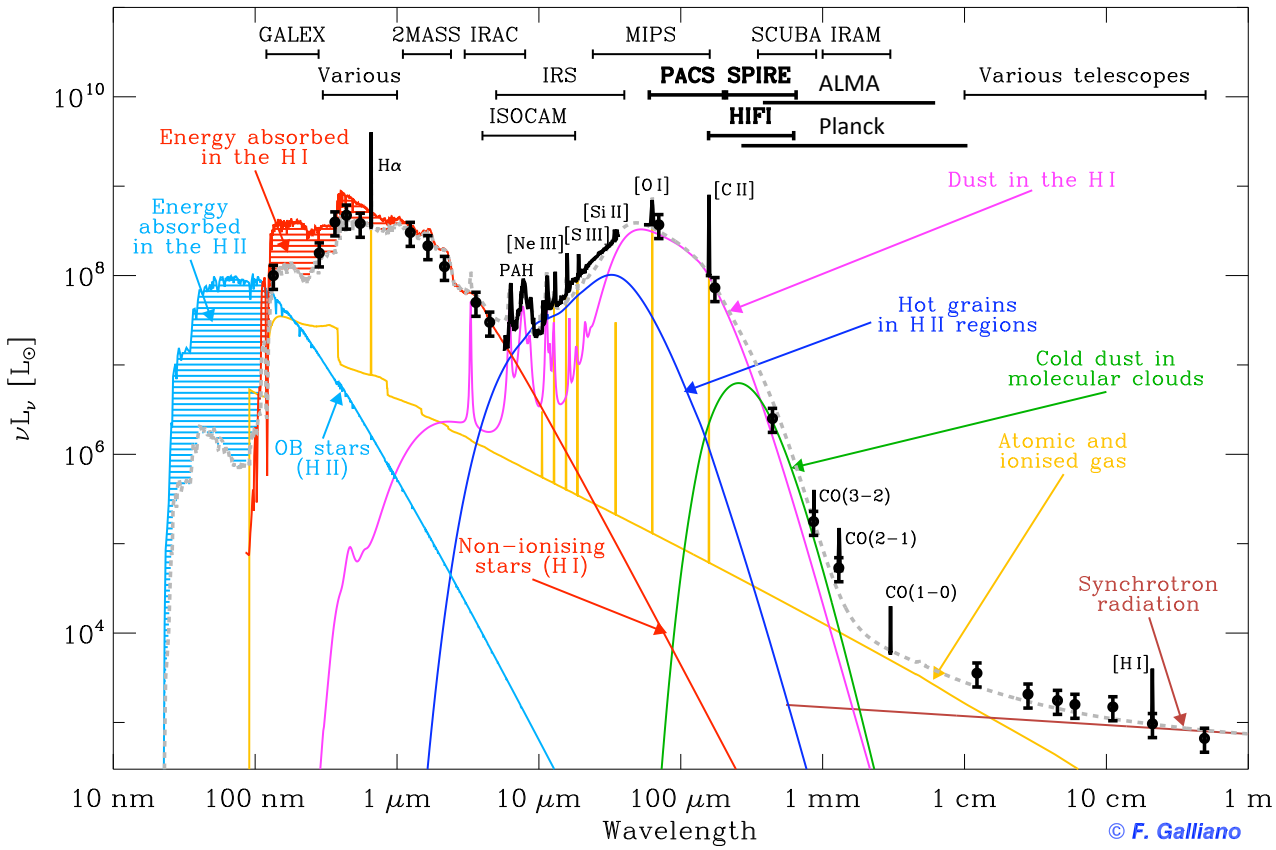

Fig. 1.15. Detailed view of the SED of a galaxy with the contributions from stars (in cyan and red), dust (in pink, green and blue) and gas (in yellow and brown). The total SED is the dashed grey line. Observations are the black points and spectrum.

Emission from older and less massive stars is shown in red, and dust heated by this radiation is shown in pink: note that here we do see the PAH emission features in the MIR. The peak of the dust emission is shifted to longer wavelengths, around 90 μm, indicative of colder grains. This corresponds to the emission from the neutral phase of the ISM. The emission from even colder dust embedded in molecular clouds, far away from any heating source, is shown in green with a peak in the submm domain ($\sim$ 300 μm). Finally the radio emission is due to emission from accelerated

[6]Note that this is not the same galaxy, nor the same model as in Fig. 1.2.

charges in the ISM (free-free and synchrotron radiation), originating in various regions, namely HII regions and the hot gas (HIM). Absorption of stellar light by dust is shown in the UV-visible by the stripped areas in the stellar emission. Note also the Lyman edge at 912 Å where the total emitted luminosity of the galaxy drops by about two orders of magnitude.

A wide range of instruments is available to probe the numerous components of the ISM of galaxies over all wavelengths, thus allowing us to obtain the necessary observational constraints. Here we present some of the telescopes and instruments that will be used in this thesis.

GALEX (GALaxy evolution EXplorer) is a space UV telescope observing at 1539 and 2316 Å.

2MASS (Two Microns All Sky Survey) is a large ground-based survey in the J (1.25 μm) H (1.65 μm) and K (2.20 μm) bands. It was conducted from the Mt. Hopkins Telescope in Arizona (USA) for the Northern hemisphere and from the Cerro Tololo Interamerican Observatory (in Chile) for the Southern hemisphere.

ISO (Infrared Space Observatory) contains an infrared camera (ISOCAM) observing between 2.5 and 17 μm.

Spitzer is a space IR telescope containing three instruments: IRAC and MIPS, both photometers observing from 3.6 to 160 μm, and IRS, the spectrometer covering 7 to 40 μm. A more complete description of these instruments is given in Chapter 6.

Herschel carries three instruments, PACS, SPIRE and HIFI, observing from 55 to 670 μm in FIR and submm wavelengths. PACS and SPIRE are both photometers and medium-resolution spectrometers and HIFI is a high-resolution spectrometer. *Herschel* is at the very heart of our study and the second part of this manuscript (Chapters 3 to 5) is entirely dedicated to *Herschel* data.

JCMT, APEX, IRAM (James Cerk Maxwell Telescope - Atacama Pathfinder EXperiment - Institute for Radio Astronomy at Millimetre wavelengths) are three ground-based facilities observing in the submm wavelength range with the instruments SCUBA (Submillimetre Common-User Bolometer Array, JCMT) in Mauna Kea (Hawaii, USA), LABOCA (Large Apex BOlometer CAmera, APEX) in Chajnantor (Chile) and MAMBO(Max-Planck-Millimetre-Bolometer, IRAM) in Grenada (Spain). SCUBA observed at 450 and 850 μm and is now replaced by SCUBA2, LABOCA observes at 870 μm and MAMBO observed at 1.2 mm. These three instruments are described in more details in Chapter 6.

Planck is another space telescope with two instruments, LFI and HFI (Low and High Frequency Instruments), observing submm to cm wavelengths from 350 μm to 1 cm.

ALMA (Atacama Large Millimetre/submillimiter Array) is a ground-based radio interferometer observing from 315 μm to 7.5 mm.

1.4.2 A wide range of SED shapes

Galaxies present a wide variety of morphological types and can be divided, in simplified terms, into three main groups: spiral galaxies, elliptical and lenticular galaxies, and irregular galaxies. Observations of different types of galaxies have shown that their SED shapes present different characteristics depending on several parameters such as their sizes, luminosities, masses, morphological

types, stellar activities, metallicities, etc., resulting in different relative proportions of the various ISM components. Our Galaxy is a classical barred spiral galaxy (SBc). Schematically spiral and irregular galaxies are more gas-rich, have a relatively young stellar population and can undergo bursts of star formation. On the contrary elliptical galaxies are neutral gas and dust deficient and their stellar population is quite old.

Figure 1.16 shows SEDs of five galaxies of different morphological types and stellar activities. We saw in Sections 1.2 and 1.3 how the SED depends on the ISM properties and Fig. 1.15 gives us the relative contribution of each ISM component. Let us now see on Fig. 1.16 what we can learn for different types of galaxies from the comparison of the different observed SED shapes, using the spiral type as a reference type.

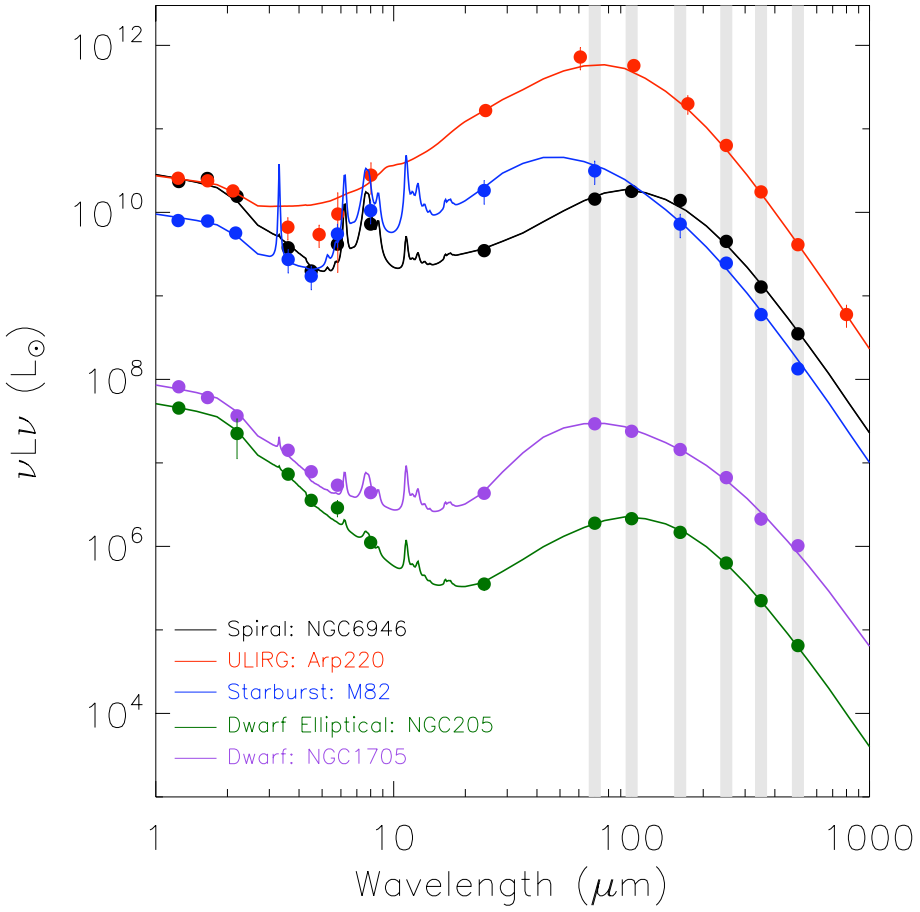

Fig. 1.16. SEDs for various galaxy types (from Madden et al. 2013): Spiral (NGC6946, in black), Dwarf (NGC1705, in purple), Dwarf Elliptical (NGC205, in green), Starburst (M82, in blue) and ULIRG (Arp220, in red). The differences in their SED shapes are due to the variations in the relative contribution of each ISM phase to the total emission of the galaxy. The grey stripes indicate the wavelength coverage of the 6 *Herschel* bands (see Chapter 3).

Spiral galaxies These galaxies usually contain large quantities of gas and dust and thus show strong dust continuum emission in the IR as well as strong emission lines. Spirals are composed of a rotating disk of stars and ISM (gas and dust), a bulge and sometimes a bar. Usually the bulge shows an older stellar population than the disk. Numerous star-forming regions can be found in the spiral arms. We see on Fig. 1.16, for the spiral NGC6946, the strong PAH features, arising from the active star-forming regions associated with PDRs in the disk, and FIR dust continuum emission

peaking around 100 μm.

Elliptical galaxies These galaxies present elliptical light radial profiles. They are known to possess a sparse and dust-poor ISM (Combes 1991) and an old stellar population. Molecular gas is rare, if detected at all, in elliptical galaxies (Sage et al. 2007), and thus they harbour a very low star formation activity. They normally show a weak dust component in their SED compared to the NIR peak, representative of the old stellar component.

Lenticular galaxies They are galaxies possessing a disk and a bulge but no spiral arms. They were originally misclassified by Hubble as intermediate between the roundest elliptical galaxies and spiral galaxies. They are now thought to be former spiral galaxies from which some gas has been removed by interaction with hot cluster gas in galaxy clusters (van den Bergh 2009). Their SEDs indeed show non-negligible dust and PAH emission.

Irregular / Dwarf galaxies As stated by their names, those galaxies are usually very small and do not possess a regular shape, making them difficult to classify. As we see in Fig. 1.16 the dwarfs are much fainter than the "normal" type galaxies, show a FIR peak of the SED shifted to shorter wavelengths, a steeper MIR continuum rise and weaker PAH features. Dwarf galaxies are presented in more details in Chapter 2 as they are the main focus of this work. In Fig. 1.16 we show the SED of NGC1705 which is a dwarf spiral galaxy and NGC205 a dwarf elliptical, and we clearly see the decreased contribution of the dust in the elliptical dwarf compared to the more active star-forming dwarf.

Besides classifying galaxies by morphological type, we can also distinguish galaxies based on their star formation activity:

Starburst galaxies are galaxies that are very actively forming stars (up to 1000 $M_\odot\,yr^{-1}$). To sustain such high star formation rates they consume their gas reservoirs very rapidly and the starburst phase only lasts a few tens of Myr. An important young stellar population creates numerous bright HII regions surrounded by PDRs. The harder and more intense radiation field they generate leads to a warmer dust component. This translates into a SED with prominent PAH features (from the PDRs) and a dust peak shifted to MIR wavelengths (see M82 in Fig. 1.16).

Active Galactic Nucleus galaxies - AGNs - These galaxies possess a very compact and luminous nucleus which dominates the total luminosity of the galaxy. This enhanced central luminosity is due to the accretion processes occurring in the accretion disk around a central super massive black hole. There are various categories of AGNs: Low-Ionisation Nuclear Emission-line Regions (LINERs galaxies), Seyfert galaxies, quasars, blazars and radio galaxies. Unified models propose that all of these different types are in fact the same object observed from a different point of view (Urry & Padovani 1995). Among the spectral characteristics of AGN is a "NIR bump" around 2 - 10 μm due to very hot dust in the accretion disk heated by the AGN.

(Ultra)-Luminous InfraRed Galaxies - (U-)LIRGs - These galaxies are extremely luminous in the IR wavelength range ($L_{TIR} > 10^{11}$ $L_\odot$ for a LIRG and $> 10^{12}$ $L_\odot$ for a ULIRG) radiating more than 90 % of their energy in the IR. LIRGs are extreme starburst and some also contain an AGN. ULIRGs are thought to be major mergers of gas-rich galaxies and they usually show strong emission lines in their spectra. They may be progenitors of elliptical galaxies (Kormendy & Sanders 1992; Genzel et al. 2001). Note the prominent MIR-to-FIR peak in the SED of Arp220, a typical ULIRG, in Fig. 1.16. The dust peak is shifted to shorter wavelengths compared to that of spirals

- a sign of hotter dust. The PAH features are absent, because the PAHs can not survive the hard radiation in the vicinity of the AGN.

The properties of irregular / dwarf galaxies, interpretation of their observed SEDs and how they vary compared to "normal" spiral galaxies together with determination of the ISM properties that are responsible for these variations, are fundamental to this thesis work. We thus now focus on a description of these specific environments for the next Chapter.

Chapter 2

Low-metallicity galaxies

Contents

In this Chapter, we focus on the characteristics of low-metallicity systems. First we define the metallicity of a galaxy and describe the importance of this parameter in characterising the ISM, before reviewing different ways of determining metallicity in Section 2.1. Physical properties of low-metallicity environments are presented in Section 2.2, where we outline the peculiarities of the ISM in these galaxies and the various motivations for studying them.

2.1 Metallicity

2.1.1 Definition

Metallicity is defined by the mass fraction of metals in the ISM, where metals encompass all elements heavier than helium. Metallicity is usually noted with the letter "Z" while "X" and "Y" are the mass fractions of hydrogen and helium respectively. We thus have:

$$X + Y + Z = 1 \tag{2.1}$$

The metallicity is then a measure of the fraction of the initial hydrogen and helium that has been converted into heavier elements. For the lightest elements, up to ^{7}Be, this conversion is done during primordial nucleosynthesis, shortly after the Big Bang. Elements up to iron are synthesised in stars, and released in the ISM when stars die (see Section 1.2.6), and elements heavier than iron are produced during supernovae events.

Primordial mass fractions (denoted by "$_P$", values from Pagel 1997) have evolved to present-day values in the solar neighbourhood (denoted by $\odot$, Asplund et al. 2009) :

$$\left\{ \begin{array}{rcl} X_P & \sim & 0.76 \\ Y_P & \sim & 0.24 \\ Z_P & = & 0 \end{array} \right. \Rightarrow \left\{ \begin{array}{rcl} X_\odot & \sim & 0.7154 \\ Y_\odot & \sim & 0.2703 \\ Z_\odot & \sim & 0.0142 \end{array} \right. \tag{2.2}$$

The hydrogen fraction has slowly decreased since the Big Bang as it is converted to heavier elements: helium or metals.

Usually the metallicity is approximated by the ratio of the abundance of one metal element, e.g., oxygen or iron, to the hydrogen abundance, (O/H) or (Fe/H), and expressed as 12+log(O/H) (or 12+log(Fe/H)). Note that abundances are in number and not in mass. We use metallicity in terms of oxygen abundance throughout this manuscript. In the solar neighbourhood, we have $(\mathrm{O/H})_\odot = (4.90 \pm 0.56) \times 10^{-4}$ i.e., $12+\log(\mathrm{O/H})_\odot = 8.69 \pm 0.05$ (Asplund et al. 2009).

We often talk about galaxies with a given fraction, f, of the solar metallicity and note it as "$Z = f\ Z_\odot$". It actually means that the oxygen abundance in the galaxy is f times the oxygen abundance of the Galaxy ($\mathrm{O/H} = f\,(\mathrm{O/H})_\odot$), and often it is assumed that the oxygen abundance scales with the total metal abundance: $(\mathrm{O/H})/(\mathrm{O/H})_\odot \sim Z/Z_\odot$.

For a galaxy, the metallicity thus traces the history of the stellar activity, i.e., schematically how many cycles of star formation it already went through (see Section 1.2.7 and the lifecycle of matter in the ISM). Metallicity is thus a key parameter of the evolution of galaxies, and is expected to increase with age as the galaxy undergoes chemical enrichment. Investigations of relations between metallicity and other physical properties of galaxies can thus place important constraints on the physical processes governing galaxy evolution. In this work, we especially focus on the relation between metallicity and dust, another key agent of galaxy evolution (Section 1.2.7).

2.1.2 Determination

There are several possible ways to determine the metallicity of a galaxy: spectroscopy of ionised gas in HII regions (Izotov et al. 2006) or planetary nebulas (Pagel 1997); photometry of resolved

stellar populations ((Fe/H) determined by the colour of the red giant branch, e.g., Lee et al. 1993); spectroscopy of individual stars (only possible in the nearest galaxies where individual stars can be resolved, e.g., Haser et al. 1998 in the Magellanic Clouds); spectroscopy or photometry of integrated light for remote galaxies without HII regions (Worthey 1994); spectroscopy of the cold neutral medium (using absorption lines, Kunth et al. 1994); or X-ray observations of the hot ionised medium (Persic et al. 1998). We refer to Kunth & Östlin (2000) for a review of the various ways of accessing the metallicity of a galaxy, and detail here only the first: spectroscopic measurements of emission lines in HII regions.

The abundance of elements in HII regions depends on the properties of the gas, namely the electron density, n_e, and the electron temperature, T_e. These two parameters determine the ionisation stages that can be found in the region for a given element. Several methods exist to derive abundances in HII regions and we describe here two most commonly used methods: the "direct" method and the "strong-line" method.

The "direct" method

This method is called "direct" because it allows the direct determination of the electron density and temperature through carefully chosen optical line ratios, after correcting the lines for extinction. We review here the physics allowing us to determine n_e and T_e from line ratios in the simple case of a two-level system. Let us consider an element collisionally excited to an upper energy level that cascades down to the lower energy level by collisional de-excitation and spontaneously emits a photon. The populations of the two levels can be found by solving the statistical equilibrium equation:

$$n_e n_l \gamma_{lu} = n_e n_u \gamma_{ul} + n_u A_{ul} \tag{2.3}$$

where n_u and n_l are the population densities of the upper and lower energy level respectively; γ_{ul} and γ_{lu} are the collisional rate coefficients between the two levels; and A_{ul} is the Einstein coefficient for spontaneous emission. In thermal equilibrium, the collisional excitation rate coefficient, γ_{lu}, is related to the collisional de-excitation rate coefficient, γ_{ul}, by:

$$\gamma_{lu} = \gamma_{ul} \frac{g_u}{g_l} e^{\frac{-E_{ul}}{kT_e}} \tag{2.4}$$

where g_u and g_l are the statistical weights of the two levels; E_{ul} is the energy difference between the two levels; and k is the Boltzmann constant. γ_{ul} is given by:

$$\gamma_{ul} = \left(\frac{2\pi}{kT_e}\right)^{1/2} \frac{\hbar^2}{m_e^{3/2}} \frac{\Omega(u,l)}{g_u} \tag{2.5}$$

where m_e is the mass of the electron; $\Omega(u,l)$ is the collision strength for upward collisions; and $\hbar$ the Planck constant, h, divided by 2π.

With Eqs. 2.3 and 2.4 we can get:

$$\frac{n_u}{n_l} = \frac{g_u}{g_l} e^{\frac{-E_{ul}}{kT_e}} \left(\frac{1}{1+\frac{n_c}{n_e}}\right) = \frac{n_e \gamma_{lu}}{A_{ul}} \left(\frac{1}{1+\frac{n_e}{n_c}}\right) \tag{2.6}$$

where we introduce n_c, the critical density: $n_c = A_{ul}/\gamma_{ul}$. The critical density determines if collisions dominate the de-excitation process. This is the case when $n_e \gg n_c$. When $n_e \ll n_c$, collisional de-excitation of the upper level is negligible.

The line intensity that we observe is directly proportional to the cooling rate Λ, given by:

$$\Lambda = n_u A_{ul} h\nu_{ul} \tag{2.7}$$

with $h\nu_{ul} = E_{ul}$.

In the high-density limit, the observed intensities are independent of the electron density and depend only on the electron temperature. Indeed for $n_e \gg n_c$, the cooling rate can be expressed as:

$$\Lambda = n_l \frac{g_u}{g_l} e^{\frac{-E_{ul}}{kT_e}} A_{ul} h\nu_{ul} \tag{2.8}$$

On the contrary, in the low-density limit, the observed intensities depend on the electron density. Indeed for $n_e \ll n_c$, the cooling rate is:

$$\Lambda = n_e n_l \gamma_{lu} h\nu_{ul} \tag{2.9}$$

Λ depends on ${T_e}^{-1/2}$ via the collisional rate coefficient γ_{lu} (through Eqs. 2.4 and 2.5). Thus the electron temperature can be determined by using two lines with very high critical densities. The typical line ratio used for the determination of the electron temperature is [OIII] λ4363/[OIII] $\lambda\lambda$4959,5007, because these lines have critical densities of 2.4×10^7 cm^{-3} and 7×10^5 cm^{-3} respectively.

The electron density is usually measured combining two lines with different critical densities. In between the two critical densities, the line ratio is a good measure of the electron density as one line is in the high-density limit (with intensity $\propto n_l$) and the other line is in the low-density limit (with intensity $\propto n_e \times n_l$). Line pairs that are commonly used are the [SII] λ6717/λ6731 ratio with respective critical densities of 1.3×10^3 cm^{-3} and 3.6×10^3 cm^{-3}, or [OII] λ3726/λ3729 with n_c of 10^4 cm^{-3} and 3×10^3 cm^{-3}.

Once n_e and T_e are known, the ionic abundance of an element can be derived from:

$$\frac{N(X^i)}{N(H^+)} = \frac{I_\lambda}{I_{H\beta}} \frac{\epsilon_{H\beta}}{\epsilon_\lambda} \tag{2.10}$$

where $N(X^i)$ is the ionic abundance of the specie of interest; I_λ is the measured intensity of the ionic emission line; $I_{H\beta}$ is the measured intensity of the Hβ recombination line and ϵ_λ and $\epsilon_{H\beta}$ are the emissivities of the respective lines. For the ion we are interested in, ϵ_λ is directly proportional to the cooling rate and thus to the number density of the ion. The formula to derive the Hβ emissivity is given in Aller (1984).

The total abundance of the element is obtained by summing the ionic abundances of all of the ionisation stages. As all of the ionisation stages can not always be observed for an element, one has to correct for the unobserved ions via the ionisation correction factors (ICFs) for each element. Fortunately for oxygen, the most abundant ions, O^+ and O^{2+}, are seen in the optical spectra of HII regions and only a small fraction is in the form of O^{3+}. In most cases, the abundance for oxygen can thus be determined directly by:

$$\frac{O}{H} = \frac{O^+}{H^+} + \frac{O^{2+}}{H^+} \tag{2.11}$$

and this is one of the reasons why the metallicity of a galaxy is usually given in terms of oxygen abundance. To derive ICFs for other elements, we need to know the ionisation structure of the HII region, that can be derived using photoionisation models.

This "direct" method is the most direct way to access the metallicity of a galaxy but is subject to a number of caveats, among which are:

- The [OIII] λ4363 line, necessary to determine T_e(OIII), is very weak and most of the time can not be observed easily in high-metallicity environments (e.g., Garnett et al. 2004).

- In high-metallicity regions, temperature fluctuations or gradients in the HII region may cause a misestimation of the electron temperature. T_e(OIII) is then not representative of the true electron temperature in the HII region leading to a systematic bias in the metallicity determination (usually underestimation, see review by Stasińska 2005; Bresolin 2007).

Other auroral lines detectable at high metallicities (such as [NII] λ5755 or [SII] λ6312) or high signal-to-noise spectra can overcome the weakness of the [OIII] λ4363 line and robust metallicities can be obtained up to roughly solar metallicity.

We refer to Izotov et al. (2006) for an example of determining the metallicity with the "direct" method. Izotov et al. (2006) use the [SII] λ6717/λ6731 ratio to determine the electron density and [OIII] λ4363/[OIII] $\lambda\lambda$4959,5007 to derive the electron temperature. However, the electron temperature is not the same in the low- and high-ionisation zones of the HII region, especially in HII regions with low metallicities (Stasińska 1990). Only T_e(OIII) is derived directly from the observations. To get the electron temperature of the different ions of interests, Izotov et al. (2006) use the most recent results from the HII photoionisation models of Stasińska & Izotov (2003) to get relations between T_e(OIII) and the temperatures characteristic of other ions. Updated relations from Pagel et al. (1992) are then used in Izotov et al. (2006) to derive ionic abundances from the corresponding electron temperatures, and are based on the three-level-atom solutions of McCall (1984). The ICFs for elements other than oxygen are determined from photoionisation models and are expressed as functions of $O^+/(O^+ + O^{2+})$ and $O^{2+}/(O^+ + O^{2+})$.

We will follow the method of Izotov et al. (2006) to determine the metallicity of the galaxies in our study (see Chapter 3). With this method, Izotov et al. (2012) determined the metallicity of 42 extremely low-metallicity galaxies (down to 12 + log(O/H) = 7.12) and compiled a sample of the 17 most metal-poor galaxies known in the local Universe. Their main finding is that there seems to be a metallicity floor around 12+log(O/H) $\sim$ 6.9, below which no galaxies are found in the local Universe, suggesting that the matter from which dwarf galaxies have formed had been previously pre-enriched to that level by (e.g.,) Population III stars.

The "strong-line" method

This method is used when the [OIII] λ4363 line is not detected, for example at higher metallicities in low-excitation HII regions. Empirical metallicity calibrations were derived by fitting the relationship between "direct" metallicities and strong-line ratios for HII regions. Typical ratios are mostly optical line ratios: [NII] λ6584/Hα (Pettini & Pagel 2004), ([OII] λ3727/Hβ)/([NII] λ6584/Hα) (Pettini & Pagel 2004), or the "R_{23}" ratio (Pilyugin 2001; Pilyugin & Thuan 2005; Liang et al. 2007; Yin et al. 2007):

$$R_{23} = \frac{[OII]\lambda 3727 + [OIII]\lambda\lambda 4959, 5007}{H\beta} \tag{2.12}$$

The bulk of cooling in dusty environments is done by the FIR fine structure lines while it is done by high-excitation optical lines in low-metallicity regions. Thus we expect R_{23} to increase as the metallicity decreases. Figure 2.1 shows the R_{23} ratio as a function of 12+log(O/H), and we observe the expected trend for high metallicities. At lower metallicities, [OIII] $\lambda\lambda$4959,5007 is not dominating the cooling anymore and the relation turns around at $\sim$ 10% of the solar metallicity, creating a degeneracy in R_{23}. This degeneracy can be lifted using another line ratio, for example [NII] λ6584/[OII] λ3727. The division between the upper and lower branch of the R_{23} calibration occurs around log([NII] λ6584/[OII] λ3727) $\sim$ -1.2 (Kewley & Ellison 2008). The "strong-line" method suffers from the same caveats as the "direct" method since the calibration is based on "direct" metallicities.

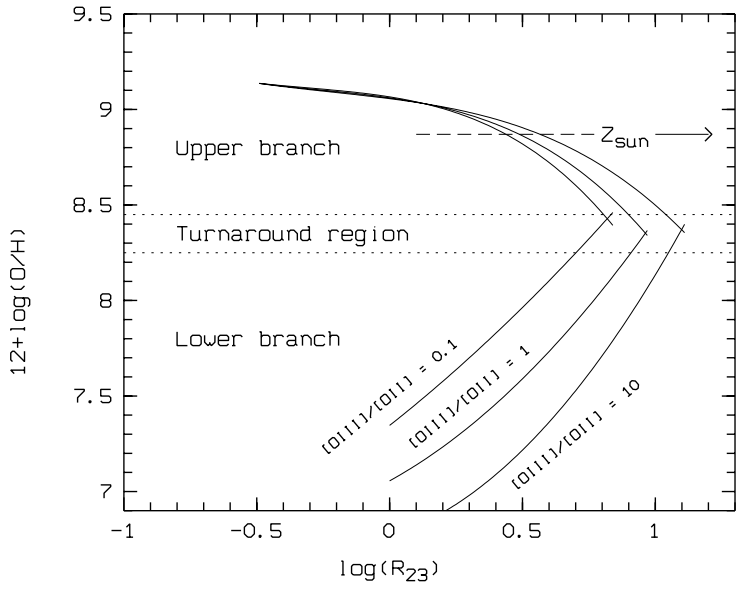

Fig. 2.1. Oxygen abundance, 12+log(O/H), as a function of R_{23}, derived from McGaugh (1991) models. The figure has been taken from Maier et al. (2004) to illustrate the degeneracy in the R_{23} calibration.

As we are spanning a wide range in metallicity in the sample we use for our study, we will also use the "strong-line" method with the calibration of Pilyugin & Thuan (2005) to determine the metallicity of our galaxies (see Chapter 3).

Other strong-line R_{23} calibrations can be derived from photoionisation models or from combining models and observations. We refer to Kewley & Ellison (2008) for a review on the various ways of determining the metallicity of a galaxy through spectroscopic observations of HII regions.

2.2 Dwarf galaxies

2.2.1 Definition and classification

General characteristics

Dwarf galaxies are commonly defined as being small in size with a low mass, a low luminosity and a low metallicity. Where to draw the line between "normal" galaxies and dwarf galaxies is still widely debated but we adopt here the luminosity criterion of Grebel et al. (2003): $M_V \geq$ -18 mag, where M_V is the absolute magnitude in the V band. A luminosity criterion is often used rather than a mass criterion as luminosity is directly observable for a galaxy, contrary to its mass, and allows a more homogeneous classification. In terms of mass, galaxies with masses smaller than 10^{10} $M_\odot$ can be considered as dwarf galaxies. Dwarf galaxies in the local Universe can have luminosities as low as 10^5 $L_\odot$, masses as low as 10^7 $M_\odot$, metallicities as low as 1/50 $Z_\odot$ and sizes in terms of R_{25}[1] smaller than 5 kpc. For comparison, the Milky Way has $M_V \sim$ - 21 mag, a total mass, M_{tot}, of $\sim 10^{12}$ $M_\odot$ (including dark matter), a total luminosity of $\sim 7 \times 10^{10}$ $L_\odot$ (see Table 1.1) and a radius of $\sim$ 18 kpc. The stellar content of dwarf galaxies is also low, $\lesssim 10^9$ $M_\odot$, two orders of magnitude below the stellar mass for the Milky Way. They form stars either via episodic bursts of star formation or continuously (see Section 2.2.2). Dwarf galaxies are the dominant population of galaxies in the Universe (Marzke & da Costa 1997) even though their low luminosities often restrict their detailed

[1] R_{25} is defined as the radius at which the surface brightness falls to a level of 25 mag/arcsec^2.

study to the nearby Universe. For example, the Local Group contains about 100 galaxies, with 70% of them being dwarf galaxies (McConnachie 2012). Dwarf galaxies in the Local Group are dominated by dark matter (Mateo 1998) and a study by Oh et al. (2011) showed for a sample of dwarf galaxies from THINGS (The HI Nearby Galaxy Survey) that the dark matter mass to total mass ratio in their sample is about 0.7. If this can be generalised to all of the dwarf galaxies, they may account for a significant mass fraction of the total mass in the Universe.

Naively one could think that considering their small sizes and young chemical ages due to their low metallicities, dwarf galaxies are simple systems that are easy to study. In fact, the star formation and chemical enrichment histories in these galaxies are very complex, and are triggered and sustained by as-yet unknown mechanisms. The wide variety of observed dwarf galaxy populations, star-formation activities, chemical enrichment histories and ISM conditions, combined with the fact that observing them is challenging because of their low luminosities, makes it difficult to build a general case for these galaxies. This is illustrated already by the numerous morphological types that have been defined to classify the dwarf galaxy population.

Morphological classification

Indeed dwarf galaxies can be separated into different families. Of course the classification of dwarf galaxies is still a debated subject. Some classes overlap with some others and the properties of the galaxies within a class are not unique. Moreover the morphology of dwarf galaxies strongly depends on the component we are looking at, e.g., spiral distribution of the atomic gas, presence of a stellar bar or irregular structure of the HII gas. We follow and describe here the classification from Grebel (2001). We refer to Mateo (1998); Kunth & Östlin (2000); Grebel (2001) for reviews on the various morphological types for dwarf galaxies and their respective properties.

Dwarf Spirals - dS They are small analogues to the "normal" spiral galaxies (S0, Sa, Sb, Sc and Sd galaxies). They are at the high mass end of the dwarf galaxy distribution, and are characterised by a central surface brightness of $\mu_V \geq 23$ mag arcsec^{-2}, HI masses of $M_{HI} \leq 10^9\ M_\odot$ and total masses of $M_{tot} \leq 10^{10}\ M_\odot$. Late-type dwarf spirals are mostly slow-rotators or exhibit solid-body rotation while early-types dwarfs spirals have rotationally supported exponential disks, and are usually more metal- and gas-rich than late types. Dwarf spirals show a slow continuous level of star formation and are found both in clusters and in the field. An example of a dwarf spiral galaxy is shown in Fig. 2.2 left[2].

Dwarf Irregulars - dIrr As their name suggest, they have an irregular shape in the optical, with scattered bright HII regions. These galaxies are characterised by $\mu_V \leq 23$ mag arcsec^{-2} (usually well described by an exponential profile), $M_{HI} \leq 10^9\ M_\odot$ and $M_{tot} \leq 10^{10}\ M_\odot$. They are gas-rich and the HI distribution can show a complicated pattern (with clumps and shells). The most massive dIrrs usually have an HI distribution that is much more extended than their optical size, and are dominated by solid-body rotation. In less massive dIrrs, rotation is not systematically observed and their HI distribution can be off-centered or can present a ring-like structure (Young & Lo 1997). They can present high levels of star-formation activity. They are also found either in clusters or in the field. An example of a dwarf irregular galaxy is shown in Fig. 2.2 center[3].

Blue Compact Dwarfs galaxies - BCDs These galaxies do not have a specific shape but are usually compact, made of several concentrated star clusters and are gas-rich and actively star-forming galaxies (i.e., with levels of star formation that can reach those of "normal" giant galaxies).

[2]Image from http://cseligman.com/text/atlas/
[3]Image from http://billsnyderastrophotography.com

Fig. 2.2. Examples of *(left)* a dwarf spiral NGC4214, *(center)* a dwarf irregular IC10, and *(right)* a blue compact dwarf IZw18.

Various subtypes of BCDs exist, among which are HII galaxies (with optical spectra reminiscent of HII regions), blue amorphous galaxies and Wolf-Rayet (WR) galaxies (which present strong signatures indicative of a significant population of WR stars). Their name is due to their blue colours (in B band) arising from the population of young, hot, massive stars recently formed. Both gas and stars show high central concentrations, thus contributing to a strong and bright central surface brightness ($\mu_V \leq 19$ mag arcsec^{-2}). They are characterised by $M_{HI} \leq 10^9\ M_\odot$, often exceeding the mass of stars, and $M_{tot} \leq 10^{10}\ M_\odot$. Their HI distribution can also be very extended and sometimes decoupled from the galaxies (van Zee et al. 1998; Cannon et al. 2006). Nonetheless solid-body rotation is observed in the central parts of BCDs. Their star formation is mostly episodic through bursts of star formation. Contrary to dS and dIrrs, they are usually isolated, away from galaxy clusters. An example of a BCD galaxy is shown in Fig. 2.2 right[4].

Dwarf Spheroidals - dSph have a spheroidal shape and are the faintest and least massive galaxies known. Indeed they are characterised by $M_V \geq$ -14 mag, $\mu_V \geq 22$ mag arcsec^{-2} with very little central stellar concentration, $M_{HI} \leq 10^5\ M_\odot$ and $M_{tot} \leq 10^7\ M_\odot$. They are often almost devoid of detectable neutral gas, and sometimes their low gaseous content is below the amounts expected from stellar mass loss. They do not show any rotation nor any HII emission. Their star formation rate is very low. They are usually found close to massive galaxies. An example of a dwarf spheroidal galaxy is shown in Fig. 2.3 left.

Fig. 2.3. Examples of *(left)* a dwarf spheroidal NGC205, *(center)* a dwarf elliptical M32 and *(right)* tidal dwarfs from the NGC7252 system. NGC7252 is in the middle of the image and the two dwarf galaxies are at the edges of the two tidal streams.

[4]Image from http://hubblesite.org

Dwarf Ellipticals - dE have spherical or elliptical shapes, with compact central stellar densities. They are characterised by a high central surface brightness but are gas-poor and not very massive: $M_V \geq$ -17 mag, $\mu_V \leq 21$ mag arcsec^{-2}, $M_{HI} \leq 10^8$ $M_\odot$ and $M_{tot} \leq 10^9$ $M_\odot$. As in the case of dSph, they are usually not supported by rotation, show little star formation and are also found close to massive galaxies. An example of a dwarf elliptical galaxy is shown in Fig. 2.3 center[5].

Tidal dwarfs are a special type of dwarf galaxies as they are the remnants of interactions between two massive galaxies (stripped material or mergers). They form from the debris torn out from massive galaxies during these interactions. Contrary to the other families of dwarfs galaxies they can be metal-rich, for their mass, as they possess the metallicity of their parent galaxies (Duc & Mirabel 1998). Their characteristics such as mass, luminosity, and gas content, thus mostly depend on the conditions of the interaction and on the properties of their progenitors. An example of an interacting system with two tidal dwarf galaxies is shown in Fig. 2.3 right[6].

Table 2.1. General characteristics for the various morphological types of dwarf galaxies (except tidal dwarfs). The Milky Way has been added on the last column for comparison.

	dS	dIrr	BCDs	dSph	dE	Milky Way
M_V [mag]	$\geq$ -18	$\geq$ -16	$\geq$ -18	$\geq$ -14	$\geq$ -17	-21
μ_V [mag arcsec^{-2}]	$\geq$ 23	$\leq$ 23	$\leq$ 19	$\geq$ 22	$\leq$ 21	-
$M_{HI}[M_\odot]$	$\leq 10^9$	$\leq 10^9$	$\leq 10^9$	$\leq 10^5$	$\leq 10^8$	4.5×10^9
M_{tot} $[M_\odot]$	$\leq 10^{10}$	$\leq 10^{10}$	$\leq 10^{10}$	$\leq 10^7$	$\leq 10^9$	$\sim 10^{12}$
Shape	spiral extended	irregular extended	compact small	elliptical small	elliptical small	barred spiral extended
Gas Content	rich	rich	rich	poor	poor	rich
Rotation	solid-body	solid-body	solid-body	no	no	yes
Star Formation	slow, cont.	episodic/cont.	episodic and bursty	low, cont.	low, cont.	cont.
Location	cluster/field	cluster/field	field	cluster	cluster	-

Note: cont. = continuous

How these different families of dwarf galaxies are related or not is still an open question. For example Thuan (1985) suggested that BCDs and dIrrs are the same type of galaxy, only differing by their present star-formation rates, and can evolve into dE. On the contrary, James (1994) claimed that dIrrs are a fundamentally different population from BCDs that are in fact dwarf ellipticals undergoing a burst of star formation. Zhao et al. (2013) separated BCDs into irregular- and elliptical-types and suggested that irregular- and (some) elliptical-type BCDs might be related and at different stages of galaxy evolution and/or have different progenitors. Additionally, very late-type dwarf spirals may be in a transition phase to dwarf irregulars, and very-low mass dIrrs may be evolving towards dwarf spheroidals (Grebel 2001). Some dIrrs and dSph may also be tidal dwarfs that formed early-on. The question of an evolutionary trend between the different families of dwarf galaxies is thus far from being solved.

In Table 2.1, we summarise the main characteristics for the various dwarf morphological types (except the tidal dwarfs). Our sample of dwarf galaxies is composed of gas-rich dwarf galaxies, mainly BCDs and star-forming dIrrs. Thus, in the next Section, we will see in more detail how the ISM of these gas-rich, star-forming dwarf galaxies differs from more metal-rich environments and we will leave aside the gas-poor types (dEs and dSph galaxies).

[5]Images of the dSph and dE from http://www.noao.edu/outreach/aop/observers/
[6]Image from Braine et al. (2001)

2.2.2 The peculiar ISM of dwarf galaxies

Due to their low metallicity, the ISM of these dwarf galaxies is quite different from the ISM of more massive galaxies, and we review here the main differences in terms of gas and dust properties.

Gas in low-metallicity galaxies

Star formation - Dwarf galaxies usually have gas densities below the threshold value for star formation (determined by Kennicutt 1989), thus one might conclude that their star-formation activity is very poor. As we saw in Section 2.2.1 this is certainly not the case for BCDs as well as dIrrs that can be actively forming stars, with star formation being concentrated in one or several knots. Star formation can be either continuous or episodic with bursts of star formation (every $\sim$ 100 Myr) between two more quiescent periods of slow continuous star formation (Searle & Sargent 1972). Without gas inflow, the star-formation activity can cease at anytime, whenever all of the gas has been consumed. Gas-poor dwarfs may thus be galaxies which have already converted most of their gas reservoir into stars. BCDs are the typical environments where episodic star formation can be found. These episodes are usually violent (up to 10 $M_{\odot}\,yr^{-1}$, Thuan 1983) and thus short, only a few Myr, as the gas reservoir is consumed extremely rapidly to sustain such a high star-formation rate.

Because of this intense star-formation activity, most dIrrs and BCDs are dominated by a young stellar population concentrated in star-forming complexes, super star clusters (SSCs) or massive O-B associations; embedded in a more extended older stellar population (e.g., Hodge et al. 1991). This older population is most of the time composed of red horizontal branch stars and can be thus younger than globular clusters in the Galaxy. The high star-formation activity in BCDs generates a high number of young and massive stars such as WR stars. When observed in a galaxy, those stars are usually the sign of intense star formation over the past 10 Myr. The presence of such young stars (usually with a higher relative fraction compared to the older stellar population) combined to a lower metallicity of the ISM results in a harder galaxy-wide radiation field (Campbell et al. 1986; Galliano et al. 2003, 2005; Madden et al. 2006). The hardness of the radiation field is defined by the proportion of hard photons, and hence by the shape of the stellar spectrum in the UV. Figure 2.4 shows the UV-visible part of the ISRF of the Galaxy compared to the ISRF of four low-metallicity galaxies, which indeed show a higher level of UV emission.

The hardness of the radiation field can be measured using emission from highly ionised species in the optical (e.g.,OIII λ4363/Hβ, NII λ6584/Hα, see Kewley et al. 2001) or in the IR domains (e.g., NeIII λ15.56μm/NeII λ12.81μm, Madden et al. 2006). The radiation field becomes softer as stars evolve off the main sequence after a few Myr (e.g., Levesque et al. 2010). As metallicity increases, the metals present in the atmospheres of massive stars can absorb much of the hard UV photons produced by the star, thus decreasing the hardness of the radiation field in the HII region. As we will see in the next paragraphs, this harder ISRF at low metallicities will have important consequences on the gas and dust properties.

Atomic gas - The absolute HI content in low-metallicity galaxies is relatively low compared to more-metal rich environments (see Table 2.1). However, for gas-rich dwarf galaxies, the atomic gas mass fraction is quite high (e.g., $\geq$ 30% of the total baryonic mass for BCDs, Thuan & Martin 1981), compared to that found in more massive galaxies (a percent, or fractions of a percent, see Table 2.1 for our Galaxy). These galaxies thus have a large gas reservoir that has not yet been converted into stars. The HI distribution is usually extended in some dwarf galaxies and goes beyond the optical radius (in terms of R_{25}) of these galaxies (see Tully et al. 1978; Thuan & Martin 1981; Thuan et al. 2004; Begum & Chengalur 2005a; Pustilnik & Martin 2007; Hunter et al. 2011). This extended HI content shows a complex structure that can be a remnant from the formation of the dwarf galaxy

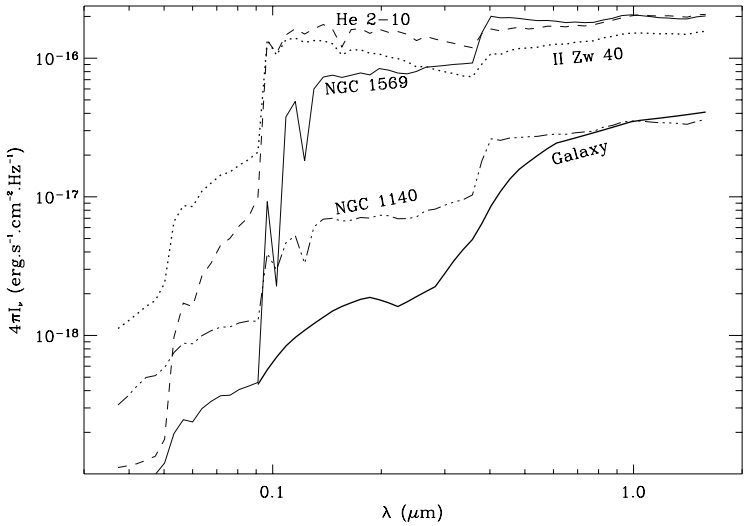

Fig. 2.4. Synthesised ISRF for four low-metallicity galaxies from Galliano et al. (2005), compared to the ISRF of the Galaxy (from Mathis et al. 1983)

or sign of external perturbations (i.e., past or present interactions with a more massive companion). This extended HI might be seen as a large available reservoir of gas slowly fuelling the centre of the galaxy for star formation, although a direct link with star formation is still debated (Hunter 1997; de Blok & Walter 2006).

HI can also trace the dark matter content in galaxies, via the rotation curves. Indeed HI observations provide information on the rotation velocities of the gas. Using rotation curve models, one can reproduce the gas and stellar radial profiles and infer the mass of the halo using the rotation curve and mass models (usually with the profile from Navarro et al. 1996). HI observations revealed that dwarf galaxies contain a larger fraction of dark matter, more concentrated in the halo, than more massive galaxies (Brinks & Taylor 1994).

Molecular gas - Molecular gas, through CO observations, is particularly difficult to detect in dwarf galaxies (i.e., Taylor et al. 1998; Leroy et al. 2009; Schruba et al. 2012), despite their intense star-formation activity and large reservoirs of HI gas. This poses the question of what fuels the star formation in these galaxies. This "CO-deficit" in dwarf galaxies can be interpreted in two ways: either the molecular gas content is indeed very low in dwarf galaxies, but then difficult to reconcile with the necessary amount of molecular gas required to fuel star formation; or CO becomes a poor tracer of H_2 at low metallicities, and there may exist a significant amount of H_2 not traced by CO. Indeed in low-metallicity ISM, the transparency of the ISM due to lower dust abundances, combined with the increased hardness of the ISRF, allows harder FUV photons to penetrate deeper into the cloud and photodissociate CO, and other molecules that are not efficient at self-shielding (because they are not abundant enough). The transition from CI to CO occurs thus deeper in the molecular cloud. Additionally, H_2 is efficient at self-shielding and can survive in regions where CO has already been photodissociated, resulting in a higher proportion of H_2 residing in the CII - CI region, outside the smaller CO core (see Fig. 2.5). This molecular gas not traced by CO has been called the "CO-free" gas (or "CO-dark" gas). Its presence was first suggested in low-metallicity galaxies via observations of [CII] at 158 μm in the Large Magellanic Cloud (Poglitsch et al. 1995; Israel 1997) and IC10 (Madden et al. 1997). Its existence has been confirmed in our Galaxy with two independent measurements: γ-rays a few years ago (Grenier et al. 2005) and *Planck* observations in the submm/mm domain more recently (Planck Collaboration et al. 2011a). Theoretical work

has shown that the "CO-free" gas effect is strongly controlled by the extinction and should have an increased importance as the metallicity decreases (Wolfire et al. 2010; Krumholz & Gnedin 2011; Glover & Clark 2012). In low-metallicity galaxies, recent *Herschel* and *Planck* observations indeed confirm that the molecular gas content appears more important that the one traced by CO alone (Roman-Duval et al. 2010; Galliano et al. 2011).

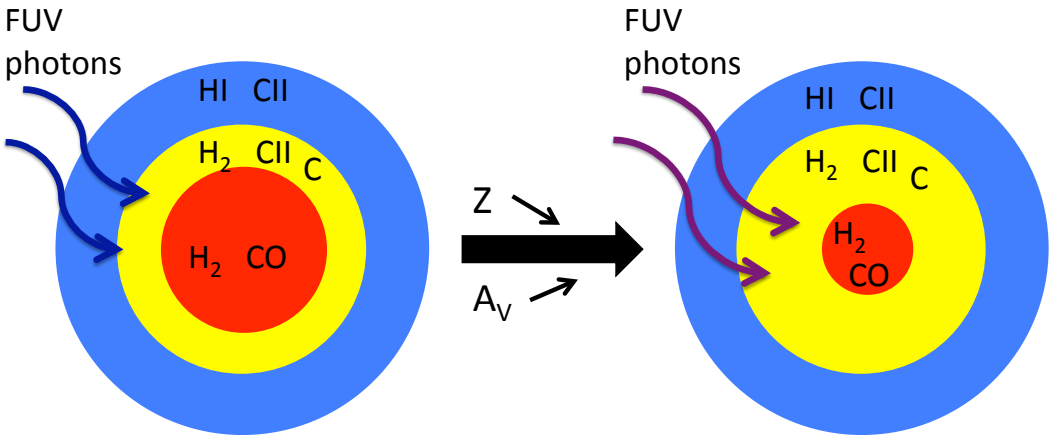

Fig. 2.5. Illustration of the impact of metallicity and extinction on the structure of the molecular clouds, inspired from Wolfire et al. (2010). The harder FUV photons penetrate deeper into the cloud at low metallicity, increasing the relative size of the region where H_2 is co-existing with CII and CI (yellow zone), compared to the region where both H_2 and CO are present (red zone). The blue zone corresponds to the atomic phase, where no H_2 is present.

Thus the relation between the total amount of H_2 and the observed CO is more ambiguous at low metallicities. Several studies have tried to determined the metallicity dependence of the X_{CO} conversion factor (Wilson 1995; Israel 1997; Taylor et al. 1998; Boselli et al. 2002; Leroy et al. 2011; Schruba et al. 2012). For example, from a sample of 16 dwarf galaxies, Schruba et al. (2012) found a X_{CO} scaling with $(O/H)^{-2}$.

Dust in low-metallicity galaxies

Dwarf galaxies have absolute dust abundances lower than those of more metal-rich galaxies, resulting in lower UV-attenuation and a porous ISM. This can be interpreted as a direct consequence of the low metallicity of these galaxies: less metals are available in the ISM to form dust. We saw in the previous section that this has an important influence on the molecular cloud structure. Moreover, despite their low metal content, for their mass, dwarf galaxies possess non-negligible amounts of dust with properties differing from their metal-rich counterparts, in extinction as well as in emission.

Extinction curve - As we saw in Section 1.2.2, the extinction curve depends on the nature and on the properties of the dust present along the line-of-sight. It can thus vary from one galaxy to another, depending on the physical conditions of the ISM. We illustrate the impact of lower metallicity on the extinction curve in Fig. 2.6, by comparing the Milky Way and two low-metallicity dwarf galaxies: the Large and Small Magellanic Clouds (LMC, Z $\sim$ 1/2 $Z_\odot$ and SMC, Z $\sim$ 1/5 $Z_\odot$). The three extinction curves are quite similar in the optical range but differ in the UV: the "UV-bump" at 2175 Å is much less pronounced in the LMC than in the Milky Way and is absent in the SMC; and the FUV slopes also differ. Weingartner & Draine (2001) reproduced these observed extinction curves in the Magellanic Clouds theoretically with an approximate mixture of silicate and carbonaceous grains. The absence of the 2175 Å feature in the SMC was explained by a deficit in very small

carbonaceous grains (including PAHs) with sizes below 0.02 μm.

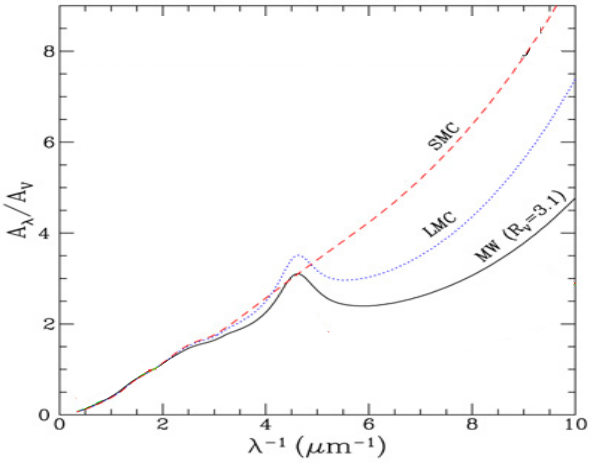

Fig. 2.6. Interstellar extinction curves for the Milky Way ($R_V = 3.1$), the LMC and the SMC (adapted from Gordon et al. 2003)

Warmer dust - Dust has been known to be warmer in dwarf galaxies since the first *IRAS* observations of high 60/100 μm flux ratios, compared to that observed for more metal-rich environments (e.g., Helou 1986; Hunter et al. 1989; Sauvage et al. 1990; Melisse & Israel 1994). These results were then confirmed with *Spitzer* (Rosenberg et al. 2006; Cannon et al. 2006; Walter et al. 2007; Engelbracht et al. 2008). The SEDs in some low-metallicity star-forming dwarf galaxies indeed peak at shorter wavelengths, sometimes well below 100 μm, and have a steeply rising MIR continuum, representative of an overall warmer dust component (Galliano et al. 2003, 2005; Galametz et al. 2009). In comparison, the peak of the SED is around 100 - 200 μm for more metal-rich galaxies (see Fig. 1.16). This overall warmer dust is a consequence of the harder and more intense ISRF interacting with the ISM of dwarf galaxies (e.g., Madden et al. 2006).

Weak MIR aromatic features - PAHs are often barely detected in these galaxies (e.g., Sauvage et al. 1990; Madden 2000; Wu et al. 2006; Hunter & Kaufman 2007; Smith et al. 2007), if at all when the metallicity drops to a level of $\sim$ 1/3 - 1/5 $Z_\odot$ (Engelbracht et al. 2005). The paucity of dust allows the harder UV photons to travel deeper into the ISM and destroy PAH molecules by photo-evaporation or photodissociation (Galliano et al. 2003, 2005; Madden et al. 2006; Wu et al. 2006). The dearth of PAH features in dwarf galaxies has also been explained by the destruction of the molecules by SN shocks (O'Halloran et al. 2006) or by a delayed carbon injection in the ISM by asymptotic giant branch (AGB) stars (Galliano et al. 2008).

Grain size distribution - Starbursting dwarf galaxies sometimes show a higher relative abundance of small grains compared to our Galaxy. Mass can indeed be transferred from big grains to smaller grains because of fragmentation and erosion of the big grains by shock waves produced by the numerous SN in these starbursting dwarf galaxies (Jones et al. 1996; Lisenfeld et al. 2002; Galliano et al. 2003, 2005). As these low-metallicity environments are devoid of PAHs grains, too small to survive in such extreme environments, the very small grains are thus the most numerous grains in the ISM. We saw in Section 1.3 that the PAHs were normally the main actors of the gas heating in PDRs around HII regions. The dearth of PAHs in low-metallicity environments may impact the thermal balance of the gas phase, as the very small grains become the available agents for gas

heating via the photoeletric effect.

Submillimetre excess - An excess emission, unaccountable by usual SED models, is appearing in the FIR to submm/millimetre (mm) domain for some dwarf galaxies (Galliano et al. 2003, 2005; Galametz et al. 2009; Bot et al. 2010; Grossi et al. 2010; Dale et al. 2012). An excess emission has also been observed in our Galaxy with COBE (Reach et al. 1995) but with an intensity less pronounced compared to that found in low-metallicity systems. Dumke et al. (2004); Bendo et al. (2006); Zhu et al. (2009) found a submm excess in some low-metallicity spiral galaxies as well. This submm excess has been one of the main sources of uncertainty in dust modelling in dwarf galaxies for the past few years, especially on the dust mass parameter. Several explanations have already been proposed to investigate the origin of this excess, although not completely satisfactory :

1. *An additional very cold dust component:* Galliano et al. (2003, 2005), Galametz et al. (2009, 2010, 2011) modelled the submm excess they detected in their metal-poor galaxies with a very cold dust (VCD) component, residing in very dense clumps. They added to their SED models an extra modified blackbody with a submm emissivity index of 1 and a low dust temperature ($\sim$ 10K). Their additional component could explain the break observed in the submm domain in some of their SEDs but it may lead to very low gas-to-dust mass ratios, considering the observed gas mass, compared to those expected from chemical evolution and from the amount of available metals in the ISM. Moreover, Galliano et al. (2011) observed that the submm excess in the LMC is more pronounced in diffuse regions, inconsistent with the assumption of very dense clumps containing this VCD component.

2. *An additional spinning dust component:* Several studies have shown that fast rotating very small dust grains from ionized gas regions in many galaxies were producing centimetre (cm) radio emission (Ferrara & Dettmar 1994; Draine & Hensley 2012). As shown by recent studies (Ysard & Verstraete 2010; Ysard et al. 2012), the peak of the "spinning" dust emission depends on many parameters such as the radiation field intensity, the dust size distribution, dipole moment distribution, physical parameters of the gas phase, etc. This hypothesis was tested to explain the submm-to-cm excess by Bot et al. (2010), Israel et al. (2010) and Planck Collaboration et al. (2011b) in the Magellanic Clouds. The spinning dust model seems sufficient for the mm/cm excess but another effect is required to explain the submm/mm excess. Indeed, the usual spinning dust models do not normally produce much emission in the submm domain but rather at longer wavelengths (as illustrated in Murphy et al. (2010) for NGC 6946). Moreover, PAHs have been assumed to be the carriers of this spinning dust emission (as shown in Draine & Lazarian 1998) and this may seem contradictory with the weakness of the observed PAH features in low-metallicity galaxies (Engelbracht et al. 2005; Madden et al. 2006).

3. *Changes in the optical properties of the grains:*

   - *via a change in the dust grain composition:* Welty et al. (2002); Serra Díaz-Cano & Jones (2008) suggested amorphous carbon as a more realistic ISM dust analogue in lieu of graphite. Amorphous carbon grains are more emissive than graphite grains: the emissivity index, β, is 1.7 instead of 2.0 (see Sections 1.2.3, and Chapter 8). Thus using amorphous carbon instead of graphite in SED models would result in a flatter submm slope and may therefore be sufficient to explain the submm excess (Galametz et al. 2013), and suppress the need to invoke any extra dust component. Additionally, the increased emissivity for the amorphous carbon grains also implies a lower dust mass as less dust is required to account for the same luminosity, and resulting in dust masses and gas-to-dust mass ratios more coherent with those expected from chemical evolution (Galametz et al.

2010; Meixner et al. 2010; O'Halloran et al. 2010; Galliano et al. 2011; Galametz et al. 2013).

- *via grain coagulation:* Paradis et al. (2009) showed that the FIR-submm excess in dense molecular clouds of the Galaxy could be explained by fractal aggregation of amorphous individual grains which induces changes in the dust submm optical properties. This grain coagulation effect had already been suggested in the past by Bazell & Dwek (1990) and Stepnik et al. (2001).
- *via a temperature-dependent emissivity index:* Meny et al. (2007) proposed a new model for FIR/submm dust emission based on the physical properties of disordered matter. They consider the interaction of electromagnetic waves with the acoustic oscillations in a disordered charge distribution (DCD) and a distribution of low energy two level tunnelling states (TLS). This interaction results in an emission spectrum strongly dependent on the temperature and in an enhanced submm/mm emission compared to more classical models. The emissivity index is no longer constant over this wavelength range. This model has been successfully applied by Bot et al. (2010) to explain the mm excess in the LMC. However, when applied to the SMC, DCD/TLS effects alone do not reproduce the excess well (Bot et al. 2010).
- *via the addition of magnetic grains:* Recent work by Draine & Hensley (2012) on the SMC focuses on magnetic grains as a possible source of submm excess. They consider nanoparticles of metallic iron, magnetite and maghemite that could be free fliers in the ISM or inclusions on larger dust grains. Magnetic grains indeed have an enhanced absorption cross section at submm wavelengths and part of the submm excess could be due to thermal emission from magnetic grain material. They show that a combination of a normal dust mixture (amorphous silicates and carbonaceous grains), spinning dust and magnetic dust could account for the observed SED in the submm/mm range of the SMC.

We will come back to the submm excess later in Chapter 8 to see how *Herschel* and new submm data can bring new constraints on this excess, and look at the impact of using amorphous carbon instead of graphite grains.

2.2.3 Motivations for dwarf galaxies studies

Besides being the most abundant galaxy population in the Universe, dwarf galaxies pose a number of interesting issues with potentially important consequences on numerous domains in cosmological and extragalactic studies. We illustrate here a few of these issues at different spatial and time scales.

Large-scale structures and galaxy formation

Dwarf galaxies are interesting objects for cosmological studies for several reasons. As they are dominated by dark matter, they provide constraints on the dark matter distribution predicted by cosmological simulations. Currently these simulations predict an increasing number of small size dark matter halos in which dwarf galaxies reside at the present epoch. However the number of observed dwarf galaxies is way too low compared to the theoretical predictions (Moore et al. 1999). Possible explanations for this discrepancy are that these halos do not contain any visible matter and are thus undetectable (Simon & Geha 2007), or that these halos host very low surface-brightness dwarf galaxies too difficult to detect. This is known as "the missing satellite problem".

In terms of galaxy formation, dwarf galaxies have long been thought to be building blocks of the larger, more evolved systems of the present-day Universe (Dekel & Silk 1986). However evidence

for downsizing (Cowie et al. 1996), where star formation occurs first in the massive systems before proceeding to lower mass objects in the local Universe, is challenging this scenario.

Approaching the primordial Universe

Because of their low metallicity, dwarf galaxies can be considered to be chemically young objects that went through only a few episodes of star formation and that are thus at an early stage of their evolution. In this picture, they can be seen as analogues to primordial environments present in the early Universe. Those systems are very difficult (if not impossible) to observe with the current instrumentation and dwarf galaxies provide interesting local probes of ISM conditions that may resemble those of the early Universe. However the dwarf galaxies we observe today are not pristine environments as the early Universe galaxies are. Indeed, most of the time they also harbour an intermediate-age or old stellar population, signs of a complex star-formation history. This poses the interesting question of the nature and existence of the link between dwarf galaxies and primordial environments beyond chemical youth.

Dwarf galaxies also offer the possibility to approach primordial helium abundances (e.g., Pagel et al. 1992; Izotov et al. 1994, 1997; Olive et al. 1997; Peimbert et al. 2002; Luridiana et al. 2003; Steigman 2005; Izotov et al. 2007, and many others). These abundances in turn provide useful constraints on critical cosmological parameters such as the baryonic mass density of the Universe, the lifetime of the neutron and the number of neutrino families. Dwarf galaxies, and especially BCDs, are ideal laboratories to constrain the helium primordial abundance to the necessary precision. As they are chemically very young, they contain very little helium manufactured by stars and most of the helium present in the ISM of these galaxies is thus primordial helium, produced during the Big Bang nucleosynthesis.

Galaxy evolution

The external evolution of a galaxy is driven by the environment, as opposed to the internal evolution, driven by chemical enrichment (see next paragraph). This external evolution is controlled by inflows, outflows, interaction with companions or mergers. Simulations show that the more massive galaxies, to reach their current mass and size, must have experienced merging events from smaller systems in the past. As the scenario of dwarf galaxies playing the role of building blocks of more massive galaxies does not seem realistic today, we can wonder if these two main populations of galaxies: dwarfs and "normal" massive galaxies, are linked or if they are two different populations. The continuous evolution of the ISM properties between the dwarfs and massive galaxies seems to point towards the first hypothesis, even if this link is not clear.

Accessing and understanding the chemical evolution history

As we saw in Section 1.2.7, the ISM matter-life cycle implies that the metallicity of a galaxy increases as the galaxy evolves through several cycles of star formation, building up its stellar mass. Thus we should expect some kind of relation between stellar mass and metallicity, providing us with crucial information on galaxy evolution and on the physical processes governing it. This relation has indeed been observed first locally for a small sample of dwarf galaxies by Lequeux et al. (1979) and extended to a sample of $\sim$ 50,000 local star-forming galaxies by Tremonti et al. (2004). The relation between mass and metallicity holds over 3 orders of magnitude, down to $M_* = 10^{8.5}$ and a factor of 10 in metallicity. The mass-metallicity relation, or *M-Z* relation, is steep for $M_* \leq 10^{10.5}$ and flattens out at larger stellar masses. Tremonti et al. (2004) explained this flattening with chemical evolution models by invoking efficient galactic-scale winds that remove metals from low mass galaxies with shallow potential wells. Using hydrodynamical simulations, Brooks et al. (2007) have shown that in

addition to gas mass loss due to SN feedback, a mass-dependent star-formation efficiency is needed to explain the *M-Z* relation at low masses: low-mass galaxies with low star-formation efficiencies have not yet converted a lot of their gas reservoirs into stars and are therefore less metal-rich. Alternatively, a lower proportion of high-mass stars in low-mass galaxies, due to low levels of star formation, and thus a slower chemical enrichment has also been proposed (Köppen et al. 2007). The *M-Z* relation has also been observed at high redshifts (Savaglio et al. 2005; Erb et al. 2006; Maiolino et al. 2008; Mannucci et al. 2009; Cresci et al. 2012) and the relation has been seen evolving until z $\sim$ 3. Thus, investigating the population of low-mass and low-metallicity galaxies, i.e., dwarf galaxies, may provide important clues to the origin of the *M-Z* relation.

However, metal enrichment is in fact a very complex process and depends on external and internal processes occurring during galaxy evolution. Indeed, the gas phase abundance can be effected by pristine, metal-poor, gas inflows, that will dilute the ISM and decrease the metallicity of the galaxy; or by outflows driven by stellar feedback. Elements are also processed by gas and dust in the ISM as we saw in Chapter 1: elements are depleted from the gas phase when dust is formed and returned to the gas phase when dust is destroyed (see Section 1.2.6). The gas-to-dust mass ratio (G/D) links the amount of metals locked up in dust and in the gas phase and is thus a powerful tracer of the evolutionary stage of the galaxy. Investigation of the relation between G/D and metallicity can thus place important constraints on the physical processes governing galaxy evolution and more specifically on chemical evolution models and their main parameters such as SN rate, initial mass function (IMF), etc. Dwarf galaxies are thus good test cases for these models at low metallicities.

We believe that part of the answer to these issues lies in the understanding of the ISM processes occurring in low-metallicity dwarf galaxies. Throughout Section 2.2.2 we saw that the ISM of dwarf galaxies present notable peculiarities and differences compared to the ISM of more-metal rich environments, and that several of them are not fully understood yet.

Having reliable probes and diagnostics of the properties of the ISM phases in low-metallicity galaxies is necessary to start tackling these issues. A complete and well-sampled wavelength coverage of the SED is also needed to disentangle the effects of various parameters, such as metallicity, star-formation activity, morphology etc., on the ISM properties and on the processes regulating them. The advent of the *Herschel Space Observatory* at the very beginning of my PhD, provided new constraints on the FIR-to-submm domain of the SED. Before *Herschel*, the wavelength ranges accessible to the scientific community with *IRAS*, *ISO*, *Spitzer*, *AKARI* and ground-based facilities (suffering from contamination by Earth's atmosphere) were indeed poorly sampling the bulk of the dust emission beyond $\sim$ 160 μm in the FIR-submm and direct observations of the most important gas cooling lines in the FIR were missing. Moreover, the sensitivities reached by these instruments enabled accurate studies only for the brightest and highest metallicity dwarf galaxies. With its unprecedented sensitivity and wavelength coverage, *Herschel* now provides a unique opportunity to study dust and gas in the lowest-metallicity galaxies, enabling more systematic studies of these environments over a larger range of metallicities.

My work focuses especially on the dust in dwarf galaxies, and on the impact of metallicity on the dust properties. The previous discussion has demonstrated the importance and the need for such a study. The first part of my work (Chapters 3 to 5) is dedicated to the study of the cold dust component uncovered by *Herschel* in low-metallicity environments. In these Chapters, we only focus on new *Herschel* data (presented in Chapter 4) and interpret it with the aid of a modified blackbody model (Chapter 5). The second part of my work (Chapters 6 to 9) broadens our view of dust in these low-metallicity systems by looking at the total dust component across the whole IR-to-submm range (data presented in Chatper 6). The SEDs are modelled with a semi-empirical model, presented in Chapter 7 and the results are then analysed and discussed in Chapter 8. We

especially focus on the variation of the dust properties with metallicity and address the submm excess issue in this chapter. The last chapter of this thesis incorporates the gas into our dust picture and is dedicated to the variations of the G/D with metallicity. Implications for chemical evolution scenarios are discussed with the aid of three chemical evolution models.

I base my work on a survey of low-metallicity galaxies observed with *Herschel*. I also include another *Herschel* survey, containing more metal-rich environments to broaden my metallicity range towards higher metallicities and study the variations dust properties from metal-poor to metal-rich systems. The uniqueness of this work is that the dust properties are derived here in a systematic way for a large number of galaxies ($\sim$ 110), with a wavelength range as broad as possible, among which more than half are dwarf galaxies, and $\sim$ 35 % have Z $\leq$ 1/5 $Z_{\odot}$. In most of the studies mentioned previously, only single systems were studied or small samples containing 10 - 20 low-metallicity galaxies, usually with a limited number of galaxies with Z $\leq$ 1/5 $Z_{\odot}$. We saw in Section 2.2.1 that dwarf galaxies are unique systems and that it is very difficult to build a general case for these galaxies. The main challenge of my work is to treat all of the galaxies the same way, to be able to systematically compare their dust properties, without neglecting their individual specificities.

Part II

The cold dust in low-metallicity ISMs revealed by *Herschel*

Chapter 3

The *Herschel* Space Observatory

Contents

In this Chapter, I present the *Herschel* mission and the two instruments on which most of my work is based. A detailed description of the two *Herschel* surveys I use for my study is given in the last two sections.

3.1 The mission

3.1.1 Description

The *Herschel* Space Observatory was approved by ESA in 1993 as the fourth "cornerstone" mission in the ESA "Horizon 2000" long-term plan. It was successfully launched on the 14^{th} of May 2009, together with *Planck*, and operated for about 4 years, providing the community with more than 25,000 hours of science data. It operated autonomously far away from Earth on an orbit around the 2^{nd} Lagrangian point of the Sun-Earth/Moon system. Initially named FIRST (Far InfraRed and Submillimetre space Telescope) at the beginning of the mission, it was renamed after the discoverer of infrared light, William Herschel, for the 200^{th} anniversary of this discovery in 2000.

Herschel was designed, following *Spitzer*, to offer a higher spatial resolution and sensitivity compared to the previous space missions and to explore the relatively unknown FIR/submm wavelength range, where dust emits the bulk of its energy (see Chapter 1). Among the widely-ranging scientific targets of the mission, we can find stars in the early-phase of formation in their birth molecular cloud in the Galaxy, ISMs of local galaxies or high-redshift star-forming galaxies (up to z $\sim$ 5). The science objectives of *Herschel* thus cover all the possible time and spatial scales: from local feedback of evolved stars in the ISM of very nearby galaxies to star-formation history of the universe and galaxy evolution over cosmological times. *Herschel* was dedicated to the study of the ISM and the cold Universe in its most general sense. In our case, we look at local ISM properties of nearby galaxies and study how dust properties vary in environments of metal content lower than in our Galaxy.

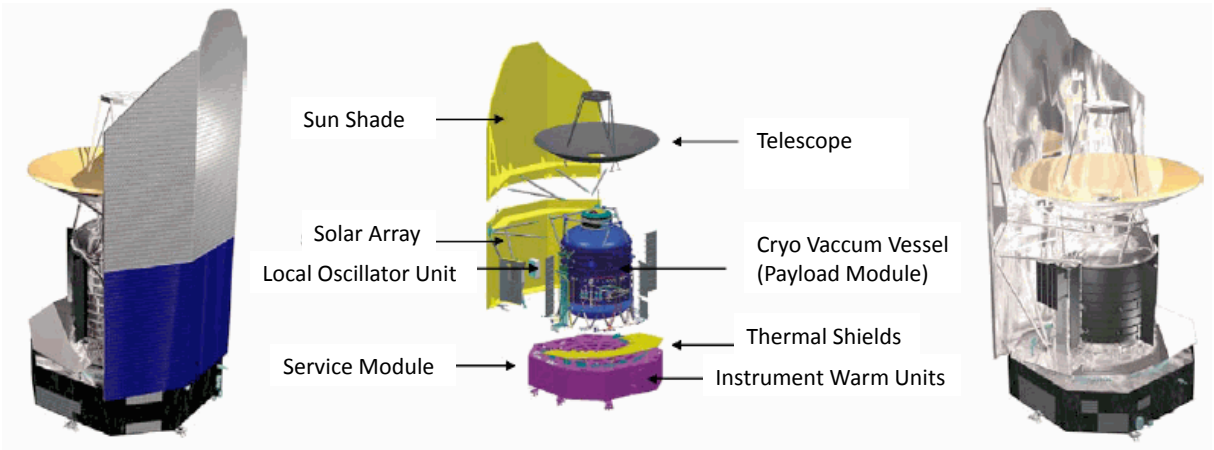

Fig. 3.1. The *Herschel* Space Observatory, seen on the "warm" side (*left*) and on the "cold" side (*right*). The various components of the spacecraft are labelled on the schematic view in the centre.

The mission consists of a spacecraft, equipped with three instruments cooled down to 0.3 K by liquid superfluid helium inside a cryostat. The spacecraft is composed of the payload module carrying the three instruments, the telescope, the service module, and the sunshield/sunshade (Fig. 3.1[1]).

[1]Image from the *Herschel* Observers' Manual, available at http://herschel.esac.esa.int/twiki/bin/view/Public/SpacecraftObservatoryWeb?template=viewprint.

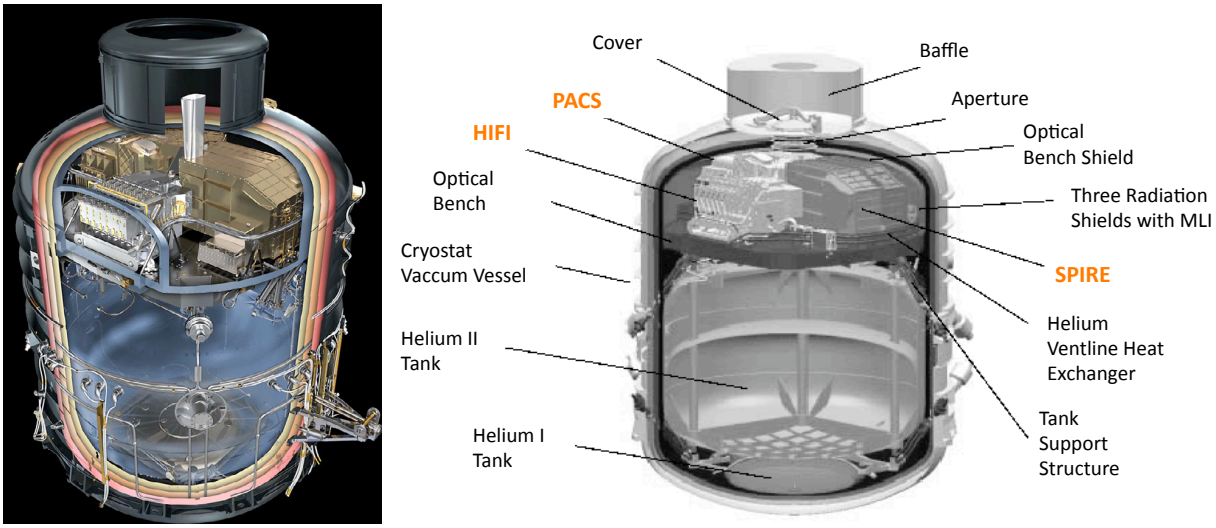

Fig. 3.2. (*left*) The payload module (from Pilbratt et al. (2010)). (*right*) Schematic view of the payload module where all of the components have been labelled. The three instruments are highlighted in orange (adapted from the *Herschel* Observers' Manual).

Autonomous observations according to the timelines, accurate pointings, on-board data handling, and communication with the ground are handled by the spacecraft. The telescope has a typical Cassegrain optical design and a diameter of 3.5 m, making it the largest mirror, that does not need a deployable structure, ever launched in space and reaches unprecedented sensitivities.

Table 3.1. Main capabilities of the three instruments on board *Herschel*. The first rows, marked with "P" describe the photometers capabilities. The last rows, marked with "S" show the spectrometers capabilities. In bold, the two instruments used in my work: PACS and SPIRE photometers.

		PACS	**SPIRE**	HIFI
P	Range	60-210 μm 70 or 110 μm and 160 μm (simultaneous)	200-670 μm 250, 350, 500 μm (simultaneous)	
	FOV	$1.75' \times 3.5'$	$4' \times 8'$ (unfilled)	
	Sensitivity (5σ/1hr)	5 mJy (70/110 μm), 10 mJy (160 μm)	Confusion limit: 5.8mJy (250 μm), 6.3mJy (350 μm), 6.8mJy (500 μm)	
S	Range	55-210 μm	194-313 and 303-671 μm	157-213 and 240-625 μm (with gap)
	FOV	$47'' \times 47''$	$2.0'$(unvignetted)	$39''$ (488 GHz) $13''$ (1408 GHz)
	Sensitivity (5σ/1hr)	$2\text{x}10^{-18}$ Wm^{-2} (130μm, 1^{st} order), $5\text{x}10^{-18}$ (70 μm, 3^{rd} order) Continuum: 100 mJy (1^{st} order), 250 mJy (3^{rd} order)	1.0-2.2x10^{-17} Wm^{-2} (high res.) 40-88 mJy (low res.)	"A few" mK (Band 1a) to 100mK (Band 7b), 1σ/1hr
	Resolution	900-2100 (1st order, 102-210 μm), 1800-3000 (2nd order, 72-98 μm), 2600-5400 (3rd order, 55-72 μm)	20-1000	1000-10^7

Note: Table adapted from Tables 3.1 and 3.2 of the *Herschel* Observers' Manual.

If we zoom into the payload module, we find the three instruments on board *Herschel* the Photodetector Array Camera and Spectrometer (PACS - Poglitsch et al. 2010), the Spectral and Photometric Imaging REceiver (SPIRE - Griffin et al. 2010) both imaging photometers and medium resolution spectrometers, and the Heterodyne Instrument for the Far Infrared (HIFI - de Graauw

et al. 2010), a very high resolution heterodyne spectrometer (Fig. 3.2). The PACS and SPIRE photometers in combination cover a 60 to 670 μm range, and the three spectrometers together cover 55 to 670 μm. The basic informations on the three instruments can be found in Table 3.1.

3.1.2 The novelty of *Herschel*

The era of infrared space astronomy began with the *InfraRed Astronomical Satellite* (*IRAS*) in 1983. Since then, several other IR telescopes have been launched including the *Infrared Space Observatory* (*ISO*), the *Spitzer* Space Telescope, the *Wide-field Infrared Survey Explorer* (*WISE*) and *AKARI*. The wavelength ranges and sensitivities covered by *Spitzer*, *ISO* and *IRAS* do not sample the cold dust component of the dust SED beyond 160 μm. Some ground-based telescopes such as *JCMT*, *APEX*, *SEST*, *IRAM* could detect the cold dust beyond 160 μm, but because of sensitivity limitations, accurate measurements of the photometry could only be obtained for the brightest and highest metallicity dwarf galaxies. With unprecedented sensitivity and spatial resolution, *Herschel* is helping to fill this gap in spectral range and complete our view of dust in the widest range of galaxy types and distances, and, in particular, constraining the cold dust contribution. Table 3.2 summarises various capabilities for the cited space telescopes. Fig. 3.3 illustrates the improvement in spatial resolution brought by *Herschel* on the nearby dwarf galaxy NGC 1705. The two knots are well separated in both *Herschel*/PACS images whereas they are blurred in *Spitzer*/MIPS images and indistinguishable at 160 μm.

Table 3.2. Comparison of the infrared telescopes capabilities.

	Launch	Wavelength (μm)	Spatial resolution at 100 μm ($''$)	Sensitivity at 100 μm (mJy)
IRAS	1983	12 - 100	150	200[a]
ISO	1995	2 - 240	90	10[a]
Spitzer	2003	3 - 180	38 (at 160 μm)	1[b]
AKARI	2006	1.7 - 180	39 (at 90 μm)	3.2[c]
WISE	2006	2.5 - 25	-	-
Herschel	2009	55 - 670	12	1
Planck	2009	350 - 10^4	-	-

[a]: The sensitivities are 1σ values for 1 hour integration time in the 100 μm broadband filter.
[b]: The sensitivities are 1σ values for 1 hour integration time in the 160 μm broadband filter.
[c]: The sensitivities are 1σ values for 2 second integration time in the 90 μm broadband filter.

3.2 The PACS and SPIRE photometers

3.2.1 PACS

Description

The PACS photometer performs dual band imaging over a field of view (FOV) of $1.75' \times 3.5'$, with full sampling of the telescope point spread function (PSF). Two bands can be observed simultaneously: either 70 and 160 μm or 100 and 160 μm. The light is spread between the blue (70 or 100 μm) and the red (160 μm) bolometers and is collected by the bolometers arrays in the focal plane (Fig.

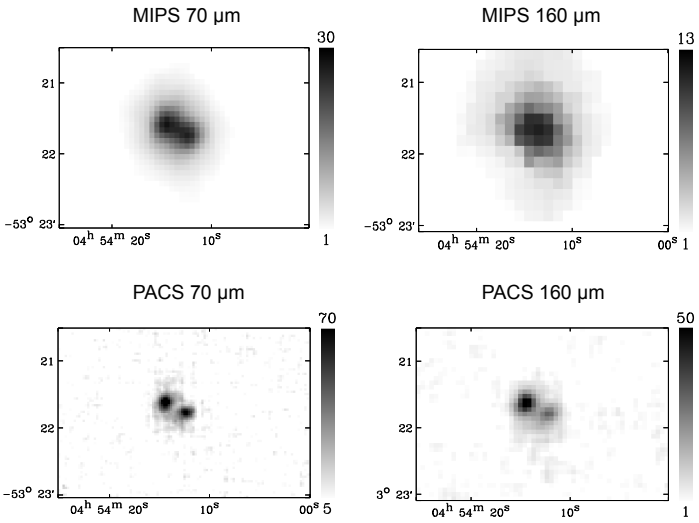

Fig. 3.3. Observations of the galaxy NGC1705 with MIPS and PACS: Illustration of the improvement in spatial resolution between *Spitzer*/MIPS (*top row*) and *Herschel*/PACS (*bottom row*) at 70 μm (*left column*) and 160 μm (*right column*) (from Madden et al. 2013). The two knots are well separated at PACS resolutions. The full width at half maximum (FWHM) of the PACS beams for the 70 and 160 μm bands are 5.6″ and 11.4″ while for the MIPS bands the FWHM values are 18″ and 38″. The colour scale is in MJy/sr.

3.4[2]). The pointing accuracy has been measured to 2″ at the 1σ level on pointed observations. The photometer characteristics are presented in Table 3.3.

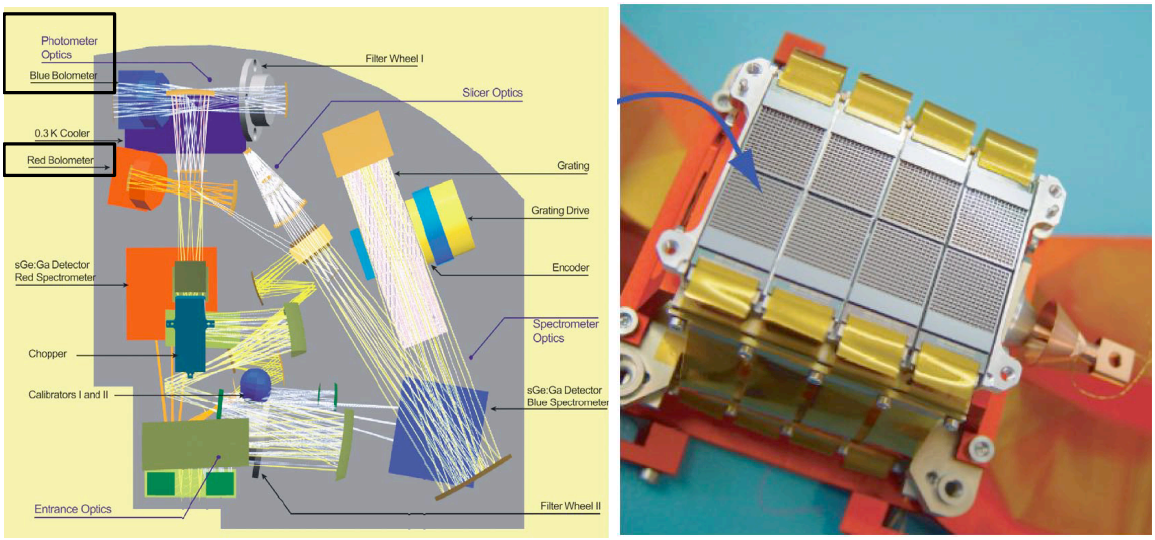

Fig. 3.4. (*left*) Optical layout of the PACS instrument. The photometer optics are on the top left of the picture (framed by the black rectangles). (*right*) Bolometer matrices of the PACS blue bolometer array. The total blue bolometer array assembly is 64x32 pixels and is composed of 4x2 monolithic matrices of 16x16 pixels, as shown here. In a similar way, the red bolometer array assembly is 16x32 pixels (2x1 monolithic matrices).

[2]Image from the PACS Observers' Manual, available at http://herschel.esac.esa.int/twiki/bin/view/Public/PacsCalibrationWeb?template=viewprint.

The PACS PSF (see Fig. 3.5 for the PSF at 100 μm [3]), which represents the way the light from a point source is spread onto the detectors, has been measured out to 1000″, using version 7 of the PACS photometric calibration tree available in the *Herschel* Interactive Processing Environment (HIPE, Ott 2010). This means that a small contribution of the flux from a point source can be found as far as 1000″ away from the centre of the source. The encircled energy fraction (*eef*) tables, given by HIPE, quantify the fraction of the total flux density contained in a given aperture on the PSFs (inverse of the aperture correction) and are presented in Fig. 3.5. This will have important consequences for determining accurate photometry of our sources (see Chapter 4).

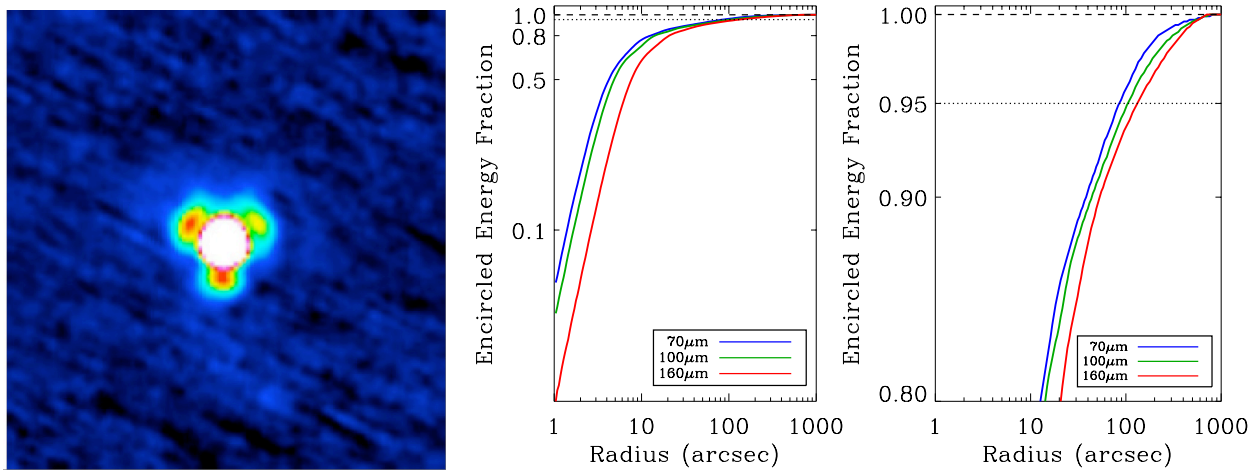

Fig. 3.5. (*left*) The PACS photometer PSF at 100 μm, displayed with a linear scale up to 10% of the peak. Note the tri-lobe pattern of the PSF, due to an imperfection on the mirror due to the secondary mirror tripod. (*centre and right*) PACS Encircled Energy Fractions as a function of radius. The right handside is a zoom between 0.8 and 1.0. The dashed line corresponds to the 100% line and the dotted line to the 95% line.

The filter transmission curves are shown in Fig. 3.9 and can be extracted from HIPE. PACS has been calibrated on 5 stars for use as primary calibrators and on asteroids plus fainter stars as secondary calibrators. The calibration accuracy is 5% in each band and is dominated by the calibration model uncertainty.

What is observed by the bolometers, $\bar{F}_S$, is directly proportional to the source flux density, $\mathrm{F}_S(\nu)$, weighted by the filter transmission, hereafter called the Relative Spectral Response Function, $\mathrm{R}(\nu)$, (RSRF, as in SPIRE Observers' Manual). $\bar{F}_S$ is given by:

$$\bar{F}_S = \frac{\int F_S(\nu) R(\nu)\,\mathrm{d}\nu}{\int R(\nu)\,\mathrm{d}\nu} \tag{3.1}$$

To obtain a monochromatic flux density, the pipeline has to assume a shape for the spectrum of the source and a standard frequency, ν_0. For PACS, the standard frequencies are the frequencies corresponding to λ_0={70,100,160} μm. Here the spectral convention is $\nu \times F_\nu$ = constant or $\mathrm{F}_S(\nu) = \mathrm{F}_S(\nu_0) \times (\nu_0/\nu)$, also used for PACS calibration. Importing this in Eq. 3.1 gives:

$$\bar{F}_S = F_S(\nu_0)\nu_0 \frac{\int R(\nu)/\nu\,\mathrm{d}\nu}{\int R(\nu)\,\mathrm{d}\nu} \tag{3.2}$$

Inverting Eq. 3.2 will give the monochromatic flux density, i.e., the output of the pipeline, $\mathrm{F}_S(\nu_0)$, as a function of what is observed by the bolometers, $\bar{F}_S$:

[3] Image from the PACS Observers' Manual.

$$F_S(\nu_0) = \bar{F}_S K_4 \tag{3.3}$$

where K_4 is:

$$K_4 = \frac{1}{\nu_0} \frac{\int R(\nu)\,\mathrm{d}\nu}{\int R(\nu)/\nu\,\mathrm{d}\nu} \tag{3.4}$$

However, there is no particular reason for the source to have a spectral shape $F_S(\nu) \propto \nu^{-1}$. Thus we need to correct the output of the pipeline to the real spectral shape of the source: this is the colour correction.

If the source "true" spectral shape, $F'_S(\nu)$, is unknown, we can derive $F'_S(\nu_0)$ via:

$$F'_S(\nu_0) = F_S(\nu_0) \frac{\bar{F}'_S}{\bar{F}_S} \tag{3.5}$$

This transforms into:

$$F'_S(\nu_0) = \frac{\int F'_S(\nu) R(\nu)\,\mathrm{d}\nu}{\int (F_S(\nu)/F_S(\nu_0)) R(\nu)\,\mathrm{d}\nu} \tag{3.6}$$

Using $F_S(\nu) = F_S(\nu_0) \times (\nu_0/\nu)$, we transform Eq. 3.6 into:

$$F'_S(\nu_0) = \frac{\int F'_S(\nu) R(\nu)\,\mathrm{d}\nu}{\int (\nu_0/\nu) R(\nu)\,\mathrm{d}\nu} \tag{3.7}$$

Observing modes

There are three different observing modes for the PACS photometer: a point source photometry chop-nod mode, a scan map technique for small or large fields, and another scan map technique within the PACS/SPIRE parallel mode. Here we describe shortly the second one as it is the one used for our observations. The map in scan map mode is made by moving the telescope on the sky along parallel lines, called scan legs, at a constant speed (Fig. 3.6). The scan leg length depends on the size of the desired map, and the scan speed for our observations is 20″/s. To obtain a smoother map, a better PSF reconstruction and to remove the striping effects due to the *1/f* noise, it is recommended to do two scan maps with two orthogonal scan directions for one source. For point sources, a mini-scan map mode is preferred over the chop-nod mode, as it increases the point source sensitivity in all bands. It is a special case of the scan map mode with 3′ scan legs and where the scanning is done along the two diagonals of the bolometer detector.

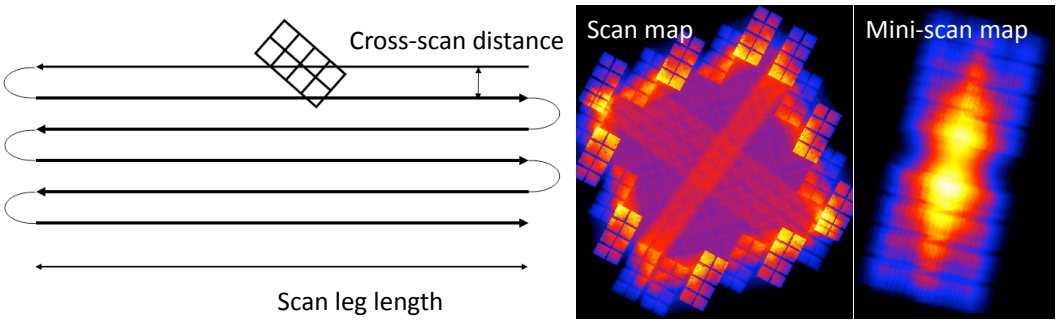

Fig. 3.6. (*left*) Example of a scan map with 6 scan line legs (from the PACS Observers' Manual). (*right*) Coverage maps of a scan map and a mini-scan map (from our observations).

3.2.2 SPIRE

Description

The SPIRE photometer observes the three bands simultaneously over a $4' \times 8'$ field of view. The detector arrays are composed of 139, 88 and 43 bolometers at 250, 350 and 500 μm respectively. Several bolometers in each array are centred on the same position on the sky for all three arrays (see blue bolometers in Fig. 3.7[4]).

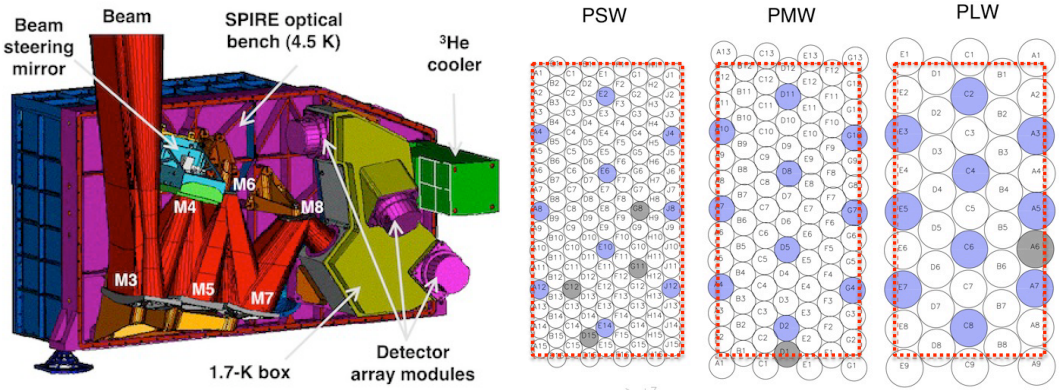

Fig. 3.7. (*left*) SPIRE focal plane unit on the photometer side. (*right*) Schematic view of the bolometers arrays. The blue bolometers are the bolometers centered on the same position on the sky for the 3 arrays. The grey bolometers are the dead bolometers. The $4' \times 8'$ field of view is delineated by the red dashed rectangle.

The SPIRE photometer characteristics are presented in Table 3.3. The beam areas are given here as they will be needed to convert the flux densities extracted from the map in Jy/beam to Jy (see Chapter 4). Neptune was used as a primary calibrator for the photometer calibration. There are two different SPIRE calibration uncertainties: a systematic uncertainty of $\sim 5\%$ coming from the models used for Neptune, which is correlated between the three bands, and a random uncertainty of $\sim 2\%$ coming from the repetitive measurement of the flux densities of Neptune. These two uncertainties are added linearly instead of in quadrature as advised in the SPIRE Observers' Manual, giving an overall 7% calibration accuracy for the SPIRE photometer[5].

To treat the signal from the source, the pipeline assumes that the source is a point source, uses the same spectral convention of $\nu \times F_\nu = \text{constant}$ as PACS, and outputs monochromatic in-beam flux densities at standard frequencies corresponding to 250, 350 and 500 μm. The reasoning will be the same as for PACS, except that the output will be in units of Jy/beam.

However, for SPIRE, the filter transmission for each band depends on the extent of the source. If the source is extended, the response function has to be weighted by λ^2 to take into account the fact that the beam width varies across the band depending on the wavelength, leading to additionnal power coupled from extended emission. The two response functions for a point source, $\mathrm{R}_P(\lambda)$, and an extended source, $\mathrm{R}_E(\lambda)$, for each band are shown in Fig. 3.9, with $\mathrm{R}_E(\lambda) = \mathrm{R}_P(\lambda) \times (\lambda_0/\lambda)^2$. The K_4 factor, to convert $\bar{F}_S$ into $\mathrm{F}_S(\nu_0)$ then depends if the source is extended, $\mathrm{K}_4 = \mathrm{K}_{4E}$, or not, $\mathrm{K}_4 = \mathrm{K}_{4P}$. As the pipeline does not know if the source is extended or compact, the default will be to assume that the source is a point source, and use K_{4P} in Eq. 3.3. Thus to get the

[4]Image from the SPIRE Observers' Manual, available at http://herschel.esac.esa.int/twiki/bin/view/Public/SpireCalibrationWeb?template=viewprint.

[5]Since this manuscript has been written, the values for the SPIRE calibration and the uncertainties may have been updated. The same goes for the beam areas. We advise the reader to treat these numbers with caution.

monochromatic flux density for an extended source, one has to multiply $F_S(\nu_0)$, the output of the pipeline, by K_{4E}/K_{4P} (see Chaper 4). The K_{4P} and K_{4E}/K_{4P} values are given in Table 3.3.

The colour corrections work the same as for PACS and Eq. 3.7 can be used for SPIRE too. Given the type of source observed by SPIRE, in most cases it could be appropriate to assume that the source spectrum follows a power law with a spectral index, α_S, i.e., $F'_S(\nu) = F'_S(\nu_0) \times (\nu_0/\nu)^{\alpha_S}$ where $F'_S(\nu_0)$ is the source flux density at ν_0 for the "true" spectral shape. In this case, Eq. 3.7 transforms into:

$$F'_S(\nu_0) = F_S(\nu_0) \frac{\nu_0}{\nu_0^{\alpha_S}} \frac{\int R(\nu)/\nu \, \mathrm{d}\nu}{\int R(\nu)/\nu^{\alpha_S} \, \mathrm{d}\nu} \tag{3.8}$$

Observing modes

SPIRE offers three observing modes: a Large area map mode, a Small area map mode and a Point Source Photometry map. We describe briefly here the first two only, as they correspond to the modes used to perform our observations. The Large map mode is used to cover large areas of the sky or extended sources ($> 5'$ diameter) and the map is made by scanning the telescope on the sky, at a given scan speed. For our observations, the speed used is the nominal scan speed of $30''$/s. The Small map mode is for sources with diameters $< 5'$, and the map is made by doing two short cross-scans with the telescope. The difference in coverage is shown in Fig. 3.8[6].

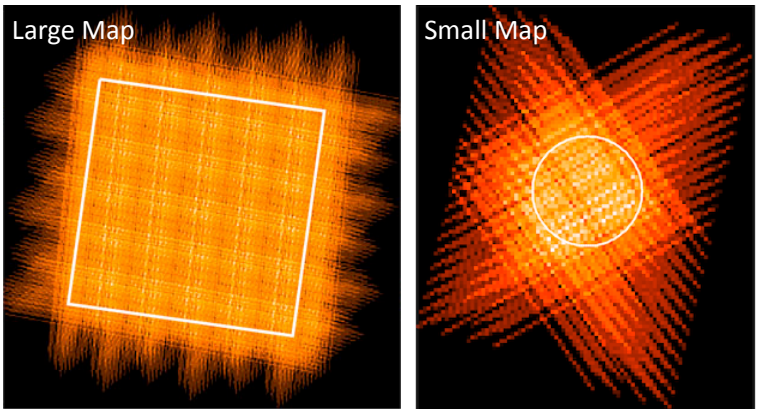

Fig. 3.8. Example of a Large (*left*) and Small (*right*) scan map coverage with SPIRE.

3.3 Low metallicity with *Herschel* : the Dwarf Galaxy Survey

3.3.1 Description

The Dwarf Galaxy Survey (DGS, PI: S. Madden) is one of the three *Herschel* Guaranteed Time Key Programs of the SPIRE Local Galaxies consortium (SAG2). The two other programs are the *Herschel* Reference Survey (HRS, PI: S. Eales) and the Very Nearby Galaxy Survey (VNGS, PI: C. Wilson). The DGS aims at studying the gas and dust properties in low-metallicity ISM with *Herschel*. It is a photometric and spectroscopic survey of 50 dwarf galaxies at FIR and submm wavelengths. For a more detailed description of the general goals of the survey and the source selection process, see the Dwarf Galaxy Survey Overview by Madden et al. (2013). In this work,

[6]Image from the SPIRE Observers' Manual.

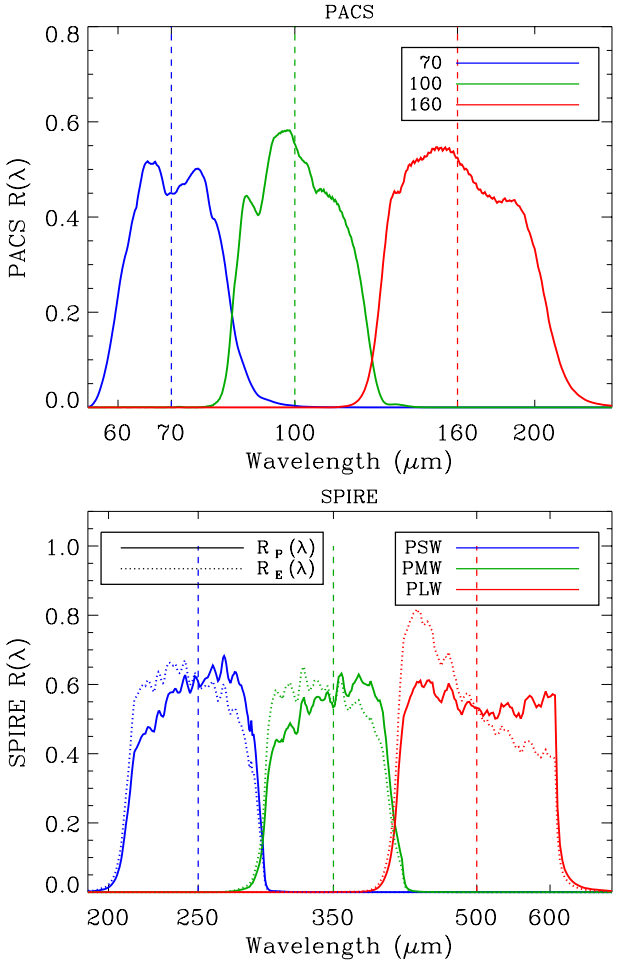

Fig. 3.9. (*top*) PACS filter transmissions, R(λ). (*bottom*) SPIRE filter transmissions for point sources, $R_P(\lambda)$, plain lines, and extended sources, $R_E(\lambda)$, dotted lines (see text for details). On both plots, the dashed lines mark the reference wavelength for each band.

Table 3.3. PACS and SPIRE characteristics.

PACS				
Band	λ (μm)	Range (μm)	FHWM ($''$)	Calibration accuracy
Blue	70	60 - 85	5.6	5%
Green	100	85 - 125	6.8	5%
Red	160	125 - 210	11.4	5%

SPIRE							
Band	λ (μm)	Range (μm)	FHWM[a] ($''$)	Beam Areas[b] ($''^2$)	Calibration accuracy	K^c_{4P}	K^c_{4E}/K_{4P}
PSW	250	200 - 300	18.2	465	7%	1.0113	0.9828
PMW	350	270 - 430	24.9	822	7%	1.0087	0.9834
PLW	500	375 - 670	36.3	1768	7%	1.0065	0.9710

[a]: The SPIRE beam FWHM values are given for maps with standard pixel size of 6, 10, 14$''$at 250, 350, 500 μm.
[b]: SPIRE photometer reference spectrum values: http://herschel.esac.esa.int/twiki/bin/view/Public/SpirePhotometerBeamProfileAnalysis, September 2012 values. The errors on the beam areas are of $\sim$ 4%.
[c]: The values have been taken from the SPIRE Observers' Manual, Version 2.4, Section 5.2.8.

we focus on the dust and thus only on the 48 targets for which complete photometry was obtained. Throughout this manuscript, we thus consider that the total sample consists of the 48 photometry targets of the DGS (leaving out the LMC and SMC only done in spectroscopy).

The DGS survey is composed of some well-known Local Group sources (such as IC10, NGC6822, NGC1569) and a selection of sources from several optical line emission surveys including the Hamburg/SAO Survey (i.e., HS0017+1055) and the Second Byurakan Survey (i.e., SBS0335-052). The DGS target sources come from follow-up observations which specifically identified the metal-deficient BCDs from the surveys (e.g., Izotov et al. 1991; Ugryumov et al. 2003; Popescu & Hopp 2000), as well as the sample of Izotov & Thuan (1999); Hopkins et al. (2002) which contain some of the better-studied BCDs.

The targets of the DGS span a wide range in various parameters such as morphology, star-formation rate, stellar and gas mass and metallicity, with objects among the most metal-poor galaxies in the local Universe (Figs. 3.11 and 3.12). The metallicities range from 12+log(O/H) = 7.14 (IZw18, Z $\sim$ 1/40 $Z_{\odot}$, Izotov et al. 1999) to 8.43 (He2-10, Z $\sim$ 0.55 $Z_{\odot}$, Kobulnicky et al. 1999). The closest source is NGC 6822 at 500 kpc and the more distant is HS0052+2536 at 191 Mpc (Fig. 3.12). Typical star-formation rates range over 4 orders of magnitude from 0.0007 $M_{\odot}\,yr^{-1}$ (UGC4483) to 28 $M_{\odot}\,yr^{-1}$ (Haro11), with many of the dwarf galaxies containing super star clusters. The DGS contains mostly objects of Irr type (VIIZw403) along with a few dwarf spiral galaxies (NGC625). Stellar masses range over 4 orders of magnitudes, from 3$\times$10^6 $M_{\odot}$ (UGC4483) to 3$\times$10^{10} $M_{\odot}$ (Haro11).

3.3.2 Metallicity determination

The most important parameter throughout my study is metallicity. Thus we have to be certain that the metallicities for our samples, are determined in a homogeneous way to avoid any discrepancy or unreliable metallicity trends.

As we saw in Chapter 2, there are several methods for estimating the metallicity of a galaxy. We explore and compare two different methods here: the so-called "direct" method based on the direct measurement of the electron temperature T_e(OIII) from the detection of the [OIII]λ4363 auroral line, and a "strong-line" method which uses an empirical calibration of metallicity from the [OII]λ3727 and [OIII]$\lambda\lambda$4959,5007 strong emission lines. The first method should be more accurate, and closer to the "true" metallicity value, but as the [OIII]λ4363 auroral line is not detected in higher-metallicity environments, we also need to have measurements from a "strong-line" method in order to have a homogeneous set of metallicity values over the largest metallicity range possible. We follow the method and the equations presented in Izotov et al. (2006), hereafter I06, for the "direct" method; and in Pilyugin & Thuan (2005), hereafter PT05, for the "strong-line" method. The PT05 method uses the R_{23} ratio[7].

Direct determination following I06

The O^+ and O^{2+} abundances are computed using the following relations:

$$12 + \log\left(\frac{O^+}{H^+}\right) = \log\frac{\lambda3727}{H\beta} + 5.961 + \frac{1.676}{t} - 0.40\log t - 0.034t + \log(1 + 1.35x) \quad (3.9)$$

$$12 + \log\left(\frac{O^{2+}}{H^+}\right) = \log\frac{\lambda4959 + \lambda5007}{H\beta} + 6.200 + \frac{1.251}{t} - 0.55\log t - 0.014t \quad (3.10)$$

[7]Remember from Chapter 2, $R_{23} = \frac{[OII]\lambda3727+[OIII]\lambda\lambda4959,5007}{H\beta}$

where $t = 10^{-4}$ T_e and $x = 10^{-4}$ N_e $t^{-0.5}$. For O^{2+} in Eq. 3.10, $T_e = T_e(OIII)$ and for O^+ in Eq. 3.9, $T_e = T_e(OII)$. $t(OIII)$ is given by the formula of Aller (1984):

$$t(OIII) = \frac{1.432}{\log[(\lambda 4959 + \lambda 5007)/\lambda 4363] - \log C_T} \tag{3.11}$$

where C_T is given by:

$$C_T = \left(8.44 - 1.09t + 0.5t^2 - 0.08t^3\right) \frac{1 + 0.0004x}{1.0.044x} \tag{3.12}$$

$t(OII)$ can be deduced from $t(OIII)$ using the relations of Stasińska & Izotov (2003).

O^{3+} only represents a small fraction of the total oxygen abundance. Photoionisation models show that O^{3+}/O is $\geq 1\%$ only in the highest excitation regions with $O^+/(O^+ + O^{2+}) \lesssim 0.1$. In these regions we can approximate O^{3+}/H^+ by:

$$\frac{O^{3+}}{H^+} = 0.5 \frac{He^{2+}}{He^+ + He^{2+}} \left(\frac{O^+}{H^+} + \frac{O^{2+}}{H^+}\right) \tag{3.13}$$

using the $\lambda 4471$ line for He^+ and the $\lambda 4686$ line for He^{2+}. When $O^+/(O^+ + O^{2+}) \geq 0.1$, $O^{3+}/H^+ \sim 0$ and we assume we can neglect it. We find that O^{3+} has to be taken into account in three galaxies only: HS0822+3542, Pox186 and Tol1214-277.

Finally the oxygen abundance is given by summing up all of the ionic abundances:

$$\frac{O}{H} = \frac{O^+}{H^+} + \frac{O^{2+}}{H^+} + \frac{O^{3+}}{H^+} \tag{3.14}$$

Empirical determination following PT05

The relations used to derive the metallicities are the following:

$$12 + \log(O/H)_{upper} = \frac{R_{23} + 726.1 + 842.2P + 337.5P^2}{85.96 + 82.76P + 43.98P^2 + 1.793R_{23}} \tag{3.15}$$

$$12 + \log(O/H)_{lower} = \frac{R_{23} + 106.4 + 106.8P - 3.40P^2}{17.72 + 6.60P + 6.95P^2 - 0.302R_{23}} \tag{3.16}$$

where P is an excitation parameter given by:

$$P = \frac{[OIII]\lambda\lambda 4959, 5007/H\beta}{R_{23}} = \frac{[OIII]\lambda\lambda 4959, 5007}{[OII]\lambda 3727 + [OIII]\lambda\lambda 4959, 5007} \tag{3.17}$$

Following Kewley & Ellison (2008), we use the upper (resp. lower) calibration branch when $\log([NII]\lambda 6584/[OII]\lambda 3727) >$ (resp. $\leq$) -1.2.

For both methods the errors from the line intensities are propagated to the oxygen abundance using:

$$\Delta f = \sqrt{\sum_{i=1}^{N} \left(\frac{\partial f}{\partial x_i} \Delta x_i\right)^2} \tag{3.18}$$

for a function f of N variables x_i, i=[1..N].

Comparison of the two methods

All of the optical line intensities and their uncertainties are collected from the literature (see references in Table 3.4). For some galaxies, metallicities were computed using the mean (O/H) of several HII regions. The DGS metallicities for the two methods are listed in Table 3.4. The references listed in Table 3.4 are the references for the original optical line intensities. The comparison between the two methods is shown in Fig. 3.10 and the mean ratio between the two methods is 0.004 dex with an average deviation of 0.10 dex. For 63% of the galaxies, the two metallicity estimates are within 0.1 dex from each other. And all of the galaxies, except two, have their two metallicity estimates corresponding within 0.2 dex. The two deviant galaxies (Tol0618-402 and UM448) show very high [OII]λ3727 intensities that can boost up their PT05 metallicity compared to their I06 metallicity.

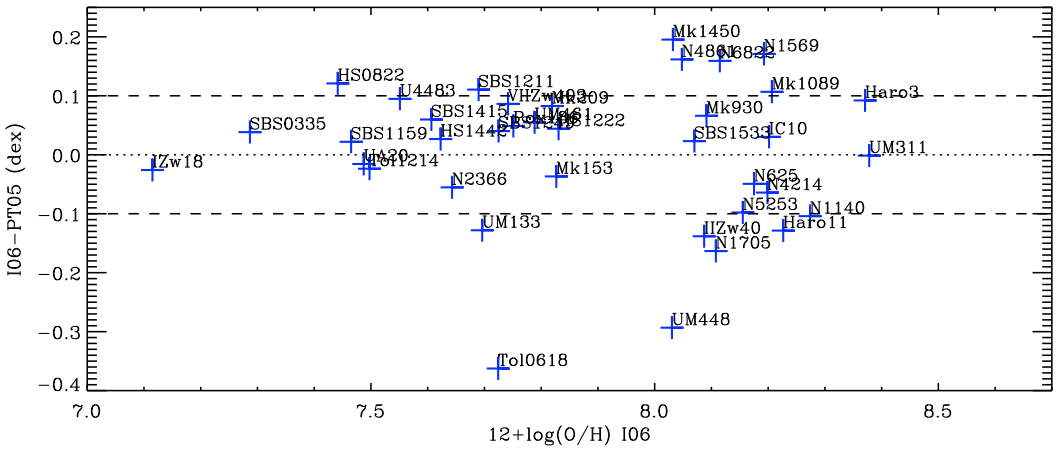

Fig. 3.10. Comparison of the metallicity estimates of the DGS using the methods of I06 and PT05. The unity line is indicated as a dotted line and the mean deviation of 0.1 dex as dashed lines.

For our study, we also use more metal-rich environments (see 3.4), for which only PT05 measurements are available (Moustakas et al. 2010; Kennicutt et al. 2011). Thus from now on, we work with the PT05 metallicity values for the DGS galaxies for consistency. The final metallicity distribution for the DGS sample is presented in Fig. 3.11.

3.3.3 Other parameters

The target list is presented in Table 3.5 along with galaxy characteristics:

- (1): Galaxy name.
- (2) and (3): RA (J2000) and DEC (J2000). Positions are from the NASA/IPAC Extragalactic Database (NED).
- (4): Distance, D. Any distance quoted here not referenced to the literature, has been determined using the velocities given in NED and the Mould et al. (2000) model, assuming $H_0 = 70$ km s^{-1} Mpc^{-1}.
- (5): Metallicity, in terms of oxygen abundances: 12+log(O/H). The values quoted here are the PT05 values, except where noted.
- (6): Absolute magnitude in band B M_B. They have been determined from the apparent magnitudes, m_B, from NED using: m_B - M_B = 5(log(D)-1) where D is the distance in pc.

Table 3.4. Metallicities for the DGS determined following either the I06 or the PT05 method.

Sources	12+log(O/H) I06	12+log(O/H) PT05	Ref
Haro11[d]	8.23 ± 0.03	8.36 ± 0.01	1
Haro2[a]	-	8.23 ± 0.03	2
Haro3	8.37 ± 0.02	8.28 ± 0.01	3
He2-10[a]	-	8.43 ± 0.01	4
HS0017+1055[b]	7.63 ± 0.10	-	5
HS0052+2536[b,d]	8.07/8.04 ± 0.20	-	5
HS0822+3542	7.44 ± 0.06	7.32 ± 0.03	6
HS1222+3741	7.83 ± 0.03	7.79 ± 0.01	7
HS1236+3937	7.47 ± 0.04	7.72 ± 0.01	8
HS1304+3529	7.66 ± 0.04	7.93 ± 0.01	8
HS1319+3224	7.59 ± 0.04	7.81 ± 0.01	8
HS1330+3651	7.66 ± 0.04	7.98 ± 0.01	8
HS1442+4250	7.62 ± 0.02	7.60 ± 0.01	9
HS2352+2733[b]	8.40 ± 0.20	-	5
IZw18[d]	7.11 ± 0.04	7.14 ± 0.01	10
IC10[d]	8.20 ± 0.06	8.17 ± 0.03	11
IIZw40	8.09 ± 0.02	8.23 ± 0.01	12
Mrk1089[c,d]	8.39/8.21 ± 0.12	8.30/8.10 ± 0.08	13
Mrk1450	8.03 ± 0.01	7.84 ± 0.01	14
Mrk153	7.83 ± 0.05	7.86 ± 0.04	15
Mrk209	7.82 ± 0.01	7.74 ± 0.01	16
Mrk930	8.09 ± 0.03	8.03 ± 0.01	17
NGC1140	8.27 ± 0.08	8.38 ± 0.01	3
NGC1569	8.19 ± 0.03	8.02 ± 0.02	18
NGC1705[d]	8.11 ± 0.13	8.27 ± 0.11	19
NGC2366	7.64 ± 0.02	7.70 ± 0.01	20
NGC4214	8.20 ± 0.03	8.26 ± 0.01	4
NGC4449[a]	-	8.20 ± 0.11	21
NGC4861	8.05 ± 0.01	7.89 ± 0.01	16
NGC5253	8.16 ± 0.03	8.25 ± 0.02	4
NGC625[d]	8.18 ± 0.03	8.22 ± 0.02	22
NGC6822[d]	8.11 ± 0.07	7.96 ± 0.01	23
Pox186	7.75 ± 0.01	7.70 ± 0.01	24
SBS0335-052	7.29 ± 0.01	7.25 ± 0.01	17
SBS1159+545	7.46 ± 0.02	7.44 ± 0.01	14
SBS1211+540	7.69 ± 0.01	7.58 ± 0.01	14
SBS1249+493	7.72 ± 0.01	7.68 ± 0.02	25
SBS1415+437	7.61 ± 0.01	7.55 ± 0.01	26
SBS1533+574[d]	8.07 ± 0.02	8.05 ± 0.01	16
Tol0618-402[d]	7.72 ± 0.01	8.09 ± 0.01	27
Tol1214-277	7.50 ± 0.03	7.52 ± 0.01	4
UGC4483	7.55 ± 0.04	7.46 ± 0.02	28
UGCA20[d]	7.49 ± 0.01	7.50 ± 0.01	29
UM133	7.70 ± 0.05	7.82 ± 0.10	4
UM311[c]	8.38/8.36 ± 0.05	8.38/8.36 ± 0.01	17,30,31
UM448	8.03 ± 0.04	8.32 ± 0.01	17
UM461	7.79 ± 0.03	7.73 ± 0.01	15
VIIZw403	7.74 ± 0.01	7.66 ± 0.01	16

Notes:
[a]: For these galaxies, the [OIII]λ4363 line was not detected and a direct determination of the metallicity with the I06 method is therefore not possible.
[b]: For these galaxies, no line intensities were available in the litterature. Ugryumov et al. (2003) use the [OIII]λ4363 line to get the electron temperature and method from Izotov et al. (1994). I06 is an updated version of the method of Izotov et al. (1994), and thus we chose to quote the results of Ugryumov et al. (2003) in the I06 column.
[c]: These objects are galaxies within compact groups of galaxies or are parts of other galaxies. We chose to quote the value of the metallicity for the galaxy only (on the left) and for the whole group (on the right), which is the mean of all of the metallicities in the group. For Mrk1089, the galaxy is region A-C, and the group is composed of regions A-C, B, E, F1, F2, H from López-Sánchez et al. (2004). For UM311, the galaxy is region 3 following the denomination of Moles et al. (1994), and the group is composed of regions 1-2-3 of Moles et al. (1994) plus NGC450 and UGC807. It was not possible to find a metallicity or lines intensities for UGC807. For HS0052+2536 the group is composed of HS0052+2536 and HS0052+2537. For all of the galaxies the group corresponds to the galaxies included in the aperture used for *Herschel* photometry (see Chapter 4).
[d]: For these galaxies, the final metallicities are derived from the mean (O/H) of several HII regions.

References for metallicities: (1) Guseva et al. (2012) ; (2) Kong et al. (2002) ; (3) Izotov et al. (2004) ; (4) Kobulnicky et al. (1999) ; (5) Ugryumov et al. (2003) ; (6) Pustilnik et al. (2003) ; (7) Izotov et al. (2007) ; (8) Popescu & Hopp (2000) ; (9) Guseva et al. (2003a) ; (10) Izotov et al. (1999) ; (11) Magrini & Gonçalves (2009) ; (12) Guseva et al. (2000) ; (13) López-Sánchez et al. (2004) ; (14) Izotov et al. (1994) ; (15) Izotov et al. (2006) ; (16) Izotov et al. (1997) ; (17) Izotov & Thuan (1998) ; (18) Kobulnicky & Skillman (1997) ; (19) Lee & Skillman (2004a) ; (20) Saviane et al. (2008) ; (21) McCall et al. (1985) ; (22) Skillman et al. (2003) ; (23) Lee et al. (2006) ; (24) Guseva et al. (2007) ; (25) Thuan et al. (1995) ; (26) Guseva et al. (2003b) ; (27) Masegosa et al. (1994) ; (28) van Zee & Haynes (2006) ; (29) van Zee et al. (1996) ; (30) Moles et al. (1994) ; (31) Pilyugin & Thuan (2007)

- (7): Galaxy size in terms of D_{25}.
- (8): Stellar mass, M_*, obtained from the formula of Eskew et al. (2012) using the 3.6 and 4.5 μm IRAC flux densities, $F_{3.6}$ and $F_{4.5}$ derived in Chapter 6:

$$M_* = 10^{5.65} F_{3.6}^{2.85} F_{4.5}^{-1.85} \left(\frac{D}{0.05}\right)^2 \tag{3.19}$$

  where D is the distance in Mpc.
- (9): Atomic HI gas mass, M_{HI}. If needed, they have been corrected for the distance used here.
- (10): Pre-*Herschel* total infrared (TIR) luminosity, L_{TIR}, determined from the formula of Dale & Helou (2002), using the 24, 70 and 160 μm *Spitzer*/MIPS luminosities, L_{24}, L_{70} and L_{160} from Bendo et al. (2012):

$$L_{TIR} = 1.559 \times (\nu_{24} L_{24}) + 0.7686 \times (\nu_{70} L_{70}) + 1.374 \times (\nu_{160} L_{160}) \tag{3.20}$$

  Some galaxies were not observed with one or more of the MIPS bands. When available, we used the IRAS luminosities and the corresponding IRAS formula from Dale & Helou (2002):

$$L_{TIR} = 2.403 \times (\nu_{25} L_{25}) + 0.7686 \times (\nu_{60} L_{60}) + 1.374 \times (\nu_{100} L_{100}) \tag{3.21}$$

- (11): Star formation rate, SFR, using the IR-based calibration of Kennicutt (1998):

$$SFR[\mathrm{M_\odot\,yr^{-1}}] = \frac{\mathrm{L_{TIR}[erg.s^{-1}]}}{2.2 \times 10^{43}} = \frac{\mathrm{L_{TIR}[L_\odot]}}{5.8 \times 10^9} \tag{3.22}$$

  with L_{TIR} from Column (10). For sources where L_{TIR} was not available, we used Hα or Hβ luminosities to convert to SFR:

$$SFR[\mathrm{M_\odot\,yr^{-1}}] = \frac{\mathrm{L_{H\alpha}[erg.s^{-1}]}}{1.26 \times 10^{41}} = \frac{2.85 \times \mathrm{L_{H\beta}[erg.s^{-1}]}}{1.26 \times 10^{41}} \tag{3.23}$$

The wide range of parameters spanned by the DGS targets is illustrated in Fig. 3.11 and 3.12.

3.3.4 Observations with *Herschel*

The design of the DGS is an attempt to obtain a statistically significant sample of about 9 galaxies in 7 bins over a wide metallicity range: 12+log(O/H) ranging from 8.4 (1/3 $Z_\odot$), in bins of

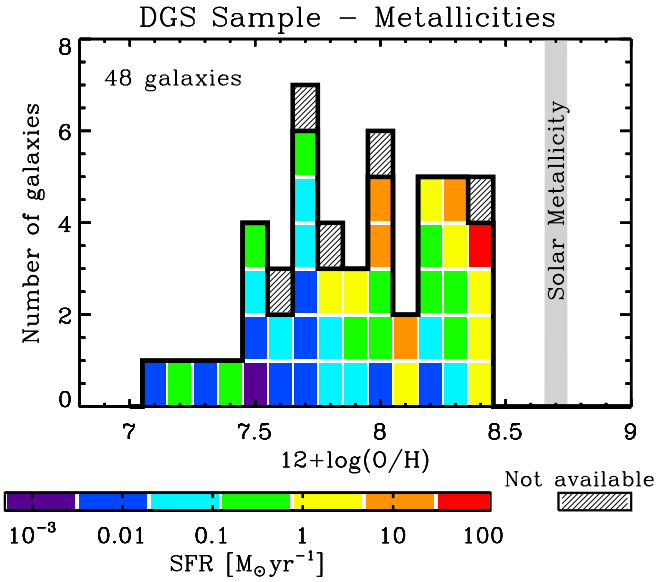

Fig. 3.11. Metallicity distribution of the DGS sample from 12+log(O/H) = 7.14 to 8.43. Solar metallicity is indicated here as a guide to the eye. The pre-*Herschel* Star Formation Rate (*SFR*) distribution is also indicated by the colour code. They have been converted from L_{TIR}(*Spitzer*) with the Kennicutt (1998) law and are given in Table 3.5. When no IR data was available, *Hα* or *Hβ* emission lines were used and converted to *SFR* (Kennicutt 1998) (see Section 3.3.3 for details). The dashed cells indicate that none of these data were available for the galaxy. The most actively star-forming galaxy (in red) corresponds to the starburst luminous infrared galaxy (LIRG) Haro 11.

12+log(O/H)=0.2 (a factor of 1.4 difference) to provide an accuracy of $\sim$ 30%. As can be seen from Figure 3.11, it was not possible to have a uniform sample in terms of metallicity, due to lack of availability or detectability of such extreme low-metallicity sources in the local Universe. We also did not insist on populating our highest metallicity bins, since metal-rich galaxies are plentiful in other surveys, such as the HRS (Boselli et al. 2010b), the *Herschel* Virgo Cluster Survey (Davies et al. 2012) and the KINGFISH survey (Kennicutt et al. 2011), for example.

The DGS was granted $\sim$ 230 hours of observations, part of which were used to observe the sample with the two *Herschel* imaging photometers: all of them (48) with PACS at 70, 100 and 160 μm and 41 with SPIRE at 250, 350 and 500 μm. Seven sources were not observed with SPIRE because they were predicted to be too faint for SPIRE.

For all of our galaxies, the PACS photometry observations have been done in the PACS scan-map mode, with map sizes varying from $4'\times4'$ to $30'\times30'$, at a medium scan speed ($20''$/s). Mapping the largest galaxies of the Local Group with the 3 PACS bands required $\sim$10h of observing time per galaxy. The SPIRE observations have been made using the SPIRE Large and Small scan-map modes, depending on the source sizes, at the nominal scan speed ($30''$/s). Mapping the 11 larger galaxies takes about 1h at most per galaxy to reach the desired sensitivities with SPIRE while the small scan mode required about 10 minutes per galaxy. We planned observations to completely cover the star-forming regions and, where possible, much of the HI structure to be able to access the low surface brightness dust in diffuse metal-poor regions. A nominal size of at least 2 $\times$ D_{25} was thus considered for most photometry maps.

The technical details of the DGS observations are summarised in Appendix A.

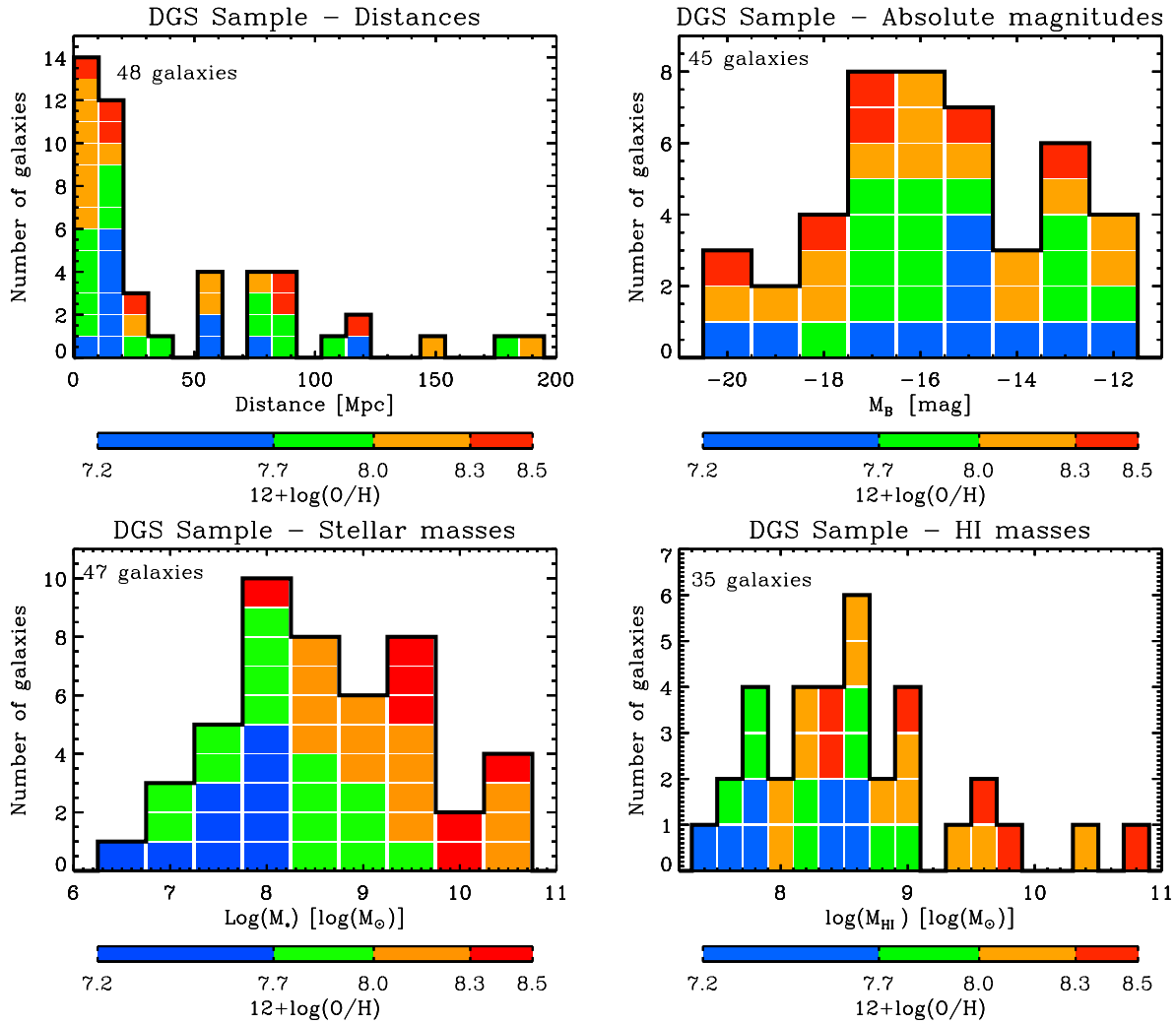

Fig. 3.12. Properties of the DGS sample: Distributions of distances, D, *(top left)*, absolute B magnitudes, M_B, *(top right)*, stellar masses, M_* *(bottom left)* and HI masses *(bottom right)*. The colour scale represents the range of metallicity values. Galaxies for which the parameter is not available or is an upper limit are not shown here. The number of DGS galaxies on the plot is indicated on the top left of each panel.

3.3.5 Ancillary data

The DGS galaxies have been observed with numerous ground-based and space-based observatories (Fig. 3.13). Having the full range of UV to radio observations available opens the door to some very powerful multiphase modelling of the dust and gas, and to a coherent picture of chemical evolution of galaxies. With the vast multi-wavelength *Herschel* data set, along with the complementary data that exists or is being collected, the physical characteristics of the nebular gas, the photodissociation regions, the neutral gas and stellar properties can be characterized.

The first step in exploiting the *Herschel* observations has been the construction of the detailed database of existing observations from UV to radio wavelengths. In addition to the new PACS and SPIRE photometry and spectroscopy, the database includes the NIR to mm bands necessary to best characterize the dust properties using existing *IRAS* data, *WISE* NIR to MIR measurements, *Spitzer* MIR to FIR observations, the critical ground-based submm observations: 850 μm, 870 μm and 1.2 mm data from SCUBA/*JCMT* or SCUBA-2/*JCMT*, LABOCA/*APEX*, MAMBO/*IRAM* as well as *Planck* data, which is complementing the longer submm to radio wavelengths. We also include *Spitzer* IRS spectroscopy to access the atomic, ionized and molecular gas phases. To characterize the stellar activity, 2MASS and GALEX data have also been collected.

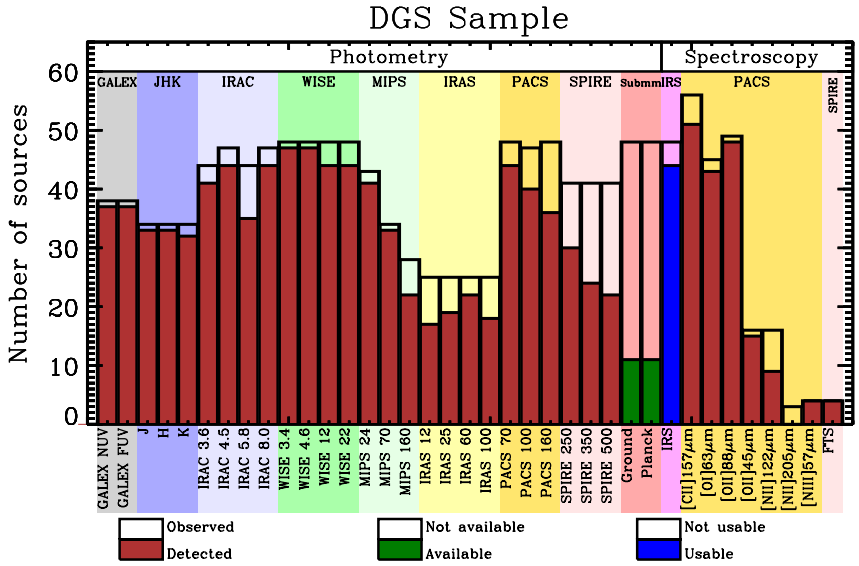

Fig. 3.13. Histogram of the number of observed and detected *Herschel* sources in the DGS program along with the accompanying ancillary data that has been collected. Note that PACS spectroscopy includes 7 individual LMC and SMC sources, thus accounting for the larger number (55 sources) in the histogram while the accompanying LMC and SMC *Herschel* photometry data is in the HERITAGE program.

The ancillary data compiled for the DGS sample to date include the following:

- GALEX maps in FUV and NUV (1528 and 2271Å). Observations are collected from the STScI MAST archive (http://galex.stsci.edu/GR6/). These data give us a view into the star-formation histories of the galaxies by capturing the direct UV emission from young stars to the most recent star-formation activity (e.g., Hunter et al. 2010). The dust absorption properties in the UV provide additional constraints on the SED modelling of the dust emission properties in the MIR to FIR. GALEX observations exist for all but 9 galaxies of the DGS sample.

- 2MASS observations have been compiled from IRSA (http://irsa.ipac.caltech.edu/) and exist for 34 galaxies in the DGS. The J, H and K_S bands from 2MASS provide direct access to the emission from the oldest stellar population.

- *Spitzer* has observed all 50 targets of the DGS with various combinations of IRAC bands at 3.6, 4.5, 5.8 and 8.0 μm and MIPS bands at 24, 70 and 160 μm. The IRAC and MIPS data consist of a combination of archival data and the cycle 5 program: Dust Evolution in Low-Metallicity Environments (P.I. F. Galliano; ID: 50550). The MIPS data are reduced and compiled in Bendo et al. (2012) and have been recently publicly released. *Spitzer* data will enable us to constrain the MIR part of the SEDs and get access, for example, to the PAH features (through the 8 and 24 μm bands) or to the old stellar population (through the first IRAC bands). Furthermore MIPS shares two bands with PACS at 70 and 160 μm. This will be very useful to compare the two instruments and confirm the reliability of our PACS results (see Chapter 6). *Spitzer* IRS spectroscopy, covering 5 to 35 μm, exists for all but 5 of the DGS galaxies and have been recently reprocessed (see Chapter 6). The IRS spectroscopy covers the PAHs bands as well as many ionized lines that are relatively bright in dwarf galaxies.

- The sensitivity of *IRAS* at 12, 25, 60 and 100 μm provides data for about half of the DGS sample (data from the NASA/IPAC IRSA database). The 12 μm observations provide an additional valuable MIR constraint useful for modelling the global SEDs of the DGS galaxies.

- Most of the DGS galaxies have also been detected by *WISE* at 3.4, 4.6, 12 and 22 μm (data from the NASA/IPAC IRSA database). The 22 μm observations, especially, will give the necessary constraints on the MIR wavelength range of the SED when neither *IRAS* 25 μm nor *Spitzer* 24 μm are available.

- Submm observations from ground-based telescopes are crucial to determine the presence and characterization of the submm excess (see Chapter 8). Usually this excess may begin to appear around 450-500 μm compelling observations beyond 500 μm. About 30% of the DGS sample have already been observed in the submm range with either the MAMBO 1.2 mm (*IRAM* - 30m telescope), LABOCA (*APEX*), SCUBA(*JCMT*) or SCUBA-2 (*JCMT*). After submitting several proposals, we obtained new observations for DGS sources with LABOCA on *APEX*, presented in Section 6.5.3, to augment the submm observations to characterize and study the submm excess.

- *Planck* has observed the sky with bands from 30 to 857 GHz. Due to the relatively large *Planck* beams (4.5' to 33') and limited sensitivity, only a handful of galaxies (eleven) are included in the *Planck* Early Release Catalog and in the *Planck* Catalog of Compact Sources.

A summary of the available ancillary data can be found in Table 3.6. Figure 3.13 gives a view of the range of existing *Herschel* and ancillary data for the DGS sample, and how many galaxies were detected for the different data sets.

3.4 Comparing with more metal-rich galaxies: the KINGFISH sample

To enrich our study of the DGS and determine the impact of metallicity on the dust properties, we perform a comparison with galaxies from another *Herschel* sample: Key Insights on Nearby Galaxies: a Far-Infrared Survey with *Herschel* (KINGFISH, Kennicutt et al. 2011). KINGFISH is a survey including more metal-rich galaxies and enables us to span a wider metallicity range, notably by populating the high-metallicity end of the metallicity distribution (Fig. 3.14).

The KINGFISH survey contains 61 galaxies: 41 spiral galaxies, 11 early-type galaxies (E and S0) and 9 irregulars (Kennicutt et al. 2011), all observed in the 6 *Herschel* bands. It has been built with 57 galaxies from the *Spitzer* Infrared Nearby Galaxies Survey (SINGS, Kennicutt et al. 2003a), to which were added IC0342, NGC2146, NGC 3077 and NGC5457. The metallicities adopted here for most of the KINGFISH sample have been determined the same way as for the DGS in Moustakas et al. (2010), using the method of Pilyugin & Thuan (2005). The KINGFISH metallicities are from Column 9 from Table 1 of Kennicutt et al. (2011). We have to note also that for 12 galaxies, no HII region measurement is available in the literature and the metallicities were estimated from the luminosity-metallicity relation. No errors for metallicities are given in Kennicutt et al. (2011) so we adopt a conservative 0.1 dex error for the KINGFISH metallicities. For the four additional sources, IC0342, NGC2146, NGC 3077 and NGC5457, Kennicutt et al. (2011) gives a reference for the metallicity but do not precise if the metallicities were just extracted from the referenced paper or recomputed from original line intensities. Thus for these four sources we recompute the metallicities using the original line intensities from the literature:

- For IC0342, the line ratios were taken from McCall et al. (1985) and we derive a PT05 metallicity of 8.46, close to the value reported by Kennicutt et al. (2011): 8.49.
- For NGC2146, Kennicutt et al. (2011) uses the metallicity determined by Engelbracht et al. (2008) which computed the metallicity using the PT05 method. We thus keep the metallicity given by Kennicutt et al. (2011) for this galaxy.
- For NGC5457, we find a metallicity of 12+log(O/H) = 8.42 using the optical line ratios of the 25 regions studied by Kennicutt et al. (2003a). This value is a bit lower than the value reported by Kennicutt et al. (2011): 8.68.
- For NGC3077, no metallicity is reported for the PT05 calibration in Kennicutt et al. (2011). We used McQuade et al. (1995) optical fluxes and derived a PT05 metallicity of 12+log(O/H) = 8.52 for this galaxy. The metallicity reported by Kennicutt et al. (2011) using the theoretical calibration of Kobulnicky & Kewley (2004) is 8.9. The difference between the two metallicity estimates, 0.4 dex, is of the same order than that observed for the other KINGFISH galaxies.

The distances, metallicities and TIR luminosities can be found in Kennicutt et al. (2011). The stellar masses are derived from the IRAC fluxes densities (from Dale et al. 2007) using Eq. 3.19, and most of the HI masses can be found in Draine et al. (2007) (see Chapter 9). The SFR are derived from the TIR luminosities and Eq. 3.22. Fig. 3.14 shows the properties of the KINGFISH sample. This sample spans a 1.2 dex range in metallicity, ranges over 4 orders of magnitudes in stellar mass and 3 orders of magnitude in HI mass. The DGS distributions for each parameter are overlaid on Fig. 3.14 to facilitate the comparison between the two samples. We see that the two samples complement each other very well in terms of metallicities, stellar and gas masses (Fig. 3.14 and Table 3.4). Indeed the KINGFISH sample brings in more metal-rich galaxies (the median metallicity is 8.4 compared to 7.9 for the DGS) with higher stellar masses (the median $\log(M_*)$ is 10.4 compared to 8.6 for the DGS) and higher gas masses (the median $\log(M_{HI})$ is 9.1 compared to 8.6 for the DGS).

Since most of the KINGFISH sources are from SINGS, a large range of ancillary data is available for these galaxies, especially UV to submm photometry (Dale et al. 2005, 2007), including 2MASS, *Spitzer*, *IRAS* and SCUBA. For a more detailed description of the available data for the KINGFISH survey, see Kennicutt et al. (2011). The *Herschel* data is presented in Dale et al. (2012).

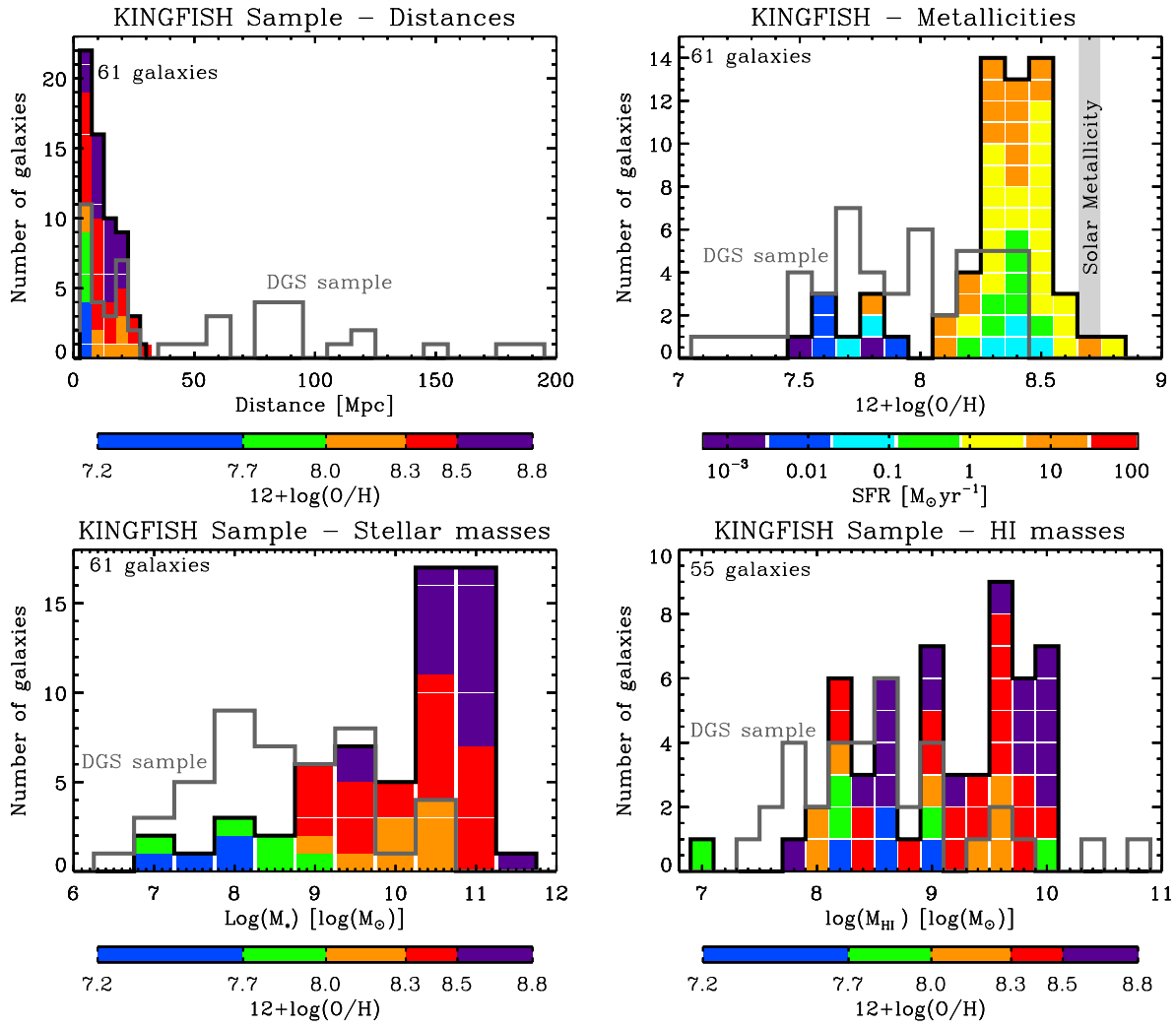

Fig. 3.14. Properties of the KINGFISH sample: Distributions of distances, D, *(top left)*, metallicities, in terms of 12+log(O/H), *(top right)*, stellar masses, M_* *(bottom left)* and HI masses *(bottom right)*. The colour scale represents the range of star-formation rate for the *top right* panel and metallicity for the others. Colour scales are identical as for Fig. 3.11 and 3.12. Galaxies for which the parameter is not available or is an upper limit are not shown here. The number of KINGFISH galaxies on the plot is indicated on the top left of each panel. The DGS distributions for each parameter are indicated in grey.

Table 3.4. Main characteristics of the DGS and KINGFISH parameters.

		D [Mpc]	12+log(O/H)	M_B	Log(M_*) [Log($M_\odot$)]	Log(M_{HI}) [Log($M_\odot$)]	Log(SFR) [Log($M_\odot$ yr^{-1})]
DGS	min: max	0.50: 191.00	7.14: 8.43	-20.00: -12.00	6.47: 10.53	6.30: 10.79	-3.70: 1.46
	median	19.80	7.93	-16.00	8.64	8.60	-1.06
KINGFISH	min: max	3.00: 30.60	7.54: 8.77	-	7.24: 11.68	7.06: 10.06	-2.93: 1.24
	median	9.70	8.35	-	10.44	9.08	0.00

Table 3.5. Characteristics of the DGS sample.

Source	RA (J2000)	DEC (J2000)	Distance Mpc (ref)	12 + log(O/H) (ref)	M_B (ref)	Size (D_{25}) arcmin × arcmin	$M_\star$ 10^8 $M_\odot$	M_{HI} 10^8 $M_\odot$(ref)	Log(L_{TIR}) Log($L_\odot$)	SFR $M_\odot$ yr^{-1}
Haro 11	00h36m52.7s	-33d33m17.0s	92.1 (1)	8.36 ± 0.01 (1)	-20.55 (1)	0.5'x0.4'	172.0	5.0 (1)	11.22	28.61
Haro 2	10h32m32.0s	+54d24m02.0s	21.7 (2)	8.23 ± 0.03 (2)	-18.28 (1)	1.2'x0.8'	36.7	3.8 (2)	9.72	0.91
Haro 3	10h45m22.4s	+55d57m37.0s	19.3 (3)	8.28 ± 0.01 (3)	-18.29 (1)	1.2'x0.8'	30.9	11.3 (3)	9.67	0.81
He 2-10	08h36m15.1s	-26d24m34.0s	8.7 (21)	8.43 ± 0.01 (4)	-17.25 (1)	1.9'x1.4'	31.8	3.1 (4)	9.66	0.79
HS 0017+1055	00h20m21.4s	+11d12m21.0s	79.1 (3)	7.63 ± 0.10[a] (5)	-16.23 (2)	-	0.69	≤ 1.7 (5)	-	-
HS 0052+2536	00h54m56.4s	+25d53m08.0s	191.0 (3)	8.07/8.04 ± 0.20[a,b] (5)	-19.56 (2)	-	204.0	≤ 482.0 (6)	-	-
HS 0822+3542	08h25m55.5s	+35d32m32.0s	11.0 (4)	7.32 ± 0.03 (6)	-12.40[d] (3)	0.27'x0.12'	0.03	0.77 (7)	≤ 7.04	≤ 0.002
HS 1222+3741	12h24m36.7s	+37d24m37.0s	181.7 (3)	7.79 ± 0.01 (7)	-17.90 (4)	0.12'x0.11'	23.7	-	-	1.51
HS 1236+3937	12h39m20.2s	+39d21m05.0s	86.3 (3)	7.72 ± 0.10[c] (8)	-16.00 (4)	0.34'x0.09'	≤ 14.9	-	-	0.09
HS 1304+3529	13h06m24.2s	+35d13m43.0s	78.7 (3)	7.93 ± 0.10[c] (8)	-17.73 (4)	0.28'x0.21'	3.8	-	-	0.50
HS 1319+3224	13h21m19.7s	+32d08m25.0s	86.3 (3)	7.81 ± 0.10[c] (8)	-15.68 (4)	0.14'x0.11'	1.1	-	-	-
HS 1330+3651	13h33m08.3s	+36d36m33.0s	79.7 (3)	7.98 ± 0.10[c] (8)	-17.81 (5)	0.29'x0.19'	8.9	-	-	0.38
HS 1442+4250	14h44m12.8s	+42d37m44.0s	14.4 (3)	7.60 ± 0.01 (9)	-15.15 (4)	1.13'x0.26'	-	3.1 (5)	≤ 7.59	≤0.007
HS 2352+2733	23h54m56.7s	+27d49m59.0s	116.7 (3)	8.40 ± 0.20[a] (5)	-17.05 (2)	-	≤1.3	≤ 230.0 (6)	-	-
I Zw 18	09h34m02.0s	+55d14m28.0s	18.2 (5)	7.14 ± 0.01 (10)	-15.22 (1)	0.3'x0.3'	0.2	1.0 (8)	≤ 7.74	≤ 0.01
II Zw 40	05h55m42.6s	+03d23m32.0s	12.1 (20)	8.23 ± 0.01 (11)	-14.93 (1)	0.56'x0.22'	4.0	5.7 (9)	9.40	0.43
IC 10	00h20m17.3s	+59d18m14.0s	0.7 (6)	8.17 ± 0.03 (12)	-12.43 (1)	6.8'x5.9'	2.6[e]	1.1 (10)	7.80[f]	0.01
Mrk 1089	05h01m37.7s	-04d15m28.0s	56.6 (3)	8.30/8.10 ± 0.08[b] (13)	-20.46 (1)	0.61'x0.23'	192.0	210.0 (11)	10.60[f]	6.86
Mrk 1450	11h38m35.7s	+57d52m27.0s	19.8 (3)	7.84 ± 0.01 (14)	-13.86[d] (3)	0.40'x0.31'	1.2	0.43 (12)	8.44	0.05
Mrk 153	10h49m05.0s	+52d20m08.0s	40.3 (3)	7.86 ± 0.04 (15)	-18.03 (1)	0.54'x0.30'	11.4	≤6.9 (13)	8.97	0.16
Mrk 209	12h26m15.9s	+48d29m37.0s	5.8 (7)	7.74 ± 0.01 (16)	-13.67 (1)	0.8'x0.6'	0.29	0.74 (13)	7.49	0.005
Mrk 930	23h31m58.3s	+28h56m50.0s	77.8 (3)	8.03 ± 0.01 (17)	-	0.43'x0.43'	27.5	31.9 (14)	10.26	3.12
NGC 1140	02h54m33.6s	-10d01m40.0s	20.0 (8)	8.38 ± 0.01 (3)	-18.55 (1)	1.7'x0.9'	44.2	35.0 (24)	9.52	0.57
NGC 1569	04h30m49.0s	+64d50m53.0s	3.1 (9)	8.02 ± 0.02 (18)	-15.75 (1)	3.6'x1.8'	8.4	1.8 (15)	9.04	0.19
NGC 1705	04h54m13.5s	-53d21m40.0s	5.1 (10)	8.27 ± 0.11 (19)	-15.73 (1)	1.9'x1.4'	2.2	0.9 (16)	7.82	0.01
NGC 2366	07h28m54.6s	+69d12m57.0s	3.2 (11)	7.70 ± 0.01 (20)	-16.18 (1)	8.1'x3.3'	1.9	7.4 (17)	8.13	0.02
NGC 4214	12h15m39.2s	+36d19m37.0s	2.9 (12)	8.26 ± 0.01 (4)	-17.11 (1)	8.5'x6.6'	8.4	4.1 (15)	8.73	0.09
NGC 4449	12h28m11.1s	+44d05m37.0s	4.2 (13)	8.20 ± 0.11 (21)	-17.94 (1)	6.2'x4.4'	26.9	11.0 (15)	9.33	0.36
NGC 4861	12h59m02.3s	+34d51m34.0s	7.5 (14)	7.89 ± 0.01 (16)	-16.84 (1)	4.0'x1.5'	3.1	4.8 (18)	8.49	0.05
NGC 5253	13h39m55.9s	-31d38m24.0s	4.0 (12)	8.25 ± 0.02 (4)	-16.87 (1)	5.0'x1.9'	5.9	1.6 (19)	9.14	0.24
NGC 625	01h35m04.6s	-41d26m10.0s	3.9 (15)	8.22 ± 0.02 (22)	-16.20 (1)	5.8'x1.9'	5.4	1.1 (29)	8.41	0.04
NGC 6822	19h44m57.7s	-14d48m12.0s	0.5 (16)	7.96 ± 0.01 (23)	-13.19 (1)	15.5'x13.5'	1.6	1.3 (20)	7.6	0.007
Pox 186	13h25m48.6s	-11d36m38.0s	18.3 (3)	7.70 ± 0.01 (24)	-12.17[d] (3)	-	0.12	≤ 0.02 (21)	-	0.04
SBS 0335-052	03h37m44.0s	-05d02m40.0s	56.0 (3)	7.25 ± 0.01 (17)	-16.02 (6)	0.23'x0.20'	1.1	4.6 (22)	≤ 9.23	≤ 0.29
SBS 1159+545	12h02m02.4s	+54d15m50.0s	57.0 (3)	7.44 ± 0.01 (14)	-15.08 (7)	0.20'x0.10'	0.70	≤ 0.63 (5)	-	0.17
SBS 1211+540	12h14m02.5s	+53d45m17.0s	19.3 (3)	7.58 ± 0.01 (14)	-13.43 (8)	0.26'x0.17'	0.40	0.56 (12)	-	0.02
SBS 1249+493	12h51m52.5s	+49d03m28.0s	110.8 (3)	7.68 ± 0.02 (25)	-	0.10'x0.10'	2.7	10.0 (23)	-	-
SBS 1415+437	14h17m01.4s	+43d30m05.0s	13.6 (17)	7.55 ± 0.01 (26)	-14.99[d] (3)	0.75'x0.15'	0.94[e]	4.4 (12)	≤ 7.78	≤ 0.01
SBS 1533+574	15h34m13.8s	+57d17m06.0s	54.2 (3)	8.05 ± 0.01 (16)	-16.69[d] (3)	0.67'x0.67'	19.9	30.0 (14)	≤ 10.30[f]	≤3.44
Tol 0618-402	06h20m02.5s	-40d18m09.0s	150.8 (3)	8.09 ± 0.01 (27)	-	0.4'x0.3'	271.0	-	≤ 9.91	≤ 1.40
Tol 1214-277	12h17m17.1s	-28d02m33.0s	120.5 (3)	7.52 ± 0.01 (4)	-17.00 (9)	0.08'x0.05'	1.5	≤3.2 (5)	≤9.33[g]	≤ 0.36
UGC 4483	08h37m03.0s	+69d46m31.0s	3.2 (11)	7.46 ± 0.02 (28)	-12.53 (1)	1.4'x0.7'	0.07	0.33 (28)	6.61	0.0007
UGCA 20	01h43m14.7s	+19d58m32.0s	11.0 (18)	7.50 ± 0.02 (29)	-14.43 (2)	3.1'x0.8'	≤ 0.35	0.20 (25)	-	0.01

Table 3.5. Characteristics of the DGS sample (continued).

Source	RA	DEC	Distance Mpc (ref)	12 + log(O/H) (ref)	M_B (ref)	Size (D_{25}) arcmin × arcmin	$M_\star$ 10^8 $M_\odot$	M_{HI} 10^8 $M_\odot$(ref)	Log(L_{TIR}) Log($L_\odot$)	SFR $M_\odot$ yr^{-1}
UM 133	01h44m41.3s	+04d53m26.0s	22.7 (3)	7.82 ± 0.01 (4)	-15.72[d] (3)	1.0'x1.0'	0.65	4.0 (26)	-	0.02
UM 311	01h15m34.4s	-00d51m46.0s	23.5 (3)	8.38/8.36 ± 0.01[b] (17,30,31)	-19.22 (10)	0.11'x0.10'	103.0[e]	620.0 (27)	9.73	0.94
UM 448	11h42m12.4s	+00d20m03.0s	87.8 (3)	8.32 ± 0.01 (17)	-20.02 (1)	0.4'x0.4'	416.0	60.0 (24)	10.86	12.36
UM 461	11h51m33.3s	-02d22m22.0s	13.2 (3)	7.73 ± 0.01 (15)	-13.73 (6)	0.30'x0.22'	0.46	1.3 (28)	7.80	0.01
VII Zw 403	11h27m59.9s	+78d59m39.0s	4.5 (19)	7.66 ± 0.01 (16)	-13.77 (1)	1.4'x0.8'	0.16	0.52 (2)	7.23	0.003

References for distances : (1) Bergvall et al. (2006) ; (2) Kennicutt et al. (2003a) ; (3) this work, calculated from the redshifts available in NED, the Hubble flow model from Mould et al. (2000) and assuming $H_0 = 70$ km s^{-1} Mpc^{-1} ; (4) Pustilnik et al. (2003) ; (5) Aloisi et al. (2007) ; (6) Kim et al. (2009) ; (7) Schulte-Ladbeck et al. (2001) ; (8) Moll et al. (2007) ; (9) Grocholski et al. (2012) ; (10) Tosi et al. (2001) ; (11) Karachentsev et al. (2002) ; (12) Karachentsev et al. (2004) ; (13) Karachentsev et al. (2003) ; (14) de Vaucouleurs et al. (1991) ; (15) Cannon et al. (2003) ; (16) Gieren et al. (2006) ; (17) Aloisi et al. (2005) ; (18) Sharina et al. (1996) ; (19) Lynds et al. (1998) ; (20) Bordalo et al. (2009) ; (21) Tully (1988)
References for metallicities: (1) Guseva et al. (2012) ; (2) Kong et al. (2002) ; (3) Izotov et al. (2004) ; (4) Kobulnicky et al. (1999) ; (5) Ugryumov et al. (2003) ; (6) Pustilnik et al. (2003) ; (7) Izotov et al. (2007) ; (8) Popescu & Hopp (2000) ; (9) Guseva et al. (2003a) ; (10) Izotov et al. (1999) ; (11) Guseva et al. (2000) ; (12) Magrini & Gonçalves (2009) ; (13) López-Sánchez & Esteban (2010) ; (14) Izotov et al. (1994) ; (15) Izotov et al. (2006) ; (16) Izotov et al. (1997) ; (17) Izotov & Thuan (1998) ; (18) Kobulnicky & Skillman (1997) ; (19) Lee & Skillman (2004b) ; (20) Saviane et al. (2008) ; (21) McCall et al. (1985) ; (22) Skillman et al. (2003) ; (23) Lee et al. (2006) ; (24) Guseva et al. (2007) ; (25) Thuan et al. (1995) ; (26) Guseva et al. (2003b) ; (27) Masegosa et al. (1994) ; (28) van Zee & Haynes (2006) ; (29) van Zee et al. (1996) ; (30) Moles et al. (1994) ; (31) Pilyugin & Thuan (2007)
References for apparent magnitudes: (1) de Vaucouleurs et al. (1991) ; (2) Ugryumov et al. (2003) ; (3) Gil de Paz & Madore (2005); (4) Vennik et al. (2000) ; (5) Ugryumov et al. (2001) ; (6) Maddox et al. (1990) ; (7) SDSS DR4 ; (8) Paturel et al. (2003) ; (9) Fricke et al. (2001) ; (10) Smoker et al. (2000)
References for HI masses: (1) Cormier et al. (2014) ; (2) Thuan et al. (2004) ; (3) Gordon & Gottesman (1981) ; (4) Sauvage et al. (1997) ; (5) Pustilnik & Martin (2007) ; (6) MacHattie et al. (in prep.) ; (7) Chengalur et al. (2006) ; (8) Lelli et al. (2012) ; (9) Bettoni et al. (2003) ; (10) Huchtmeier & Richter (1988) ; (11) Williams et al. (1991) ; (12) Huchtmeier et al. (2005) ; (13) Thuan & Martin (1981) ; (14) Thuan et al. (1999a) ; (15) Walter et al. (2008) ; (16) Meurer et al. (1998) ; (17) Hunter et al. (2011) ; (18) van Eymeren et al. (2009) ; (19) López-Sánchez et al. (2012) ; (20) de Blok & Walter (2006) ; (21) Begum & Chengalur (2005b) ; (22) Ekta et al. (2009) ; (23) Pustilnik et al. (2002) ; (24) Davoust & Contini (2004) ; (25) Paturel et al. (2003) ; (26) Ekta & Chengalur (2010) ; (27) Moles et al. (1994) ; (28) van Zee et al. (1998) ; (29) Cannon et al. (2004)
[a] For these galaxies, no line intensities were available in the literature to determine the metallicities using the PT05 method. We use Ugryumov et al. (2003) where the [OIII]λ4363 line is used to obtain the electron temperature and the method from Izotov et al. (1994). I06 is an updated version of the method of Izotov et al. (1994).
[b] These objects are galaxies within compact groups of galaxies or are parts of other galaxies. We list the value of the metallicity for the galaxy only (1^{st} value quoted) and for the whole group (2^{nd} value quoted), which is the mean of all of the metallicities in the group. For Mrk1089, the galaxy is region A-C, and the group is composed of regions A-C, B, E, F1, F2, H from López-Sánchez & Esteban (2010). For UM311, the galaxy is region 3 following the denomination of Moles et al. (1994), and the group is composed of regions 1-2-3 of Moles et al. (1994) plus NGC450 and UGC807. It was not possible to find a metallicity or lines intensities for UGC807. For HS0052+2536 the group is composed of HS0052+2536 and HS0052+2537. For all of the galaxies the group corresponds to the galaxies inlcuded in the aperture used for *Herschel* photometry (see Chap 4).
[c] For these galaxies, no line intensity uncertainties, from which the metallicities are determined, are quoted. We assume a conservative value of 0.1 which is the mean of the variation of the difference between this metallicity calibration, PT05, and the I06 method (see Section 3.3.2).
[d] corrected for Galactic extinction.
[e] computed with synthesised IRAC fluxes from the SED modelled in Chapter 7.
[f] IRAS fluxes from NED.
[g] MIPS fluxes from Engelbracht et al. (2008).

Table 3.6. Summary of available *Herschel* photometry and ancillary data for the DGS galaxies.

Source	*Herschel* FIR/submm	GALEX[a] NUV/FUV	2MASS[b] NIR	IRAS[b] IR	*Spitzer*[c] MIR/FIR	WISE[b] NIR/MIR	Ground-Based [d] submm	*Planck*[e] bands (GHz) submm
Haro 11	PACS - SPIRE	GALEX	JHK	IRAS	IRAC - MIPS - IRS[f]	WISE	LABOCA	-
Haro 2	PACS - SPIRE	GALEX	JHK	IRAS	IRAC - MIPS - IRS[g]	WISE	SCUBA	-
Haro 3	PACS - SPIRE	GALEX	JHK	IRAS	IRAC - MIPS - IRS[f]	WISE	-	857
He 2-10	PACS - SPIRE	-	JHK	IRAS	IRAC - MIPS - IRS[f]	WISE	SCUBA MAMBO	857 - 545
HS 0017+1055	PACS - SPIRE	-	JHK	-	IRAC - MIPS24 - IRS[f]	WISE	-	-
HS 0052+2536	PACS - SPIRE	GALEX	JHK	IRAS	IRAC - MIPS24 - IRS[f]	WISE	LABOCA	-
HS 0822+3542	PACS	GALEX	JHK	-	IRAC - MIPS - IRS[f]	WISE	-	-
HS 1222+3741	PACS	GALEX	JHK	-	IRAC - MIPS70 - IRS[f]	WISE	-	-
HS 1236+3937	PACS - SPIRE	GALEX	-	-	IRAC - IRS[f]	-	-	-
HS 1304+3529	PACS - SPIRE	-	JHK	-	IRAC - MIPS24 - IRS[f]	WISE	-	-
HS 1319+3224	PACS	-	-	-	IRAC - IRS[f]	WISE	-	-
HS 1330+3651	PACS	-	-	-	IRAC - IRS[f]	WISE	-	-
HS 1442+4250	PACS - SPIRE	GALEX	-	-	IRAC4.5/8 - MIPS - IRS[f]	WISE	-	-
HS 2352+2733	PACS - SPIRE	GALEX	-	-	MIPS24 - IRS[f]	WISE	-	-
I Zw 18	PACS - SPIRE	GALEX	JHK	-	IRAC - MIPS - IRS[f,g]	WISE	-	-
II Zw 40	PACS - SPIRE	GALEX	JHK	IRAS	IRAC - MIPS[h] - IRS[f]	WISE	SCUBA - MAMBO	-
IC 10	PACS - SPIRE	-	JHK	IRAS	IRAC - MIPS[h] - IRS[f,g]	WISE	SCUBA	857 - 545
Mrk 1089	PACS - SPIRE	GALEX	JHK	IRAS	IRAC - MIPS24/70 - IRS[f,g]	WISE	LABOCA	-
Mrk 1450	PACS - SPIRE	-	JHK	IRAS	IRAC - MIPS - IRS[f]	WISE	-	-
Mrk 153	PACS - SPIRE	GALEX	JHK	IRAS	IRAC - MIPS[h] - IRS[f]	WISE	-	-
Mrk 209	PACS - SPIRE	GALEX	JHK	-	IRAC4.5/8 - MIPS - IRS[f]	WISE	-	-
Mrk 930	PACS - SPIRE	GALEX	JHK	IRAS	IRAC - MIPS - IRS[f]	WISE	LABOCA	-
NGC 1140	PACS - SPIRE	GALEX	JHK	IRAS	IRAC - MIPS - IRS[f]	WISE	SCUBA - MAMBO	857
NGC 1569	PACS - SPIRE	GALEX	JHK	IRAS	IRAC - MIPS - IRS[f,g]	WISE	SCUBA - MAMBO	-
NGC 1705	PACS - SPIRE	GALEX	JHK	IRAS	IRAC - MIPS - IRS[g]	WISE	LABOCA	-
NGC 2366	PACS - SPIRE	GALEX	JHK	IRAS	IRAC - MIPS - IRS[f,g]	WISE	-	857
NGC 4214	PACS - SPIRE	GALEX	JHK	IRAS	IRAC - MIPS - IRS[f,g]	WISE	SCUBA	857 - 545 - 353 - 217
NGC 4449	PACS - SPIRE	GALEX	JHK	IRAS	IRAC - MIPS - IRS[g]	WISE	SCUBA - MAMBO	857 - 545 - 353 - 217
NGC 4861	PACS - SPIRE	GALEX	JHK	IRAS	IRAC - MIPS - IRS[f,g]	WISE	-	-
NGC 5253	PACS - SPIRE	GALEX	JHK	IRAS	IRAC - MIPS[h] - IRS[g]	WISE	SCUBA - LABOCA	857 - 545 - 353
NGC 625	PACS - SPIRE	GALEX	JHK	IRAS	MIPS - IRS[f]	WISE	LABOCA	857 - 545
NGC 6822	PACS - SPIRE	GALEX	JHK	IRAS	IRAC - MIPS - IRS[f,g]	WISE	LABOCA	857
Pox 186	PACS - SPIRE	-	-	-	IRAC - MIPS24 - IRS[f]	WISE	-	-
SBS 0335-052	PACS - SPIRE	GALEX	JHK	-	IRAC - MIPS - IRS[f]	WISE	-	-
SBS 1159+545	PACS - SPIRE	-	-	-	IRAC - MIPS24 - IRS[f]	WISE	-	-
SBS 1211+540	PACS - SPIRE	GALEX	-	-	IRAC - MIPS24 - IRS[f]	WISE	-	-
SBS 1249+493	PACS - SPIRE	GALEX	-	-	IRAC - MIPS24 - IRS[f]	WISE	-	-
SBS 1415+437	PACS	GALEX	-	-	IRAC4.5/8 - MIPS - IRS[f]	WISE	-	-
SBS 1533+574	PACS - SPIRE	GALEX	JHK	IRAS	IRAC - MIPS70 - IRS[f]	WISE	-	-
Tol 0618-402	PACS	GALEX	JHK	-	IRAC - MIPS - IRS[f]	WISE	-	-
Tol 1214-277	PACS - SPIRE	GALEX	-	-	IRAC - MIPS[h] - IRS[f]	WISE	-	-
UGC 4483	PACS - SPIRE	GALEX	JHK	IRAS	IRAC - MIPS - IRS[f]	WISE	-	-
UGCA 20	PACS	GALEX	-	-	IRAC - MIPS24 - IRS[f]	WISE	-	-

Table 3.6. Summary of available *Herschel* photometry and ancillary data for the DGS galaxies.

Source	*Herschel* FIR/submm	GALEX[a] NUV/FUV	2MASS[b] NIR	IRAS[b] IR	*Spitzer*[c] MIR/FIR	WISE[b] NIR/MIR	ground-based [d] submm	*Planck*[e] bands (GHz) submm
UM 133	PACS - SPIRE	GALEX	-	-	IRAC - MIPS24 - IRS[g]	WISE	-	-
UM 311	PACS - SPIRE	GALEX	-	-	IRAC4.5/8 - MIPS - IRS[f]	WISE	LABOCA	857 - 545
UM 448	PACS70/160 - SPIRE	GALEX	JHK	IRAS	IRAC - MIPS - IRS[f]	WISE	SCUBA - LABOCA	-
UM 461	PACS - SPIRE	GALEX	JHK	IRAS	IRAC - MIPS - IRS[f]	WISE	-	-
VII Zw 403	PACS - SPIRE	GALEX	JHK	IRAS	IRAC - MIPS - IRS[f,g]	WISE	-	-

[a]: Data from STScI MAST archive (http://galex.stsci.edu/GR6/).
[b]: Data collected from the NASA/IPAC Infrared Science Archive (IRSA).
[c]: Data from Bendo et al. (2012).
[d]: Data collected from the literature: SCUBA/*JCMT*: 450 and/or 850 μm; LABOCA/*APEX*: 870 μm; MAMBO/*IRAM*: 1.2 mm (e.g., Bolatto et al. 2000; James et al. 2002; Lisenfeld et al. 2002; Böttner et al. 2003; Galliano et al. 2003; Kiuchi et al. 2004; Galliano et al. 2005; Galametz et al. 2009, 2011) or recent follow-up observations (Rémy-Ruyer et al., in preparation).
[e]: Data collected from the *Planck* database and the Early Release Source Catalog. *Planck* bands at 857, 545, 353, 217 and 143 GHz respectively correspond to 350, 550, 850, 1380 and 2100 μm.
[f]: *Spitzer* IRS 1D spectrum available for at least one of the modules: ShortLow, ShortHigh, LongLow, LongHigh. Data is extracted using the database tool, CASSIS (Lebouteiller et al. 2011).
[g]: *Spitzer* IRS maps available and extracted for the whole galaxy and/or part of it only, using the database tool, CASSIS (Lebouteiller et al. 2011).
[h]: While MIPS data are technically available for all MIPS bands, the data from one or two of the bands may have limited usefulness (limited coverage in the case of IC 10; confusion issues in the 160 μm images for Mrk 153 and Tol 1214-277; saturated emission at 24 μm in NGC 5253; problems with background subtraction in the 160 μm image of II Zw40 (see Bendo et al. 2012)).

Chapter 4

Building the cold dust SEDs

Contents

In this Chapter, we describe the data reduction process followed to produce the final *Herschel* maps for the DGS sample (Section 4.1). In Sections 4.2 and 4.3, we describe how we obtain the different PACS and SPIRE flux densities, together with their uncertainties (Tables 4.1 and 4.2).

4.1 Reducing DGS *Herschel* data

Herschel data can be reduced using the HIPE environment. During my PhD, HIPE was constantly evolving and several versions of HIPE have been used for the data reduction. We mention each time which version is used for the PACS and SPIRE data reduction[1].

4.1.1 PACS

For the PACS data reduction we use HIPE, with version 7 of the photometric calibration[2], and a modified version of the pipeline provided by the *Herschel* Science Center. We describe the main steps of the data reduction that we follow.

The pipeline begins with the Level 0 Products, at a purely instrumental level. All of the auxiliary data (such as "housekeeping" parameters, pointings, etc) is stored as Products. Level 0 also contains the Calibration Tree, needed for flux conversion. Then we perform the usual steps such as flagging the "bad" saturated pixels, converting the signal into Jy pix^{-1} and applying flatfield correction. We systematically mask the column 0 of all the matrices (the PACS array is composed of groups of 16×16 bolometers) to avoid electrical crosstalk issues. We perform second level deglitching to remove all of the glitches, which represent on average $\sim 0.3\%$ of the data.

After performing all of the above steps we reach the Level 1 stage of data reduction. Note that we still have the bolometer drifts (the so-called "$1/f$" noise) at this stage of the data reduction. This low-frequency noise originates from two sources: thermal noise, strongly correlated between the bolometers, and uncorrelated non-thermal noise. The method employed to remove the drifts will greatly affect the final reconstructed map (also called Level 2 data). We thus analyse three different map-making methods in order to systematically compare the maps and extract flux densities, to determine if there is an optimized method for each galaxy. The first two map-making methods are provided in HIPE: the PhotProject and the MADmap method. The last method is the Scanamorphos method (Roussel 2013).

The first technique we use for the final reconstruction of the map is PhotProject. We first remove the $1/f$ noise (corresponding to data with low spatial frequencies or large scale structures in the map) using a high-pass filter. We then use the PhotProject routine to reproject the data on the sky. The high-pass filtering step is optimum for compact sources but can lead to suppression of extended features (corresponding to low spatial frequencies) in extended sources.

MADmap (Microwave Anisotropy Dataset mapper) produces maximum likelihood maps from the time ordered data (Cantalupo et al. 2010). The main assumption here is that the noise is uncorrelated from pixel to pixel. However, one component of the $1/f$ noise is strongly correlated from pixel to pixel, as it is due to the thermal drift of the bolometers, and thus not treated by MADmap. Nevertheless, MADmap is more efficient than PhotProject in reconstructing the extended structures within a map.

[1] However, the reader must keep in mind that the current version of HIPE might not be the same than that used for the data reduction and photometry in this Chapter and that the maps and flux densities might need some updating. The flux densities presented here are the same as in Rémy-Ruyer et al. (2013).

[2] The version 7 cited here corresponds to the value of the calFileVersion metadata of the Responsitivity Calibration Product in HIPE.

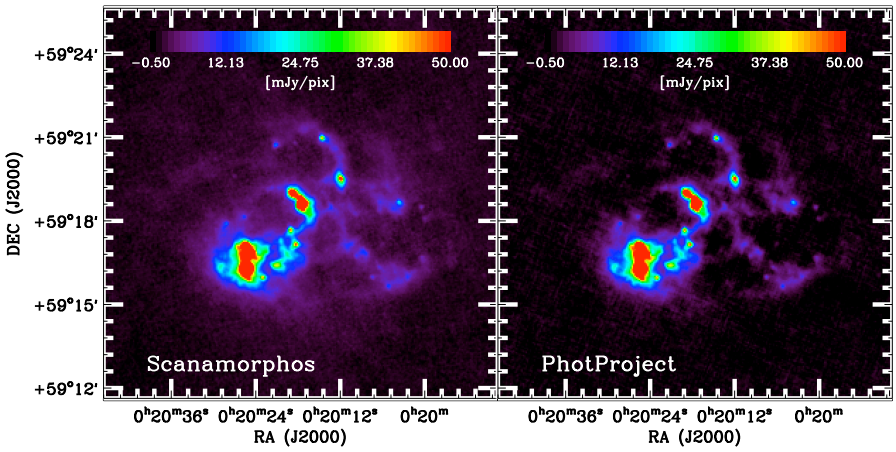

Fig. 4.1. Scanamorphos (*left*) and PhotProject (*right*) images of IC 10 at 70 μm to illustrate how PhotProject tends to clip out the extended features. The colours and spatial scales are the same on both images. Here the diffuse extended emission is best visible on the Scanamorphos map. The comparison of the total flux densities coming from the 2 methods confirms that PhotProject misses the extended emission: in this case, F_{70}(Scanamorphos)/F_{70}(PhotProject) = 1.5.

Scanamorphos is another technique specially developed to process scan observations (Roussel 2013). The particularity of Scanamorphos, compared to MADmap, is that no particular noise model is assumed to deal with the low-frequency noise (the $1/f$ noise). Indeed Scanamorphos takes advantage of the redundancy in the observations, i.e., of the fact that a portion of the sky is observed more than once and by more than one bolometer. The two noise sources contributing to the low-frequency noise are inferred from the redundancy of the data and removed (Roussel 2013). The maps are made using the default parameters. We add the minimap option when reducing data with a field size of the order of 8.4 arcmin. For consistency in the following flux computation, we produce maps with the same pixel sizes for all of the methods: 2″, 2″and 4″ for 70, 100 and 160 μm respectively.

Adapting the map-making method to the source

To determine the best map-making method for each galaxy (summarised in Table 4.1), we compute the flux densities (see Section 4.2.1 for PACS flux extraction) for the three bands for the three methods for each galaxy and compare the photometry for the three different methods. For consistency, we use the same apertures for the three different types of maps.

As mentioned above, the PhotProject method is optimized for compact sources. Indeed, the filtering step partly removes large scale structures in the map. It is not adapted for extended sources as this filtering step can sometimes also remove the large scale structures of our large sources with diffuse extended emission (Figure 4.1), also noted by Aniano et al. (2012) for two extended KINGFISH galaxies. Moreover the source is automatically masked before the high-pass filtering step, and this mask may be too small for extended sources with peculiar morphology, leading to suppression of extended features during the filtering step. Therefore, we decide to take as final, the maps produced by PhotProject for compact sources only.

Some galaxies are not detected in one or several bands. When deriving upper limits on the flux densities for these galaxies, the three methods give very different results. As the "non-detection" criterion is directly linked to the background determination through its contribution to the total flux density and the corresponding uncertainty, we need to choose the method that gives the most reliable background structure. MADmap and Scanamorphos do not have any constraints on

the background values, whereas PhotProject is constrained to an average statistically-null background. Because Scanamorphos does not make any assumptions on the background, sometimes positive residual noise structures can remain in the maps. MADmap presents features, such as a curved background for some maps, due to an oversimplified treatment of missing data. Again, the PhotProject maps here are used because they are the most constrained as far as the background is concerned. Moreover, when the galaxy is not detected at 160 μm it is usually a compact point source at the other PACS wavelengths. Thus this choice is consistent with the previous choice for compact sources.

For more extended sources, we only consider MADmap and Scanamorphos. As mentioned before, MADmap maps sometimes present a curved background: the source in the map centre is surrounded by lower background levels than those used in the background aperture for the photometry. This therefore results in a high background leading to an underestimation of the source flux density. Moreover this is not consistent with the assumption of a flat background made for the photometry (see Section 4.2.1). After some tests, to avoid this problem, we decide to use the Scanamorphos maps for the extended sources.

4.1.2 SPIRE

Following the same method as in Ciesla et al. (2012) for the Herschel Reference Survey, or in Auld et al. (2013) for the HErschel VIrgo Cluster Survey, the SPIRE maps are processed through HIPE[3] using a modified version of the available SPIRE pipeline. The steps from the Level 0 to Level 1 are basically the same as in the official version provided by the SPIRE Instrument Control Centre (ICC). The pipeline starts with a first deglitching step, then a time response correction is applied to match the detector timelines to the astronomical pointing timelines. A second deglitching step is then performed as it improves the removal of residual glitches. After an additional time response correction, the flux calibration step is performed, where non-linearity corrections are taken into account. An additional correction is applied to the bolometer timelines to account for the fact that there is a delay in the response of the bolometers to the incoming signal. The temperature drifts of the bolometers are then removed. For this step, the pipeline temperature drift removal is not run. Instead a custom temperature drift correction (BriGAdE, Smith et al. in prep) is applied to the whole observation timeline (rather than to an individual scan-leg). Finally, the Naive mapper is used to construct the final map with pixel sizes of 6, 8, 12$''$ for the 250, 350, 500 μm band respectively. For galaxies with heavy cirrus contamination, an additional destriping step is performed. A complete description of the data processing step will be given in Smith et al. in prep.

4.2 DGS PACS photometry

Throughout this study we focus on the *global* SED modelling of the samples. Due to the intrinsically faint luminosities of dwarf galaxies, the total integrated photometry for the DGS must be done with great care, paying close attention to the evaluation of uncertainties on the flux densities.

4.2.1 Extracting the fluxes

For PACS measurements, we perform aperture photometry, placing an aperture on the source and a background region away from the source to estimate the sky level. As mentioned in Section 3.2.1, the PACS PSFs have been measured out to 1000$''$ with version 7 of the PACS photometric calibration. Most of our maps are smaller than this, which means, in principle, that some contribution from the

[3]The version 5 of HIPE was used for producing the SPIRE maps.

PSF of the source can basically be found everywhere on the map, and, any emission from the source falling in the background region must be taken into account when estimating the total source flux density.

Taking into account this aperture correction, aperture photometry is performed, using circular apertures of 1.5 times the optical radius whenever possible. For cases where it is not, we adjust our apertures to be sure to encompass all of the FIR emission of the galaxy (Table 4.1). There are three special cases. For HS0052+2536 the chosen aperture also encompasses the neighbouring, very faint galaxy HS0052+2537. Mrk1089 is a galaxy within a compact group of galaxies and UM311 is part of another galaxy and the chosen apertures encompass the whole group of objects. For these galaxies, the spatial resolution of the SPIRE bands makes it very difficult, if not impossible, to separate them from the other objects in their respective groups. For these few cases, the entire group is considered and noted in Tables 3.4, 4.1 and 4.2. The background region is a circular annulus around the source. In most cases, the inner radius of the background region is the same as that of the source aperture and the outer radius is about two times the source aperture radius.

The maps are assumed to consist of the sum of a constant, flat background plus the contribution from the source. Flux densities are measured in the aperture (f_{ap}) and in the background annulus (f_{an}) by summing the pixels in both regions. The contribution to the measured flux densities (f_{ap} and f_{an}) from the total flux density of the galaxy (f_{tot}) and from the background (b) is determined for each aperture using the encircled energy fraction (eef) tables. These tables, given by HIPE, are measurements of the fraction of the total flux density contained in a given aperture on the PSFs (inverse of the aperture correction). This gives us a simple linear system of two equations with two unknowns: the total flux density from the galaxy (f_{tot}) and the background level (b):

$$\begin{cases} f_{ap} &= f_{tot} \times eef_{r_0} + N_{ap} \times b \\ f_{an} &= f_{tot} \times (eef_{r_2} - eef_{r_1}) + N_{bg} \times b \end{cases} \tag{4.1}$$

where r_0, r_1, r_2 are the source aperture radius and the background annulus radii respectively, and eef_{r_0}, eef_{r_1} and eef_{r_2} are the encircled energy fractions at radii r_0, r_1, r_2. N_{ap} (resp. N_{bg}) is the number of pixels in the source (resp. background) aperture. Inverting this system gives us the values for f_{tot} and b.

If one considers that there is no contribution from the source outside of the source aperture, i.e., setting eef_{r_0}=1 and eef_{r_1}=eef_{r_2}=0, the flux density will be underestimated, as some contribution from the source will have been removed during the background subtraction. This underestimation depends on the source aperture size, r_0, and can be important for small apertures. The error made on the flux density becomes greater than the calibration error, which is the dominant source of uncertainty ($\sim 5\%$, see Section 4.2.2), when $r_0 \lesssim 1'$. Given that the median r_0 in the DGS sample is $\sim 0.6'$, it is thus important to take into account the contribution from the source falling outside the source aperture.

4.2.2 Computing the uncertainties

The uncertainties on the flux density arise from the non-systematic errors due to the measurement of the flux density on the maps, ($unc_{f_{tot}}$), and the systematic errors due to calibration, (unc_{calib}).

For the measurement on the maps, the system of equations being linear, the uncertainties arising from the two measurements on the map (unc_{ap} and unc_{an}) can be linearly propagated to the total flux density and the background level, giving us the uncertainty on the total flux density ($unc_{f_{tot}}$) and the uncertainty on the background level (unc_b). The determination of unc_{ap} and unc_{an} is the same for both errors as the measure is the same: summing pixels in a given region of the map. Thus we detail the calculation for unc_{ap} only.

There are two sources of errors to unc_{ap}: one coming from the sum of the pixels, unc_{sum}, one

coming from the intrinsic error on the flux density value in each pixel, unc_{int}.

Determination of unc_{sum}: For each pixel there is a contribution from the background noise to the total measured flux density. This error, σ_{sky}, is the same for a pixel in the source aperture as well as in the background aperture, repeated N_{ap} times here. The error, σ_{sky}, is the standard deviation of all pixels in the background aperture. The final uncertainty, unc_{sum}, is then:

$$unc_{sum} = \sqrt{N_{ap}}\sigma_{sky} \tag{4.2}$$

Determination of unc_{int}: For each pixel there is an underlying uncertainty for the flux density value in the pixel, $\sigma_{int,i}$, and is independent from pixel to pixel. This uncertainty arises from the data reduction step when the flux density for each pixel is computed. A map of these uncertainties is produced during the data reduction process. The uncertainty, unc_{int}, is then derived by adding quadratically all of the errors in the considered pixels:

$$unc_{int} = \sqrt{\sum_{i=0}^{N_{ap}} \sigma_{int,i}^2} \tag{4.3}$$

Note that the assumption of pixel-to-pixel independent uncertainty is not applicable for PACS maps and this can result in an underestimation of unc_{int}.

The total error on the source aperture measurement is then:

$$unc_{ap} = \sqrt{unc_{sum}^2 + unc_{int}^2} \tag{4.4}$$

The unc_{an} is derived the same way and we can then compute $unc_{f_{tot}}$ and unc_b. The quantity $unc_{f_{tot}}$ is thus the total error on the flux density due to measurement on the map. To this uncertainty, we add in quadrature the systematic calibration uncertainty, unc_{calib}, of 5% for the three PACS bands (M. Sauvage & T. Müller, priv. com.), giving, in the end, the $\sigma_{70-100-160}$ reported in Table 4.1:

$$\sigma_\lambda = \sqrt{unc_{f_{tot}}^2 + unc_{calib}^2} \tag{4.5}$$

Note that in unc_{sum}, we have a combination of uncertainties from small-scale astronomical noise and instrumental uncertainties. These instrumental uncertainties can be redundant with part of the instrumental uncertainties taken into account in unc_{int}, leading to an overestimate of unc_{ap} and thus $unc_{f_{tot}}$. However, it has a minor impact on the final uncertainties, $\sigma_{70-100-160}$, as the calibration uncertainty is dominant.

4.2.3 Case of upper limits

Some galaxies in our sample are not detected in some or all of the PACS bands. We classify these galaxies as "upper limits" when the computed flux density is lower than five times the corresponding uncertainty on the flux density (e.g., Tol 0618-402, Figure 4.2). We take as the final upper limit, five times the uncertainty on the flux density value in order to have a 5σ upper limit (reported in Table 4.1).

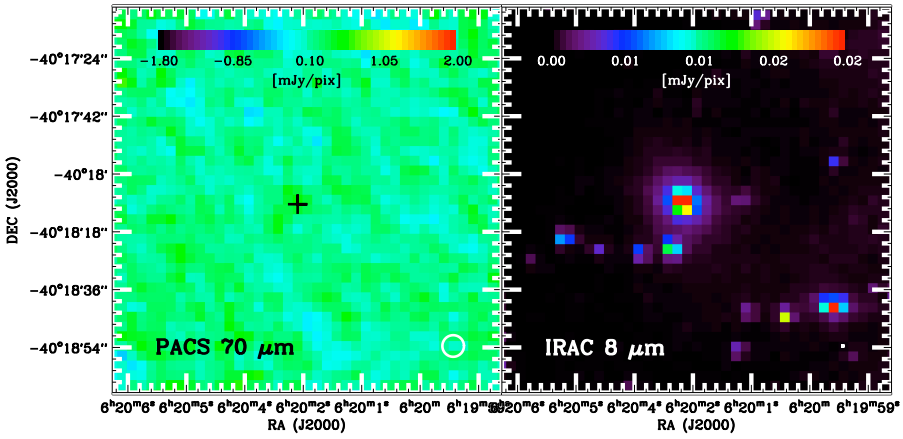

Fig. 4.2. Example of a PACS non-detection: *(left)* PACS 70 μm image of Tol 0618-402. The position of the galaxy is marked with a black cross. The IRAC 8 μm image has been added on the right for comparison. The PACS 70 μm (FWHM=5.6″) and the IRAC 8 μm (FWHM=2.0″) beams are indicated as white circles on the bottom right of the images.

4.3 DGS SPIRE photometry

For the SPIRE photometre, the RSRFs are different for a point source or for an extended source (see Fig. 3.9 and Section 3.2.2). As explained in Section 3.2.2, the output of the pipeline will be, *by definition*, a monochromatic flux density of a *point source*. To obtain monochromatic flux densities of extended sources we apply the ratio of K_4 corrections for extended and point-like sources, K_{4E}/K_{4P}, defined in Section 3.2.2. In order to determine which sources need this extra-correction, we have to distinguish between extended and point-like (unresolved) sources in our sample, as well as non-detected sources. Extended sources are defined as galaxies whose spatial extension is larger than the FWHM of the SPIRE beam, and non-detected sources are galaxies that are not visible at SPIRE wavelengths.

4.3.1 Extracting the fluxes

The photometry method is adapted for each type of galaxy. However, as the data reduction has been performed with HIPE v5, the 350 μm maps are first scaled by a factor of 1.0067 to update the maps to the latest version of the 350 μm flux calibration (SPIRE Observers' Manual (Section 5.2.8))

Point source photometry

To determine the flux densities of point sources, we fit a Gaussian function (which is representative of the shape of the PSF) to the timeline data from the bolometers, using a timeline-based source fitter that is used for deriving the flux calibration for the individual bolometers[4]. We then check a posteriori that our "unresolved" classification was correct: if the FWHM of the fitted Gaussian is $< 20''$, $29''$ and $37''$ at 250, 350 and 500 μm respectively, then the source can be considered as truly point-like. As the timeline data is in Jy beam^{-1}, the flux density will simply be the amplitude of the fitted Gaussian. This is the most accurate way of computing flux densities for point-like sources as it matches the measurement techniques used for the SPIRE calibration. Moreover we avoid all pixelization issues when using the timeline data rather than the map. On top of that, applying any

[4]The last version of this source fitter is incorporated into HIPE v10 (Bendo et al. in prep.).

map-making process would also smear the PSFs, causing the peak signal values to decrease by $\sim$ 5% for point sources.

Extended source photometry

For the extended sources, we perform aperture photometry on the maps, using the same source and background apertures as those used for the PACS photometry, and check that the PACS apertures do fully encompass the SPIRE emission from the entire galaxy. The maps are converted from Jy beam^{-1} to Jy pix^{-1} considering that the beam area values are 465, 822 and 1768 square arcseconds[5] at 250, 350, 500 μm respectively and the pixel sizes are given in Section 4.1.2.

The background level is determined by the median of all of the pixels in the background aperture. The median is preferred rather than the mean because the SPIRE background is contaminated by prolific background sources due to some observations reaching the confusion limit. The background level is then subtracted from our maps and the total flux density is the sum of all of the pixels encompassed in the source aperture, corrected for K_{4E}/K_{4P}. These K_{4E}/K_{4P} correction factors, given in the SPIRE Observers' Manual (Section 5.2.8), are 0.98279, 0.98344 and 0.97099 at 250, 350, 500 μm respectively.

However there are also "marginally" extended sources (e.g., IIZw40) that do not require this K_{4E}/K_{4P} correction. To identify these sources, we first check that the source is truly resolved by applying the point source method on the timeline data. We verify that the FWHM is indeed greater than the chosen threshold values for the "unresolved" classification. As an additional check, the fitted Gaussian is subtracted from the map and the resulting map is visually checked for any remaining emission from the source. If this condition is satisfied, then the source is truly resolved. If the FWHM of the fitted Gaussian is lower than 24″, 34″ and 45″ at 250, 350, 500 μm respectively then the source is considered to be "marginally" extended only, and thus to not require the K_{4E}/K_{4P} correction.

4.3.2 Computing the uncertainties

As for the PACS photometry, there are two types of uncertainties for SPIRE photometry: the errors arising from the determination of the flux density, unc_{flux}, and the calibration errors, unc_{calib}. As we used different methods for flux extraction depending on the type of the source, the errors contributing to unc_{flux} are determined differently. The method described here has been adapted from the method described in Ciesla et al. (2012).

Point sources

The uncertainty on the flux density for a point source is determined through a test in which we add 100 artificial sources with the same flux density as the original source. They are added at random locations in the maps, within a 0.3 deg box centred on the original source. The same photometry procedure was applied to the artificial sources and the final uncertainty is the standard deviation in the flux densities derived for the artificial sources. We quote the following uncertainties (unc_{flux}) for point-like sources:

- 6 mJy at 250 μm;
- 7 mJy (for flux densities $>$ 50 mJy) and 10 mJy (for flux densities $\lesssim$ 50 mJy) at 350 μm;
- 9 mJy at 500 μm.

[5]SPIRE photometre reference spectrum values: http://herschel.esac.esa.int/twiki/bin/view/Public/SpirePhotometerBeamProfileAnalysis, September 2012 values.

Extended sources

For the aperture photometry performed on the extended sources, we have four types of uncertainties contributing to unc_{flux}:

- the uncertainty arising from the background level determination, unc_{bg},
- the uncertainty due to background noise in the source aperture, unc_{source},
- the underlying uncertainty for the flux density value in the pixel coming from the data reduction, unc_{int}, and
- the uncertainty in the beam area value: unc_{beam}, which is given to be 4%[6].

The determination of the background level generates an uncertainty that will affect each pixel in the source aperture when subtracting the background level from the map. The uncertainty on the background level is $unc_{bg_{level}} = \sigma_{sky}/\sqrt{N_{bg}}$, with σ_{sky} being here again the standard deviation of all of the pixels in the background aperture. This will affect the determination of the flux density for each pixel summed in the aperture:

$$unc_{bg} = N_{ap} unc_{bg_{level}} \tag{4.6}$$

The uncertainty due to background noise in the source aperture, unc_{source}, is determined the same way as the PACS unc_{ap} since it is the uncertainty arising from summing the pixels in a given aperture:

$$unc_{source} = \sqrt{N_{ap}}\sigma_{sky} \tag{4.7}$$

The uncertainty arising from the underlying uncertainties of the flux density value in each pixel is computed the same way as for PACS. Here again, this uncertainty arises from the data reduction step when the flux density for each pixel is computed, and the pipeline produces the corresponding error map:

$$unc_{int} = \sqrt{\sum_{i=0}^{N_{ap}} \sigma_{int,i}^2} \tag{4.8}$$

The total uncertainty coming from the determination of the flux density for an extended source, is then:

$$unc_{flux} = \sqrt{unc_{bg}^2 + unc_{source}^2 + unc_{int}^2 + unc_{beam}^2} \tag{4.9}$$

For both types of sources, we also add calibration uncertainties to unc_{flux} to get the final total uncertainty. There are two different SPIRE calibration uncertainties: a systematic uncertainty of $\sim$ 5% coming from the models used for Neptune, the primary calibrator, which is correlated between the three bands, and a random uncertainty of $\sim$ 2% coming from the repetitive measurement of the flux densities of Neptune. These two uncertainties were not added in quadrature but linearly, as advised in the SPIRE Observer's Manual, giving an overall 7% calibration uncertainty unc_{calib}. The final total uncertainty, $\sigma_{250-350-500}$ reported in Table 4.2, is obtained by adding unc_{flux} and unc_{calib} in quadrature.

As for PACS, with SPIRE we also have a redundancy in the error estimation in unc_{source} and unc_{int}, again with only a minor impact on the final uncertainties, $\sigma_{250-350-500}$, as the calibration uncertainty dominates.

[6]This value is given in: http://herschel.esac.esa.int/twiki/bin/view/Public/SpirePhotometerBeamProfileAnalysis.

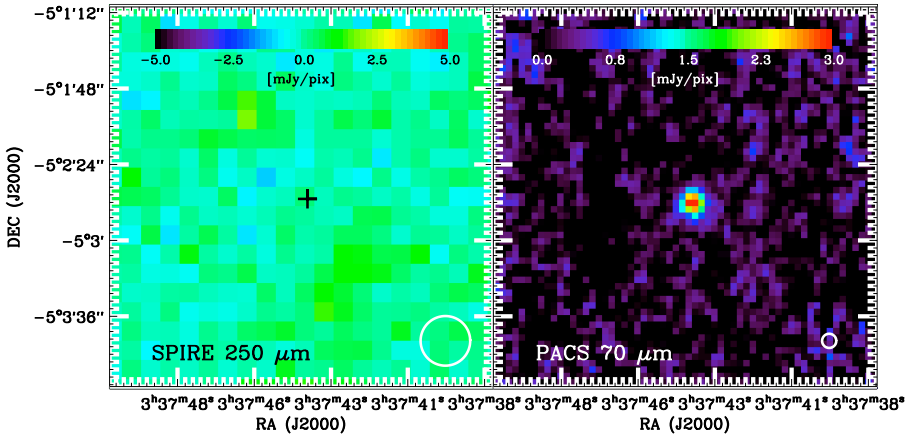

Fig. 4.3. Example of a SPIRE non-detection: *(left)* SPIRE 250 μm and *(right)* PACS 70 μm image of SBS 0335-052. The position of the galaxy is indicated by a black cross on the SPIRE image. The SPIRE 250 μm (FWHM=18.2″) and the PACS 70 μm (FWHM=5.6″) beams are indicated as white circles on the bottom right of the images.

4.3.3 Case of upper limits

When the galaxy is not detected in the SPIRE bands (e.g., SBS 0335-052, Figure 4.3), we can only derive upper limits on the flux density. Also, when the source is blended with another source in the beam and we are unable to confidently separate them (e.g., Pox186 and a background galaxy separated by 20″, Figure 4.4), upper limits are reported. Since the undetected sources are point sources, we use five times the uncertainties reported for point sources in Section 4.3.2. The only exception is SBS1533+574 which is blended with another source and slightly extended at 250 μm. The method described above gives an upper limit too low. The extended source photometry method is thus used to derive a 5σ upper limit at this wavelength.

4.3.4 Special cases: heavy cirrus contamination

For NGC 6822 and IC 10, the cirrus contamination from our Galaxy is significant in the SPIRE bands.

NGC 6822 - Galametz et al. (2010) determined that the contribution from the cirrus to the total emission of the galaxy is of the order of 30% for all SPIRE bands. To determine the cirrus contribution here, we assume that the entire galaxy is in a homogeneous and flat cirrus region. We determine this cirrus level by considering regions at the same cirrus level outside of the galaxy. This level is used as the background level for the flux determination. We then compare this flux density with the flux density obtained when we consider an uncontaminated background region and determine the contamination from the cirrus. We also find that the contribution of the cirrus to the total flux densities is about 30%, which is coherent with the results from Galametz et al. (2010). Thus for this galaxy, the flux densities cited in Table 4.2 are flux densities where the cirrus contribution has been subtracted. We also include a conservative 30% uncertainty in the error for these flux densities to account for the estimation of the cirrus contribution, and for the fact that the cirrus emission may not be flat.

IC 10 - We apply the same method here. Again, we find that the cirrus contributes $\sim$ 30% on average, to each SPIRE band. We took this contribution into account by adding this cirrus

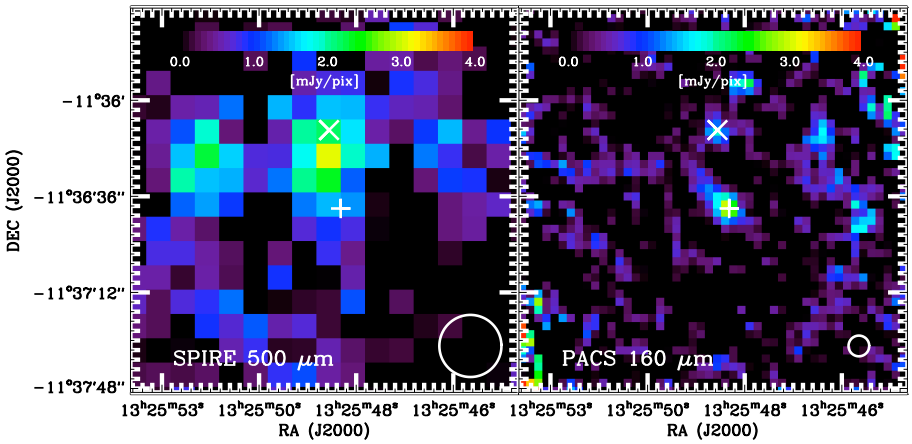

Fig. 4.4. Example of a "mixed" source. SPIRE 500 μm (left) and PACS 160 (right) images of Pox186 and a contaminating background source. The sources are 20″ apart, and are well separated at 160 μm, but are completely blended at SPIRE 500 μm resolution. Pox186 corresponds to the bottom cross, whereas the contaminating background source is the X. The SPIRE 500 μm (FWHM=36.3″) and the PACS 160 μm (FWHM=11.3″) beams are indicated as white circles on the bottom right of the images.

uncertainty to the other sources of uncertainties for this galaxy.

This method can be improved, by using the HI maps to better determine the cirrus emission and the background level and thus reducing the uncertainties on the measurements for these two galaxies.

4.4 KINGFISH data

The *Herschel* KINGFISH flux densities are taken from Dale et al. (2012). They have been extracted from SCANAMORPHOS maps. The KINGFISH SPIRE fluxes and corresponding uncertainties are updated to match the latest SPIRE beam areas (see Section 4.3.1). The beam areas used in this paper were released in September 2012, after the publication of Dale et al. (2012) in January 2012.

Table 4.1. Table of PACS flux densities for the DGS galaxies. The map-making method is indicated for each galaxy as well as the radius of the circular aperture used for the flux extraction. When an upper limit is given, it is the 5σ upper limit computed in 4.2.3.

Source	F_{70} (Jy)	σ_{70} (Jy)	F_{100} (Jy)	σ_{100} (Jy)	F_{160} (Jy)	σ_{160} (Jy)	Method	Circular aperture radius ($''$)
Haro11	6.14	0.31	4.96	0.25	2.42	0.12	Scanamorphos	45^{b}
Haro2	4.99	0.25	5.33	0.27	3.95	0.20	Scanamorphos	50^{a}
Haro3	5.30	0.26	6.41	0.32	4.83	0.24	Scanamorphos	60^{a}
He2-10	25.6	1.3	26.6	1.3	18.8	0.9	Scanamorphos	108^{a}
HS0017+1055	0.046	0.005	0.033	0.004	0.019	0.004	PhotProject	16^{b}
HS0052+2536	0.22	0.01	0.21	0.01	0.139	0.008	PhotProject	$23^{a,f}$
HS0822+3542	$\leq 0.014^{j}$ / $\leq 0.041^{k}$	-	$\leq 0.013^{j}$ / $\leq 0.048^{k}$	-	0.034	0.003	PhotProject	12^{a}
HS1222+3741	0.025	0.004	≤ 0.036	-	≤ 0.022	-	PhotProject	14^{b}
HS1236+3937	≤ 0.029	-	≤ 0.035	-	≤ 0.028	-	PhotProject	15^{a}
HS1304+3529	0.121	0.007	0.150	0.009	0.069	0.005	PhotProject	18^{b}
HS1319+3224	0.012	0.003	0.013	0.002	≤ 0.015	-	PhotProject	8^{b}
HS1330+3651	0.093	0.006	0.112	0.007	0.091	0.005	PhotProject	20^{b}
HS1442+4250	0.09	0.01	≤ 0.016	-	≤ 0.047	-	PhotProject	51^{a}
HS2352+2733	0.039	0.003	0.016	0.002	≤ 0.016	-	PhotProject	15^{a}
IZw18	0.045	0.003	0.018	0.002	≤ 0.011	-	PhotProject	14^{a}
IC10	140.	7.	207.	10.	225.	11.	Scanamorphos	306^{a}
IIZw40	6.39	0.32	5.79	0.29	3.53	0.18	Scanamorphos	66^{b}
Mrk1089	4.27	0.21	4.97	0.25	4.68	0.23	Scanamorphos	$75^{b,f}$
Mrk1450	0.30	0.02	0.25	0.01	0.127	0.007	PhotProject	20^{a}
Mrk153	0.28	0.02	0.30	0.02	0.137	0.009	PhotProject	35^{b}
Mrk209	0.32	0.02	0.35	0.02	0.16	0.01	Scanamorphos	24^{c}
Mrk930	1.19	0.06	1.40	0.07	0.98	0.05	Scanamorphos	60^{b}
NGC1140	4.04	0.20	4.62	0.23	4.58	0.23	Scanamorphos	118^{b}
NGC1569	60.4	3.0	57.3	2.9	39.7	2.0	Scanamorphos	150^{d}
NGC1705	1.37	0.07	1.46	0.07	1.10	0.06	PhotProject^{g}	72^{d}
NGC2366	5.30	0.26	6.23	0.31	4.08	0.20	Scanamorphos	$150^{d,e}$
NGC4214	24.5	1.2	32.2	1.6	33.7	1.7	Scanamorphos	300^{d}
NGC4449	49.3	2.5	75.9	3.8	79.5	4.0	Scanamorphos	250^{d}
NGC4861	2.31	0.12	2.17	0.11	1.99	0.10	Scanamorphos	120^{d}
NGC5253	32.9	1.6	32.3	1.6	23.2	1.2	Scanamorphos	120^{d}
NGC625	6.49	0.32	9.47	0.47	8.20	0.41	Scanamorphos	170^{d}
NGC6822	54.9	2.8	63.6	3.2	77.1	3.9	Scanamorphos	440^{d}
Pox186	0.038^{j}	0.005	0.052^{j}	0.005	0.047^{j}	0.004	PhotProject	16^{a}
SBS0335-052	0.056	0.004	0.024^{h}	0.001	0.007^{h}	0.001	PhotProject	$10^{a,h}$
SBS1159+545	0.019	0.003	0.019	0.003	≤ 0.018	-	PhotProject	8^{a}
SBS1211+540	0.034	0.003	0.018	0.002	0.013	0.002	PhotProject	15^{b}
SBS1249+493	0.032	0.005	≤ 0.034	-	≤ 0.042	-	PhotProject	12^{b}
SBS1415+437	0.18	0.01	0.16	0.01	0.065	0.007	PhotProject	34^{a}
SBS1533+574	0.19	0.01	0.24	0.01	0.19	0.01	Scanamorphos	30^{a}
Tol0618-402	≤ 0.014	-	≤ 0.005	-	≤ 0.013	-	PhotProject	18^{a}
Tol1214-277	0.017	0.003	0.018	0.002	≤ 0.018	-	PhotProject	12^{b}
UGC4483	0.16	0.02	$-^{i}$	$-^{i}$	$\leq 0.037^{j}/\leq 0.072^{k}$	-	PhotProject	63^{a}
UGCA20	≤ 0.052	-	≤ 0.057	-	≤ 0.048	-	PhotProject	20^{c}

Table 4.1. Table of PACS flux densities for the DGS galaxies (continued).

Source	F_{70} (Jy)	σ_{70} (Jy)	F_{100} (Jy)	σ_{100} (Jy)	F_{160} (Jy)	σ_{160} (Jy)	Method	Circular aperture radius ($''$)
UM133	0.15^{j}	0.01	0.066	0.010	0.053	0.009	Scanamorphos	26^{c}
UM311	2.94	0.15	5.63	0.28	6.10	0.31	Scanamorphos	$140^{b,f}$
UM448	5.17	0.26	-	-	3.22	0.17	Scanamorphos	64^{b}
UM461	0.21^{j}	0.01	0.145	0.009	0.113	0.007	PhotProject	17^{b}
VIIZw403	0.47	0.03	0.56	0.03	0.34	0.02	PhotProject	40^{c}

^{a,b,c}: The radius is: ^{a}: 1.5 times the optical radius. ^{b}: larger than 1.5 times the optical radius. ^{c}: smaller than 1.5 times the optical radius.
^{d,e}: The aperture is: ^{d}: adapted from elliptical shape. ^{e}: off-centred to match the particular shape of the galaxy.
^{f}: These objects are galaxies within compact groups of galaxies or are parts of other galaxies and the photometry given here is for the whole group (see Section 4.2.1 for details).
^{g}: The Scanamorphos maps of NGC1705 are not satisfactory because of a non uniform background. Therefore we use the PhotProject maps. To preserve as much of the diffuse extended emission as possible we manually mask out the galaxy before performing the high-pass filtering step.
^{h}: New observations were obtained for SBS0335-052 at 100 and 160 μm with longer integration times (Sauvage et al. in prep). We chose to quote the flux density values from the newest observations for 100 and 160 μm.
^{i}: Interferences on the detector are strongly polluting the map for the 100 μm observation of UGC4483. We thus do not report any flux density nor give any 100 μm map for this galaxy.
^{j}: These flux densities might present some discrepancies with other FIR measurements (i.e., MIPS, other PACS and/or SPIRE wavelengths).
^{k}: These fluxes densities are more coherent with the rest of the IR photometry for this galaxy (see Section 7.2.4). Thus we recommend to use these values when studying this object.

Table 4.2. Table of SPIRE flux densities for the DGS galaxies. When an upper limit is given, it is the 5σ upper limit computed in 4.3.3.

Source	F_{250} (Jy)	σ_{250} (Jy)	F_{350} (Jy)	σ_{350} (Jy)	F_{500} (Jy)	σ_{500} (Jy)
Haro11	0.63	0.05	0.23	0.02	0.09	0.01
Haro2	1.28[a]	0.10	0.53[a]	0.04	0.15[a]	0.01
Haro3	1.79[a]	0.15	0.77[a]	0.07	0.23[a]	0.02
He2-10	6.67[a]	0.54	2.64[a]	0.22	0.79[a]	0.07
HS0017+1055	≤0.030	-	≤0.050	-	≤0.045	-
HS0052+2536[b]	0.058	0.007	0.03	0.01	0.018	0.009
HS0822+3542[c]	-	-	-	-	-	-
HS1222+3741[c]	-	-	-	-	-	-
HS1236+3937	≤0.030	-	≤0.050	-	≤0.045	-
HS1304+3529	0.038	0.007	≤0.050	-	≤0.045	-
HS1319+3224[c]	-	-	-	-	-	-
HS1330+3651[c]	-	-	-	-	-	-
HS1442+4250	≤0.030	-	≤0.050	-	≤0.045	-
HS2352+2733	≤0.030	-	≤0.050	-	≤0.045	-
IZw18	≤0.030	-	≤0.050	-	≤0.045	-
IC10[d]	101.[a]	31.	47.6[a]	14.8	16.3[a]	5.1
IIZw40	1.33[a]	0.12	0.58[a]	0.06	0.18	0.02
Mrk1089[b]	1.75[a]	0.15	0.78[a]	0.07	0.24[a]	0.03
Mrk1450	0.049	0.007	≤0.050	-	≤0.045	-
Mrk153	0.048[a]	0.008	≤0.050	-	≤0.045	-
Mrk209	0.062	0.007	0.03	0.01	≤0.045	-
Mrk930	0.40[a]	0.04	0.13[a]	0.01	0.049[a]	0.007
NGC1140	1.97[a]	0.17	0.94[a]	0.08	0.28[a]	0.03
NGC1569	12.0[a]	1.0	5.02[a]	0.41	1.55[a]	0.13
NGC1705	0.60[a]	0.05	0.29[a]	0.03	0.10[a]	0.01
NGC2366	2.04[a]	0.17	1.01[a]	0.09	0.39[a]	0.04
NGC4214	18.6[a]	1.5	9.92[a]	0.80	3.79[a]	0.31
NGC4449	32.4[a]	2.6	14.8[a]	1.2	5.01[a]	0.41
NGC4861	1.10[a]	0.10	0.54[a]	0.05	0.20[a]	0.03
NGC5253	7.82[a]	0.63	3.64[a]	0.29	1.18[a]	0.10
NGC625	4.33[a]	0.35	2.18[a]	0.18	0.80[a]	0.07
NGC6822[d]	48.4[a]	15.0	29.7[a]	9.2	13.6[a]	4.2
Pox186	0.045	0.007	≤0.050	-	≤0.045	-
SBS0335-052	≤0.030	-	≤0.050	-	≤0.045	-
SBS1159+545	≤0.030	-	≤0.050	-	≤0.045	-
SBS1211+540	≤0.030	-	≤0.050	-	≤0.045	-
SBS1249+493	≤0.030	-	≤0.050	-	≤0.045	-
SBS1415+437[c]	-	-	-	-	-	-
SBS1533+574	≤0.122[a]	-	≤0.050	-	≤0.045	-
Tol0618-402[c]	-	-	-	-	-	-
Tol1214-277	≤0.030	-	≤0.050	-	≤0.045	-
UGC4483	0.024	0.006	≤0.050	-	≤0.045	-
UGCA20[c]	-	-	-	-	-	-
UM133	0.032	0.006	≤0.050	-	≤0.045	-
UM311[b]	3.84[a]	0.31	1.87[a]	0.16	0.66[a]	0.06
UM448	0.99[a]	0.08	0.38[a]	0.03	0.13	0.01
UM461	0.027	0.006	0.03	0.01	≤0.045	-
VIIZw403	0.14[a]	0.01	0.053	0.008	0.028	0.009

[a]: The flux densities are derived from aperture photometry, with the same aperture used for PACS.
[b]: These objects are galaxies within compact groups of galaxies or are parts of other galaxies and the photometry given here is for the whole group (see Section 4.2.1 for details).
[c]: These sources were not observed at all by SPIRE.
[d]: The quoted flux densities for these sources have been corrected for cirrus contamination.

Chapter 5

Cold dust from low-metallicity environments to normal galaxies

Contents

This Chapter is dedicated to the comparison the cold dust properties of dwarf galaxies with that of more metal-rich environments, first qualitatively with colour-colour diagrams (Section 5.1), and then quantitatively with the aid of a modified blackbody model (Section 5.2). The cold dust properties are thus characterised with the following parameters: the temperature (T), the emissivity index (β), the dust mass ($M_{dust,BB}$) and the FIR luminosity (L_{FIR}).

5.1 Characterising the SED shapes

In order to obtain a qualitative view of the FIR-to-submm behaviour of the DGS sample, and to compare with the KINGFISH sample, we inspect the observed *Herschel* SEDs as well as several *Herschel* colour-colour diagrams combining both PACS and SPIRE observations. Indeed, recent studies have shown how colours can be used to explore the dust properties of galaxies (e.g., Bendo et al. 2010a; Galametz et al. 2010; Boselli et al. 2010a, 2012; Dale et al. 2012; Galametz et al. 2013).

5.1.1 Observed spectral energy distributions

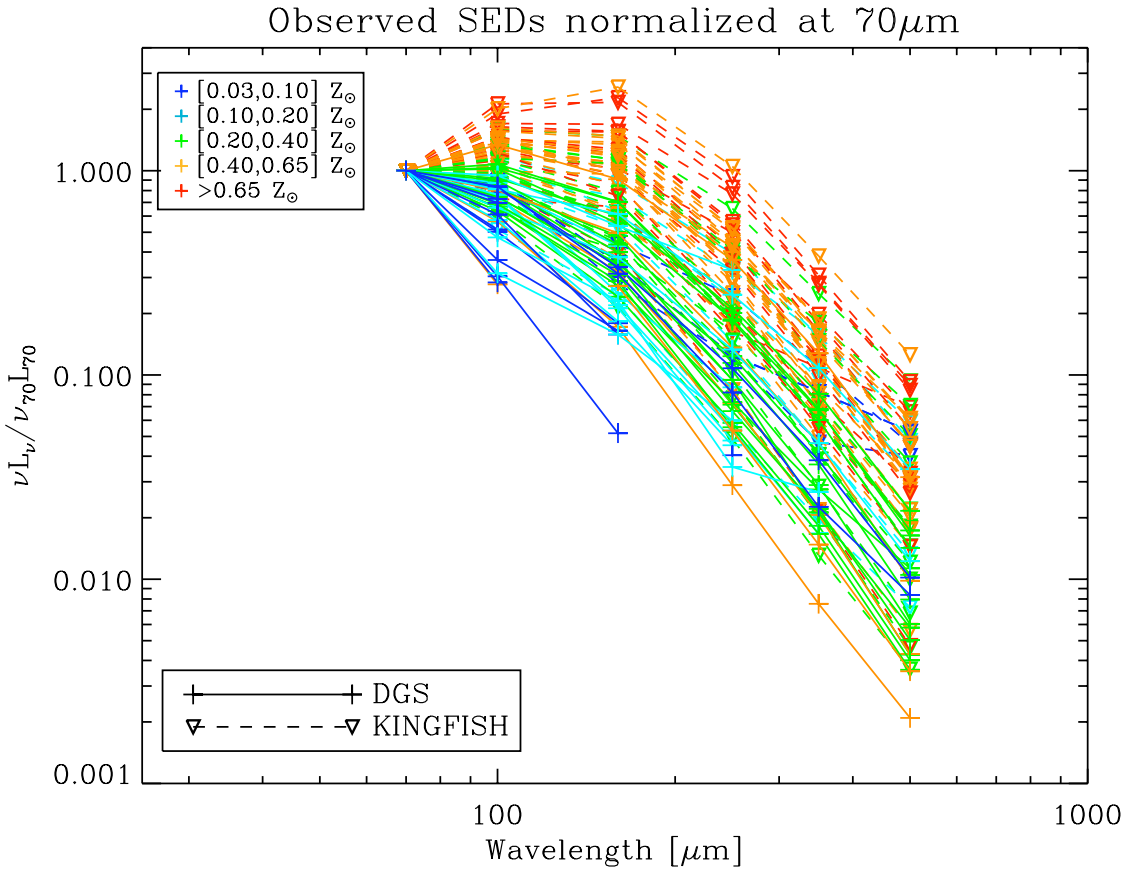

Fig. 5.1. Total *Herschel* observed SEDs for both DGS and KINGFISH samples, normalized at 70 μm. The colours delineate the different metallicity bins, and the lines and symbols differentiate DGS (plain lines and crosses) and KINGFISH galaxies (dashed lines and downward triangles).

Total observed SEDs for both samples are computed for a first look at the characteristic SED shapes in the DGS and KINGFISH samples (Figure 5.1). The upper limits are not indicated here for clarity. The most metal-poor galaxies are also the faintest and therefore not detected with

Herschel beyond 160 μm. The observed SEDs are normalized at 70 μm, and we see here that the peak of the SED shifts towards longer wavelengths as the metallicity increases, reflecting the impact of metallicity on the observed dust properties.

5.1.2 Dwarf Galaxy Survey colours

Constructing the colour-colour diagrams

The *Herschel* colour-colour diagrams are constructed first by computing the observed flux ratios and the corresponding error bars, for both DGS and KINGFISH, and omitting the galaxies with more than one upper limit in the considered bands.

We then compute the theoretical *Herschel* flux ratios of simulated modified blackbodies spanning a range in temperature (T from 0 to 40 K in 2 K bins and from 40 to 100 K in 10 K bins) and emissivity indices (β from 0.0 to 2.5). From now on, we define the emissivity index fixed for modelling the simulated *Herschel* flux ratios as "β_{theo}", and "β_{obs}" when we leave the emissivity index as a free parameter in modified blackbody fits (see Section 5.2). In our simulated modified blackbody, the emitted fluxes are proportional to $\lambda^{-\beta_{theo}} \times B_\nu(\lambda, T)$, where $B_\nu(\lambda, T)$ is the Planck function (see Section 5.2).

The pipeline we use for the data reduction gives us monochromatic flux densities for our data points for both PACS and SPIRE. To mimic the output of the pipeline for our theoretical points we weight our theoretical flux density estimates by the RSRF of the corresponding bands. For SPIRE simulated measurements, we then convert our RSRF-weighted flux densities into monochromatic flux densities by applying the K_4 correction given on the SPIRE Observers' Manual (see Section 3.2.2). For PACS, we also colour correct the RSRF-weighted modelled flux densities to a spectrum where νF_ν is constant (i.e., multiply by the analogous of K_4 for PACS, see Eq. 3.4). These simulated flux ratios from a simple model are useful indicators to interpret the colour-colour diagrams.

FIR/submm colours

The spread of galaxies on the colour-colour diagrams (Figures 5.2 and 5.3) reflects broad variations in the SED shape and physical properties in our survey.

The F_{70}/F_{100} vs F_{100}/F_{160} diagram (Figure 5.2) traces best the peak of the SED. Galaxies usually exhibit a peak in their SED around $\sim$ 100 - 160 μm. Galaxies with FIR flux densities $F_{70} > F_{100} > F_{160}$ may be quite warm as they peak at wavelengths less than 70 μm. Colder galaxies would lie in the lower left corner of the plot ($F_{70} < F_{100} < F_{160}$), as shown by the simulated flux ratio lines. KINGFISH galaxies indeed cluster in the corresponding lower-left corner of the plot while DGS galaxies span a wider space (Fig 5.2, top), reflecting the differences in the dust properties between the low-metallicity dwarf galaxies and the generally more metal-rich environments probed by the KINGFISH survey. Nonetheless both samples follow the trends outlined by the theoretical flux ratio lines from simulated modified blackbodies. There are some outliers, all of them being very faint, extremely metal-poor galaxies (from 0.03 to 0.20 $Z_\odot$). There is also a metallicity trend in Fig. 5.2 (bottom), between the KINGFISH sample and the DGS galaxies, as well as within both samples, i.e., low-metallicity (dwarf) galaxies peak at much shorter wavelengths and thus have overall warmer dust (several tens of K), compared to more metal-rich galaxies.

As we saw in Section 2.2.2, the warmer dust of dwarf galaxies is due to the very energetic environment in which the grains reside: the dust grains are exposed to harder and more intense ISRF than in a more metal-rich environment. This increases the contribution of hot and warm dust to the total dust emission resulting in higher equilibrium dust temperatures. This confirms what has already been observed by *IRAS* and *Spitzer* on smaller samples of dwarf galaxies (e.g., Hunter et al. 1989; Sauvage et al. 1990; Melisse & Israel 1994; Walter et al. 2007).

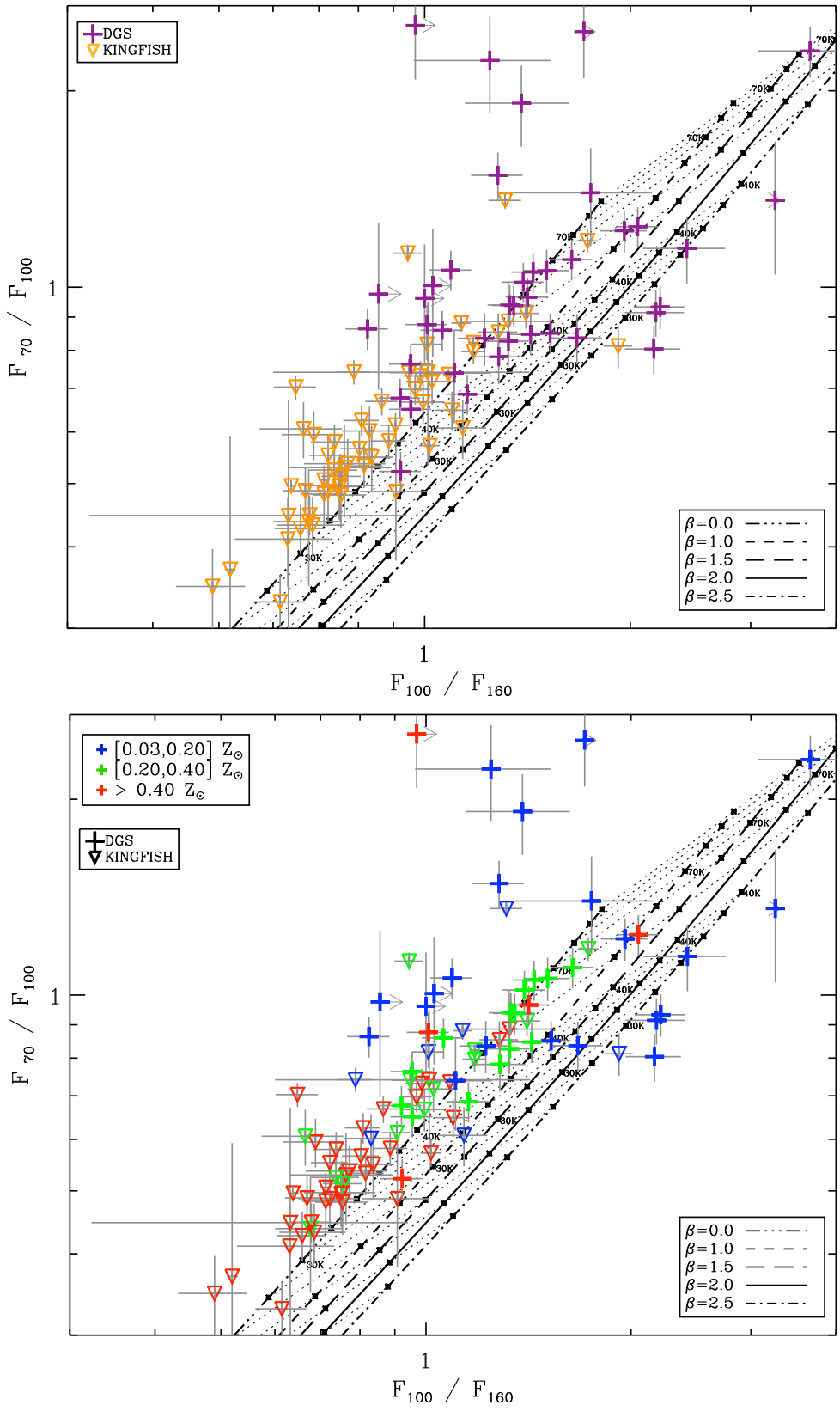

Fig. 5.2. Colour-colour diagram: PACS/PACS diagram: F_{70}/F_{100} versus F_{100}/F_{160}. *(top)* The colour and symbol code differentiates DGS (purple crosses) and KINGFISH galaxies (orange downward triangles). *(bottom)* The colour code delineates the different metallicity bins this time. Crosses and downward triangles are still representing DGS and KINGFISH galaxies, respectively. For both plots, the curves give theoretical Herschel flux ratios for simulated modified blackbodies for $\beta_{theo} = 0.0$ to 2.5 and T from 0 to 40 K in 2 K bins and from 40 to 100 K in 10 K bins, as black dots, increasing in T from left to right. Lines of constant T are indicated as dotted lines, and a few temperatures have been marked on the plots.

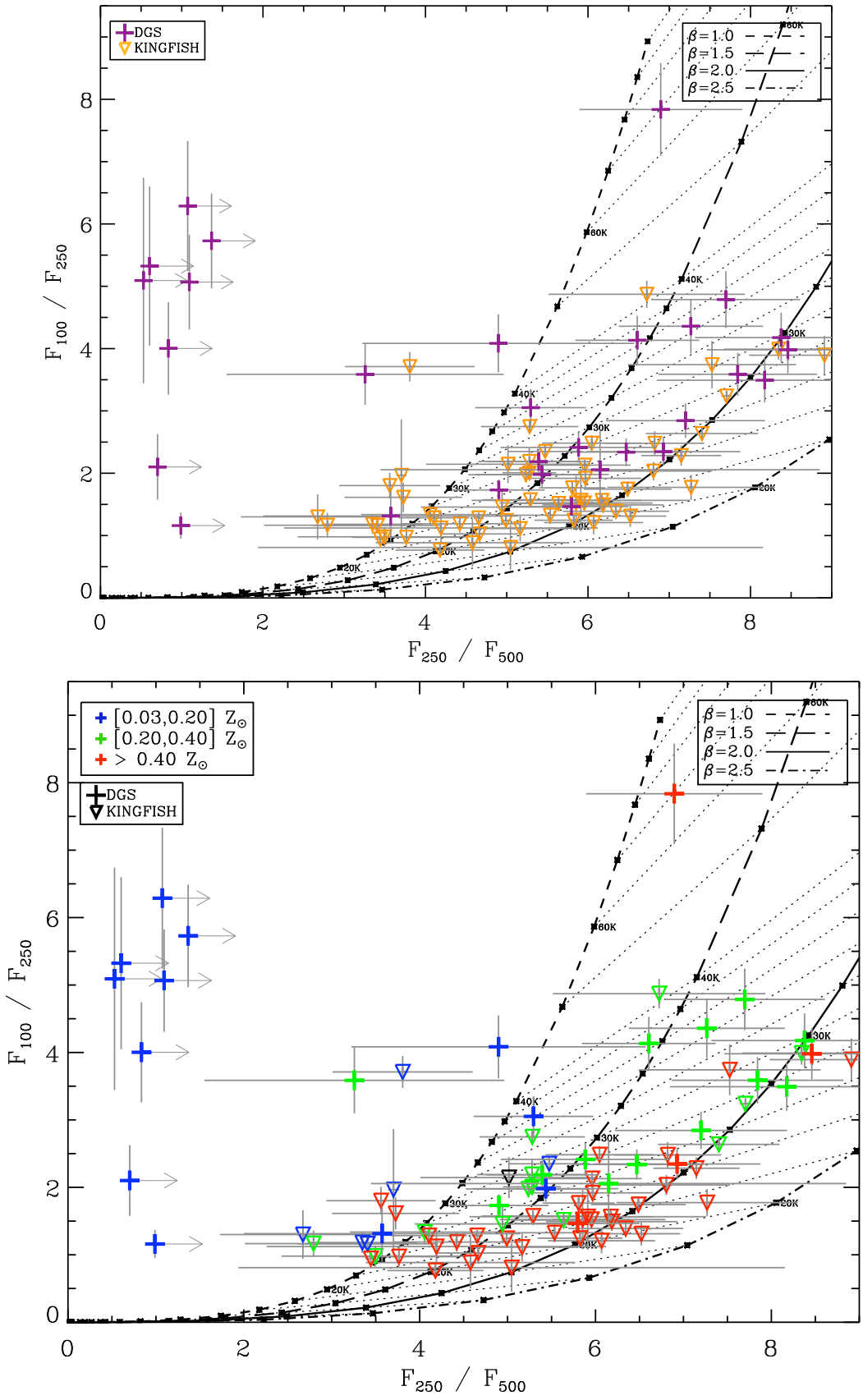

Fig. 5.3. Colour-colour diagram: PACS/SPIRE diagram: F_{100}/F_{250} versus F_{250}/F_{500}. The colour and symbol choices are the same as in Figure 5.2 for both figures. Note that the most metal-poor galaxies (from 0.03 to 0.20 $Z_{\odot}$) are very faint and even not detected anymore at long wavelengths. We were only able to derive upper limits beyond 160 μm for these galaxies and, thus, some galaxies do not appear on this diagram anymore.

Note that there is a small excess at 70 μm for most of the galaxies compared to our simulated modified blackbodies, causing them to fall above the lowest β_{theo} line to artifically low β_{obs}. This means that if we were to fit modified blackbodies *only* to the FIR flux densities (from 70 μm to 160 μm) we would get very low values of β_{obs}, i.e., very flat SEDs in the FIR, which reflects a broad peak in the observed SED. This is due to the crudeness of the isothermal approximation made in the modified blackbody modelling. In a real galaxy, the dust grains have a range of temperatures, (e.g., hotter dust around star-forming regions vs colder dust in the diffuse ISM). Such a low β_{obs} here is only a side effect of the distribution in temperature of the grains in the galaxy. The extremely metal-poor outliers noted before may have an even wider temperature distribution than in more metal-rich galaxies, causing the broadening of the peak in their dust SED and their peculiar location on the diagrams in Fig. 5.2. Part of this excess at 70 μm could also be due to non-thermal heating, i.e., dust grains whose emission can not be represented by a modified blackbody, such as stochastically heated small grains.

More accurate values of T and β_{theo} may be illustrated by including submm data in the colour-colour diagrams. At submm wavelengths (beyond $\sim$ 250 μm), the emissivity index this time represents an intrinsic grain property: the efficiency of the emission from the dust grain. A theoretical emissivity index $\beta_{theo} = 2$ is commonly used to describe the submm SED for local and distant galaxies in the models as it represents the intrinsic optical properties of Galactic grains (mixture of graphite and silicate grains; see Sections 1.2.3 and 1.2.5). More recently β_{theo} between 1.5 and 2 have also been used for galaxies (e.g., Amblard et al. 2010; Dunne et al. 2011). The F_{100}/F_{250} *vs* F_{250}/F_{500} diagram (Figure 5.3) reflects best the variations in emissivity index β_{theo}. Here again the DGS galaxies are more widely spread than the KINGFISH galaxies (Figure 5.3, top) spanning larger ranges of F_{100}/F_{250} and F_{250}/F_{500} ratios, that is, wider ranges in temperature and β (such as higher T and lower β). As far as metallicity is concerned, the trend with temperature already noted in Fig. 5.2 is still present (Figure 5.3, bottom). But hardly any trend between β and metallicity can be noticed: as the extremely low-metallicity galaxies are not detected at 500 μm, it is rather difficult to conclude on this point relying only on the FIR/submm colour-colour diagram.

Modelling low-metallicity dwarf galaxies with grain properties derived from the Galaxy (i.e., using β_{theo} =2), may thus not be appropriate. The galaxies showing a lower β_{obs} ($\beta_{obs} < 2$) will have a flatter submm slope. Smaller F_{250}/F_{500} ratios, that can be seen as a sign of lower β_{obs}, indicative of a flatter submm slope, have already been noted with *Herschel* by, e.g., O'Halloran et al. (2010); Grossi et al. (2010); Boselli et al. (2012) for subsolar-metallicity galaxies. This flatter slope may be the sign of a contribution from an extra emission in excess of the commonly used $\beta_{theo} = 2$ models. Thus the flattening of the observed submm slope ($\beta_{obs} < 2$) could be used as a diagnosis for possible excess emission appearing at 500 μm (see Section 5.4).

5.2 FIR/submm modelling of the cold dust properties

To complete our observational and qualitative view of the FIR-submm behaviour of the DGS and KINGFISH galaxies, we use a modified blackbody model to quantitatively determine the parameters discussed above: T and β_{obs}, as well as $M_{dust,BB}$ and L_{FIR} in the DGS and KINGFISH samples. In the following, we note the dust mass estimated from a modified blackbody $M_{dust,BB}$, as opposed to the dust mass derived from a semi-empirical dust model, M_{dust} (see Chapter 7).

5.2.1 Modelling the cold dust

Here we are considering *Herschel* data covering in the FIR-submm, where the bulk of the IR luminosity is emitted and where most of the mass of the cold dust can be traced. We know that cold grains are also large grains and thus the dust grains are likely to be in equilibrium with the

radiation field. If we assume that all of the grains have the same equilibrium temperature (i.e., the same size), their emission can be represented by a modified blackbody.

A single modified blackbody is thus fitted to the *Herschel* data of each galaxy from both DGS and KINGFISH samples and the modelled flux densities are given by:

$$F_\nu(\lambda) = \frac{M_{dust,BB}\kappa(\lambda_0)}{D^2}\left(\frac{\lambda}{\lambda_0}\right)^{-\beta_{obs}} B_\nu(\lambda, T) \tag{5.1}$$

where $\kappa(\lambda_0) = 4.5$ m^2 kg^{-1} is the dust mass absorption opacity at the reference wavelength, $\lambda_0 = 100$ μm (see Eq. 1.13 from Section 1.2.3). The free parameters are the temperature (T) and dust mass ($M_{dust,BB}$) as well as the emissivity index (β_{obs}), where we leave β_{obs} free in the [0.0, 2.5] range. D is the distance to the source (given in Table 3.5) and $B_\nu(\lambda, T)$ is the Planck function. Colour corrections, described in Sections 3.2.1 and 3.2.2, are included in the fitting procedure.

$\kappa(\lambda_0)$ has been calculated from the grain properties of Zubko et al. (2004), as in Galliano et al. (2011)[1], and is consistent with a $\beta_{theo} = 2$ (see Section 7.1.2 and Fig. 7.3). Leaving β_{obs} to vary in our fit can produce lower dust masses for lower β_{obs} (Bianchi 2013). This effect is discussed for the two dust masses relations we derive in Section 5.3. Moreover, this particular choice for the value $\kappa(\lambda_0)$ will only affect the absolute values of the dust masses. Choosing another model to derive $\kappa(\lambda_0)$ would not affect the intrinsic variations noted in Section 5.3.

At 70 μm, possible contamination by dust grains that are not in thermal equilibrium, and whose emission cannot be represented by a modified blackbody, can occur in galaxies. An excess at 70 μm compared to a modified blackbody model can also appear, as seen in Fig. 5.2, because dust grains in a galaxy are more likely to have a temperature distribution rather than a single temperature. For example in spiral galaxies (present in the KINGFISH sample), the dust emission at 70 - 500 μm can originate from two components with different heating sources and potentially different temperatures (Bendo et al. 2010a, 2012; Boquien et al. 2011; Smith et al. 2012b). Therefore, we restrict our wavelength fitting range to 100 - 500 μm. The 70 μm observation can be useful as an upper limit for a single temperature dust component. We redo the fit including the 70 μm point only if the modelled point from the fit without 70 μm data violates this upper limit condition, i.e., if it is greater than the observed point (e.g., Mrk 209 in Figure 5.4).

Some of our galaxies are not detected at some wavelengths. To have enough constraints for the fit, at least a detection up to 250 μm is required. If the galaxy is not detected beyond 160 μm, we fit a modified blackbody including the 70 μm point. Indeed some galaxies peaking at very short wavelengths have their Rayleigh Jeans contribution already dropping at FIR and submm wavelengths, and are often not detected by SPIRE. For these galaxies, the 70 μm point is already on the Rayleigh Jeans side of the modified blackbody, and in this case we also include it in our fit.

All of these conditions are matched for 35 DGS galaxies, and we use the 70 μm point for 11 of them (five because of the violation of the upper limit condition at 70 μm, four because the galaxy is not detected beyond 160 μm, and two because the galaxy is not observed by SPIRE, see Table 5.1 for details). However, none of the 56 galaxies from KINGFISH requires using the 70 μm point.

From the fitted modified blackbodies, we also derive the FIR luminosity, L_{FIR}, by integrating the modelled curve between 50 and 650 μm. The resulting parameters from the fits are given in Table 5.1. The SEDs are shown in Fig. 5.13 for all 35 DGS galaxies and Fig. 5.14 for the 56 KINGFISH galaxies.

5.2.2 Rigorous error estimation

In order to derive conservative errors for our T, β, $M_{dust,BB}$ and L_{FIR} parameters we performed Monte Carlo iterations for each fit, following the method in Galliano et al. (2011). For each galaxy,

[1] for their "Standard Model", see Appendix A of Galliano et al. (2011).

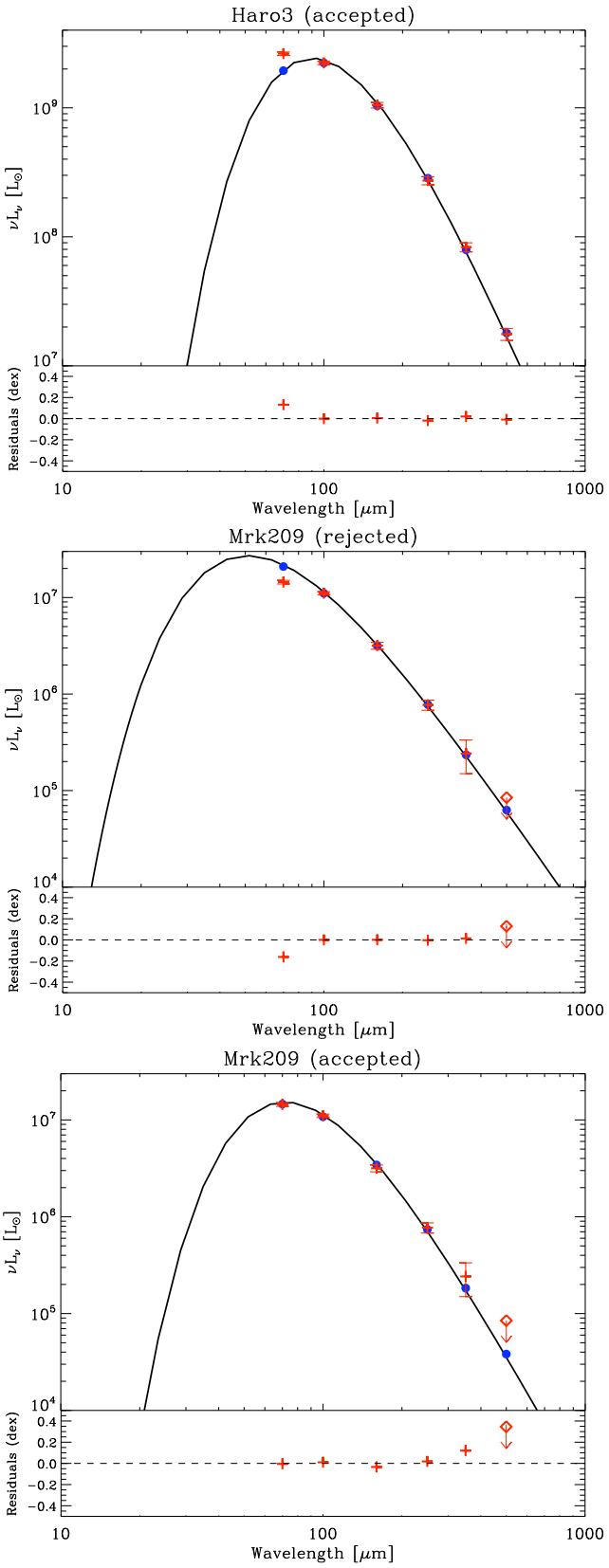

Fig. 5.4. Examples of modified blackbody fits: the observed points are the red crosses whereas the modelled points are the filled blue circles. Upper limits are indicated with red diamonds. The bottom panel of each plot indicates the residuals from the fit. (*top*) Fit for Haro3, the observed 70 μm point which is not considered at first in our fitting procedure, is above the modelled one. (*centre*) Fit for Mrk209. Here the observed 70 μm point is below the modelled one, and the fit should be redone, giving us: (*bottom*) Fit for Mrk209 using the 70 μm point. Note how the shape of the modified blackbody varies between the two: for example, the dust temperature for Mrk209 goes from 56 K (without 70 μm) to 33K (with 70 μm).

we randomly perturb our fluxes within the error bars and perform fits of the perturbed SEDs (300 for each galaxy). To be able to do so, we must first carefully identify the various types of error and take special care for errors which are correlated between different bands.

As explained in Sections 4.2.2 and 4.3.2, we have measurement errors and calibration errors in our error estimates. The measurement errors are independent from one band to another and are usually well represented by a Gaussian distribution. The calibration errors, however, are correlated between different bands as it is the error on the flux conversion factor. It can be summarized for our case as follow:

PACS: Although the total calibration error is 5% in the three PACS bands it can be decomposed into two components:

- the uncertainty on the calibration model is 5% (according to the PACS photometer point-source flux calibration documentation[2]) and is correlated between the three bands.
- the uncertainties due to noise in the calibration observations are: 1.4, 1.6, 3.5 % at 70, 100, 160 μm, respectively (PACS photometer point-source flux calibration). These uncertainties are independent from one band to another.

SPIRE: The SPIRE ICC recommend using 7% in each band but here again we can decompose it:

- the uncertainty on the calibration model is 5% (SPIRE Observer's Manual) and is correlated between the three bands.
- the uncertainties due to noise in the calibration observations are 2% for each band (SPIRE Observer's Manual). These uncertainties are independent.
- As SPIRE maps are given in Jy beam^{-1}, the error on the beam area will also affect the calibration. The uncertainty on the beam area is given to be 4% in each band[3] and are independent. This error is applied only to the extended sources, as the photometry for the point sources has been done directly on the timeline data.

The perturbation of the observed fluxes will then be the sum of two components:

- A normal random independent variable representing the measurement errors.
- A normal random variable describing the calibration errors that takes into account the correlation between the wavebands as described above, the same for each galaxy.

After performing 300 Monte-Carlo iterations, a distribution for each of the three model parameters T, β, $M_{dust,BB}$ as well as for L_{FIR} is obtained for each galaxy (see example on Fig. 5.5). We chose to quote the 66.67% confidence level for our parameters defined by the range of the parameter values between 0.1667 and 0.8333 of the repartition function. As the distributions are often asymmetric we obtain asymmetric error bars on our parameters. These error bars are given in Table 5.1.

5.3 Dust FIR properties

We now have the T, β, $M_{dust,BB}$ and L_{FIR} distributions of the DGS and KINGFISH samples (Figures 5.6 and 5.7). Note that KINGFISH is not a volume- or flux-limited sample but a cross-section of galaxies with different properties. Due to the heterogeneity of both samples we thus quote the median rather than the mean to compare the samples.

[2]This documentation is available at: http://herschel.esac.esa.int/twiki/bin/view/Public/PacsCalibrationWeb?template=viewprint

[3]This value is given in: http://herschel.esac.esa.int/twiki/bin/view/Public/SpirePhotometerBeamProfileAnalysis.

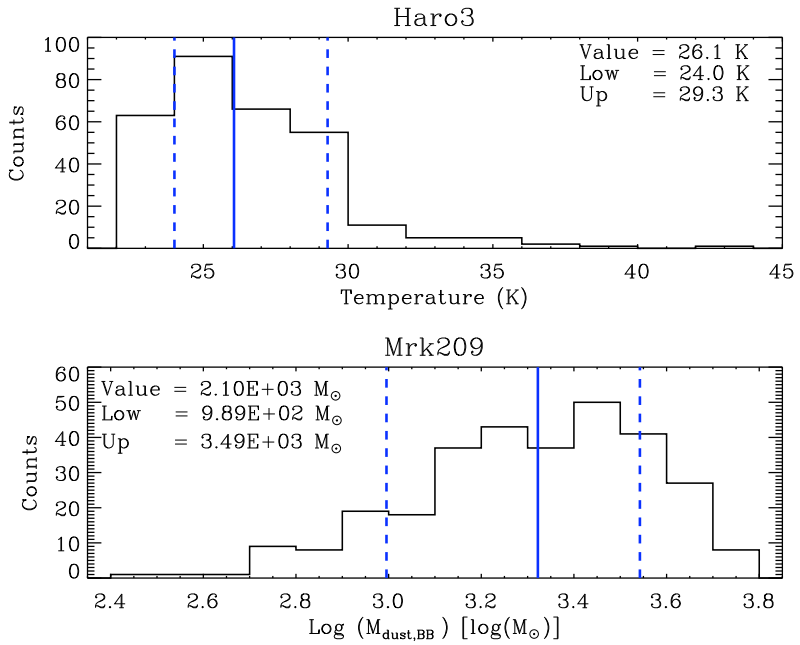

Fig. 5.5. Examples of the obtained parameter distributions for the 300 Monte-Carlo iterations for the modified blackbody fits: (*top*) distribution of temperature, T, for Haro3, (*bottom*) distribution of dust mass, $M_{dust,BB}$, for Mrk209 with the 70 μm point included in the fit. The plain blue line notes the value of the parameter and the dashed blue lines note the 66.67% confidence level for the parameters.

5.3.1 Temperature

The range in dust temperature of the DGS galaxies is 21 to 98 K with a median $T \sim 32$ K (Figure 5.6a). The most metal-poor galaxies are among the warmer ones. If we compare the KINGFISH to the DGS galaxies, our lowest temperatures are quite comparable (17 vs 21 K), but the DGS galaxies have higher maximal dust temperatures (39 vs 98 K). In Figure 5.6a, we see that the KINGFISH dust temperature distribution has a narrow peak around ∼20-25 K whereas the DGS distribution is broader. This difference is due to some galaxies in our sample that peak at extremely short wavelengths, a distinguishing feature of star-forming dwarf galaxies, resulting in very high dust temperatures for a single modified blackbody fit. The dust in DGS galaxies is thus overally warmer than that in more metal-rich galaxies ($T^{med}_{DGS} = 32$ K and $T^{med}_{KINGFISH} = 23$ K). This is coherent with the temperature trends presented in the previous section. Note that the high temperature tail of the DGS temperature distribution could be even more prominent than presented here: some galaxies are not detected beyond 100 - 160 μm rendering impossible the determination of their dust temperature with a modified blackbody fit (13 galaxies in the DGS). The SEDs for these galaxies likely peak at very short wavelengths giving very warm averaged dust temperatures (see Chapter 7 for the complete SED modelling of these galaxies).

5.3.2 Emissivity index

The "observed" emissivity index (β_{obs}, see Eq. 5.1) distribution is shown on Fig. 5.6b, spanning a range from 0.0 to 2.5 with a median $\beta_{obs} \sim 1.7$ for the DGS. There does not appear to be any clear correlation with metallicity here. Nonetheless, even if some DGS galaxies are nicely fitted by an often-presumed $\beta_{obs} = 2.0$ blackbody, some require a $\beta_{obs} \leq 2.0$, and those are primarily metal-poor to moderately metal-poor galaxies (0.10 to 0.4 $Z_{\odot}$). Note also that for the KINGFISH sample, all of the galaxies, but two, within this metallicity range have $0.5 \leq \beta_{obs} \leq 2.0$. From SPIRE band ratios,

Boselli et al. (2012) also found that low-metallicity galaxies from the HRS sample were presenting submm colours consistent with an emissivity index ≤ 2.0. Arbitrarily fixing $\beta = 2.0$ in a blackbody modelling, in order to mimic the emissivity index appropriate for a mixture of amorphous silicate and graphite (reproducing the Milky Way observations), may not always be appropriate for low-metallicity galaxies. However, we note that several DGS galaxies suggest a β_{obs} = 0.0 - 0.5 from our modified blackbody model (Fig. 5.6b). These six galaxies with $\beta_{obs} < 0.5$ in the DGS, are not detected beyond 160 μm and such a low β_{obs}, physically unrealistic, is probably due to the poorly constrained submm part of the SED.

In summary, there are metal-poor to moderately metal-poor galaxies, with metallicities between 0.1 and 0.4 $Z_{\odot}$, for which $0.5 \leq \beta_{obs} \leq 2.0$. These lower β_{obs} values, not necessarily realistic in term of actual grain properties, are representative of a flatter submm slope in the FIR observations, and could perhaps be an indicator of the presence of a submm excess in these sources (see Section 5.4).

5.3.3 Dust mass

The dust masses estimated from our modified blackbody fits for the DGS range from 1.0×10^2 $M_{\odot}$ to 2.5×10^7 $M_{\odot}$ (Figure 5.6c), with a median of $\sim 1.2 \times 10^5$ $M_{\odot}$. From Figure 5.6c we see that the most metal-poor galaxies are the least massive galaxies compared to the moderately metal-poor galaxies. The dwarf galaxies are, not surprisingly, less massive in dust than the galaxies from the KINGFISH sample: the median dust mass of the KINGFISH sample is about two orders of magnitude higher than for the DGS: $\sim 1.1 \times 10^7$ $M_{\odot}$. In order to determine if this is only an effect due to the smaller sizes of dwarfs, we consider the ratio between the dust and stellar masses. The stellar masses for the DGS and KINGFISH samples have been computed in Chapter 3. Figure 5.7 shows that there is a strong decrease (about an order of magnitude) of the proportion of dust mass relative to the stellar mass with decreasing metallicity: we have a Spearman rank coefficient[4] ρ=0.51. The median for the ratio $M_{dust,BB}/M_{\star}$ is 0.02% for DGS versus 0.04% for KINGFISH. The best power-law fit gives:

$$M_{dust,BB}/M_{\star} = 1.5 \times 10^{-20} \times (12 + log(O/H))^{18.4} \quad (5.2)$$

However the dust masses derived here for both samples are probably lower limits of the real dust masses in many cases (see Dale et al. 2012 and Section 8.2.1). Indeed we allow our β_{obs} to go to very low values, giving lower dust masses than if we fixed it to 1.5 or even 2.0: as we allow a greater emission effciency for the grains, we need less mass than if we were using a higher emissivity index, to account for the same amount of luminosity. We perform the test by fixing the emissivity index parameter to 2.0 and find that the correlation between the dust-to-stellar mass ratios with metallicity almost vanishes: with $\beta = 2.0$ modified blackbody dust masses, the Spearman rank coefficient for the relation decreases to ρ=0.08. Additionally, with our modified blackbody fits we are considering only one temperature and grain size. We may be missing here a fraction of the dust mass coming from warmer big grains, and this contribution may be more important in low-metallicity galaxies rather than in more metal-rich ones. The mass corresponding to the stochastically heated grains is, however, negligible. In Chapter 7, we will obtain total dust masses from a full semi-empirical SED model, which will allow us to study the dust-to-stellar mass ratios in more details.

5.3.4 FIR luminosity

The FIR luminosities in the DGS sample range from 1.2×10^7 $L_{\odot}$ to 5.3×10^{10} $L_{\odot}$ (Figure 5.6d), with a median of $\sim 5.3 \times 10^8$ $L_{\odot}$. We see in Figure 5.6d that dwarf galaxies are less luminous in the

[4]The Spearman rank coefficient, ρ, indicates how well the relationship between X and Y can be described by a monotonic function: monotonically increasing: $\rho > 0$, or monotonically decreasing: $\rho < 0$.

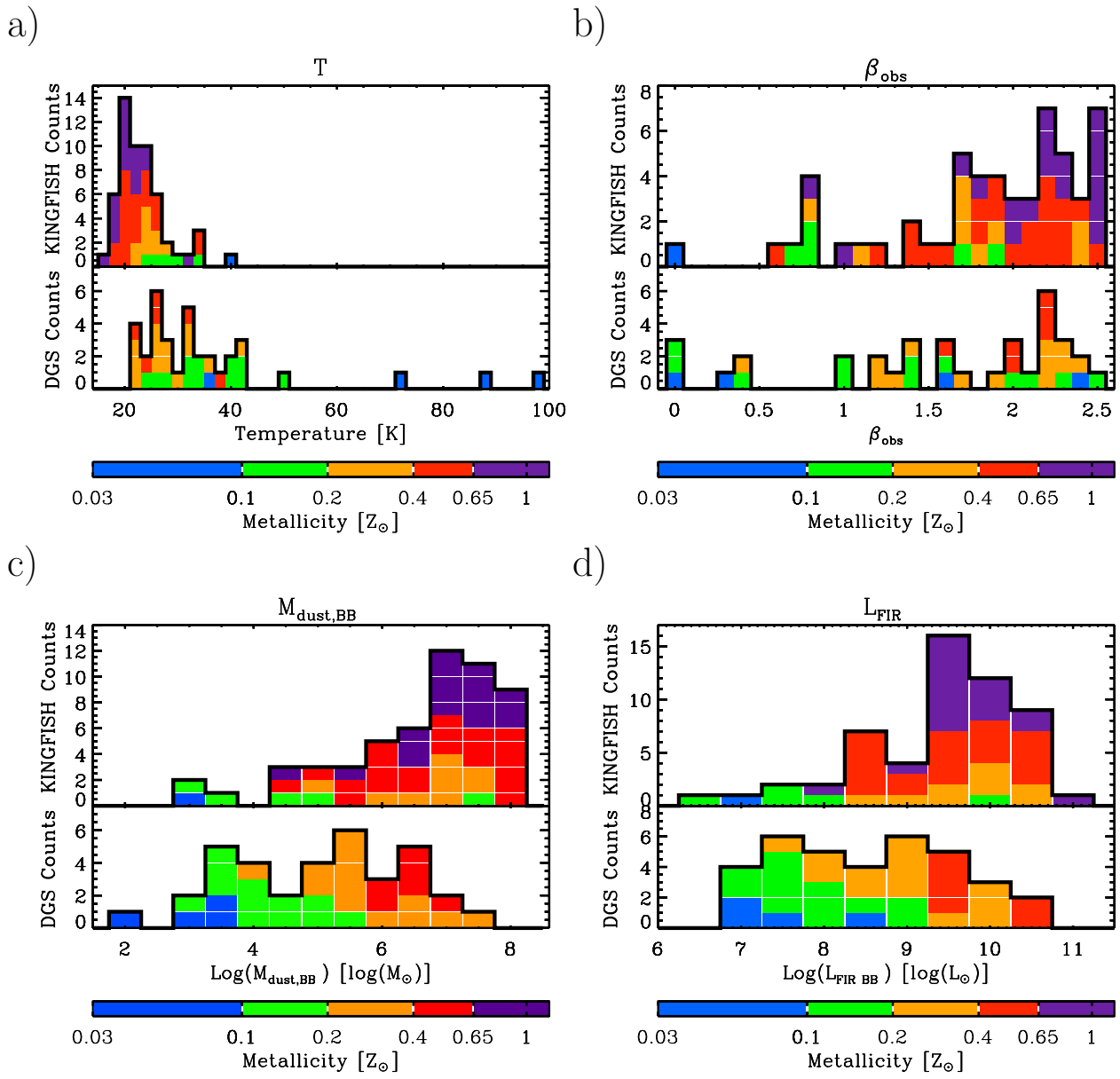

Fig. 5.6. Distributions of temperature *(a)*, emissivity index *(b)*, dust mass *(c)* and FIR luminosity *(d)* from modified blackbody fits for *Herschel* data for the DGS and KINGFISH samples. The colour scale represents the range of metallicity values. On each panel, the upper/lower histogram is the KINGFISH/DGS distribution for the parameter.

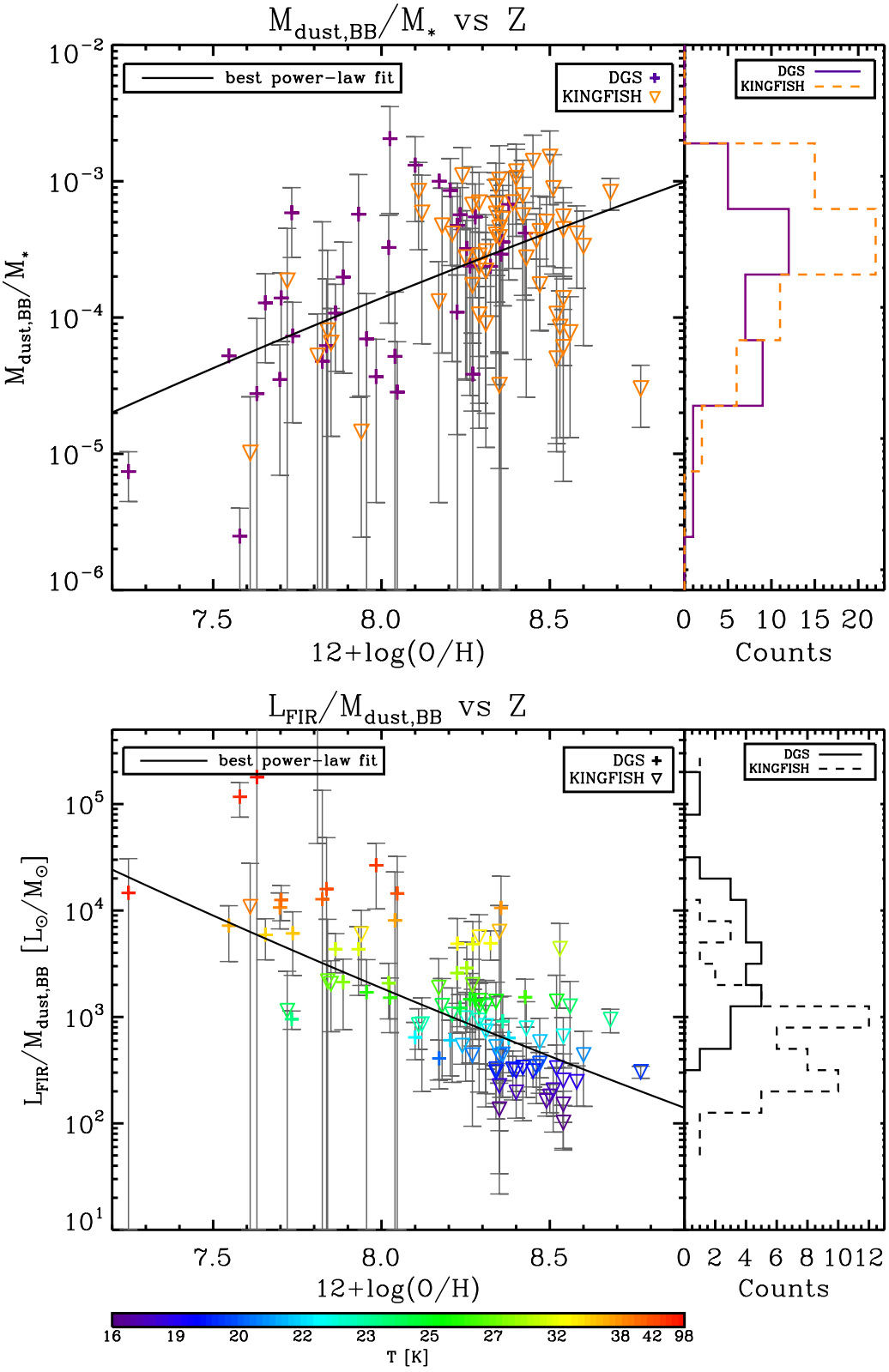

Fig. 5.7. *(top)* $M_{dust,BB}/M_\star$ as a function of metallicity for DGS (purple crosses) and KINGFISH (orange downward triangles). The best power-law fit is indicated as a black line, and corresponds to: $\log(M_{dust,BB}/M_\star)$ = (-20.4 ± 1.6) + (18.4 ± 1.8) × log(12+log(O/H)). The distribution of $M_{dust,BB}/M_\star$ is indicated on the side for both samples: plain purple line for DGS and dashed orange line for KINGFISH. *(bottom)* $L_{FIR}/M_{dust,BB}$ as a function of metallicity for DGS (crosses) and KINGFISH (downward triangles). The colours code the temperature, T. The best power-law fit line is indicated as a black line, and corresponds to: $\log(L_{FIR}/M_{dust,BB})$ = (24.4 ± 1.1) + (-23.6 ± 1.2) × log(12+log(O/H)). The distribution of $L_{FIR}/M_{dust,BB}$ is indicated on the side for both samples: solid line for DGS and dashed line for KINGFISH. On both plots: the errors on the metallicities are omitted for clarity. They are of about 0.1 dex on average.

FIR than the galaxies from the KINGFISH sample. However if we consider $L_{FIR}/M_{dust,BB}$, which represents the quantity of light emitted by the available amount of dust, there is a strong trend of increasing $L_{FIR}/M_{dust,BB}$ with decreasing metallicity (Figure 5.7): here we have a Spearman rank coefficient ρ=-0.72. The best power-law fit gives:

$$L_{FIR}/M_{dust,BB} = 4.2 \times 10^{24} \times (12 + log(O/H))^{-23.6} \quad (5.3)$$

Despite their lower dust masses, dwarf galaxies emit more in the FIR/submm than more metal-rich galaxies, per unit dust mass ($\sim$ 6 times more for the DGS). Here fixing β_{obs}=2 only decreases the strength of the correlation (ρ = -0.46) but the correlation still holds. This difference in $L_{FIR}/M_{dust,BB}$ between the two samples is a direct consequence of the higher temperature of dust grains in dwarf galaxies, as shown by the colours on Fig. 5.7, due to the stronger and harder ISRF in which the grains are embedded. However, as mentioned above, the total dust mass may be underestimated by the modified blackbody model in lower metallicity galaxies and this trend could be weaker. This will be explored in Chapter 8.

5.3.5 Temperature - emissivity index relation

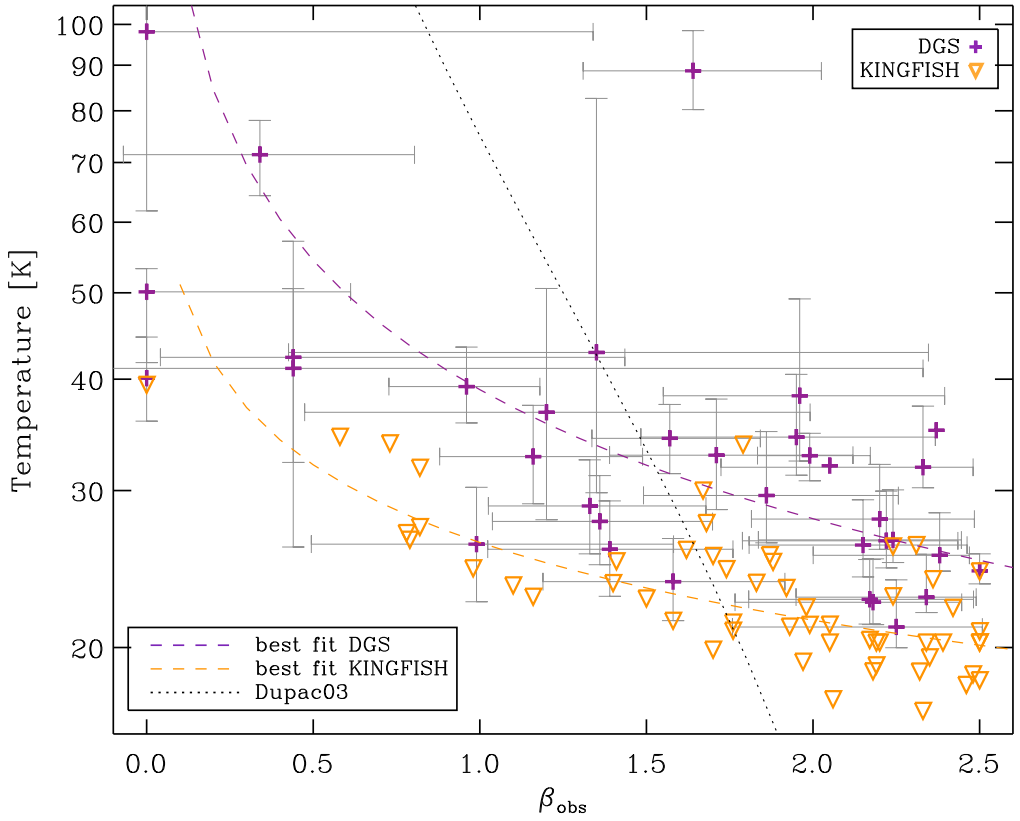

Fig. 5.8. Temperature versus β_{obs} from the modified blackbody fits for the DGS (purple crosses) and for KINGFISH galaxies (orange downward triangles). The dashed lines correspond to the best power-law fit for the DGS (purple line) and KINGFISH (orange line) galaxies, excluding the galaxies for which β_{obs}=0.0. They correspond to: $\log(T_{DGS}) = (1.59 \pm 0.01) + (-0.48 \pm 0.04) \times \log(\beta_{obs,DGS})$, and $\log(T_{KINGFISH}) = (1.41 \pm 0.02) + (-0.29 \pm 0.05) \times \log(\beta_{obs,KINGFISH})$. For comparison, the analysis of Dupac et al. (2003) has been overplotted on our data (black dotted line). For clarity the error bars on the parameters have been displayed only for the DGS sample.

Some studies have noted an inverse β / temperature correlation in objects from starless cores to galaxies (Dupac et al. 2003; Yang & Phillips 2007; Anderson et al. 2010; Paradis et al. 2010; Planck Collaboration et al. 2011a; Galametz et al. 2012; Smith et al. 2012a). To investigate this possible effect in our samples, we plot these two parameters from our modified blackbody fits (T and β_{obs}) (Figure 5.8).

First we note that the DGS galaxies have overall higher dust temperature than the KINGFISH galaxies as already noted in Figures 5.2, 5.3 and 5.6. We also have the DGS galaxies where the fit gives $\beta_{obs} = 0.0$, without detections beyond 160 μm that we believe to be due to a poorly constrained submm SED. If we exclude these galaxies, the KINGFISH and DGS samples present an anticorrelation between T and β_{obs}, and this anticorrelation seems to be steeper in the DGS: the best power-law fit gives $T \propto \beta_{obs}^{-0.48}$ for the DGS and $T \propto \beta_{obs}^{-0.29}$ for the KINGFISH galaxies. However, the anticorrelation seems stronger in KINGFISH than in the DGS sample ($\rho_{KINGFISH}$ = -0.69 vs ρ_{DGS} = -0.56).

Shetty et al. (2009a,b) and Juvela & Ysard (2012a,b) showed that such an observed anticorrelation comes from the assumption of a constant temperature along the line-of-sight in modified blackbody fits and from noise in the measurements. They advise caution when interpreting this β / temperature relationship when derived from χ^2 modified blackbody fits. Kelly et al. (2012) show that a χ^2 fit can artificially produce an anticorrelation between T and β_{obs}, whereas a Bayesian fit does not, and recovers the true parameters more accurately.

Nonetheless, if we assume that the differences in the observed (T, β_{obs}) relations between DGS and KINGFISH can be due to changes in dust optical grain properties in the submm (as suggested by Meny et al. 2007; Paradis et al. 2010), this may be the sign that the assumption of a single grain temperature, the presence of noise in the measurements and the use of a χ^2 fitting procedure may only be *partially* responsible for the observed trends. However, given the very large errors on the T and β parameters, it is difficult to draw a solid conclusion on this issue.

5.4 The intriguing submm excess: the modified blackbody view

A submm excess has been observed in the past in several low-metallicity galaxies (Galliano et al. 2003, 2005; Dumke et al. 2004; Bendo et al. 2006; Zhu et al. 2009; Galametz et al. 2009; Bot et al. 2010; Grossi et al. 2010; Galametz et al. 2011; Dale et al. 2012). It has been called "excess" because the current available models are unable to fully explain the submm emission of these galaxies. This submm excess has been one of the main sources of uncertainty in dust modelling in dwarf galaxies for the past few years, especially on the dust mass parameter.

5.4.1 Characterisation of the excess

In most models, $\beta_{theo} = 2$ is often assumed in order to mimic the optical properties of the dust grain mixture of the Galaxy. In spiral galaxies, a modified blackbody with a fixed β_{theo} to 2 reproduces well the FIR emission (Bendo et al. 2003, 2010a). In the colour-colour diagrams we hinted that a low β_{obs} may be the sign of a possible presence of an excess emission adding its contribution to a $\beta_{theo} = 2$ submm SED. Boselli et al. (2012) also showed that the F_{250}/F_{500} colour was more consistent with an effective emissivity index of 1.5 for the lowest metallicity galaxies in the HRS sample. Here we want to determine, systematically, which galaxies of the DGS and KINGFISH samples present an excess. A modified blackbody with a fixed emissivity index β_{theo} of 2.0 is fit to the data for both DGS and KINGFISH samples. Here again, we use the 70 μm point only if the modelled flux is larger than the observed flux.

We take the relative residual at 500 μm to be:

$$R(500) = \frac{L_\nu^{observed}(500) - L_\nu^{model}(500)}{L_\nu^{model}(500)} \tag{5.4}$$

In order to define a residual, R, at 500 μm the galaxy must be detected out to 500 μm. This, unfortunately, reduces our sample to 78 galaxies due to the high number of faint galaxies in the DGS sample.

Following the same procedure as in Section 5.2.2, we randomly perturb the fluxes within the errors bars and perform fits of the perturbed SEDs (300 for each galaxy). A distribution of *R(500)* is generated and the 66.67% confidence level of the distribution gives the error on the residual at 500 μm: $\Delta R(500)$. The values of *R(500)* and $\Delta R(500)$ are listed in Table 5.3.

A galaxy is then flagged with "excess" if the relative residual at 500 μm is greater than the corresponding error: $R(500) > \Delta R(500)$ (see Table 5.3). As the 500 μm point is included in the fit, the procedure will also try to achieve a good fit of the 500 μm point, and this will give lower *R(500)* than if the 500 μm point was not included in the fit. That is why we fix our "excess" criterion to a 1σ detection only. For both samples, the *R(500)* distribution is shown in Figure 5.9, and excess galaxies are indicated by hashed cells.

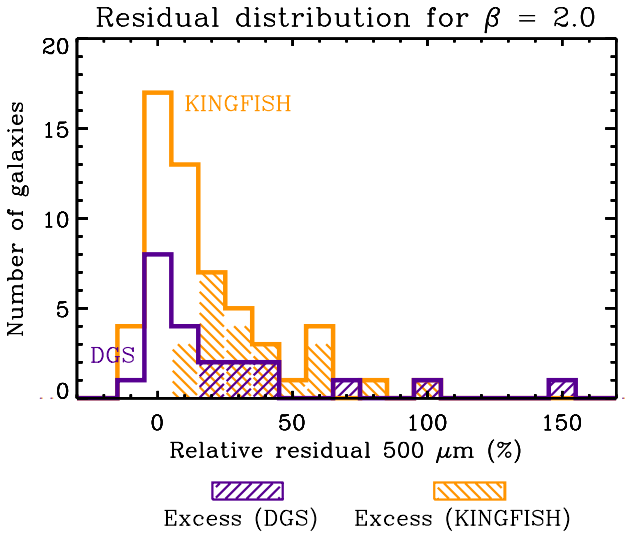

Fig. 5.9. Relative residual distribution at 500 μm for modified blackbody fits with a fixed β_{theo} of 2.0 for DGS (purple) and KINGFISH (orange) samples. Galaxies for which the residual at 500 μm is greater than the corresponding error bar ($R(500) > \Delta R(500)$) have been marked by hashed cells.

Out of 78 galaxies, 42% presents an excess at 500 μm with respect to a $\beta_{theo} = 2$ modified blackbody: nine are from DGS and 24 from KINGFISH. It is interesting to note that seven out of the nine KINGFISH galaxies of Irregular type (Im, I0 or Sm) detected at 500 μm, are among the 24 "excess" KINGFISH galaxies. The ones missing are M81dwB and HoII which both have a very large error bar on the 500 μm flux and thus a very wide *R(500)* distribution. Dale et al. (2012) looked at the residual at 500 μm for a Draine & Li (2007) model fit (see Dale et al. 2012 for details) and also found that most of these Irregular galaxies presented an excess at 500 μm. They mention a dozen KINGFISH galaxies with a *R(500)* above 60%. However as their study is based on a different model than ours, we will not go deeper into any further comparison.

Figure 5.10 shows the metallicity distribution of the 33 excess galaxies (black line) together with the joint metallicity distribution of DGS and KINGFISH samples (grey line). Note how the absence of detections at 500 μm reduces the low-metallicity tail of the joint metallicity distribution.

The metallicity distribution for the excess galaxies peaks around 12+log(O/H) $\sim$ 8.3 and is skewed towards the low-metallicity end of the distribution: 64 % of the excess galaxies are galaxies with $Z < 0.4\ Z_{\odot}$, whereas, in the total distribution of galaxies detected at 500 μm, (grey line on Fig. 5.10), only 46% of the total number of galaxies are galaxies with $Z < 0.4\ Z_{\odot}$. Moreover, the proportion of excess galaxies in the [7.5 - 8.3] metallicity range is $\sim$ 58% versus $\sim$ 29% in the]8.3 - 8.8] range. This shows that the submm excess seems to occur mainly in metal-poor galaxies, at least when a $\beta_{theo} = 2$ modified blackbody model is used. The colours on Fig. 5.10 code the signal-to-noise ratio of the residual at 500 μm for the excess galaxies. There seems to be a dichotomy in the distribution around 12+log(O/H) $\sim$ 8.3, with the strongest excesses being detected in the lowest metallicity galaxies.

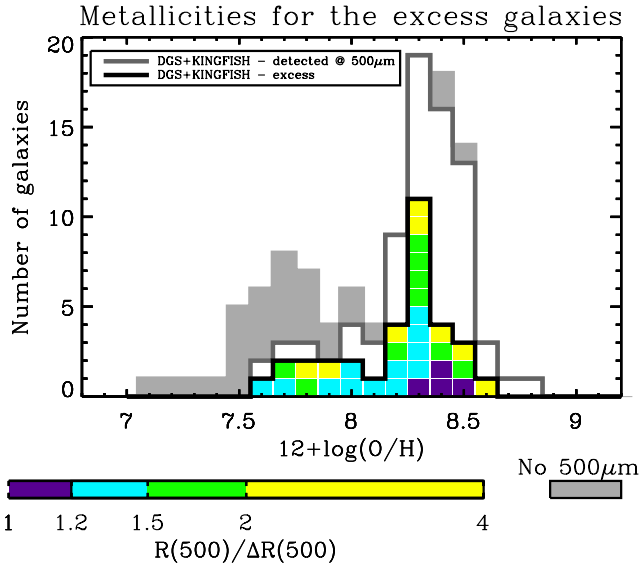

Fig. 5.10. Metallicity distribution for the excess galaxies in black. The colours mark the presence of an excess at 500 μm and code the intensity of this excess: $R(500)/\Delta R(500)$. The metallicity distribution for the DGS & KINGFISH galaxies detected at 500 μm is outlined in grey. The grey cells mark all of the galaxies for which no detection is available at 500 μm.

On Fig. 5.11, we have a clear anti-correlation between $R(500)$ and β_{obs} from the modified blackbody fits from Section 5.3: ρ=-0.78. For galaxies with a "naturally" flatter slope (i.e., a low β_{obs}), forcing a steeper slope (i.e., fixing $\beta_{theo} = 2.0$) will naturally increase the residuals at the longest wavelengths, thus generating the correlation between $R(500)$ and β_{obs}.

All of the galaxies showing an excess (i.e., $R(500) > \Delta R(500)$) have indeed a low β_{obs} ($\beta_{obs} \leq 2.0$) (Fig. 5.11). It is also interesting to note that this corresponds to 80% of the 44 galaxies with $\beta_{obs} \leq 2.0$. On the colour-colour diagram of Fig. 5.3, all of the excess galaxies fall on the left side of the $\beta_{theo} = 2.0$ line. Moreover, all of the galaxies falling on the left side of the $\beta_{theo} = 1.5$ line, except one, present an excess. This is coherent with what is observed on Fig. 5.11, and can be useful to select potential targets for FIR/submm follow-up observations.

5.4.2 A word of caution: submm excess appearing beyond 500 μm

In the previous analysis we are considering only *Herschel* wavelengths, and any galaxy for which a submm excess is appearing beyond *Herschel* wavelengths would not be detected here. This is illustrated with two galaxies of the DGS sample with observations beyond 500 μm, Haro 11 and II Zw 40, both modelled with modified blackbodies, with the same procedure as in Section 5.4.1. Haro

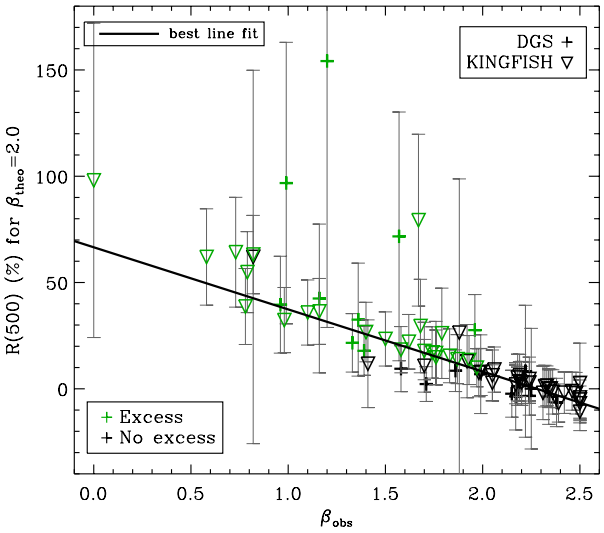

Fig. 5.11. Relative residual at 500 μm versus β_{obs} (from Section 5.3) for DGS (crosses) and KINGFISH (downward triangles) galaxies. The green symbols mark the galaxies presenting an excess at 500 μm. The best fit line is indicated as a solid black line, and corresponds to: R(500)= (66.6 ± 7.1) + (-29.2 ± 3.4) × β_{obs}.

11 falls to the left side of the $\beta = 1.5$ line and has been identified as an "excess" galaxy in Table 5.3 whereas II Zw 40 falls to the right side of the $\beta = 1.5$ line (Figure 5.3) and does not present any excess at 500 μm when using only *Herschel* bands (Table 5.3).

As shown in Figure 5.12, Haro 11 presents an excess at 500 μm ($R(500) \sim 28\% \pm 17\%$), confirmed at 870 μm ($R(870) \sim 360\% \pm 15\%$). However, the submm excess is clearly appearing at longer wavelengths ($\geq$ 500 μm) for II Zw 40 when including observations beyond 500 μm. At 500 μm $R(500) \sim 2 \pm 8$ %, and $R(450) \sim 6 \pm 34$ % but at 850 and 1200 μm we have $R(850) \sim 265 \pm 16$ % and $R(1200) \sim 370 \pm 40$ %. This illustrates the need for submm data, to complement the existing *Herschel* data.

5.5 Limitations of the modified blackbody approach

Throughout this Chapter we saw that the modified blackbody modelling presents some limitations due to the very strong assumption of a single temperature for the dust grains. Although this approach, popular in the literature, provided useful constraints on the dust properties, a more realistic dust model is now needed to really pinpoint the dust properties, and their variations with metallicity (i.e., dust-to-stellar mass and (F)IR luminosity-to-dust mass ratios). A semi-empirical dust SED model is thus used in Part III and now allows the grains to vary in sizes (and thus temperatures). The necessary ancillary data is collected for the two samples and presented in Chapter 6. The dust model is presented in Chapter 7 and the dust properties analysed in Chapter 8.

Table 5.1. Table of modified blackbody fit parameters for the DGS galaxies.

Source	Temperature (K)	β_{obs}	$M_{dust,BB}$ ($M_\odot$)	L_{FIR-BB} ($L_\odot$)
Haro11	38^{+11}_{-6}	$1.96^{+0.44}_{-0.41}$	$5.0^{+6.5}_{-3.3} \times 10^6$	$5.3^{+1.1}_{-0.5} \times 10^{10}$
Haro2	25^{+3}_{-1}	$2.38^{+0.09}_{-0.38}$	$2.1^{+0.5}_{-0.9} \times 10^6$	$2.5^{+0.1}_{-0.1} \times 10^9$
Haro3	26^{+3}_{-2}	$2.15^{+0.31}_{-0.34}$	$1.7^{+1.1}_{-0.8} \times 10^6$	$2.4^{+0.2}_{-0.1} \times 10^9$
He2-10	26^{+4}_{-1}	$2.24^{+0.21}_{-0.40}$	$1.3^{+0.5}_{-0.7} \times 10^6$	$2.0^{+0.1}_{-0.1} \times 10^9$
HS0017+1055[2a]	98^{+34}_{-36}	$0.00^{+1.34}_{-0.00}$	$1.9^{+8.2}_{-1.4} \times 10^3$	$3.4^{+0.3}_{-0.4} \times 10^8$
HS0052+2536	37^{+14}_{-9}	$1.20^{+0.79}_{-0.73}$	$1.1^{+3.1}_{-0.8} \times 10^6$	$8.5^{+1.6}_{-1.0} \times 10^9$
HS0822+3542	-	-	-	-
HS1222+3741	-	-	-	-
HS1236+3937	-	-	-	-
HS1304+3529[1]	32^{+7}_{-3}	$2.05^{+0.47}_{-0.72}$	$2.2^{+1.5}_{-1.3} \times 10^5$	$9.4^{+0.5}_{-0.4} \times 10^8$
HS1319+3224	-	-	-	-
HS1330+3651[2b]	50^{+3}_{-8}	$0.00^{+0.61}_{-0.00}$	$3.3^{+3.4}_{-0.6} \times 10^4$	$8.8^{+0.4}_{-0.4} \times 10^8$
HS1442+4250	-	-	-	-
HS2352+2733	-	-	-	-
IZw18	-	-	-	-
IC10	21^{+3}_{-1}	$2.25^{+0.26}_{-0.49}$	$2.6^{+1.1}_{-1.4} \times 10^5$	$1.1^{+0.05}_{-0.05} \times 10^8$
IIZw40	33^{+5}_{-4}	$1.71^{+0.41}_{-0.32}$	$1.9^{+1.8}_{-0.9} \times 10^5$	$9.2^{+0.9}_{-0.7} \times 10^8$
Mrk1089	23^{+3}_{-1}	$2.34^{+0.15}_{-0.39}$	$2.5^{+0.7}_{-1.2} \times 10^7$	$1.6^{+0.1}_{-0.1} \times 10^{10}$
Mrk1450	43^{+40}_{-13}	$1.35^{+1.00}_{-0.92}$	$7.6^{+24.6}_{-6.1} \times 10^3$	$1.2^{+0.4}_{-0.2} \times 10^8$
Mrk153[1]	32^{+5}_{-2}	$2.33^{+0.15}_{-0.61}$	$1.2^{+0.4}_{-0.6} \times 10^5$	$5.3^{+0.3}_{-0.2} \times 10^8$
Mrk209[1]	34^{+6}_{-3}	$1.95^{+0.42}_{-0.47}$	$2.1^{+1.4}_{-1.1} \times 10^3$	$1.3^{+0.1}_{-0.1} \times 10^7$
Mrk930	26^{+4}_{-2}	$2.22^{+0.21}_{-0.43}$	$5.7^{+3.0}_{-3.0} \times 10^6$	$8.6^{+0.6}_{-0.5} \times 10^9$
NGC1140	23^{+2}_{-1}	$2.17^{+0.31}_{-0.36}$	$3.0^{+1.7}_{-1.5} \times 10^6$	$1.9^{+0.1}_{-0.1} \times 10^9$
NGC1569	28^{+4}_{-2}	$2.20^{+0.28}_{-0.38}$	$2.8^{+1.5}_{-1.4} \times 10^5$	$5.7^{+0.5}_{-0.4} \times 10^8$
NGC1705	33^{+5}_{-4}	$1.16^{+0.33}_{-0.28}$	$8.4^{+6.7}_{-3.7} \times 10^3$	$4.1^{+0.3}_{-0.3} \times 10^7$
NGC2366	39^{+4}_{-4}	$0.96^{+0.22}_{-0.23}$	$6.8^{+2.9}_{-2.1} \times 10^3$	$7.3^{+0.3}_{-0.2} \times 10^7$
NGC4214	26^{+3}_{-3}	$1.39^{+0.37}_{-0.37}$	$2.0^{+2.0}_{-1.0} \times 10^5$	$2.9^{+0.2}_{-0.1} \times 10^8$
NGC4449	22^{+3}_{-1}	$2.18^{+0.27}_{-0.41}$	$2.3^{+1.2}_{-1.2} \times 10^6$	$1.4^{+0.1}_{-0.1} \times 10^9$
NGC4861	28^{+3}_{-3}	$1.36^{+0.34}_{-0.32}$	$6.1^{+5.2}_{-2.7} \times 10^4$	$1.3^{+0.1}_{-0.1} \times 10^8$
NGC5253	30^{+5}_{-3}	$1.86^{+0.40}_{-0.37}$	$1.9^{+1.8}_{-1.0} \times 10^5$	$5.5^{+0.5}_{-0.4} \times 10^8$
NGC625	29^{+4}_{-3}	$1.33^{+0.35}_{-0.30}$	$5.9^{+5.9}_{-2.7} \times 10^4$	$1.5^{+0.1}_{-0.1} \times 10^8$
NGC6822	26^{+4}_{-4}	$0.99^{+0.59}_{-0.50}$	$1.1^{+1.6}_{-0.6} \times 10^4$	$1.8^{+0.1}_{-0.1} \times 10^7$
Pox186	40^{+4}_{-4}	$0.00^{+0.00}_{-0.00}$	$1.6^{+0.7}_{-0.5} \times 10^3$	$2.0^{+0.2}_{-0.2} \times 10^7$
SBS0335-052[2a,3]	89^{+10}_{-8}	$1.64^{+0.39}_{-0.33}$	$8.0^{+1.8}_{-1.4} \times 10^2$	$1.2^{+1.4}_{-1.2} \times 10^7$
SBS1159+545	-	-	-	-
SBS1211+540[2a,3]	71^{+7}_{-7}	$0.34^{+0.46}_{-0.41}$	$1.0^{+0.4}_{-0.3} \times 10^2$	$1.2^{+0.1}_{-0.1} \times 10^7$
SBS1249+493	-	-	-	-
SBS1415+437[2b]	35^{+16}_{-3}	$2.37^{+0.15}_{-1.20}$	$4.9^{+2.1}_{-3.1} \times 10^3$	$3.5^{+0.3}_{-0.3} \times 10^7$
SBS1533+574[2a]	42^{+8}_{-10}	$0.44^{+1.00}_{-0.40}$	$5.6^{+11.4}_{-2.5} \times 10^4$	$8.2^{+0.4}_{-0.4} \times 10^8$
Tol0618-402	-	-	-	-
Tol1214-277	-	-	-	-
UGC4483	-	-	-	-
UGCA20	-	-	-	-
UM133	41^{+16}_{-15}	$0.44^{+1.89}_{-0.57}$	$3.1^{+56.4}_{-2.8} \times 10^3$	$4.0^{+0.9}_{-0.5} \times 10^7$
UM311	24^{+3}_{-2}	$1.58^{+0.34}_{-0.39}$	$3.7^{+3.5}_{-1.9} \times 10^6$	$3.4^{+0.2}_{-0.1} \times 10^9$
UM448[1]	33^{+2}_{-2}	$1.99^{+0.18}_{-0.16}$	$9.9^{+3.5}_{-2.5} \times 10^6$	$4.9^{+0.2}_{-0.2} \times 10^{10}$
UM461	24^{+1}_{-1}	$2.50^{+0.00}_{-0.00}$	$2.7^{+0.5}_{-0.5} \times 10^4$	$2.5^{+0.2}_{-0.2} \times 10^7$
VIIZw403[1]	34^{+3}_{-3}	$1.57^{+0.27}_{-0.23}$	$2.1^{+1.1}_{-0.7} \times 10^3$	$1.2^{+0.1}_{-0.05} \times 10^7$

[1]: 70 μm point included in fit: violation of the upper limit condition at 70 μm.
[2a]: 70 μm point included in fit: no detections beyond 160 μm.
[2b]: 70 μm point included in fit: no observations beyond 160 μm.
[3]: For these particular galaxies, we included the 24 μm point in the fit as the 24 μm point fell below the modelled modified blackbody when we just overlaid it on the plot.

Table 5.2. Table of modified blackbody fit parameters for the KINGFISH galaxies.

Source	Temperature (K)	β_{obs}	$M_{dust,BB}$ ($M_\odot$)	L_{FIR-BB} ($L_\odot$)
NGC0337	$25.^{+3.}_{-3.}$	$1.70^{+0.46}_{-0.39}$	$6.0^{+7.0}_{-2.6} \times 10^6$	$7.7^{+0.4}_{-0.4} \times 10^9$
NGC0584	-	-	-	-
NGC0628	$19.^{+2.}_{-2.}$	$2.19^{+0.54}_{-0.31}$	$2.0^{+1.9}_{-0.5} \times 10^7$	$4.5^{+0.2}_{-0.2} \times 10^9$
NGC0855	$25.^{+3.}_{-3.}$	$1.41^{+0.36}_{-0.37}$	$1.7^{+1.5}_{-0.9} \times 10^5$	$2.1^{+0.1}_{-0.1} \times 10^8$
NGC0925	$23.^{+3.}_{-3.}$	$1.10^{+0.45}_{-0.41}$	$2.6^{+2.7}_{-1.2} \times 10^6$	$2.5^{+0.1}_{-0.1} \times 10^9$
NGC1097	$22.^{+3.}_{-2.}$	$1.98^{+0.46}_{-0.36}$	$4.3^{+4.0}_{-1.8} \times 10^7$	$2.5^{+0.1}_{-0.1} \times 10^{10}$
NGC1266	$26.^{+4.}_{-2.}$	$2.31^{+0.18}_{-0.42}$	$1.1^{+0.4}_{-0.5} \times 10^7$	$1.5^{+0.1}_{-0.1} \times 10^{10}$
NGC1291	$20.^{+2.}_{-2.}$	$1.70^{+0.42}_{-0.41}$	$5.2^{+4.4}_{-2.2} \times 10^6$	$1.7^{+0.1}_{-0.1} \times 10^9$
NGC1316	$20.^{+1.}_{-0.2}$	$2.50^{+0.00}_{-0.18}$	$1.4^{+0.1}_{-0.2} \times 10^7$	$4.4^{+0.2}_{-0.2} \times 10^9$
NGC1377	$34.^{+8.}_{-4.}$	$1.79^{+0.35}_{-0.43}$	$7.0^{+5.1}_{-3.5} \times 10^5$	$3.9^{+0.5}_{-0.4} \times 10^9$
NGC1404	-	-	-	-
IC0342	$20.^{+3.}_{-1.}$	$2.17^{+0.34}_{-0.46}$	$3.0^{+1.6}_{-1.7} \times 10^7$	$1.0^{+0.05}_{-0.04} \times 10^{10}$
NGC1482	$24.^{+4.}_{-1.}$	$2.36^{+0.14}_{-0.49}$	$3.0^{+0.9}_{-1.6} \times 10^7$	$2.6^{+0.2}_{-0.1} \times 10^{10}$
NGC1512	$25.^{+3.}_{-3.}$	$0.98^{+0.46}_{-0.35}$	$1.8^{+1.8}_{-0.8} \times 10^6$	$2.2^{+0.1}_{-0.1} \times 10^9$
NGC2146	$24.^{+2.}_{-1.}$	$2.50^{+0.00}_{-0.37}$	$7.3^{+1.2}_{-2.3} \times 10^7$	$6.9^{+0.5}_{-0.4} \times 10^{10}$
HoII	$25.^{+9.}_{-3.}$	$1.88^{+0.55}_{-0.89}$	$3.2^{+5.6}_{-2.9} \times 10^4$	$3.6^{+0.4}_{-0.4} \times 10^7$
DDO053	-	-	-	-
NGC2798	$26.^{+4.}_{-2.}$	$2.24^{+0.28}_{-0.40}$	$1.3^{+0.8}_{-0.6} \times 10^7$	$1.8^{+0.1}_{-0.1} \times 10^{10}$
NGC2841	$17.^{+2.}_{-1.}$	$2.33^{+0.19}_{-0.57}$	$6.6^{+2.2}_{-3.7} \times 10^7$	$6.7^{+0.3}_{-0.3} \times 10^9$
NGC2915	$34.^{+10.}_{-6.}$	$0.73^{+0.41}_{-0.41}$	$4.5^{+4.0}_{-2.0} \times 10^3$	$2.7^{+0.3}_{-0.2} \times 10^7$
HoI	$39.^{+7.}_{-8.}$	$0.00^{+0.68}_{-0.00}$	$7.0^{+18.5}_{-3.1} \times 10^2$	$7.6^{+1.4}_{-1.2} \times 10^6$
NGC2976	$21.^{+3.}_{-2.}$	$1.99^{+0.31}_{-0.46}$	$1.1^{+0.7}_{-0.6} \times 10^6$	$4.9^{+0.2}_{-0.2} \times 10^8$
NGC3049	$32.^{+6.}_{-4.}$	$0.82^{+0.39}_{-0.36}$	$4.3^{+3.9}_{-2.4} \times 10^5$	$1.9^{+0.1}_{-0.1} \times 10^9$
NGC3077	$26.^{+4.}_{-3.}$	$1.62^{+0.43}_{-0.41}$	$3.1^{+3.1}_{-1.5} \times 10^5$	$4.3^{+0.2}_{-0.2} \times 10^8$
M81dwB	$27.^{+10.}_{-7.}$	$0.82^{+1.09}_{-0.79}$	$1.4^{+6.9}_{-0.9} \times 10^3$	$3.0^{+0.4}_{-0.4} \times 10^6$
NGC3190	$18.^{+2.}_{-1.}$	$2.50^{+0.01}_{-0.52}$	$2.7^{+0.4}_{-1.1} \times 10^7$	$4.5^{+0.2}_{-0.2} \times 10^9$
NGC3184	$19.^{+1.}_{-3.}$	$2.18^{+0.51}_{-0.36}$	$2.7^{+2.6}_{-0.7} \times 10^7$	$5.6^{+0.2}_{-0.2} \times 10^9$
NGC3198	$21.^{+2.}_{-2.}$	$1.58^{+0.44}_{-0.39}$	$9.1^{+10.2}_{-4.3} \times 10^6$	$4.8^{+0.2}_{-0.2} \times 10^9$
IC2574	$27.^{+3.}_{-3.}$	$0.78^{+0.38}_{-0.30}$	$6.3^{+5.7}_{-2.5} \times 10^4$	$1.3^{+0.1}_{-0.1} \times 10^8$
NGC3265	$28.^{+5.}_{-3.}$	$1.68^{+0.38}_{-0.43}$	$6.2^{+5.5}_{-3.6} \times 10^5$	$1.2^{+0.1}_{-0.1} \times 10^9$
NGC3351	$21.^{+3.}_{-2.}$	$2.05^{+0.43}_{-0.44}$	$9.8^{+7.9}_{-5.3} \times 10^6$	$4.3^{+0.2}_{-0.2} \times 10^9$
NGC3521	$20.^{+2.}_{-1.}$	$2.20^{+0.32}_{-0.33}$	$6.9^{+3.9}_{-2.7} \times 10^7$	$2.2^{+0.1}_{-0.1} \times 10^{10}$
NGC3621	$21.^{+3.}_{-2.}$	$1.93^{+0.45}_{-0.47}$	$1.1^{+1.1}_{-0.6} \times 10^7$	$4.7^{+0.2}_{-0.2} \times 10^9$
NGC3627	$20.^{+1.}_{-0.3}$	$2.50^{+0.02}_{-0.22}$	$5.7^{+0.3}_{-1.3} \times 10^7$	$1.7^{+0.1}_{-0.1} \times 10^{10}$
NGC3773	$23.^{+3.}_{-3.}$	$1.92^{+0.42}_{-0.38}$	$3.8^{+4.3}_{-1.6} \times 10^5$	$3.0^{+0.2}_{-0.2} \times 10^8$
NGC3938	$20.^{+2.}_{-2.}$	$2.05^{+0.48}_{-0.38}$	$3.1^{+2.8}_{-1.4} \times 10^7$	$1.0^{+0.04}_{-0.04} \times 10^{10}$
NGC4236	$26.^{+5.}_{-4.}$	$0.79^{+0.46}_{-0.48}$	$1.6^{+1.9}_{-0.8} \times 10^5$	$2.9^{+0.1}_{-0.1} \times 10^8$
NGC4254	$20.^{+2.}_{-0.5}$	$2.39^{+0.09}_{-0.34}$	$7.6^{+1.3}_{-3.1} \times 10^7$	$2.4^{+0.1}_{-0.1} \times 10^{10}$
NGC4321	$19.^{+2.}_{-1.}$	$2.48^{+0.09}_{-0.43}$	$1.1^{+0.2}_{-0.4} \times 10^8$	$1.9^{+0.1}_{-0.1} \times 10^{10}$
NGC4536	$24.^{+4.}_{-3.}$	$1.74^{+0.49}_{-0.37}$	$1.1^{+1.2}_{-0.5} \times 10^7$	$1.2^{+0.1}_{-0.1} \times 10^{10}$
NGC4559	$24.^{+4.}_{-3.}$	$1.40^{+0.42}_{-0.44}$	$1.9^{+2.0}_{-1.0} \times 10^6$	$1.8^{+0.1}_{-0.1} \times 10^9$
NGC4569	$20.^{+2.}_{-1.}$	$2.35^{+0.29}_{-0.37}$	$1.3^{+0.6}_{-0.5} \times 10^7$	$3.3^{+0.1}_{-0.1} \times 10^9$
NGC4579	$18.^{+2.}_{-1.}$	$2.46^{+0.08}_{-0.49}$	$4.8^{+1.0}_{-2.1} \times 10^7$	$7.2^{+0.3}_{-0.3} \times 10^9$
NGC4594	$19.^{+1.}_{-3.}$	$1.97^{+0.58}_{-0.36}$	$9.5^{+11.8}_{-2.8} \times 10^6$	$2.4^{+0.1}_{-0.1} \times 10^9$
NGC4625	$21.^{+3.}_{-2.}$	$1.76^{+0.52}_{-0.39}$	$7.3^{+10.3}_{-3.5} \times 10^5$	$3.1^{+0.1}_{-0.1} \times 10^8$
NGC4631	$24.^{+3.}_{-3.}$	$1.83^{+0.43}_{-0.42}$	$1.6^{+1.7}_{-0.7} \times 10^7$	$1.4^{+0.1}_{-0.1} \times 10^{10}$
NGC4725	$18.^{+3.}_{-1.}$	$2.06^{+0.51}_{-0.56}$	$3.2^{+3.0}_{-1.9} \times 10^7$	$4.4^{+0.2}_{-0.2} \times 10^9$
NGC4736	$25.^{+4.}_{-3.}$	$1.87^{+0.43}_{-0.41}$	$2.9^{+2.8}_{-1.5} \times 10^6$	$3.6^{+0.2}_{-0.2} \times 10^9$
DDO154	-	-	-	-
NGC4826	$23.^{+3.}_{-2.}$	$2.24^{+0.32}_{-0.37}$	$4.2^{+2.4}_{-1.8} \times 10^6$	$2.8^{+0.1}_{-0.1} \times 10^9$
DDO165	-	-	-	-

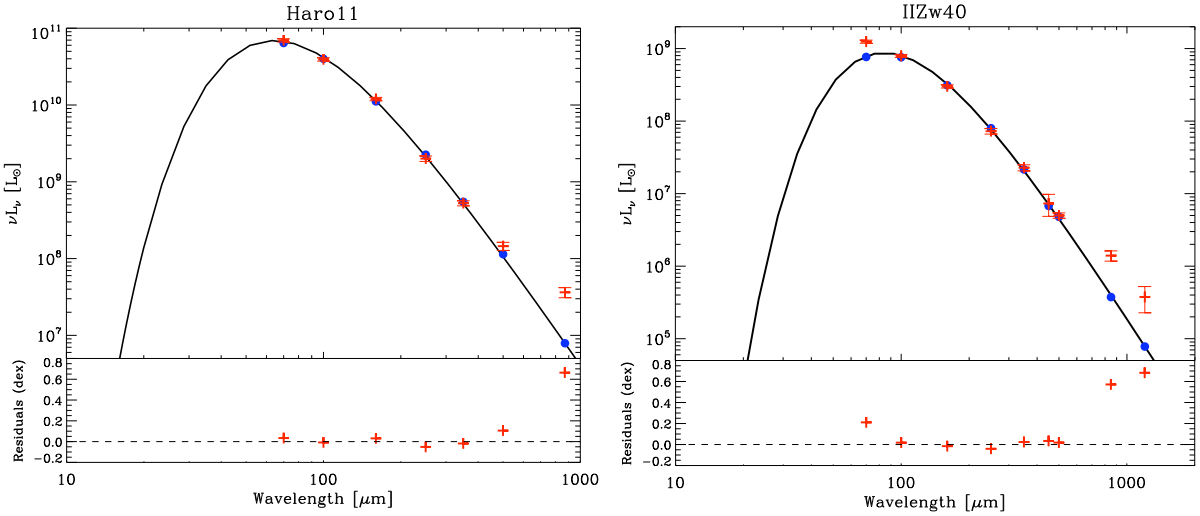

Fig. 5.12. SEDs of Haro 11 *(left)* and II Zw 40 *(right)*. They have been obtained with a modified blackbody model with a fixed $\beta_{theo} = 2.0$. The 870 μm point for Haro 11 is from LABOCA (Galametz et al. 2009). For II Zw 40, the 450 and 850 μm points are from SCUBA, and the 1.2 mm point is from MAMBO (Galliano et al. 2005). All submm points have been corrected for non-dust contamination (free-free and synchrotron radiations and CO line contamination, see Section 6.5). The filled blue circles are the modelled fluxes in each band. The red crosses are the observations. The total SEDs are displayed in black. The bottom panel of each plot indicates the residuals from the fit.

Table 5.2. Table of modified blackbody fit parameters for the KINGFISH galaxies (continued).

Source	Temperature (K)	β_{obs}	$M_{dust,BB}$ ($M_\odot$)	L_{FIR-BB} ($L_\odot$)
NGC5055	$19._{-1.}^{+2.}$	$2.32^{+0.27}_{-0.42}$	$6.2^{+2.9}_{-2.4} \times 10^7$	$1.2^{+0.1}_{-0.1} \times 10^{10}$
NGC5398	$34._{-6.}^{+7.}$	$0.58^{+0.38}_{-0.36}$	$3.1^{+3.1}_{-1.6} \times 10^4$	$2.0^{+0.1}_{-0.1} \times 10^8$
NGC5408	$30._{-5.}^{+6.}$	$1.67^{+0.55}_{-0.44}$	$2.1^{+2.8}_{-1.1} \times 10^4$	$1.3^{+0.1}_{-0.1} \times 10^{10}$
NGC5457	$21._{-3.}^{+2.}$	$1.76^{+0.52}_{-0.37}$	$2.6^{+3.0}_{-1.1} \times 10^7$	$6.5^{+0.7}_{-0.4} \times 10^7$
NGC5474	$23._{-2.}^{+3.}$	$1.16^{+0.45}_{-0.41}$	$3.2^{+3.7}_{-1.7} \times 10^5$	$2.7^{+0.1}_{-0.1} \times 10^8$
NGC5713	$22._{-1.}^{+3.}$	$2.42^{+0.06}_{-0.46}$	$3.5^{+0.7}_{-1.6} \times 10^7$	$1.9^{+0.1}_{-0.1} \times 10^{10}$
NGC5866	$21._{-1.}^{+2.}$	$2.50^{+0.00}_{-0.41}$	$1.1^{+0.2}_{-0.4} \times 10^7$	$4.1^{+0.2}_{-0.2} \times 10^9$
NGC6946	$20._{-1.}^{+2.}$	$2.34^{+0.18}_{-0.42}$	$7.0^{+1.7}_{-3.3} \times 10^7$	$2.2^{+0.1}_{-0.1} \times 10^{10}$
NGC7331	$20._{-1.}^{+2.}$	$2.19^{+0.37}_{-0.38}$	$9.6^{+5.5}_{-4.5} \times 10^7$	$3.1^{+0.1}_{-0.1} \times 10^{10}$
NGC7793	$23._{-2.}^{+3.}$	$1.50^{+0.44}_{-0.40}$	$1.6^{+1.6}_{-0.7} \times 10^6$	$1.2^{+0.04}_{-0.05} \times 10^9$

Table 5.3. Table of relative residuals at 500 μm for a modified blackbody fit with β_{theo} fixed to 2.0 for the DGS and KINGFISH samples. A column with the β_{obs} values from Table 5.1 have been added.

	β_{obs}	β_{theo} = **2.0**		
Source		*R(500)* (%)	$\Delta R(500)$ (%)	Excess ?
DGS				
Haro11	1.96	27.6	16.7	yes
Haro2	2.38	-6.4	11.4	
Haro3	2.15	-2.3	11.0	
He2-10	2.24	-3.3	9.1	
HS0052+2536	1.20	154.2	125.3	yes
IC10	2.25	0.1	28.4	
IIZw40	1.71	2.2	8.2	
Mrk1089	2.34	-3.6	13.1	
Mrk930	2.22	8.3	31.0	
NGC1140	2.17	-3.6	15.8	
NGC1569	2.20	1.4	9.2	
NGC1705	1.16	42.5	35.0	yes
NGC2366	0.96	39.6	22.8	yes
NGC4214	1.39	17.9	11.5	yes
NGC4449	2.18	1.2	9.0	
NGC4861	1.36	32.5	26.6	yes
NGC5253	1.86	8.5	9.8	
NGC625	1.33	21.6	13.7	yes
NGC6822	0.99	96.8	66.2	yes
UM311	1.58	9.4	10.8	
UM448	1.99	6.9	18.5	
VIIZw403	1.57	71.7	58.5	yes
KINGFISH				
NGC0337	1.70	17.8	13.5	yes
NGC0628	2.19	6.3	9.9	
NGC0855	1.41	11.8	20.6	
NGC0925	1.10	35.9	15.3	yes
NGC1097	1.98	7.6	11.3	
NGC1266	2.31	-1.9	12.6	
NGC1291	1.70	10.8	12.4	
NGC1316	2.50	2.7	18.8	
NGC1377	1.79	26.1	21.2	yes
IC0342	2.17	2.1	9.1	
NGC1482	2.36	-1.5	10.4	
NGC1512	0.98	32.3	15.3	yes
NGC2146	2.50	-6.8	8.2	
HoII	1.88	26.4	72.3	
NGC2798	2.24	4.6	10.3	
NGC2841	2.33	1.4	9.4	
NGC2915	0.73	64.2	25.8	yes
HoI	0.00	98.1	73.9	yes
NGC2976	1.99	7.9	11.1	
NGC3049	0.82	63.1	18.4	yes
NGC3077	1.62	22.1	12.8	yes
M81dwB	0.82	62.0	87.8	

Table 5.3. (continued).

	β_{obs}	β_{theo} = **2.0**		
Source		*R(500)* (%)	Δ*R(500)* (%)	Excess ?
NGC3190	2.50	-5.1	9.2	
NGC3184	2.18	5.3	11.0	
NGC3198	1.58	18.4	10.9	yes
IC2574	0.78	38.7	17.9	yes
NGC3265	1.68	29.5	22.0	yes
NGC3351	2.05	2.8	8.5	
NGC3521	2.20	3.0	9.9	
NGC3621	1.93	13.5	11.5	yes
NGC3627	2.50	-10.8	8.9	
NGC3773	1.92	13.0	17.2	
NGC3938	2.05	6.3	11.9	
NGC4236	0.79	54.9	19.1	yes
NGC4254	2.39	-6.7	9.0	
NGC4321	2.48	-2.1	9.8	
NGC4536	1.74	17.1	12.1	yes
NGC4559	1.40	26.7	14.0	yes
NGC4569	2.35	0.1	9.0	
NGC4579	2.46	-1.1	9.0	
NGC4594	1.97	9.9	9.0	yes
NGC4625	1.76	16.8	14.9	yes
NGC4631	1.83	15.5	12.7	yes
NGC4725	2.06	9.0	10.6	
NGC4736	1.87	13.9	11.5	yes
NGC4826	2.24	2.9	9.7	
NGC5055	2.32	1.3	9.8	
NGC5398	0.58	62.0	22.7	yes
NGC5408	1.67	79.3	40.4	yes
NGC5457	1.76	14.8	12.9	yes
NGC5474	1.16	36.4	15.5	yes
NGC5713	2.42	-1.8	9.8	
NGC5866	2.50	-4.1	9.7	
NGC6946	2.34	0.1	8.9	
NGC7331	2.19	3.5	9.3	
NGC7793	1.50	23.4	12.7	yes

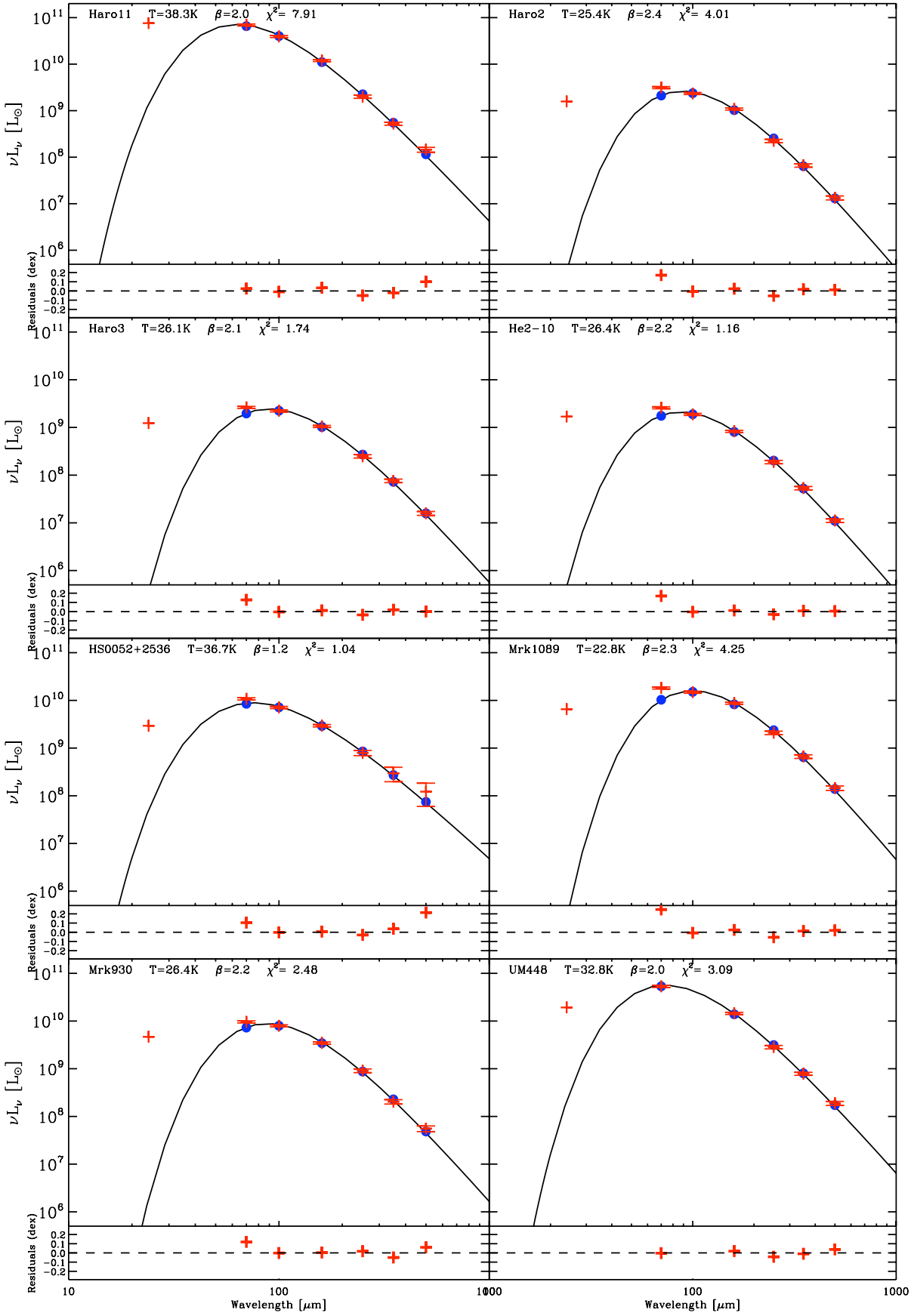

Fig. 5.13. Modified blackbody fits of the 70 to 500 μm range for the DGS. The solid black line is the modelled modified blackbody, the blue circles are the modelled points. The red symbols are the observations: crosses are for detections and diamonds are for upper limits. We overlaid the MIPS 24 μm point from Bendo et al. (2012). The T and β parameters have been indicated on the top of each plot along with the χ^2 value of the fit. The bottom panel of each plot indicates the residuals from the fit.

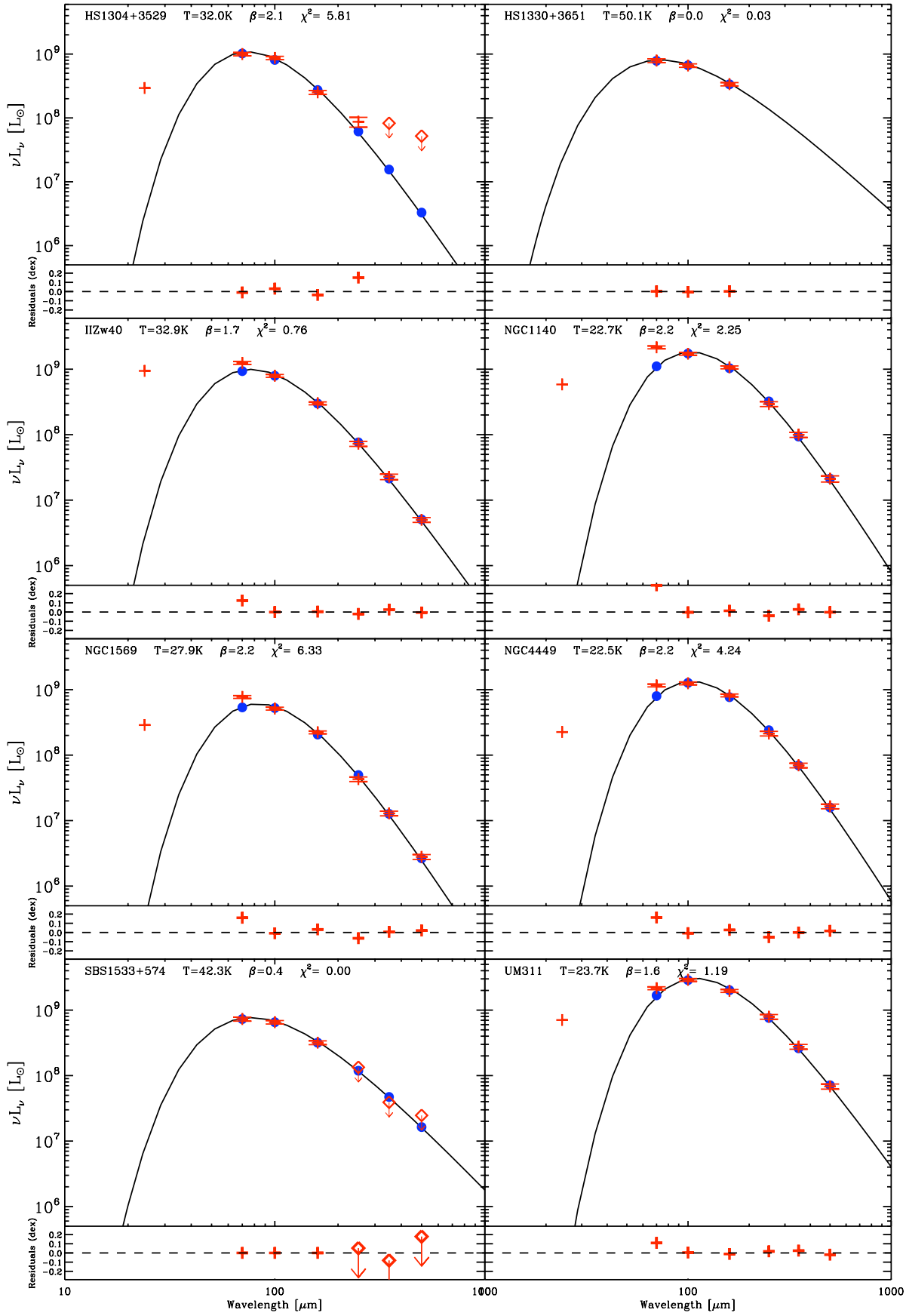

Fig. 5.13. *(continued)* Modified blackbody fits of the 70 to 500 μm range for the DGS.

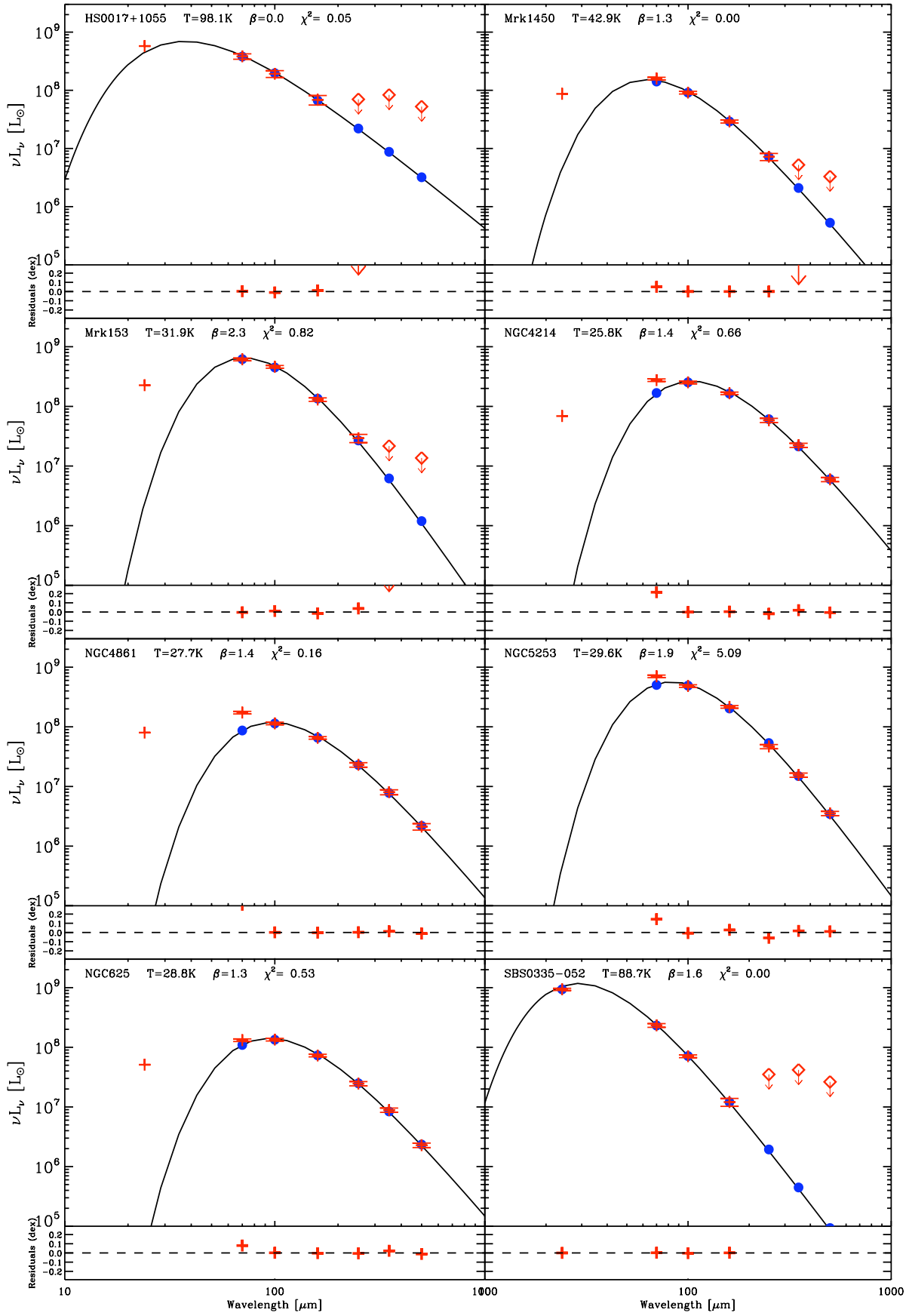

Fig. 5.13. *(continued)* Modified blackbody fits of the 70 to 500 μm range for the DGS. Note: for SBS0335-052, we included the 24 μm point in the fit as the 24 μm point fell below the modelled modified blackbody when we just overlaid it on the plot.

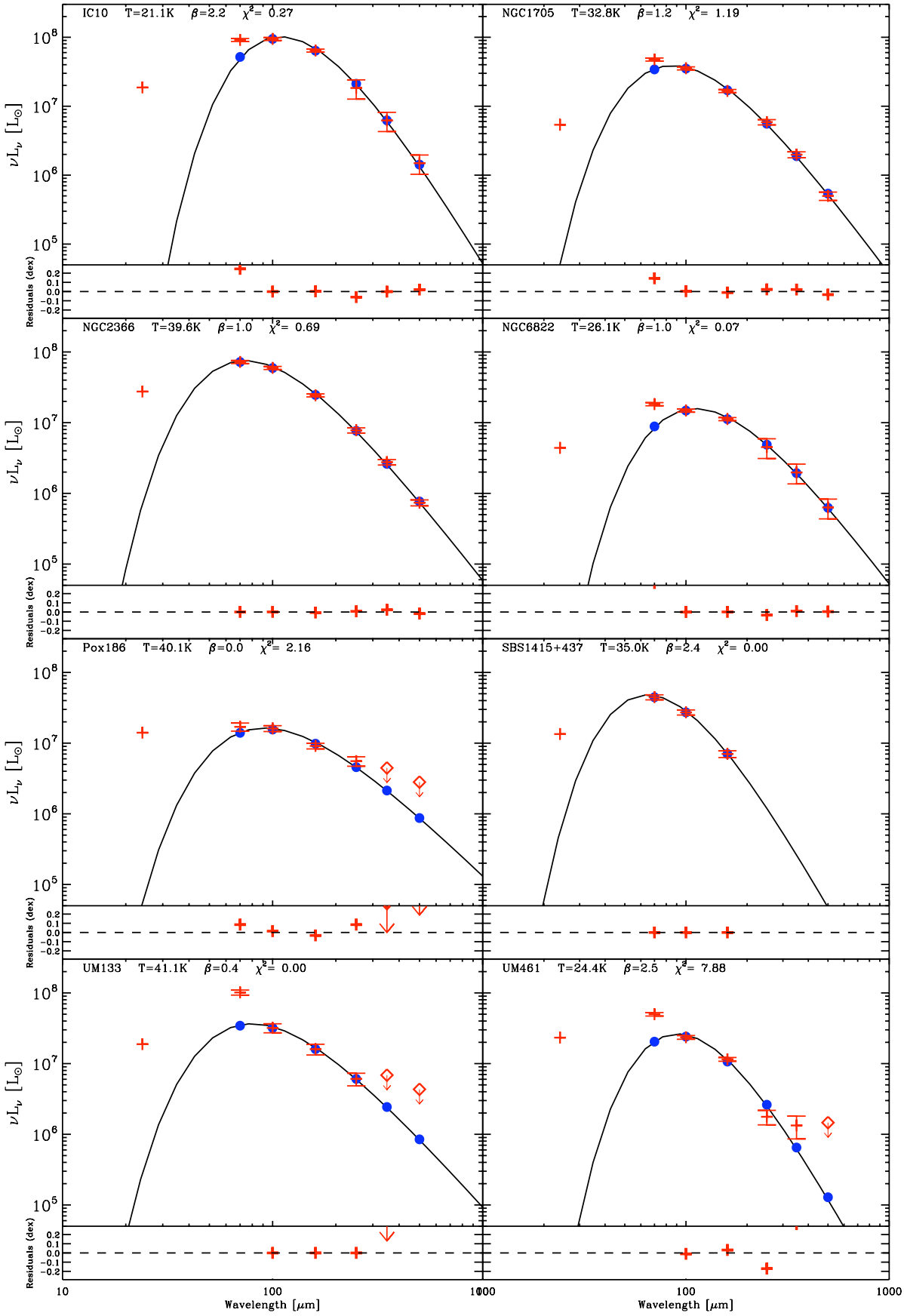

Fig. 5.13. *(continued)* Modified blackbody fits of the 70 to 500 μm range for the DGS.

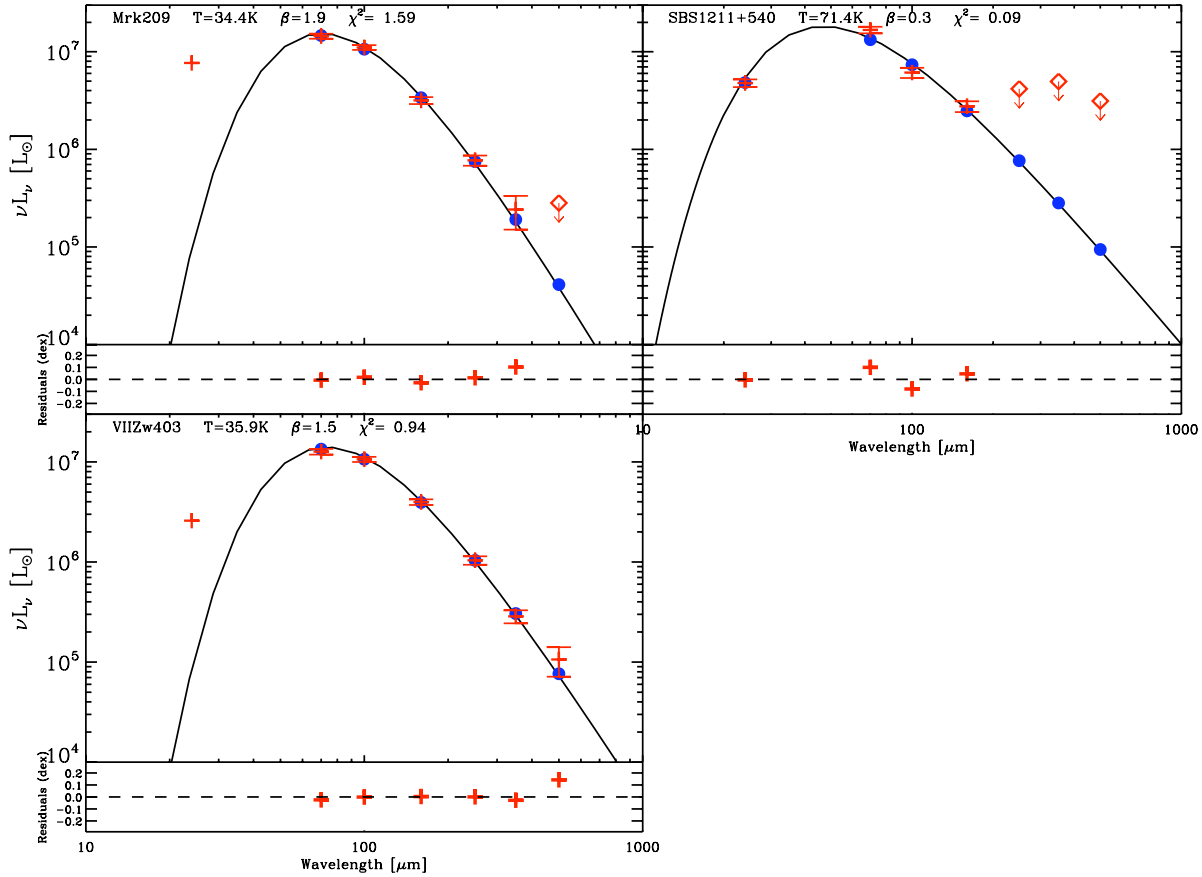

Fig. 5.13. *(continued)* Modified blackbody fits of the 70 to 500 μm range for the DGS. Note: for SBS1211+540, we included the 24 μm point in the fit as the 24 μm point fell below the modelled modified blackbody when we just overlaid it on the plot.

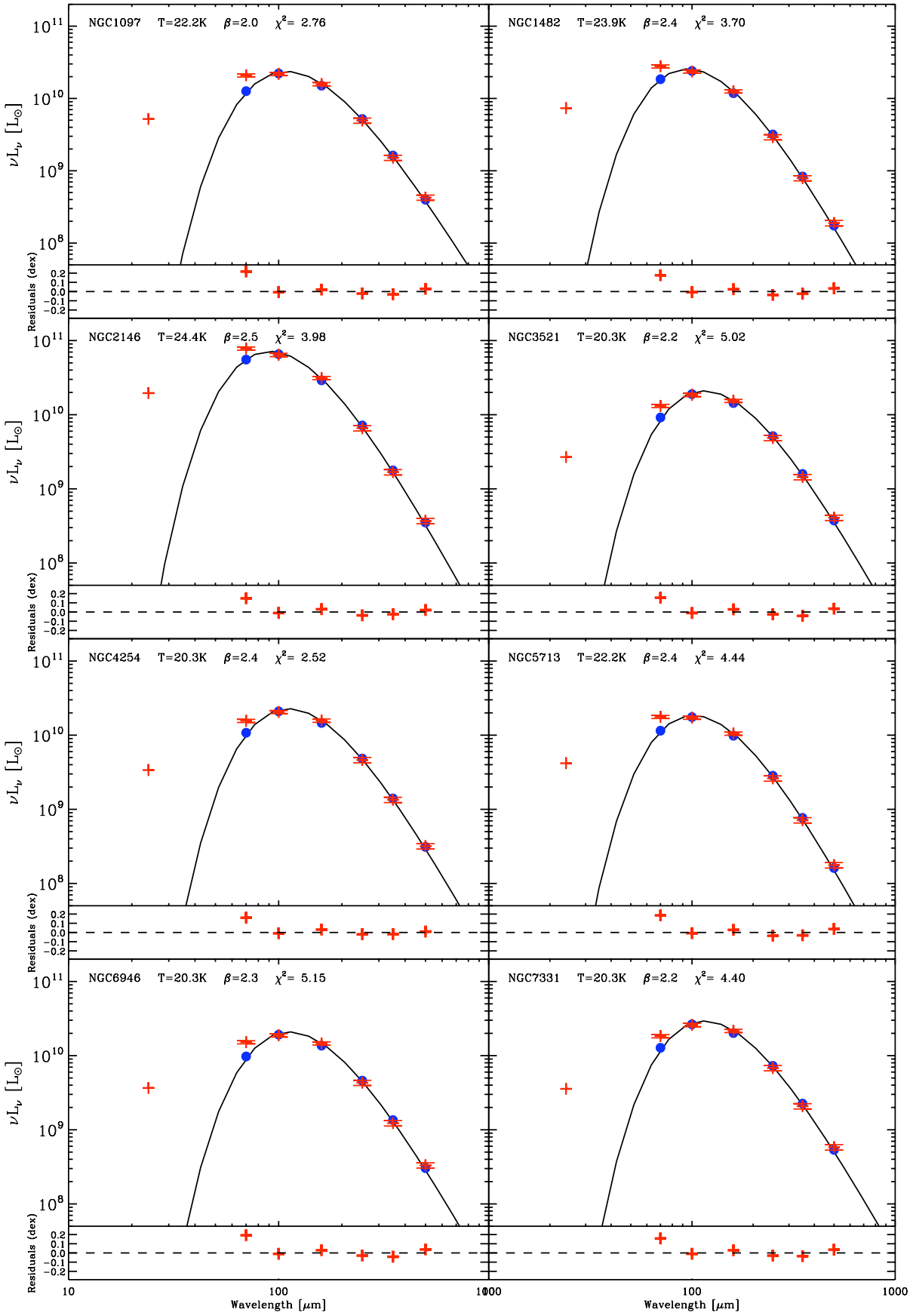

Fig. 5.14. Modified blackbody fits of the 70 to 500 μm range for the KINGFISH galaxies. The solid black line is the modelled modified blackbody, the blue circles are the modelled points. The red symbols are the observations: crosses are for detections and diamonds are for upper limits. We overlaid the MIPS 24 μm point from Dale et al. (2007). The T and β parameters have been indicated on the top of each plot along with the χ^2 value of the fit. The bottom panel of each plot indicates the residuals from the fit.

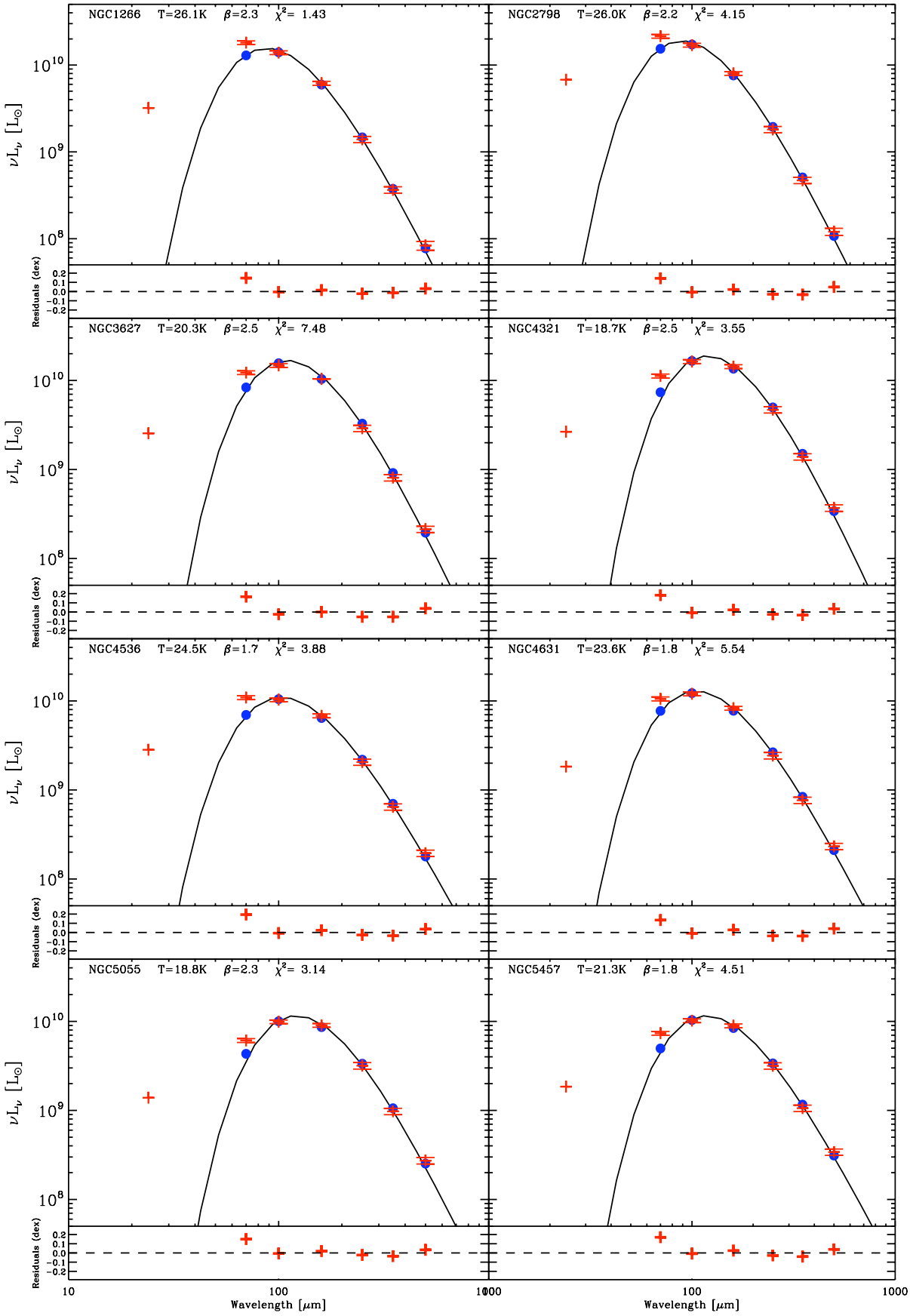

Fig. 5.14. *(continued)* Modified blackbody fits of the 70 to 500 μm range for the KINGFISH galaxies.

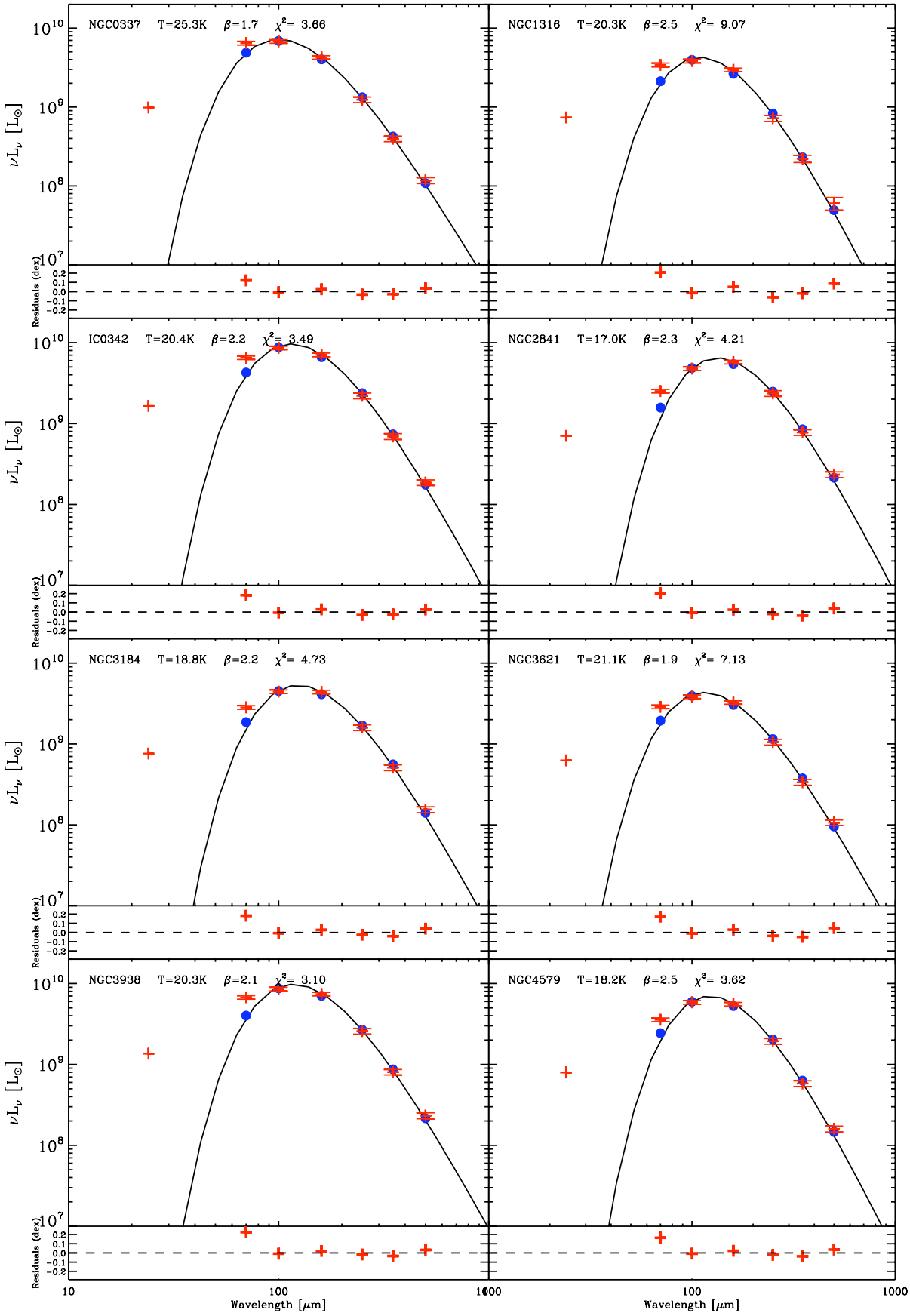

Fig. 5.14. *(continued)* Modified blackbody fits of the 70 to 500 μm range for the KINGFISH galaxies.

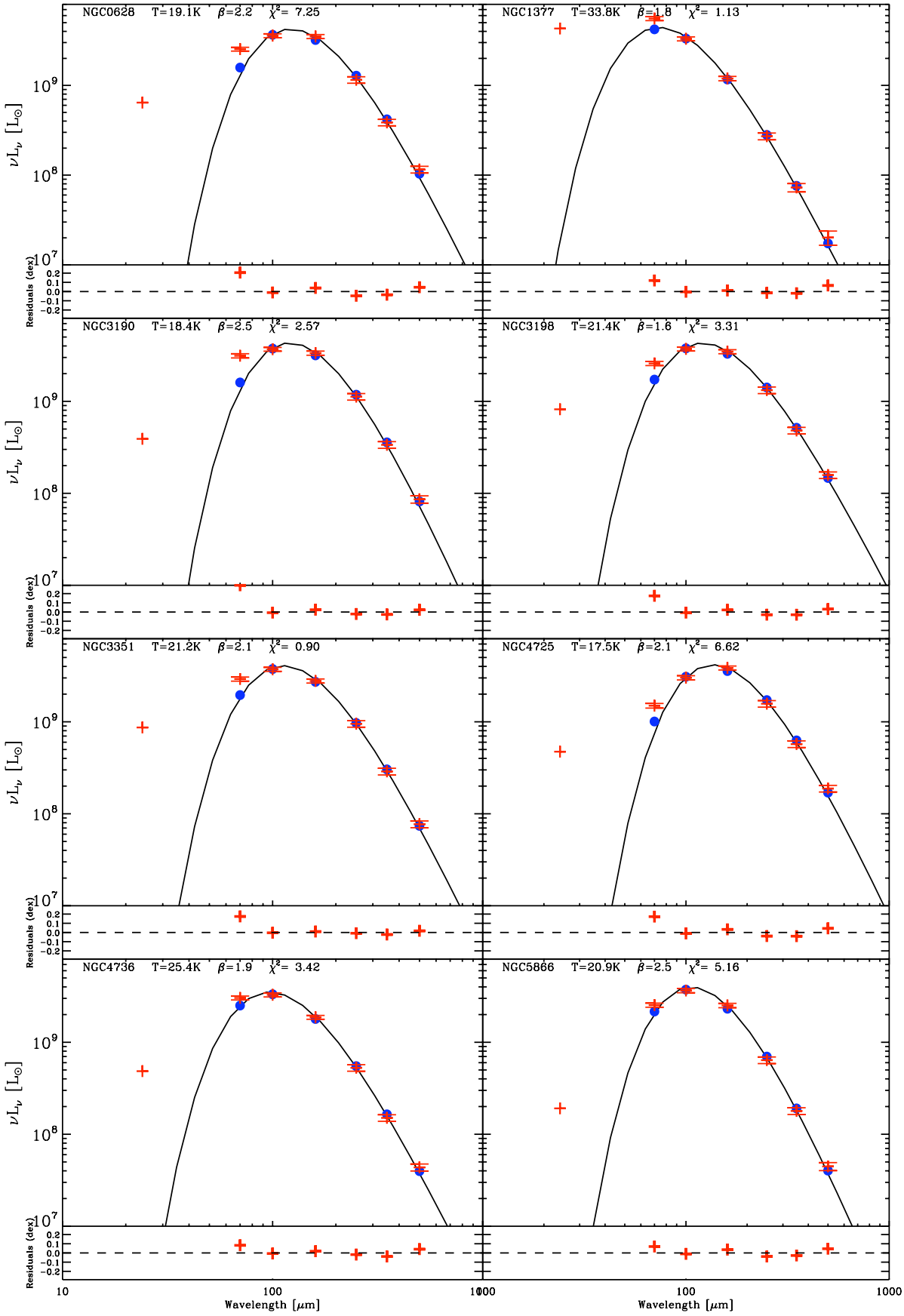

Fig. 5.14. *(continued)* Modified blackbody fits of the 70 to 500 μm range for the KINGFISH galaxies.

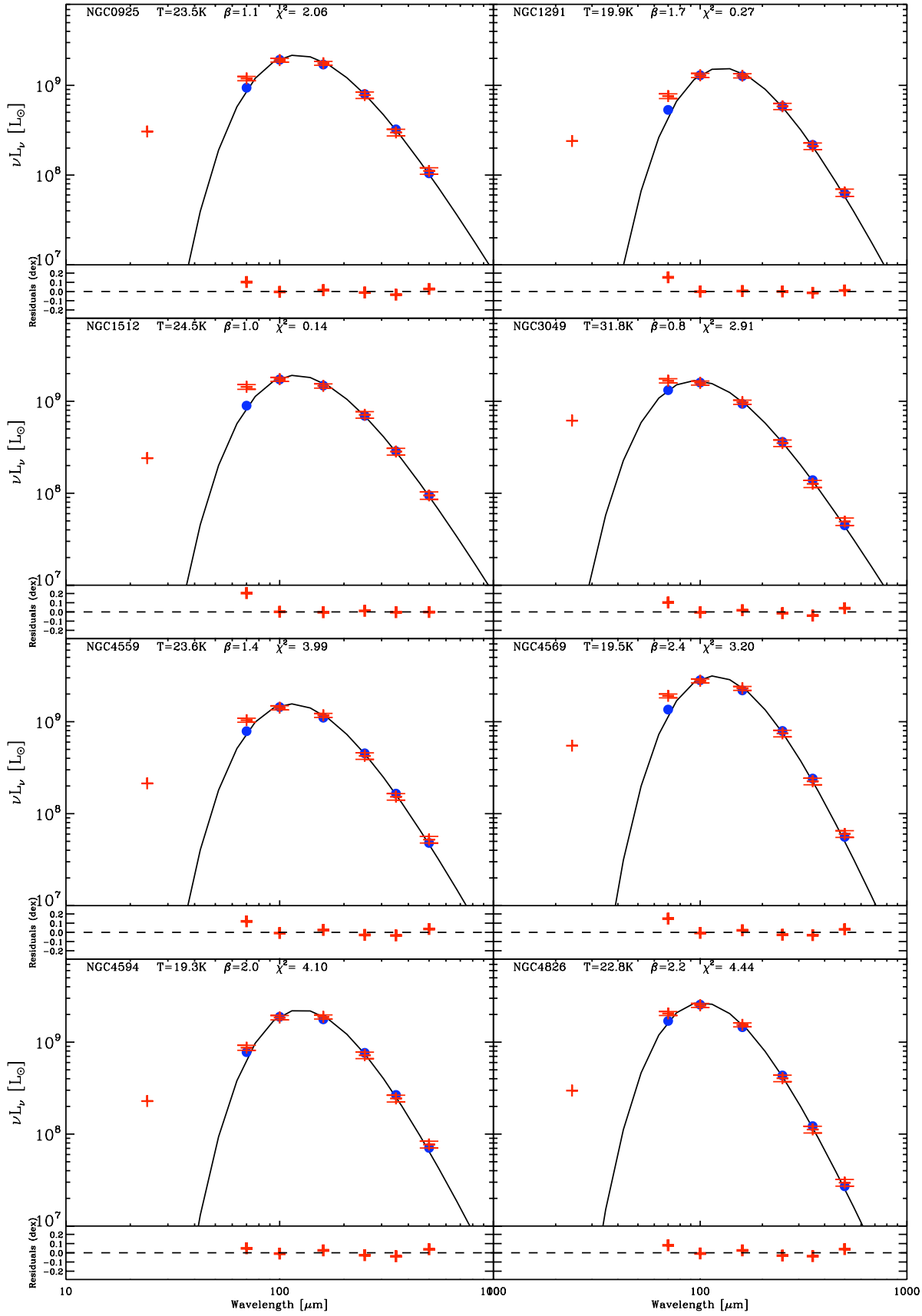

Fig. 5.14. *(continued)* Modified blackbody fits of the 70 to 500 μm range for the KINGFISH galaxies.

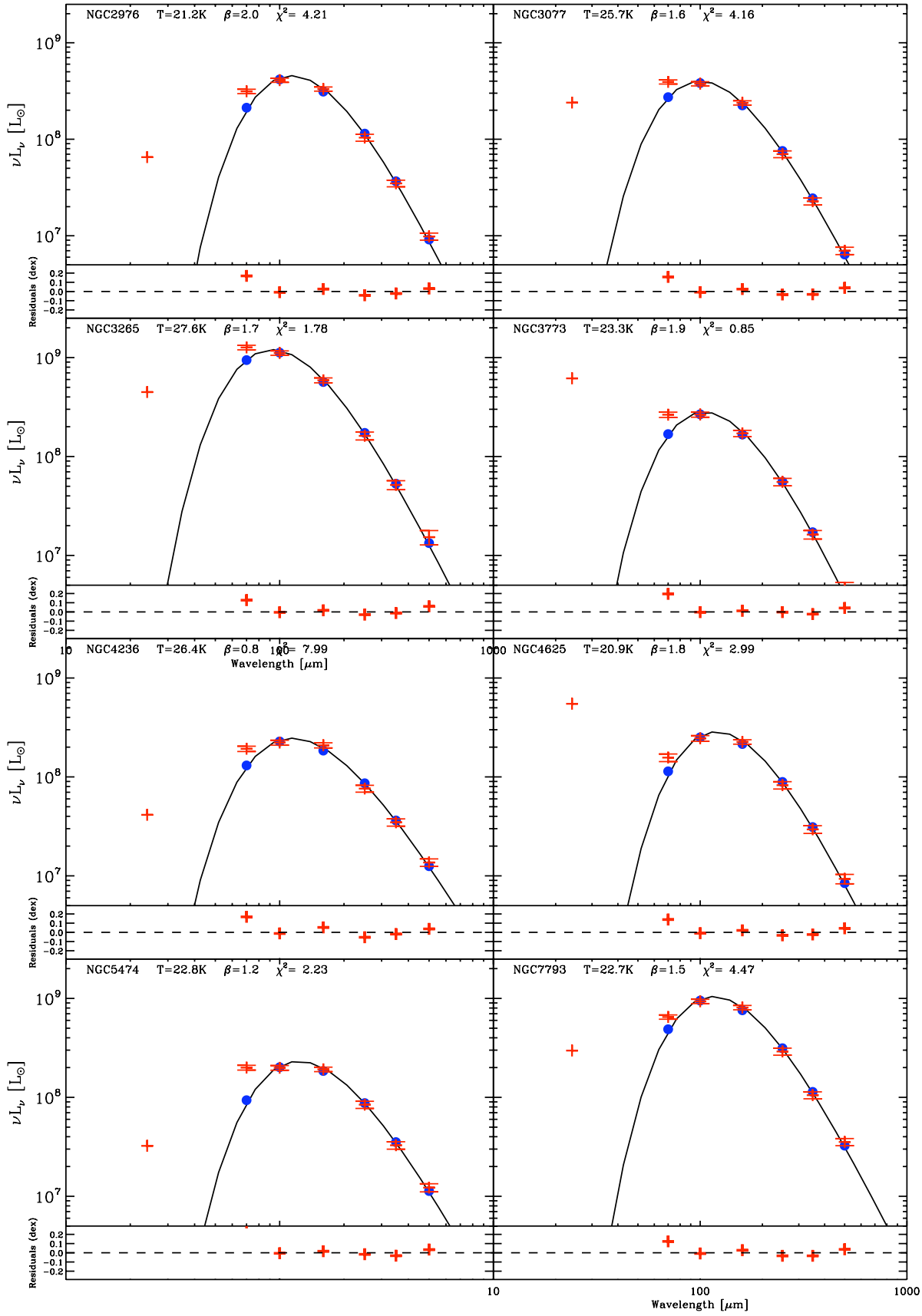

Fig. 5.14. *(continued)* Modified blackbody fits of the 70 to 500 μm range for the KINGFISH galaxies.

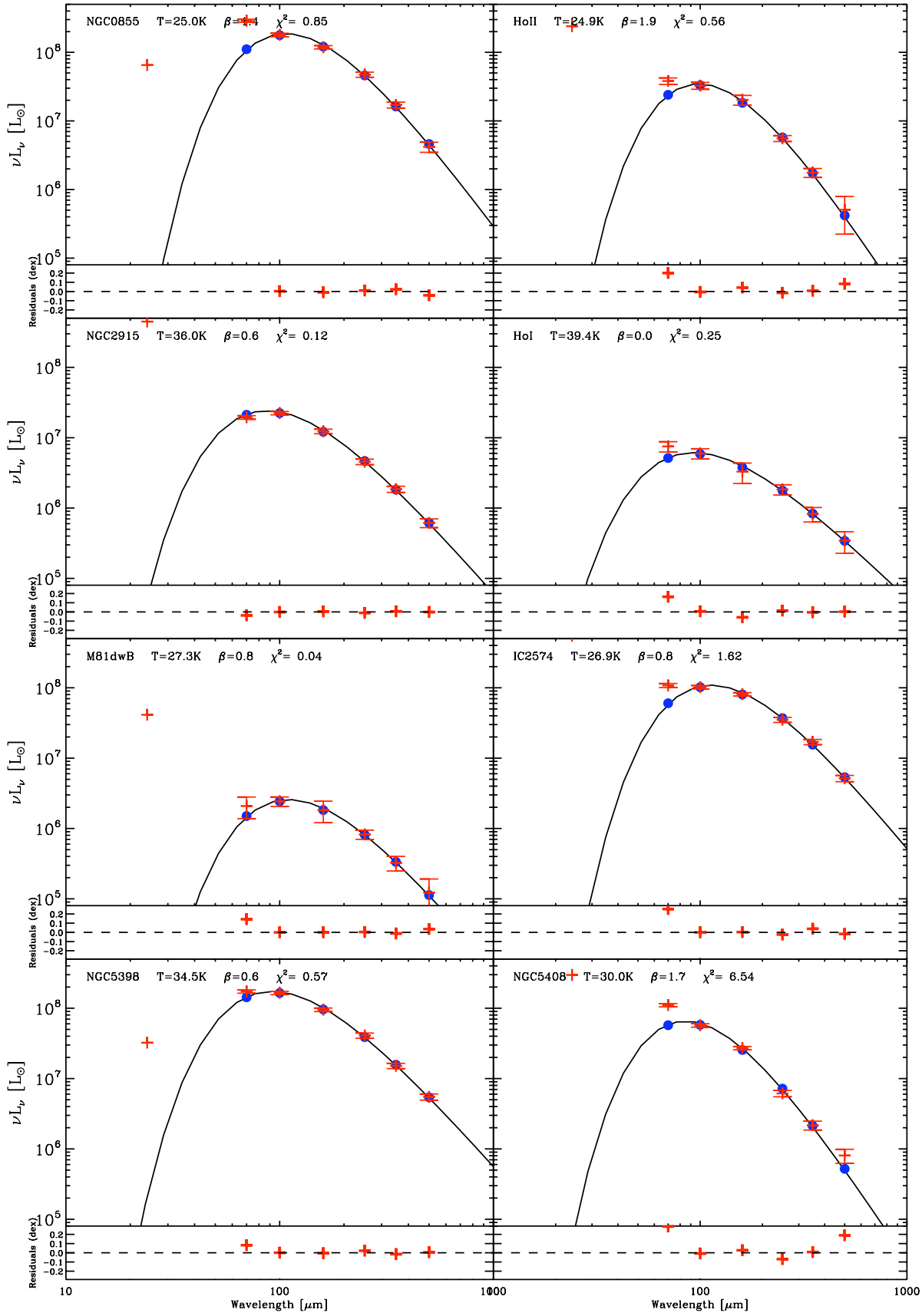

Fig. 5.14. *(continued)* Modified blackbody fits of the 70 to 500 μm range for the KINGFISH galaxies.

Part III

Evolution of ISM properties with metallicity : a complete IR-to-submillimetre view

Chapter 6

Sampling the IR-to-submm observed dust SEDs

Contents

In this Chapter we collect all of the ancillary data needed to properly sample the IR-to-submm dust SEDs of the DGS galaxies. We intensively use the archives whenever it is possible. Otherwise we treat the data ourselves. References for finding the corresponding KINGFISH data we use is given at the end of each section.

6.1 2MASS: Searching the literature

2MASS (Two Microns All Sky Survey) observed the entire sky in the J (1.24 μm), H (1.66 μm) and K_s (2.16 μm) bands. The RSRFs (relative spectral response functions) for each band is shown in Fig. 6.1. The RSRF for 2MASS are designed to be integrated directly over spectra in F_λ (with $\nu F_\nu = \lambda F_\lambda$), in order to calculate synthetic photometry.

The 2MASS data for the DGS sample is compiled from the literature: the NASA/IPAC ISA 2MASS Point Source Catalog, the 2MASS Extended Objects Final Release, the 2MASS Large Galaxy Atlas (Jarrett et al. 2003), Engelbracht et al. (2008); Dale et al. (2009) and is given in Table 6.8. In some cases, the original data is given in magnitudes in the databases. To convert this into flux densities, we use the zero-magnitude flux values from Cohen et al. (2003), F_0:

$$F_\nu = F_0 \times 10^{-mag/2.5} \tag{6.1}$$

The error on the flux density is given by Eq. 6.2 and is derived by propagating the errors on F_0 and on the magnitude, mag, σ_{F_0} and σ_{mag}, in Eq. 6.1. F_0 and σ_{F_0} are given in Table 6.1 along with some characteristics of the 2MASS data.

$$\sigma_{F_\nu} = F_\nu \times \sqrt{\left(\frac{\sigma_{F_0}}{F_0}\right)^2 + \left(\frac{ln(10)}{2.5}\sigma_{mag}\right)^2} \tag{6.2}$$

Table 6.1. Characteristics of 2MASS (from Cohen et al. 2003; Jarrett et al. 2003).

Band	λ [μm]	F_0 [Jy]	σ_{F_0} [Jy]	Calibration accuracy
J	1.25	1594.0	27.8	3%
H	1.65	1024.0	20.0	3%
Ks	2.20	666.7	12.6	3%

KINGFISH 2MASS photometry is presented in Dale et al. (2007) and has been taken from Jarrett et al. (2003).

6.2 *Spitzer* observations

Spitzer observations of some dwarf galaxies of the DGS were already available through the *Spitzer* database[1]. When the DGS was designed, complementary *Spitzer* observations were scheduled in the cycle 5 program to complete the set of existing *Spitzer* data in order to have NIR and MIR complementary observations for a maximum number of targets in the DGS sample (Dust Evolution in Low-Metallicity Environments: P.I. F. Galliano; ID: 50550). These new observations are presented here, along with those previously available.

[1]The query form is available at: http://sha.ipac.caltech.edu/applications/Spitzer/SHA/#id=SearchByPosition&startIdx=0&pageSize=0&shortDesc=Position%20Search&isBookmarkAble=true

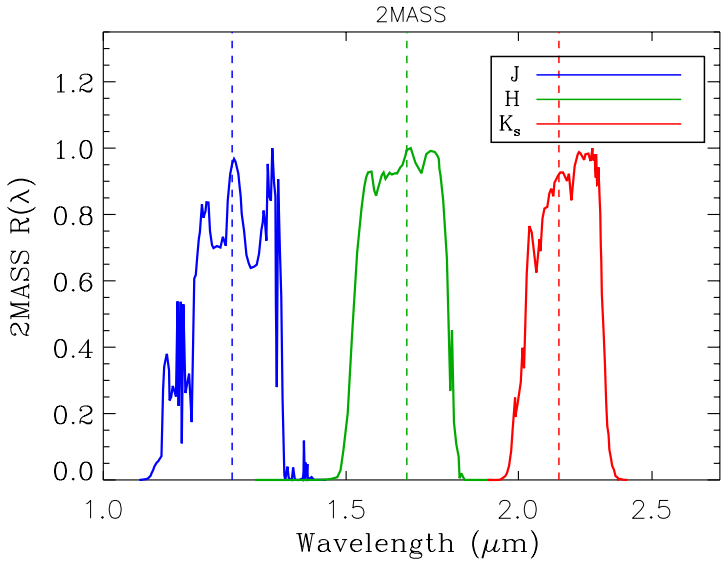

Fig. 6.1. 2MASS filter transmissions, R(λ). The dashed lines mark the reference wavelength for each band.

6.2.1 IRAC

Instrument

The InfraRed Array Camera (IRAC) is a four-channel camera providing simultaneous 5.2′× 5.2′ images at 3.6, 4.5, 5.8 and 8.0 μm. All four detectors arrays are 256 × 256 pixels in size, with pixel sizes of 1.2″. The main characteristics of IRAC are given in Table 6.2. Several stars were used for the calibration. The total calibration uncertainty is $\sim$ 10%.

The convention for the spectral response function here is that R(ν) is proportional to the number of electrons produced by a single photon of energy $h\nu$. Thus the number of electrons collected from the source, N_e^S, during an integration time t and though a telescope area $\mathcal{A}$, is directly proportional to the source flux density, $F_S(\nu)$, divided by the energy of the collected photons, weighted by the spectral response of the telescope, R(ν):

$$N_e^S = t\mathcal{A}\int \frac{F_S(\nu)}{h\nu} R(\nu)\,\mathrm{d}\nu \tag{6.3}$$

The spectral response for each band is shown in Fig. 6.2. Here the spectral convention is $\nu \times F_\nu$ = cst or $\mathrm{F}_S(\nu) = \mathrm{F}_S(\nu_0) \times (\nu_0/\nu)$, with ν_0 corresponding to λ_0={3.6, 4.5, 5.8, 8.0}μm. Importing this into Eq. 6.3 gives:

$$N_e^S = \frac{t\mathcal{A}F_S(\nu_0)}{h\nu_0}\int \left(\frac{\nu_0}{\nu}\right)^2 R(\nu)\,\mathrm{d}\nu \tag{6.4}$$

and thus:

$$F_S(\nu_0) = \frac{t\mathcal{A}}{N_e^S h\nu_0}\int \left(\frac{\nu_0}{\nu}\right)^2 R(\nu)\,\mathrm{d}\nu \tag{6.5}$$

However, as for PACS and SPIRE, there is no particular reason for the source to have a spectral shape $\mathrm{F}_S(\nu) \propto \nu^{-1}$. Thus we need to apply a colour correction. If the source "true" spectral shape, $\mathrm{F}'_S(\nu)$, is unknown, we have from Eq. 6.3:

$$N_e'^S = t\mathcal{A}\int \frac{F'_S(\nu)}{h\nu} R(\nu)\,\mathrm{d}\nu \tag{6.6}$$

By definition the calibration factor, C, is the ratio between the number of electrons collected from an arbitrary source to the flux density of this source at the nominal wavelength, i.e., N_e /$\mathrm{F}(\nu_0)$. Using the fact that: N_e^S / $\mathrm{F}_S(\nu_0) = \mathrm{N}_e'^S$ / $\mathrm{F}'_S(\nu_0)$, we get:

$$F'_S(\nu_0) = t\mathcal{A}\int \frac{F'_S(\nu)}{h\nu} R(\nu)\,\mathrm{d}\nu \times \frac{h\nu_0}{t\mathcal{A}\int(\nu_0/\nu)^2 R(\nu)\,\mathrm{d}\nu} \tag{6.7}$$

which gives in the end:

$$F'_S(\nu_0) = \frac{\int F'_S(\nu)(\nu_0/\nu)R(\nu)\,\mathrm{d}\nu}{\int(\nu_0/\nu)^2 R(\nu)\,\mathrm{d}\nu} \tag{6.8}$$

Eq. 6.8 can be generalised to any flux convention in the form $\mathrm{F}_S(\nu) \propto \nu^{-\alpha_S}$ chosen for a photomultiplier (such as MIPS, *WISE* or IRAS presented in the next Sections):

$$F'_S(\nu_0) = \frac{\int F'_S(\nu)(\nu_0/\nu)R(\nu)\,\mathrm{d}\nu}{\int(\nu_0/\nu)^{\alpha_S+1} R(\nu)\,\mathrm{d}\nu} \tag{6.9}$$

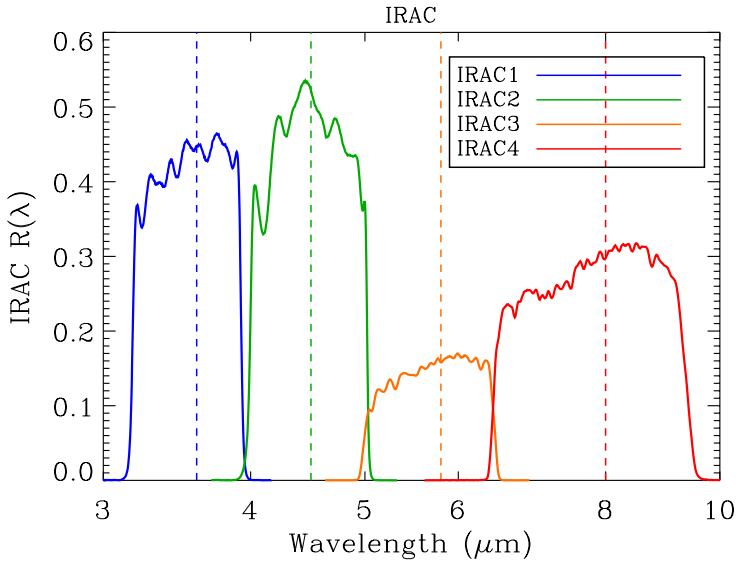

Fig. 6.2. IRAC filter transmissions, R(λ). The dashed lines mark the reference wavelength for each band.

Table 6.2. IRAC characteristics (from the IRAC Instrument Handbook, version 2.0.1).

IRAC							
Band	Wavelength (μm)	Bandwidth (μm)	FWHM ($''$)	Calibration accuracy	A[a]	B[a]	C[a]
IRAC 1	3.6	0.750	1.66	10%	0.82	0.370	0.910
IRAC 2	4.5	1.015	1.72	10%	1.16	0.433	0.94
IRAC 3	5.8	1.425	1.88	10%	1.49	0.207	0.66
IRAC 4	8.0	2.905	1.98	10%	1.37	0.330	0.740

[a]: Extended aperture corrections coefficients, see Section 6.2.1, Photometry.

Photometry

The IRAC maps are retrieved from the NASA/IPAC ISA database for *Spitzer* data, and the AORkeys for the IRAC observations are summarised in Appendix A. After a step of background subtraction, similar to what was done for SPIRE (Chapter 4), flux densities are extracted from the maps through aperture photometry, and are given in Table 6.9. The apertures are in most cases the same as the ones used for *Herschel* photometry. Some contamination which can occur from background sources or foreground stars has also been removed from the source aperture.

The IRAC calibration is based on point-source photometry for a 12″ radius aperture. Extra aperture correction is needed to account for the emission from the wings of the PSF and the scattering of diffuse emission across the IRAC focal plane. This correction is given by:

$$\frac{F_{\nu_0}(true)}{F_{\nu_0}(measured)} = A(\nu_0)e^{-r^{B(\nu_0)}} + C(\nu_0) \tag{6.10}$$

where, $A(\nu_0)$, $B(\nu_0)$ and $C(\nu_0)$ are given in Table 6.2 and r is the source aperture radius. Following the recipe given in the IRAC Instrument Handbook (version 2.0.1 Section 4.11.1[2]) we do not apply this correction to small and compact sources (see Table 6.9).

Errors

The uncertainty on the flux density is determined the same way as for SPIRE. Adapting Eq. 4.9 to IRAC gives:

$$unc_{flux} = \sqrt{unc_{bg}^2 + unc_{source}^2} \tag{6.11}$$

where:

$$\begin{cases} unc_{bg} &= N_{ap}\frac{\sigma_{sky}}{\sqrt{N_{bg}}} \\ unc_{source} &= \sqrt{N_{ap}}\sigma_{sky} \end{cases} \tag{6.12}$$

where σ_{sky} is the standard deviation of all of the pixels in the background aperture. N_{ap} and N_{bg} are the number of pixels in the source and background apertures respectively. The final total uncertainty, $\sigma_{3.6-4.5-5.8-8.0}$ reported in Table 6.9, is obtained by adding unc_{flux} and the 10% calibration error in quadrature.

We consider that galaxies are not detected when the computed flux density is lower than three times the corresponding uncertainty on the flux density in a given band. The final upper limit is then three times the uncertainty on the flux density value (3σ upper limit, reported in Table 6.9).

IRAC photometry for KINGFISH galaxies is presented in Dale et al. (2007).

Comparison with the literature

IRAC photometry is available in the literature for 29 DGS sources: Hunt et al. (2006); Dale et al. (2007, 2009); Engelbracht et al. (2008); Galametz et al. (2009). We use the ratios of our IRAC to the literature IRAC flux densities to assess how well the measurements agree with each other; a ratio of 1 corresponds to a very good agreement. If we compare our measurements to those from the literature we get a fairly good agreement between them (see Fig. 6.3), with some outliers:

Haro2: The comparison to the literature values agrees for the first three IRAC bands (ratios of 0.92, 0.96 and 0.93 at 3.6 μm, 4.5 μm, and 5.8 μm respectively) except for the IRAC 8.0 μm band

[2]This document is available at http://irsa.ipac.caltech.edu/data/SPITZER/docs/irac/iracinstrumenthandbook/

where the ratio goes to ~ 2. We check the photometry at 8.0 μm by recomputing the flux density with the aperture given in Dale et al. (2007) and find a flux in very close agreement to the one we find with our own aperture (ratio of 1.009 at 8.0 μm), and also for the three other IRAC bands. As an additional check, we find that Marble et al. (2010) performed photometry for Haro2 in a IRS-matched aperture and their result is in good agreement with ours (ratio = 1.036 at 8.0 μm). Thus we discard the 8.0 μm point from Dale et al. (2007) in our comparison with literature measurements.

NGC4861: Our measurements are systematically larger than the flux from Engelbracht et al. (2008). A possible explanation could be that we include Mrk39 with which NGC4861 is interacting in our aperture and that Engelbracht et al. (2008) did not. However, no precise information is given in Engelbracht et al. (2008) about the size of the apertures used for IRAC photometry, so it is hard to see if we are really comparing similar measurements. Thus we discard this galaxy in our comparison with literature measurements.

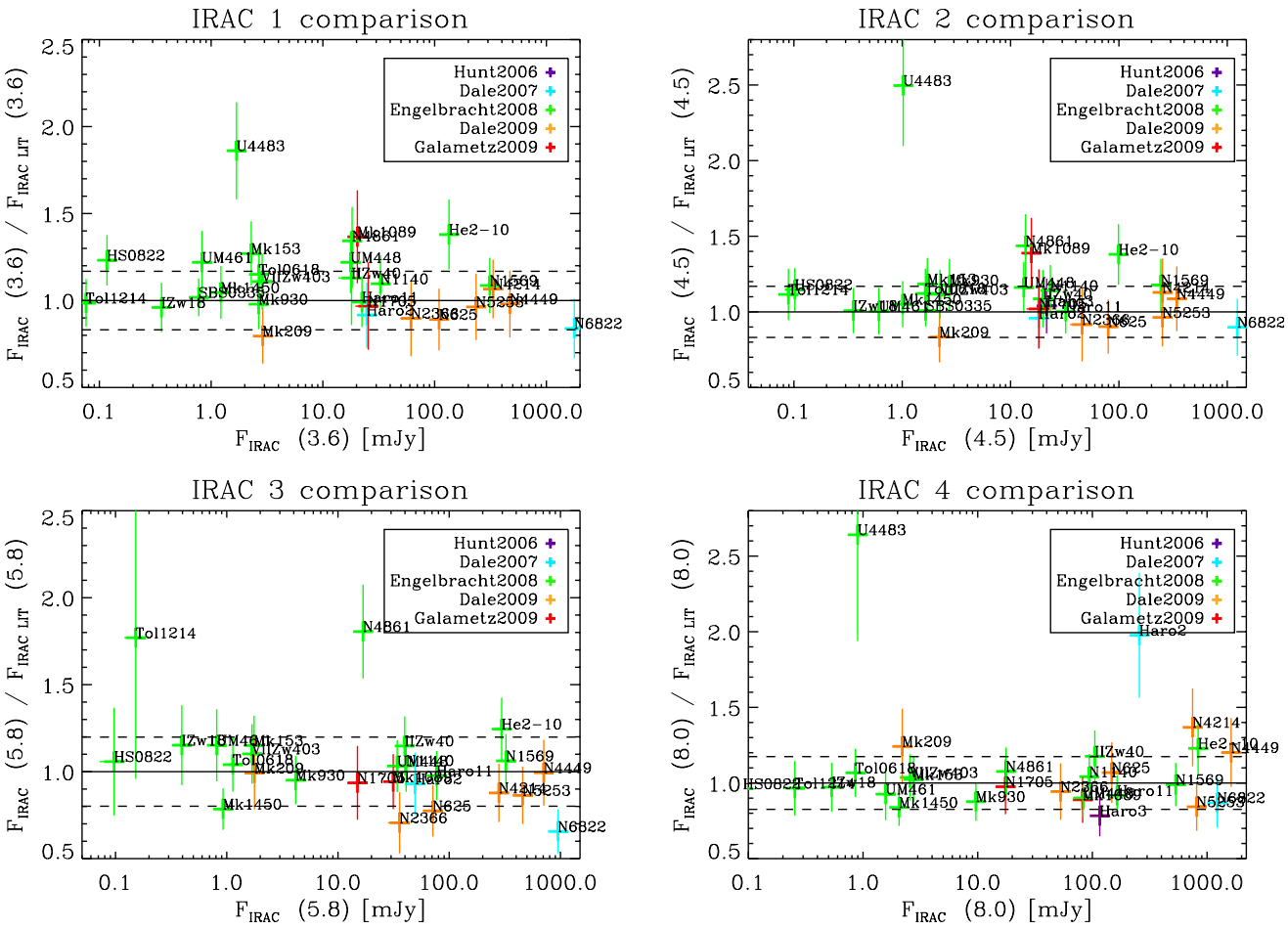

Fig. 6.3. Comparison of our IRAC flux densities and literature IRAC flux densities: $F_{IRAC}(\lambda_0)/F_{IRACLIT}(\lambda_0)$ flux density ratios as a function of our IRAC flux density, $F_{IRAC}(\lambda_0)$, at 3.6 μm *(top left)*, 4.5 μm *(top right)*, 5.8 μm *(bottom left)* and 8.0 μm *(bottom right)*. As a guide to the eye, the unity line is added as a solid line as well as the average uncertainties on the ratio in each bands as dotted lines. These average uncertainties are 17%, 17%, 19% and 17% at 3.6, 4.5, 5.8 and 8.0 μm. Colours distinguish the reference for the literature measurement.

UGC4483: We do not detect this galaxy at 5.8 μm. For the other three IRAC bands, our measurements are systematically larger than the flux density from Engelbracht et al. (2008). However, no precise information is given in Engelbracht et al. (2008) about the size of the aperture used for IRAC photometry. Nonetheless they mention an aperture for 2MASS measurements which is very similar to the one we use. IRAC photometry within this 2MASS aperture is consistent with what we find with our aperture. Thus we discard this galaxy in our comparison with literature measurements.

Tol1214-277: The comparison is fine at all wavelengths except for IRAC 5.8 μm. Again, because of the lack of information about the apertures used in Engelbracht et al. (2008) we cannot assess that we are really comparing similar measurements. Nonetheless, the ratio between the two measurements is coherent, within its error bar, with photometric agreement because of the large uncertainties on both measurements ($\sim$ 20% (Table 6.9) and 41% (Engelbracht et al. 2008)). Thus we keep this point in our comparison with literature measurements.

Excluding these outliers, and points where one of the two measurements (ours or the literature's) is an upper limit, we get a mean ratio of our IRAC measurements to those in the literature of 1.05 $\pm$ 0.11 for IRAC 3.6 μm, 1.06 $\pm$ 0.11 for IRAC 4.5 μm, 1.02 $\pm$ 0.14 for IRAC 5.8 μm and 1.01 $\pm$ 0.11 for IRAC 8.0 μm. This is to be compared to an average uncertainty on the ratios of 17%, 17%, 19% and 17% at 3.6, 4.5, 5.8 and 8.0 μm. The error on the average ratio is comparable to the average uncertainties on the ratio for all of the bands. Thus there is a good photometric agreement between our measurements and previously published measurements.

6.2.2 IRS

Instrument

The InfraRed Spectrograph[3] (IRS) is composed of four modules providing low (R$\sim$ 60 - 130) and moderate (R$\sim$ 600) resolution spectroscopic capabilities over 5.8 - 40 μm (ShortLow and LongLow modules) and over 9.9 - 37.2 μm (ShortHigh and LongHigh modules). IRS also provide imaging in two filters: Blue (13 - 18 μm) and Red (18 - 26 μm). The basic informations for the four spectroscopy modules can be found in Table 6.3, and a schematic view of the IRS slits is shown in Fig. 6.4.

Table 6.3. IRS characteristics (from the IRS Instrument Handbook, version 5.0).

IRS						
Module	Range (μm)	Resolving Power R	Plate scale ($''$/pix)	Slit Width ($''$)	Slit Length ($''$)	Cut-offs (μm)
SL1	7.46 - 14.29	61 - 120		3.6		[λ_{min} - 7.53, 14.02 - λ_{max}]
SL2	5.13 - 7.60	60 - 127	1.8	3.7	57	[λ_{min} - 5.23, 7.49 - λ_{max}]
SL3	7.33 - 8.66					[λ_{min} - 7.4, 8.5 - λ_{max}]
LL1	19.91 - 39.90	58 - 112		10.5		[λ_{min} - 20.5, 37.4 - λ_{max}]
LL2	13.90 - 21.27	57 - 126	5.1	10.7	168	[λ_{min} - 14.0, 20.52 - λ_{max}]
LL3	19.23 - 21.61					[λ_{min} - 19.8, 21.5 - λ_{max}]
SH	9.89 - 19.51	600	2.3	4.7	11.3	
LH	18.83 - 37.14	600	4.5	11.1	22.3	

[3] see the IRS Handbook, available at http://irsa.ipac.caltech.edu/data/SPITZER/docs/irs/irsinstrumenthandbook/

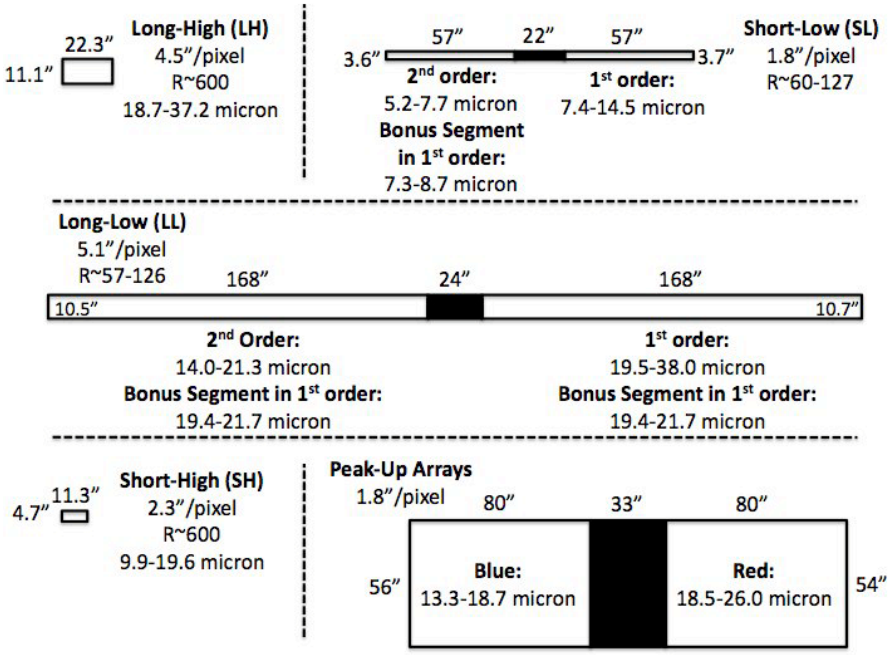

Fig. 6.4. Schematic view of the IRS slits. Note that the slits are not parallel in the *Spitzer* plane as shown here. Actual slit position angles relative to a *Spitzer* roll angle of 0° are SL = +84.7°, LL = +181.2°, SH = +221.5°, LH = +136.7°, and IRS Peak-up = +177.0°.

Reduction

The IRS spectra for the DGS galaxies have been extracted from the Cornell AtlaS of *Spitzer* Infrared spectrograph Sources[4] (CASSIS v5, Lebouteiller et al. 2011) which provides optimal extraction of a large collection of spectra from staring mode observations. Most of the DGS galaxies were observed using the staring mode, except for a few extended ones that were observed with the mapping mode, for which the spectra were reduced manually. We were able to obtain SL and LL data for 43 galaxies in total.

Two versions of the spectra are available in CASSIS: an "optimal" extraction better suited for point sources and a "tapered column" extraction, better suited for partially extended sources. A message advises the user if the "tapered column" extraction or the "optimal" extraction method should be chosen. The chosen extraction for each of the DGS targets, as well as AORkeys, are summarised in Appendix A. CASSIS uses the AdOpt algorithm (Advanced Optimal extraction, Lebouteiller et al. 2010) within the Spectroscopic Modeling Analysis and Reduction Tool (SMART, Higdon et al. 2004). AdOpt enables optimal extraction of spectra using a super-sampled PSF. The pipeline includes such steps as image cleaning, individual exposure combination and background subtraction. Specific attention is given to identification and removal of bad pixels and outlier rejection at the image and spectra levels.

Preparing the spectra

The IRS spectra for the DGS galaxies are presented in Appendix **??**. Several steps are necessary before including them in the SEDs. First some wavelengths at the edges of each orders have to be

[4]http://cassis.astro.cornell.edu/atlas/

cut off the spectra. These cut-off wavelengths are given in Table 6.3.

For the extended galaxies, there is a conversion step from MJy/sr to Jy where the IRS spectrum is multiplied by the area over which it has been extracted.

We collect IRS data in order to constrain the MIR slope of the SED, thus we are more interested in the continuum rather than in the spectral lines. It is then necessary to rescale the SL and LL spectra in order to match the photometry. The idea is to derive synthetic IRS photometry to correct the two modules and to use all of the constraints we have in this wavelength range: the IRAC 5.8 and 8.0 μm, *WISE* 12 and 22 μm and MIPS 24 μm bands. IRAC 5.8, 8.0 and *WISE* 12 μm are used simultaneously to derive a correction factor for the SL module that depends on the wavelength. However, for the LL module, we only have two constraints that do not sample well the LL spectrum. Deriving a wavelength-dependant correction factor is not possible here, and the LL correction factor is thus a constant. We use MIPS 24 μm for most cases, while *WISE* 22 μm is only considered whenever MIPS 24 μm is not available. SL and LL can be treated separately as they are two independent observations.

The correction factor for LL, C_{LL} is then:

$$C_{LL} = F_{24}/F_{IRS}(M_{24}) \tag{6.13}$$

where F_{24} is the observed 24 μm MIPS flux density (from Bendo et al. (2012)) and $F_{IRS}(M_{24})$ is the synthetic photometry for the IRS LL, spectrum at 24 μm. $F_{IRS}(M_{24})$ is derived using Eq. 6.16. Eq. 6.13 is adapted for *WISE* 22 μm when MIPS 24 μm is not available.

As we have several constraints available for the SL module, we can use them simultaneously to derive a correction that smoothly depends on wavelength, $C_{SL}(\lambda)$. To derive $C_{SL}(\lambda)$, we fit a spline function, using the IDL SPLINE_P procedure, to $C_{SL}(I3)$, $C_{SL}(I4)$, $C_{SL}(W3)$ and C_{LL}. We use C_{LL} here to have a better constraint at the end of the spline. We also impose a derivative of 0 at the end of the spline in order to have a smooth function. We also assume that the correction factor $C_{SL}(\lambda)$ should always be ≥ 1.0.

$C_{SL}(I3)$, $C_{SL}(I4)$, $C_{SL}(W3)$ are given by:

$$\begin{cases} C_{SL}(I3) &= F_{5.8}/F_{IRS}(I_{5.8}) \\ C_{SL}(I4) &= F_{8.0}/F_{IRS}(I_{8.0}) \\ C_{SL}(W3) &= F_{12}/F_{IRS,SL}(W_{12}) \end{cases} \tag{6.14}$$

where $F_{5.8}$, $F_{8.0}$ and F_{12} are the observed 5.8 and 8.0 μm IRAC and the 12 μm WISE flux densities (from Tables 6.9 and 6.10); and $F_{IRS}(I_{5.8})$, $F_{IRS}(I_{8.0})$ and $F_{IRS,SL}(W_{12})$ are the synthetic photometry for the IRS SL spectrum at 5.8, 8.0 and 12 μm. $F_{IRS}(I_{5.8})$, $F_{IRS}(I_{8.0})$ are derived using Eq. 6.8.

However, there is an overlap between the *WISE* 12 μm filter and the LL wavelengths (Fig. 6.5). As the LL part of the spectrum has already been corrected, we must find the flux missing in the SL part of the spectrum, i.e., $F_{IRS,SL}(W_{12})$, to match F_{12}. But the integration over the *WISE* bandpass is not linear, i.e.,: $F_{IRS,SL}(W_{12}) \neq F_{IRS}(W_{12})$ - $F_{IRS,LL}(W_{12})$. In other words, we can not use Eq. 6.18 on the SL wavelength range to derive $F_{IRS,SL}(W_{12})$. Thus there is no simple way of deriving $C_{SL}(W3)$. Instead, we apply the following method:

1. We generate a grid of potential $C_{SL}(W3)$, {x}, from 0.01 to 10 ;
2. find the spline going through $C_{SL}(I3)$, $C_{SL}(I4)$, C_{LL}, and each x_i, $sp(x_i)$;
3. correct the SL spectrum with each $sp(x_i)$ and
4. compute the synthetic *WISE* 12 μm photometry for each corrected *total* IRS spectrum, $F_{IRS}(W_{12})(sp(x_i))$.

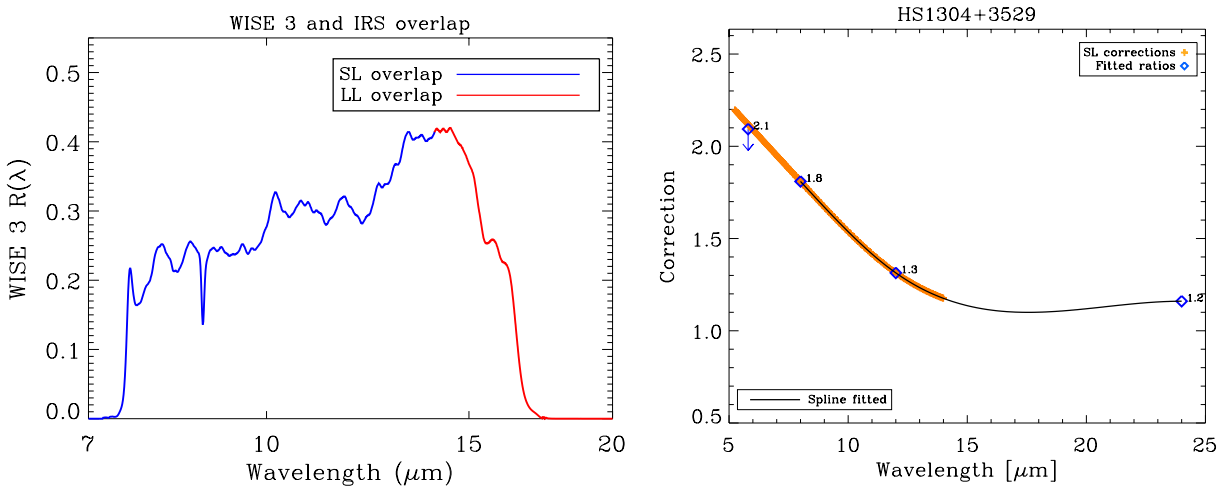

Fig. 6.5. *(left)* Illustration of the overlap between the *WISE* 12 μm band and the IRS LL wavelengths. *(right)* Example of a spline used to rescale SL in the case of HS1304+3529. The spline has been fitted to the blue diamonds, except for the 5.8 μm band as the galaxy is not detected at this wavelength. The diamonds represent the ratio between the observed and the synthetic photometry at each wavelength. The black curve is the final adopted spline, sp(x_0), where $x_0 = 1.3$. The orange crosses are the corrections applied to the SL part of the spectrum.

$C_{SL}(W3)$ is the x_0 that gives $F_{IRS}(W_{12})(sp(x_0)) = F_{W_{12}}$.

The final IRS spectrum, $F_{IRS,corr}(\lambda_{SL})$ and $F_{IRS,corr}(\lambda_{LL})$, is given by:

$$\begin{cases} F_{IRS,corr}(\lambda_{SL}) &= F_{IRS}(\lambda_{SL}) \times C_{SL}(\lambda_{SL}) \\ F_{IRS,corr}(\lambda_{LL}) &= F_{IRS}(\lambda_{LL}) \times C_{LL} \end{cases} \quad (6.15)$$

The method presented here is adapted depending on the number of constraints for each galaxy. Upper limits are not considered for the correction of IRS spectrum. An example of this treatment of IRS spectrum is shown in Fig. 6.6 along with the spline used to correct the SL spectrum in Fig. 6.5. Note that this correction assumes that the spectral shape of the area observed by the IRS slits likewise describes the expected spectral shape of the full galaxy. This is true for compact sources but can be erroneous for more extended galaxies, except if the region falling within the IRS slits dominates the total emission of the galaxy in the MIR.

For some galaxies, the IRS spectrum is very noisy (e.g. HS1304+3529, Fig 6.6, top panel). To improve the quality of the spectrum, we smooth the spectrum until we reach a signal-to-noise of 3 for each point in the spectrum. This smoothing step is applied for 22 DGS galaxies.

6.2.3 MIPS

Instrument

The Multiband Imaging Photometer for Spitzer (MIPS) provides broad-band imaging and photometry at 24, 70 and 160 μm. The broad-band filters are shown in Fig. 6.7. The three detector arrays are separated and view the sky simultaneously. The size of the arrays, FOV and pixel sizes are given in Table 6.4. Primary and secondary calibrators for MIPS are stars. MIPS colours corrections are based on a 10^4K blackbody, i.e., $F_S(\nu) \propto B_\nu(\nu_0, T_0 = 10^4 K)$ where $B_\nu(\nu, T_0)$ is the Planck function. Eq. 6.9 can thus be transformed into:

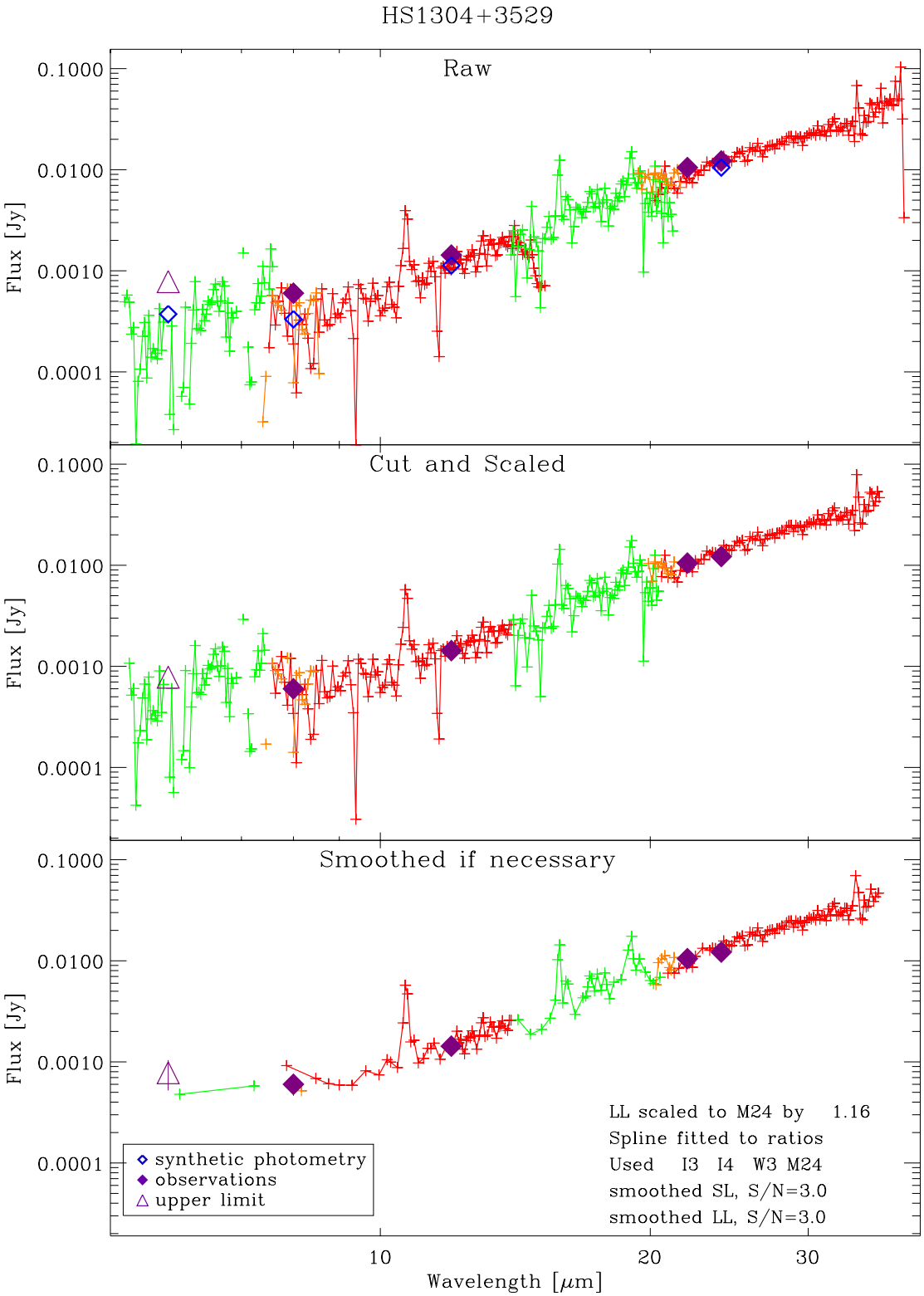

Fig. 6.6. Example of IRS treatment for HS1304+3529: the raw spectrum is presented in the *top* panel. The photometry points have been overlaid in filled purple diamonds as well as synthetic photometry as blue open diamonds. The galaxy is not detected at 5.8 μm as indicated by the open purple triangle. Green, orange and red parts of the spectrum represents the SL2 and LL2, SL3 and LL3, SL1 and LL1 spectra, respectively. The *middle* panel shows the spectra after cutting-off the bad wavelengths and rescaling to match the photometry. The spline used to rescale SL is shown in Fig. 6.5. The *bottom* panel shows the spectra smoothed to a S/N of 3.

$$F'_S(\nu_0) = \frac{\int F'_S(\nu)(\nu_0/\nu)R(\nu)\,\mathrm{d}\nu}{\int \left(\frac{\nu_0}{\nu}\right)\left(\frac{B_\nu(\nu,T_0)}{B_\nu(\nu_0,T_0)}\right)R(\nu)\,\mathrm{d}\nu} \tag{6.16}$$

with $T_0 = 10^4$ K.

Table 6.4. MIPS characteristics (from the MIPS Instrument Handbook, version 2).

MIPS							
Band	λ (μm)	Bandwidth (μm)	FWHM ($''$)	Calibration accuracy	FOV ($' \times '$)	Array size (pix $\times$ pix)	Pixel size ($'' \times ''$)
MIPS 1	24	4.7	6	4%	5.4 $\times$ 5.4	128 $\times$ 128	2.5 $\times$ 2.6
MIPS 2	70	19	18	7%	5.2 $\times$ 2.6	32 $\times$ 16	9.9 $\times$ 10.1
MIPS 3	160	35	38	12%	5.3 $\times$ 2.1	20 $\times$ 2	16 $\times$ 18

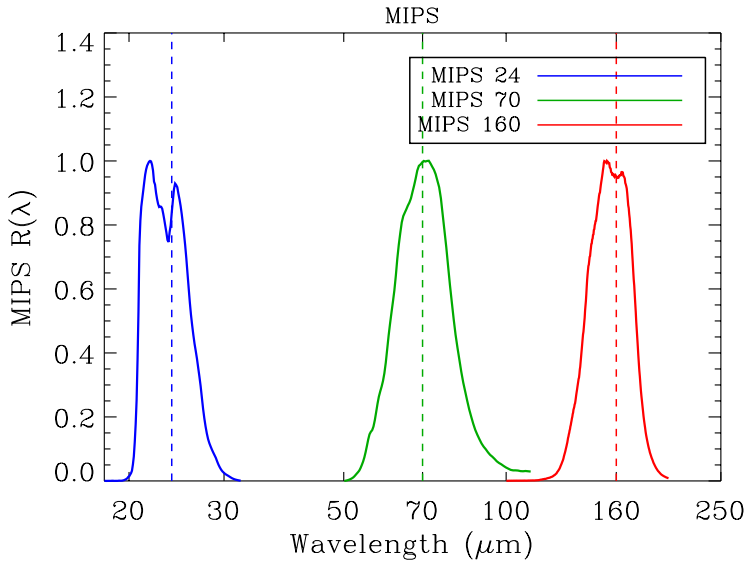

Fig. 6.7. MIPS filter transmissions, R(λ). The dashed lines mark the reference wavelength for each band.

Data Reduction and Photometry

The table of the available MIPS data for the DGS is given in Table 3.6 and in Bendo et al. (2012) who give a detailed description of the data reduction and of the photometry for integrated flux densities. Bendo et al. (2012) reprocessed the raw *Spitzer* data using the MIPS Data Analysis Tool (Gordon et al. 2005). The maps are given in units of MJy sr^{-1}. A non-linearity correction is applied to the 70 μm pixels that exceeded 66 MJy sr^{-1}. This correction is given in Dale et al. (2007) based on data from Gordon et al. (2007):

$$F_{70}(true) = 0.581 \times F_{70}(measured)^{1.13} \tag{6.17}$$

The fluxes were extracted from the maps via aperture photometry. Bendo et al. (2012) used elliptical apertures with minor and major axes that were the greater of either 1.5 times the D_{25} isophotes of de Vaucouleurs et al. (1991) or $3'$. This is to ensure that they do not need to apply aperture corrections on the 160 μm measurements. The whole group for Mrk1089 and UM311 was

taken into account in the aperture used for these sources as it is impossible to properly separate them at FIR wavelengths. Some of the DGS galaxies do not have an optical disk defined anywhere in the literature, so the 3′ aperture was used. For some very faint galaxies (fainter than 10 mJy at 24 μm), 1′ apertures were used to minimize the effect of background noise in very large apertures (see Bendo et al. 2012). Special treatments were necessary for HS0052+2536, IC10, IIZw40, Mrk153, NGC5253, NGC6822, SBS1249+493, Tol0618-402 and Tol1214-277; and are detailed in Bendo et al. (2012).

Of the DGS sample, 43, 34 and 28 galaxies have been observed by MIPS at 24, 70 and 160 μm respectively (see Fig. 3.13). Bendo et al. (2012) MIPS flux densities compare well with previously published MIPS samples containing a subset of the DGS galaxies (Dale et al. 2007; Engelbracht et al. 2008). Therefore we are confident about the reliability of these results and will use them to perform the comparison with our PACS flux densities.

MIPS photometry for KINGFISH galaxies is presented in Dale et al. (2007).

Comparison with PACS measurements for the DGS

The PACS flux densities correspond to monochromatic values for sources with spectra where νF_ν is constant, while the MIPS flux densities are monochromatic values for sources with the spectra of a 10^4K blackbody, so colour corrections need to be applied to measurements from both instruments before they are compared to each other. We first assume that the source spectral shape will be very close to that of the Rayleigh Jeans side of a modified blackbody: $F_S(\nu) \propto \nu^{\alpha_S}$. We fit a modified blackbody through the three PACS data points to determine the spectral index α_S, and apply the corresponding colour corrections from the available PACS documentation[5]. For the MIPS flux densities, we fit a blackbody through the 70 and 160 μm data points (not using the 24 μm point) and apply the corrections from the MIPS Handbook[6]. The typical colour corrections for MIPS are of the order of 10% and 4% on average at 70 and 160 μm. However, they are of the order of 1% or 2% in the 70 and 160 μm PACS bands. For non detected galaxies, where we, for PACS, and/or Bendo et al. (2012), for MIPS, reported upper limits (9 galaxies), we are not able to properly fit a blackbody and therefore derive a proper colour correction. We do not compare PACS and MIPS flux densities for these galaxies for now.

We use the ratios of the PACS and MIPS flux densities to assess how well the measurements from the instrument agree with each other; a ratio of 1 corresponds to a very good agreement. The PACS/MIPS ratios at 70 and 160 μm are shown in Figure 6.8, and the correspondence is relatively good. The PACS/MIPS ratio is 1.019 ± 0.112 at 70 μm and 0.995 ± 0.153 at 160 μm. This is to be compared to an average uncertainty of ∼12% (∼11% from MIPS and ∼5% for PACS, added in quadrature) and ∼16% (∼15% from MIPS and ∼7% for PACS, added in quadrature) on the ratios at 70 and 160 μm respectively.

If we now consider galaxies detected at 70 μm and not at 160 μm, indicated by a different symbol on the left panel of Figure 6.8, we are still able to compare, with extra caution, the measurements at 70 μm. Indeed, as we are not able to derive a proper colour correction for those galaxies, we add to the MIPS 70 μm flux densities a 10% uncertainty and a 1% uncertainty to the PACS 70 μm flux densities to account for the colour correction effect. When adding these extra galaxies at 70 μm, the PACS/MIPS ratio is 0.985 ± 0.158 at 70 μm. This is to compare with an average uncertainty of ∼14% on the 70 μm ratio (∼12% from MIPS and ∼7% for PACS, added in quadrature, including the extra galaxies). The very faint and discrepant galaxies at 70 μm are HS1222+3741 (ratio of 0.40)

[5]The corresponding documentation for PACS colour corrections is available at http://herschel.esac.esa.int/twiki/pub/Public/PacsCalibrationWeb/cc_report_v1.pdf. The values presented in this documentation can also be rederived from Eq. 3.8.

[6]The MIPS Instrument Handbook is available at http://irsa.ipac.caltech.edu/data/SPITZER/docs/mips/mipsinstrumenthandbook/home/

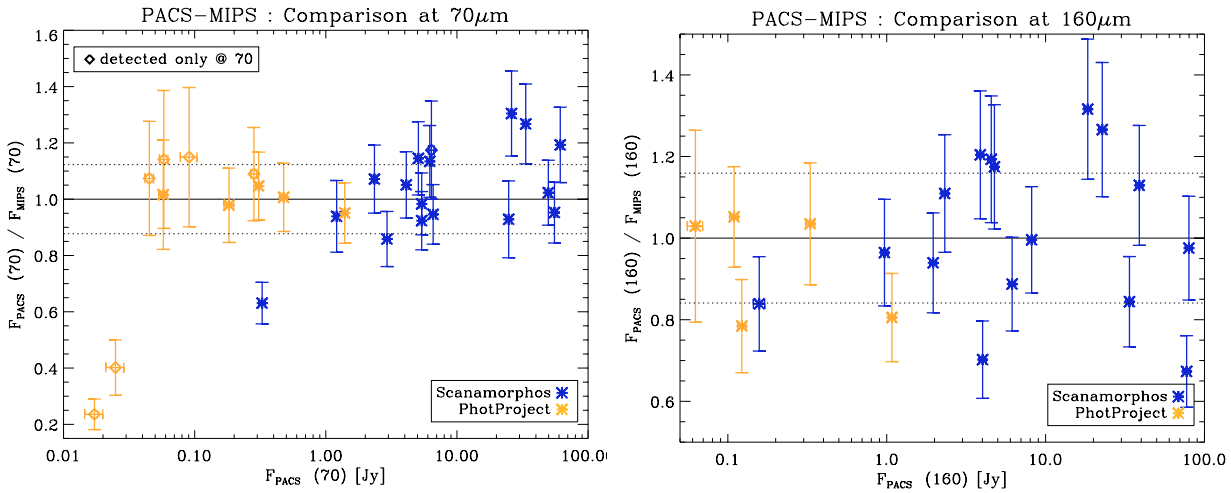

Fig. 6.8. Comparison of PACS flux densities and MIPS flux densities: PACS-to-MIPS flux density ratios as a function of PACS flux density at 70 μm *(left)* and 160 μm *(right)*. As a guide to the eye, the unity line is added as a solid line as well as the average uncertainties on the ratio in both bands as dotted lines. These average uncertainties are ∼12% and ∼16% at 70 and 160 μm. Colours distinguish the selected mapping method (see Chapter 4).

and Tol1214-277 (ratio of 0.24). For HS1222+3741, the MIPS image contains some bright pixels near the edge of the photometry aperture used for MIPS, and this may have driven the 70 μm MIPS flux density up. For Tol1214-277, a nearby source is present in the MIPS data and, although its contribution has been subtracted when computing the MIPS 70 μm flux, some contribution from this source may still be present. Additionally, measuring accurate flux densities at $\leq$ 50 mJy in both MIPS and PACS data is difficult and may have led to the discrepancies.

The error on the average ratio of the PACS to MIPS flux densities is comparable to the average uncertainties on the ratio for both bands. Thus there is a good photometric agreement between PACS and MIPS photometry for the DGS sample.

The same test has been done by Dale et al. (2012) for the KINGFISH galaxies. They found that the *Spitzer* and *Herschel* flux densities were also in good agreement.

6.3 WISE

Instrument

The Wide-field Infrared Survey Explorer (WISE, Wright et al. 2010) surveyed the entire sky at 3.4, 4.6, 12 and 22 μm. The telescope contains four mid-infrared focal plane array detectors that observed the sky simultaneously in a $47' \times 47'$ FOV. The main characteristics for WISE are given in Table 6.5 and the 4 broad-band MIR filters are shown in Fig. 6.9. The spectral convention for *WISE* is $F_S(\nu) \propto \nu^{-2}$ and thus Eq. 6.9 gives:

$$F'_S(\nu_0) = \frac{\int F'_S(\nu)(\nu_0/\nu)R(\nu)\,\mathrm{d}\nu}{\int (\nu_0/\nu)^3 R(\nu)\,\mathrm{d}\nu} \tag{6.18}$$

Table 6.5. WISE characteristics.

WISE				
Band	Wavelength (μm)	Bandwidth (μm)	FWHM ($''$)	F_0 [Jy]
WISE 1	3.4	0.750	6.1	306.682
WISE 2	4.6	1.015	6.4	170.663
WISE 3	12.0	1.425	6.5	29.045
WISE 4	22.0	2.905	12.0	8.284

Photometry: Searching the literature

The WISE data have been extracted from the NASA/IPAC ISA database and the WISE all-sky catalog[7]. Magnitudes are given, and can be converted into flux densities using Eq. 6.1 and the zero-magnitude flux values from Wright et al. (2010), reported in Table 6.5.

According to the WISE documentation[8], the optimal flux measurement for point sources is the WiMPRO (with i={1,2,3,4}) measurement from the database, as it comes from profile-fitting photometry. However when the source is resolved or extended, it is better to use the circular aperture photometry reported: WiMAG. This is indicated by an EXTFLG value of 5 in the database. The WISE flux densities for 40 DGS galaxies are reported in Table 6.10.

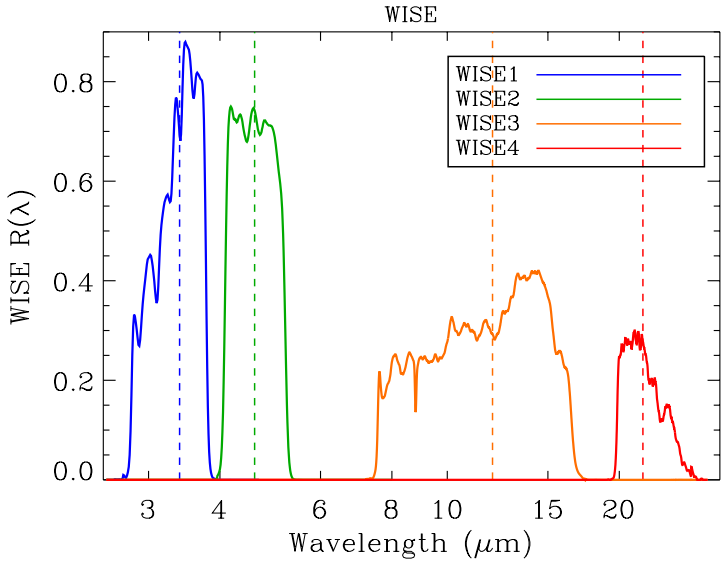

Fig. 6.9. WISE filter transmissions, R(λ). The dashed lines mark the reference wavelength for each band.

6.4 IRAS

The InfraRed Astronomical Satellite (*IRAS*) was designed to observe the entire sky in four wavelengths bands centred on 12, 25, 60 and 100 μm. The basic characteristics of *IRAS* are given in Table 6.6 and the four broadband filters are shown in Fig. 6.10. *IRAS* data for the DGS have been compiled from the literature: the NASA/IPAC ISA IRAS Faint Source (v2.0 1990) and Point

[7]available at: http://irsa.ipac.caltech.edu/cgi-bin/Gator/nph-dd
[8]available at: http://wise2.ipac.caltech.edu/docs/release/allsky/expsup/index.html

Source (v2.1) Catalogs, Rice et al. (1988); Sanders et al. (2003); Engelbracht et al. (2008) and is given in Table 6.11. The spectral convention for *IRAS* is $F_S(\nu) \propto \nu^{-1}$ and thus Eq. 6.9 gives:

$$F'_S(\nu_0) = \frac{\int F'_S(\nu)(\nu_0/\nu)R(\nu)\,\mathrm{d}\nu}{\int (\nu_0/\nu)^2 R(\nu)\,\mathrm{d}\nu} \tag{6.19}$$

Table 6.6. *IRAS* characteristics.

IRAS			
Band	λ (μm)	Bandwidth (μm)	Calibration accuracy
IRAS 1	12	4.7	2%
IRAS 2	25	19	5%
IRAS 3	100	35	5%
IRAS 4	160	35	10%

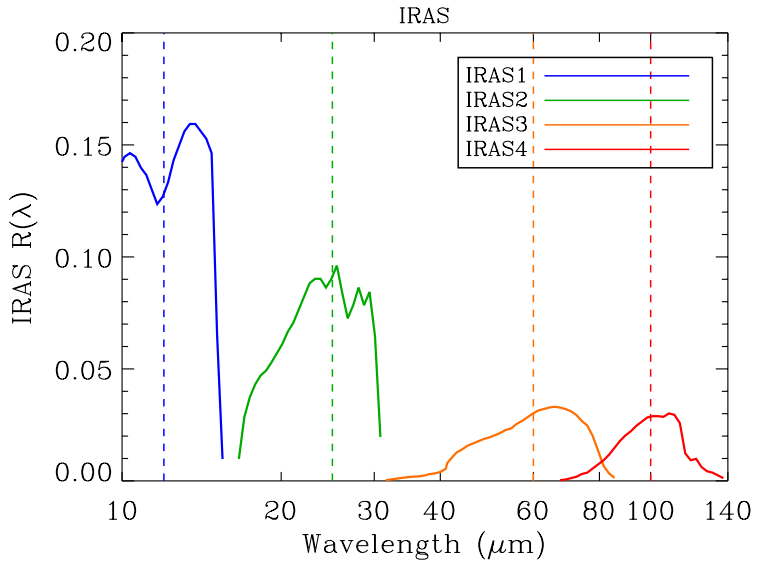

Fig. 6.10. IRAS filter transmissions, R(λ). The dashed lines mark the reference wavelength for each band.

Note that *IRAS* is not very sensitive and that the resolution varies from $\sim 30''$ at 12 μm to $\sim 120''$at 100 μm. Even for the detected sources, such a low resolution may imply that several sources are mixed in the beam and indistinguishable. Thus some of the *IRAS* fluxes of Table 6.11 may be unreliable and *IRAS* photometry should be treated with caution. 25 galaxies have *IRAS* measurements and only 15 are detected in all of the IRAS bands.

6.5 Ground-based submm data

6.5.1 Instruments

SCUBA The Submillimeter Common-User Bolometer Array (SCUBA) is a submm bolometre receiver, mounted on the JCMT (James Clerk Maxwell Telescope) in Hawaii, composed of two arrays: the Long-Wave (LW) array observing the sky at 850 μm and the Short-Wave (SW) array observing the sky at 450 μm. The FOV is $2.3'$ in diameter and the sky is observed simultaneously

by the two arrays, with FWHM of 7.5″ and 14″ for the SW and LW arrays respectively. SCUBA was upgraded to SCUBA2 in the Fall 2011.

LABOCA The Large APEX BOlometer CAmera (LABOCA) is one of the instruments mounted on APEX (Atacama Pathfinder EXperiment) in Chile, and was designed by the MPIfR. It is a multi-beam bolometric receiver observing in the submillimetric atmospheric window at 870 μm with a FOV of 11.4′× 11.4′ and a beam FWHM of 19.5″.

MAMBO MAMBO (the MAx-planck Millimeter-BOlometer) was a submm/mm bolometre array, mounted on the IRAM 30-m telescope in Spain, observing at 1.2 mm with a FOV of 4′× 4′ and a FWHM of 11″. MAMBO has been decommissioned in April 2011.

The main characteristics for these three instruments are presented in Table 6.7 and the bandpass filters are shown in Fig. 6.11.

Table 6.7. SCUBA, LABOCA and MAMBO characteristics.

Band	λ [μm]	Bandwidth [μm]	FWHM (″)	FOV (′× ′)
SCUBA SW[a]	450	90[d]	7.5	2.3 (diameter)
SCUBA LW[a]	850	170[d]	14	2.3 (diameter)
LABOCA[b]	870	160	19.5[e]	11.4 × 11.4
MAMBO[c]	1200	430	11	4 × 4

[a]: Values from: http://www.jach.hawaii.edu/JCMT/continuum/scuba/intro.html.
[b]: Values from: http://www3.mpifr-bonn.mpg.de/staff/gsiringo/laboca/laboca_at_the_mpifr_bolometer_group.html.
[c]: Values from: http://www.iram.es/IRAMES/mainWiki/PoolObserving.
[d]: Holland et al. (1999).
[e]: Albrecht et al., in prep.

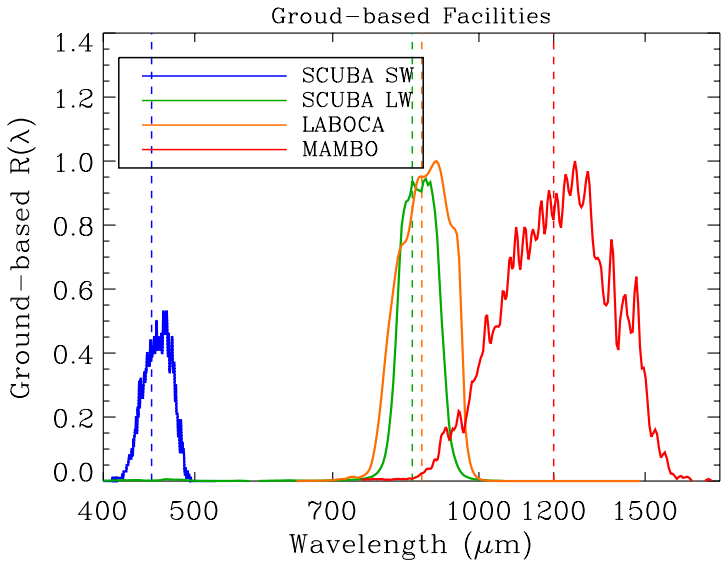

Fig. 6.11. Ground-based submm filter transmissions, R(λ). The dashed lines mark the reference wavelength for each band.

6.5.2 Literature measurements

SCUBA data for 21 KINGFISH galaxies (34% of the sample) is presented in Dale et al. (2007). We find submm literature measurements for 11 galaxies of the DGS: Haro11, Mrk1089, NGC1705 and UM311 with LABOCA (Galametz et al. 2009), Haro2 with SCUBA Dale et al. (2007), He2-10, IIZw40, NGC1140, NGC1569, NGC4214 and NGC4449 with SCUBA and MAMBO (Lisenfeld et al. 2002; Böttner et al. 2003; Galliano et al. 2003, 2005; Kiuchi et al. 2004; Hermelo et al. 2013).

We are interested here in the analysis of the *global* dust properties of galaxies. For NGC4214 and NGC4449 we do not use SCUBA data as the field of view of the observations is very small and the cold diffuse dust emission is missed by the observations: the maps presented in Kiuchi et al. (2004) for NGC4214 only show the centre of the galaxy in a $2' \times 1.40'$ field of view, and Böttner et al. (2003) present maps of NGC4449 on a $2.8' \times 3'$ field of view. Galametz et al. (2009) report a flux density at 870 μm for UM311 corresponding to the regions 1 2 and 3 of Moles et al. (1994) and not for the full group that we are considering. Thus we do not use this flux density either.

6.5.3 New LABOCA observations

In order to complete this sample of submm observations, we wrote 8 proposals for the three instruments: one for MAMBO, two for SCUBA2 and five for LABOCA, out of which 7 were accepted. However MAMBO was decommissioned right after the acceptance of our proposal and thus no observations could be carried on. For SCUBA2 observations, because of bad weather conditions and a medium priority for our program, we were not able to observe the proposed sources down to the required rms. For LABOCA the strategy was to separate our requested time between two of the owners of the APEX telescope time: ESO (European Southern Observatory) and OSO (Onsala Space Observatory, Sweden). Our proposals were accepted and we were able to successfully observe three sources out of the four requested (HS0052+2536 was dropped because it was not detected after all of the allocated time). Thus we present here LABOCA observations for Mrk930, NGC5253 and UM448.

Observations and data reduction

The sources were observed with LABOCA on APEX between May 2012 and May 2013 from programs 089.B0922, 089.F9306, 091.B0724 and 091.F9306. The sources were mapped using the spiral raster map mode with map sizes adjusted from the extent of the SPIRE 250 μm emission as the two beam sizes are comparable ($\sim$ 18 - 19$''$). The focus settings of the telescope were regularly checked during the observations using planets (Uranus and Neptune). The pointing of the telescope was checked on strong sources located close to the target galaxy. Skydips were performed regularly during the observations in order to derive the zenith opacity needed to correct the observations for atmospheric attenuation. Calibration of the flux densities was derived mostly from observations of planets (Mars, Uranus and Neptune as primary calibrators). The calibration was found to be accurate to 12%.

The data reduction is performed with the BoA software package[9] (BOlometer Array analysis software, Schuller 2012). The following steps are applied to the raw time series:

- calibration correction;
- opacity correction using the interpolation of the opacity at the elevation of the scan (from the skydips);
- correction for the thermal drift of the bolometres;

[9] http://www.astro.uni-bonn.de/boawiki/Boa

- flat fielding;
- conversion from counts to Jy;
- flagging of bad channels: Additionally to the known dead and noisy channels, all channels that deviate from the median rms of all of the channels were flagged after checking all of the time series to identify them. After this step, about 83% of the total 295 channels remains unflagged;
- removal of correlated noise on the full array and on groups of channels sharing the same amplifier box and the same wiring (this noise on groups of channels was found during the commissioning period of LABOCA);
- baseline subtraction;
- despiking;
- low-frequency filtering;
- flagging of the data taken outside reasonable telescope scanning velocity and acceleration limits.

Then each reduced scan is gridded in a rms-weighted intensity map with $4'' \times 4''$ pixels. Individuals maps are coadded and noise-weighted again to derive the final maps. As our sources are extended, it is important to differentiate between correlated noise and extended emission. However the "blind" skynoise removal step in the data reduction can not separate correlated atmospheric noise from the real diffuse extended emission of the sources. To avoid this effect, an iterative method is applied where a model of the flux distribution of the source is determined from the observations and improved at each new iteration of the data reduction. This data reduction method and the reduction parameters have been tested and improved in order to get the best recovery of the faint diffuse emission of extended sources. The data reduction is presented in more details in Albrecht et al., (in prep.) on another sample of galaxies. The new LABOCA maps are presented in Fig. 6.12. The rms level in the maps is 0.04 mJy/beam for Mrk930 and NGC5253 and 0.05 mJy/beam for UM448.

Photometry

Aperture photometry is performed on the maps to derive flux densities. Maps are first converted from mJy/beam to mJy/pix using an effective beam area of 521 arcsec^2 (Albrecht et al. in prep.). For NGC5253, we use the same aperture as for *Herschel* measurements. For Mrk930 and UM448, the aperture used for *Herschel* photometry encompass a small fraction of nearby sources (to the east of Mrk930 and to the north of UM448, see Fig. 6.12). For these two sources, we adapt the shape of the *Herschel* aperture to only encompass the emission of the galaxy at 870 μm. The *Herschel* background aperture is used for NGC5253. For Mrk930 and UM448, the nearby sources may bias our estimation of the background if we take an annulus around the source aperture. Thus we use small circular apertures of $30''$ radius spread around the galaxy for these two sources. Errors on the flux density are estimated by adapting the method presented in Chap 4 to LABOCA.

We get a total flux density at 870 μm for the sources of $F_{870} = 41 \pm 5$ mJy for Mrk930, $F_{870} = 494 \pm 59$ mJy for NGC5253 and $F_{870} = 76 \pm 9$ mJy for UM448. These flux densities are reported in Table 6.12. If we use the apertures used previously for *Herschel* photometry, we get $F_{870} = 42 \pm 6$ mJy for Mrk 930 and $F_{870} = 75 \pm 9$ mJy for UM448 which is consistent with our results.

James et al. (2002) observed NGC5253 and UM448 at 850 μm with SCUBA and reported flux densities at 850 μm of 192 $\pm$ 23 mJy for NGC5253 (39% of our value) and 40 $\pm$ 9 mJy for UM448 (53% of our value). We believe that these discrepancies are due to the apertures used by James et al. (2002) which are much smaller than ours: 41″ in diameter for NGC5253 and 34″ in diameter for UM448. Indeed when using the apertures from James et al. (2002), we find a flux density at 870 μm of 212 $\pm$ 25 mJy for NGC5253 and 29.6 $\pm$ 3.4 mJy for UM448, much closer to their findings at 850 μm. Additionally, our data reduction paid particular attention to recover the diffuse extended emission whereas James et al. (2002) do not mention any particular treatment of the extended emission in their galaxies.

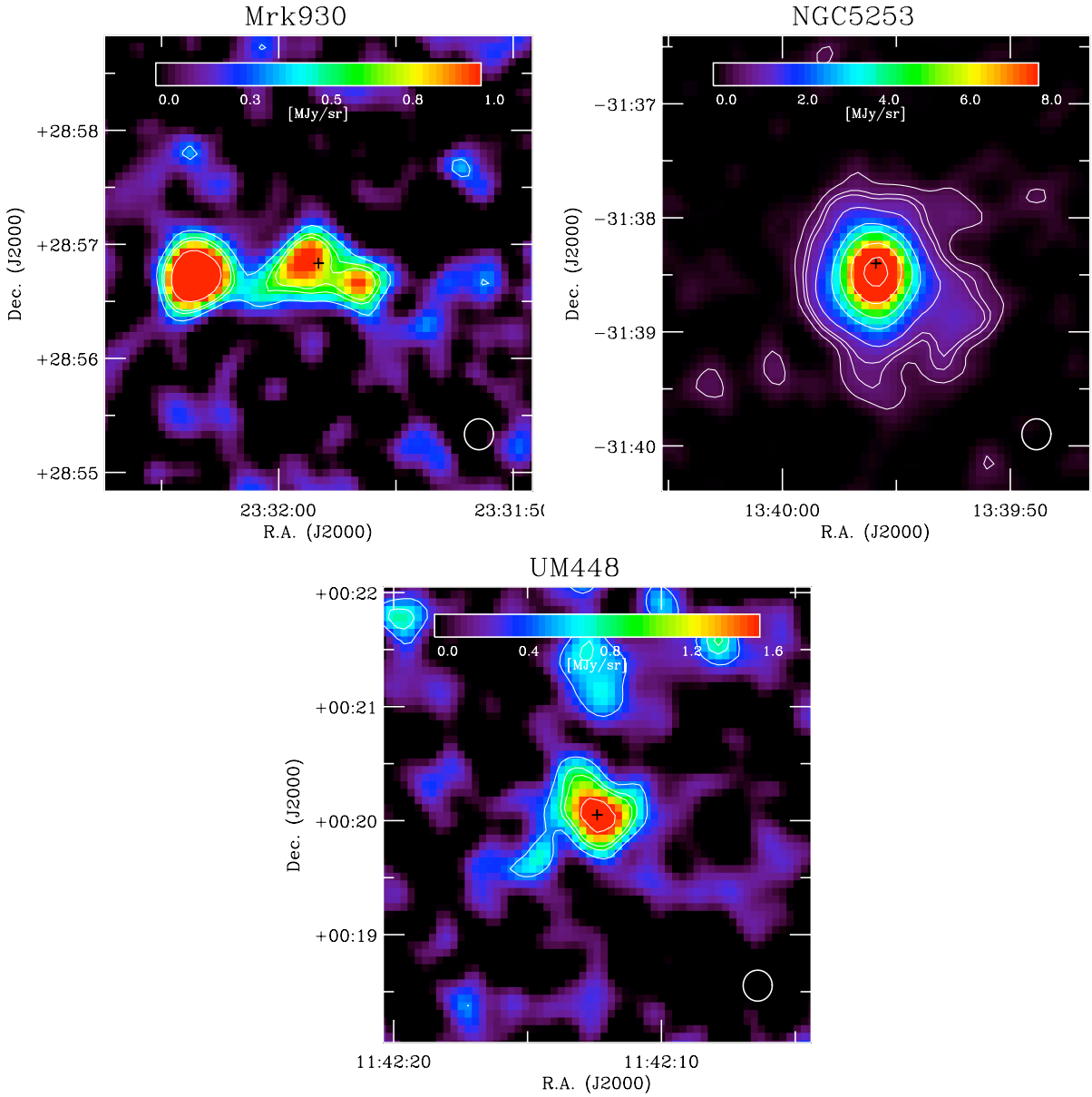

Fig. 6.12. LABOCA 870 μm maps for Mrk930 *(top left)*, NGC5253 *(top right)* and UM448 *(bottom)*, in units of MJy/sr. The contours are S/N contours with S/N = 3, 5 and 6 for Mrk930, S/N= 3, 5, 6, 10, 20, 30, 50, 80 for NGC5253 and S/N=3, 5, 6, 10 for UM448. The black cross marks the position of the galaxy from NED and the LABOCA beam is shown on the bottom right corner of the maps.

6.5.4 Non-dust contaminations

Possible contamination from non-dust sources can occur at submm wavelengths and we need to take them into account when using the submm flux densities to constrain a SED dust model. We can identify two sources of contamination at our wavelengths of interest:

Radio emission: There are two sources of radio emission: thermal (bremsstrahlung, also called free-free) and non-thermal (synchrotron) emission. Free-free emission comes from charged particles when they are accelerated during collisions. It arises from the interaction of very fast charged particles with a gas and is emitted from the ionised phase of the ISM (e.g., HII regions, see Section 1.3). This emission can be estimated using the radio tendency: $L_\nu^{ff} \propto \nu^{-0.1}$ or emission from the Hα recombination line. Synchrotron emission arises when relativistic electrons are gyrating about a magnetic field. The synchrotron emission is also well described by a power law of spectral index α_{sync}: $L_\nu^{sync} \propto \nu^{-\alpha_{sync}}$. A typical value for α_{sync} is 0.8±0.1. Usually, if no strong AGN is present, the free-free component dominates over the synchrotron component of the radio emission. For a review on radio emission in normal galaxies, see the review by Condon (1992).

CO emission: Some CO transitions can fall within the wavelength range we cover: CO(2-1) at 1.3 mm in the MAMBO 1.2 mm band, CO(3-2) at 867 μm in the LABOCA 870 μm and the SCUBA 850 μm bands. CO(1-0) can be difficult to detect in low-metallicity dwarf galaxies (e.g. Leroy et al. 2005; Schruba et al. 2012), but, in principle, other higher excitation states could be present (Cormier et al. 2014).

Estimating the contaminations: To estimate the contamination from radio emission, we assume that we can neglect synchrotron emission compared to the free-free emission. We collect at least one radio flux density for each galaxy and extrapolate to 850, 870 and 1200 μm using the power-law description of the radio emission: $L_\nu^{radio} \propto \nu^{-0.1}$. For some galaxies, several radio flux densities are available. In this case the radio contamination from each available flux density is estimated and we use the mean and standard deviation of all of the estimated contaminations for the final radio contamination. The mean radio contamination to the total flux density at 850 μm for the DGS galaxies is 15.8 % and 16.8 % for the KINGFISH sample (giving 16.6% for the total sample). At 870 μm and 1200 μm respectively the mean radio contaminations are 15.3% and 22.5%.

The CO emission in the submm filters can be estimated using:

$$F_{CO} = \frac{2k\nu^3}{c^3\Delta\nu}\int_{\Omega_s} I_{CO}\,\mathrm{d}\Omega \tag{6.20}$$

in the case where a CO map is available (for the most extended sources). k is the Boltzmann constant, ν is the frequency of the CO transition, $\Delta\nu$ is the bandwidth of the submm bolometre (70 GHz for SCUBA at 850 μm, 60 GHz for LABOCA and 80 GHz for MAMBO), Ω_s is the solid angle covering the source and I_{CO} is the velocity integrated intensity given by: $I_{CO} = \int T_{mb}\,\mathrm{d}v$ where T_{mb} is the main beam temperature. In some cases, CO luminosities, L_{CO}, are given using the distance D to the source. We convert these luminosities using: $\int_{\Omega_s} I_{CO}\,\mathrm{d}\Omega = L_{CO}/D^2$.

For compact sources, where a single pointing encompasses the whole galaxy, Eq. 6.20 transforms into:

$$F_{CO} = \frac{2k\nu^3}{c^3\Delta\nu} I_{CO}\Omega_{mb} \tag{6.21}$$

where the solid angle Ω_{mb} is given by $\frac{\pi\theta^2}{4\ln(2)}$ with θ the FWHM of the main beam. In some cases, CO(3-2) or CO(2-1) measurements are not available to directly estimate the CO contribution to the

850 and 870 μm, and 1200 μm bands respectively. For these galaxies, we use CO(2-1) or CO(1-0) in lieu of CO(3-2), and CO(1-0) in lieu of CO(2-1) if lower J CO transition measurements are available. We convert the CO intensities of the lower J transitions to the higher J transitions using the band ratios from Wilson et al. (2012) obtained on a sample of 47 galaxies:

$$\left\{ \begin{array}{lcl} R_{3-2/2-1} & = & 0.36 \pm 0.04 \\ R_{3-2/1-0} & = & 0.18 \pm 0.02 \\ R_{2-1/1-0} & = & 0.50 \pm 0.08 \end{array} \right. \tag{6.22}$$

These lines ratios are relatively consistent too with the line ratios derived by Cormier et al. (2014) on a sample of 5 dwarf galaxies. We did not find any CO measurement in the literature for NGC1705 and we use the mean CO line contamination to the submm flux densities. This mean CO line contamination to the total flux density at 850 μm for the DGS galaxies is 2.9 % and 7.8 % for the KINGFISH sample (giving 6.8% for the total sample). At 870 μm and 1200 μm respectively the mean line contaminations are 0.8% and 1.7%. When we have CO non detections, we consider the upper limit for the CO line contamination to be conservative.

The final submm flux densities, presented in Tables 6.12 and 6.13, are derived by removing both the radio and CO line contaminations from the original flux densities. The mean radio+CO contamination to the total flux density at 850 μm for the DGS galaxies is 18.7 % and 24.5 % for the KINGFISH sample (giving 23.4% for the total sample). At 870 μm and 1200 μm respectively the mean radio+CO contaminations are 16.1% and 24.3%. Note that the lower mean contaminations in the 870 μm for the radio, CO, or radio+CO contaminations, compared to the same contaminations at 850 μm, is only representative of the smaller number of sources observed at 870 μm (6 galaxies) compared to the number of sources observed at 850 μm (26 galaxies).

Table 6.8. 2MASS flux densities for the DGS galaxies. When an upper limit is given, it is the 95% confidence upper limit given by the database.

Source	F_J [mJy]	σ_{F_J} [mJy]	F_H [mJy]	σ_{F_H} [mJy]	F_{K_s} [mJy]	$\sigma_{F_{K_s}}$ [mJy]	Ref
Haro11	13.0	0.4	13.0	0.6	14.1	0.7	1
Haro2	43.6	1.4	53.5	2.3	44.9	2.3	2
Haro3	44.7	1.4	53.2	2.3	37.9	1.9	1
He2-10	178	6	201	9	167	8	1
HS0017+1055	0.38	0.01	0.59	0.03	0.36	0.02	3
HS0052+2536	0.54	0.02	0.55	0.02	0.40	0.02	3
HS0822+3542	0.15	0.02	0.34	0.04	0.16	0.03	4
HS1222+3741	0.90	0.03	1.18	0.05	0.83	0.04	3
HS1236+3937	-	-	-	-	-	-	3
HS1304+3529	0.32	0.01	0.27	0.01	$\leq$ 0.385	-	3
HS1319+3224	-	-	-	-	-	-	3
HS1330+3651	-	-	-	-	-	-	3
HS1442+4250	-	-	-	-	-	-	3
HS2352+2733	-	-	-	-	-	-	3
IZw18	0.75	0.08	0.64	0.07	0.52	0.06	3
IC10	2052	64	2972	129	2632	133	2
IIZw40	15.1	1.5	21.0	2.2	20.3	2.1	4
Mrk1089	12.2	0.4	13.9	0.6	12.2	0.6	1
Mrk1450	1.05	0.03	0.90	0.04	0.66	0.03	3
Mrk153	4.64	0.56	4.27	0.59	3.63	0.51	4
Mrk209	7.42	1.34	8.22	2.00	7.28	2.40	5
Mrk930	3.52	0.36	4.64	0.48	3.53	0.36	4
NGC1140	48.9	1.5	57.2	2.5	41.8	2.1	2
NGC1569	473	49	547	57	479	50	2
NGC1705	52.1	1.6	50.9	2.2	41.1	2.1	2
NGC2366	145	10	147	13	110.	14.	5
NGC4214	521	16	614	27	458	23	2
NGC4449	916	29	1068	46	839	42	2
NGC4861[a]	16.9	0.5	14.0	0.6	13.1	0.7	2
NGC5253	380	12	414	18	334	17	2
NGC625	218	7	236	10	184	9	2
NGC6822[a]	1619	50	1754	76	1363	69	2
Pox186	-	-	-	-	-	-	3
SBS0335-052	0.30	0.01	0.28	0.01	$\leq$ 0.38	-	3
SBS1159+545	-	-	-	-	-	-	3
SBS1211+540	-	-	-	-	-	-	3
SBS1249+493	-	-	-	-	-	-	3
SBS1415+437	-	-	-	-	-	-	3
SBS1533+574	1.95	0.06	2.14	0.09	1.54	0.08	3
Tol0618-402	4.32	0.13	5.84	0.25	4.04	0.20	4
Tol1214-277	-	-	-	-	-	-	3
UGC4483	2.20	0.23	0.94	0.12	3.11	0.39	4
UGCA20	-	-	-	-	-	-	3
UM133	-	-	-	-	-	-	3
UM311	-	-	-	-	-	-	3
UM448	19.3	0.6	22.2	1.0	19.4	1.0	2
UM461	2.03	0.21	1.49	0.16	1.27	0.14	4
VIIZw403	4.31	0.44	3.89	0.40	2.97	0.31	4

[a]: The aperture used does not cover the total emission from the galaxy and the magnitudes reported in the database are not consistent with the rest of the IR photometry. Thus we do not consider them for the modelling.
References: (1) 2MASS Extended Objects Final Release 2003 ; (2) Jarrett et al. (2003) ; (3) NASA/IPAC ISA Point Source Catalog, available at http://irsa.ipac.caltech.edu/cgi-bin/Gator/nph-dd?catalog=fp_psc ; (4) Engelbracht et al. (2008) ; (5) Dale et al. (2009)

Table 6.9. IRAC flux densities for the DGS galaxies. When an upper limit is given, it is the 3σ upper limit computed in Section 6.2.1 Photometry.

Source	$F_{3.6}$ [mJy]	$\sigma_{3.6}$ [mJy]	$F_{4.5}$ [mJy]	$\sigma_{4.5}$ [mJy]	$F_{5.8}$ [mJy]	$\sigma_{5.8}$ [mJy]	$F_{8.0}$ [mJy]	$\sigma_{8.0}$ [mJy]	Radius ($''$)	Aper corr ?
Haro11	22.4	3.2	32.3	4.6	77.1	10.9	164	23	45^a	yes
Haro2	24.7	3.5	18.2	2.6	49.3	7.0	257	36	50^a	yes
Haro3	28.2	4.0	21.5	3.1	43.9	6.3	116	16	60^a	yes
He2-10	134	19	99.2	14.1	296	42	836	118	108^a	yes
HS0017+1055	0.17	0.02	0.31	0.03	0.76	0.08	1.53	0.16	12^b	
HS0052+2536	0.72	0.12	0.32	0.09	0.66	0.17	3.17	0.46	17^c	yes
HS0822+3542	0.12	0.01	0.10	0.01	0.10	0.03	0.09	0.03	5^b	
HS1222+3741	0.25	0.03	0.19	0.02	0.27	0.05	0.57	0.07	14^a	
HS1236+3937	≤ 0.56	-	≤ 0.38	-	≤ 0.66	-	≤ 0.32	-	15^a	
HS1304+3529	0.38	0.08	0.41	0.09	≤ 0.78	-	0.60	0.14	18^a	
HS1319+3224	0.06	0.01	0.05	0.01	0.10	0.02	0.12	0.02	8^a	
HS1330+3651	0.56	0.09	0.46	0.10	≤ 0.80	-	0.97	0.17	20^a	
HS1442+4250	-	-	1.24	0.21	-	-	1.59	0.25	51^a	yes
HS2352+2733	≤ 0.04	-	≤ 0.04	-	≤ 0.13	-	≤ 0.11	-	15^a	
IZw18	0.36	0.05	0.35	0.05	0.39	0.07	0.53	0.08	12^b	yes
IC10[f]	-	-	-	-	-	-	-	-	-	-
IIZw40	18.1	4.3	19.9	3.5	39.8	5.7	105	15	45×33 $(39)^c$	yes
Mrk1089	20.4	2.9	15.5	2.2	31.4	4.4	82.2	11.6	75^a	yes
Mrk1450	1.22	0.17	1.01	0.14	0.93	0.14	2.06	0.29	20^a	yes
Mrk153	2.29	0.33	1.70	0.24	1.76	0.25	2.75	0.39	25^b	yes
Mrk209	2.90	0.41	2.21	0.32	1.78	0.27	2.20	0.32	39^d	yes
Mrk930	2.66	0.38	2.73	0.39	4.17	0.59	9.65	1.37	13^b	yes
NGC1140	32.8	4.8	23.3	3.4	41.0	5.8	93.9	13.3	118^a	yes
NGC1569	312	45	244	35	324	46	533	75	150^a	yes
NGC1705	25.5	5.9	18.3	4.2	15.0	2.8	17.5	2.6	72^a	yes
NGC2366	61.5	12.4	45.7	10.4	35.8	7.6	52.8	8.1	200^d	yes
NGC4214	334	47	253	36	280	40	748	106	205×160 $(181)^c$	yes
NGC4449	472	67	342	48	709	100	1622	229	190×170 $(180)^c$	yes
NGC4861	18.3	2.6	13.8	2.0	16.8	2.5	17.7	2.5	150×100 $(71)^c$	yes
NGC5253	235	34	252	36	458	65	812	115	120^a	yes
NGC625	110	16	79.7	11.4	71.3	10.1	147	21	170^a	yes
NGC6822	1780	272	1240	196	951	141	1226	175	440^a	yes
Pox186	0.18	0.02	0.18	0.02	0.14	0.03	0.64	0.07	9^b	
SBS0335-052	0.78	0.08	1.64	0.17	4.50	0.45	12.3	1.2	10^a	
SBS1159+545	0.11	0.01	0.10	0.01	0.12	0.03	0.59	0.07	12^d	
SBS1211+540	0.16	0.02	0.08	0.01	≤ 0.12	-	0.30	0.05	15^a	

Table 6.9. IRAC flux densities for the DGS galaxies. When an upper limit is given, it is the 3σ upper limit computed in Section 6.2.1 Photometry.

Source	$F_{3.6}$ [mJy]	$\sigma_{3.6}$ [mJy]	$F_{4.5}$ [mJy]	$\sigma_{4.5}$ [mJy]	$F_{5.8}$ [mJy]	$\sigma_{5.8}$ [mJy]	$F_{8.0}$ [mJy]	$\sigma_{8.0}$ [mJy]	Radius ($''$)	Aper corr ?
SBS1249+493	0.08	0.02	0.07	0.02	≤ 0.20	-	0.26	0.04	5[b]	
SBS1415+437	-	-	0.80	0.11	-	-	0.50	0.08	34[a]	yes
SBS1533+574	2.09	0.34	1.52	0.24	2.26	0.33	3.32	0.48	30[a]	yes
Tol0618-402	2.68	0.38	1.64	0.23	1.13	0.16	0.86	0.12	18[a]	yes
Tol1214-277	0.08	0.01	0.09	0.01	0.15	0.03	0.25	0.03	8[b]	
UGC4483	1.69	0.25	1.02	0.15	≤ 0.33 / ≤ 0.85[g]	-	0.90	0.15	43 × 24 (32)[c]	yes
UGCA20	≤ 0.85	-	≤ 0.60	-	≤ 1.07	-	≤ 0.46	-	20[a]	
UM133	≤ 0.62	-	≤ 0.46	-	≤ 0.86	-	≤ 0.54	-	8[a]	
UM311	-	-	33.4	4.7	-	-	114	16	115[e]	yes
UM448	17.7	2.5	13.2	1.9	34.1	4.8	83.0	11.7	53 × 31 (41)[c]	yes
UM461	0.83	0.12	0.61	0.09	0.81	0.14	1.58	0.29	17[a]	yes
VIIZw403	2.86	0.41	2.23	0.32	1.69	0.25	2.56	0.37	40[a]	yes

[a]: The aperture is the same as the one used for *Herschel*.
[b]: The *Herschel* aperture has been shorten to avoid a contaminating source.
[c]: The *Herschel* aperture has been adapted to match the peculiar morphology of the source in the NIR. The radius indicated in between parenthesis is the equivalent radius r= $\sqrt{ab}$ to be used in Eq. 6.10.
[d]: The *Herschel* aperture has been enlarged to encompass all of the NIR emission.
[e]: The IRAC map is too small for the *Herschel* aperture. The aperture thus had to be shorten.
[f]: For this galaxy, the IRAC maps do not cover the full galaxy. Thus we do not feel comfortable in reporting flux densities for this source.
[g]: This flux density is more coherent with the rest of the IR photometry for this galaxy (see Section 7.2.4). Thus we recommend to use this value when studying this object.

Table 6.10. WISE flux densities for the DGS galaxies.

Source	$F_{3.4}$ [mJy]	$\sigma_{3.4}$ [mJy]	$F_{4.6}$ [mJy]	$\sigma_{4.6}$ [mJy]	F_{12} [mJy]	σ_{12} [mJy]	$F_{22.0}$ [mJy]	$\sigma_{22.0}$ [mJy]	Extended source ?
Haro11	17.3	0.1	33.2	0.2	322	1	1957	12	yes
Haro2	16.0	0.1	11.8	0.1	138	1	743	5	yes
Haro3	12.5	0.1	9.8	0.1	130	1	739	5	yes
He2-10	66.7	0.4	53.0	0.3	775	4	4696	29	yes
HS0017+1055	0.148	0.001	0.291	0.002	3.54	0.02	12.1	0.1	
HS0052+2536	0.534	0.003	0.397	0.002	3.28	0.02	19.6	0.1	
HS0822+3542	0.106	0.001	0.0823	0.0004	$\leq$ 0.47	-	3.85	0.02	
HS1222+3741	0.125	0.001	0.122	0.001	1.08	0.01	5.94	0.04	
HS1236+3937[a]	-	-	-	-	-	-	-	-	-
HS1304+3529	0.221	0.001	0.221	0.001	1.43	0.01	10.5	0.1	
HS1319+3224	0.0392	0.0002	0.0801	0.0004	0.504	0.002	1.93	0.01	
HS1330+3651	0.274	0.002	0.212	0.001	1.09	0.01	7.64	0.05	
HS1442+4250	0.128	0.001	0.090	0.001	$\leq$ 0.15	-	$\leq$ 1.05	-	
HS2352+2733	0.0664	0.0004	0.0406	0.0002	$\leq$ 0.42	-	$\leq$ 2.98	-	
IZw18	0.212	0.001	0.207	0.001	0.773	0.004	5.44	0.03	
IC10	1204	7	769	4	2563	12	9088	93	yes
IIZw40	6.29	0.03	11.5	0.1	289	1	1456	9	yes
Mrk1089	5.74	0.03	5.18	0.03	69.0	0.3	412	3	yes
Mrk1450	0.92	0.01	0.712	0.004	7.03	0.03	49.6	0.3	
Mrk153	1.64	0.01	1.03	0.01	3.92	0.02	25.4	0.2	only at 3.4 μm
Mrk209	0.93	0.01	0.588	0.003	5.95	0.03	48.1	0.3	only at 3.4 μm
Mrk930	1.63	0.01	1.41	0.01	15.3	0.1	114	1	yes
NGC1140	15.0	0.1	10.2	0.1	57.3	0.3	310	2	yes
NGC1569[b]	-	-	-	-	-	-	-	-	-
NGC1705	9.89	0.05	6.42	0.04	8.16	0.04	30.7	0.2	yes
NGC2366[c]	-	-	-	-	-	-	-	-	-
NGC4214	10.9	0.1	8.94	0.05	86.7[e]	0.4	689[e]	4	yes
NGC4449	389	2	249	1	905	4	255	16	yes
NGC4861[b]	-	-	-	-	-	-	-	-	-
NGC5253	62.0	0.3	168	1	1391	6	6562	58	yes
NGC625[c]	7.24	0.04	5.01	0.03	35.1	0.2	380	2	yes
NGC6822[b]	-	-	-	-	-	-	-	-	-
Pox186	0.106	0.001	0.087	0.001	2.18	0.01	13.3	0.1	
SBS0335-052	0.460	0.003	1.67	0.01	24.4	0.1	74.1	0.5	
SBS1159+545	0.0652	0.0004	0.095	0.001	1.00	0.01	7.18	0.04	
SBS1211+540	0.094	0.001	0.0642	0.0003	0.225	0.001	1.86	0.01	

Table 6.10. WISE flux densities for the DGS galaxies.

Source	$F_{3.4}$ [mJy]	$\sigma_{3.4}$ [mJy]	$F_{4.6}$ [mJy]	$\sigma_{4.6}$ [mJy]	F_{12} [mJy]	σ_{12} [mJy]	$F_{22.0}$ [mJy]	$\sigma_{22.0}$ [mJy]	Extended source ?
SBS1249+493	0.0507	0.0003	0.0684	0.0004	0.726	0.003	3.40	0.02	
SBS1415+437	0.283	0.002	0.286	0.002	1.75	0.01	17.9	0.1	
SBS1533+574	0.96	0.01	0.779	0.004	8.04	0.04	49.7	0.3	only at 3.4 μm
Tol0618-402	1.70	0.01	0.92	0.01	0.281	0.001	$\leq$ 1.00	-	
Tol1214-277	0.0513	0.0003	0.0786	0.0004	1.24	0.01	6.89	0.04	
UGC4483[c]	-	-	-	-	-	-	-	-	-
UGCA20	0.0667	0.0004	0.0346	0.0002	$\leq$ 0.19	-	$\leq$ 1.30	-	
UM133	0.209	0.001	0.171	0.001	0.695	0.003	5.75	0.04	
UM311[d]	-	-	-	-	-	-	-	-	-
UM448	11.8	0.1	9.74	0.05	93.5	0.4	543	3	yes
UM461	0.346	0.002	0.372	0.002	5.51	0.03	29.2	0.2	
VIIZw403[c]	-	-	-	-	-	-	-	-	-

[a]: This source was not found in the database.
[b]: No good measurement was available from the database as the source is too extended or present very low surface brightness areas.
[c]: This source is extended but no W_iMAG measurement was available.
[d]: The photometry is not done on the whole complex and thus we do not report it here.
[e]: The aperture used by the database do not encompass the total galaxy at these wavelengths.

Table 6.11. *IRAS* flux densities for the DGS galaxies.

Source	F_{12} [Jy]	$\sigma_{F_{12}}$ [Jy]	F_{25} [Jy]	$\sigma_{F_{25}}$ [Jy]	F_{60} [Jy]	$\sigma_{F_{60}}$ [Jy]	F_{100} [Jy]	$\sigma_{F_{100}}$ [Jy]	Ref
Haro11	0.42	0.05	2.49	0.03	6.48	0.39	5.01	0.35	1
Haro2	0.21	0.03	0.95	0.01	4.68	0.28	5.32	0.32	1
Haro3	0.21	0.03	0.94	0.01	4.95	0.40	6.75	0.41	1
He2-10	1.18	0.13	6.78	0.72	23.4	2.9	26.3	3.9	2
HS0017+1055	-	-	-	-	-	-	-	-	-
HS0052+2536	0.11[a]	0.02	0.14[a]	0.01	0.25[a]	0.01	0.71[a]	0.07	1
HS0822+3542	-	-	-	-	-	-	-	-	-
HS1222+3741	-	-	-	-	-	-	-	-	-
HS1236+3937	-	-	-	-	-	-	-	-	-
HS1304+3529	-	-	-	-	-	-	-	-	-
HS1319+3224	-	-	-	-	-	-	-	-	-
HS1330+3651	-	-	-	-	-	-	-	-	-
HS1442+4250	-	-	-	-	-	-	-	-	-
HS2352+2733	-	-	-	-	-	-	-	-	-
IZw18	-	-	-	-	-	-	-	-	-
IC10	-	-	-	-	-	-	-	-	-
IIZw40	0.41	0.04	1.88	0.02	6.02	0.42	$\leq$ 19.7	-	1
Mrk1089	0.25[a]	0.01	0.70	0.01	4.06	0.20	5.64	0.56	3
Mrk1450	$\leq$ 0.06	-	$\leq$ 0.10	-	0.28	0.04	$\leq$ 0.58	-	1
Mrk153	$\leq$ 0.08	-	$\leq$ 0.09	-	0.28	0.04	$\leq$ 0.48	-	1
Mrk209	-	-	-	-	-	-	-	-	-
Mrk930	$\leq$ 0.08	-	0.23	0.01	1.25	0.09	$\leq$ 2.15	-	1
NGC1140	0.10	0.03	0.49	0.06	3.34	0.31	4.92	0.64	2
NGC1569	0.87	0.07	7.73	0.62	44.0	3.5	47.1	5.9	2
NGC1705	$\leq$ 0.05	-	$\leq$ 0.11	-	$\leq$ 0.87	-	$\leq$ 1.82	-	1
NGC2366	$\leq$ 0.12	-	0.70	0.07	3.51[a]	0.18	4.67[a]	0.28	1
NGC4214	0.65	0.07	2.58	0.19	17.9	1.2	29.0	3.2	2
NGC4449	2.14[a]	0.23	5.15	0.65	36.6	4.0	73.0	11.3	2
NGC4861	0.25[a]	0.03	0.41	0.09	1.82	0.38	2.39	0.55	2
NGC5253	2.81[a]	0.20	12.3	1.0	29.0	2.3	29.1	3.6	2
NGC625	0.20	0.03	1.30	0.03	5.73	0.04	8.63	0.13	4
NGC6822	0.25[a]	0.04	2.46	0.37	47.6	7.1	95.4	14.3	5
Pox186	-	-	-	-	-	-	-	-	-
SBS0335-052	-	-	-	-	-	-	-	-	-
SBS1159+545	-	-	-	-	-	-	-	-	-
SBS1211+540	-	-	-	-	-	-	-	-	-
SBS1249+493	-	-	-	-	-	-	-	-	-
SBS1415+437	-	-	-	-	-	-	-	-	-
SBS1533+574	$\leq$ 0.06	-	$\leq$ 0.07	-	0.26[a]	0.03	0.41[a]	0.11	1
Tol0618-402	-	-	-	-	-	-	-	-	-
Tol1214-277	-	-	-	-	-	-	-	-	-
UGC4483	$\leq$ 0.09	-	$\leq$ 0.09	-	$\leq$ 0.12	-	$\leq$ 0.57	-	2
UGCA20	-	-	-	-	-	-	-	-	-
UM133	-	-	-	-	-	-	-	-	-
UM311	-	-	-	-	-	-	-	-	-
UM448	0.15[a]	0.04	0.78	0.11	4.01	0.40	4.30	0.61	2
UM461	$\leq$ 0.09	-	$\leq$ 0.09	-	$\leq$ 0.12[a]	-	$\leq$ 0.57	-	2
VIIZw403	0.07[a]	0.01	0.06	0.01	0.39	0.04	0.90[a]	0.20	2

[a]: This flux density is not consistent with the rest of the IR photometry. Thus we do not consider it for the modelling.

References: (1) the NASA/IPAC ISA IRAS Faint Source Catalog (v2.0) available at: http://irsa.ipac.caltech.edu/cgi-bin/Gator/nph-dd?catalog=irasfsc ; (2) Engelbracht et al. (2008) ; (3) the NASA/IPAC ISA IRAS Point Source Catalog (v2.1) available at: http://irsa.ipac.caltech.edu/cgi-bin/Gator/nph-dd?catalog=iraspsc ; (4) Sanders et al. (2003) ; (5) Rice et al. (1988)

Table 6.12. Submm flux densities for the DGS sample.

Name	F_{450} μm [mJy]	Ref	F_{850} μm [mJy]	Ref	F_{870} μm [mJy]	Ref	F_{1200} μm [mJy]	Ref
Haro11	-	-	-	-	44.0 ± 6.0	1	-	-
- Radio	-	-	-	-	12.2 ± 8.2	2,3	-	-
- CO(3-2)	-	-	-	-	0.3 ± 0.1	4[a]	-	-
- CO(2-1)	-	-	-	-	-	-	-	-
F_{dust}	-	-	-	-	31.5 ± 10.2	-	-	-
Haro2	-	-	40.0 ± 10.0	5	-	-	-	-
- Radio	-	-	9.8 ± 1.2	5	-	-	-	-
- CO(3-2)	-	-	3.2 ± 0.7	6[a]	-	-	-	-
- CO(2-1)	-	-	-	-	-	-	-	-
F_{dust}	-	-	27.0 ± 10.1	-	-	-	-	-
He2-10	342 ± 65	7	130 ± 12	7	-	-	60 ± 14	7
- Radio	-	-	20.0 ± 6.7	8	-	-	20.7 ± 7.0	8
- CO(3-2)	-	-	3.0 ± 0.0	7,9[a]	-	-	-	-
- CO(2-1)	-	-	-	-	-	-	5.0 ± 0.0	7,10[b]
F_{dust}	342 ± 65	-	107 ± 14	-	-	-	34.3 ± 15.6	-
IIZw40	248 ± 81	7	98 ± 14	7	-	-	43.0 ± 13.0	7
- Radio	-	-	13.5 ± 4.5	3,11	-	-	14.0 ± 4.7	3,11
- CO(3-2)	-	-	≤ 3.4	7,9[a]	-	-	-	-
- CO(2-1)	-	-	-	-	-	-	0.1 ± 0.0	7,12[b]
F_{dust}	248 ± 81	-	81.1 ± 14.7	-	-	-	28.9 ± 13.8	-
Mrk1089	-	-	-	-	74.8 ± 10.1	1	-	-
- Radio	-	-	-	-	4.6 ± 0.0	11	-	-
- CO(3-2)	-	-	-	-	0.6 ± 0.2	4[a]	-	-
- CO(2-1)	-	-	-	-	-	-	-	-
F_{dust}	-	-	-	-	69.5 ± 10.1	-	-	-
Mrk930	-	-	-	-	41.0 ± 5.0	13	-	-
- Radio	-	-	-	-	7.0 ± 0.5	3	-	-
- CO(3-2)	-	-	-	-	≤ 0.03	4[b]	-	-
- CO(2-1)	-	-	-	-	-	-	-	-
F_{dust}	-	-	-	-	33.9 ± 5.0	-	-	-
NGC1140	272 ± 55	7	69.0 ± 28.0	7	-	-	≤ 48.0	7
- Radio	-	-	7.8 ± 0.0	14	-	-	8.1 ± 0.0	14
- CO(3-2)	-	-	≤ 0.01	15[b]	-	-	-	-
- CO(2-1)	-	-	-	-	-	-	≤ 0.02	15[b]
F_{dust}	272 ± 55	-	61.2 ± 28.0	-	-	-	≤ 39.9	-
NGC1569	1280 ± 450	16	345 ± 40	16	-	-	250 ± 99	17
- Radio[e]	-	-	49.0 ± 0.0	16	-	-	55.5 ± 0.0	16
- CO(3-2)	-	-	1.7 ± 0.2	9[a]	-	-	-	-
- CO(2-1)	-	-	-	-	-	-	0.11 ± 0.01	18[b]
F_{dust}	1280 ± 450	-	294 ± 40	-	-	-	194 ± 99	-
NGC1705	-	-	-	-	127 ± 17	1	-	-
- Radio	-	-	-	-	7.0 ± 0.5	19	-	-
- CO(3-2)	-	-	-	-	1.0 ± 0.0	-[d]	-	-
- CO(2-1)	-	-	-	-	-	-	-	-
F_{dust}	-	-	-	-	119 ± 17	-	-	-
NGC4214	-	-	-	-	-	-	350 ± 106	20
- Radio	-	-	-	-	-	-	23.6 ± 6.7	21
- CO(3-2)	-	-	-	-	-	-	-	-
- CO(2-1)	-	-	-	-	-	-	0.12 ± 0.02	22[c]
F_{dust}	-	-	-	-	-	-	326 ± 106	-
NGC5253	-	-	-	-	494 ± 59	13	-	-
- Radio	-	-	-	-	50.4 ± 2.0	3	-	-
- CO(3-2)	-	-	-	-	≤ 0.4	23[a]	-	-
- CO(2-1)	-	-	-	-	-	-	-	-
F_{dust}	-	-	-	-	443 ± 59	-	-	-
UM448	-	-	-	-	76.0 ± 9.0	13	-	-
- Radio	-	-	-	-	18.8 ± 0.8	3	-	-
- CO(3-2)	-	-	-	-	1.9 ± 0.6	12[c]	-	-
- CO(2-1)	-	-	-	-	-	-	-	-
F_{dust}	-	-	-	-	55.4 ± 9.1	-	-	-

[a]: From CO(3-2).
[b]: From CO(2-1).
[c]: From CO(1-0).
[d]: Mean line contamination.
[e]: For this galaxy, Galliano et al. (2003) used a spectral index for the radio contamination α_{radio} = -0.36 determined by Israel & de Bruyn (1988) from the full radio spectrum of NGC1569.
Note : When the error is 0.0, it means that no error was given on the original radio or CO measurement.
References : (1) Galametz et al. (2009) ; (2) Mauch et al. (2008) ; (3) Condon et al. (1998) ; (4) Cormier et al. (2014); (5) Dale et al. (2007) ; (6) Wilson et al. (2012); (7) Galliano et al. (2005); (8) Kobulnicky & Johnson (1999); (9) Meier et al. (2001); (10) Baas et al. (1994); (11) Sramek & Weedman (1986); (12) Sage et al. (1992); (13) this work; (14) Klein et al. (1983); (15) Hunter & Sage (1993); (16) Galliano et al. (2003); (17) Lisenfeld et al. (2002); (18) Greve et al. (1996); (19) Meurer et al. (1998); (20) Hermelo et al. (2013); (21) Kepley et al. (2011); (22) Walter et al. (2001); (23) Hirashita (2013)

Table 6.13. Submm flux densities for the KINGFISH sample.

Name	$F_{450\ \mu m}$ [Jy]	Ref	$F_{850\ \mu m}$ [mJy]	Ref
NGC0337	-	-	350 ± 50	1
- Radio	-	-	63.7 ± 6.4	1
- CO(3-2)	-	-	$\leq$ 6.4	2[a]
F_{dust}	-	-	280 ± 50	-
NGC1097	-	-	1440 ± 780	1
- Radio	-	-	240 ± 24	1
- CO(3-2)	-	-	108 ± 1	3[a]
F_{dust}	-	-	1092 ± 780	-
NGC1482	-	-	330 ± 50	1
- Radio	-	-	138 ± 14	1
- CO(3-2)	-	-	2.8 ± 0.3	4[b]
F_{dust}	-	-	189 ± 52	-
NGC2798	-	-	190 ± 30	1
- Radio	-	-	48.1 ± 5.2	1
- CO(3-2)	-	-	20.2 ± 2.2	5[b]
F_{dust}	-	-	122 ± 31	-
NGC2976	-	-	610 ± 240	1
- Radio	-	-	29.5 ± 2.9	1
- CO(3-2)	-	-	23.4 ± 3.7	2[a]
F_{dust}	-	-	557 ± 240	-
NGC3190	-	-	190 ± 40	1
- Radio	-	-	24.9 ± 2.9	1
- CO(3-2)	-	-	$\leq$ 3.6	2[a]
F_{dust}	-	-	162 ± 40	-
NGC3521	-	-	2110 ± 820	1
- Radio	-	-	207 ± 21	1
- CO(3-2)	-	-	174 ± 12	2[a]
F_{dust}	-	-	1729 ± 820	-
NGC3627	-	-	1860 ± 700	1
- Radio	-	-	265 ± 27	1
- CO(3-2)	-	-	303 ± 17	2[a]
F_{dust}	-	-	1292 ± 701	-
NGC4254	-	-	1010 ± 540	1
- Radio	-	-	245 ± 24	1
- CO(3-2)	-	-	161 ± 10	2[a]
F_{dust}	-	-	604 ± 541	-
NGC4321	-	-	880 ± 490	1
- Radio	-	-	197 ± 20	1
- CO(3-2)	-	-	119 ± 12	2[a]
F_{dust}	-	-	564 ± 491	-
NGC4536	-	-	420 ± 110	1
- Radio	-	-	112 ± 11	1
- CO(3-2)	-	-	20.7 ± 2.3	6[c]
F_{dust}	-	-	287 ± 111	-
NGC4569	-	-	470 ± 80	1
- Radio	-	-	48.1 ± 5.2	1
- CO(3-2)	-	-	43.8 ± 3.7	2[a]
F_{dust}	-	-	378 ± 80	-
NGC4579	-	-	440 ± 70	1
- Radio	-	-	56.8 ± 5.8	1
- CO(3-2)	-	-	17.2 ± 3.0	2[a]
F_{dust}	-	-	366 ± 70	-
NGC4594	-	-	370 ± 110	1
- Radio	-	-	79.4 ± 8.1	1
- CO(3-2)	-	-	$\leq$ 4.4	2[a]
F_{dust}	-	-	286 ± 110	-
NGC4631	30.7 ± 10.0	1	5730 ± 1210	1
- Radio	-	-	695 ± 70	1
- CO(3-2)	-	-	150 ± 7	2[a]
F_{dust}	30.7 ± 10.0	-	4885 ± 1212	-
NGC4736	-	1	1540 ± 660	1
- Radio	-	-	157 ± 16	1
- CO(3-2)	-	-	117 ± 9	2[a]
F_{dust}	-	-	1266 ± 660	-
NGC4826	-	1	1230 ± 310	1
- Radio	-	-	58.5 ± 5.8	1
- CO(3-2)	-	-	218 ± 11	2[a]
F_{dust}	-	-	954 ± 310	-

Table 6.13. Submm flux densities for the KINGFISH sample.

Name	F_{450} μm [Jy]	Ref	F_{850} μm [mJy]	Ref
NGC5713	-	-	570 ± 120	1
- Radio	-	-	92.7 ± 9.3	1
- CO(3-2)	-	-	6.4 ± 0.7	4^b
F_{dust}	-	-	471 ± 120	-
NGC5866	0.8 ± 0.2	1	140 ± 20	1
- Radio	-	-	13.3 ± 1.7	1
- CO(3-2)	-	-	14.1 ± 1.7	7^c
F_{dust}	0.8 ± 0.2	-	113 ± 20	-
NGC6946	18.5 ± 4.6	1	2980 ± 450	1
- Radio	-	-	808 ± 81	1
- CO(3-2)	-	-	553 ± 61	5^b
F_{dust}	18.5 ± 4.6	-	1619 ± 461	-
NGC7331	20.6 ± 8.1	1	2110 ± 380	1
- Radio	-	-	216 ± 21	1
- CO(3-2)	-	-	114 ± 13	5^b
F_{dust}	20.6 ± 8.1	-	1780 ± 381	-

[a]: From CO(3-2).
[b]: From CO(2-1).
[c]: From CO(1-0).
References : (1) Dale et al. (2007) ; (2) Wilson et al. (2012) ; (3) Petitpas & Wilson (2003) ; (4) Albrecht et al. (2007) ; (5) Leroy et al. (2009) ; (6) Schruba et al. (2012); (7) Welch & Sage (2003)

Chapter 7

Modelling the dust emission of galaxies

Contents

In this Chapter, we present the semi-empirical SED model that will enable us to derive more accurate estimates of the dust properties (especially the dust masses) compared to those determined using modified blackbodies in Chapter 5 (Section 7.1). In Section 7.2, we then describe how this model is applied it to the DGS and KINGFISH galaxies.

7.1 Description of the model

7.1.1 Philosophy of the model

As we already understood from Chapter 1, modelling the dust emission of a galaxy is a very complex process. Several regions of the galaxy such as star forming regions, molecular clouds, diffuse ISM, etc. contribute differently to the dust SED at each wavelength, and all of these contributions can be captured in the telescope beam. The illumination conditions and the dust composition can vary between the different regions or within the region itself. However, due to lack of observational constraints and spatial resolution we can not access this level of detail in galaxies at the longest wavelengths, except perhaps for the closest galaxies (i.e., LMC/SMC: D$\sim$ 50 kpc, or M31: D$\sim$ 800 kpc). We thus model here the global emission of our galaxies.

In a given region within a galaxy the dust physical conditions are directly linked to the illumination conditions. For example, dust within molecular clouds, where little radiation can penetrate, is colder than dust in the diffuse ISM. In the model, we suppose that each region of the galaxy is subject to uniform illumination conditions and that the dust composition and properties are the same throughout the galaxy. We account for the different regions in a galaxy by combining different regions with different interstellar radiation field intensities. The model has thus two steps:

1. First, we model the dust SED of a mass-element of the ISM, characterised by a uniform intensity of the radiation field, and controlled by the microscopic grain properties.

2. Then, we combine several mass-elements to account for the wide variety of illumination conditions within the galaxy.

This model is a simplified version of the model from Galliano et al. (2008), and is presented in Galliano et al. (2011). It has been used to model galaxies before by Galametz et al. (2009, 2010, 2011); Hony et al. (2010); Meixner et al. (2010); O'Halloran et al. (2010).

7.1.2 Grain properties

To build the dust model, we require a set of dust components. Each dust specie is characterised by a chemical composition and a size distribution function. The chemical composition of the grains then determines the set of optical properties that is used. We adopt a standard dust composition from Zubko et al. (2004): the Galactic grain composition made of 3 dust species: PAHs, graphite and silicate grains (i.e., the BARE-GR-S model from Zubko et al. 2004). To determine the contribution to the total emission of each dust specie, one needs to know the size distribution function and the optical properties of each dust component.

Size distribution

The size distribution of each dust component that we use in our modelling has been determined by Zubko et al. (2004) and was constrained by fitting simultaneously the UV extinction curve, the IR emission and the elemental depletions of the diffuse Galactic ISM. We outline here the method followed by Zubko et al. (2004).

Let F_i[1] be the size distribution of the ith dust specie with i={1,2,3}={PAH, graphite, silicate} and $F_i(a)da$ the number of grains per H atom in the radius range [a, a+da]. Let k be the number of chemical elements constituting the dust. Observations of the diffuse Galactic ISM give the following set of constraints, used by Zubko et al. (2004):

1. Constraints from the abundance of elements locked up into the solid phase of the ISM:

$$\frac{N_j}{N_H} = \sum_{i=1}^{3} \int \frac{4}{3}\pi a^3 \rho_i \frac{\alpha_{ij}}{m_j} F_i(a)\,\mathrm{d}a \tag{7.1}$$

   where N_j is the column density of the jth chemical element constituting the dust specie (j = 1... k), locked up in the dust; N_H is the line-of-sight hydrogen column density; ρ_i is the mass density of the ith dust component; m_j is the atomic mass of the jth chemical element; and α_{ij} is the mass fraction of the jth element in the ith dust specie.

   Input from the observations of the diffuse Galactic ISM: The relative abundance of an element locked up in dust, N_j/N_H, is given by the elemental depletion in the gas phase: the difference between the total ISM abundance of the elements and its observed gas phase abundance. The first is determined via the combination of stellar surface abundances (solar, B, F and G types) from Snow & Witt (1996); Holweger (2001); Sofia & Meyer (2001). The observed gas phase abundances are from Cardelli et al. (1996); Dwek et al. (1997); Meyer et al. (1997, 1998). The densities, ρ_i, are given in Table 7.1, and the mass fractions, α_{ij}, can be calculated from the atomic and molecular masses of the dust constituents.

2. Constraints from the UV-visible interstellar extinction curve:

$$\frac{\tau_H(\lambda)}{N_H} = \sum_{i=1}^{3} \int \pi a^2 Q^i_{ext}(\lambda, a) F_i(a)\,\mathrm{d}a \tag{7.2}$$

   where $\tau_H(\lambda)$ is the extinction per H column density; and $Q_{ext}(a, \lambda)$ is the extinction efficiency of the ith dust component at radius a. Eq. 7.2 is similar to Eq. 1.35 from Section 1.2.3.

   Input from the observations of the diffuse Galactic ISM: To characterise the extinction from the diffuse ISM, Zubko et al. (2004) use the mean extinction curve for R_V=3.1 of Fitzpatrick (1999). The extinction cross-section is calculated using Mie theory for spherical dust particles (Bohren & Huffman 1983) and the dielectric function for the dust component. The references for the dielectric functions are listed in Table 7.1.

3. Constraints from the IR emission spectrum:

$$\frac{I_\lambda(\lambda)}{N_H} = \sum_{i=1}^{3} \int \pi a^2 Q^i_{abs}(\lambda, a) S^i_\lambda(\lambda, a) F_i(a)\,\mathrm{d}a \tag{7.3}$$

   where $I_\lambda(\lambda)$ is the specific intensity per unit solid angle; $Q^i_{abs}(a, \lambda)$ is the absorption efficiency of the ith dust component at radius a; and $S^i_\lambda(\lambda, a)$ is the corresponding source function[2].

[1] We adopt the notation F_i instead of f_i in Zubko et al. (2004) to avoid confusion with the parameters f_{PAH} and f_{sil} of the model, see Section 7.2.1.

[2] We adopt the notation $S^i_\lambda(\lambda, a)$ instead of $E^i_\lambda(\lambda, a)$ as in Zubko et al. (2004) because this quantity actually correspond to the source function: S_λ=j_λ/α_λ rather than to an "emissivity" as it is called in Zubko et al. (2004). For isotropic emission, the emissivity is defined as: $\epsilon_\lambda = \frac{4\pi j_\lambda(\lambda)}{\rho_{ISM}}$.

For all dust particles, we have:

$$S^i_\lambda(\lambda, a) = \int_{T_{CMB}}^{T_{sub}} B_\lambda(\lambda, T) P(a, T)\, \mathrm{d}T \tag{7.4}$$

where T is the dust grain temperature and can range between the CMB radiation temperature, T_{CMB}, and the grain sublimation temperature, T_{sub}; and $P(a,T)$ is the temperature probability distribution defined in Chapter 1, Section 1.2.4 (see Eqs. 1.33 and 1.34).

This is where we link the emission of the dust particles to the ISRF to which they are exposed: dust is heated by the ISRF and the heating depends on the grain size (see Section 1.2.3). Small grains undergo stochastic heating and present temperature and internal energy fluctuations depending on the flux of photons they receive. Big grains are in thermodynamical equilibrium with the ISRF and have an equilibrium temperature $T_d(a)$, i.e., $P(a,T)$ can be approximated by a delta function at $T_d(a)$, corresponding to the equilibrium temperature. In this case, $S^i_\lambda(\lambda, a) \simeq \mathrm{B}_\lambda(\lambda, T_d(a))$.

As we saw in Chapter 1, $T_d(a)$ is controlled by the balance between what the dust particle absorbs and re-emits:

$$\int_0^\infty \pi a^2 Q_{abs}(\lambda, a) J^{Gal}_\lambda(\lambda)\, \mathrm{d}\lambda = \int_0^\infty \pi a^2 Q_{abs}(\lambda, a) B_\lambda(\lambda, T_d(a))\, \mathrm{d}\lambda \tag{7.5}$$

where J^{Gal}_λ is the mean intensity of the ISRF in the solar neighbourhood.

Input from the observations of the diffuse Galactic ISM: IR data from the COBE[3] all-sky survey in 8 DIRBE bands and in the FIRAS[4] channels (Dwek et al. 1997; Arendt et al. 1998), is used to constrain the IR emission spectrum of the diffuse Galactic ISM, $I_\lambda(\lambda)$. The absorption cross-sections are computed the same way as the extinction cross-sections. The source functions, $S^i_\lambda(\lambda, a)$, are computed by Zubko et al. (2004) using the Thermal Discrete Approximation (TDA, as in Draine & Li 2001) for small grains and is the Planck function at $T_d(a)$ for big grains. For the ISRF, Zubko et al. (2004) adopt the empirical representation for the solar neighbourhood from Mathis et al. (1983) with a mean intensity, J^{Gal}_λ:

$$J^{Gal}_\lambda(\lambda) = J^{UV}_\lambda(\lambda) + \sum_{i=1}^{3} W_i B_\lambda(\lambda, T_i) + B_\lambda(\lambda, T_{CMB}) \tag{7.6}$$

where J^{UV}_λ is the UV component, the second term represents three effective blackbody sources with dilution factors $W_{\{1,2,3\}} = \{10^{-14}, 10^{-13}, 4 \times 10^{-13}\}$ and temperatures $T_{\{1,2,3\}} = \{7500, 4000, 3000\}$ K; and the third term represents the cosmic microwave background (CMB) radiation, $B_\lambda(\lambda, T_{CMB})$ at the temperature $T_{CMB} = 2.73$ K (Mather et al. 1994).

The set of constraints used by Zubko et al. (2004) is presented in Fig. 7.1. Zubko et al. (2004) use the method of regularization to solve this set of constraints and obtain a size distribution for the chosen dust composition coherent with the observations.

For each dust specie, the size distribution, $F_i(a)$, is expressed as $F_i(a) = A \times G_i(a)$, where A is a normalisation coefficient in H^{-1}, a, the grain radius, is expressed in μm and $G_i(a)$ is in units of $\mu\mathrm{m}^{-1}$ and follows:

[3] COsmic Background Explorer.

[4] DIRBE (Diffuse InfraRed Background Experiment) and FIRAS (Far InfraRed Absolute Spectrometer) are two instruments on board COBE.

$$\int_{a_{i,min}}^{a_{i,max}} G_i(a)\,\mathrm{d}a = 1 \tag{7.7}$$

where $a_{i,min}$ and $a_{i,max}$ are the minimum and maximum grain size for the ith dust specie (given in Table 7.1). An analytical function $\bar{G}$ is used to approximate the numerical values of *G(a)*:

$$log(\bar{G}(a)) = c_0 + b_0\ log(a) - b_1 \left| log\left(\frac{a}{a_1}\right)\right|^{m_1} - b_2 \left| log\left(\frac{a}{a_2}\right)\right|^{m_2} - b_3\,|a-a_3|^{m_3} - b_4\,|a-a_4|^{m_4} \tag{7.8}$$

The 14 parameters $\{c_0, b_0, b_1, b_2, b_3, b_4, a_0, a_1, a_2, a_3, a_4, m_1, m_2, m_3, m_4\}$ are given in Zubko et al. (2004).

The resulting size distribution is presented in Fig. 7.2.

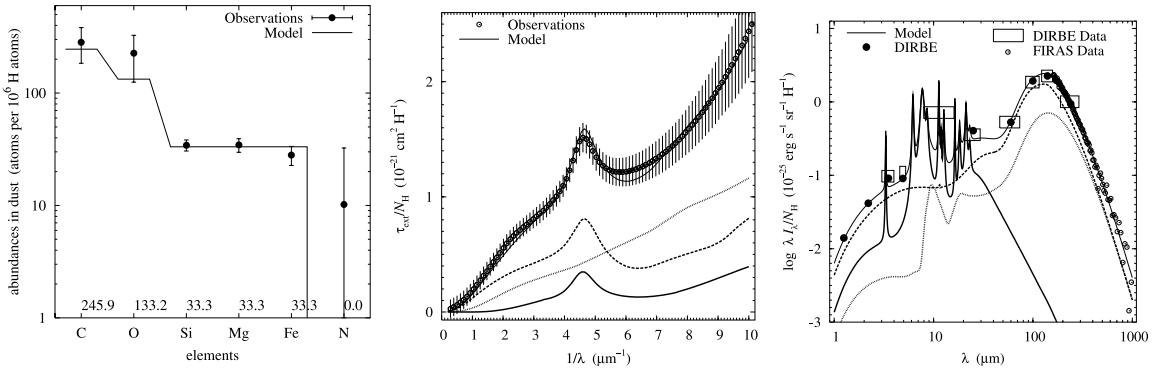

Fig. 7.1. Constraints from the diffuse Galactic ISM used by Zubko et al. (2004): *(left)* Abundances *(centre)* UV-visible extinction curve *(right)* IR emission. In each plot, the "model" curve corresponds to what is obtained for the final size distribution. In the *(centre)* and *(right)* panels the plain, dashed and dotted lines are the PAH, graphite and silicate contributions to the model curve.

Table 7.1. Properties of the dust components (adapted for our dust composition from Table 2 of Zubko et al. 2004).

Constituent	Composition	Mass density [g.cm^{-3}]	a_{min} [μm]	a_{max} [μm]	References for Optical properties
PAHs	C	2.24	3.5×10^{-4}	5×10^{-3}	Li & Draine (2001)[a], Draine & Li (2007)[b]
Graphite	C	2.24	3.5×10^{-4}	0.33	Laor & Draine (1993)
Silicate	$MgFeSiO_4$	3.5	3.5×10^{-4}	0.37	Weingartner & Draine (2001)

[a]: This reference is used by Zubko et al. (2004) in his model to get the size distribution.

[b]: This reference is the updated version by Draine & Li (2007) of the PAH optical properties that are used in our model to compute the grain absorption cross-sections.

Optical properties

Now that we have a size distribution, we need to compute the absorption efficiencies, $Q^i_{abs}(a,\lambda)$, of each of our dust species. These optical properties are derived using a Mie code and the method presented in Laor & Draine (1993). The PAH optical properties have been updated by Draine & Li (2007) who use more accurate band profiles constrained by *Spitzer* spectra compared to Li & Draine (2001). In the PAHs component we distinguish between the neutral and ionised PAHs. The absorption efficiencies are shown in Fig. 7.2 for the four dust species: neutral PAHs, ionised

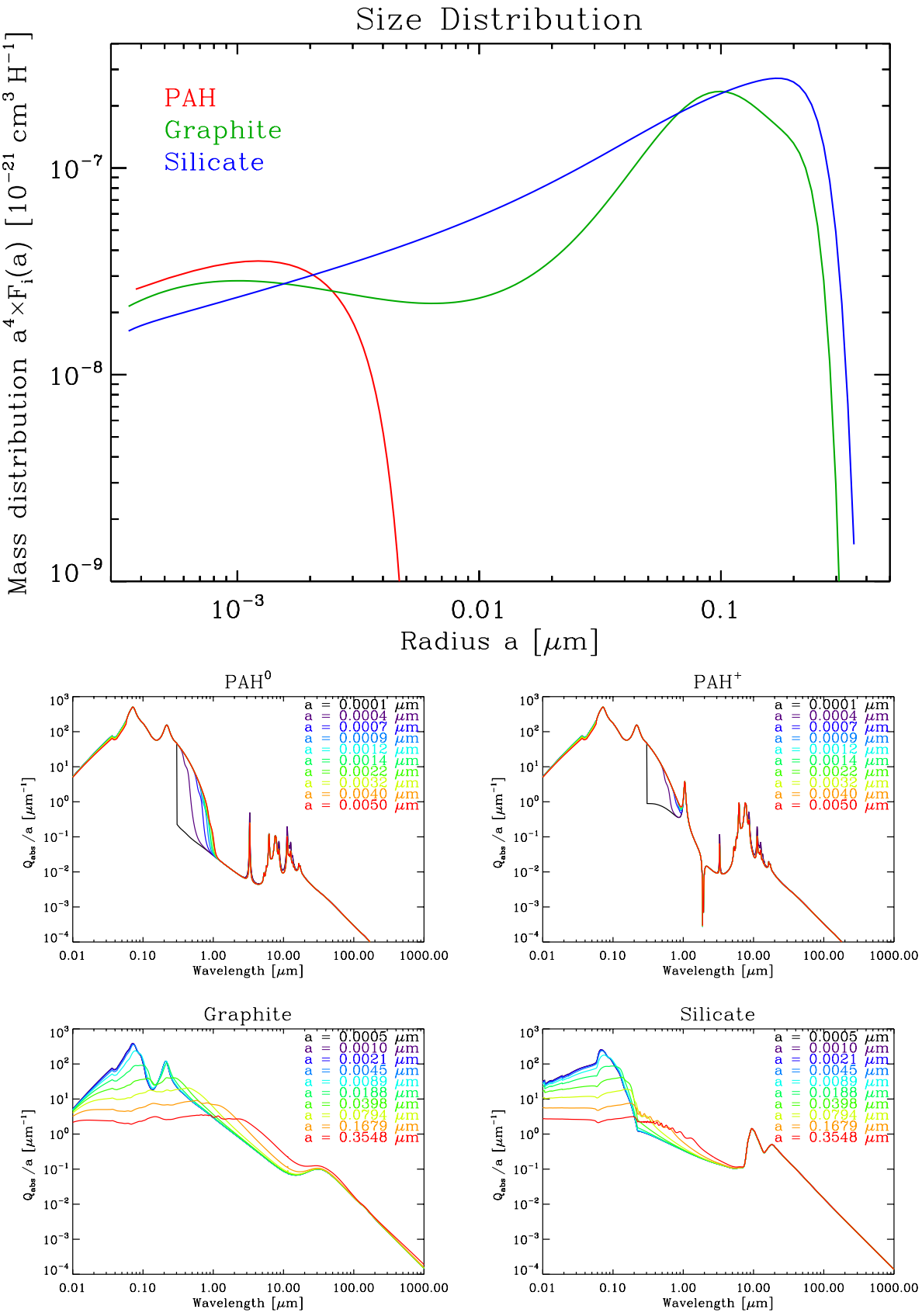

Fig. 7.2. Grain properties: *(top)* Size distributions from Zubko et al. (2004) for PAHs (red), graphite (green) and silicate grains (blue) *(bottom)* Absorption efficiencies, normalised to a given grain radius a, $Q_{abs}(\lambda)/a$, for neutral PAHs *(top left panel)*, ionised PAHs *(top right panel)*, graphite *(bottom left panel)* and silicate *(bottom right panel)* grains. The colours indicate different values for the grain radius a.

PAHs, graphite and carbon grains for different grain radius a. The opacity of the adopted dust composition, κ_{abs}, is the sum of the opacity for each dust specie: PAHs, carbon and silicate grains. Following Eq. 1.13 the opacity for the ith dust specie is given by:

$$\kappa^i_{abs}(\lambda) = \frac{\int \pi a^2 Q^i_{abs}(a,\lambda) G_i(a)\,\mathrm{d}a}{\int \frac{4}{3}\pi \rho_i a^3 G_i(a)\,\mathrm{d}a} \tag{7.9}$$

The submm emissivity index β is defined by the logarithmic submm slope of the absorption efficiency (see Section 1.2.3) or equivalently of the opacity:

$$Q_{abs}(\lambda) = Q_{abs}(\lambda_0)\left(\frac{\lambda_0}{\lambda}\right)^{\beta} \leftrightarrow \kappa_{abs}(\lambda) = \kappa_{abs}(\lambda_0)\left(\frac{\lambda}{\lambda_0}\right)^{-\beta} \tag{7.10}$$

Fig. 7.3 shows the total opacity for our dust mixture. In our case, the fit of the submm part of the opacity gives an emissivity index $\beta = 2.0$ (Fig. 7.3), where we chose to normalise at $\lambda_0 = 160$ μm with $\kappa_{abs}(\lambda_0) = 1.4$ m^{2}kg^{-1}.

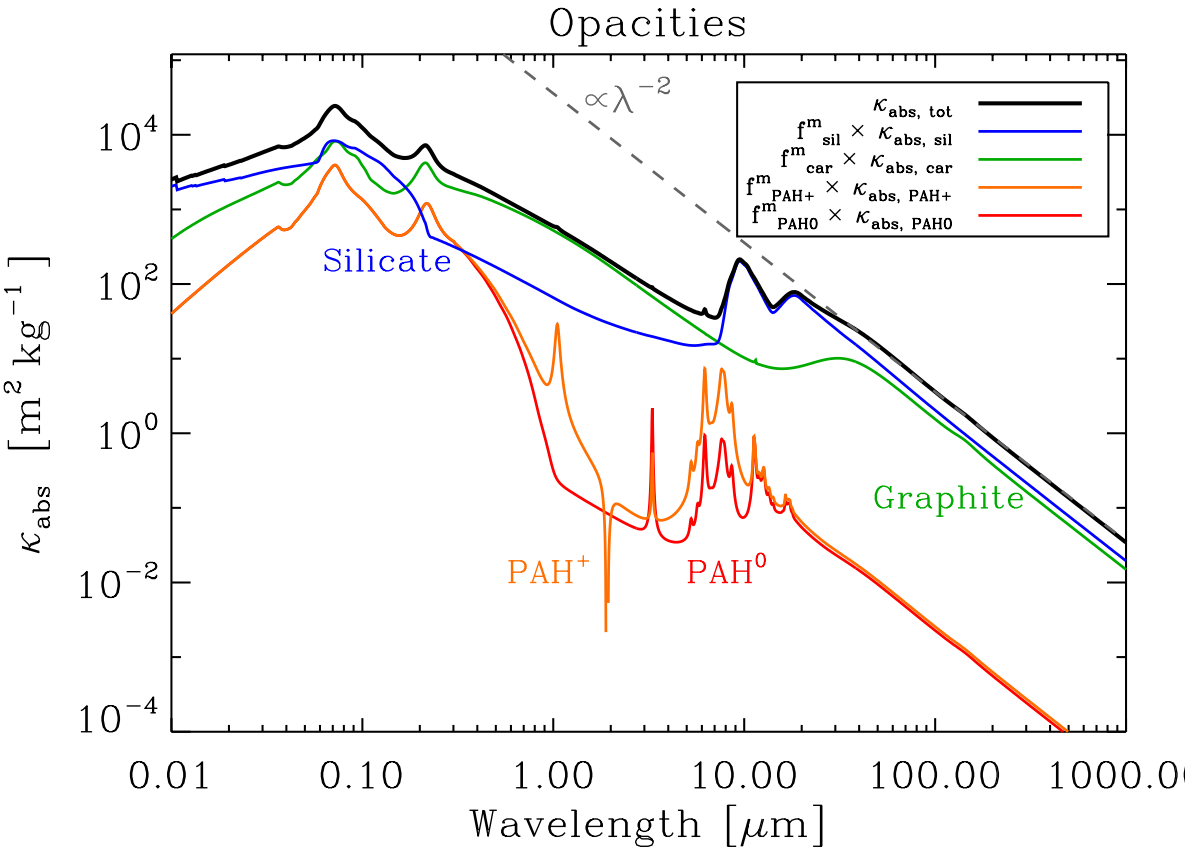

Fig. 7.3. Opacities for the adopted dust composition (in black) and for each dust specie: silicates in blue, graphite in green, neutral PAHs in red and ionised PAHs in orange. The κ_{abs} for each specie has been calculated using Eq. 7.9 and f^m_{PAH+}, f^m_{PAH0}, f^m_{gr} and f^m_{sil} are the corresponding mass fractions (see Section 7.1.3). The total opacity for our dust mixture (in black) is the sum of the different contributions displayed in colours. The λ^{-2} dependence of the submm part of the total opacity is shown in grey.

Note that when we say "grain properties" we encompass two things: the size distribution and the optical properties. The optical properties are *intrinsic* properties of the grains. The size distribution, however, assumes certain abundances for the elements constituting the dust and a given

illumination (solar abundances and Galactic ISRF in our case). Technically this size distribution is *not* directly applicable to other galaxies where abundances and illumination conditions differ from the diffuse Galactic ISM (especially for dwarf galaxies, see Section 2.2.2). Ideally we would need to reproduce the method presented by Zubko et al. (2004) for each galaxy we want to model and get a size distribution that simultaneously reproduces the elemental abundances, UV extinction, and IR emission *of the considered galaxy*. However, the lack of observational constraints does not enable us to follow such method, and, in order to move forward we *approximate* the grain size distribution in the galaxy we want to model by that from the BARE-GR-S model of Zubko et al. (2004).

7.1.3 One ISM mass element

The first step of the model is to compute the SED emitted by a single mass-element of the ISM, $l_\nu^{dust}(U,\lambda)$, illuminated by a stellar radiation field with uniform intensity U. $l_\nu^{dust}(U,\lambda)$ is given by:

$$l_\nu^{dust}(U,\lambda) = f_{PAH}^m \left[f_{PAH+}^m l_\nu^{PAH+}(U,\lambda) + (1 - f_{PAH+}^m) l_\nu^{PAH0}(U,\lambda) \right] + f_{gr}^m l_\nu^{gr}(U,\lambda) + f_{sil}^m l_\nu^{sil}(U,\lambda) \tag{7.11}$$

where:

- f_{PAH+}^m is the mass fraction of ionised PAHs compared to the total PAHs mass,
- f_{PAH}^m the mass fraction of total PAHs (neutral and ionised),
- f_{gr}^m the mass fraction of graphite grains, and
- f_{sil}^m is the mass fraction of silicate grains.

We have $f_{PAH}^m + f_{gr}^m + f_{sil}^m = 1$. $l_\nu^{PAH+}(U,\lambda)$, $l_\nu^{PAH0}(U,\lambda)$, $l_\nu^{gr}(U,\lambda)$ and $l_\nu^{sil}(U,\lambda)$ are the corresponding size distribution integrated monochromatic luminosities per unit dust mass.

Following Eq. 1.37, the monochromatic luminosities per unit dust mass are given by[5]:

$$l_\lambda^i(\lambda) = \frac{1}{M_i} \int 4\pi^2 a^2 Q_{abs}^i(\lambda,a) S_\lambda^i(\lambda,a) G_i(a)\,\mathrm{d}a \tag{7.12}$$

where M_i is the mass of the ith dust specie and is given by: $M_i = \int \frac{4}{3}\pi a^3 \rho_i G_i(a)\,\mathrm{d}a$.

Note that this time in Eq. 7.12, compared to Eq. 7.3, $G_i(a)$ is known and we want to compute the l_λ^i using the optical properties computed in 7.1.2.

However, as mentioned in Section 7.1.2, the assumed size distribution $G_i(a)$ is the size distribution of dust grains in the Galaxy. In another galaxy, the grain size distribution could be different. Schematically, a larger number of SN shocks or very intense radiation field will tend to erode the bigger grains, transferring mass into smaller grains. On the contrary, in dense and cold environments, grains can accrete and coagulate thus transferring mass from small to big grains. Thus we separate the graphite and silicate grains into very small grains (VSGs) and big grains (BGs), to account for an eventual variation of the proportion of small grains compared to the proportion of big grains. The transition size between the two is fixed at $a_t = 0.01$ μm. A larger number of small grains compared to that in the Galaxy will appear as a higher NIR continuum in the modelled SED. The last two members of the right hand side of Eq. 7.11 thus become:

$$f_{gr}^m l_\nu^{gr}(U,\lambda) = f_{VSG,gr}^m l_\nu^{VSG,gr}(U,\lambda) + f_{BG,gr}^m l_\nu^{BG,gr}(U,\lambda) \tag{7.13}$$

[5]Notations: L_ν is the monochromatic luminosity and I_λ from Eq. 7.3 is the specific monochromatic intensity per unit solid angle: $L_\nu = 4\pi\ I_\nu = 4\pi\ \frac{\lambda}{\nu}\ I_\lambda$. The monochromatic luminosities per unit dust mass of a given dust specie, l_ν^i, is given by $l_\nu^i = L_\nu^i / \mathrm{M}_i$.

and:

$$f_{sil}^{m} l_{\nu}^{sil}(U,\lambda) = f_{VSG,sil}^{m} l_{\nu}^{VSG,sil}(U,\lambda) + f_{BG,sil}^{m} l_{\nu}^{BG,sil}(U,\lambda) \tag{7.14}$$

with: $f_{PAH}^{m} + f_{VSG,gr}^{m} + f_{BG,gr}^{m} + f_{VSG,sil}^{m} + f_{BG,sil}^{m} = 1$. The integration on the size distribution in Eq. 7.12 is performed over the $[a_{i,min},\ a_t]$ range to get $l_{\nu}^{VSG,i}(U,\lambda)$; and over the $[a_t,\ a_{i,max}]$ range to get $l_{\nu}^{BG,i}(U,\lambda)$ with i={gr, sil}.

The transition radius a_t implies that the VSGs always undergo stochastic heating, and that BG are either stochastically heated or in thermal equilibrium. The source functions $S_{\lambda}^{i}(\lambda,a)$ are computed accordingly:

- For BGs at thermal equilibrium, $S_{\lambda}^{i}(\lambda,a) \simeq \mathrm{B}_{\lambda}(\lambda, T_d(a))$, where $T_d(a)$ is determined from Eq. 7.5.
- For stochastically heated VSGs or BGs, their temperature probability distributions are computed following the method of Guhathakurta & Draine (1989).

Fig. 7.4 shows the temperature probability distributions for the different grain species for different grain radiuses a, and the enthalpies[6] used in their derivation. We see that large graphite and silicate grains have a narrow temperature probability distribution: their temperature does not oscillate much around their equilibrium temperatures. PAHs, small graphite grains and small silicate grains have, on the contrary, broad temperature distributions, showing the large range of temperatures these grains can span.

Here we assume that the ISRF heating the grains has the spectral shape of the solar neighbourhood (Mathis et al. 1983), and we parameterise its mean intensity, J_{ν}, by:

$$J_{\nu}(\lambda) = U \times J_{\nu}^{Gal}(\lambda) \tag{7.15}$$

where $J_{\nu}^{Gal}(\lambda)$ is the mean intensity of the ISRF from Mathis et al. (1983), normalised to the solar neighbourhood value: $4\pi \times \int J_{\nu}^{Gal}\,\mathrm{d}\nu = 2.2 \times 10^{5}$ W.m^{-2}. When U = 1, it means that the ISM mass element is illuminated by a stellar radiation field having the intensity of the solar neighbourhood ISRF from Mathis et al. (1983).

We now have all of the elements to generate dust SED templates for a mass-element of the ISM with this dust composition at a given intensity of the ISRF. We generate these templates for a grid of starlight intensities, U, from 10^{-2} to 10^{7}.

7.1.4 Combining several ISM mass elements

Now that we have the emission from a single ISM mass-element, we want to find the proper combination of mass-elements, i.e., of illumination conditions, that fits the observations we have for our sources. Indeed the emission from a galaxy will likely be a combination of different regions with different physical conditions. Here, as mentioned in 7.1.1, we assume that the dust properties are uniform throughout the galaxy, i.e., the size distribution and the optical properties are constant within the galaxy, and that only the starlight intensity varies.

The total specific monochromatic luminosity emitted by dust in the galaxy is given by:

$$L_{\nu}^{tot,dust} = \int l_{\nu}^{dust}(U(M),\lambda)\,\mathrm{d}M \tag{7.16}$$

or:

[6] The enthalpy is linked to the heat capacity, C(T), defined in Section 1.2.4 by: H(T)= $\frac{4}{3}\pi a^3 \int_0^T C(T_g)\,\mathrm{d}T_g$ where T_g is the grain temperature.

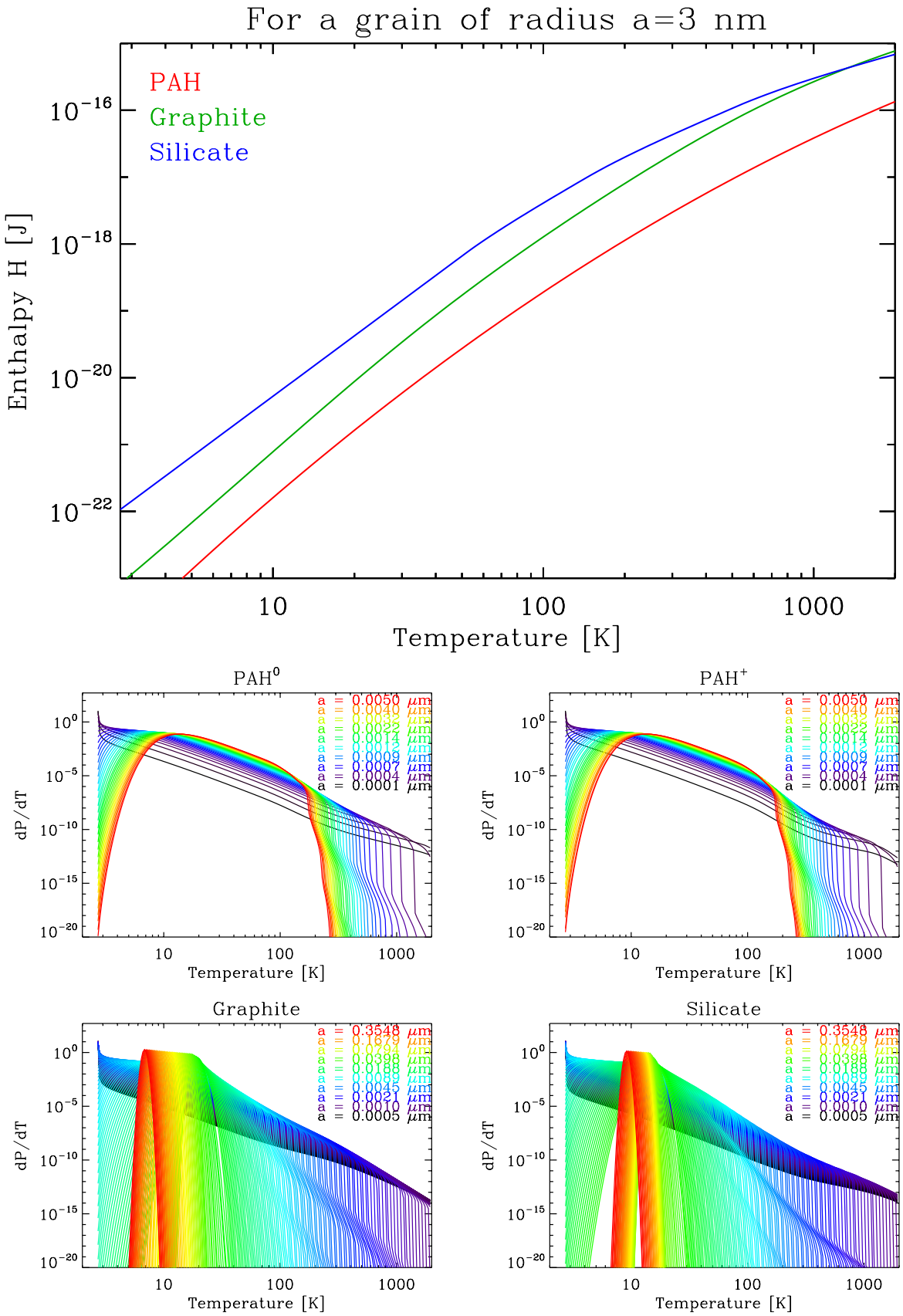

Fig. 7.4. *(top)*: Enthalpies for the considered dust species. *(bottom row)* Temperature probability distributions for the different grain species. The colour codes the grain size: from black (small radius) to red (big radius).

$$L_\nu^{tot,dust} = \int \left(\sum_{i=1}^{4} f_i^m l_\nu^i \right) \frac{dM}{dU} \, \mathrm{d}U \tag{7.17}$$

where i={PAH+, PAH0, gr, sil} (see Eq. 7.11).

We use the empirical prescription from Dale et al. (2001a) to describe the distribution of starlight intensities per unit dust mass: it can be approximated by a power law of index α:

$$\frac{dM}{dU} = cst \times U^{-\alpha} \tag{7.18}$$

In most cases, this prescription is flexible enough to reproduce dense and diffuse media, and provides a simple parameterization of the physical conditions in the ISM. With the total dust mass, given by:

$$M_{dust} = \int_{U_{min}}^{U_{min}+\Delta U} \frac{dM}{dU} \, \mathrm{d}U \tag{7.19}$$

we get:

$$M_{dust} = \frac{cst}{1-\alpha} (U_{max}^{1-\alpha} - U_{min}^{1-\alpha}) \tag{7.20}$$

with $U_{max} = U_{min} + \Delta U$. Let K $= \frac{U_{max}^{1-\alpha} - U_{min}^{1-\alpha}}{1-\alpha}$, we have $cst = M_{dust}/K$. Injecting this into Eq. 7.17 gives:

$$L_\nu^{tot,dust} = \frac{M_{dust}}{K} \int \left(\sum_{i=1}^{3} f_i l_\nu^i \right) U^{-\alpha} \, \mathrm{d}U \tag{7.21}$$

Emission from old stars can also contribute to the IR emission and especially in the NIR. Thus we add a stellar continuum to the dust emission, parameterised by the stellar mass of the galaxy $M_\star$:

$$L_\nu^\star = M_\star l_\nu^\star \tag{7.22}$$

$l_\nu^\star$ is the specific monochromatic luminosity per unit stellar mass of a 1 Gyr stellar population, synthesised with the PEGASE[7] model (Fioc & Rocca-Volmerange 1997), assuming a Salpeter Initial Mass Function (IMF): $N(M)dM = M^{-1.35}dM$ and an initial metallicity Z=$Z_\odot$. The age of the stellar population is not of great importance here as this population will essentially be constrained by the NIR bands up to IRAC 4.5 μm. However, the stellar mass is poorly determined and does not give a reliable estimate of the true stellar mass of the galaxy. The point of this stellar component is to have a good fit in the NIR, in order to extrapolate the stellar contribution in the MIR.

The total emission from the galaxy is thus:

$$L_\nu^{tot} = L_\nu^{dust,tot} + L_\nu^\star \tag{7.23}$$

For each band at a wavelength λ_i we can compute the synthetic luminosity, $L_\nu^{model}(\lambda_i)$ by convolving the model with the RSRF of each band and using the appropriate spectral convention of each instrument. The various $L_\nu^{model}(\lambda_i)$ are computed using Eqs. 6.8, 6.16, 6.18 and 6.19.

The fitting procedure is an iterative process where we combine all of the templates of one ISM mass-element we need to fit the observations and stops when observational constraints are

[7]Projet d'Étude des GAlaxies par Synthèse Évolutive

minimized. The fit is performed with the MPCURVEFIT procedure in IDL based on the Levenberg-Marquardt methods.

7.1.5 Limitations of the model

This model has been built on a certain number of assumptions, and thus presents some limitations. We argue here that these limitations do not biais our final results.

Geometry : Ideally, radiative transfer models are a more rigorous way of reconstructing the total emission of a galaxy. In these models, the emission from a mass-element of the ISM is computed via a radiation transfer model, and then is propagated to the observer. In order to do so, we need to know about the geometry of the stellar sources and of the dust and gas within the galaxy. In our case, we do not have access to such level of detail for all of our galaxies. Moreover we are interested by total dust masses and the dust mass is dominated by the mass of the large dust grains, in equilibrium with the radiation field of the galaxy. The spectrum of these large dust grains is determined by the stellar power absorbed by the grains and not by the spatial distribution of the stellar sources.

Local variations of grain properties : Dust grains emissivity values could vary in different regions of the modelled galaxy. In this case, our model would lead to a misestimate of the dust mass in regions where the emissivity differs from the emissivity assumed here. However these variations are very poorly known, and difficult to constrain. Grain-grain coagulation for example could be responsible for a local increase of the FIR opacity in dense clouds (Stepnik et al. 2003). The emissivity of the dust grain could also increase with the grain temperature (Meny et al. 2007), and thus we would overestimate the dust mass in hot dust regions. However here we are interested in dust masses for *total* galaxies, and not in *local variations* of the dust mass within these galaxies. Thus we believe that the effects described here would not have too much impact on the total dust mass (i.e., if they have any, it would affect the dust mass within its error bar).

Radiation field : In this model, we assume that the ISRF has the shape of the Galactic diffuse ISM. However, some studies (e.g., Madden et al. 2006) have shown that the ISRF of dwarf galaxies differs from the radiation field of "normal" more metal-rich galaxies. The ISRF in low-metallicity dwarf galaxies is often more intense and harder, due to the predominance of massive stars, and a larger mean free path length of the ionizing photons, attributed to the lower dust attenuation in these galaxies. The shape of the radiation field determines the emission of out-of-equilibrium small grains. Increasing the hardness of the radiation field increases the maximum temperature the small grains can reach when they fluctuate. However, these small grains only have a minor contribution to the total dust mass, and thus the assumed shape of the ISRF does not bias our estimation of the total dust mass.

7.2 Modelling the DGS and KINGFISH galaxies

The model described in the previous Section is applied to the DGS and KINGFISH galaxies. For the DGS galaxies, the observational constraints are from 2MASS, *Spitzer*, *WISE*, *IRAS* (presented in Chapter 6) and *Herschel* instruments (presented in Chapter 4). For the KINGFISH galaxies, the observational constraints originate from the same instruments (except *WISE* and *Spitzer*/IRS).

Some galaxies are not detected at one or several wavelengths. We do not consider the upper limits in the fits by imposing a zero weight on the points and imposing to the best fit model to be consistent with the non-detections.

In order to study the submm excess in more details in Section 8.3, we do not include in the fit the SPIRE 500 μm point nor any available ground-based submm data (i.e., we put a zero weight on these points). Indeed, the submm excess can already be observed for some dwarfs galaxies at this wavelength, thus trying to fit this point can, in some cases, bias our estimation of the dust mass in these galaxies.

7.2.1 Setting the parameters

In our case, the model can be described by 8 parameters:

- M_{dust}: the total dust mass,
- U_{min}: the minimum of the starlight intensity distribution,
- ΔU: the difference between the maximum and minimum of the starlight intensity distribution,
- α: the index of the power law describing the starlight intensity distribution,
- f_{PAH}: the PAHs mass fraction, normalised to the Galactic PAH mass fraction (when f_{PAH}= 0.5 it means that the mass fraction of PAH in the modelled galaxy is half the mass fraction of PAHs in the Galaxy),
- f_{ion}: the ionised-to-total PAH mass ratio (when $f_{ion} = 0.5$ it means that 50% of the PAHs are ionised),
- f_{vsg}: the very small grains mass fraction, i.e., the mass fraction of grains with radius $a \leq 10$ nm, normalised to the Galactic value (when $f_{vsg} = 0.5$ it means that the mass fraction of very small grains in the modelled galaxy is half the mass fraction of very small grains in the Galaxy), and
- f_{sil}: the silicate-to-(silicate+graphite) grains mass fraction (when $f_{sil} = 0.5$ it means that there is the same mass of silicate and graphite grains in the ISM.)

The different mass fractions f^m_{PAH}, f^m_{PAH+}, $f^m_{VSG,gr}$, $f^m_{BG,gr}$, $f^m_{VSG,sil}$ and $f^m_{BG,sil}$ can be computed from the above parameters and Galactic mass fractions:

$$\begin{cases} f^m_{PAH} &= f^m_{PAH,\odot} \times f_{PAH} \\ f^m_{PAH+} &= f^m_{PAH,\odot} \times f_{PAH} \times f_{ion} \\ \\ f^m_{VSG,gr} &= (1 - f^m_{PAH}) \times (1 - f_{sil}) \times f_{VSG,gr,\odot} f_{vsg} \\ f^m_{BG,gr} &= (1 - f^m_{PAH}) \times (1 - f_{sil}) \times (1 - f_{VSG,gr,\odot} f_{vsg}) \\ \\ f^m_{VSG,sil} &= (1 - f^m_{PAH}) \times f_{sil} \times f_{VSG,sil,\odot} f_{vsg} \\ f^m_{BG,sil} &= (1 - f^m_{PAH}) \times f_{sil} \times (1 - f_{VSG,sil,\odot} f_{vsg}) \end{cases} \tag{7.24}$$

where $f^m_{PAH,\odot} = 0.0457$ is the Galactic PAH mass fraction; $f_{VSG,gr,\odot} = 0.1846$ is the proportion of graphite VSGs in the Galaxy; and $f_{VSG,sil,\odot} = 0.1655$ is the proportion of silicate VSGs in the Galaxy. These values can be obtained from the dust properties given by Zubko et al. (2004).

We fix the f_{sil} parameter to its Galactic value, leaving us with 7 free parameters:

$$f_{sil} = \frac{f^m_{sil,\odot}}{f^m_{sil,\odot} + f^m_{gr,\odot}} = \frac{0.6596}{0.6596 + 0.2947} = 0.6912 \tag{7.25}$$

where $f^m_{sil,\odot}$ and $f^m_{gr,\odot}$ are the Galactic mass fraction of silicate and graphite grains respectively, taken from Zubko et al. (2004).

As IRS spectra are available for the DGS sample, we can put constraints on the f_{ion} and f_{PAH} parameters. When no IRS constraints are available, we leave these parameters free. However, whenever PAH features are absent from the IRS spectrum, we fix $f_{PAH} = 0$. When there are no PAHs, the value of f_{ion} does not have any importance and so we fix it arbitrarily to $f_{ion} = 0.5$. If the IRS spectrum provides good SL constraints on the ionised PAH lines we leave this parameter free, otherwise, we also fix $f_{ion} = 0.5$. These choices for f_{ion} and f_{PAH} are done in order to improve the quality of the fit. The value of f_{ion} has no influence on the dust mass as it controls the proportion of ionised PAHs.

For some DGS galaxies, the MIR continuum shape outlined by the IRS spectrum cannot be well fitted by our model. In these cases, we add an extra modified blackbody component in the MIR, with a fixed $\beta = 2.0$ and a temperature varying between 80 and 300 K. It can be physically interpreted as the contribution from a hot HII region to the total emission of the galaxy. As dwarf galaxies have small physical sizes and low dust attenuation, the emission from the energetic HII regions can indeed affect the total emission from the whole galaxy. In these cases, this tells us that the Dale et al. (2001a) prescription of $\frac{dM}{dU} \propto U^{-\alpha}$ may not be flexible enough to provide a satisfactory fit for these galaxies. This can have a small impact on the dust mass, as we are adding warm equilibrium dust grains (Fig. 7.5). However, we demonstrate in Section 7.2.4 for cases where the impact on the dust mass is important (i.e., greater than the dust mass error bar, red points in Fig. 7.5) that the addition of a warm modified blackbody is necessary to have a coherent MIR to submm shape of the SED.

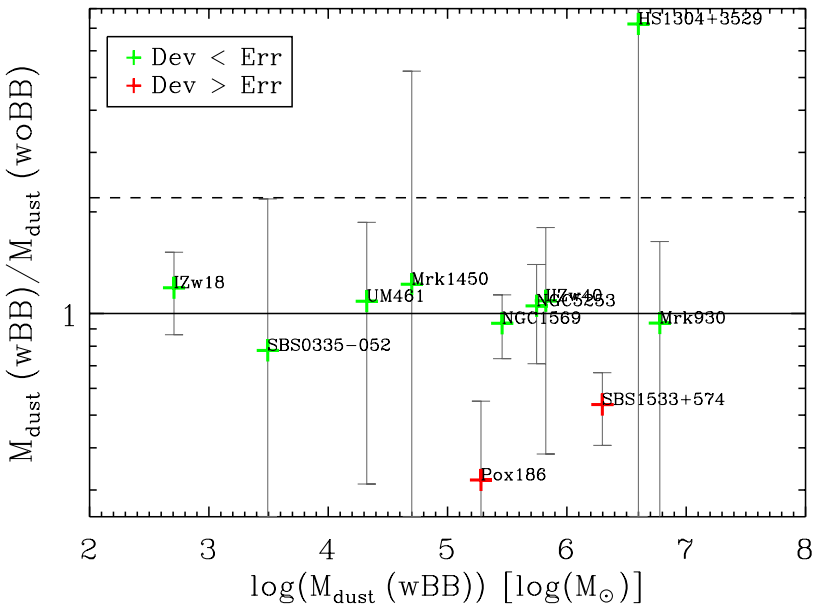

Fig. 7.5. Comparison of the dust masses estimated with an additional warm MIR blackbody ($M_{dust}(wBB)$) compared to the dust masses obtained without this extra-component ($M_{dust}(woBB)$) for galaxies for which this additional blackbody is needed (see Section 7.2.1). The colours show whether $M_{dust}(wBB)$ and $M_{dust}(woBB)$ are consistent within errors (in green) or not (in red).

7.2.2 Extracting total infrared luminosities, mean radiation field intensities and star-formation rates

From the best fit model we can extract two quantities derived from the parameters for the galaxy: the TIR luminosity L_{TIR} and the mass-averaged starlight intensity $< U >$. These two parameters are given by:

$$L_{TIR} = \int_0^\infty L_\nu^{tot,dust}(\nu)\,\mathrm{d}\nu = \int_{1\mu m}^{1000\mu m} L_\nu^{tot,dust}(\nu)\,\mathrm{d}\nu \tag{7.26}$$

and:

$$< U >= \frac{1}{M_{dust}} \int_{U_{min}}^{U_{max}} U \times \frac{dM_{dust}}{dU}\,\mathrm{d}U \tag{7.27}$$

Eq. 7.27 translates into:

$$< U > \quad = \quad \begin{cases} \frac{1-\alpha}{2-\alpha}\frac{U_{max}^{2-\alpha}-U_{min}^{2-\alpha}}{U_{max}^{1-\alpha}-U_{min}^{1-\alpha}} & \text{if } \alpha \neq 1 \;\&\; \alpha \neq 2 \\ \frac{\Delta U}{\ln(1+\Delta U/U_{min})} & \text{if } \alpha = 1 \\ U_{min}\ln(1+\Delta U/U_{min})\left(\frac{U_{min}+\Delta U}{\Delta U}\right) & \text{if } \alpha = 2 \end{cases} \tag{7.28}$$

From the L_{TIR} we can also compute an estimation of the star-formation rate (SFR) for the galaxies in our sample, using the formula of Kennicutt (1998) presented in Eq. 3.22.

7.2.3 Errors

As in Chapter 5 the errors on the various parameters are estimated by generating 300 random realisations of the SEDs within errors in order to get a distribution for the parameters. For each galaxy, we randomly perturb our fluxes within the errors bars and perform fits of the perturbed SEDs. Here again we must take special care for errors which are correlated between different bands. We detail here the decomposition of the errors for all the instruments we use, except *Herschel* as this decomposition has already been presented in Section 5.2.2.

2MASS: Jarrett et al. (2003) quote a 2 - 3% uncertainty on the zero-magnitude flux values. To be conservative, we assume a non-correlated error of 3%.

IRAC: The total calibration uncertainty used for the DGS and KINGFISH IRAC fluxes is $\sim 10\%$. This can be decomposed into two parts:

- Reach et al. (2005) give a 2% uncertainty in all of the IRAC bands. This error is correlated between the four bands.
- The IRAC Instrument Handbook (Section 4.3) also recommends using a 10% error to account for several systematic effects in the calibration. This error is independent from band to band.

IRS: The IRS spectra extracted from the CASSIS database already provide a decomposition of the total error on the flux densities into three parts:

- Part of the error is the peak-to-peak uncertainty and represents the measurement error, independent for the different wavelengths.

- Part of the error is due to the flux difference between the two nod spectra and is correlated for all of the wavelengths over both SL and LL ranges.
- The third component of the error in IRS spectra is the correlation error. It is not clear whether this error is correlated between the two SL and LL modules, so, to be conservative, we assume that the correlation errors are correlated for all of the SL wavelengths on one side and for all of the LL wavelengths on the other side. According to Lebouteiller et al. (2011), the global IRS calibration is better than the 2% level.

MIPS: For the DGS MIPS photometry, Bendo et al. (2012) used a 4% calibration error at 24 μm (Engelbracht et al. 2007), 10% at 70 μm (Gordon et al. 2007) and 12% at 160 μm (Stansberry et al. 2007). For the KINGFISH, the same uncertainties were used by Dale et al. (2007) except for MIPS 70 μm where they adopted a 7% calibration error. According to the MIPS Instrument Handbook, the calibration of the MIPS 160 μm band has been done using the 24 μm and 70 μm observations of asteroids. We can thus consider that the calibration errors for MIPS 24 μm and MIPS 70 μm are independent but that they are correlated with MIPS 160 μm.

WISE: *WISE* calibration has been performed on stars and is tied to *Spitzer* calibration according to Jarrett et al. (2011). For each wavelength, the correlations between the bands can be summarised this way:

- The *WISE* 3.4 μm calibration error is decomposed in an independent part, proper to *WISE*, of 2.4 %, and is correlated with the IRAC 3.6 μm band. Thus we add the IRAC 3.6 μm calibration uncertainty to the *WISE* 3.4 μm calibration error.
- Following the *WISE* 3.4 μm band, the *WISE* 4.6 μm error has an independent part of 2.8% and is correlated with the IRAC 4.5 μm band.
- Similarly, the *WISE* 12 μm error has an independent part of 4.5% and is correlated with the IRS-SL/LL modules.
- And finally, the *WISE* 22 μm error has an independent part of 5.7% and is correlated with the MIPS 24 μm band.

IRAS: According to the IRAS explanatory supplement[8], the calibration of *IRAS* has been tied to the Rieke et al. (1984) ground-based photometric system at 12 μm. The three *IRAS* bands at 12, 25 and 60 μm have been calibrated using stellar models, and the *IRAS* 100 μm calibration used asteroids. The relative uncertainties relative to the ground-based 12 μm are 2%, 5% and 5% for *IRAS* 12, 25 and 60 μm respectively, independent from band to band. The absolute uncertainty on the 12 μm flux density is 4%, in common and correlated between the three bands. The uncertainty at 100 μm is 10%, and is not correlated with any of the other *IRAS* bands.

SCUBA for KINGFISH: Dale et al. (2005) give a calibration uncertainty of 25% and 15% for the 450 and 850 μm bands respectively. We assume that these errors are independent between the two bands.

[8]Available at: http://lambda.gsfc.nasa.gov/product/iras/docs/exp.sup/

Other ground-based instruments: For the other submm measurements (SCUBA, LABOCA and MAMBO), the calibration is derived directly from the observations as it depends on the conditions during the observations. It will be different from galaxy to galaxy. The values for the calibration errors can be found in the references quoted for the submm flux densities in Table 6.12. The errors from the different instruments are independent from one another.

As in Section 5.2.2, the perturbation of the observed fluxes is the sum of two components:

- A normal random independent variable representing the measurement errors at each wavelength.
- A normal random variable describing the calibration errors that takes into account the correlation between the wavebands as described above.

Here again we quote the 66.67% confidence level for our parameters.

7.2.4 Notes on individual DGS galaxies

- *Haro 11* - As this galaxy has silicate absorption features around 10 μm, we add extinction in our modelling. The output luminosity is modified by:

$$L_\nu^{tot,dust}(\lambda, A_V) = L_\nu^{tot,dust}(\lambda, A_V = 0) \times e^{-\tau_0(\lambda) A_V / 1.086} \tag{7.29}$$

where τ_0 is the optical depth, determined from the optical properties and the size distribution of our dust composition:

$$\tau_0(\lambda) = \sum_{i=1}^{3} \frac{\int \pi a^2 Q_{ext}^i(a, \lambda) F_i(a)\, \mathrm{d}a}{\int \frac{4}{3} \pi \rho_i a^3 F_i(a)\, \mathrm{d}a} \tag{7.30}$$

The extinction parameter A_V is left varying between 1 and 20, and the best fit value is $A_V = 5$. The fit is clearly improved in the NIR-MIR range after introducing A_V (see Fig. 7.6). The stellar continuum is also affected by extinction and the PEGASE stellar template can not provide a reliable fit of the 2MASS NIR points. Instead, we replace it by a blackbody (fixing $\beta = 0$) and imposing a temperature $T \geq 1000$ K. We obtain a best fit temperature $T = 30\,000$ K, corresponding to a peak of the blackbody emission around 0.1 μm, in the UV - a sign of quite a young stellar population. This is consistent with what is found by Adamo et al. (2010) who found a peak of cluster formation at ~ 3.5 Myr ago, and with the UV part of the SED presented in Cormier et al. (2012). Fig. 7.6 shows the improvement of this additional component compared to the default model.

- *HS 0822+3542* - The PACS upper limits at 70 and 100 μm are not consistent at all with the rest of the MIR to FIR photometry (see Fig. 7.23). Thus we do not impose that these upper limits are respected in the fit. We decide to change the reported upper limits for the 70 and 100 μm PACS wavelengths and we recommend using the synthetic photometry provided by the model, i.e., $F_{70} \leq 41$ mJy and $F_{100} \leq 48$ mJy. These values are reported in Table 4.1.

- *HS 1236+3937* - Only *Spitzer* IRAC and IRS, and *Herschel* PACS and SPIRE data are available for this galaxy, and the galaxy is not detected with any of these instruments. So we can not report a SED for this galaxy.

- *HS 1304+3529* - To obtain a better fit at MIR wavelengths, we add an extra MIR modified blackbody (β fixed to 2.0 and best fit temperature $T = 100$ K). Additionally, this extra MIR modified

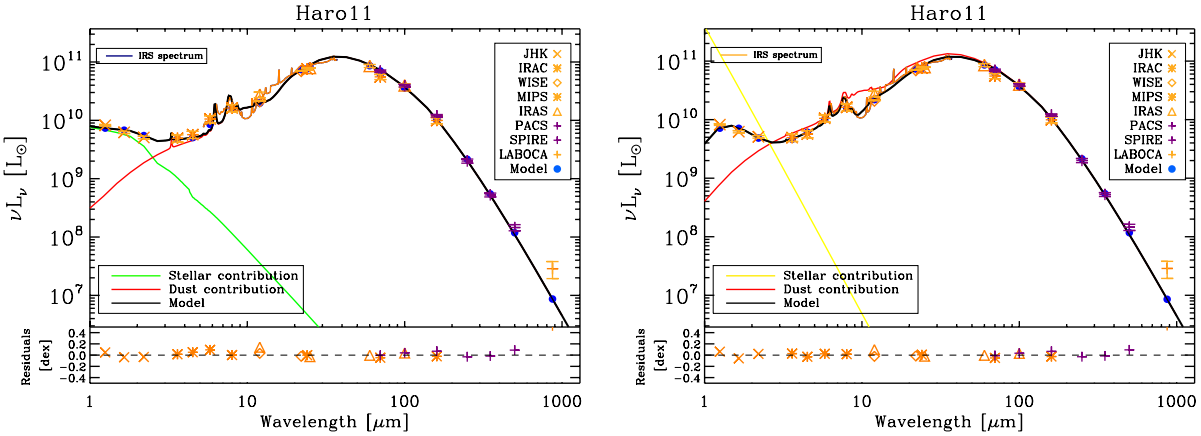

Fig. 7.6. SED for Haro11 when no extinction is assumed *(left)* and with extinction *(right)*. The colours and symbols for all of the SEDs presented in this Section are described in Fig.7.23.

blackbody improves the fit in the FIR. This is shown in Fig. 7.7.

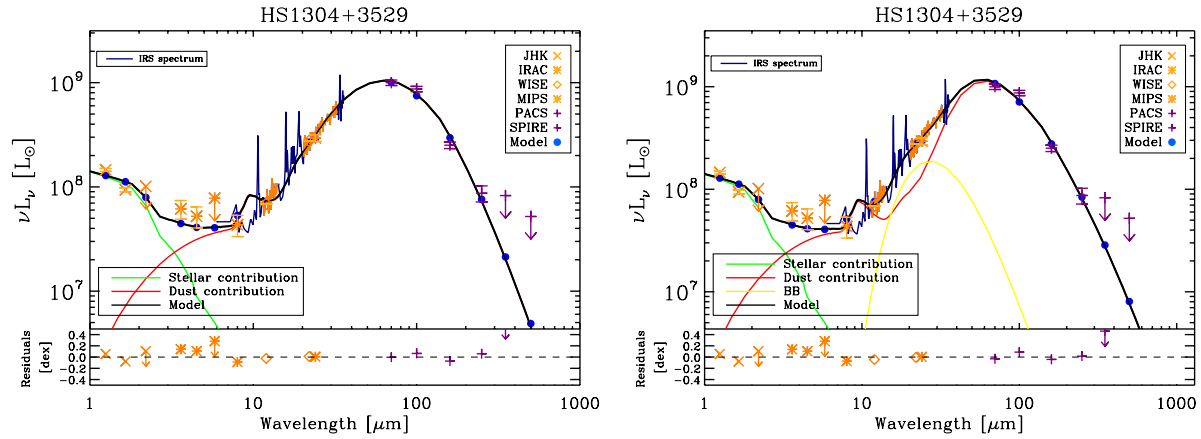

Fig. 7.7. SED for HS1304+3529 without *(left)* and with *(right)* the extra MIR modified blackbody.

- *HS 1442+4250* - There are only 4 detected points for this galaxy: IRAC 5.8 μm, IRAC 8.0 μm, MIPS 24 μm and PACS 70 μm, and thus not enough constraints to fit a SED.

- *HS 2352+2733* - There are only 3 detected points for this galaxy: MIPS 24 μm, PACS 70 μm and PACS 100 μm, and thus not enough constraints to fit a SED. However, we can get a rough estimate of the dust mass by fitting a modified blackbody with a fixed β=2.0, through these 3 points. We obtain a temperature of T= 52 K and $M_{dust,BB} = 1.01 \times 10^4\ M_\odot$ (see Fig. 7.8). This mass can bee seen as a lower limit of the real dust mass (see Chapter 8). Taking the median ratio of the dust masses estimated with the full dust model to the dust masses estimated with a $\beta = 2.0$ modified blackbody for the DGS (0.51, see Section 8.2.1 where this ratio is derived), we can estimate a total dust mass of $\sim M_{dust} = 1.98 \times 10^4\ M_\odot$.

- *I Zw 18* - To get a better match of the IRS spectrum, we add an extra MIR modified blackbody (β fixed to 2.0 and best fit temperature $T = 100$ K). This is shown in Fig. 7.9.

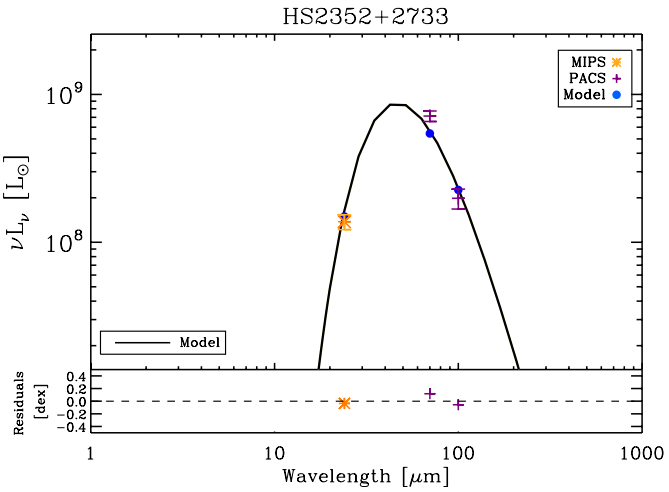

Fig. 7.8. Modified blackbody fit for HS2352+2733 with a fixed β=2.0.

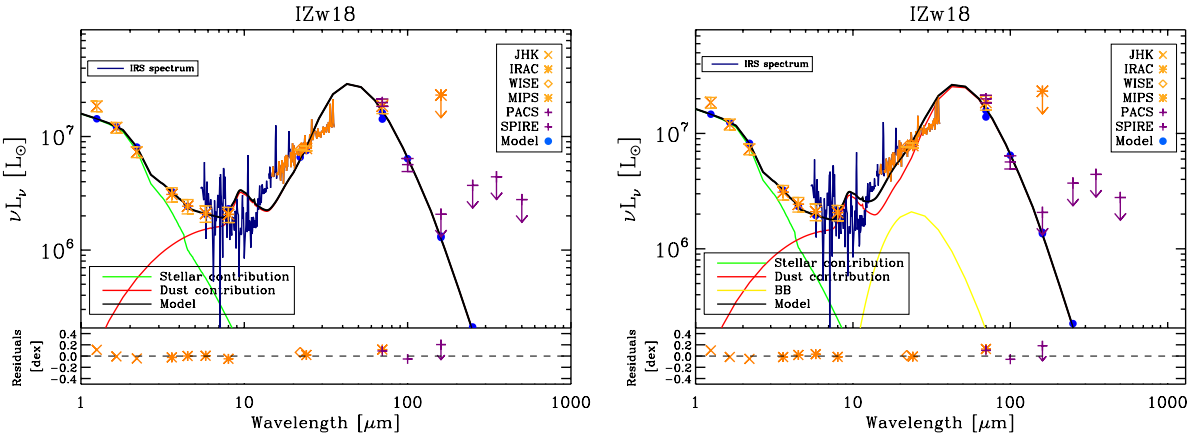

Fig. 7.9. SED for IZw18 without *(left)* and with *(right)* the extra MIR modified blackbody.

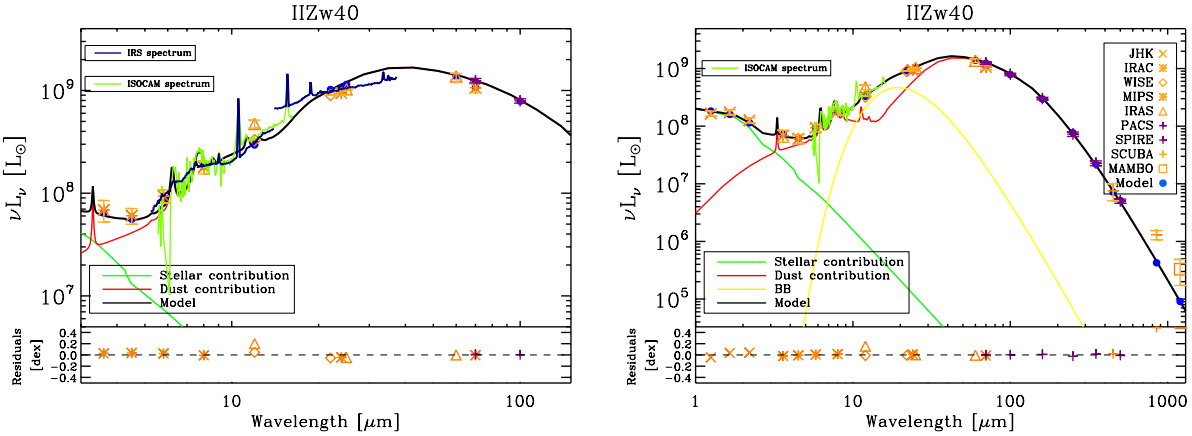

Fig. 7.10. SED for IIZw40 without *(left)* and with *(right)* the extra MIR modified blackbody. On the *left* panel, we zoom into the 3 - 150 μm range with the IRS spectrum overlaid on the figure in dark blue.

- *II Zw 40* - This galaxy has a good IRS spectrum. However, when compared to other MIR measurements, it seems that the *Spitzer* IRS-LL spectrum is not consistent with the rest of the MIR - FIR photometry (see Fig. 7.10). We thus looked for the ISOCAM spectrum for this galaxy. ISOCAM covers a 5.6 to 16.3 μm range. We match the ISOCAM spectrum with the photometry by applying the same rescaling process as for the IRS SL spectrum, i.e., find a spline going through the IRAC 8 μm and WISE 12 μm bands. The comparison of the ISOCAM and the IRS spectra shows that ISOCAM is consistent with the SL part of the IRS spectrum. However the slope of the LL spectrum does not seem coherent with the slope outlined by the end of the ISOCAM spectrum. This means that for this galaxy, a wavelength dependent correction might also be needed for the IRS LL part of the spectrum. Unfortunately, the 3 constraints we have in the MIR, (*WISE* 22 μm, MIPS 24 μm and *IRAS* 25 μm) do not properly sample the LL spectrum and thus we cannot derive this wavelength dependent correction. Thus we use the ISOCAM spectrum in the modelling for this galaxy. To properly match the end of the ISOCAM spectrum, we add an extra modified blackbody (β fixed to 2.0 and best fit temperature $T = 124$ K). This is shown in Fig. 7.10.

- *Mrk 1450* - To get a better match of the IRS spectrum, we add an extra MIR modified blackbody (β fixed to 2.0 and best fit temperature $T = 100$ K). This is shown in Fig. 7.11.

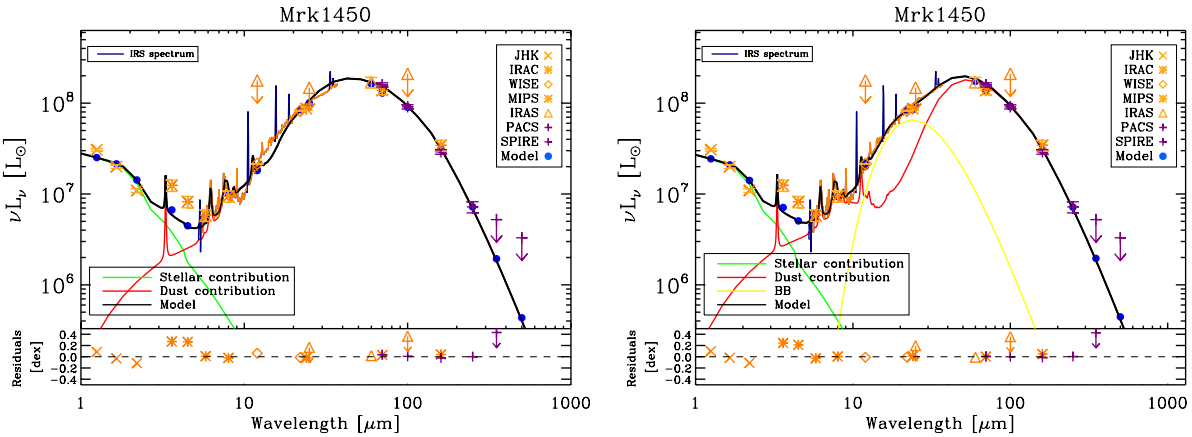

Fig. 7.11. SED for Mrk1450 without *(left)* and with *(right)* the extra MIR modified blackbody.

-*Mrk 153* - This galaxy has a silicate emission feature in its IRS spectrum around 10 μm. This galaxy is known to harbour an AGN and this emission feature could be originating from hot small silicate grains in the accretion disk around the AGN. Thus we leave the f_{sil} parameter free for this galaxy. We get $f_{sil} = 0.9104$ (i.e., 1.3 times the Galactic value).

- *Mrk 930* - To get a better match of the IRS spectrum, we add an extra MIR modified blackbody (β fixed to 2.0 and best fit temperature $T = 100$ K). This is shown in Fig. 7.12.

- *NGC1140 and NGC 1569* - The IRS SL slit only covers a small part of these galaxies. As they both are extended, we wonder if the SL rescaling is consistent with the rest of the NIR - MIR spectrum. We use the ISOCAM spectrum for comparison after applying the same rescaling step. The two spectra are consistent with each other and with the general NIR - MIR shape of the SED for both galaxies. Thus we consider that the IRS spectrum is reliable and we use it in the modelling. In the case of NGC1569, we also add an extra MIR modified blackbody (β fixed to 2.0 and best fit temperature $T = 100$ K), to get a better match of the IRS spectrum. This is shown in Fig. 7.13.

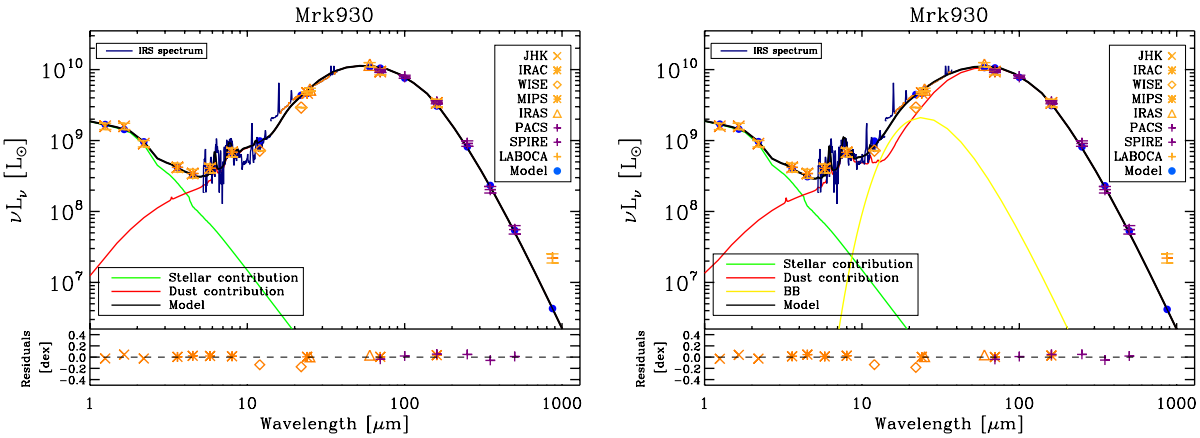

Fig. 7.12. SED for Mrk930 without *(left)* and with *(right)* the extra MIR modified blackbody.

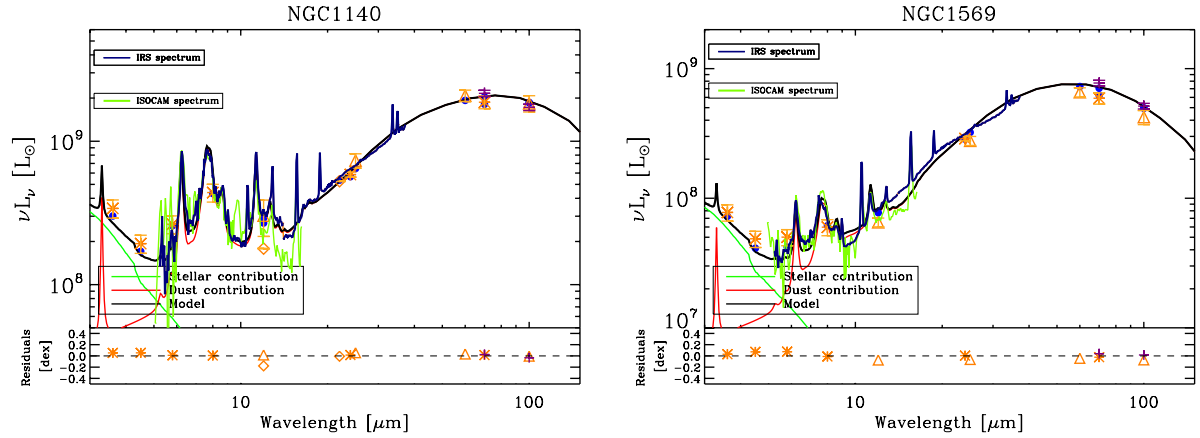

Fig. 7.13. Zoom on the SED between 3 and 150 μm for NGC1140 *(left)* where the ISOCAM spectrum is overlaid on the SED in light green. Same for NGC1569 *(right)*. See Fig. 7.23 for the final SEDs.

- *NGC 5253* - To get a better match of the IRS spectrum, we add an extra MIR modified blackbody (β fixed to 2.0 and best fit temperature $T = 100$ K). This is shown in Fig. 7.14.

- *NGC 6822* - If we leave the f_{vsg} parameter free, this leads to unrealistically prominent PAH features for this galaxy. Thus we fix the f_{vsg} parameter to the Galactic value for this galaxy. This leads to an increase of the dust mass of $\sim$ 15 % which is within the $\sim$ 112% error bar[9]. This is shown in Fig. 7.15.

- *Pox 186* - To get a better match of the IRS spectrum, we add an extra MIR modified blackbody (β fixed to 2.0 and best fit temperature $T = 137$ K) (see Fig. 7.16). Pox 186 has a very broad FIR peak of the SED, and is not detected beyond 250 μm. It has a very uncommon SED shape and a limited number of constraints. It looks like a very wide modified blackbody, i.e., a giant HII region, that should be surrounded by some diffuse colder dust. Thus we introduce a single starlight intensity component, to mimic the emission of a colder diffuse ISM around this giant HII region.

[9]Note the very large error bar for the dust mass due to the large error bar on the SPIRE observations.

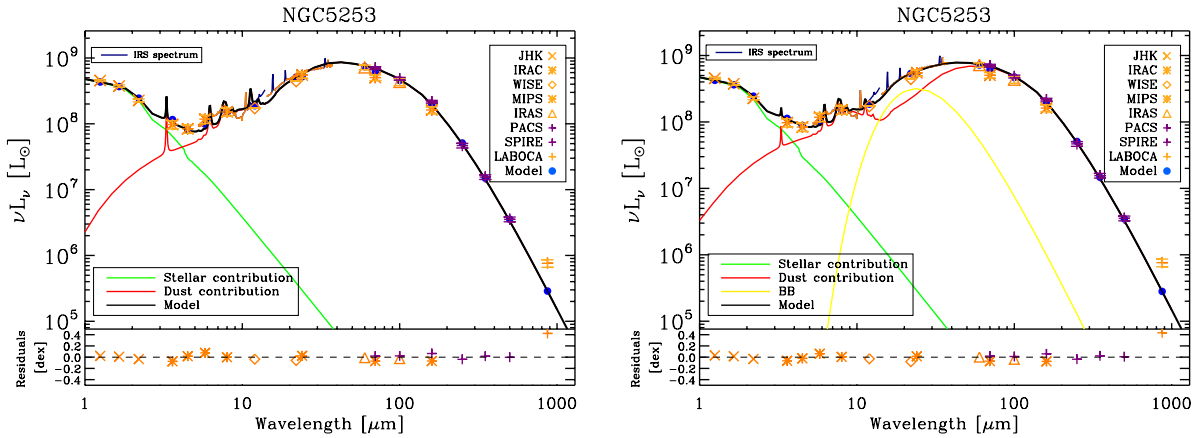

Fig. 7.14. SED for NGC5253 without *(left)* and with *(right)* the extra MIR modified blackbody.

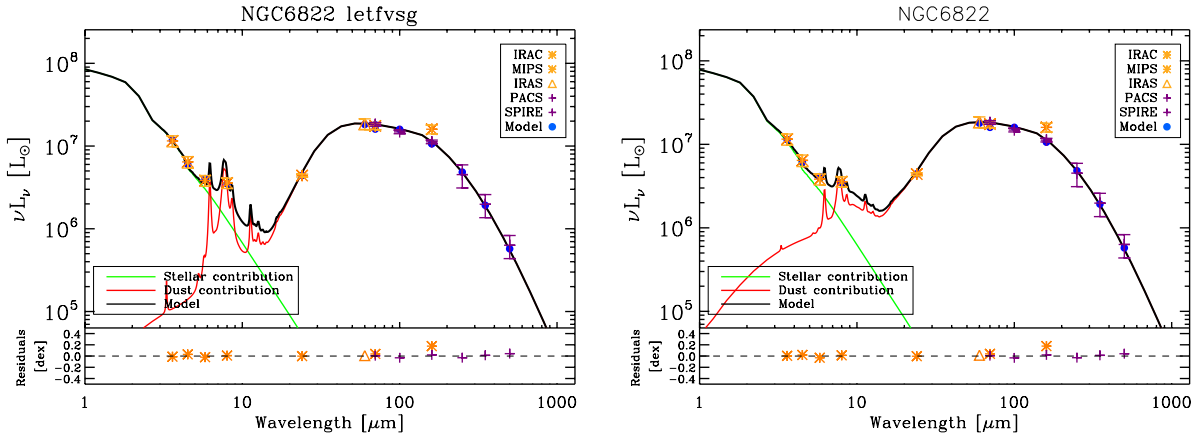

Fig. 7.15. SEDs for NGC6822 with f_{vsg} free *(left)* and fixed *(right)*.

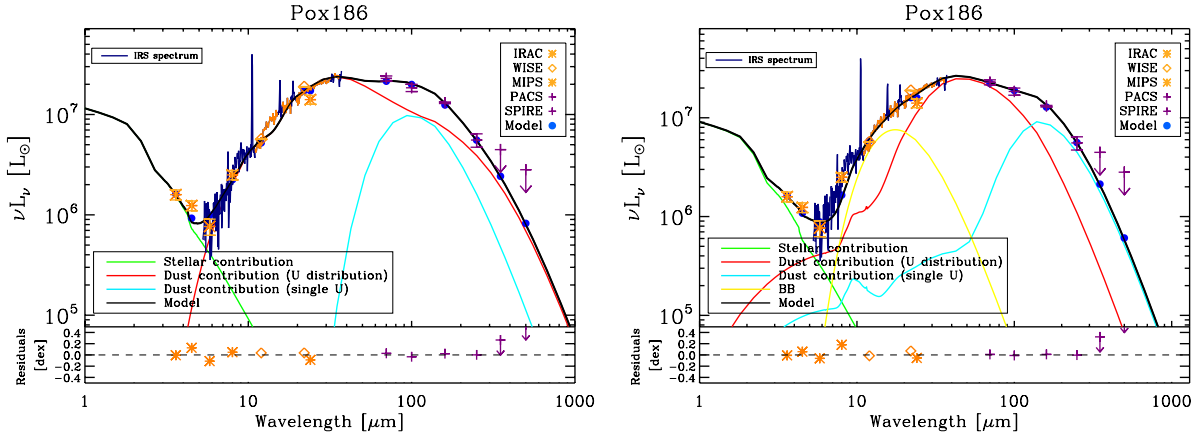

Fig. 7.16. SED for Pox186 with the extra diffuse component (in cyan), without *(left)* and with *(right)* the extra MIR modified blackbody.

We get a best fit $U = 0.40$.

- *SBS 0335-052* - This galaxy has a very surprising SED with a IR peak around 15 - 30 μm, and an IRS spectrum showing silicate absorption features superimposed on a featureless continuum (see also Thuan et al. 1999b). The silicate absorption feature around 10 μm observed in the IRS spectrum indicates that extinction is prominent in this galaxy. Thus we add extinction in our model as for Haro 11, and get $A_V = 1.1$. The peculiar shape of the IRS spectrum requires two MIR modified blackbodies to get a satisfactory fit (β fixed to 2.0 and best fit temperatures $T_1 = 281$ K and $T_2 = 125$ K). This is shown in Fig. 7.17.

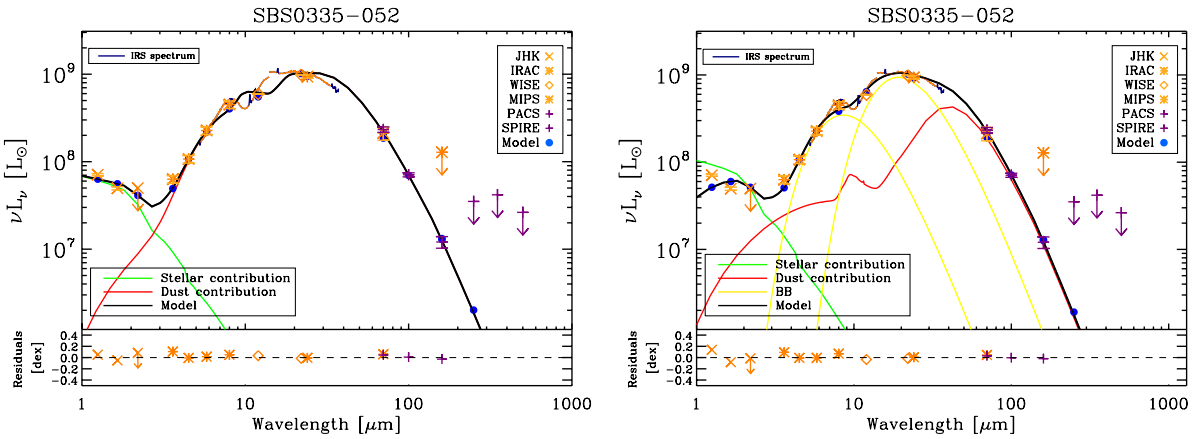

Fig. 7.17. *(left)* SED for SBS0335-052 without extinction nor the additional MIR modified blackbodies. On the *right* panel, extinction and two extra MIR modified blackbodies have been added to improve the quality of the fit in the NIR - MIR range.

- *SBS 1533+574* - To get a better match of the IRS spectrum, we add an extra MIR modified blackbody (β fixed to 2.0 and best fit temperature $T = 100$ K). This is shown in Fig. 7.18.

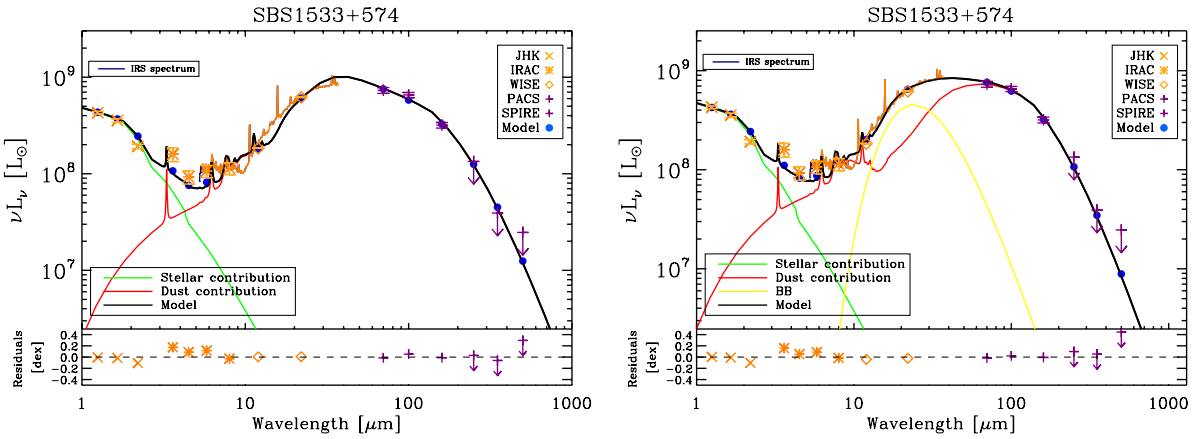

Fig. 7.18. SED for SBS1533+574 without *(left)* and with *(right)* the extra MIR modified blackbody.

- *Tol 0618-402* - The longest wavelength detected for this galaxy is 12 μm in the *WISE* band. As we do not have any constraints in the FIR to get an accurate dust mass, we do not report a SED

for this galaxy.

- *Tol 1214-277* - The MIPS 70 μm point is not coherent with the rest of the photometry: IRS and MIPS 24 μm on one side and PACS 70 and 100 μm on the other side (see Fig. 7.23). It is another confirmation that this point is discrepant (see Chapter 6, Section 6.2.3), and thus we do not consider it in the modelling. Similarly to Pox 186, Tol 1214-277 has a very broad SED peak in the FIR, resembling a giant HII region. Here again we add a single starlight intensity component, and get a best fit $U = 19.5$.

- *UGC 4483* - The IRAC upper limit at 5.8 μm and the PACS upper limit at 160 μm do not seem consistent at all with the rest of the NIR to FIR photometry (see Fig. 7.23). Thus we do not impose that these upper limits are respected in the fit. We advise using the synthetic photometry provided by the model, i.e., $F_{5.8} \leq 0.85$ mJy and $F_{160} \leq 72$ mJy. These flux densities are reported in Tables 4.1 and 6.9.

- *UM 133* - This galaxy is not detected in the IRAC bands. However we still include the upper limits in the fit, in order to have (even approximative) constraints in the NIR (see Fig. 7.23).

- *UM 461* - To get a better match of the IRS spectrum, we add an extra MIR modified blackbody (β fixed to 2.0 and best fit temperature $T = 150$ K). This is shown in Fig. 7.19.

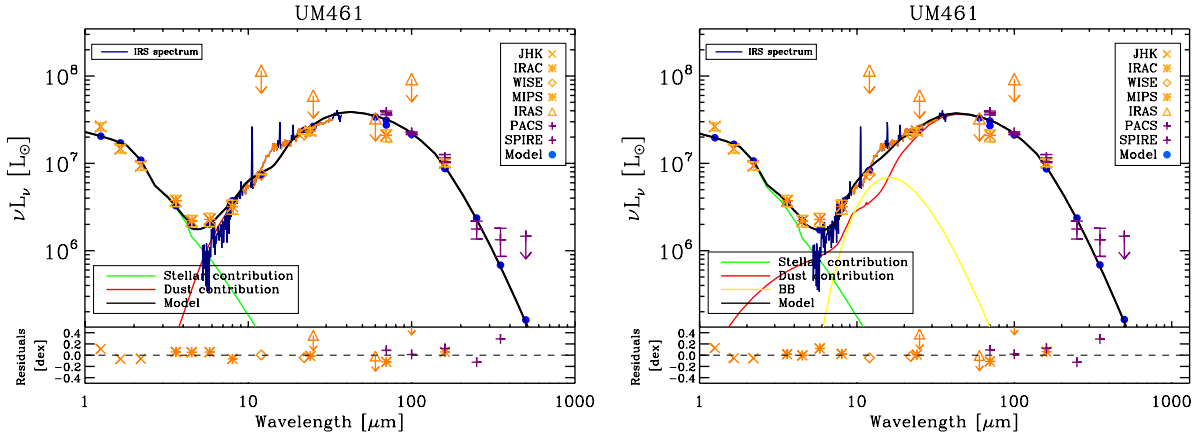

Fig. 7.19. SED for UM461 without *(left)* and with *(right)* the extra MIR modified blackbody.

7.2.5 Notes on individual KINGFISH galaxies

As we are interested in getting SEDs with *Herschel* constraints to have an accurate estimation of the dust mass with submm constraints, and also in the comparison of *Spitzer*-only versus *Herschel* dust masses, we do not consider some KINGFISH galaxies which have no *Herschel* detections: NGC 0584 - NGC 1404 - DDO 154 - DDO 165.

- *NGC 0855* - If we leave the f_{vsg} parameter free, this leads to unrealistically prominent PAH features for this galaxy. Thus we fix the f_{vsg} parameter to the Galactic value for this galaxy. This leads to an increase of the dust mass of ~ 38 % which is within the ~ 40% error bar. This is shown in Fig. 7.20.

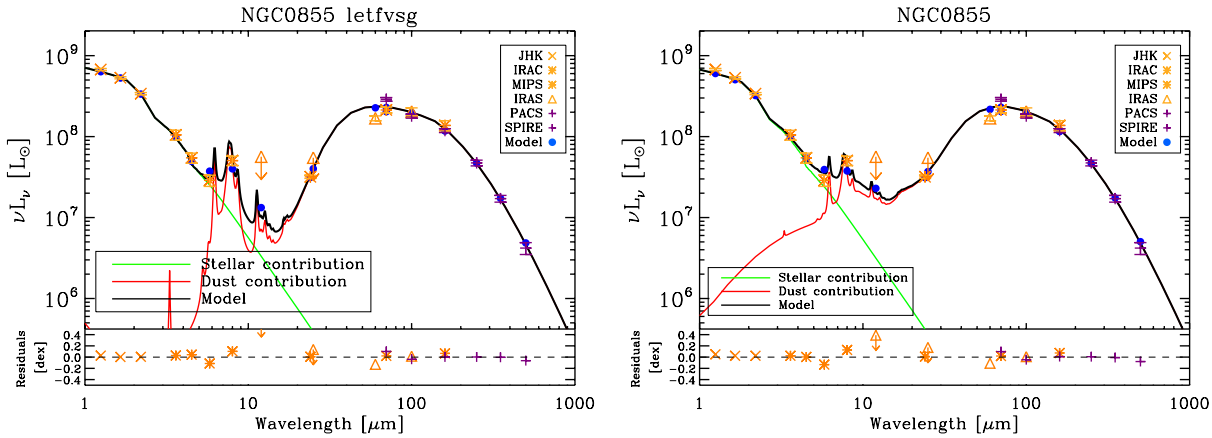

Fig. 7.20. SEDs for NGC0855 with f_{vsg} free *(left)* and fixed *(right)*.

- *Ho I* - As for NGC 0855, we fix the f_{vsg} parameter to the Galactic value for this galaxy. This leads to an increase of the dust mass of $\sim$ 14 % which is within the $\sim$ 47% error bar.

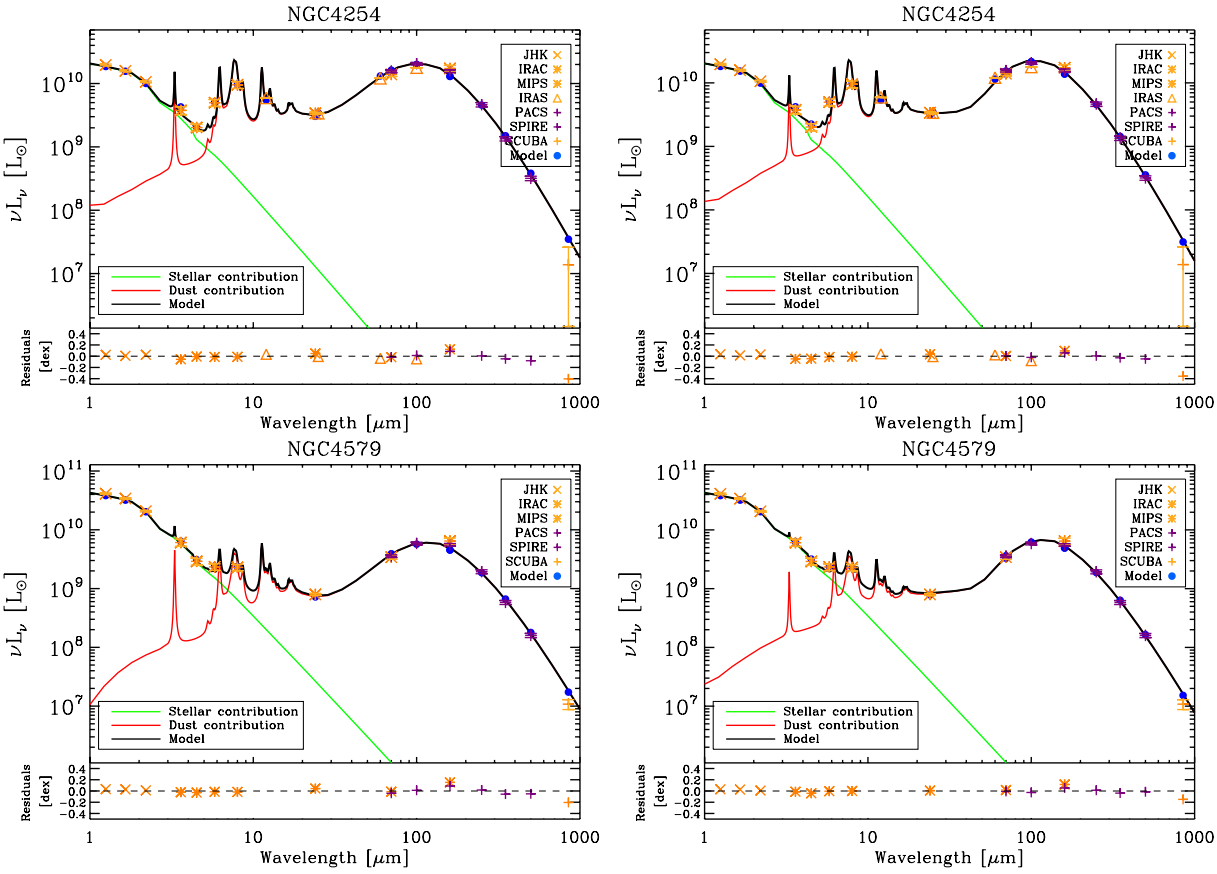

Fig. 7.21. SEDs for NGC4254 *(top)* and NGC4579 *(bottom)* with f_{vsg} free *(left)* and fixed *(right)*.

- *NGC 1512* - As for NGC 0855, we fix the f_{vsg} parameter to the Galactic value for this galaxy. This leads to an increase of the dust mass of $\sim$ 17 % which is within the $\sim$ 28% error bar.

- *NGC 4254 and NGC 4579* - We fix the f_{vsg} parameter to the Galactic value for these galaxies as it enables a better fit in the FIR. This is shown in Fig. 7.21. The dust mass for these two galaxies thus decreases by $\sim$ 20 %.

- *NGC 5408* - As for NGC 0855, we fix the f_{vsg} parameter to the Galactic value for this galaxy. This leads to an increase of the dust mass of $\sim$ 16 % which is within the $\sim$ 26% error bar.

7.2.6 Results

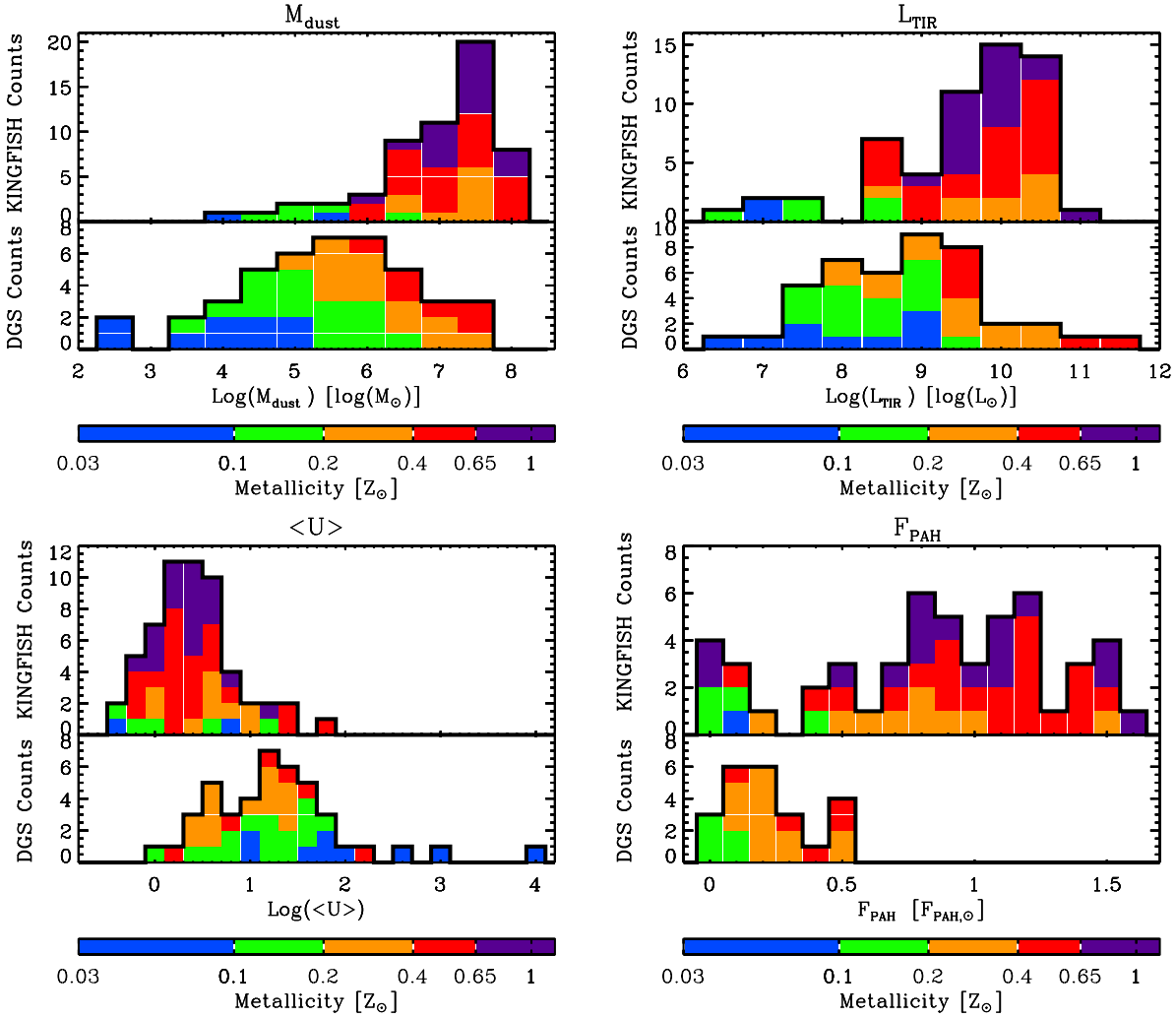

Fig. 7.22. Distributions of M_{dust} *(top left)*, L_{TIR} *(top right)*, $< U >$ *(bottom left)* and f_{PAH} *(bottom right)* from our SED fits for the DGS and KINGFISH samples. The colour scale represents the range of metallicity values. On each panel, the upper/lower histogram is the KINGFISH/DGS distribution for the parameter.

The individual SEDs for the DGS and KINGFISH galaxies are presented in Figs. 7.23 and 7.24. Note that in Figs. 7.23 and 7.24 the last fitted point is the 350 μm point, as explained in the beginning of Section 7.2. All longer wavelength points are just overlaid on the plots. The resulting parameters and their errors are given in Tables 7.3, 7.4, 7.5 and 7.6. The dust mass, TIR

luminosity, averaged starlight intensity and PAH mass fraction are presented in Fig. 7.22 and the main informations on these four parameters are summarised in Table 7.2.

The two samples span a range of 6 orders of magnitude in dust mass and in TIR luminosity. The mean starlight intensity ranges from 0.335 (Ho I) and 8.9 $\times$ 10^3 (Tol 1214-277). To determine the PAH mass fraction range, we consider only galaxies for which the f_{vsg} parameter is free. For these galaxies, the PAH mass fraction ranges from 0.06 (for NGC 2366) to 1.6 (for IC 0342) times the Galactic value.

With these histograms we can already note a trend between all of the parameters and metallicity. The dust masses, TIR luminosities and PAH mass fractions are higher in the sample containing more metal-rich galaxies: the median M_{dust} is 2.9 $\times$ 10^5 $M_\odot$ for the DGS galaxies versus 1.6 $\times$ 10^7 $M_\odot$ for the KINGFISH sample, the median L_{TIR} is 9.3 $\times 10^8$ $L_\odot$ for the DGS galaxies versus 6.1 $\times$ 10^9 $L_\odot$ for the KINGFISH sample, and $f^{med}_{PAH,DGS}$ = 0.18 $f_{PAH,\odot}$ compared to $f^{med}_{PAH,KINGFISH}$ = 0.89 $f_{PAH,\odot}$. This is consistent with the main dwarf galaxies characteristics we reviewed in Chapter 2: dwarf galaxies are less massive, less luminous and show weak PAH features. The mean starlight intensity behaves the opposite way as it decreases with increasing metallicity. This is consistent with dwarf galaxies harbouring a more intense galaxy wide radiation field.

Table 7.2. Main characteristics of the DGS and KINGFISH SED parameters.

	Log(M_{dust}) [Log($M_\odot$)]	Log(L_{TIR}) [Log($L_\odot$)]	Log($< U >$)	f_{PAH}
DGS	2.57 - 7.42	6.50 - 11.30	0.002 - 3.95	0.00* - 0.54
	median: 5.46	median: 8.97	median: 1.25	median: 0.18
KINGFISH	4.02 - 8.02	6.67 - 11.13	-0.48 - 1.80	0.00* - 1.59
	median: 7.21	median: 9.78	median: 0.34	median: 0.89

*: 0.00 for the minimum f_{PAH} value means that no PAHs are detected in at least one galaxy in the sample.

7.2.7 SEDs fits for the DGS and KINGFISH samples

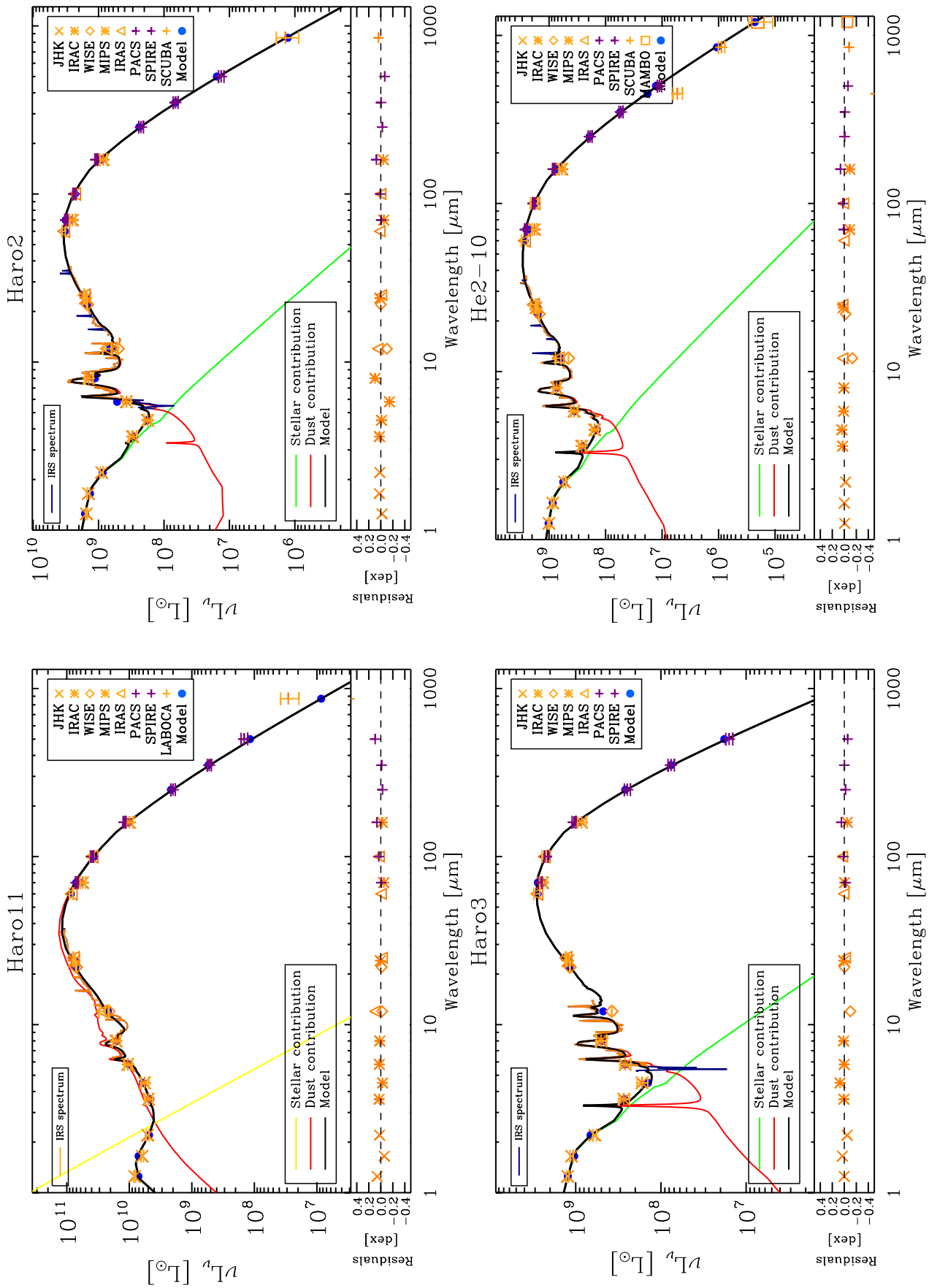

Fig. 7.23. SEDs for Haro11 *(top left)*, Haro2 *(top right)*, Haro3 *(bottom left)*, He2-10 *(bottom right)*. The observed SED includes the *Herschel* data (purple crosses) as well as any available ancillary data (in orange). The different symbols code for the different instruments: Xs for 2MASS bands, stars for *Spitzer* IRAC and MIPS, diamonds for WISE, triangles for IRAS, orange crosses for SCUBA or LABOCA, squares for MAMBO. The IRS spectrum is displayed in dark blue, with the fitted parts in orange. The total modelled SED in black is the sum of the stellar (green) and dust (red) contributions, and eventually an extra MIR modified blackbody contribution (yellow). The modelled points in the different bands are the filled blue circles.

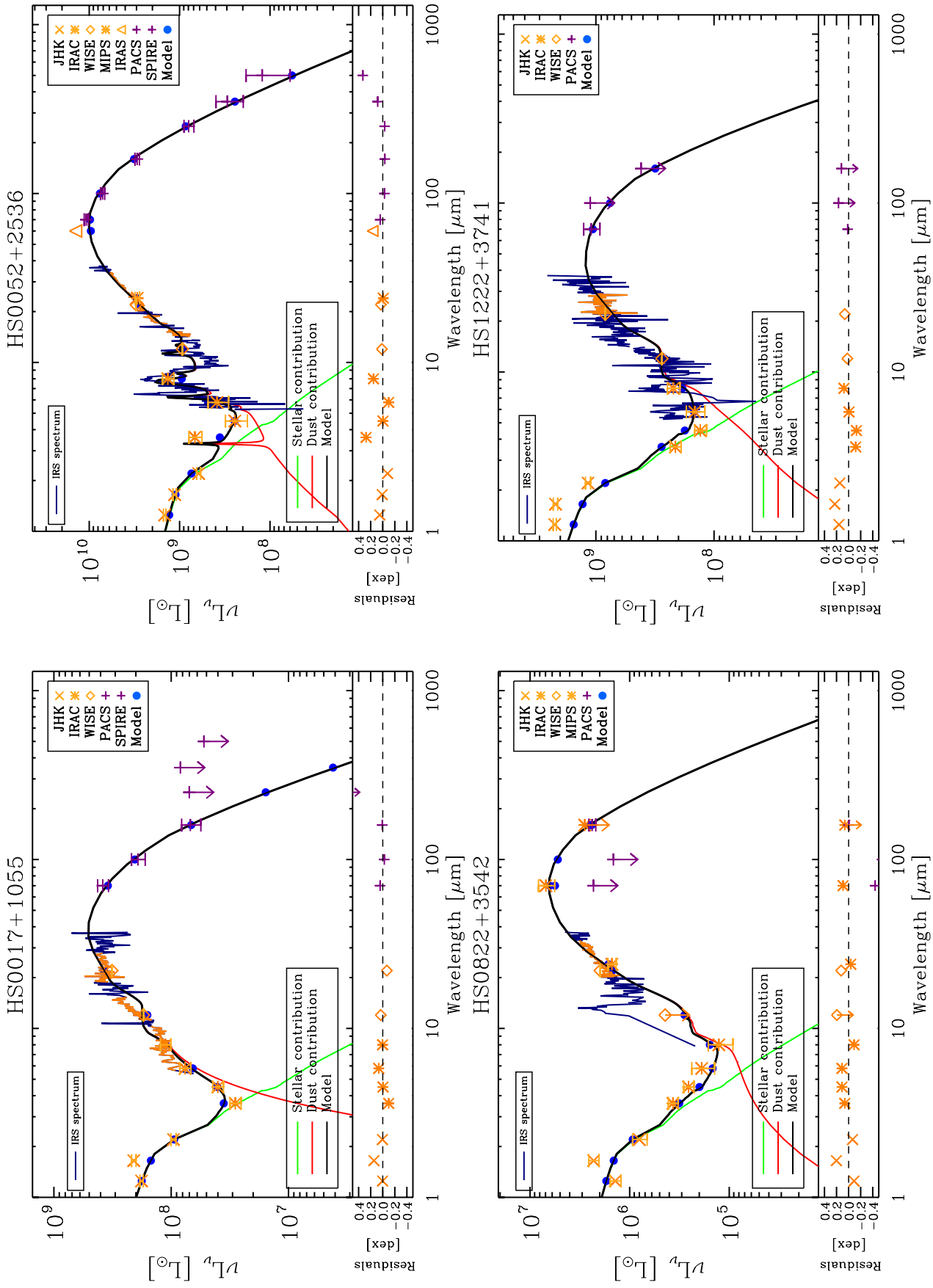

Fig. 7.23. (continued) for HS0017+1055 *(top left)*, HS0052+2536 *(top right)*, HS0822+3542 *(bottom left)*, HS1222+3741 *(bottom right)*.

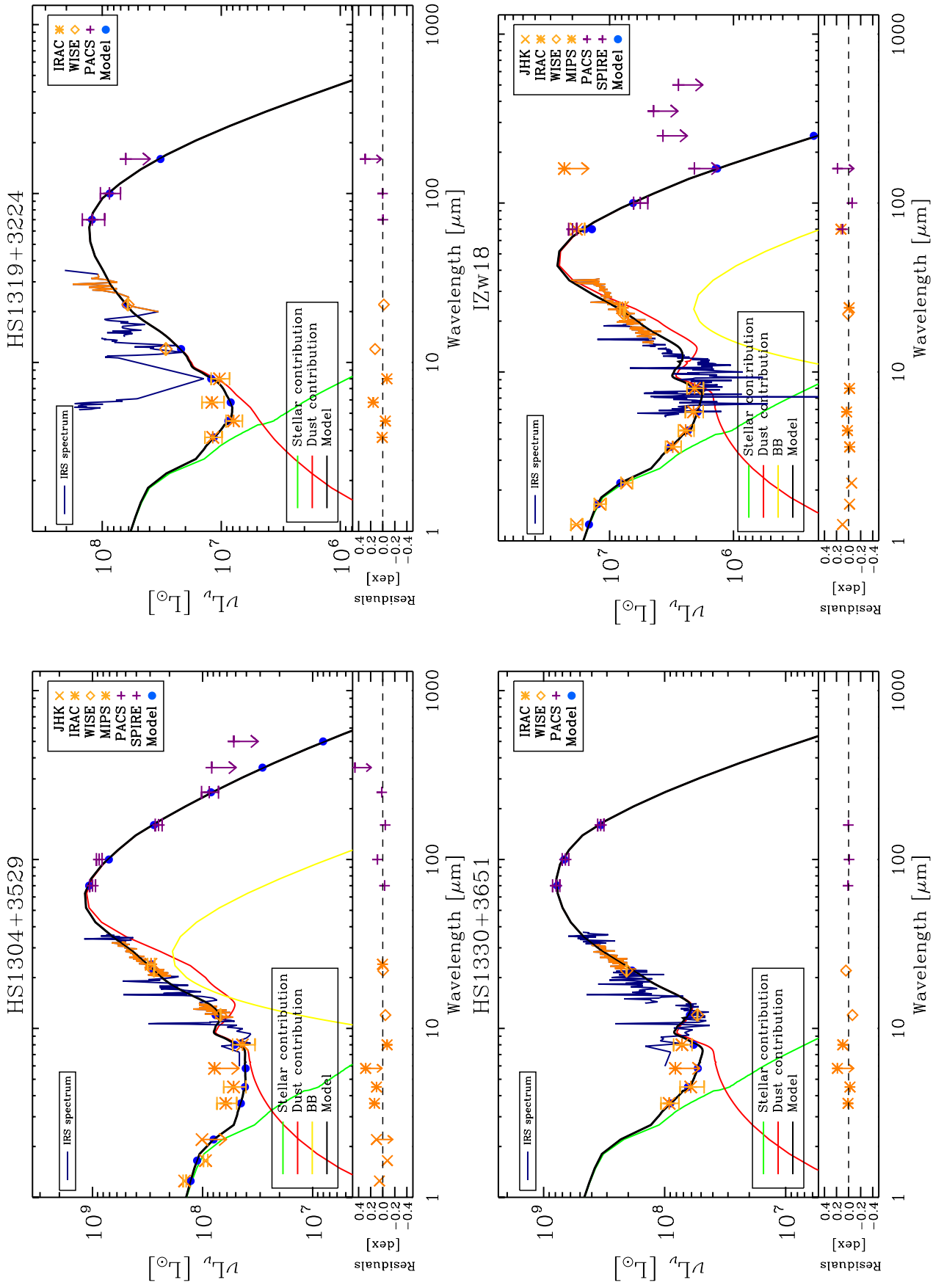

Fig. 7.23. (continued) for HS1304+3529 *(top left)*, HS1319+3224 *(top right)*, HS1330+3651 *(bottom left)*, IZw18 *(bottom right)*.

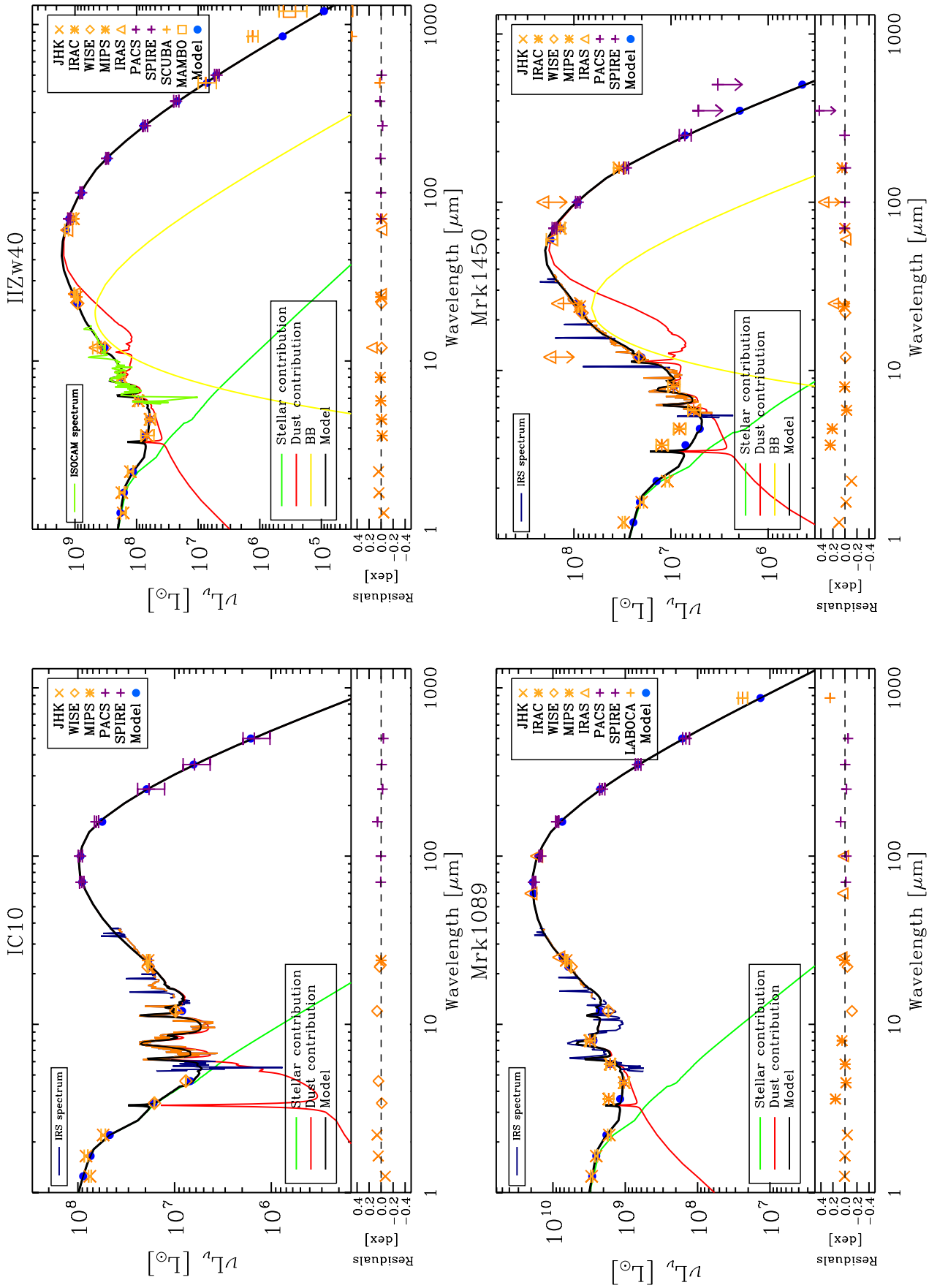

Fig. 7.23. (continued) for IC10 *(top left)*, IIZw40 *(top right)*, Mrk1089 *(bottom left)*, Mrk1450 *(bottom right)*.

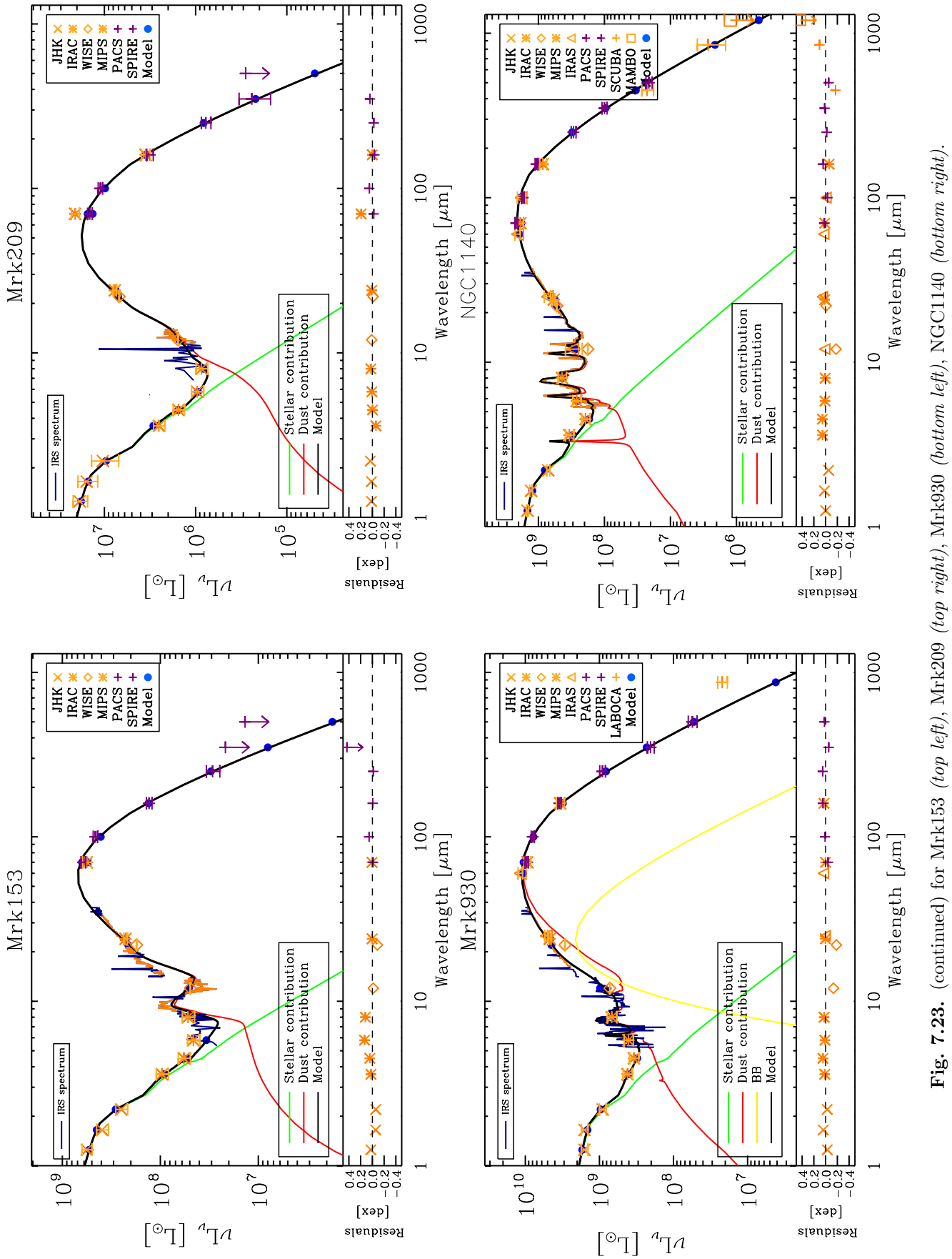

Fig. 7.23. (continued) for Mrk153 *(top left)*, Mrk209 *(top right)*, Mrk930 *(bottom left)*, NGC1140 *(bottom right)*.

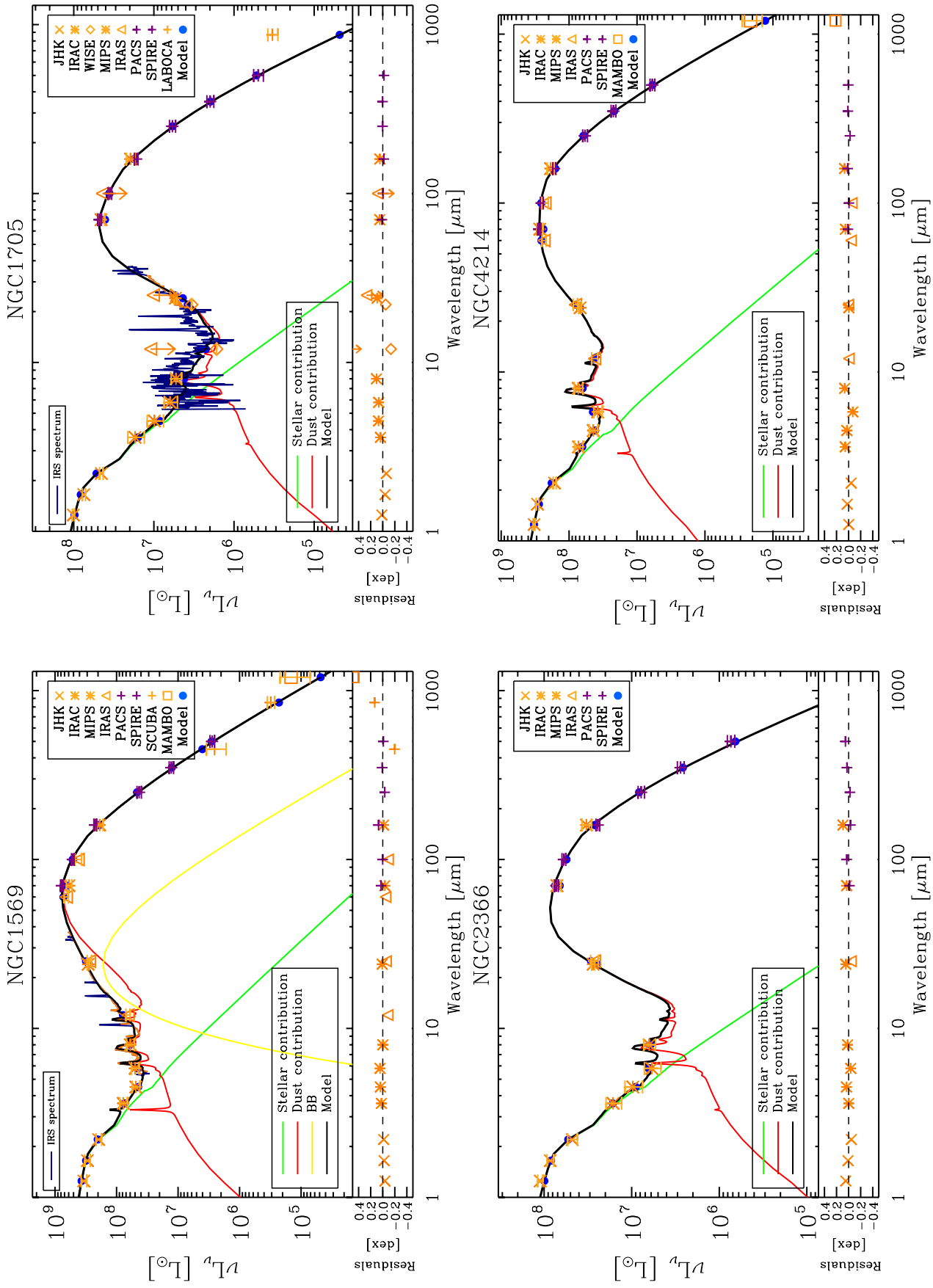

Fig. 7.23. (continued) for NGC1569 *(top left)*, NGC1705 *(top right)*, NGC2366 *(bottom left)*, NGC4214 *(bottom right)*.

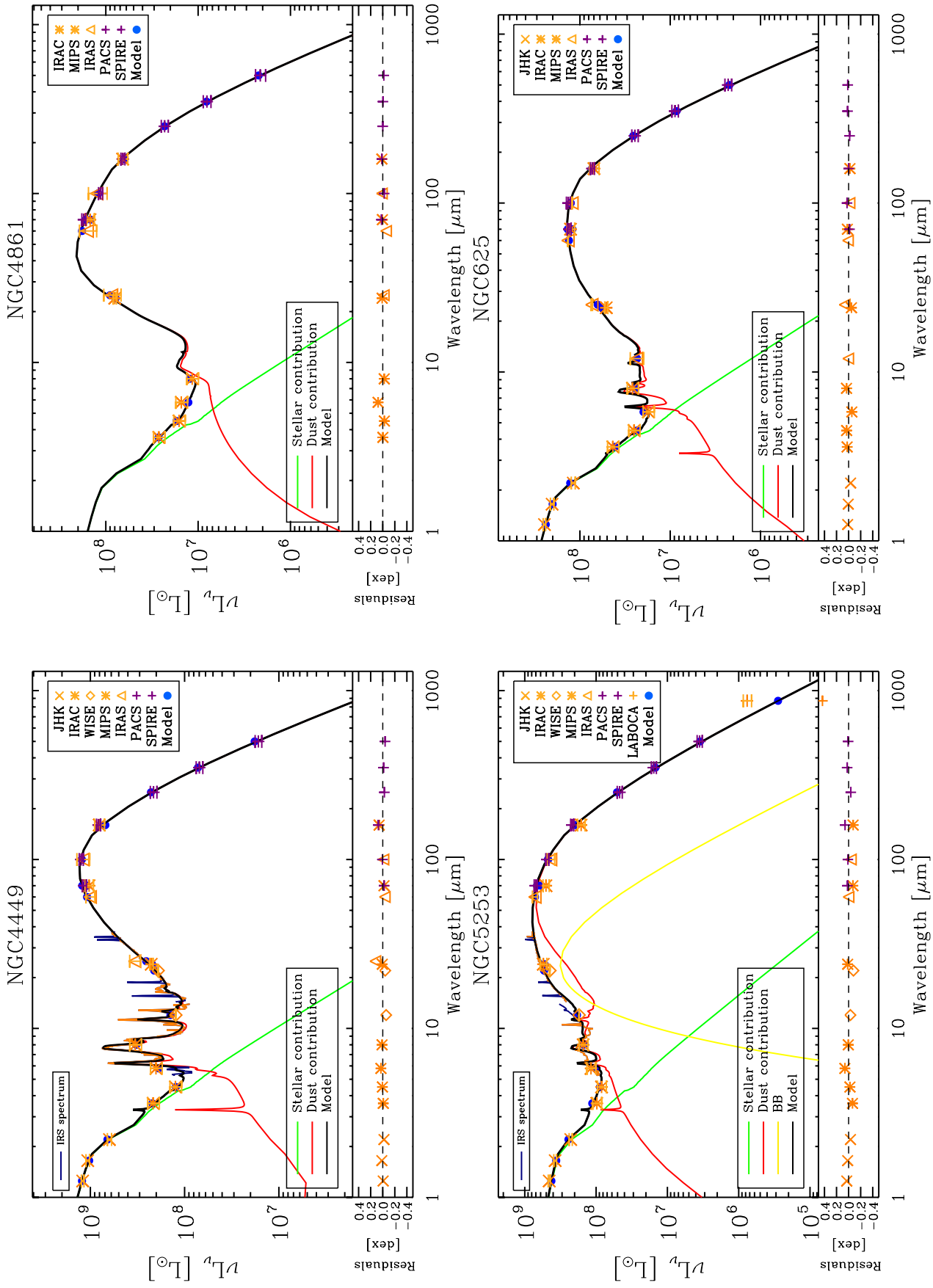

Fig. 7.23. (continued) for NGC4449 *(top left)*, NGC4861 *(top right)*, NGC5253 *(bottom left)*, NGC625 *(bottom right)*.

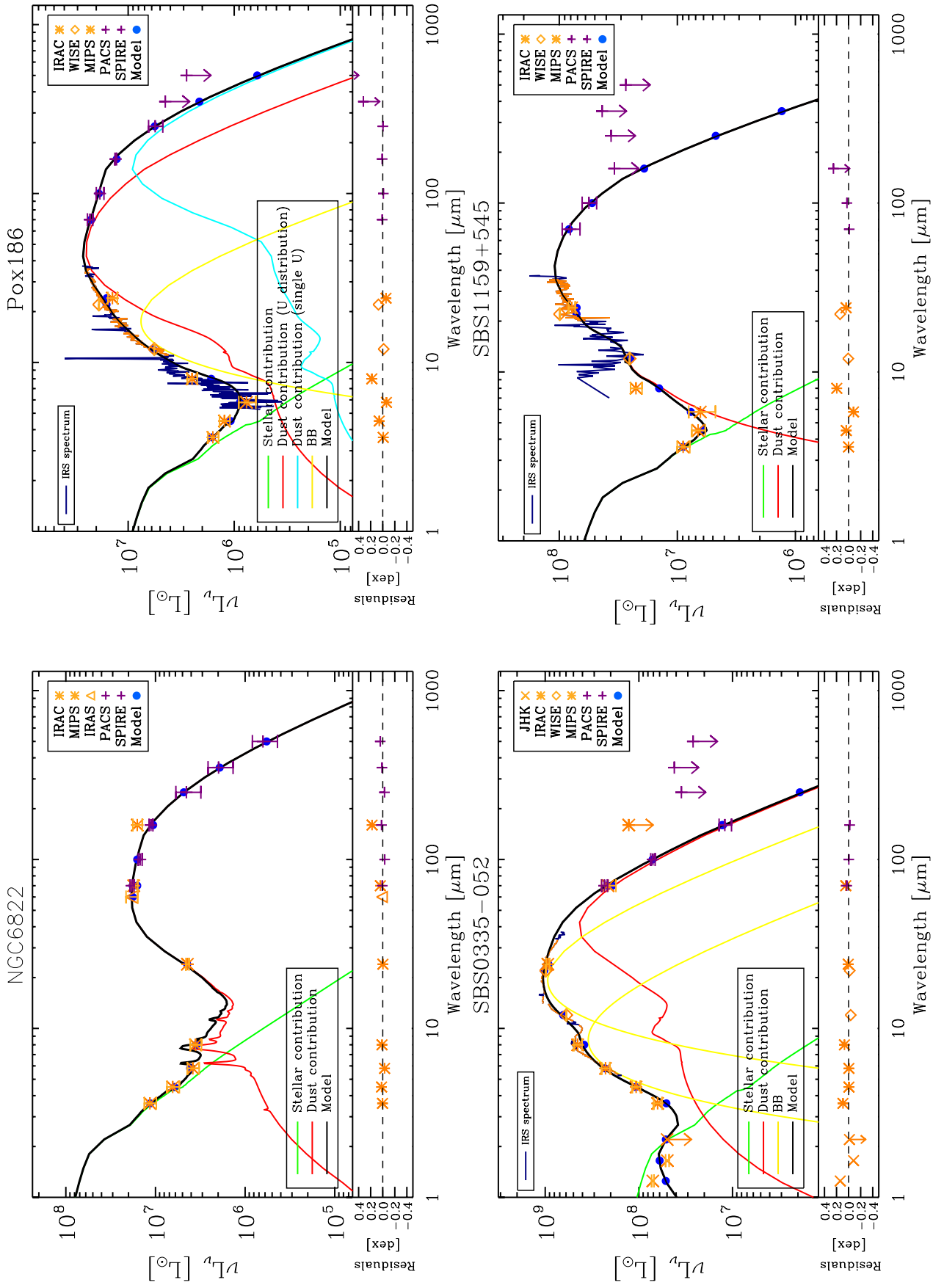

Fig. 7.23. (continued) for NGC6822 *(top left)*, Pox186 *(top right)*, SBS0335-052 *(bottom left)*, SBS1159+545 *(bottom right)*.

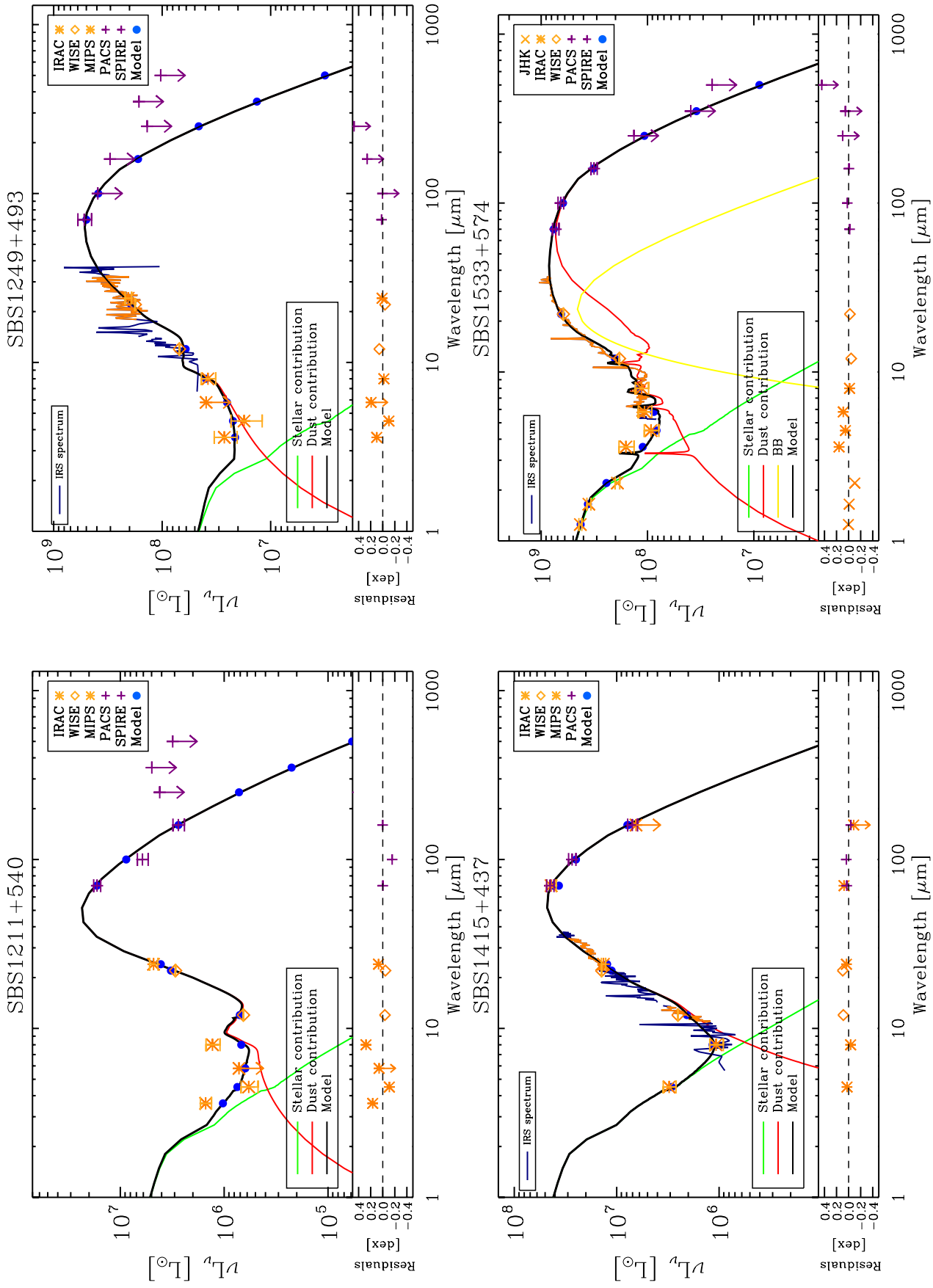

Fig. 7.23. (continued) for SBS1211+540 *(top left)*, SBS1249+493 *(top right)*, SBS1415+437 *(bottom left)*, SBS1533+574 *(bottom right)*.

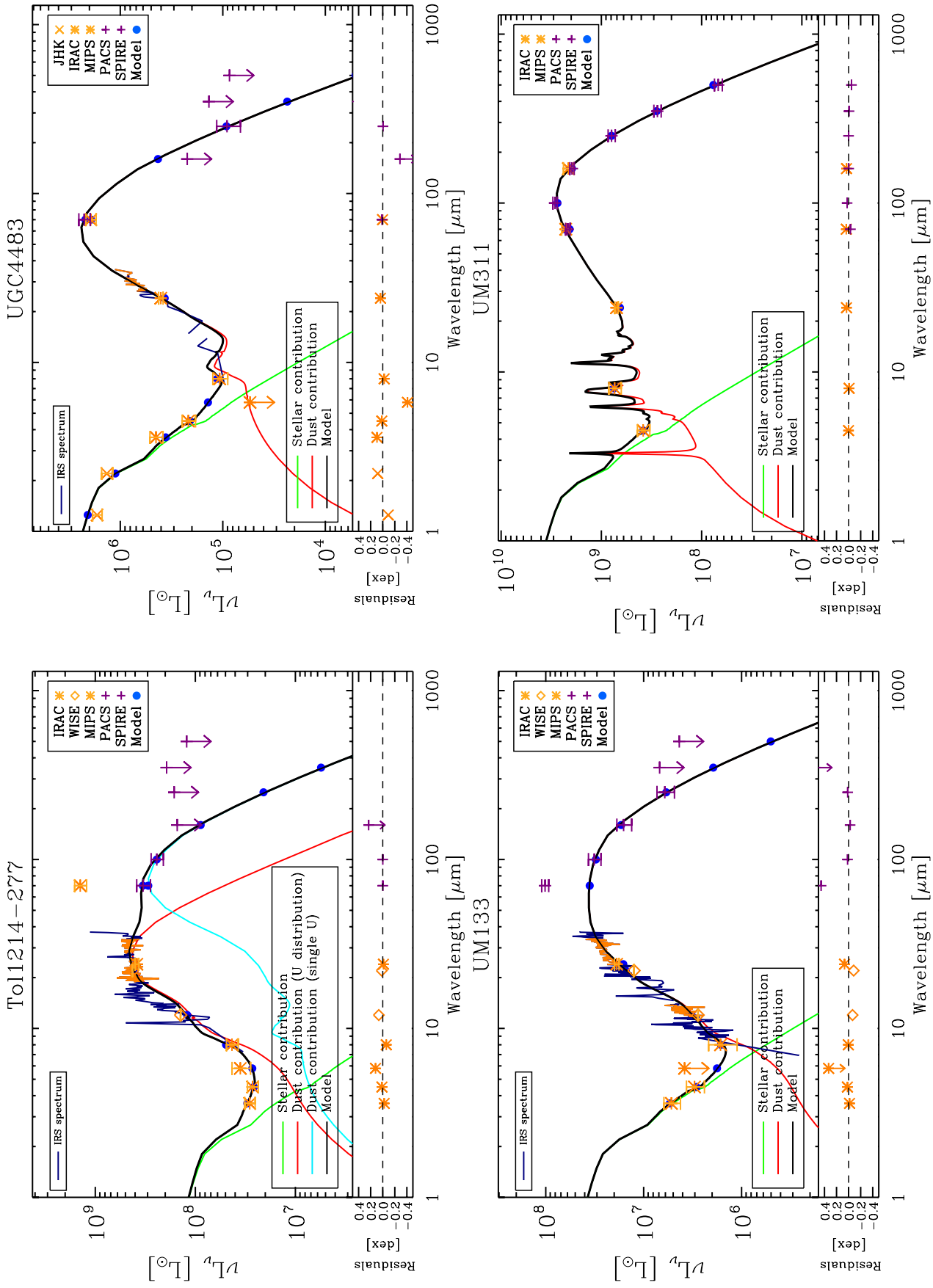

Fig. 7.23. (continued) for Tol1214-277 *(top left)*, UGC4483 *(top right)*, UM133 *(bottom left)*, UM311 *(bottom right)*.

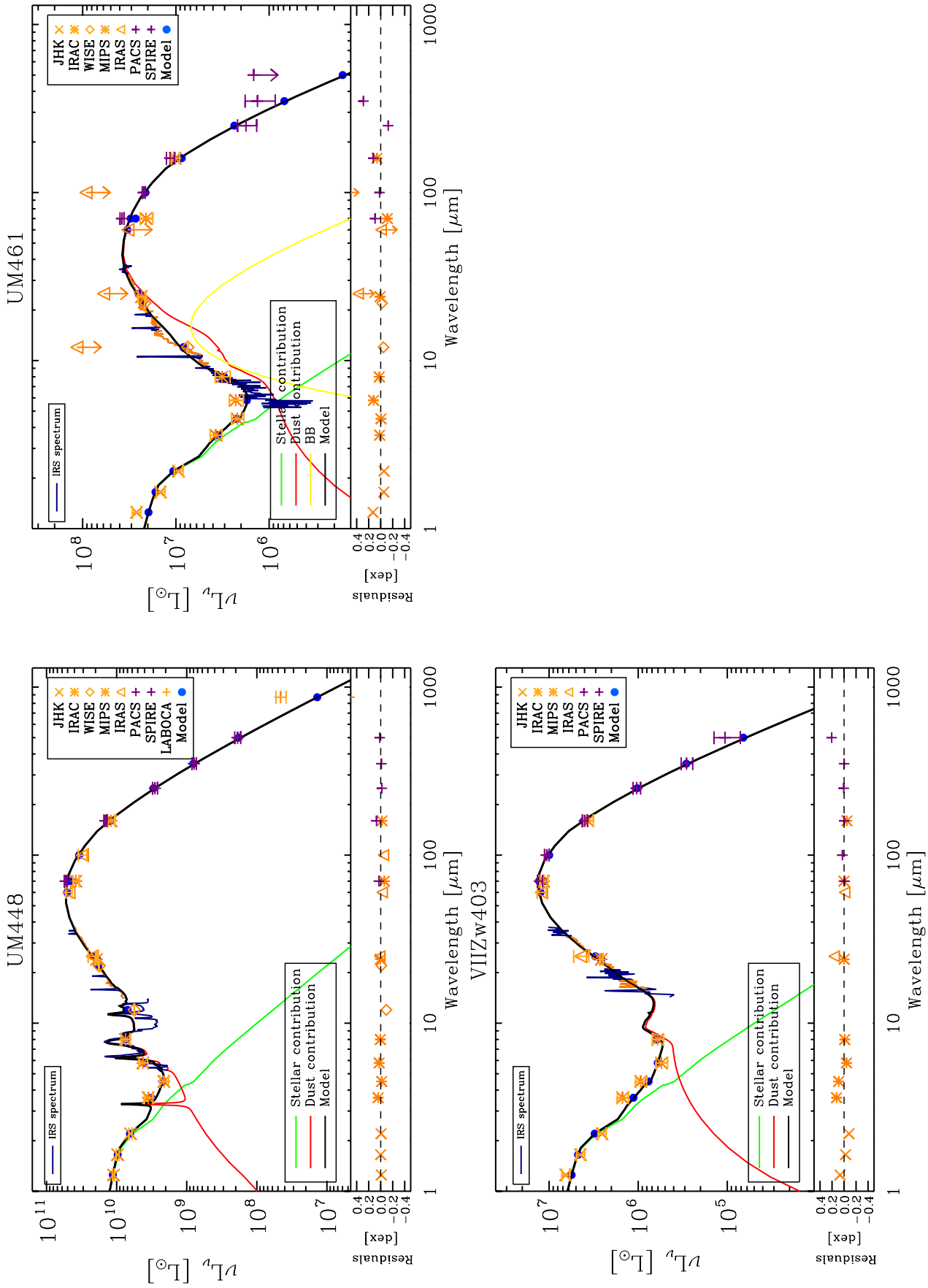

Fig. 7.23. (continued) for UM448 *(top left)*, UM461 *(top right)*, VIIZw403 *(bottom left)*.

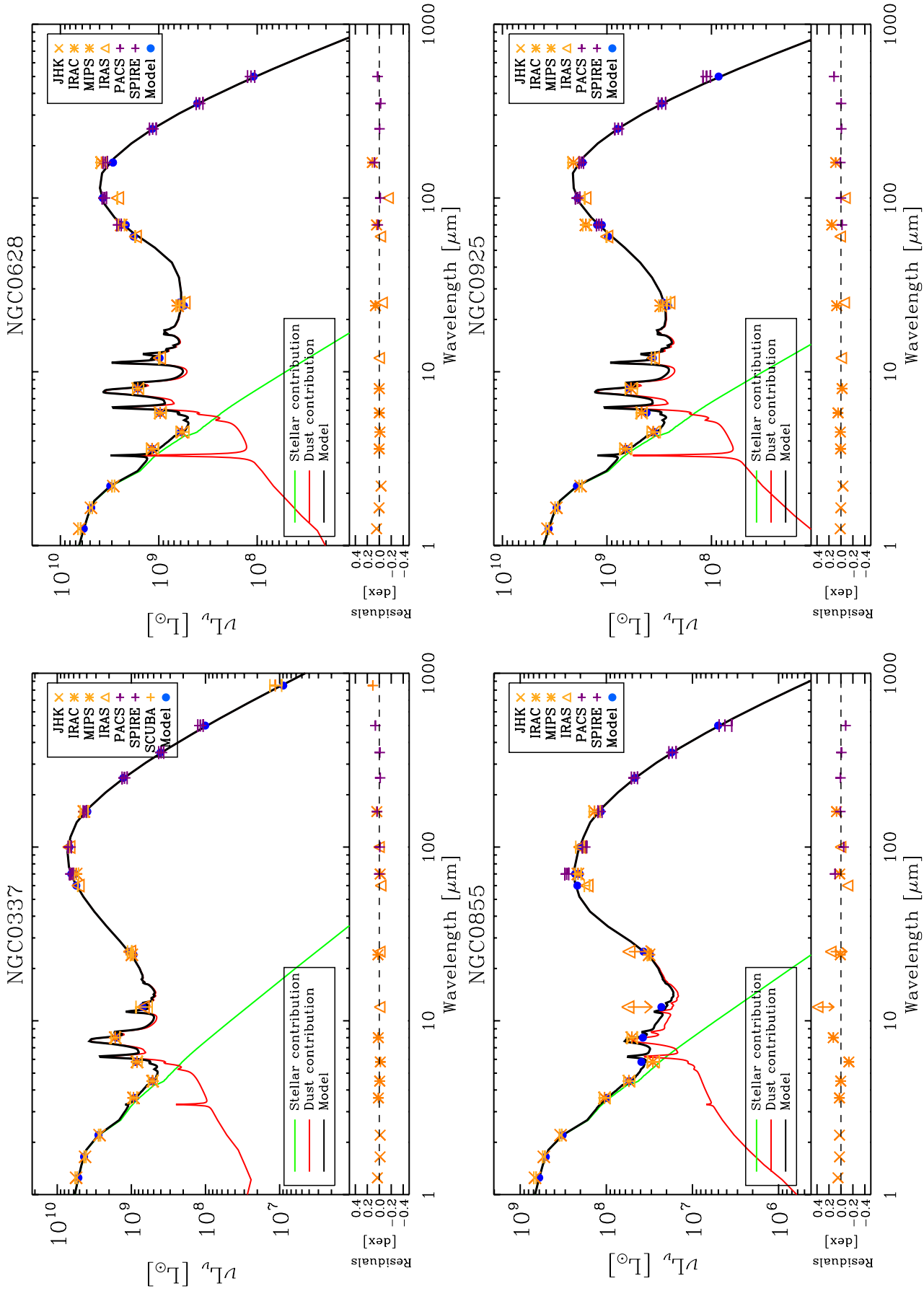

Fig. 7.24. Same as Fig. 7.23 for NGC0337 *(top left)*, NGC0628 *(top right)*, NGC0855 *(bottom left)*, NGC0925 *(bottom right)*.

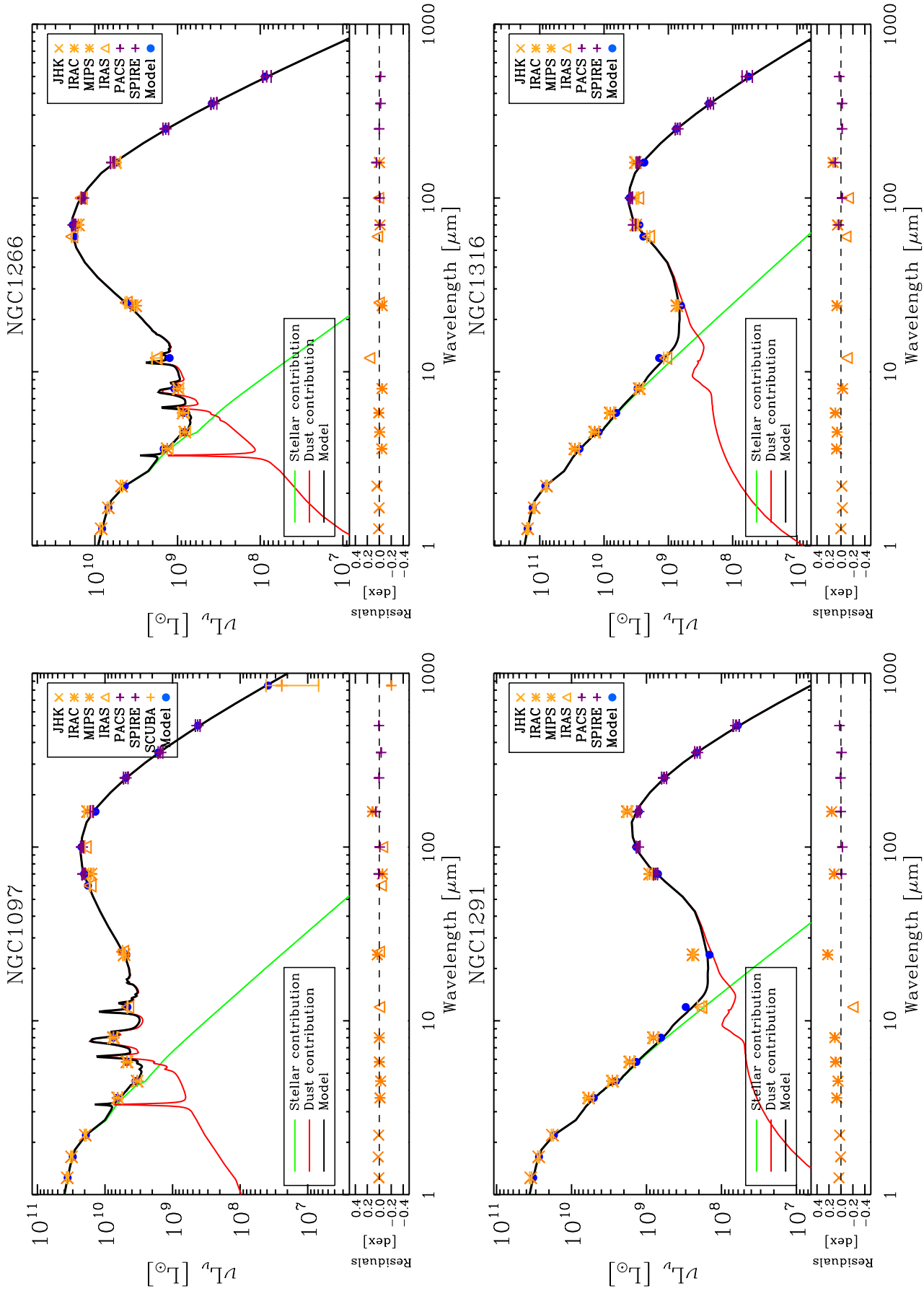

Fig. 7.24. (continued) for NGC1097 *(top left)*, NGC1266 *(top right)*, NGC1291 *(bottom left)*, NGC1316 *(bottom right)*.

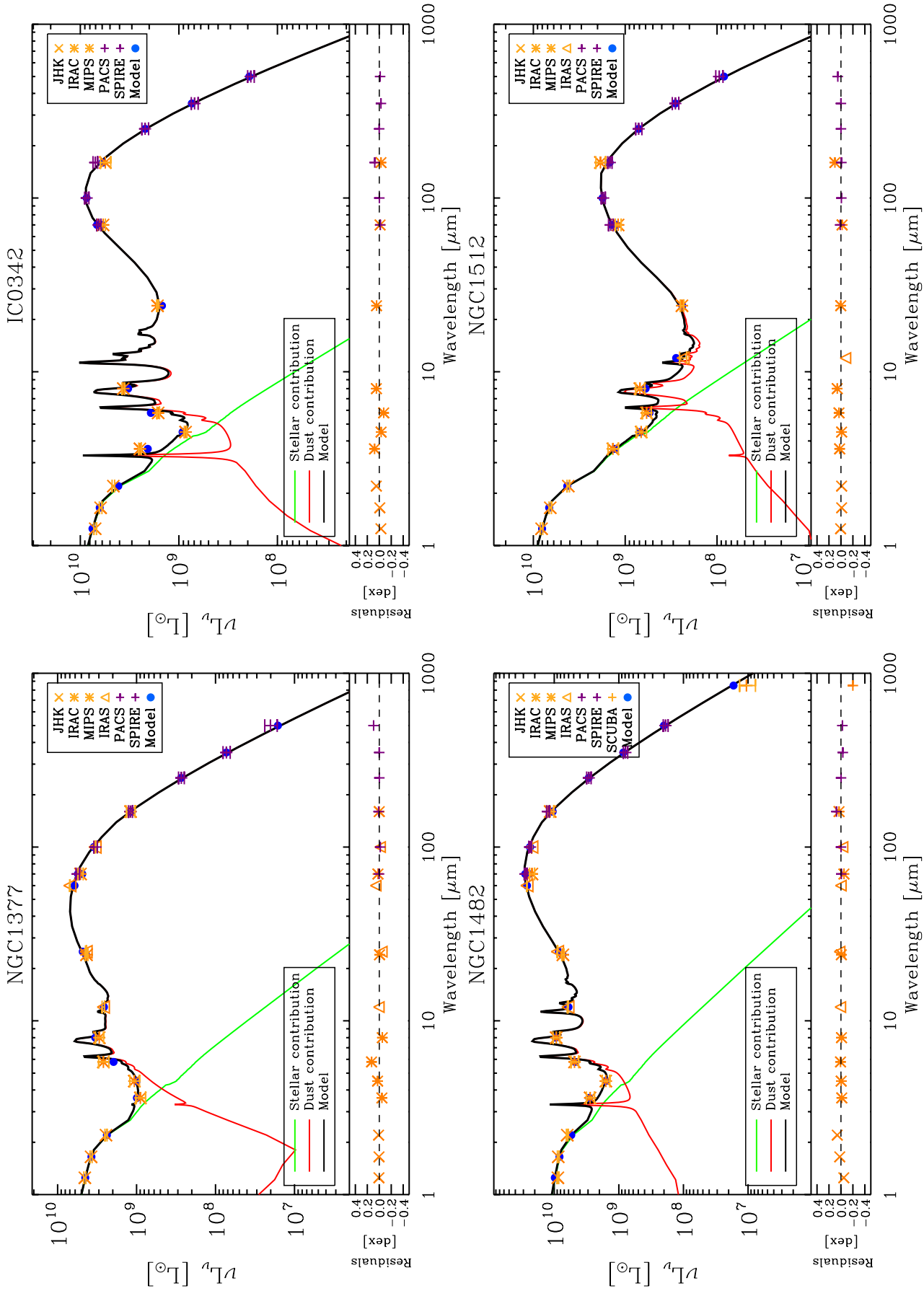

Fig. 7.24. (continued) for NGC1377 *(top left)*, IC0342 *(top right)*, NGC1482 *(bottom left)*, NGC1512 *(bottom right)*.

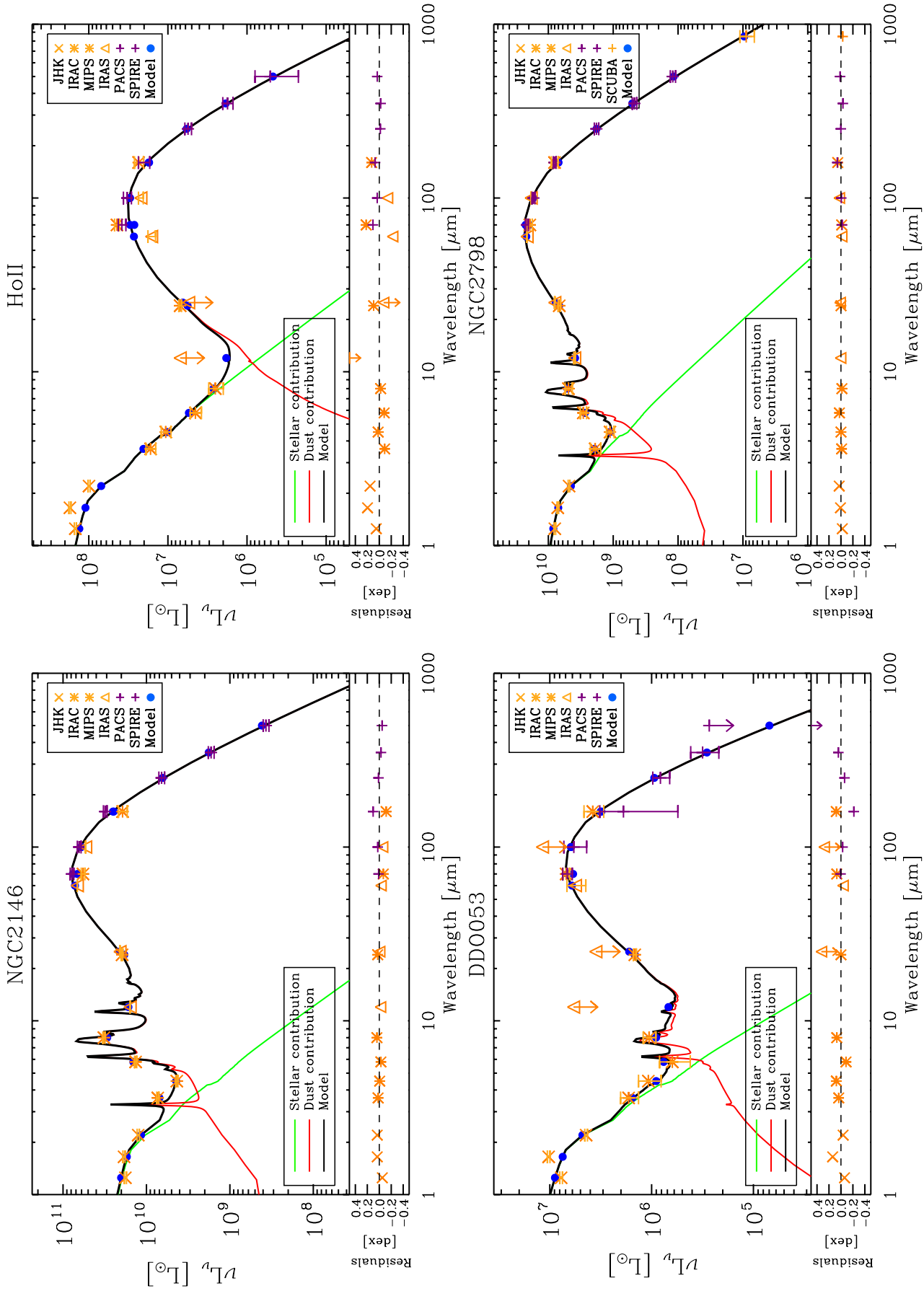

Fig. 7.24. (continued) for NGC2146 *(top left)*, HoII *(top right)*, DDO053 *(bottom left)*, NGC2798 *(bottom right)*.

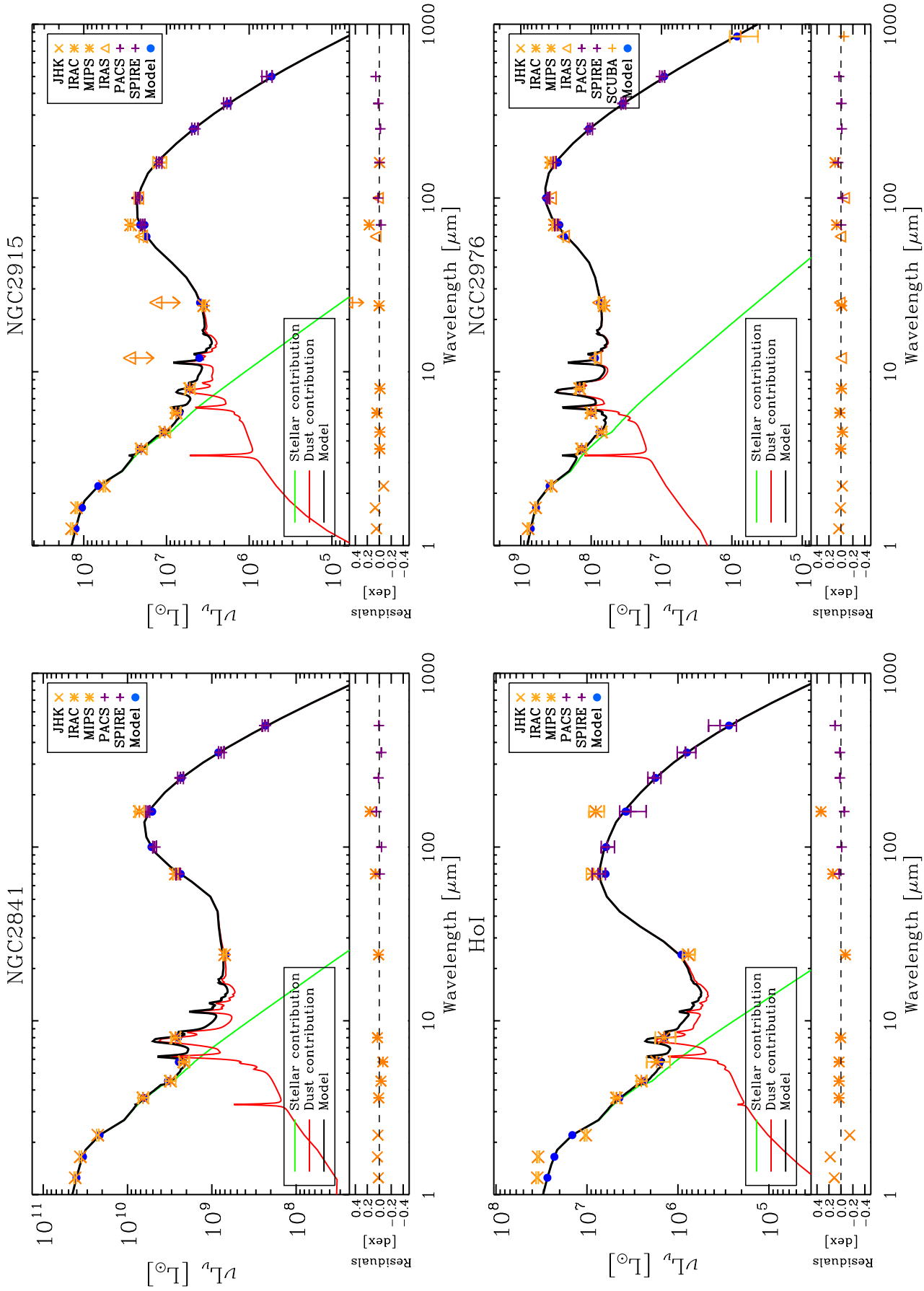

Fig. 7.24. (continued) for NGC2841 *(top left)*, NGC2915 *(top right)*, HoI *(bottom left)*, NGC2976 *(bottom right)*.

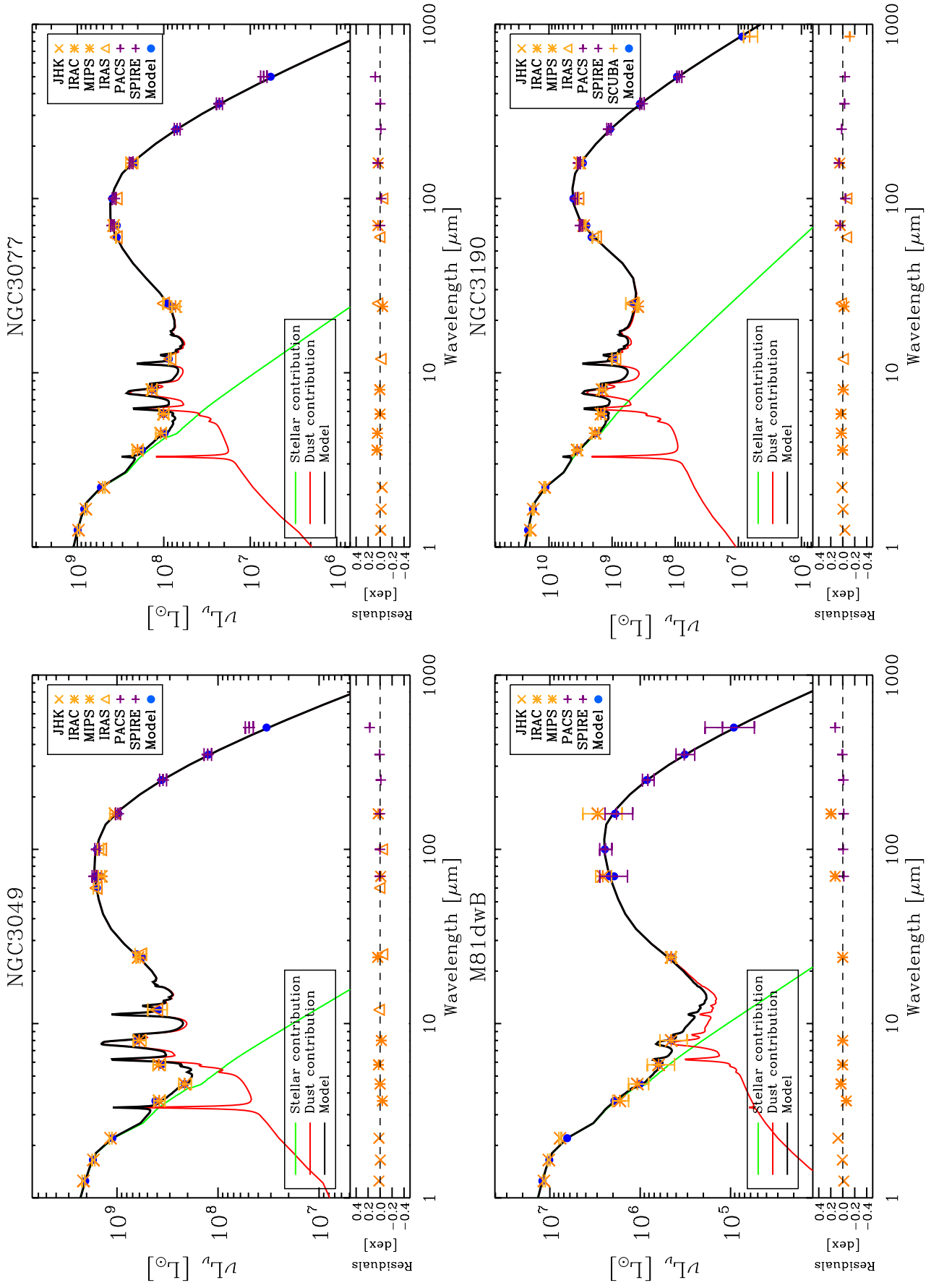

Fig. 7.24. (continued) for NGC3049 *(top left)*, NGC3077 *(top right)*, M81dwB *(bottom left)*, NGC3190 *(bottom right)*.

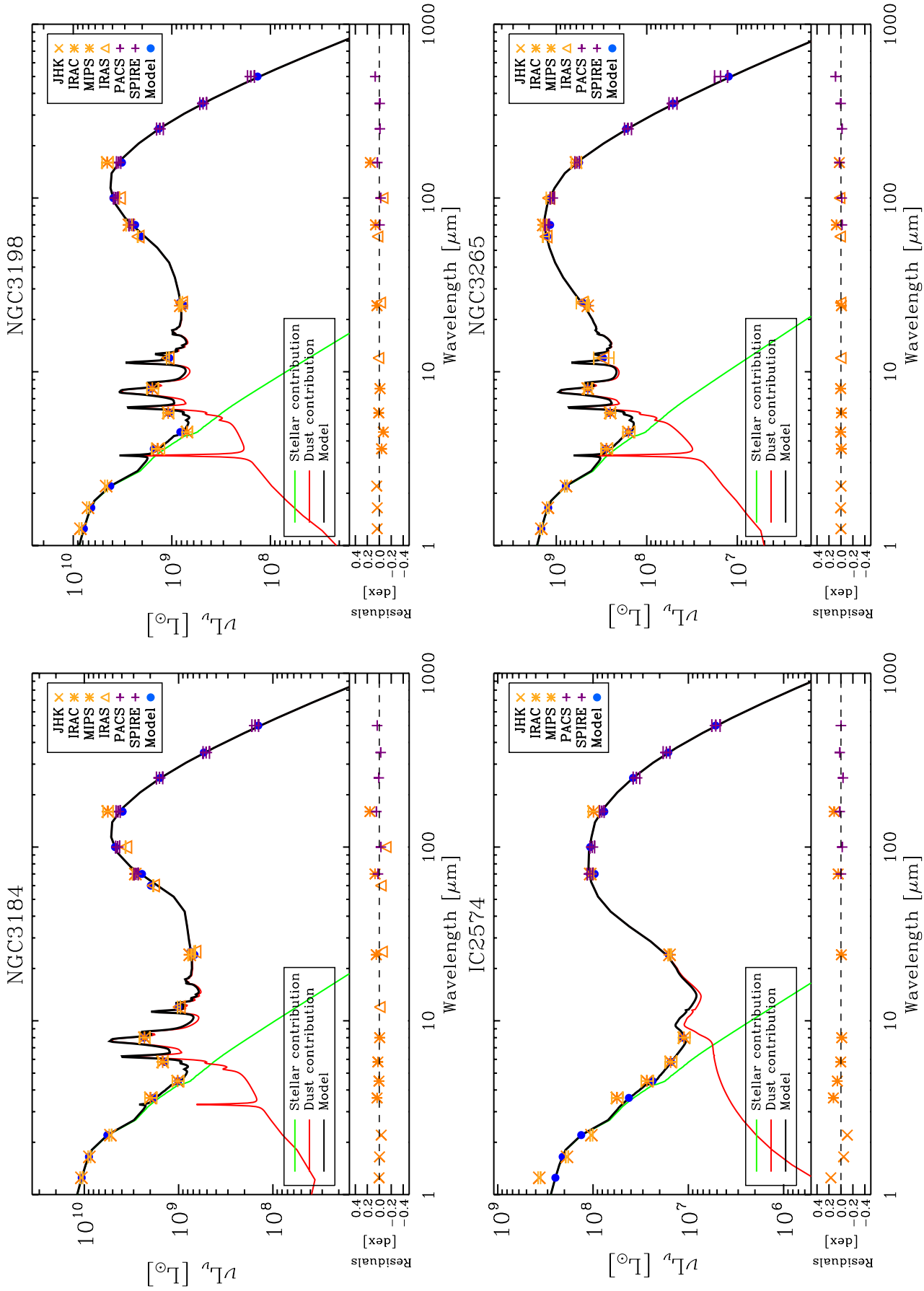

Fig. 7.24. (continued) for NGC3184 *(top left)*, NGC3198 *(top right)*, IC2574 *(bottom left)*, NGC3265 *(bottom right)*.

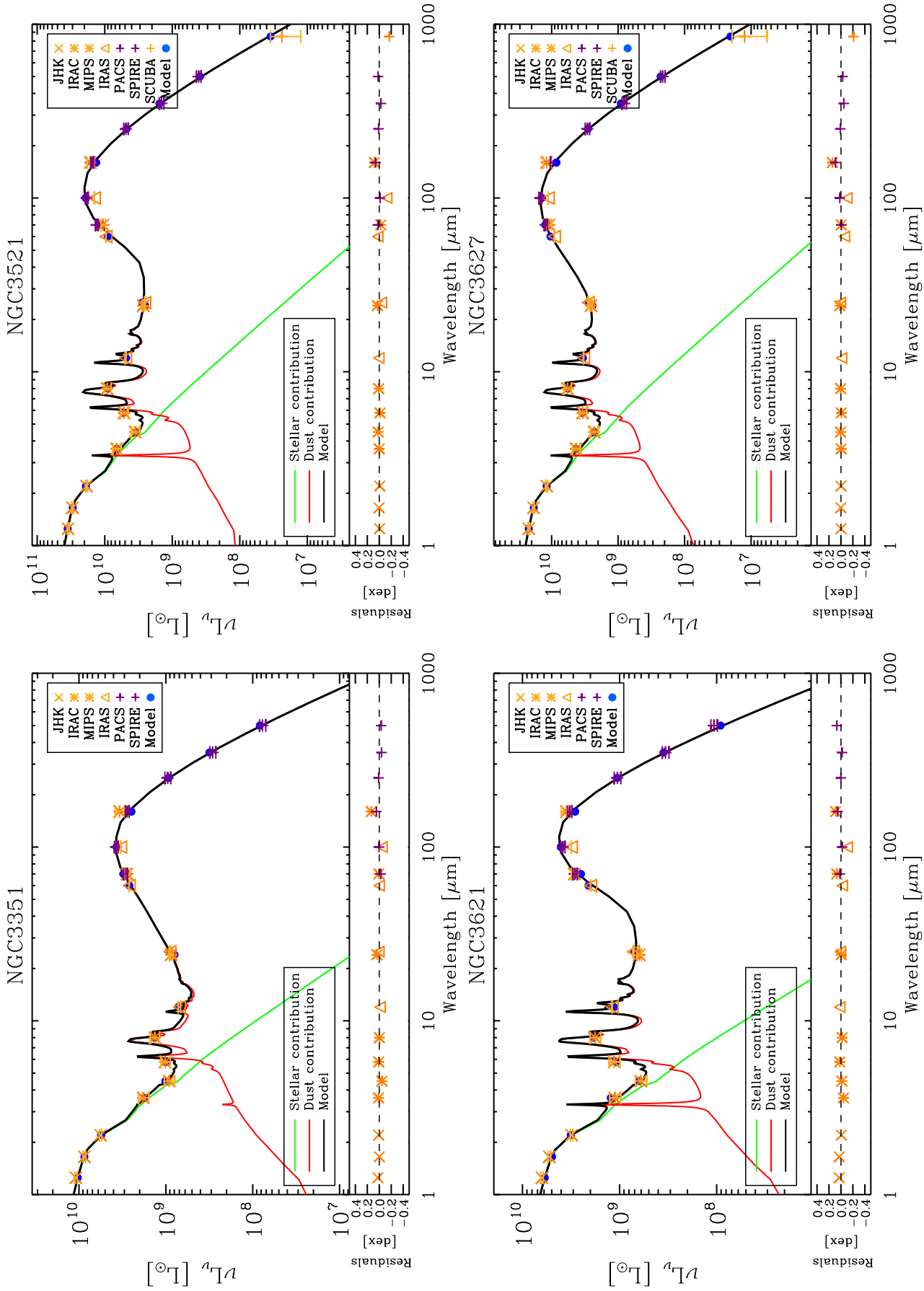

Fig. 7.24. (continued) for NGC3351 *(top left)*, NGC3521 *(top right)*, NGC3621 *(bottom left)*, NGC3627 *(bottom right)*.

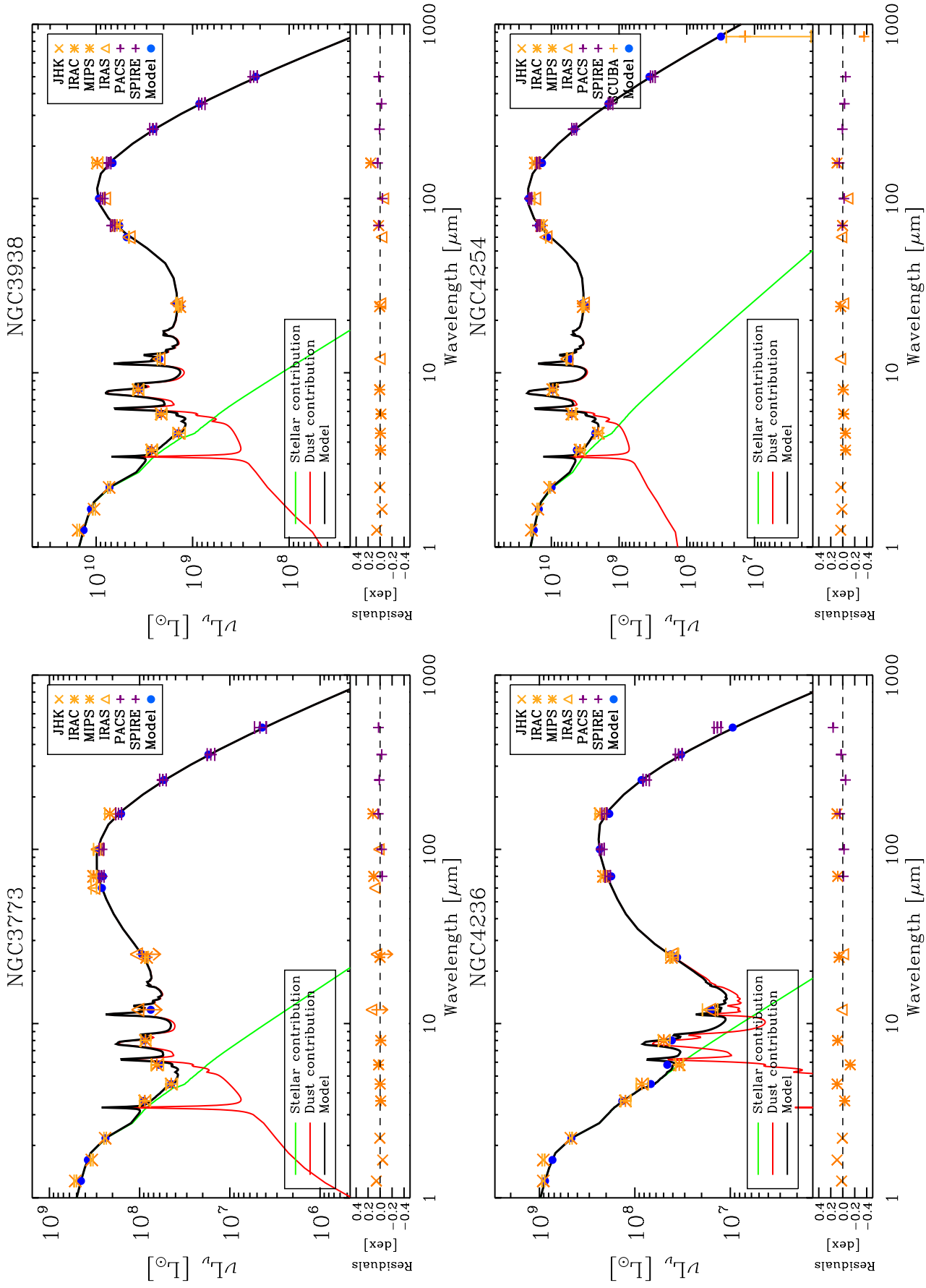

Fig. 7.24. (continued) for NGC3773 *(top left)*, NGC3938 *(top right)*, NGC4236 *(bottom left)*, NGC4254 *(bottom right)*.

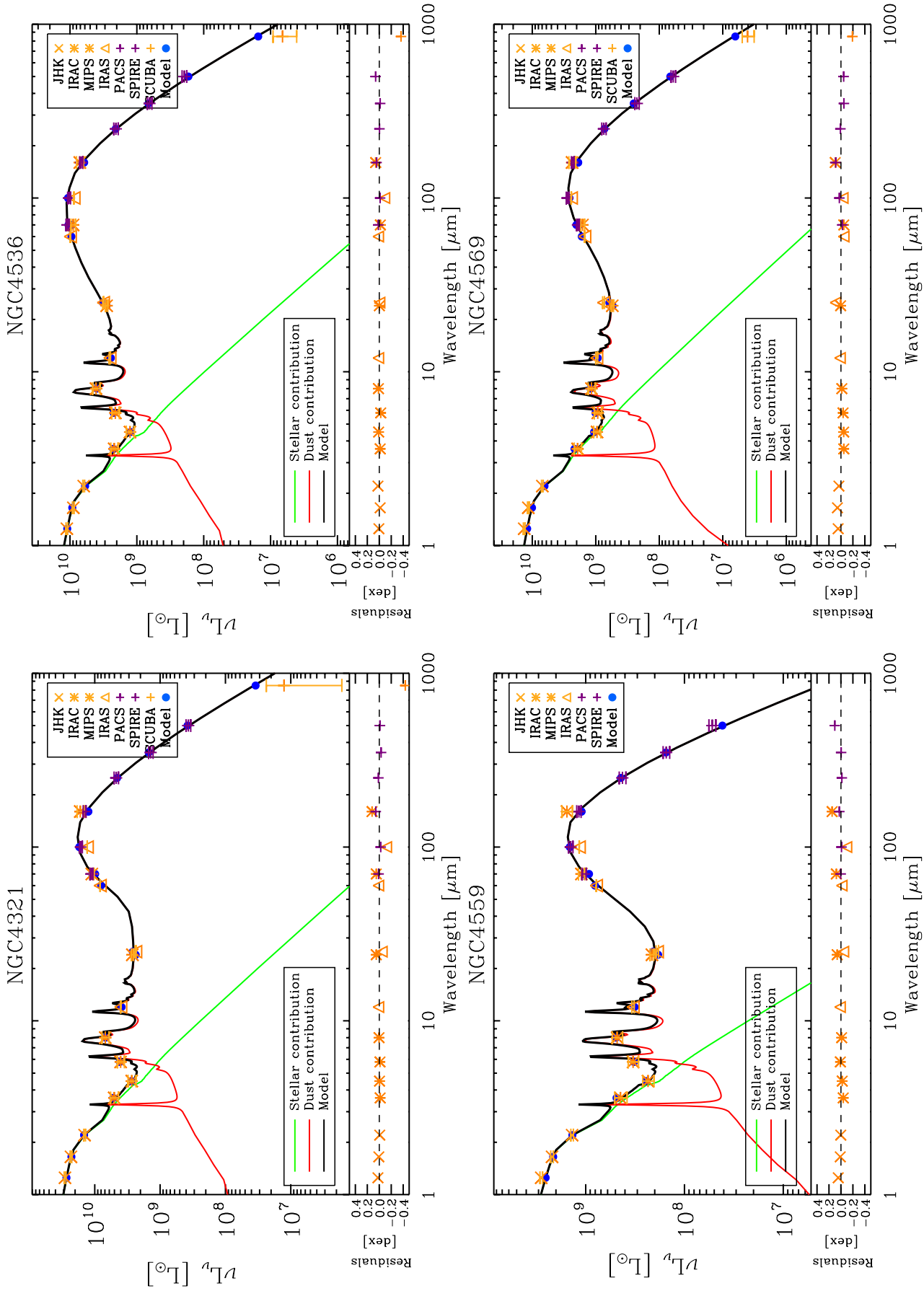

Fig. 7.24. (continued) for NGC4321 *(top left)*, NGC4536 *(top right)*, NGC4559 *(bottom left)*, NGC4569 *(bottom right)*.

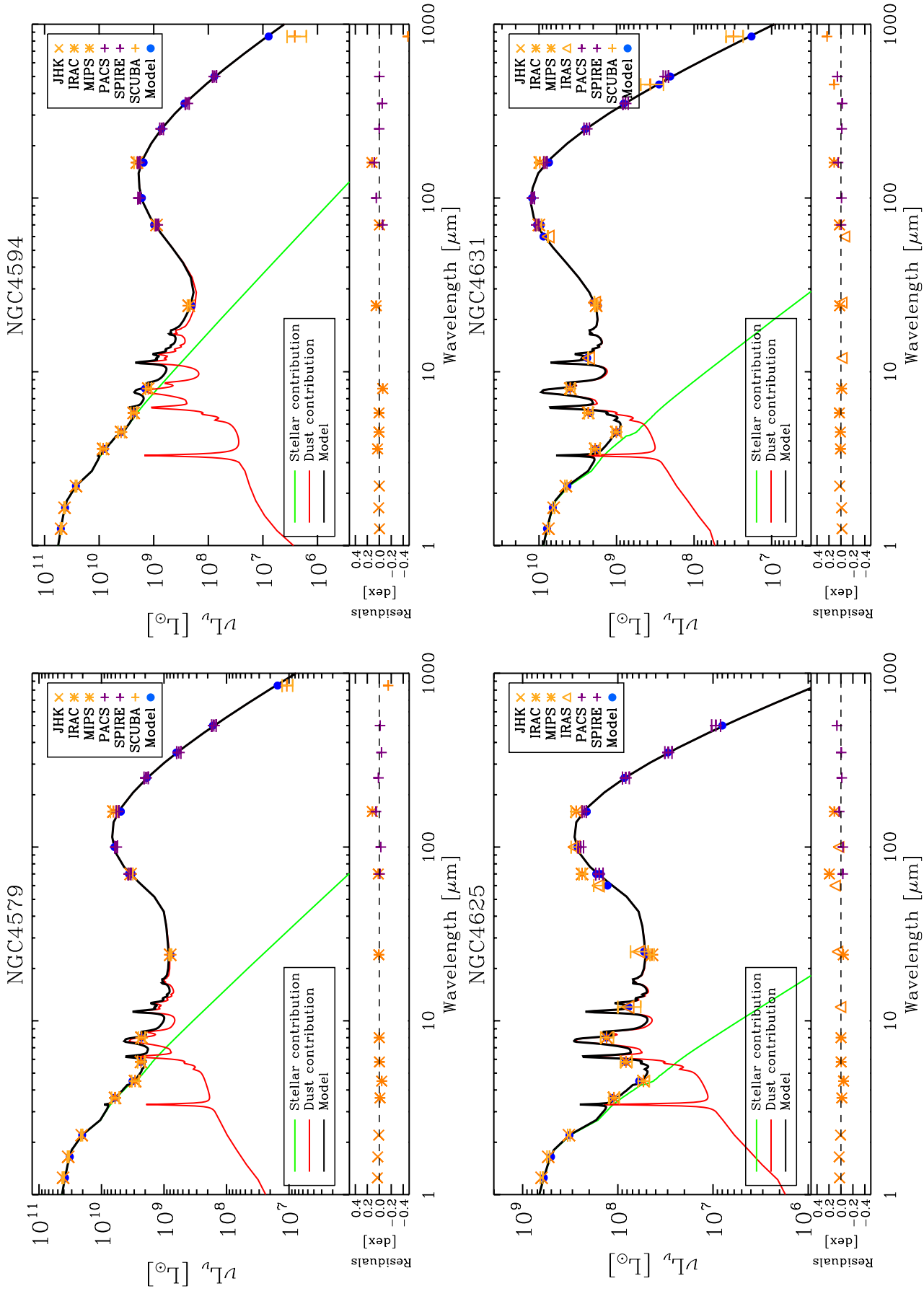

Fig. 7.24. (continued) for NGC4579 *(top left)*, NGC4594 *(top right)*, NGC4625 *(bottom left)*, NGC4631 *(bottom right)*.

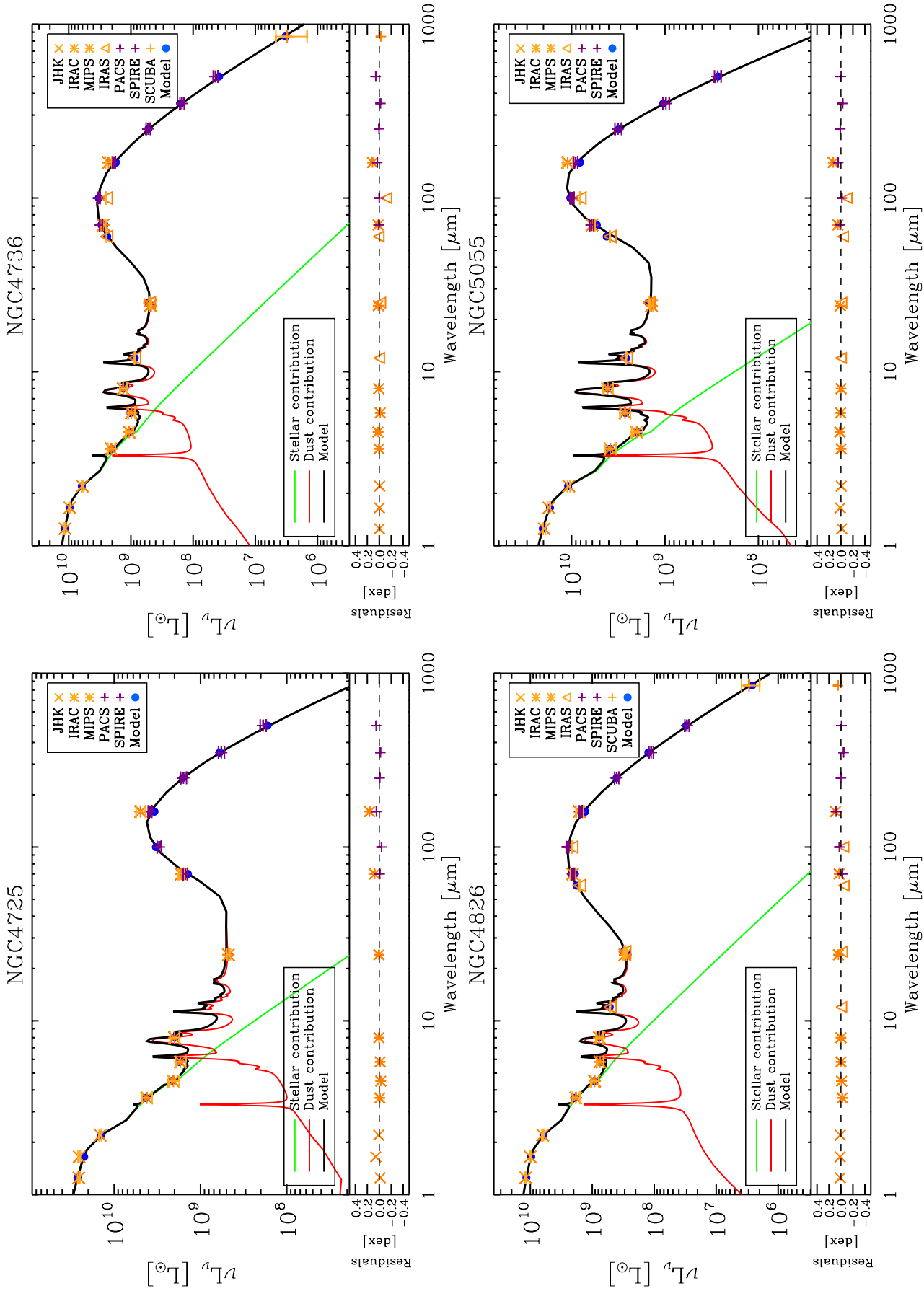

Fig. 7.24. (continued) for NGC4725 *(top left)*, NGC4736 *(top right)*, NGC4826 *(bottom left)*, NGC5055 *(bottom right)*.

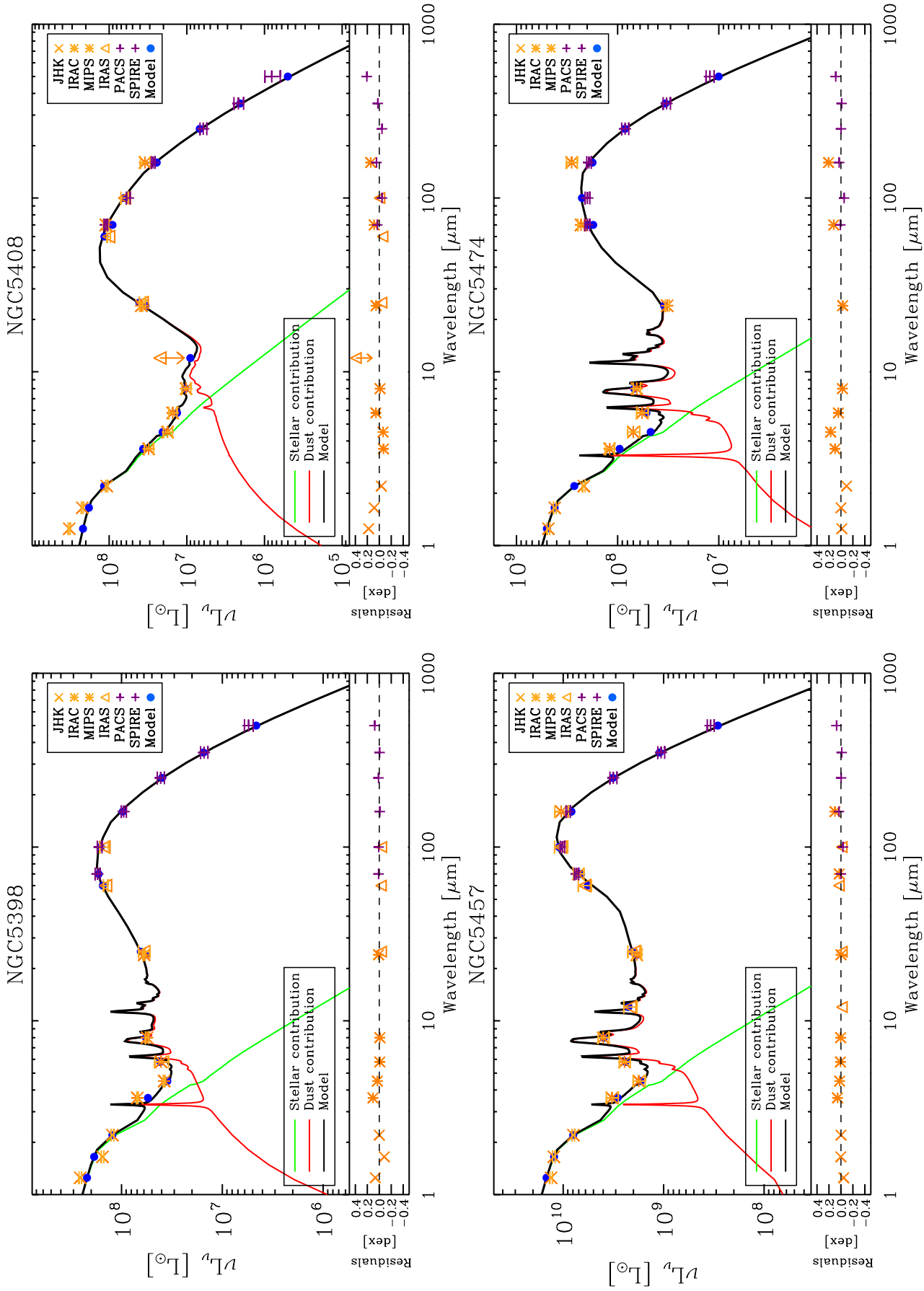

Fig. 7.24. (continued) for NGC5398 *(top left)*, NGC5408 *(top right)*, NGC5457 *(bottom left)*, NGC5474 *(bottom right)*.

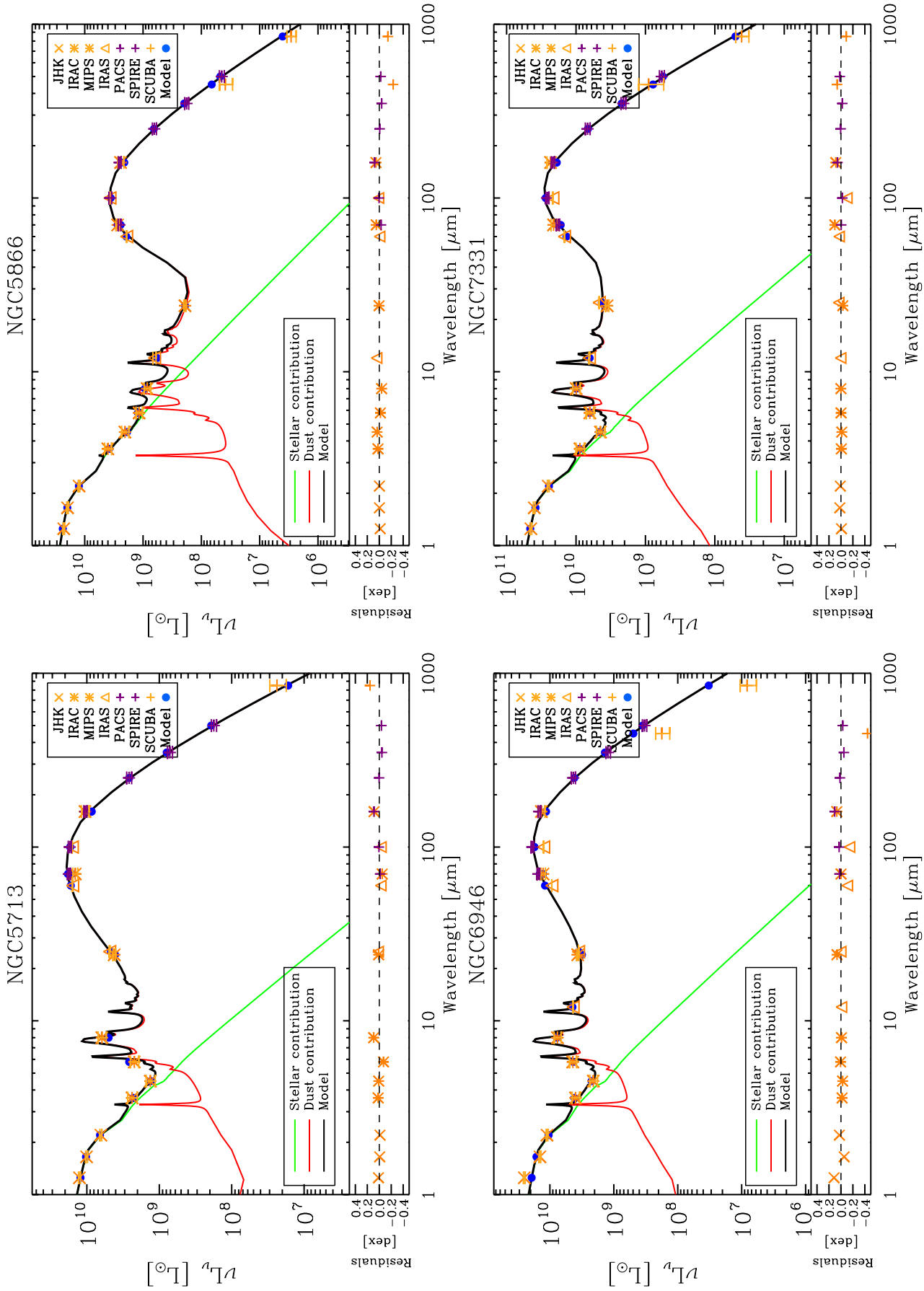

Fig. 7.24. (continued) for NGC5713 *(top left)*, NGC5866 *(top right)*, NGC6946 *(bottom left)*, NGC7331 *(bottom right)*.

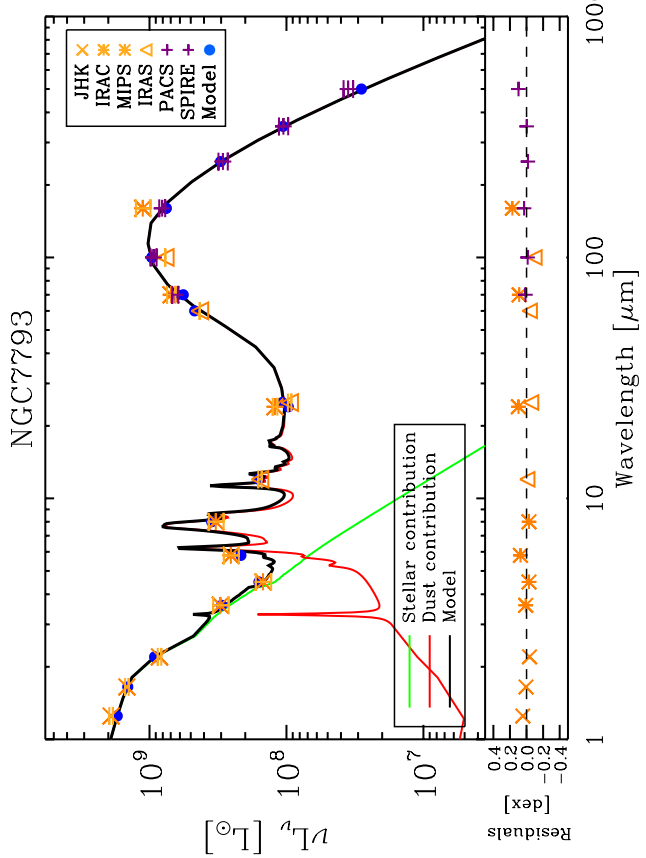

Fig. 7.24. (continued) for NGC7793 *(top left)*.

Table 7.3. SED parameters: M_{dust}, L_{TIR}, SFR, $< U >$, U_{min}, ΔU and α for the DGS sample.

Source	M_{dust} $[M_\odot]$	L_{TIR} $[L_\odot]$	SFR $[\mathrm{M_\odot\,yr^{-1}}]$	$< U >$	U_{min}	ΔU	α
Haro11	$9.9^{+1.0}_{-0.8} \times 10^6$	$2.0^{+0.04}_{-0.04} \times 10^{11}$	$3.4^{+0.08}_{-0.07} \times 10^1$	$1.4^{+0.2}_{-0.2} \times 10^2$	$11.60^{+2.24}_{-2.6}$	$3.6^{+3.4}_{-1.6} \times 10^5$	$1.96^{+0.01}_{-0.02}$
Haro2	$1.7^{+0.2}_{-0.2} \times 10^6$	$6.4^{+0.13}_{-0.14} \times 10^9$	$1.1^{+0.02}_{-0.02}$	$2.3^{+0.3}_{-0.2} \times 10^1$	$3.03^{+0.50}_{-0.4}$	$7.3^{+2.0}_{-2.0} \times 10^5$	$2.10^{+0.01}_{-0.01}$
Haro3	$2.3^{+0.3}_{-0.2} \times 10^6$	$5.4^{+0.13}_{-0.16} \times 10^9$	$9.3^{+0.22}_{-0.28} \times 10^{-1}$	$1.5^{+0.2}_{-0.2} \times 10^1$	$2.03^{+0.36}_{-0.4}$	$6.3^{+6.3}_{-1.8} \times 10^5$	$2.11^{+0.02}_{-0.02}$
He2-10	$1.6^{+0.2}_{-0.2} \times 10^6$	$5.5^{+0.13}_{-0.12} \times 10^9$	$9.5^{+0.22}_{-0.22} \times 10^{-1}$	$2.3^{+0.3}_{-0.2} \times 10^1$	$2.21^{+0.45}_{-0.3}$	$3.7^{+0.6}_{-0.5} \times 10^5$	$2.03^{+0.02}_{-0.01}$
HS0017+1055	$8.3^{+7.9}_{-2.8} \times 10^4$	$9.7^{+0.55}_{-0.49} \times 10^8$	$1.7^{+0.09}_{-0.08} \times 10^{-1}$	$8.0^{+5.0}_{-4.5} \times 10^1$	$5.14^{+4.52}_{-3.6}$	$2.9^{+0.5}_{-0.5} \times 10^6$	$1.97^{+0.03}_{-0.04}$
HS0052+2536	$6.6^{+2.4}_{-2.1} \times 10^6$	$1.7^{+0.08}_{-0.08} \times 10^{10}$	$2.9^{+0.14}_{-0.13}$	$1.7^{+0.8}_{-0.4} \times 10^1$	$2.90^{+1.78}_{-1.0}$	$3.4^{+3.0}_{-1.9} \times 10^5$	$2.18^{+0.04}_{-0.05}$
HS0822+3542	$6.2^{+4.2}_{-1.9} \times 10^3$	$1.1^{+0.10}_{-0.09} \times 10^7$	$1.8^{+0.18}_{-0.15} \times 10^{-3}$	$1.1^{+0.5}_{-0.5} \times 10^1$	$1.92^{+1.34}_{-1.0}$	$1.1^{+0.5}_{-0.2} \times 10^5$	$2.17^{+0.06}_{-0.06}$
HS1222+3741	$8.0^{+2.9}_{-2.6} \times 10^5$	$2.4^{+0.17}_{-0.24} \times 10^9$	$4.2^{+0.30}_{-0.42} \times 10^{-1}$	$1.9^{+0.9}_{-0.5} \times 10^1$	$1.96^{+1.07}_{-0.5}$	$9.3^{+3.6}_{-2.4} \times 10^5$	$2.05^{+0.03}_{-0.03}$
HS1236+3937	-	-	-	-	-	-	-
HS1304+3529	$4.0^{+2.5}_{-2.2} \times 10^6$	$1.7^{+0.09}_{-0.07} \times 10^9$	$3.0^{+0.15}_{-0.13} \times 10^{-1}$	$2.6^{+15.4}_{-1.6}$	$0.01^{+3.90}_{-0.0}$	$3.0^{+12.5}_{-0.8} \times 10^2$	$1.44^{+0.67}_{-0.16}$
HS1319+3224	$2.9^{+14.8}_{-2.3} \times 10^4$	$2.4^{+0.24}_{-0.26} \times 10^8$	$4.1^{+0.42}_{-0.45} \times 10^{-2}$	$4.2^{+5.9}_{-3.4} \times 10^1$	$7.73^{+12.10}_{-4.8}$	$1.2^{+33.8}_{-8.8} \times 10^5$	$2.18^{+0.08}_{-0.09}$
HS1330+3651	$1.3^{+0.3}_{-0.2} \times 10^6$	$1.4^{+0.06}_{-0.06} \times 10^9$	$2.4^{+0.10}_{-0.10} \times 10^{-1}$	$6.9^{+1.7}_{-1.5}$	$1.31^{+0.39}_{-0.3}$	$2.5^{+3.9}_{-1.3} \times 10^4$	$2.19^{+0.03}_{-0.04}$
HS1442+4250	-	-	-	-	-	-	-
HS2352+2733	-	-	-	-	-	-	-
IZw18	$5.1^{+1.1}_{-0.7} \times 10^2$	$3.3^{+0.20}_{-0.19} \times 10^7$	$5.8^{+0.34}_{-0.33} \times 10^{-3}$	$3.9^{+0.3}_{-0.8} \times 10^2$	$383.54^{+24.81}_{-107.9}$	$2.1^{+7.6}_{-1.6} \times 10^1$	$1.00^{+0.001}_{-0.00}$
IC10	$2.8^{+1.1}_{-0.8} \times 10^5$	$1.7^{+0.06}_{-0.07} \times 10^8$	$2.9^{+0.11}_{-0.13} \times 10^{-2}$	$3.9^{+1.4}_{-1.1}$	$0.72^{+0.30}_{-0.2}$	$1.0^{+0.2}_{-0.2} \times 10^6$	$2.21^{+0.02}_{-0.02}$
IIZw40	$6.7^{+4.2}_{-1.6} \times 10^5$	$2.9^{+0.10}_{-0.16} \times 10^9$	$5.0^{+0.17}_{-0.27} \times 10^{-1}$	$2.3^{+0.8}_{-1.0} \times 10^1$	$1.98^{+2.00}_{-1.4}$	$1.3^{+4.3}_{-0.9} \times 10^4$	$1.92^{+0.16}_{-0.29}$
Mrk1089	$2.6^{+0.4}_{-0.3} \times 10^7$	$3.6^{+0.10}_{-0.10} \times 10^{10}$	$6.2^{+0.17}_{-0.17}$	$8.6^{+1.4}_{-1.1}$	$1.45^{+0.31}_{-0.3}$	$6.8^{+2.9}_{-1.9} \times 10^4$	$2.16^{+0.03}_{-0.03}$
Mrk1450	$5.0^{+18.9}_{-1.9} \times 10^4$	$3.0^{+0.10}_{-0.08} \times 10^8$	$5.2^{+0.16}_{-0.14} \times 10^{-2}$	$3.1^{+2.0}_{-2.7} \times 10^1$	$1.88^{+6.78}_{-2.6}$	$1.1^{+7.0}_{-0.4} \times 10^3$	$1.63^{+0.44}_{-0.21}$
Mrk153	$1.7^{+0.4}_{-0.3} \times 10^5$	$1.0^{+0.04}_{-0.04} \times 10^9$	$1.8^{+0.07}_{-0.06} \times 10^{-1}$	$7.0^{+1.9}_{-1.6} \times 10^1$	$15.48^{+6.49}_{-4.8}$	$1.1^{+0.6}_{-0.3} \times 10^5$	$2.25^{+0.05}_{-0.05}$
Mrk209	$4.6^{+2.1}_{-1.4} \times 10^3$	$2.8^{+0.16}_{-0.13} \times 10^7$	$4.9^{+0.27}_{-0.23} \times 10^{-3}$	$4.1^{+2.0}_{-1.4} \times 10^1$	$5.28^{+4.09}_{-2.5}$	$1.9^{+1.2}_{-0.8} \times 10^5$	$2.07^{+0.06}_{-0.06}$
Mrk930	$6.0^{+0.9}_{-5.6} \times 10^6$	$1.9^{+0.13}_{-0.08} \times 10^{10}$	$3.3^{+0.22}_{-0.14}$	$1.9^{+0.3}_{-0.7} \times 10^1$	$3.18^{+0.56}_{-0.6}$	$3.6^{+0.3}_{-1.9} \times 10^4$	$2.15^{+0.34}_{-0.04}$
NGC1140	$3.9^{+0.5}_{-0.5} \times 10^6$	$3.7^{+0.13}_{-0.12} \times 10^9$	$6.5^{+0.23}_{-0.22} \times 10^{-1}$	$6.1^{+0.8}_{-0.8}$	$1.07^{+0.22}_{-0.2}$	$7.7^{+4.5}_{-2.1} \times 10^4$	$2.18^{+0.02}_{-0.02}$
NGC1569	$2.9^{+0.5}_{-0.4} \times 10^5$	$1.3^{+0.03}_{-0.03} \times 10^9$	$2.2^{+0.05}_{-0.06} \times 10^{-1}$	$2.4^{+0.4}_{-0.4} \times 10^1$	$5.53^{+1.46}_{-1.9}$	$1.1^{+0.8}_{-0.7} \times 10^4$	$2.23^{+0.06}_{-0.13}$
NGC1705	$1.3^{+0.8}_{-0.7} \times 10^5$	$6.9^{+0.31}_{-0.39} \times 10^7$	$1.2^{+0.05}_{-0.07} \times 10^{-2}$	$3.6^{+4.1}_{-1.6}$	$0.18^{+1.58}_{-0.2}$	$4.6^{+230.1}_{-1.3} \times 10^2$	$1.73^{+0.52}_{-0.10}$
NGC2366	$1.2^{+0.5}_{-0.3} \times 10^5$	$1.4^{+0.06}_{-0.06} \times 10^8$	$2.4^{+0.10}_{-0.10} \times 10^{-2}$	$8.0^{+2.8}_{-2.3}$	$0.61^{+0.62}_{-0.3}$	$1.2^{+1.9}_{-0.5} \times 10^4$	$1.93^{+0.11}_{-0.08}$
NGC4214	$1.7^{+0.5}_{-0.4} \times 10^6$	$5.4^{+0.16}_{-0.15} \times 10^8$	$9.4^{+0.28}_{-0.27} \times 10^{-2}$	$2.0^{+0.6}_{-0.5}$	$0.31^{+0.15}_{-0.1}$	$3.3^{+7.4}_{-3.3} \times 10^3$	$2.10^{+0.07}_{-0.06}$
NGC4449	$3.0^{+0.3}_{-0.3} \times 10^6$	$2.2^{+0.06}_{-0.07} \times 10^9$	$3.8^{+0.10}_{-0.11} \times 10^{-1}$	$4.6^{+0.6}_{-0.5}$	$1.05^{+0.17}_{-0.1}$	$4.7^{+1.1}_{-1.1} \times 10^4$	$2.28^{+0.02}_{-0.02}$
NGC4861	$6.0^{+1.9}_{-1.2} \times 10^5$	$3.5^{+0.11}_{-0.12} \times 10^8$	$6.0^{+0.20}_{-0.21} \times 10^{-2}$	$3.8^{+1.1}_{-0.9}$	$0.20^{+0.09}_{-0.1}$	$1.6^{+0.9}_{-0.5} \times 10^4$	$1.90^{+0.03}_{-0.04}$
NGC5253	$5.6^{+1.6}_{-0.9} \times 10^5$	$1.6^{+0.03}_{-0.03} \times 10^9$	$2.8^{+0.05}_{-0.05} \times 10^{-1}$	$1.4^{+0.3}_{-0.3} \times 10^1$	$2.38^{+1.03}_{-1.2}$	$5.6^{+10.4}_{-3.8} \times 10^3$	$2.12^{+0.10}_{-0.18}$
NGC625	$4.5^{+0.8}_{-0.7} \times 10^5$	$2.9^{+0.07}_{-0.08} \times 10^8$	$5.0^{+0.12}_{-0.15} \times 10^{-2}$	$4.1^{+0.8}_{-0.7}$	$0.55^{+0.13}_{-0.1}$	$7.0^{+6.8}_{-4.2} \times 10^5$	$2.12^{+0.03}_{-0.03}$
NGC6822	$2.3^{+3.8}_{-1.5} \times 10^5$	$3.6^{+0.20}_{-0.18} \times 10^7$	$6.3^{+0.35}_{-0.31} \times 10^{-3}$	$1.0^{+1.1}_{-0.6}$	$0.08^{+0.18}_{-0.1}$	$3.9^{+4.3}_{-1.9} \times 10^3$	$1.97^{+0.09}_{-0.09}$

Table 7.3. SED parameters: M_{dust}, L_{TIR}, SFR, $< U >$, U_{min}, ΔU and α for the DGS sample.

Source	M_{dust} $[M_\odot]$	L_{TIR} $[L_\odot]$	SFR $[\mathrm{M_\odot\ yr^{-1}}]$	$< U >$	U_{min}	ΔU	α
Pox186	$1.9^{+1.9}_{-0.7} \times 10^5$	$5.7^{+0.31}_{-0.37} \times 10^7$	$9.9^{+0.53}_{-0.64} \times 10^{-3}$	$3.4^{+8.7}_{-1.2} \times 10^1$	$3.44^{+1.90}_{-0.1}$	$4.6^{+0.4}_{-0.1} \times 10^4$	$1.99^{+0.28}_{-0.71}$
SBS0335-052	$3.1^{+160.0}_{-4.5} \times 10^3$	$1.8^{+0.03}_{-0.06} \times 10^9$	$3.0^{+0.06}_{-0.11} \times 10^{-1}$	$1.1^{+0.3}_{-0.3} \times 10^3$	$1070.37^{+5.39}_{-0.0}$	$1.0^{+1429.7}_{-3248.6}$	$1.00^{+0.69}_{-0.00}$
SBS1159+545	$3.0^{+6.8}_{-2.1} \times 10^4$	$2.0^{+0.09}_{-0.10} \times 10^8$	$3.5^{+0.15}_{-0.16} \times 10^{-2}$	$4.6^{+3.3}_{-2.4} \times 10^1$	$3.33^{+3.65}_{-1.9}$	$1.2^{+0.3}_{-0.3} \times 10^6$	$1.99^{+0.05}_{-0.04}$
SBS1211+540	$1.8^{+0.9}_{-0.9} \times 10^4$	$2.9^{+0.17}_{-0.15} \times 10^7$	$4.9^{+0.30}_{-0.26} \times 10^{-3}$	$1.0^{+1.2}_{-0.4} \times 10^1$	$0.02^{+0.02}_{-0.02}$	$1.4^{+0.3}_{-0.3} \times 10^3$	$1.42^{+0.08}_{-0.11}$
SBS1249+493	$4.2^{+1.7}_{-1.0} \times 10^5$	$9.3^{+0.88}_{-0.71} \times 10^8$	$1.6^{+0.15}_{-0.12} \times 10^{-1}$	$1.4^{+0.6}_{-0.7} \times 10^1$	$2.30^{+1.03}_{-1.1}$	$4.8^{+1.8}_{-0.8} \times 10^5$	$2.16^{+0.04}_{-0.03}$
SBS1415+437	$6.4^{+1.2}_{-1.1} \times 10^3$	$6.5^{+0.27}_{-0.31} \times 10^7$	$1.1^{+0.05}_{-0.05} \times 10^{-2}$	$6.9^{+1.4}_{-1.0} \times 10^1$	$14.63^{+3.95}_{-3.2}$	$3.2^{+1.0}_{-0.7} \times 10^5$	$2.24^{+0.03}_{-0.03}$
SBS1533+574	$2.0^{+0.5}_{-0.4} \times 10^6$	$1.9^{+0.05}_{-0.07} \times 10^9$	$3.3^{+0.09}_{-0.13} \times 10^{-1}$	$4.4^{+1.1}_{-1.1}$	$0.67^{+0.24}_{-0.2}$	$6.0^{+2.9}_{-2.5} \times 10^3$	$2.10^{+0.05}_{-0.05}$
Tol0618-402	-	-	-	-	-	-	-
Tol1214-277	$1.3^{+2.3}_{-0.7} \times 10^5$	$8.8^{+0.40}_{-0.49} \times 10^8$	$1.5^{+0.07}_{-0.08} \times 10^{-1}$	$8.9^{+4.5}_{-0.6} \times 10^3$	$0.89^{+1.25}_{-0.0}$	$1.0^{+0.9}_{-0.2} \times 10^5$	$1.00^{+0.6}_{-0.2}$
UGC4483	$3.7^{+1.7}_{-1.4} \times 10^2$	$3.1^{+0.25}_{-0.25} \times 10^6$	$5.4^{+0.44}_{-0.44} \times 10^{-4}$	$5.4^{+2.9}_{-1.7} \times 10^1$	$18.27^{+8.03}_{-5.9}$	$4.6^{+14.6}_{-3.3} \times 10^4$	$2.50^{+0.04}_{-1.46}$
UGCA20	-	-	-	-	-	-	-
UM133	$9.5^{+7.3}_{-3.9} \times 10^4$	$7.2^{+0.65}_{-0.59} \times 10^7$	$1.2^{+0.11}_{-0.10} \times 10^{-2}$	$5.1^{+4.0}_{-2.3}$	$0.50^{+0.58}_{-0.3}$	$1.8^{+0.6}_{-0.7} \times 10^5$	$2.04^{+0.05}_{-0.04}$
UM311	$2.0^{+0.4}_{-0.3} \times 10^7$	$5.5^{+0.21}_{-0.20} \times 10^9$	$9.4^{+0.37}_{-0.35} \times 10^{-1}$	$1.6^{+0.3}_{-0.3}$	$0.38^{+0.11}_{-0.1}$	$1.0^{+0.0}_{-0.4} \times 10^7$	$2.30^{+0.05}_{-0.04}$
UM448	$1.8^{+0.1}_{-0.2} \times 10^7$	$8.9^{+0.22}_{-0.26} \times 10^{10}$	$1.5^{+0.04}_{-0.04} \times 10^1$	$3.2^{+0.3}_{-0.2} \times 10^1$	$5.66^{+0.72}_{-0.7}$	$5.7^{+6.6}_{-2.1} \times 10^5$	$2.19^{+0.02}_{-0.02}$
UM461	$2.1^{+1.4}_{-0.7} \times 10^4$	$7.1^{+0.25}_{-0.21} \times 10^7$	$1.2^{+0.04}_{-0.04} \times 10^{-2}$	$2.0^{+0.9}_{-0.9} \times 10^1$	$1.79^{+1.21}_{-1.0}$	$1.3^{+0.3}_{-0.3} \times 10^5$	$2.00^{+0.03}_{-0.04}$
VIIZw403	$7.2^{+1.3}_{-1.1} \times 10^3$	$2.0^{+0.07}_{-0.07} \times 10^7$	$3.5^{+0.12}_{-0.12} \times 10^{-3}$	$1.8^{+0.3}_{-0.3} \times 10^1$	$4.29^{+1.15}_{-1.0}$	$3.6^{+3.9}_{-1.9} \times 10^4$	$2.28^{+0.04}_{-0.05}$

Table 7.4. SED parameters: f_{vsg}, f_{PAH}, f_{ion} and $M_\star$ for the DGS sample.

Source	f_{vsg}	f_{PAH}	f_{ion}	$M_\star$ $[M_\odot]$
Haro11	$1.63^{+0.22}_{-0.38}$	$0.09^{+0.01}_{-0.01}$	1.00	–
Haro2	$0.25^{+0.19}_{-0.19}$	$0.54^{+0.02}_{-0.02}$	1.00	$7.7^{+0.23}_{-0.23} \times 10^{9}$
Haro3	$0.23^{+0.28}_{-0.12}$	$0.36^{+0.02}_{-0.02}$	$0.22^{+0.04}_{-0.05}$	$6.0^{+0.19}_{-0.16} \times 10^{9}$
He2-10	$0.39^{+0.09}_{-0.09}$	$0.48^{+0.03}_{-0.02}$	$0.46^{+0.05}_{-0.04}$	$4.9^{+0.12}_{-0.12} \times 10^{9}$
HS0017+1055	0.00	0.00	0.50	$8.6^{+0.34}_{-0.34} \times 10^{8}$
HS0052+2536	$0.37^{+0.21}_{-0.22}$	$0.18^{+0.07}_{-0.07}$	0.50	$6.2^{+0.25}_{-0.23} \times 10^{9}$
HS0822+3542	$0.31^{+0.10}_{-0.09}$	0.00	0.50	$8.3^{+0.60}_{-0.66} \times 10^{6}$
HS1222+3741	1.00	0.00	0.50	$7.4^{+0.33}_{-0.37} \times 10^{9}$
HS1236+3937	-	-	-	-
HS1304+3529	$1.06^{+0.20}_{-0.24}$	0.00	0.50	$6.1^{+0.27}_{-0.27} \times 10^{8}$
HS1319+3224	$0.90^{+0.91}_{-0.40}$	0.00	0.50	$2.5^{+0.82}_{-1.40} \times 10^{8}$
HS1330+3651	$1.22^{+0.17}_{-0.19}$	0.00	0.50	$2.0^{+0.45}_{-0.48} \times 10^{9}$
HS1442+4250	-	-	-	-
HS2352+2733	-	-	-	-
IZw18	$2.07^{+0.29}_{-0.30}$	0.00	0.50	$7.0^{+0.58}_{-0.45} \times 10^{7}$
IC10	$0.00^{+0.01}_{-0.01}$	$0.29^{+0.01}_{-0.01}$	$0.22^{+0.01}_{-0.01}$	$4.3^{+0.07}_{-0.06} \times 10^{8}$
IIZw40	$0.99^{+0.39}_{-0.33}$	$0.17^{+0.05}_{-0.04}$	0.50	$8.6^{+0.61}_{-0.59} \times 10^{8}$
Mrk1089	$1.23^{+0.22}_{-0.24}$	$0.18^{+0.07}_{-0.07}$	$0.70^{+0.28}_{-0.42}$	$1.3^{+0.04}_{-0.04} \times 10^{10}$
Mrk1450	$0.66^{+0.19}_{-0.26}$	$0.12^{+0.01}_{-0.02}$	$0.04^{+0.19}_{-0.05}$	$1.2^{+0.03}_{-0.03} \times 10^{8}$
Mrk153	$0.93^{+0.08}_{-0.09}$	0.00	0.50	$2.6^{+0.20}_{-0.17} \times 10^{9}$
Mrk209	$0.26^{+0.28}_{-0.24}$	0.00	0.50	$8.7^{+0.88}_{-1.06} \times 10^{7}$
Mrk930	$0.52^{+0.28}_{-0.12}$	$0.07^{+0.03}_{-0.02}$	1.00	$8.1^{+0.79}_{-0.55} \times 10^{9}$
NGC1140	$0.66^{+0.12}_{-0.12}$	$0.47^{+0.02}_{-0.02}$	$0.44^{+0.03}_{-0.03}$	$7.1^{+0.23}_{-0.21} \times 10^{9}$
NGC1569	$0.70^{+0.03}_{-0.03}$	$0.17^{+0.01}_{-0.01}$	$0.25^{+0.03}_{-0.03}$	$1.8^{+0.08}_{-0.10} \times 10^{9}$
NGC1705	$0.60^{+0.08}_{-0.58}$	$0.07^{+0.12}_{-0.05}$	1.00	$4.7^{+0.27}_{-0.28} \times 10^{8}$
NGC2366	$0.46^{+0.57}_{-0.33}$	$0.06^{+0.07}_{-0.08}$	$1.00^{+0.00}_{-0.94}$	$4.8^{+0.29}_{-0.32} \times 10^{8}$
NGC4214	$1.52^{+0.45}_{-0.52}$	$0.27^{+0.16}_{-0.12}$	$0.89^{+0.05}_{-0.70}$	$1.6^{+0.05}_{-0.05} \times 10^{9}$
NGC4449	$0.57^{+0.04}_{-0.03}$	$0.54^{+0.02}_{-0.02}$	$0.78^{+0.01}_{-0.02}$	$5.9^{+0.22}_{-0.26} \times 10^{9}$
NGC4861	$0.91^{+0.20}_{-0.43}$	$0.00^{+0.10}_{-0.01}$	0.00	$6.8^{+1.17}_{-1.20} \times 10^{8}$
NGC5253	$2.40^{+0.11}_{-0.12}$	$0.24^{+0.07}_{-0.05}$	$0.57^{+0.49}_{-0.30}$	$2.0^{+0.07}_{-0.06} \times 10^{9}$
NGC625	$0.76^{+0.63}_{-0.60}$	$0.14^{+0.13}_{-0.10}$	$0.71^{+0.50}_{-0.50}$	$1.2^{+0.04}_{-0.04} \times 10^{9}$
NGC6822	1.00	$0.12^{+0.08}_{-0.06}$	$1.00^{+0.00}_{-1.00}$	$3.4^{+0.32}_{-0.40} \times 10^{8}$
Pox186	$0.46^{+0.45}_{-0.72}$	0.00	0.50	$3.9^{+0.92}_{-1.15} \times 10^{7}$
SBS0335-052	$3.07^{+0.88}_{-0.78}$	0.00	0.50	$4.5^{+0.19}_{-0.25} \times 10^{8}$
SBS1159+545	$0.00^{+0.64}_{-0.05}$	0.00	0.50	$2.7^{+0.35}_{-0.80} \times 10^{8}$
SBS1211+540	$0.69^{+0.06}_{-0.06}$	0.00	0.50	$2.2^{+0.46}_{-0.47} \times 10^{7}$
SBS1249+493	1.00	0.00	0.50	$2.0^{+1.96}_{-1.96} \times 10^{8}$
SBS1415+437	0.00	0.00	0.50	$1.8^{+0.26}_{-0.20} \times 10^{8}$
SBS1533+574	$1.84^{+0.14}_{-0.14}$	$0.17^{+0.01}_{-0.01}$	$0.14^{+0.06}_{-0.07}$	$2.0^{+0.06}_{-0.06} \times 10^{9}$
Tol0618-402	-	-	-	-
Tol1214-277	1.00	0.00	0.50	5.0×10^{8}
UGC4483	$0.79^{+0.20}_{-0.22}$	0.00	0.50	$1.0^{+0.08}_{-0.08} \times 10^{7}$
UGCA20	-	-	-	-
UM133	$0.21^{+0.32}_{-0.18}$	0.00	0.50	$1.6^{+0.24}_{-0.33} \times 10^{8}$
UM311	1.00	$0.78^{+0.22}_{-0.19}$	0.00	$1.5^{+0.31}_{-0.33} \times 10^{10}$
UM448	$0.63^{+0.20}_{-0.20}$	$0.27^{+0.09}_{-0.09}$	$0.36^{+0.34}_{-0.29}$	$5.4^{+0.14}_{-0.16} \times 10^{10}$
UM461	$0.55^{+0.14}_{-0.16}$	0.00	0.50	$9.5^{+0.53}_{-0.55} \times 10^{7}$
VIIZw403	$0.85^{+0.13}_{-0.12}$	0.00	0.50	$2.7^{+0.16}_{-0.14} \times 10^{7}$

When no errors are given, it means that either this parameter was fixed in the fit or that the parameter reached the minimum or maximum value allowed for this parameter. If fixed: $f_{vsg} = 1$, $f_{PAH} = 0.0$, $f_{ion} = 0.5$, and $f_{vsg} \geq 0.0$, $f_{PAH} \geq 0.0$ and $f_{ion} \in [0.0,1.0]$.

Table 7.5. SED parameters: M_{dust}, L_{TIR}, SFR, $< U >$, U_{min}, ΔU and α for the KINGFISH sample.

Source	M_{dust} $[M_\odot]$	L_{TIR} $[L_\odot]$	SFR $[\mathrm{M_\odot\ yr^{-1}}]$	$< U >$	U_{min}	ΔU	α
NGC0337	$1.6^{+0.2}_{-0.1} \times 10^7$	$1.1^{+0.03}_{-0.03} \times 10^{10}$	$2.0^{+0.05}_{-0.05}$	$4.5^{+0.3}_{-0.4} \times 10^1$	$1.22^{+0.18}_{-0.2}$	$8.9^{+1.8}_{-4.7} \times 10^5$	$2.37^{+0.03}_{-0.03}$
NGC0584	-	-	-	-	-	-	-
NGC0628	$2.6^{+0.3}_{-0.3} \times 10^7$	$6.5^{+0.15}_{-0.17} \times 10^9$	$1.1^{+0.03}_{-0.03}$	$1.4^{+0.2}_{-0.2} \times 10^1$	$0.57^{+0.16}_{-0.1}$	$1.8^{+2.2}_{-0.9} \times 10^1$	$2.50^{+0.00}_{-0.00}$
NGC0855	$1.8^{+0.5}_{-0.4} \times 10^6$	$3.9^{+0.09}_{-0.10} \times 10^8$	$6.8^{+0.15}_{-0.17} \times 10^{-2}$	$1.4^{+0.3}_{-0.3} \times 10^1$	$0.09^{+0.04}_{-0.03}$	$4.2^{+1.1}_{-1.0} \times 10^2$	$1.83^{+0.03}_{-0.04}$
NGC0925	$2.5^{+0.5}_{-0.3} \times 10^7$	$3.5^{+0.09}_{-0.10} \times 10^9$	$6.0^{+0.15}_{-0.17} \times 10^{-1}$	$0.8^{+0.1}_{-0.1} \times 10^1$	$0.28^{+0.05}_{-0.1}$	$3.1^{+2.9}_{-1.0} \times 10^2$	$2.50^{+0.01}_{-0.11}$
NGC1097	$8.3^{+0.7}_{-0.6} \times 10^7$	$4.2^{+0.10}_{-0.11} \times 10^{10}$	$7.3^{+0.17}_{-0.19}$	$3.1^{+0.2}_{-0.3} \times 10^1$	$0.72^{+0.22}_{-0.1}$	$1.5^{+0.4}_{-0.3} \times 10^6$	$2.30^{+0.11}_{-0.04}$
NGC1266	$8.4^{+0.7}_{-0.5} \times 10^6$	$2.8^{+0.10}_{-0.09} \times 10^{10}$	$4.9^{+0.17}_{-0.16}$	$21.9^{+1.7}_{-2.3} \times 10^1$	$5.03^{+0.63}_{-0.7}$	$6.1^{+0.8}_{-0.5} \times 10^6$	$2.29^{+0.02}_{-0.02}$
NGC1291	$1.6^{+0.3}_{-0.2} \times 10^7$	$2.2^{+0.07}_{-0.08} \times 10^9$	$3.7^{+0.12}_{-0.14} \times 10^{-1}$	$0.8^{+0.1}_{-0.1} \times 10^1$	$0.33^{+0.09}_{-0.1}$	$1.2^{+24708.6}_{-1.4} \times 10^1$	$2.50^{+0.00}_{-0.28}$
NGC1316	$9.4^{+1.3}_{-0.8} \times 10^6$	$5.9^{+0.19}_{-0.20} \times 10^9$	$1.0^{+0.03}_{-0.03}$	$4.0^{+0.4}_{-0.5} \times 10^1$	$3.55^{+1.45}_{-1.1}$	$1.0^{+971986.8}_{-8.3}$	$2.45^{+0.00}_{-0.52}$
NGC1377	$1.5^{+0.2}_{-0.1} \times 10^6$	$1.4^{+0.04}_{-0.03} \times 10^{10}$	$2.5^{+0.06}_{-0.06}$	$63.8^{+5.5}_{-9.0} \times 10^1$	$5.52^{+0.83}_{-1.1}$	$1.0^{+0.0}_{-0.04} \times 10^7$	$2.04^{+0.01}_{-0.02}$
NGC1404	-	-	-	-	-	-	-
IC0342	$4.0^{+0.3}_{-0.3} \times 10^7$	$1.6^{+0.04}_{-0.04} \times 10^{10}$	$2.8^{+0.07}_{-0.07}$	$2.2^{+0.2}_{-0.2} \times 10^1$	$0.75^{+0.06}_{-0.1}$	$6.4^{+0.9}_{-0.4} \times 10^5$	$2.50^{+0.00}_{-0.00}$
NGC1482	$2.5^{+0.2}_{-0.2} \times 10^7$	$5.1^{+0.13}_{-0.14} \times 10^{10}$	$8.8^{+0.22}_{-0.24}$	$12.2^{+1.1}_{-1.1} \times 10^1$	$2.65^{+0.37}_{-0.3}$	$2.2^{+0.4}_{-0.5} \times 10^6$	$2.27^{+0.02}_{-0.02}$
NGC1512	$3.1^{+1.1}_{-0.6} \times 10^7$	$3.3^{+0.09}_{-0.11} \times 10^9$	$5.7^{+0.16}_{-0.18} \times 10^{-1}$	$0.7^{+0.2}_{-0.2} \times 10^1$	$0.14^{+0.07}_{-0.1}$	$3.4^{+4.0}_{-2.8} \times 10^2$	$2.19^{+0.12}_{-0.18}$
NGC2146	$4.8^{+0.5}_{-0.3} \times 10^7$	$1.3^{+0.03}_{-0.03} \times 10^{11}$	$2.3^{+0.06}_{-0.06} \times 10^1$	$16.5^{+1.4}_{-1.7} \times 10^1$	$4.49^{+0.63}_{-0.7}$	$3.6^{+2.0}_{-1.9} \times 10^5$	$2.37^{+0.03}_{-0.03}$
HoII	$7.6^{+0.7}_{-0.5} \times 10^4$	$5.1^{+0.12}_{-0.13} \times 10^7$	$8.9^{+0.21}_{-0.23} \times 10^{-3}$	$4.6^{+0.3}_{-0.5} \times 10^1$	$0.85^{+0.10}_{-0.1}$	$4.6^{+0.7}_{-0.7} \times 10^5$	$2.21^{+0.02}_{-0.02}$
DDO053	$1.0^{+0.2}_{-0.1} \times 10^4$	$1.1^{+0.03}_{-0.03} \times 10^7$	$2.0^{+0.05}_{-0.05} \times 10^{-3}$	$7.0^{+0.8}_{-0.9} \times 10^1$	$1.67^{+0.34}_{-0.5}$	$5.6^{+1.1}_{-5.5} \times 10^5$	$2.30^{+0.04}_{-0.12}$
NGC2798	$1.2^{+0.1}_{-0.1} \times 10^7$	$4.0^{+0.11}_{-0.11} \times 10^{10}$	$6.9^{+0.19}_{-0.19}$	$20.4^{+1.6}_{-1.8} \times 10^1$	$3.59^{+0.42}_{-0.4}$	$6.1^{+1.1}_{-1.0} \times 10^6$	$2.20^{+0.01}_{-0.01}$
NGC2841	$5.9^{+0.5}_{-0.6} \times 10^7$	$9.0^{+0.32}_{-0.33} \times 10^9$	$1.6^{+0.06}_{-0.06}$	$0.9^{+0.1}_{-0.1} \times 10^1$	$0.60^{+0.07}_{-0.1}$	$1.0^{+0.0}_{-0.0}$	$2.50^{+0.00}_{-0.00}$
NGC2915	$3.4^{+0.8}_{-0.6} \times 10^5$	$3.8^{+0.11}_{-0.11} \times 10^7$	$6.5^{+0.19}_{-0.20} \times 10^{-3}$	$0.7^{+0.2}_{-0.1} \times 10^1$	$0.01^{+0.00}_{-0.00}$	$3.3^{+1.0}_{-0.7} \times 10^1$	$1.45^{+0.08}_{-0.08}$
HoI	$2.4^{+0.2}_{-0.2} \times 10^5$	$1.2^{+0.03}_{-0.03} \times 10^7$	$2.1^{+0.06}_{-0.06} \times 10^{-3}$	$0.3^{+0.03}_{-0.03} \times 10^1$	$0.01^{+0.00}_{-0.00}$	$2.6^{+0.5}_{-0.4} \times 10^2$	$1.76^{+0.02}_{-0.02}$
NGC2976	$1.9^{+0.2}_{-0.1} \times 10^6$	$7.3^{+0.21}_{-0.19} \times 10^8$	$1.3^{+0.04}_{-0.03} \times 10^{-1}$	$2.2^{+0.2}_{-0.3} \times 10^1$	$0.96^{+0.17}_{-0.1}$	$1.6^{+999995.3}_{-3.1} \times 10^1$	$2.50^{+0.00}_{-0.00}$
NGC3049	$7.7^{+1.7}_{-1.5} \times 10^6$	$3.6^{+0.08}_{-0.07} \times 10^9$	$6.2^{+0.14}_{-0.13} \times 10^{-1}$	$2.8^{+0.8}_{-0.5} \times 10^1$	$0.38^{+0.14}_{-0.1}$	$4.8^{+471.5}_{-2.3} \times 10^4$	$2.11^{+0.04}_{-0.04}$
NGC3077	$1.1^{+0.2}_{-0.1} \times 10^6$	$7.5^{+0.17}_{-0.18} \times 10^8$	$1.3^{+0.03}_{-0.03} \times 10^{-1}$	$3.9^{+0.6}_{-0.6} \times 10^1$	$0.98^{+0.39}_{-0.3}$	$1.0^{+0.5}_{-0.4} \times 10^3$	$2.26^{+0.13}_{-0.10}$
M81dwB	$2.8^{+3.1}_{-0.4} \times 10^4$	$4.7^{+0.11}_{-0.17} \times 10^6$	$8.1^{+0.19}_{-0.30} \times 10^{-4}$	$1.1^{+0.2}_{-0.5} \times 10^1$	$0.18^{+0.06}_{-0.1}$	$1.5^{+1.6}_{-1.1} \times 10^4$	$2.17^{+0.06}_{-0.52}$
NGC3190	$1.8^{+0.2}_{-0.2} \times 10^7$	$6.4^{+0.16}_{-0.17} \times 10^9$	$1.1^{+0.03}_{-0.03}$	$2.1^{+0.2}_{-0.2} \times 10^1$	$0.80^{+0.17}_{-0.1}$	$3.7^{+9.7}_{-2.5} \times 10^1$	$2.50^{+0.00}_{-0.00}$
NGC3184	$3.2^{+0.5}_{-0.3} \times 10^7$	$8.0^{+0.19}_{-0.20} \times 10^9$	$1.4^{+0.03}_{-0.03}$	$1.5^{+0.2}_{-0.2} \times 10^1$	$1.00^{+0.23}_{-0.4}$	$1.4^{+3.8}_{-0.3}$	$2.50^{+0.00}_{-0.28}$
NGC3198	$3.8^{+0.6}_{-0.4} \times 10^7$	$7.4^{+0.17}_{-0.17} \times 10^9$	$1.3^{+0.03}_{-0.03}$	$1.1^{+0.2}_{-0.1} \times 10^1$	$0.42^{+0.10}_{-0.1}$	$2.8^{+8.0}_{-1.7} \times 10^1$	$2.50^{+0.00}_{-0.00}$
IC2574	$2.8^{+2.0}_{-0.6} \times 10^6$	$2.1^{+0.06}_{-0.08} \times 10^8$	$3.6^{+0.10}_{-0.15} \times 10^{-2}$	$0.5^{+0.1}_{-0.2} \times 10^1$	$0.04^{+0.02}_{-0.03}$	$3.5^{+2.0}_{-2.7} \times 10^2$	$1.93^{+0.05}_{-0.16}$
NGC3265	$1.8^{+0.3}_{-0.2} \times 10^6$	$2.6^{+0.06}_{-0.06} \times 10^9$	$4.5^{+0.11}_{-0.11} \times 10^{-1}$	$8.8^{+0.9}_{-1.3} \times 10^1$	$1.45^{+0.24}_{-0.2}$	$3.0^{+1.0}_{-2.3} \times 10^6$	$2.18^{+0.02}_{-0.02}$
NGC3351	$1.9^{+0.1}_{-0.1} \times 10^7$	$6.9^{+0.17}_{-0.18} \times 10^9$	$1.2^{+0.03}_{-0.03}$	$2.1^{+0.2}_{-0.2} \times 10^1$	$0.70^{+0.09}_{-0.1}$	$1.4^{+0.3}_{-1.2} \times 10^6$	$2.50^{+0.00}_{-0.00}$
NGC3521	$7.1^{+1.2}_{-0.5} \times 10^7$	$3.1^{+0.07}_{-0.08} \times 10^{10}$	$5.4^{+0.13}_{-0.14}$	$2.5^{+0.2}_{-0.4} \times 10^1$	$1.57^{+0.71}_{-0.6}$	$3.2^{+9.3}_{-2.5}$	$2.50^{+0.00}_{-0.14}$
NGC3621	$1.9^{+0.3}_{-0.2} \times 10^7$	$7.0^{+0.17}_{-0.16} \times 10^9$	$1.2^{+0.03}_{-0.03}$	$2.1^{+0.3}_{-0.3} \times 10^1$	$0.89^{+0.32}_{-0.2}$	$1.4^{+3.1}_{-1.0} \times 10^1$	$2.50^{+0.00}_{-0.00}$

Table 7.5. SED parameters: M_{dust}, L_{TIR}, SFR, $< U >$, U_{min}, ΔU and α for the KINGFISH sample.

Source	M_{dust} $[M_\odot]$	L_{TIR} $[L_\odot]$	SFR $[\mathrm{M_\odot\,yr^{-1}}]$	$< U >$	U_{min}	ΔU	α
NGC3627	$4.0^{+0.3}_{-0.3} \times 10^7$	$2.5^{+0.06}_{-0.07} \times 10^{10}$	$4.4^{+0.10}_{-0.12}$	$3.6^{+0.3}_{-0.3} \times 10^1$	$1.20^{+0.11}_{-0.1}$	$9.9^{+4.3}_{-3.2} \times 10^6$	$2.50^{+0.00}_{-0.00}$
NGC3773	$7.6^{+1.3}_{-0.6} \times 10^5$	$5.9^{+0.14}_{-0.15} \times 10^8$	$1.0^{+0.02}_{-0.03} \times 10^{-1}$	$4.8^{+0.4}_{-0.8} \times 10^1$	$0.83^{+0.14}_{-0.2}$	$1.0^{+0.0}_{-1.0} \times 10^7$	$2.20^{+0.03}_{-0.03}$
NGC3938	$4.6^{+0.7}_{-0.5} \times 10^7$	$1.6^{+0.04}_{-0.04} \times 10^{10}$	$2.7^{+0.07}_{-0.06}$	$1.9^{+0.3}_{-0.3} \times 10^1$	$0.81^{+0.26}_{-0.2}$	$1.6^{+2.9}_{-1.1} \times 10^1$	$2.50^{+0.00}_{-0.00}$
NGC4236	$2.7^{+0.4}_{-0.4} \times 10^6$	$4.2^{+0.13}_{-0.16} \times 10^8$	$7.3^{+0.23}_{-0.27} \times 10^{-2}$	$1.0^{+0.2}_{-0.1} \times 10^1$	$0.17^{+0.04}_{-0.03}$	$6.1^{+10.3}_{-6.4} \times 10^4$	$2.17^{+0.02}_{-0.04}$
NGC4254	$5.8^{+0.8}_{-0.3} \times 10^7$	$3.5^{+0.08}_{-0.09} \times 10^{10}$	$6.1^{+0.15}_{-0.15}$	$3.4^{+0.2}_{-0.4} \times 10^1$	$2.89^{+0.32}_{-1.2}$	$1.1^{+6.3}_{-0.1}$	$2.38^{+0.10}_{-0.03}$
NGC4321	$7.2^{+1.1}_{-0.6} \times 10^7$	$2.8^{+0.07}_{-0.07} \times 10^{10}$	$4.9^{+0.12}_{-0.12}$	$2.2^{+0.2}_{-0.3} \times 10^1$	$1.57^{+0.43}_{-0.7}$	$1.9^{+8.3}_{-1.4}$	$2.50^{+0.00}_{-0.36}$
NGC4536	$3.1^{+0.5}_{-0.2} \times 10^7$	$2.1^{+0.05}_{-0.05} \times 10^{10}$	$3.7^{+0.09}_{-0.08}$	$4.2^{+0.4}_{-0.6} \times 10^1$	$0.87^{+0.15}_{-0.2}$	$2.0^{+0.6}_{-1.7} \times 10^6$	$2.25^{+0.02}_{-0.05}$
NGC4559	$9.6^{+1.4}_{-0.8} \times 10^6$	$2.5^{+0.06}_{-0.07} \times 10^9$	$4.3^{+0.10}_{-0.11} \times 10^{-1}$	$1.5^{+0.2}_{-0.2} \times 10^1$	$0.53^{+0.10}_{-0.1}$	$2.4^{+22618.9}_{-1.5} \times 10^2$	$2.50^{+0.00}_{-0.13}$
NGC4569	$1.6^{+0.1}_{-0.1} \times 10^7$	$5.1^{+0.11}_{-0.11} \times 10^9$	$8.8^{+0.19}_{-0.20} \times 10^{-1}$	$1.8^{+0.1}_{-0.1} \times 10^1$	$0.59^{+0.05}_{-0.04}$	$1.4^{+0.1}_{-0.1} \times 10^6$	$2.50^{+0.00}_{-0.00}$
NGC4579	$3.3^{+0.2}_{-0.2} \times 10^7$	$9.9^{+0.25}_{-0.23} \times 10^9$	$1.7^{+0.04}_{-0.04}$	$1.8^{+0.1}_{-0.1} \times 10^1$	$1.36^{+0.09}_{-0.1}$	$1.0^{+0.0}_{-0.0}$	$2.50^{+0.00}_{-0.00}$
NGC4594	$2.1^{+0.2}_{-0.5} \times 10^7$	$3.0^{+0.10}_{-0.09} \times 10^9$	$5.2^{+0.16}_{-0.15} \times 10^{-1}$	$0.8^{+0.3}_{-0.1} \times 10^1$	$0.28^{+0.56}_{-0.02}$	$4.3^{+1.1}_{-4.2} \times 10^6$	$2.50^{+0.00}_{-0.00}$
NGC4625	$2.0^{+0.3}_{-0.3} \times 10^6$	$4.9^{+0.12}_{-0.12} \times 10^8$	$8.4^{+0.21}_{-0.21} \times 10^{-2}$	$1.4^{+0.3}_{-0.2} \times 10^1$	$0.59^{+0.29}_{-0.1}$	$9.4^{+12.9}_{-5.8}$	$2.50^{+0.00}_{-0.00}$
NGC4631	$3.5^{+0.3}_{-0.3} \times 10^7$	$2.1^{+0.07}_{-0.07} \times 10^{10}$	$3.6^{+0.12}_{-0.12}$	$3.5^{+0.4}_{-0.4} \times 10^1$	$1.17^{+1.38}_{-0.2}$	$1.0^{+0.9}_{-0.0} \times 10^7$	$2.50^{+0.00}_{-0.10}$
NGC4725	$4.4^{+0.4}_{-0.5} \times 10^7$	$6.1^{+0.25}_{-0.27} \times 10^9$	$1.1^{+0.04}_{-0.05}$	$0.8^{+0.1}_{-0.1} \times 10^1$	$0.50^{+0.07}_{-0.1}$	$1.0^{+0.0}_{-0.0}$	$2.50^{+0.00}_{-0.00}$
NGC4736	$5.6^{+0.7}_{-0.6} \times 10^6$	$5.5^{+0.12}_{-0.13} \times 10^9$	$9.6^{+0.20}_{-0.22} \times 10^{-1}$	$5.5^{+0.8}_{-0.6} \times 10^1$	$2.26^{+1.33}_{-0.5}$	$6.0^{+49.3}_{-5.9} \times 10^1$	$2.50^{+0.00}_{-0.09}$
DDO154	-	-	-	-	-	-	-
NGC4826	$4.3^{+0.4}_{-0.3} \times 10^6$	$3.9^{+0.10}_{-0.11} \times 10^9$	$6.7^{+0.17}_{-0.19} \times 10^{-1}$	$5.3^{+0.4}_{-0.6} \times 10^1$	$1.76^{+0.60}_{-3.2}$	$3.6^{+3.1}_{-0.0} \times 10^6$	$2.50^{+0.19}_{-0.58}$
DDO165	-	-	-	-	-	-	-
NGC5055	$5.4^{+0.6}_{-0.3} \times 10^7$	$1.7^{+0.04}_{-0.05} \times 10^{10}$	$3.0^{+0.07}_{-0.08}$	$1.8^{+0.1}_{-0.2} \times 10^1$	$1.39^{+0.11}_{-0.4}$	$1.0^{+1.8}_{-0.0}$	$2.50^{+0.00}_{-0.22}$
NGC5398	$3.1^{+1.4}_{-1.2} \times 10^6$	$3.7^{+0.10}_{-0.12} \times 10^8$	$6.5^{+0.18}_{-0.20} \times 10^{-2}$	$0.7^{+0.4}_{-0.2} \times 10^1$	$0.04^{+0.09}_{-0.03}$	$5.0^{+8.3}_{-2.7} \times 10^1$	$1.69^{+0.19}_{-0.16}$
NGC5408	$8.5^{+2.6}_{-1.8} \times 10^4$	$1.9^{+0.05}_{-0.04} \times 10^8$	$3.3^{+0.08}_{-0.08} \times 10^{-2}$	$14.7^{+3.5}_{-3.3} \times 10^1$	$0.64^{+0.48}_{-0.3}$	$3.7^{+0.9}_{-0.6} \times 10^3$	$1.75^{+0.06}_{-0.05}$
NGC5457	$6.6^{+1.1}_{-0.9} \times 10^7$	$1.9^{+0.05}_{-0.05} \times 10^{10}$	$3.3^{+0.08}_{-0.08}$	$1.7^{+0.3}_{-0.2} \times 10^1$	$0.75^{+0.39}_{-0.2}$	$9.0^{+13.6}_{-6.5}$	$2.50^{+0.00}_{-0.00}$
NGC5474	$3.7^{+0.5}_{-0.4} \times 10^6$	$4.5^{+0.10}_{-0.12} \times 10^8$	$7.8^{+0.18}_{-0.21} \times 10^{-2}$	$0.7^{+0.1}_{-0.1} \times 10^1$	$0.11^{+0.03}_{-0.02}$	$5.8^{+1.3}_{-1.7} \times 10^2$	$2.10^{+0.05}_{-0.04}$
NGC5713	$2.8^{+0.2}_{-0.2} \times 10^7$	$3.2^{+0.10}_{-0.10} \times 10^{10}$	$5.6^{+0.17}_{-0.18}$	$7.3^{+0.7}_{-0.6} \times 10^1$	$1.56^{+0.20}_{-0.2}$	$9.3^{+0.7}_{-1.5} \times 10^5$	$2.26^{+0.02}_{-0.01}$
NGC5866	$6.0^{+0.7}_{-0.4} \times 10^6$	$4.8^{+0.17}_{-0.16} \times 10^9$	$8.3^{+0.30}_{-0.28} \times 10^{-1}$	$4.8^{+0.4}_{-0.5} \times 10^1$	$4.15^{+0.31}_{-0.3}$	$1.5^{+0.8}_{-0.3}$	$2.42^{+0.12}_{-0.04}$
NGC6946	$7.3^{+0.5}_{-0.4} \times 10^7$	$3.2^{+0.07}_{-0.08} \times 10^{10}$	$5.6^{+0.13}_{-0.14}$	$2.5^{+0.2}_{-0.2} \times 10^1$	$0.84^{+0.06}_{-0.1}$	$1.6^{+0.5}_{-0.2} \times 10^6$	$2.50^{+0.00}_{-0.00}$
NGC7331	$1.0^{+0.1}_{-0.1} \times 10^8$	$4.5^{+0.13}_{-0.12} \times 10^{10}$	$7.7^{+0.22}_{-0.21}$	$2.4^{+0.2}_{-0.2} \times 10^1$	$1.33^{+0.32}_{-0.1}$	$5.5^{+9999968.0}_{-23.5}$	$2.50^{+0.00}_{-0.00}$
NGC7793	$6.4^{+1.0}_{-0.7} \times 10^6$	$1.5^{+0.04}_{-0.04} \times 10^9$	$2.7^{+0.07}_{-0.08} \times 10^{-1}$	$1.4^{+0.2}_{-0.2} \times 10^1$	$0.54^{+0.13}_{-0.1}$	$3.5^{+4.0}_{-1.6} \times 10^1$	$2.50^{+0.00}_{-0.08}$

Table 7.6. SED parameters: f_{vsg}, f_{PAH}, f_{ion} and $M_\star$ for the KINGFISH sample.

Source	f_{vsg}	f_{PAH}	f_{ion}	$M_\star$ $[M_\odot]$
NGC0337	$0.47^{+0.07}_{-0.08}$	$0.47^{+0.03}_{-0.02}$	$0.96^{+0.04}_{-0.08}$	$2.5^{+0.03}_{-0.03} \times 10^{10}$
NGC0584	-	-	-	-
NGC0628	$0.94^{+0.06}_{-0.08}$	$1.40^{+0.06}_{-0.06}$	$0.34^{+0.04}_{-0.04}$	$2.8^{+0.03}_{-0.04} \times 10^{10}$
NGC0855	1.00	$0.16^{+0.01}_{-0.01}$	1.00	$2.9^{+0.03}_{-0.04} \times 10^{9}$
NGC0925	$0.96^{+0.06}_{-0.06}$	$0.78^{+0.04}_{-0.05}$	$0.44^{+0.06}_{-0.06}$	$1.7^{+0.02}_{-0.02} \times 10^{10}$
NGC1097	$0.74^{+0.42}_{-0.23}$	$0.81^{+0.05}_{-0.08}$	$0.41^{+0.09}_{-0.07}$	$1.7^{+0.03}_{-0.04} \times 10^{11}$
NGC1266	$0.10^{+0.06}_{-0.07}$	$0.12^{+0.01}_{-0.01}$	0.00	$4.0^{+0.05}_{-0.05} \times 10^{10}$
NGC1291	$0.96^{+0.06}_{-0.28}$	0.00	1.00	$1.6^{+0.03}_{-0.03} \times 10^{11}$
NGC1316	$1.55^{+0.14}_{-0.40}$	0.00	$1.00^{+0.48}_{-0.52}$	$7.5^{+0.11}_{-0.10} \times 10^{11}$
NGC1377	$0.00^{+0.11}_{-0.00}$	$0.43^{+0.04}_{-0.02}$	1.00	$2.2^{+0.03}_{-0.04} \times 10^{10}$
NGC1404	-	-	-	-
IC0342	$0.67^{+0.10}_{-0.08}$	$1.59^{+0.06}_{-0.05}$	0.00	$3.6^{+0.04}_{-0.05} \times 10^{10}$
NGC1482	$0.55^{+0.07}_{-0.07}$	$0.90^{+0.03}_{-0.03}$	$0.42^{+0.03}_{-0.02}$	$4.7^{+0.05}_{-0.06} \times 10^{10}$
NGC1512	1.00	$0.46^{+0.03}_{-0.03}$	1.00	$3.9^{+0.04}_{-0.05} \times 10^{10}$
NGC2146	$0.93^{+0.05}_{-0.05}$	$1.04^{+0.04}_{-0.03}$	$0.56^{+0.02}_{-0.02}$	$9.5^{+0.12}_{-0.11} \times 10^{10}$
HoII	$0.00^{+0.01}_{-0.01}$	0.00	$0.87^{+0.13}_{-0.24}$	$6.4^{+0.09}_{-0.08} \times 10^{8}$
DDO053	$0.93^{+0.12}_{-0.11}$	$0.13^{+0.01}_{-0.01}$	1.00	$4.3^{+0.05}_{-0.05} \times 10^{7}$
NGC2798	$0.00^{+0.001}_{-0.00}$	$0.53^{+0.02}_{-0.02}$	$0.35^{+0.03}_{-0.03}$	$4.0^{+0.05}_{-0.05} \times 10^{10}$
NGC2841	$1.00^{+0.11}_{-0.40}$	$0.78^{+0.46}_{-0.08}$	$0.87^{+0.17}_{-0.57}$	$2.0^{+0.03}_{-0.03} \times 10^{11}$
NGC2915	$1.44^{+0.08}_{-0.09}$	$0.35^{+0.03}_{-0.03}$	0.00	$6.1^{+0.06}_{-0.07} \times 10^{8}$
HoI	1.00	$0.18^{+0.01}_{-0.01}$	1.00	$1.3^{+0.01}_{-0.02} \times 10^{8}$
NGC2976	$1.31^{+0.09}_{-0.41}$	$0.88^{+0.08}_{-0.06}$	$0.49^{+0.08}_{-0.09}$	$3.5^{+0.05}_{-0.05} \times 10^{9}$
NGC3049	$0.58^{+0.10}_{-0.57}$	$0.89^{+0.04}_{-0.17}$	$0.37^{+0.07}_{-0.06}$	$9.9^{+0.16}_{-0.14} \times 10^{9}$
NGC3077	$1.39^{+0.10}_{-0.11}$	$0.72^{+0.05}_{-0.05}$	$0.41^{+0.09}_{-0.08}$	$4.8^{+0.05}_{-0.05} \times 10^{9}$
M81dwB	$0.76^{+0.83}_{-0.31}$	$0.11^{+0.03}_{-0.08}$	1.00	$5.9^{+0.08}_{-0.13} \times 10^{7}$
NGC3190	$0.52^{+0.05}_{-0.06}$	$1.15^{+0.06}_{-0.06}$	$0.15^{+0.05}_{-0.05}$	$1.0^{+0.01}_{-0.01} \times 10^{11}$
NGC3184	$1.11^{+0.07}_{-0.07}$	$1.12^{+0.05}_{-0.05}$	$0.87^{+0.07}_{-0.06}$	$5.1^{+0.05}_{-0.07} \times 10^{10}$
NGC3198	$1.40^{+0.08}_{-0.10}$	$1.11^{+0.06}_{-0.06}$	$0.32^{+0.05}_{-0.05}$	$3.8^{+0.05}_{-0.06} \times 10^{10}$
IC2574	$1.13^{+0.11}_{-0.08}$	$0.00^{+0.003}_{-0.00}$	0.00	$1.2^{+0.02}_{-0.02} \times 10^{9}$
NGC3265	$0.45^{+0.22}_{-0.19}$	$0.67^{+0.06}_{-0.04}$	$0.46^{+0.07}_{-0.07}$	$7.1^{+0.09}_{-0.09} \times 10^{9}$
NGC3351	$1.66^{+0.30}_{-0.15}$	$0.53^{+0.04}_{-0.03}$	$1.00^{+0.00}_{-0.10}$	$5.0^{+0.06}_{-0.06} \times 10^{10}$
NGC3521	$0.79^{+0.06}_{-0.07}$	$1.54^{+0.06}_{-0.06}$	$0.45^{+0.05}_{-0.04}$	$1.7^{+0.02}_{-0.02} \times 10^{11}$
NGC3621	$1.00^{+0.07}_{-0.09}$	$1.54^{+0.06}_{-0.07}$	$0.32^{+0.04}_{-0.04}$	$2.8^{+0.03}_{-0.04} \times 10^{10}$
NGC3627	$0.90^{+0.10}_{-0.09}$	$1.15^{+0.04}_{-0.05}$	$0.39^{+0.05}_{-0.05}$	$1.1^{+0.01}_{-0.01} \times 10^{11}$
NGC3773	$0.20^{+0.34}_{-0.28}$	$0.85^{+0.05}_{-0.05}$	$0.01^{+0.06}_{-0.03}$	$2.2^{+0.03}_{-0.02} \times 10^{9}$
NGC3938	$1.00^{+0.06}_{-0.08}$	$1.23^{+0.05}_{-0.06}$	$0.34^{+0.04}_{-0.05}$	$6.5^{+0.08}_{-0.09} \times 10^{10}$
NGC4236	$0.00^{+0.01}_{-0.01}$	$0.23^{+0.02}_{-0.02}$	$1.00^{+0.00}_{-0.09}$	$4.2^{+0.05}_{-0.05} \times 10^{9}$
NGC4254	1.00	$1.48^{+0.07}_{-0.07}$	$0.46^{+0.04}_{-0.04}$	$8.7^{+0.11}_{-0.14} \times 10^{10}$
NGC4321	$1.00^{+0.07}_{-0.08}$	$1.23^{+0.06}_{-0.06}$	$0.43^{+0.05}_{-0.05}$	$1.3^{+0.02}_{-0.02} \times 10^{11}$
NGC4536	$0.67^{+0.11}_{-0.11}$	$0.83^{+0.07}_{-0.04}$	$0.45^{+0.05}_{-0.05}$	$5.3^{+0.06}_{-0.06} \times 10^{10}$
NGC4559	$0.78^{+0.07}_{-0.29}$	$1.10^{+0.09}_{-0.06}$	$0.24^{+0.05}_{-0.05}$	$1.2^{+0.02}_{-0.02} \times 10^{10}$
NGC4569	$1.03^{+0.10}_{-0.10}$	$1.51^{+0.05}_{-0.05}$	0.00	$5.8^{+0.07}_{-0.07} \times 10^{10}$
NGC4579	1.00	$0.84^{+0.10}_{-0.10}$	$0.37^{+0.17}_{-0.12}$	$1.9^{+0.02}_{-0.02} \times 10^{11}$
NGC4594	$0.00^{+0.38}_{-0.00}$	$1.55^{+0.10}_{-0.28}$	0.00	$2.4^{+0.03}_{-0.03} \times 10^{11}$
NGC4625	$1.24^{+0.08}_{-0.09}$	$1.40^{+0.07}_{-0.07}$	$0.40^{+0.05}_{-0.05}$	$2.9^{+0.03}_{-0.04} \times 10^{9}$
NGC4631	$0.70^{+0.25}_{-0.15}$	$1.01^{+0.06}_{-0.06}$	$0.40^{+0.07}_{-0.05}$	$3.8^{+0.05}_{-0.05} \times 10^{10}$
NGC4725	$0.84^{+0.19}_{-0.35}$	$1.20^{+0.44}_{-0.23}$	$0.63^{+0.38}_{-0.34}$	$1.3^{+0.02}_{-0.02} \times 10^{11}$
NGC4736	$0.89^{+0.09}_{-0.13}$	$1.32^{+0.07}_{-0.07}$	$0.18^{+0.05}_{-0.05}$	$5.6^{+0.06}_{-0.07} \times 10^{10}$
DDO154	-	-	-	-
NGC4826	$0.19^{+0.10}_{-0.53}$	$1.12^{+0.12}_{-0.08}$	$0.04^{+0.08}_{-0.06}$	$5.6^{+0.07}_{-0.07} \times 10^{10}$
DDO165	-	-	-	-

Table 7.6. SED parameters: f_{vsg}, f_{PAH}, f_{ion} and $M_\star$ for the KINGFISH sample.

Source	f_{vsg}	f_{PAH}	f_{ion}	$M_\star$ $[M_\odot]$
NGC5055	$0.79^{+0.07}_{-0.08}$	$1.42^{+0.07}_{-0.06}$	$0.25^{+0.05}_{-0.04}$	$9.8^{+0.11}_{-0.13} \times 10^{10}$
NGC5398	$2.67^{+0.10}_{-0.10}$	$0.65^{+0.06}_{-0.04}$	0.00	$1.1^{+0.01}_{-0.01} \times 10^{9}$
NGC5408	1.00	$0.02^{+0.01}_{-0.005}$	1.00	$1.1^{+0.01}_{-0.01} \times 10^{9}$
NGC5457	$1.46^{+0.07}_{-0.08}$	$0.84^{+0.04}_{-0.05}$	$0.61^{+0.07}_{-0.06}$	$7.1^{+0.07}_{-0.09} \times 10^{10}$
NGC5474	$0.72^{+0.08}_{-0.06}$	$0.95^{+0.04}_{-0.04}$	0.00	$2.4^{+0.02}_{-0.02} \times 10^{9}$
NGC5713	$0.40^{+0.05}_{-0.05}$	$0.57^{+0.03}_{-0.03}$	$0.78^{+0.05}_{-0.04}$	$5.9^{+0.07}_{-0.07} \times 10^{10}$
NGC5866	$0.18^{+0.04}_{-0.04}$	$0.81^{+0.04}_{-0.04}$	0.00	$1.2^{+0.01}_{-0.01} \times 10^{11}$
NGC6946	$0.99^{+0.12}_{-0.09}$	$1.24^{+0.04}_{-0.06}$	$0.45^{+0.05}_{-0.04}$	$9.3^{+0.14}_{-0.13} \times 10^{10}$
NGC7331	$1.02^{+0.12}_{-0.42}$	$1.22^{+0.09}_{-0.08}$	$0.28^{+0.07}_{-0.06}$	$2.2^{+0.03}_{-0.03} \times 10^{11}$
NGC7793	$0.71^{+0.05}_{-0.06}$	$0.92^{+0.04}_{-0.04}$	$0.73^{+0.06}_{-0.06}$	$8.3^{+0.09}_{-0.11} \times 10^{9}$

When no errors are given, it means that either this parameter was fixed in the fit or that the parameter reached the minimum or maximum value allowed for this parameter. If fixed: $f_{vsg} = 1$, $f_{PAH} = 0.0$, $f_{ion} = 0.5$, and $f_{vsg} \geq 0.0$, $f_{PAH} \geq 0.0$ and $f_{ion} \in [0.0,1.0]$.

Chapter 8

Characterisation of the dust properties

Contents

In this Chapter, we analyse the results of the SED model fits that were performed and presented in the previous Chapter. In the first section, we demonstrate the importance of *Herschel* observations to properly constrain the model solutions for the dust properties. In Section 8.2, we explore the various dust properties that were exploited in Chapter 5 and study their variations with metallicity now using a realistic description of dust. In Section 8.3 we investigate the submm excess, and the conditions for its presence with other galactic properties.

Throughout this Chapter we would like to remind the reader that the results presented here have been obtained assuming the SPIRE beam areas and calibration values from September 2012. These values are currently[1] being updated by the SPIRE ICC with a new model for the beam. The new numbers for the beam areas may imply a difference for the SPIRE fluxes of the extended sources between 5 and 10%. This will necessarily affect the quantitative values of the results that are presented here, especially for Section 8.3. However, we believe that the qualitative trends presented in Sections 8.1 and 8.2 would not be too affected. Thus we refer any future reader to the papers that should be published soon[2] for the updated results.

8.1 Input from *Herschel* : Importance of submm observational constraints

8.1.1 On the dust mass

Galametz et al. (2011) demonstrated the importance of submm constraints beyond 160 μm on a sample of 52 galaxies and found that the dust mass estimate can be biased in a non-trivial way, apparently depending on the metallicity of the galaxy, if no submm constraints are used in the modelling. Dale et al. (2012) showed with the KINGFISH sample that the dust masses estimated without *Herschel* constraints were consistent within a factor of 2 with the dust masses estimated with both *Herschel* and *Spitzer* constraints. Nonetheless, they noted that for galaxies with 12+log(O/H) $\leq$ 8.0, dust masses tend to be underestimated if no *Herschel* constraints are used in the fit, in agreement with the results at low metallicities of Galametz et al. (2011).

We perform the test on both DGS and KINGFISH samples and estimate the dust masses using only *Spitzer* constraints, $M_d(S)$, and using both *Herschel* and *Spitzer* constraints, $M_d(S+H)$. We restrict our sample to galaxies detected in the MIPS 160 band which reduces the number of low-metallicity galaxies for this comparison. The results are presented in Fig. 8.1 as a function of metallicity. Additionally we colour code the galaxies depending on their FIR colour, F_{70}/F_{160}, that can be indicative of the global dust temperature.

The median ratio of the two dust mass estimates: $M_d(S)/M_d(S+H)$ is 1.1 for the DGS sample and 1.5 for KINGFISH galaxies with a higher dispersion in the values for the KINGFISH sample (Fig. 8.1): 0.52 dex compared to 0.37 dex for the DGS galaxies. The dust masses estimated without *Herschel* constraints are overestimated for cold high-metallicity galaxies (i.e., 12+log(O/H) $\gtrsim$ 8.1 and $F_{70}/F_{160} < 1$) in agreement with the conclusions of Galametz et al. (2011). We also find that for low-metallicity galaxies the dust masses tend to be lower when estimated without *Herschel* constraints (for galaxies with 12+log(O/H) $\lesssim$ 8.1 the median ratio drops to 0.9). This is consistent with the trends presented in Galametz et al. (2011) and Dale et al. (2012).

Herschel data provide constraints to the submm slope of the dust SED by probing the cold dust component and thus constrain the minimum starlight intensity parameter, U_{min}. This parameter significantly influences the final dust mass: the lower U_{min}, the higher the dust mass. The middle panel of Fig. 8.1 shows the ratio of the two estimates of U_{min} and we see that the U_{min} parameter

[1] as of January2014.
[2] 2014 or 2015.

tends to be underestimated for high-metallicity galaxies when no submm constraints are used, thus leading to the observed overestimation of the dust mass. The fit without submm constraints indeed needs to invoke more cold dust in order to reproduce the available constraints. However, note that this is model-dependent: we use a model with a distribution of starlight intensity between U_{min} and $U_{min} + \Delta U$, whereas Dale et al. (2012) use the Draine & Li (2007) model which also includes a single starlight intensity component modelled by a δ-function: $\delta(U - U_{min})$. The results for U_{min} will necessarily be different, but this will not change the fact that we need submm constraints to accurately determine the dust mass parameter.

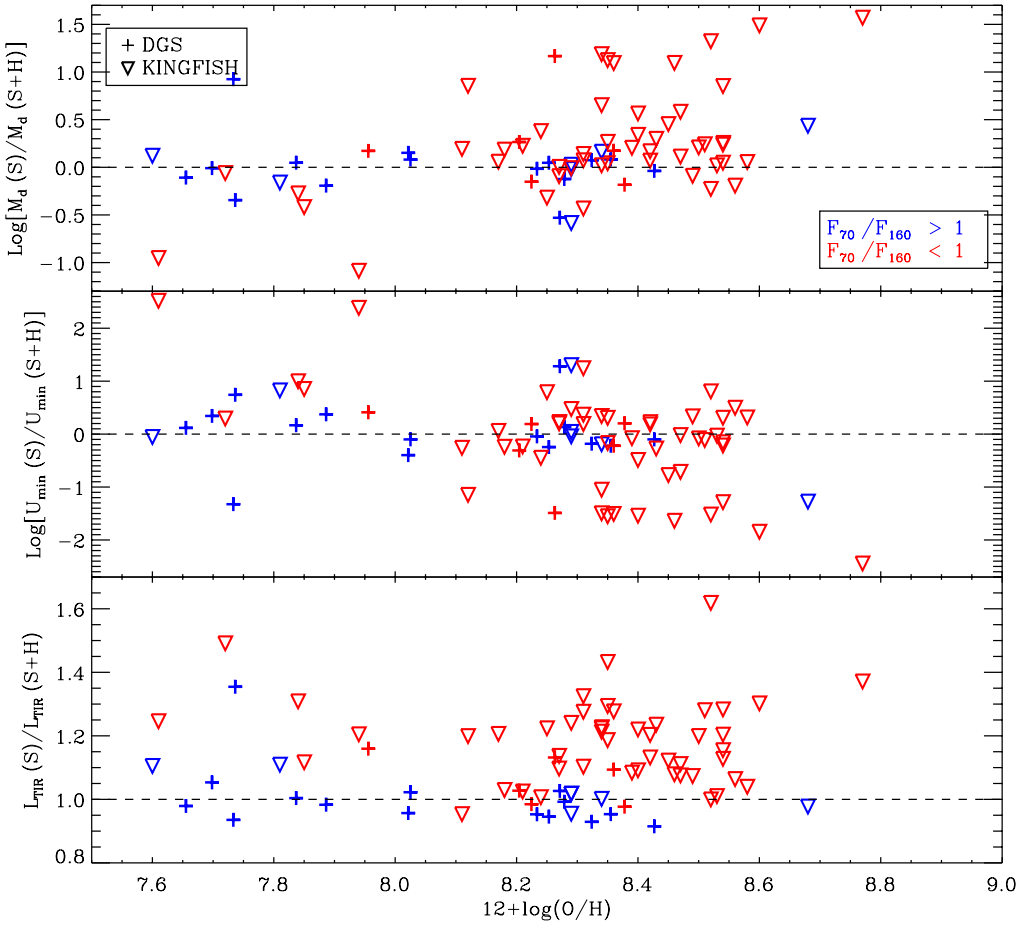

Fig. 8.1. Comparison of the dust mass, M_d, minimum starlight intensity, U_{min}, and TIR luminosity, L_{TIR}, estimated with both *Herschel* and *Spitzer* constraints (S+H) and only *Spitzer* (S). The crosses indicate DGS galaxies and the downward triangles show KINGFISH galaxies. The colours code the FIR colour 70/160 estimated with PACS fluxes.

8.1.2 On the TIR luminosity

From the previous section, we see that submm constraints are crucial to properly probe the cold dust component of the SED. However, the cold dust is not the main contributor to the TIR luminosity[3] and thus we do not expect a big difference between $L_{TIR}(S+H)$ and $L_{TIR}(S)$. Indeed the median ratio for both samples is 1.11 with a dispersion of 0.05 dex. For the DGS sample alone, the median

[3]The TIR luminosity is defined in Eq. 7.26 and estimated between 1 and 1000 μm.

ratio is 0.98, and 1.15 for the KINGFISH sample with, again, a slightly higher dispersion: 0.05 dex compared to 0.04 dex for the DGS galaxies. On the bottom panel of Fig. 8.1 we note that the TIR luminosity for cold galaxies with $F_{70}/F_{160} < 1$, is systematically overestimated by $\sim 16\%$ when the submm constraints are omitted.

For the three parameters we investigate in this section, the sampling of the peak of the SED determines if the parameter needs submm constraints to be accurately determined. Indeed, galaxies with $F_{70}/F_{160} > 1$ (blue points in Fig. 8.1) have the peak of their SED at shorter wavelengths, around 70 μm, and the last MIPS point at 160 μm already provides a sufficient constraint on the Rayleigh-Jeans slope of the dust SED. On the contrary, if $F_{70}/F_{160} < 1$, the last constraint available before the advent of *Herschel* did not enable a good sampling of the peak and of the Rayleigh Jeans slope of the dust SED and the estimation of the dust parameters was more uncertain. This is illustrated in Fig. 8.2 for two galaxies with $F_{70}/F_{160} > 1$ (Haro 2) and $F_{70}/F_{160} < 1$ (NGC 6946).

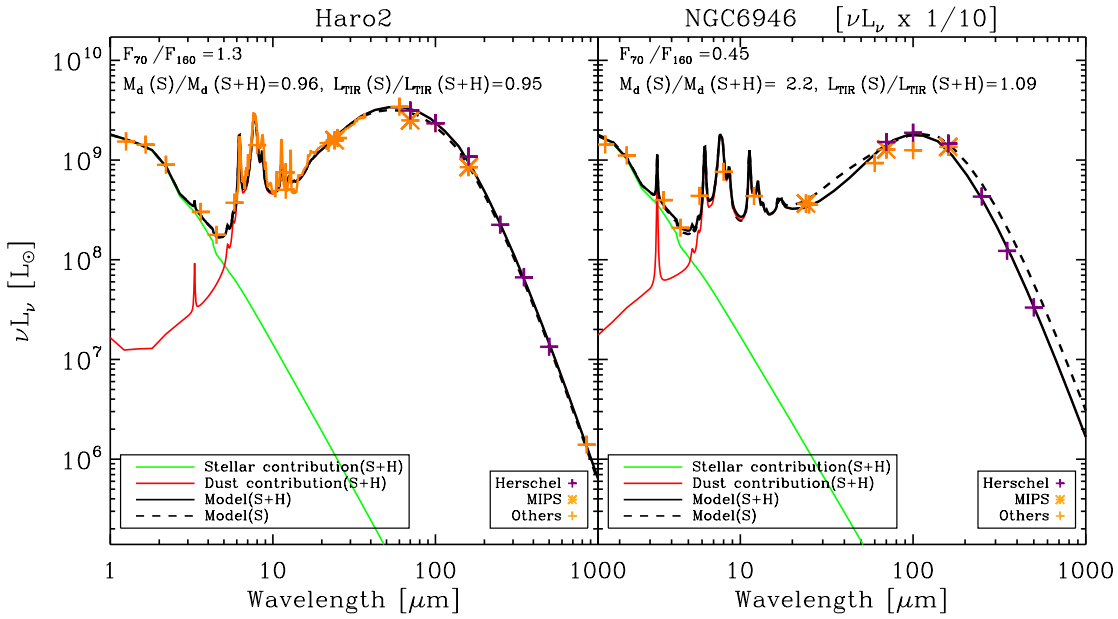

Fig. 8.2. Comparison between the SEDs obtained with and without *Herschel* constraints for Haro 2 *(left)*, a DGS galaxy with $F_{70}/F_{160} > 1$, and NGC6946 *(right)*, a KINGFISH galaxy with $F_{70}/F_{160} < 1$. *Herschel* constraints are indicated with the purple crosses, MIPS with orange stars and other ancillary data with orange crosses. The SED models obtained with and without *Herschel* constraints are shown with the solid (S+H model) and dashed (S model) lines respectively. Note that for Haro2, the submm point at 850 μm is *not* taken into account in both fits (S+H and S) as explained in Section 7.2 (zero weight): the last constraint for the (S) model is the MIPS point at 160 μm.

8.2 Dust from low-metallicity environments to "normal" galaxies

8.2.1 Importance of a realistic description of dust

In Chapter 5 we conducted a first study of the dust properties in low-metallicity environments using a modified blackbody (modBB) model to describe the dust emission. However, in a modBB model the constraints from the dust emitting at short wavelengths, tracing the warmer dust contribution, are not taken into account and this can affect the total dust mass and properties.

Fig. 8.3 (left) shows the ratios of the dust masses estimated with a modified blackbody model, $M_{dust,BB}$, and with a semi-empirical SED model, M_{dust}, for the DGS and KINGFISH samples, as

a function of metallicity and colour-coded with β_{obs}. The masses are from Tables 5.1, 5.2, 7.3 and 7.5.

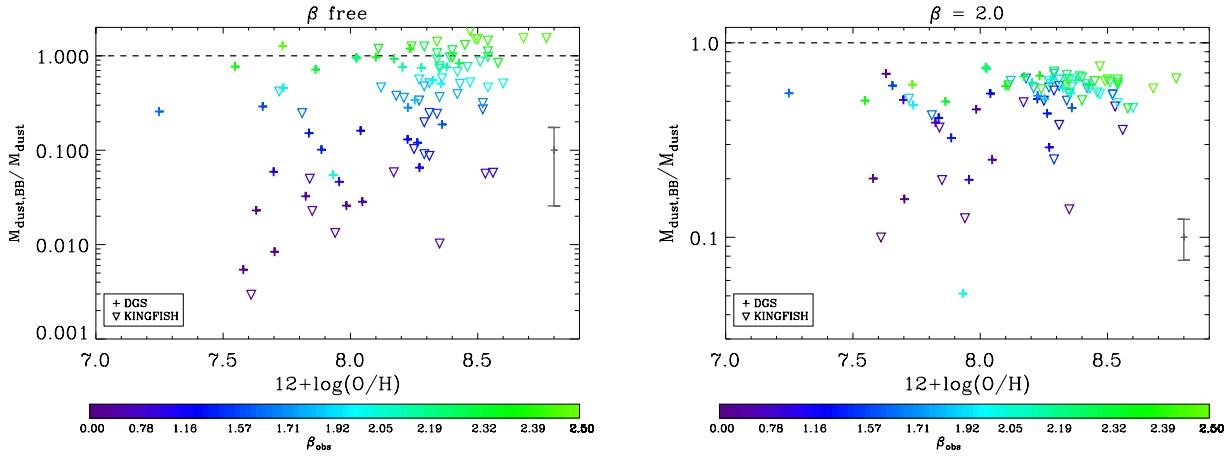

Fig. 8.3. Ratios of the dust masses estimated with a modified blackbody model and with a semi-empirical SED model, $M_{dust,BB}/M_{dust}$, for the DGS (crosses) and KINGFISH (downward triangles) samples, as a function of the metallicity. The colour codes the modBB emissivity index β_{obs} of the sources (from Chapter 5, Tables 5.1, 5.2). The median error on the ratio is shown with the dark grey point on the right of the plot. On the *left* panel, β is a free parameter in the modBB fits, whereas it is fixed to 2.0 on the *right* panel.

We see in Fig. 8.3 (left) that the dust mass estimated from a modBB model is misestimated compared to the mass estimated with a more realistic dust model. The median ratio of $M_{dust,BB}/M_{dust}$ is 0.46 for the total sample and 0.28 and 0.51 for the DGS and KINGFISH samples alone respectively. Our results for KINGFISH are in agreement with Dale et al. (2012) who report a factor of 1.9 difference between M_{dust} and $M_{dust,BB}$. We note that the underestimation of the dust masses from a modBB model compared to a full semi-empirical dust SED model increases with decreasing metallicity, and that at a given metallicity $M_{dust,BB}/M_{dust}$ decreases with β_{obs}.

However comparing dust masses from a semi-empirical dust model with a given emissivity to dust masses estimated with a modified blackbody where the emissivity index β is left varying is inconsistent, as the two estimates of the dust mass arise from two different optical properties: $\beta = 2.0$ for the full dust model and $\beta = \beta_{obs}$ for the modBB model (Bianchi 2013). Thus we do the same test, using this time modBB dust masses estimated with a modified blackbody model where β has been fixed to 2.0. The result is shown on the right plot of Fig. 8.3.

When consistently estimated, we find that the ratio $M_{dust,BB}/M_{dust}$ is systematically < 1.0: i.e., the modified blackbody model *systematically underestimates* the dust mass compared to a semi-empirical SED model. The median ratios are now: 0.55 for both samples, 0.51 for the DGS and 0.58 for KINGFISH galaxies. The trend with metallicity noted on the left panel of Fig.8.3 is not visible anymore on the right panel of Fig. 8.3. This is because for a given galaxy with $\beta_{obs} < 2.0$ (resp. > 2.0), fixing $\beta = 2.0$ imposes less (resp. more) emissive grains which translates into a higher (resp. lower) dust mass to account for the same luminosity. Thus galaxies with $\beta_{obs} < 2.0$, mostly metal-poor galaxies, have $M_{dust,BB}(\beta = 2.0)$ higher than their original modBB dust mass, resulting in an increased $M_{dust,BB}/M_{dust}$ ratio. On the contrary, galaxies with a $\beta_{obs} > 2.0$, which are mostly metal-rich galaxies, have a $M_{dust,BB}(\beta = 2.0)$ lower than their original modBB dust mass, resulting in a decreased $M_{dust,BB}/M_{dust}$ ratio. The observed trend with metallicity in the left panel of Fig. 8.3 is thus *only a side effect* of the inconsistency of the two dust mass estimates.

Although less obvious than in the left panel of Fig. 8.3, the trend of decreasing $M_{dust,BB}/M_{dust}$ with decreasing β_{obs} at a given metallicity can still be noted on the right panel of Fig. 8.3. Galaxies

well represented by a low β_{obs} have a shallow Rayleigh Jeans slope of the SED, representative of a broad SED peak. In these cases, imposing $\beta = 2.0$ imposes a steeper slope, not representative of the real shape of the SED and thus underestimates even more the dust mass. This shows the importance of the assumption of the dust temperature distribution and its impact on the dust mass: the broader the distribution of temperature, the lower the emissivity index found by a modBB and the larger the dust mass missed by modBB fits.

8.2.2 A characteristic temperature distribution

We saw in Chapter 5 that dwarf galaxies present overally warmer dust and potentially a broad dust SED peak. A temperature distribution is thus necessary to properly describe the dust in low-metallicity galaxies. The dust temperature distribution is directly linked to the range of starlight intensities, ΔU, to which the dust is exposed (see Eq. 1.30 from Chapter 1 linking U and T_d).

Fig. 8.4 shows the range of starlight intensities to which the dust is exposed ΔU as a function of the average starlight intensity $< U >$ for both samples. We use:

$$T_d[K] = 17.5 \times U^{1/(4+\beta)} = 17.5 \times U^{1/6} \tag{8.1}$$

adapted from Eq. 1.30 to relate the starlight intensity and the dust equilibrium temperature.

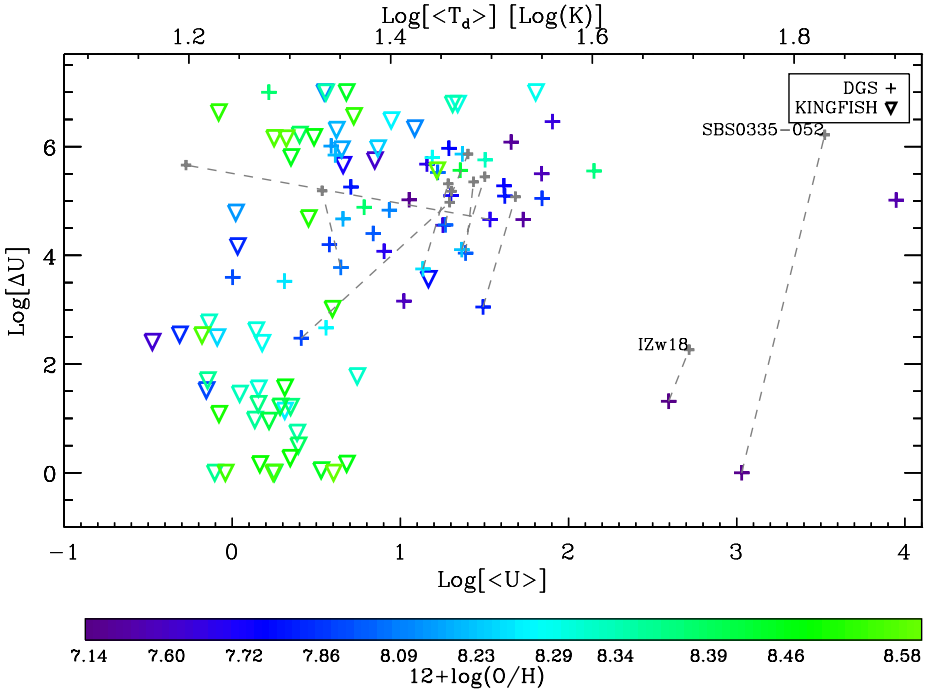

Fig. 8.4. ΔU as a function of the average starlight intensity $< U >$ for the DGS (crosses) and KINGFISH (downward triangles) samples. The average dust equilibrium temperature is shown on the top axis. The colour codes the metallicity of the sources. Grey points are where the galaxy should be if no additional MIR modified blackbody is included in the fits.

The median $< U >$ is 17.9 for the DGS and 2.2 for the KINGFISH sample. The median ΔU is $7.7\times\ 10^4$ for the DGS and $3.5\ \times\ 10^2$ for the KINGFISH sample. We see that DGS galaxies have a higher mean starlight intensity and are described by a larger range of starlight intensity values. This manifests in a broader SED peak that is shifted to shorter wavelengths for the DGS galaxies. On the contrary, the more metal-rich environments probed by KINGFISH have lower $< U >$ and lower

ΔU. This is consistent with low-metallicity galaxies harbouring warmer dust than more-metal rich environments: in the DGS the median dust temperature estimated with Eq. 8.1 is 28 K, compared to 20 K for the KINGFISH galaxies. Dust grains are not only warmer in dwarf galaxies but they also span a broader range in equilibrium temperatures. This can be estimated from ΔU and Eq. 8.1: the range of temperatures spanned by the DGS galaxies is $\sim$ 94 K while it is 36 K for the KINGFISH galaxies.

The two DGS galaxies with very high $< U >$ and low ΔU are IZw18 ($< U >$ = 390 and ΔU = 21) and SBS0335-052 ($< U >$ = 1100 and ΔU = 1). These galaxies indeed peak at very short wavelengths (around 40 μm for IZw18 and 20 μm for SBS0335-052). IZw18 has a rather narrow peak of its dust SED, consistent with its low ΔU, in contrast to SBS0335-052 (see Fig. 7.23). This is due to the additional modified blackbodies that were added in the MIR to obtain a satisfactory fit of the IRS spectrum shape for SBS0335-052. This additional MIR modBB has a great impact on the ΔU parameter preventing it from reaching higher values. Thus for all DGS galaxies for which we added the MIR modBB, we show with smaller grey points in Fig. 8.4 the place the galaxy would have if we did not add the extra MIR modBB. For most galaxies for which we added the MIR modBB we get a set of parameters that is consistent with the general trend presented for the rest of the sample. For IZw18, the fit without the MIR modBB gives an even higher $< U >$ ($\sim$ 520) but a ΔU = 184 still lower than that found for the dwarf sample: IZw18 harbours very hot dust spanning a small range of equilibrium temperatures. For SBS0335-052, the new position reflects better the observed SED shape: hot dust ($< U >$ = 3340) and very broad SED peak (ΔU = 1.6$\times$ 10^6), and is consistent with the general trend observed for dwarf galaxies.

8.2.3 Dust-to-stellar mass ratios

In Chapter 7, we saw that the dust mass is lower in low-metallicity galaxies (Fig. 7.22): there is a difference of about two orders of magnitude between the DGS and KINGFISH median dust masses. We noted the same trend in Chapter 5 when we only used modBB dust masses. In Chapter 5 it also appeared that the proportion of dust mass relative to stellar mass slightly increases between the metal-poor and metal-rich galaxies. However, as shown in Section 8.2.1, the dust masses estimated with a modBB model using a free β, as we did in Chapter 5, are systematically misestimations of the real dust masses at low-metallicities. Moreover, when estimated with a β=2.0 modBB, we saw in Chapter 5 that the correlation between the dust-to-stellar mass ratios with metallicity almost vanishes.

Fig. 8.5 shows the dust-to-stellar mass ratio for the DGS and KINGFISH galaxies as a function of metallicity, this time using dust masses from our semi-empirical SED model. The Spearman rank coefficient is 0.06, confirming what we saw with β=2.0 modBB dust masses. The median dust-to-stellar mass ratios are now very similar for the DGS and KF samples: 0.07% vs 0.09%. The scatter in the DGS dust-to-stellar mass ratios is 0.6 dex versus 0.4 dex for the KINGFISH galaxies. So the trend observed in Section 5.3 was due to the adopted dust model. Thus on average, low-metallicity dwarf galaxies contain as much dust as their metal-rich counterparts when compared to their respective stellar masses.

8.2.4 L_{TIR}-to-M_{dust} ratios

In Chapter 5 we also saw that the dwarf galaxies emit more in the FIR/submm than more metal-rich galaxies, per unit dust mass ($\sim$ 6 times more for the DGS) by looking at the $L_{FIR}/M_{dust,BB}$ ratio. Here again we want to check if this trend still holds when using dust masses estimated from our semi-empirical dust model. Thus we now consider the L_{FIR}/M_{dust} ratio, plotted on the left panel of Fig. 8.6.

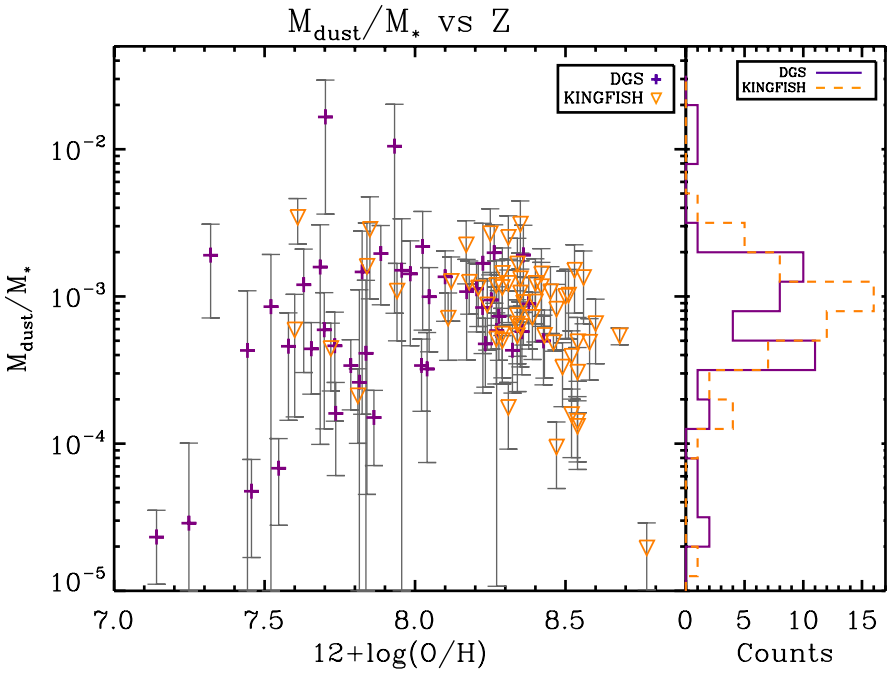

Fig. 8.5. Dust-to-stellar mass ratios for the DGS (purple crosses) and KINGFISH (orange downward triangles) samples as a function of metallicity. The distribution of $M_{dust}/M_\star$ is indicated on the side for both samples: plain purple line for DGS and dashed orange line for KINGFISH.

The median L_{FIR}/M_{dust} is 1.3 × 10^3 $L_\odot/M_\odot$ for the DGS sample, with a standard deviation of 0.5 dex, and 2.7 × 10^2 $L_\odot/M_\odot$ for the KINGFISH galaxies, with a standard deviation of 0.4 dex. The correlation is a bit weaker than in Chapter 5: we have a Spearman rank coefficient ρ=-0.49, but the difference between the DGS and KINGFISH galaxies remains: the DGS galaxies emit $\sim$ 4.7 times more in the FIR/submm domain than the KINGFISH sample. Thus this time, only part of the trend observed in Chapter 5 was due to the adopted dust modelling.

The comparison here is performed with L_{FIR} estimated between 50 and 650 μm. Because the peak of the dust SED for the dwarf galaxies is typically around 40-70 μm, the estimation of L_{FIR} does not consider the whole peak of the dust SED contrary to more-metal rich environments that have a SED peak around 100 μm. Thus we expect the L_{FIR}/L_{TIR} ratio to be lower for galaxies harbouring warmer dust, i.e., low-metallicity galaxies with a high mean starlight intensity, compared to galaxies with colder dust, i.e., more metal-rich galaxies with low $< U >$. This is indeed what we observe on the right panel of Fig. 8.6. The median L_{FIR}/L_{TIR} is 0.5 for the DGS sample, with a standard deviation of 0.14 dex, and 0.7 for the KINGFISH galaxies, with a standard deviation of 0.06 dex. There is indeed a good correlation between L_{FIR}/L_{TIR} and metallicity: $\rho = 0.54$, and an even stronger correlation between L_{FIR}/L_{TIR} and $< U >$: ρ = -0.82.

Comparing L_{FIR} to the total dust mass is thus not really appropriate as we compare the total dust mass with only a fraction of the power emitted by the dust grains. A more meaningful comparison is presented in Fig. 8.7 where the *total* IR luminosity, estimated between 1 and 1000 μm, is used.

The median L_{TIR}/M_{dust} is 2.7 × 10^3 $L_\odot/M_\odot$ for the DGS sample, with a standard deviation of 0.6 dex, and 3.8 × 10^2 $L_\odot/M_\odot$ for the KINGFISH galaxies, with a standard deviation of 0.4 dex. The Spearman rank coefficient for this trend is ρ=-0.52, similar to the Spearman rank coefficient obtained for the L_{FIR}/M_{dust} relation with metallicity. However the difference between the DGS and KINGFISH galaxies is more important: the DGS emit $\sim$ 7 times more in the infrared domain than

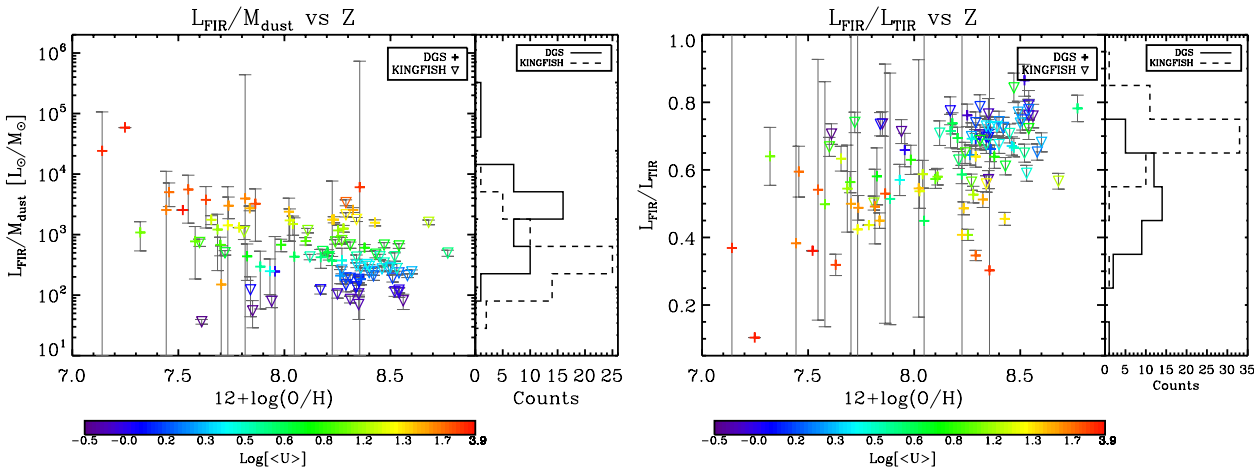

Fig. 8.6. *(left)* L_{FIR}/M_{dust} ratios for the DGS (crosses) and KINGFISH (downward triangles) samples as a function of metallicity. The distribution of L_{FIR}/M_{dust} is indicated on the side for both samples. *(right)* L_{FIR}/L_{TIR} for the DGS (purple crosses) and KINGFISH (orange downward triangles) samples as a function of metallicity. The distribution of L_{FIR}/L_{TIR} is indicated on the side for both samples. For both panels, the colours code the mean starlight intensity of the galaxies.

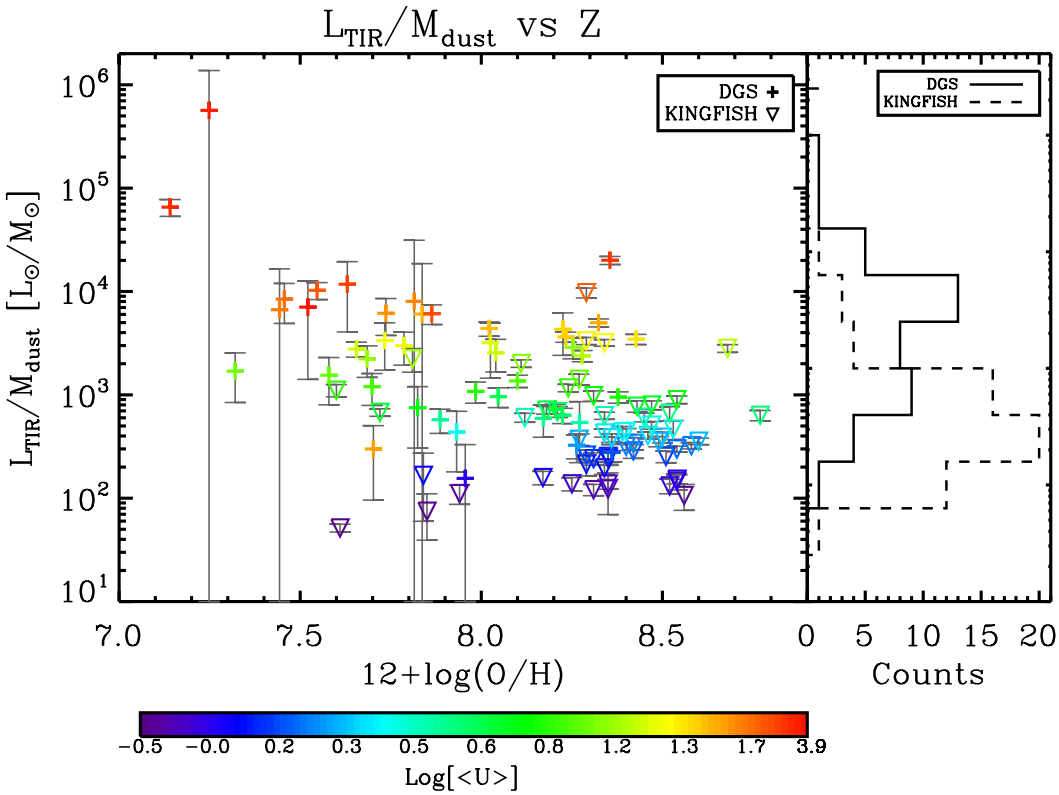

Fig. 8.7. L_{TIR}/M_{dust} ratios for the DGS (crosses) and KINGFISH (downward triangles) samples as a function of metallicity. The distribution of L_{TIR}/M_{dust} is indicated on the side for both samples. The colours code the mean starlight intensity, $< U >$, of the galaxies.

the KINGFISH sample per unit dust mass. This is directly linked to the mean starlight intensity $< U >$, as shown by the colours on Fig 8.7, where galaxies with a high $< U >$ emit more per unit dust mass than galaxies with a lower $< U >$, simply reflecting the fact that warmer dust is more luminous. Thus the trend observed in Chapter 5, Section 5.3.4, in the FIR is confirmed and enhanced when we consider the total IR range.

8.2.5 Specific star-formation rates

We finalize our view of the dust properties in galaxies by looking at the specific star-formation rate, $SSFR = SFR\ /\ M_{star}$, for our two samples. The SSFR can be seen as a measure of the efficiency of the star formation. The SFR have been estimated from the TIR luminosities in Chapter 7 and presented in Tables 7.3 and 7.5. The result is shown in Fig. 8.8. The median $SSFR$ is 2.7 $\times$ 10^{-10} yr^{-1} for the DGS sample with a standard deviation of 0.4 dex, and 5.7 $\times$ 10^{-11} yr^{-1} for the KINGFISH galaxies with a standard deviation of 0.5 dex. There is a small anti-correlation between the SSFR and metallicities: ρ = -0.35. Low-metallicity galaxies are thus more efficient in forming stars than more metal-rich galaxies: we have a difference of a factor of $\sim$ 5 between our two samples.

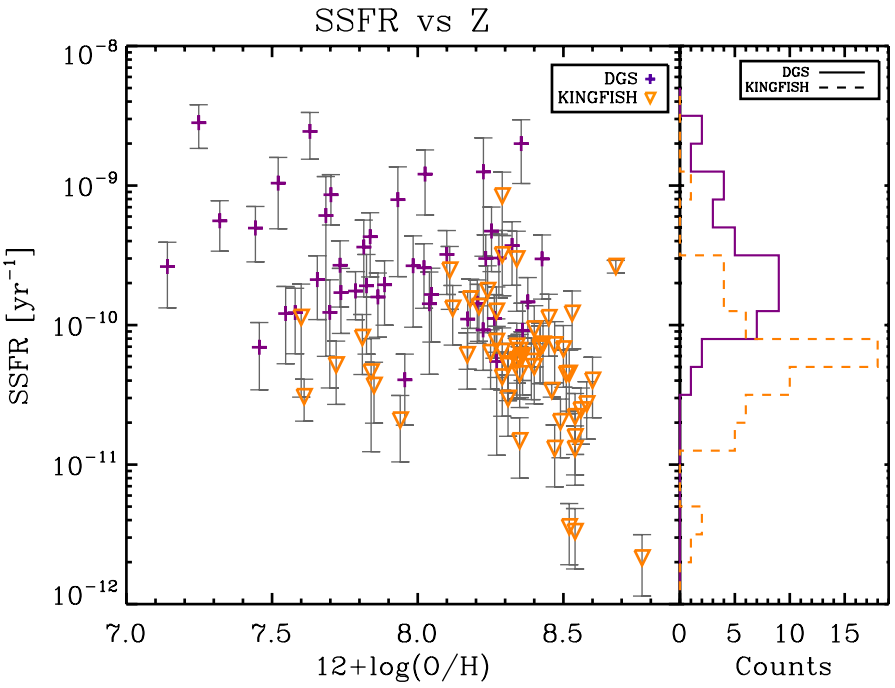

Fig. 8.8. Specific star-formation rates for the DGS (purple crosses) and KINGFISH (orange downward triangles) samples as a function of metallicity. The distribution of $SSFR$ is indicated on the side for both samples.

Note that this relation has been obtained using a L_{TIR}-calibrated SFR. Other SFR tracers, such as a combination of FUV + 24 μm or Hα + 24 μm, could be more appropriate to estimate the SFR in low-metallicity galaxies where the ratio of obscured versus unobscured star formation is lower than in more metal-rich galaxies (DeLooze et al., in prep). Additionally, we remind the reader here that our sample of dwarf galaxies contain only gas-rich star-forming dwarf galaxies and that we do not consider gas-poor dwarf galaxies in this analysis. Gas-poor dwarfs may present a lower SSFR than that observed in our sample and thus the trend presented here may be weaker if gas-poor dwarfs would be included.

8.3 The intriguing submm excess

A submm excess has been observed in the past in several low-metallicity galaxies (Galliano et al. 2003, 2005; Dumke et al. 2004; Bendo et al. 2006; Zhu et al. 2009; Galametz et al. 2009; Bot et al. 2010; Grossi et al. 2010; Galametz et al. 2011). It has been called "excess" because the current available models are unable to fully explain the submm emission of these galaxies (see Section 2.2.2). This submm excess has been one of the main sources of uncertainty in the dust modelling of dwarf galaxies for the past few years.

8.3.1 Identifying the galaxies with submm excess

For this study we select galaxies that are detected at 500 μm which gives us 78 galaxies out of the initial sample of 109 galaxies. Following the same procedure as in Section 5.4 we compute the residuals at each observed submm wavelength for the DGS and KINGFISH galaxies: $R(500)$, $R(850)$, $R(870)$ and $R(1200)$. For each residual we compute the error on the residual $\Delta R(\lambda)$ with the same method as in Section 5.4 (using the 300 random realisations of the SEDs). If the residual, $R(\lambda)$, is greater than the error on the observed flux density and greater than $\Delta R(\lambda)$, then the galaxy possesses an excess at the wavelength λ. We define "signal-to-noise ratio" or "intensity" of the excess, $S/N(\lambda)$, the quantity $R(\lambda)/\Delta R(\lambda)$. The results are shown in Table 8.1. The error shown for the residuals is the larger value between the error on the datapoint and $\Delta R(\lambda)$. As the observations at 850 μm and 870 μm are complementary, we regroup them under $R(850-870)$.

Out of the 78 galaxies detected at 500 μm, 27 of them (35%) show an excess at 500 μm. Kirkpatrick et al. (2013) investigate the presence of a submm excess at 500 μm for a subsample of the KINGFISH galaxies, including spiral and dwarf/irregular galaxies, using a two modified blackbodies model. They conclude that even if a small excess is present at 500 μm it is compensated by the same amount of 500 μm "deficiencies". In our study, we find that 23 KINGFISH galaxies have an excess with S/N > 1.0, among which 6 with S/N > 3.0; and only 3 galaxies with S/N(500) < -1, NGC2146, NGC4254 and NGC4569, which are not in the subsample considered by Kirkpatrick et al. (2013). Thus we cannot say in our study that our 500 μm excesses are compensated by "deficiencies". Kirkpatrick et al. (2013) use a two modified blackbodies model which only allows for two dust temperatures with a warm dust component and a cold dust component. We saw in Section 8.2.2, that a temperature distribution is essential to properly model the dust emission, especially in dwarf galaxies, to account for a possibly broad SED peak. We believe that the difference in the adopted dust SED models may be the main reason for their different findings.

32 of these 78 galaxies have been observed at 850 or 870 μm[4]. However, Draine et al. (2007) advised caution when working with SCUBA data for some of the KINGFISH galaxies: galaxies that have been scan-mapped and for which the data processing can remove some diffuse extended emission; galaxies that have been incompletely mapped with SCUBA and one galaxy, NGC4594 where the 850 μm flux density is dominated by AGN emission. For galaxies where the SCUBA map does not cover the extent of the whole galaxy, Dale et al. (2005) applied a correction factor to account for the missing emission based on the 160 μm emission. But the 160/850 μm ratio can vary spatially within the galaxy and Draine et al. (2007) discarded any galaxy with a correction factor greater than 1.6. If we consider all of these criteria, we must remove from our SCUBA sample the following seven galaxies: NGC1097 (corr > 1.6), NGC4254 (scan-mapped and corr > 1.6), NGC4321 (corr > 1.6), NGC4579 (scan-mapped), NGC4594 (dominated by AGN emission), NGC4736 (corr > 1.6) and NGC6946 (scan-mapped). These galaxies have indeed very low SCUBA flux densities compared to the rest of the FIR/submm photometry, with $R(850)/\Delta R(850) \sim$ -1.0. Three additional galaxies also have an even lower $R(850)/\Delta R(850)$ ($\leq$ -1.3): NGC1482, NGC4536 and NGC4569. For these

[4] We remind the reader here that non-dust contaminations have already been removed from the total submm flux densities at 850, 870 and 1200 μm (see Section 6.5).

three galaxies, the SCUBA flux density may also be underestimated. Thus in the following, we discard the SCUBA residuals for these ten galaxies.

Finally 22 galaxies out of the 78 galaxies detected at 500 μm have reliable 850 or 870 μm observations (28 %) and 11 show an excess at 850 or 870 μm (50% of the 22 galaxies). Among these 11 galaxies with excess at 850 or 870 μm, only 3 already have an excess at 500 μm Haro11, NGC0337 and NGC4631. Thus if we consider only galaxies with both observations at 500 and 850/870 μm (22 galaxies), the proportion of submm excess increases with wavelength from 14% to 50%.

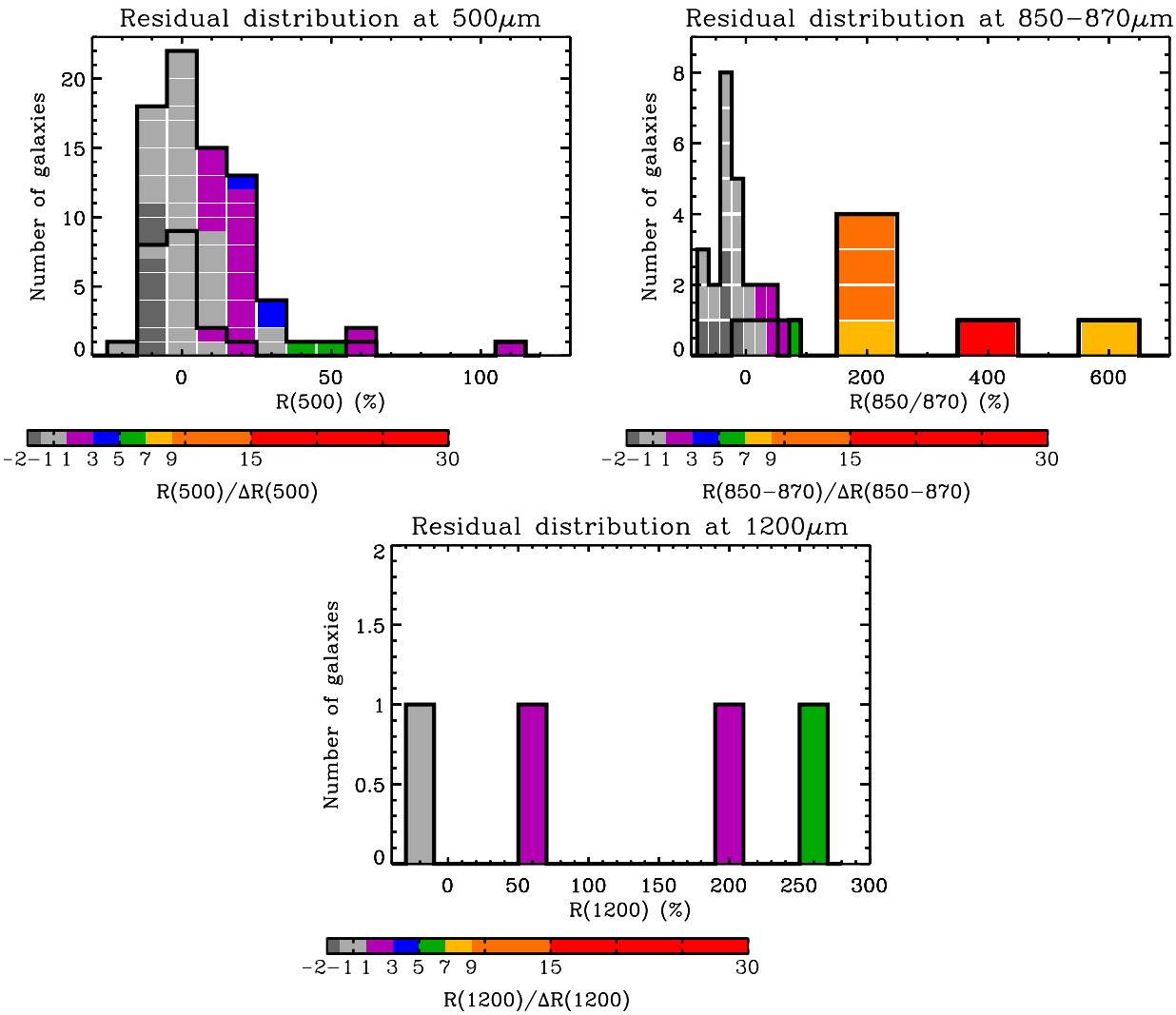

Fig. 8.9. Distribution of the residuals at 500 μm *(top left)*, 850 and 870 μm *(top right)*, and 1200 μm *(bottom)*, for the DGS and KINGFISH galaxies. The KINGFISH distribution is shown on top of the DGS distribution. For all of the panels, the colours code the S/N of the excess: $R(\lambda)/\Delta R(\lambda)$ from -1.6 to 29. A grey cell means a S/N < 1 and thus no excess.

For the 5 galaxies observed with MAMBO, three galaxies have an excess: IIZw40 and NGC1569 which also show an excess at 850 μm but not at 500 μm; and NGC4214 which does not have an excess at 500 μm and for which no reliable measurements are available at 850 or 870 μm. The other two are He2-10 which does not show any excess in the submm wavelengths and NGC1140 which is not detected with MAMBO.

The residual distribution at each wavelength is presented in Fig. 8.9. In total, out of the 78 galaxies detected at 500 μm, 36 galaxies (46%) have an excess in the submm for at least one of the considered wavelengths: 500, 850/870 and 1200 μm.

8.3.2 Excess in the submm with a modified blackbody

In this Section, we compare these findings on the 500 μm submm excess determined from a full dust SED model to that obtained when we looked at the 500 μm submm excess using a modBB model with a fixed $\beta = 2.0$ (Section 5.4). A $\beta = 2.0$ modBB detected 33 submm excess in the 78 galaxies detected at 500 μm. We find that for 8 galaxies the $\beta = 2.0$ modBB detects an excess which is not present in the full dust SED model, and for two galaxies, the $\beta = 2.0$ modBB does not detect an excess whereas the full dust SED model does. However, the modBB fits were performed including the 500 μm point whereas in the full dust SED model, we did not include the 500 μm point in the fit. We perform the test by removing the 500 μm point in the modBB fits. We find that all of the galaxies presenting an excess when using the 500 μm point also present an excess when the 500 μm point is not included, except one: NGC4594, for which the result is now coherent with the full dust SED model (i.e., no excess).

The two galaxies where the submm excess appears with the full dust SED model and not with the $\beta = 2.0$ modBB are NGC 3184 and NGC 4725. For NGC3184, the excess is barely detected at 500 μm: $R(500)_{SED} = 8.3 \pm 8.1$, and thus is not significant. For the second galaxy, $R(500)_{BB} = 9.0 \pm 10.6$ but $R(500)_{SED} = 12.4 \pm 8.0$. The excess is indeed significant here in the full dust SED model and has been missed by the modBB.

The $\beta = 2.0$ modBB thus overpredicts the number of excess galaxies by $\sim 20\%$. On the contrary, a galaxy showing an excess with a full dust SED model also shows an excess with a $\beta = 2.0$ modBB in 96% of the cases considered here.

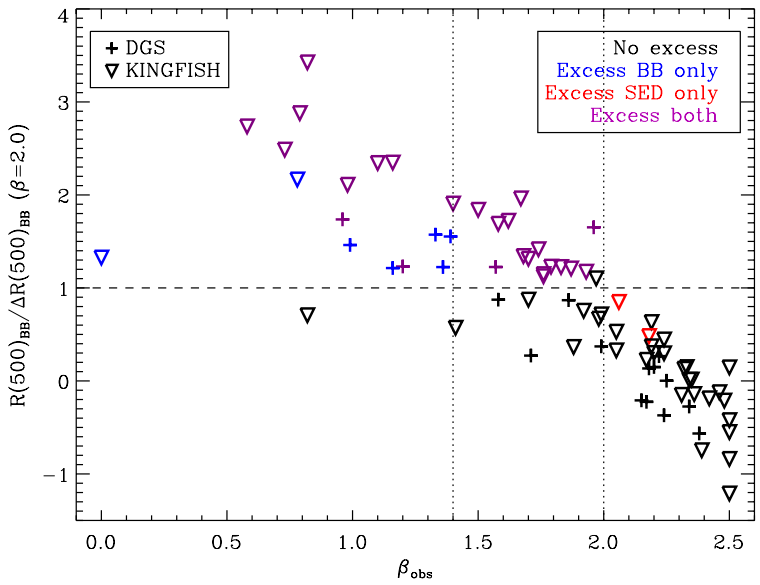

Fig. 8.10. $R(500)_{BB}/\Delta R(500)_{BB}$ as a function of β_{obs} for the 78 galaxies of the DGS (crosses) and KINGFISH samples (downward triangles) detected at 500 μm. The colours code if the excess is detected by the $\beta = 2.0$ modBB only (blue), by the full dust model only (red) or by both (purple). Galaxies with no excess are shown in black. The $\beta_{obs} = 1.4$ and $\beta_{obs} = 2.0$ lines are added to guide the eye. The $R(500)_{BB}/\Delta R(500)_{BB}$=1 threshold is indicated with the dashed line.

Fig. 8.10 shows the strength of the modBB submm excess, $R(500)_{BB}/\Delta R(500)_{BB}$ as a function of the emissivity index, β_{obs}, determined in Chapter 5. We see that all of the galaxies where only the $\beta = 2.0$ modBB predicts an excess have $\beta_{obs} \leq 1.4$. All of the galaxies with $\beta_{obs} \leq 1.4$ show an excess either only with the $\beta = 2.0$ modBB or with both models, except one. This galaxy is M81dwB which is only detected at the 1.8σ level at 500 μm and thus for which it would have been difficult to detect any excess. For galaxies with $\beta_{obs} \leq 1.4$, the excesses detected only with a $\beta = 2.0$ modBB (blue points in Fig. 8.10) have average excess signal-to-noise ratios $R(500)_{BB}/\Delta R(500)_{BB}$ ~ 1.5, whereas the excesses detected with both models (purple points in Fig. 8.10) are stronger: $R(500)_{BB}/\Delta R(500)_{BB} \sim 2.4$.

A low β_{obs} means a flatter submm Rayleigh Jeans slope of the modBB, indicative of a relatively broad peak of the dust SED, compared to a $\beta = 2.0$ modBB. Our small excess at 500 μm may just be due to the fact that the β=2.0 modBB cannot account for the particular shape of the SED with a broad peak, which is possible on the other hand with the full dust model. That is why our $\beta = 2.0$ modBB model detects an excess in some galaxies even if they do not show an excess when modelled with the full dust model.

To determine if one galaxy has a chance of harbouring a submm excess with a full dust model using only FIR/submm measurements, the few steps to follow would be:

- First, fit a modBB (including the 500 μm point) with a *free* emissivity index to determine β_{obs}.
- Then if the obtained β_{obs} is $\lesssim 1.4$, the second step would be to fit a modBB this time with a *fixed* emissivity index to 2.0 (still including the 500 μm point), obtain the 500 μm residual, $R(500)_{BB}$, and carefully estimate the error on this residual, $\Delta R(500)_{BB}$.
- If the ratio $R(500)_{BB}/\Delta R(500)_{BB}$ is $\gtrsim 2.0$, then there is a very strong chance that this galaxy presents a submm excess when modelled with a full dust model.
- If the obtained β_{obs} is between 1.4 and 2.0 *and* if the $\beta = 2.0$ modBB detects an excess ($R(500)_{BB}/\Delta R(500)_{BB} > 1.0$), then the galaxy will also present a submm excess when modelled with a full dust model.
- If β_{obs} is greater than 2.0, then there is a strong chance that the galaxy does not harbour a submm excess when modelled with a full dust model.

8.3.3 Characterising the submm excess

Evolution with wavelength

From Fig 8.11, we see that the submm excess becomes more pronounced as we go to longer wavelengths, from 500 μm to 850/870 μm (except for one galaxy: NGC0337). The difference between the S/N of the excess at 850/870 μm and the S/N of the excess at 500 μm is ~ 6.3 for galaxies with an excess at 850/870 μm. For galaxies with excess detected at both wavelengths, the S/N of the excess increases by a factor of ~ 1.5.

Only two galaxies have both measurements at 850 and 1200 μm and present excess at these wavelengths. The excess in these three galaxies shows three different behaviours: for NGC1569 the excess increases at 1200 (the S/N goes from 1.7 at 850 μm to 2.9 at 1200 μm), and for IIZw40, the excess peaks at 850 μm (the S/N decreases from 11.4 at 850 μm to 5.5 at 1200 μm). The evolution of the intensity of the excess at wavelengths greater than ~ 1000 μm appears to be dependant on the galaxy. More measurements at both wavelengths are needed to observe a more general trend.

From the colours in Fig.8.11, we hint that the excess may appear preferentially in lower-metallicity galaxies. Thus we now look at the S/N of the excess as a function of metallicity.

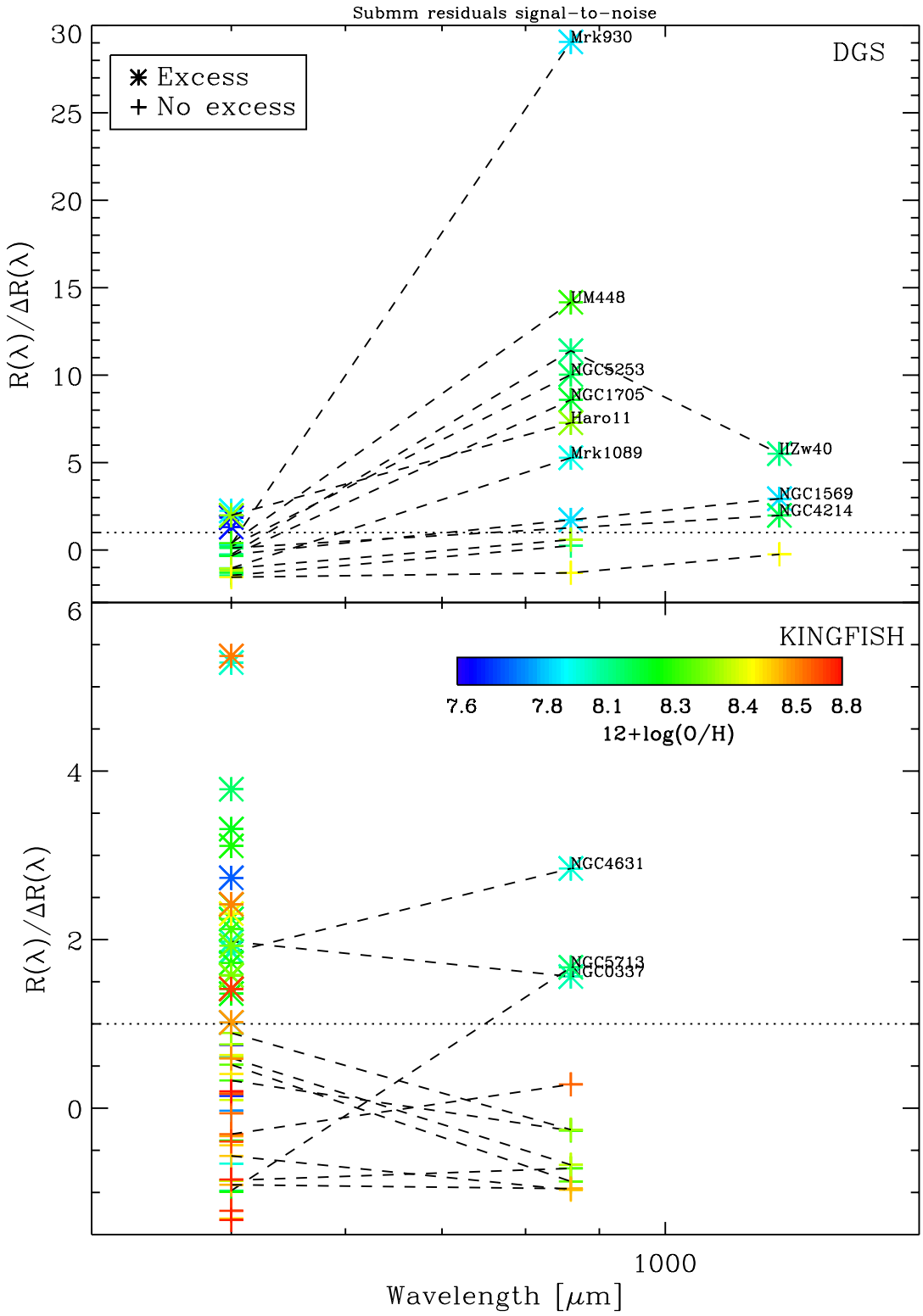

Fig. 8.11. Evolution of the S/N of the excess from 500 to 1200 μm, for the DGS *(top)* and the KINGFISH *(bottom)* samples. The stars indicate an excess i.e., $R(\lambda)/\Delta R(\lambda) \geq 1.0$. The dashed lines connect the datapoints for each galaxy if more than one submm observation is available. The dotted line indicates the $R(\lambda)/\Delta R(\lambda) = 1.0$ threshold. The galaxies are colour coded by metallicity.

Evolution with metallicity

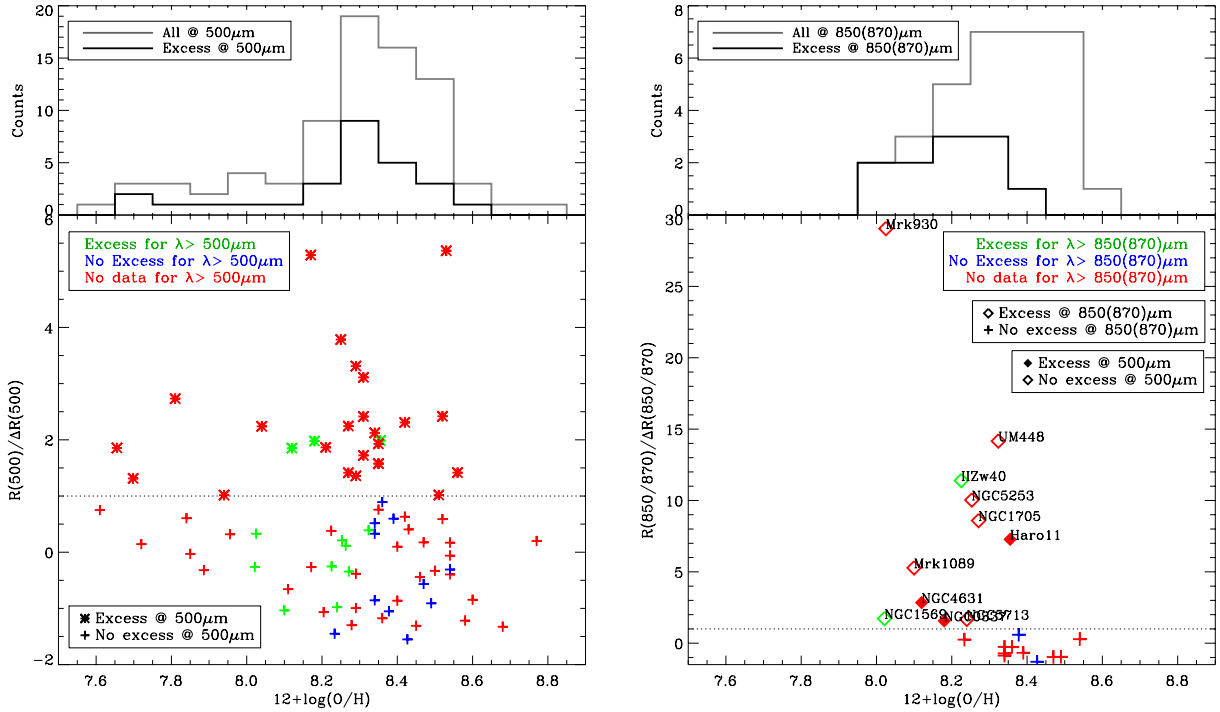

Fig. 8.12. Left: *(bottom)*$R(500)/\Delta R(500)$ as a function of metallicity for the 78 galaxies detected at 500 μm. The dotted line indicates the $R(500)/\Delta R(500) = 1.0$ threshold. The colours indicate the status of the excess at longer wavelength: no data available (red), data available but no excess (blue), data available and excess (green). On the *top* panel, we show the distribution of metallicity for the 78 500 μm-detected galaxies in grey and for the galaxies with an excess at 500 μm in black. **Right:** Same at 850/870 μm for galaxies with data at these wavelengths. The symbols now additionally code if the excess was already present at 500 μm (filled symbols) or not (empty symbols).

Fig. 8.12 shows the S/N of the excess as a function of metallicity at 500 and 850-870 μm. From Fig. 8.12 left, no trend between the S/N of the excess at 500 μm and metallicity can be observed: the Spearman rank coefficient is ρ=-0.08: i.e., the intensity of the excess does not depend on metallicity. However, if we consider only the presence versus the absence of submm excess, we see that the submm excess appears preferentially in metal-poor galaxies: 56 % of the excess galaxies have $Z < 0.4\ Z_{\odot}$ (12+log(O/H) < 8.3), whereas, in the total distribution of galaxies detected at 500 μm, (grey line on Fig. 8.12 (left)), only 46% of the total number of galaxies are galaxies with $Z < 0.4\ Z_{\odot}$. Moreover, the proportion of excess galaxies in the [7.5 - 8.3] metallicity range is $\sim$ 39% versus $\sim$ 31% in the]8.3 - 8.8] range. This confirms the first results obtained with the β=2.0 modBB. However with the β=2.0 modBB we found that the strongest excesses seems to appear in the most metal-poor galaxies, which is *not* what we see here. This is due to the fact that the S/N of the excess for the β=2.0 modBB model is anti-correlated with β_{obs} (see Fig. 8.10) and that the lowest β_{obs} were observed in the most metal-poor galaxies.

Additionally, if we compare the appearance of the excess at longer wavelength (i.e., green vs blue crosses in Fig.8.12), we see that this trend is confirmed: for galaxies without excess at 500 μm, the submm excess appears at longer wavelengths preferentially in low-metallicity galaxies. This is also confirmed by the right plot of Fig. 8.12: 81 % of the excess galaxies at 850(870) μm are galaxies

with $Z < 0.4\ Z_{\odot}$ (12+log(O/H) < 8.3), whereas, in the total distribution of galaxies detected at 850(870) μm, (grey line on Fig. 8.12 (right)), only 38% of the total number of galaxies are galaxies with $Z < 0.4\ Z_{\odot}$. Moreover, the proportion of excess galaxies in the [8.0 - 8.3] metallicity range is $\sim$ 75% versus $\sim$ 10% in the]8.3 - 8.6] range. However, here again, no trend between the strength of the excess and metallicity can be noted: the Spearman rank coefficient is ρ=-0.09.

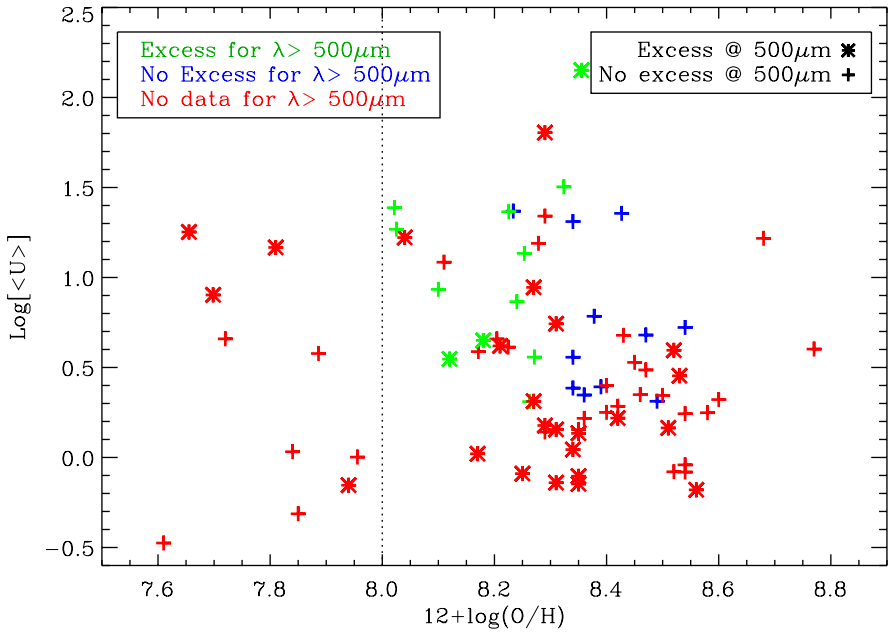

Fig. 8.13. $< U >$ as a function of metallicity for the 78 galaxies detected at 500 μm. The colours and symbols are the same as in Fig. 8.12.

We see in Fig. 8.12 that there are six galaxies for which 12+log(O/H) is lower than 8.0 but for which no excess is detected at 500 μm. From Fig.8.13, we see that all of these galaxies with 12+log(O/H) < 8.0 and that do not harbour an excess at 500 μm have very low mean starlight intensities, i.e., relatively cold dust given their metallicity. Only one galaxy with 12+log(O/H) < 8.0 and low $< U >$ has an excess: NGC 2915. For this galaxy, we have $R(500)/\Delta R(500) = 1.01$ and therefore this excess is not really significant. Thus, from Fig. 8.13, we infer that the value of $< U >$, which is related to the average temperature of the dust, discriminates between galaxies with and without submm excess at 500 μm when 12+log(O/H) ≤ 8.0.

Colour-colour diagrams

We now explore several FIR/submm colour diagrams in order to see if the submm excess galaxies fall on specific regions in these diagrams. Fig. 8.14 shows two FIR/submm colour-colour diagrams: F_{160}/F_{250} as a function of F_{250}/F_{500} on the left column and F_{160}/F_{250} as a function of $F_{500}/F_{850(870)}$ on the right column. On the top left panel of Fig. 8.14, we also plot the median ratio $\frac{F_{160}/F_{250}}{F_{250}/F_{500}}$ which is ~ 0.37. We see that all of the galaxies with an excess at 500 μm fall above this line i.e., they have *larger* $\frac{F_{160}/F_{250}}{F_{250}/F_{500}}$ values than those observed for the total sample. If we consider galaxies with longer submm data (green and blue points) we also see that it is very difficult to distinguish, using these FIR/submm colours only, which galaxies will present an excess at longer wavelengths. Nonetheless galaxies combining high F_{250}/F_{500} ($\gtrsim 6.5$) and high F_{160}/F_{250} ratios ($\gtrsim 3.0$), i.e., the most extreme cases, will show an excess at longer submm wavelengths.

If we now look at the top right panel of Fig. 8.14 where we consider the F_{160}/F_{250} and the $F_{500}/F_{850(870)}$ ratios, we see that the $F_{500}/F_{850(870)}$ is the main driver of the excess at longer submm wavelengths. In our sample of 21 galaxies detected at 850 or 870 μm, all of the galaxies having $F_{500}/F_{850(870)} \lesssim 5.5$ present an excess at wavelengths ≥ 850 μm.

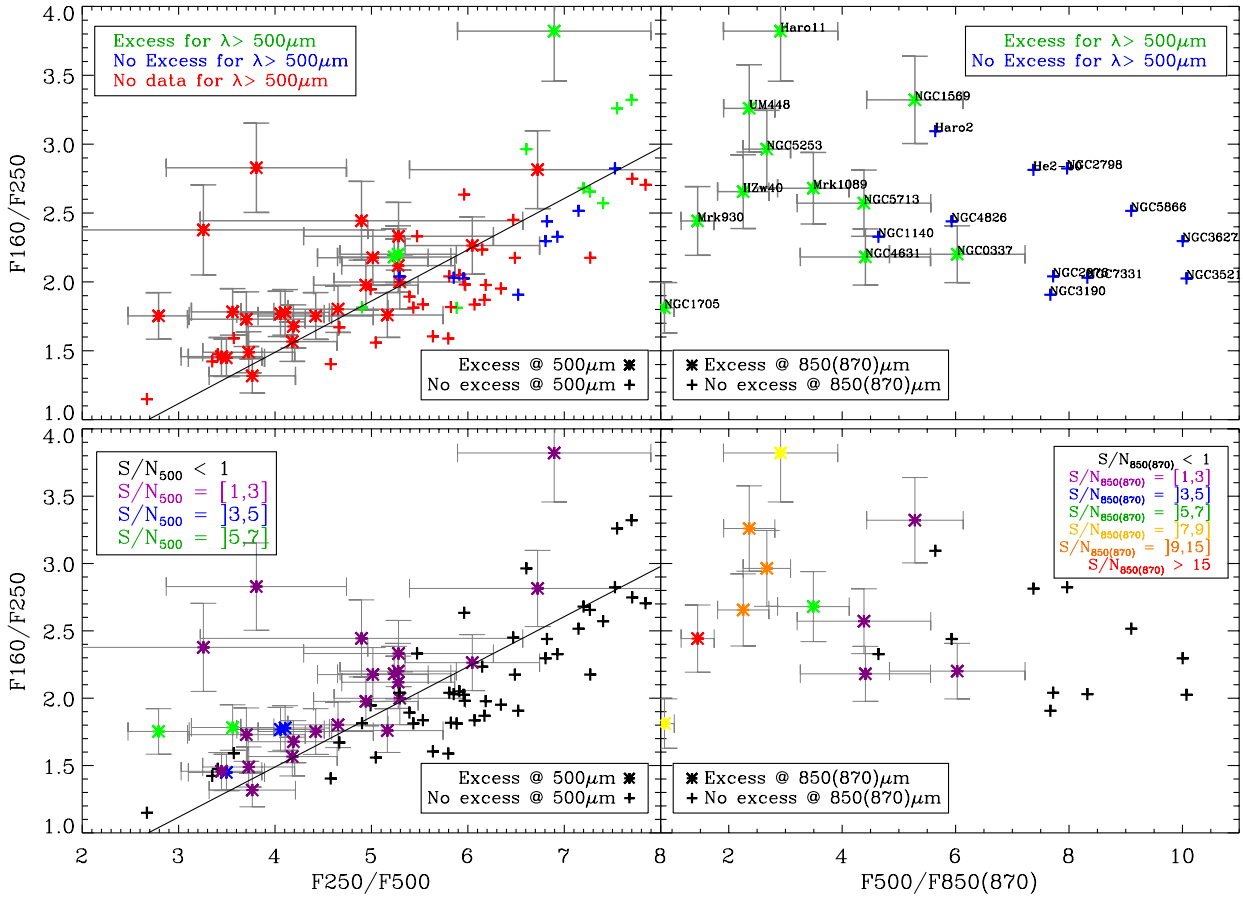

Fig. 8.14. *(left)* F_{160}/F_{250} as a function of F_{250}/F_{500} for the galaxies detected at 500 μm. Stars and crosses differentiate between galaxies with or without excess at 500 μm, respectively. The solid line denotes the median ratio of $\frac{F_{160}/F_{250}}{F_{250}/F_{500}} \sim 0.37$. *(right)* F_{160}/F_{250} as a function of $F_{500}/F_{850(870)}$ for the galaxies detected at 850 or 870 μm. Stars and crosses differentiate this time between galaxies with or without excess at 850(870) μm, respectively. On the *top* panels, the colours indicate the status of the excess at longer wavelength: no data available (red), data available but no excess (blue), data available and excess (green) (same as in Fig. 8.12). On the *bottom* panels, the colours indicate the S/N of the excess at 500 μm *(bottom left)* and 850(870) μm *(bottom right)*.

The bottom panels of Fig. 8.14 shows the same colour-colour diagrams as in the top panels but this time colour coded by S/N of the excess at 500 and 850(870) μm. We see that the S/N of the excess is mainly driven by the submm colours F_{250}/F_{500} for the S/N at 500 μm, and $F_{500}/F_{850(870)}$ for the S/N at 850(870) μm. This is not surprising given that a lower F_{250}/F_{500} or $F_{500}/F_{850(870)}$ ratio implies a shallower slope of the SED and thus a potentially stronger excess.

8.3.4 Explaining the excess: testing another dust composition

In this section we want to explore one of the hypotheses put forward to explain the submm excess in our galaxies: use another dust composition with grains more emissive in the submm. In our dust

model, we replace graphite (Gr) carbon grains by amorphous carbon (Ac) grains. As a consequence, the emissivity index of this dust composition is $\beta = 1.7$, instead of 2.0 with our previous model: we show in Fig. 8.15 the comparison between the opacities of the two models.

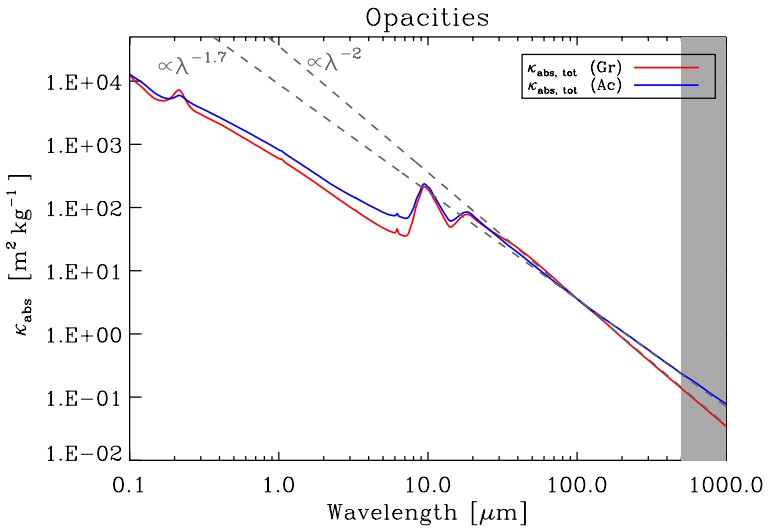

Fig. 8.15. Comparison of the opacities, κ_{abs} for the two dust compositions: Gr (red) and Ac (blue). The 500 μm to 1000 μm zone is outlined in grey.

We regenerate the SEDs for our sub-sample of 78 galaxies using this alternative dust composition, and follow the same procedure to access to the residual at a given wavelength, $R(\lambda)_{AC}$, and the corresponding S/N, $\mathrm{S/N}_{AC} = R(\lambda)_{AC}/\Delta R(\lambda)_{AC}$. The Ac model SEDs for the 37 galaxies with a submm excess from the Gr model, are shown in Fig. 8.20 along with the Gr model SEDs.

The new residual distributions at each wavelength are presented in Fig. 8.16. We see that at all wavelengths, the number of galaxies presenting an excess decreases but some galaxies still show an excess when modelled with amorphous carbon grains. The number of galaxies with a submm excess at 500 μm is now 14, about half of the number of galaxies showing submm excess at 500 μm with the Gr model. At 850/870 μm, the decrease in the presence of submm excess is less important: from 11 excess galaxies with graphite grains to eight with amorphous carbons. As for the four galaxies detected at 1200 μm, two of them still present an excess with the Ac model. Thus in total, with the Ac model, 25 galaxies have a submm excess at least at one submm wavelength.

The S/N of the excess in these galaxies is lower than those determined when using the Gr model (see Fig. 8.17): on average the S/N has decreased by 27%, 31% and 53% at 500 μm, 850/870 μm and 1200 μm respectively. Fig. 8.17 also shows that galaxies with the flattest submm slopes, and the highest S/N are the ones for which the excess remains with the Ac model: only part of the excess observed with the graphite grains model can be explained by the new dust composition.

Using more emissive dust grains - replacing graphite grains by amorphous carbons grains - can thus account for the submm excess observed in galaxies modelled with the Gr model for the weakest excesses. However, another mechanism needs to be invoked to explain the strongest submm excesses.

Fig. 8.18 shows where the submm excess galaxies lie for both models in the $< U >$ vs 12+log(O/H) plane. We see that most galaxies for which the excess is explained by the amorphous carbon grains model are moderately metal-poor galaxies, with $8.2 \leq 12+\log(\mathrm{O/H}) \leq 8.4$. This dust composition has already been shown to be more appropriate for LMC regions by Galliano et al. (2011) and Galametz et al. (2013), where the metallicity is $\sim 0.47\ Z_{\odot}$ (as estimated by Galliano et al. 2011, i.e., $12+\log(\mathrm{O/H}) = 8.36$). Thus we believe that for galaxies with 12+log(O/H)

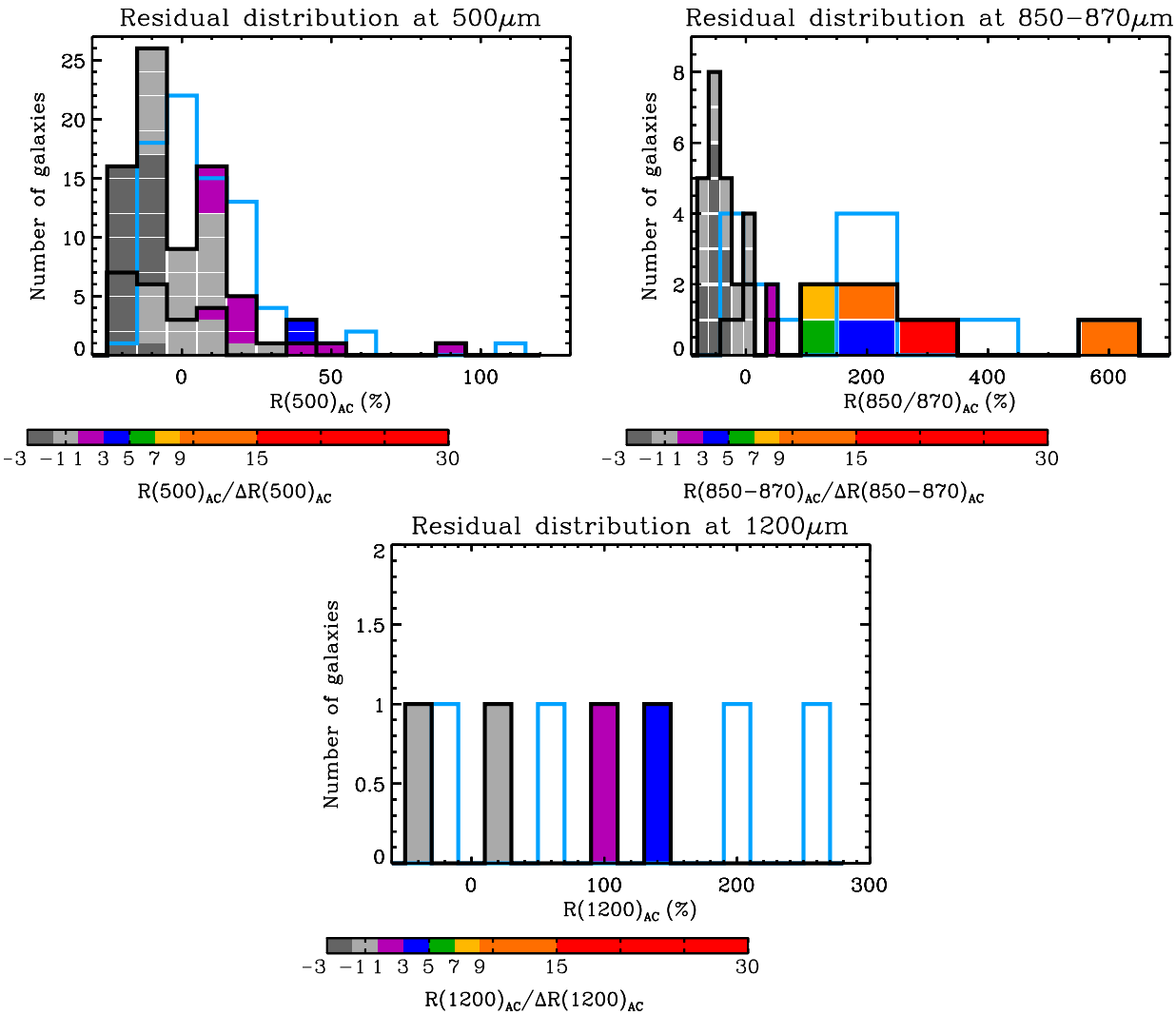

Fig. 8.16. Distribution of the residuals at 500 μm *(left)*, 850 and 870 μm *(centre)*, and 1200 μm*(right)*, for the DGS and KINGFISH galaxies. The KINGFISH distribution is shown on top of the DGS distribution. For all panels, the colours code the S/N of the excess: $R(\lambda)/\Delta R(\lambda)$. A grey cell means a S/N < 1 and thus no excess. The distribution of $R(\lambda)$ for the previous model using graphite grains is shown in light blue.

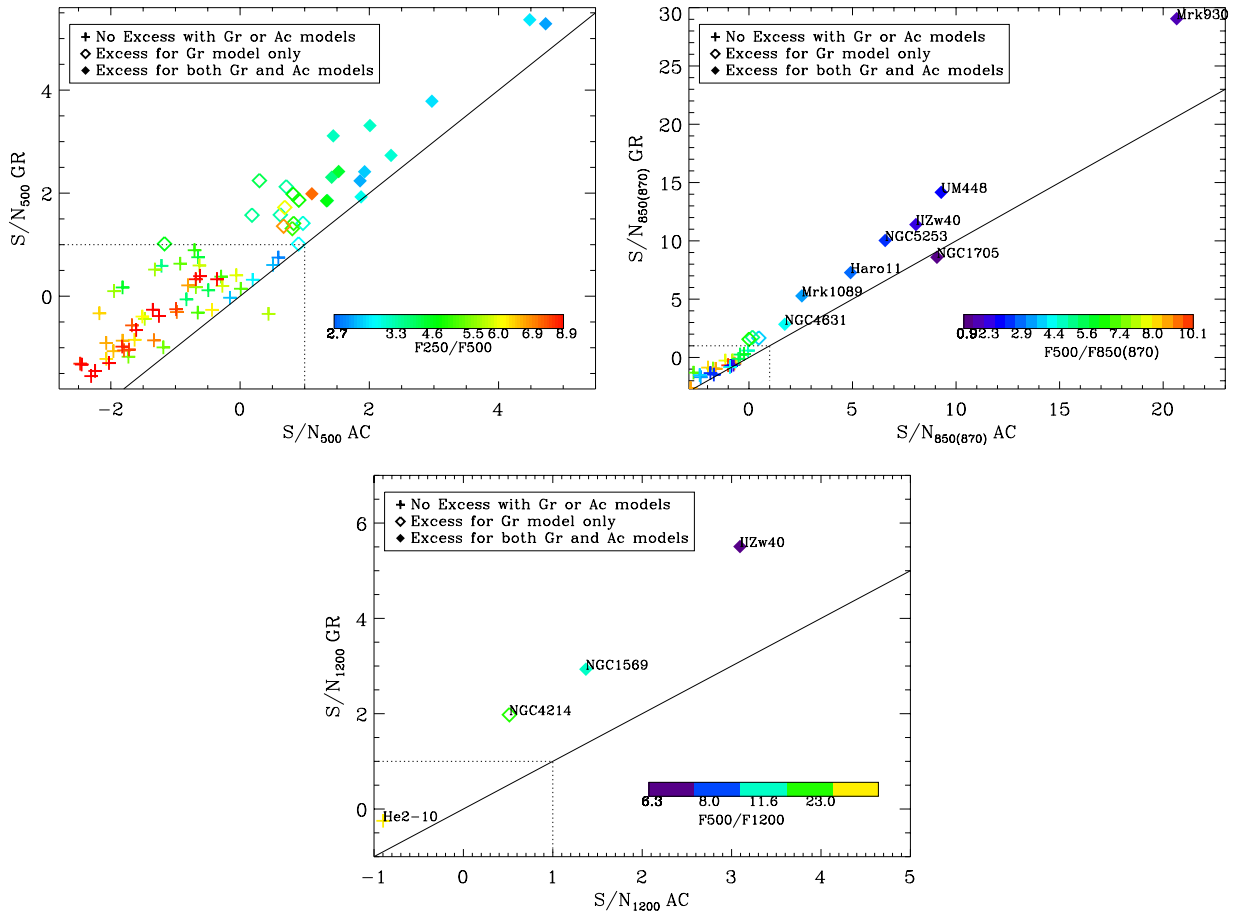

Fig. 8.17. S/N_{Gr} versus S/N_{AC} for the three submm wavelengths 500 *(top left)*, 850(870) *(top right)* and 1200 μm *(bottom)*. For each panel, the symbols differentiate between galaxies without submm excess (crosses), with submm excess only with the graphite grains model ("Gr model", open diamonds) and with submm excess with both models ("Gr and Ac models", filled diamonds). The colour indicates the submm colour: F_{250}/F_{500} *(top left)*, $F_{500}/F_{850(870)}$ *(top right)*, or F_{500}/F_{1200} *(bottom)*. Names are indicated for filled diamonds for the top right and bottom panel.

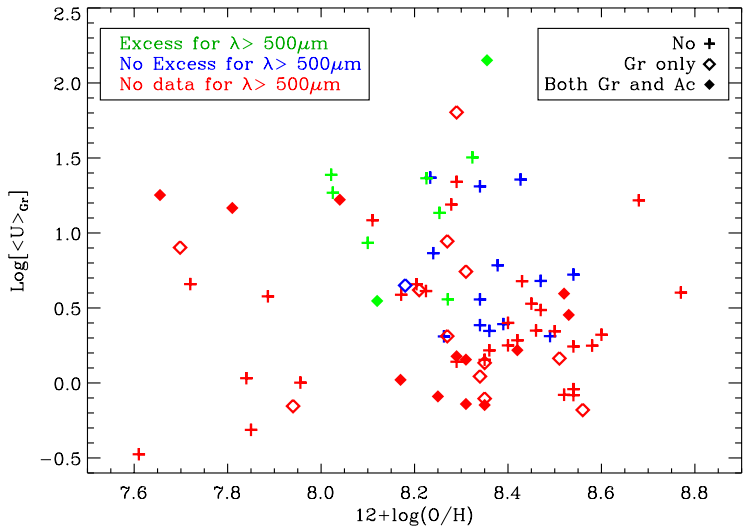

Fig. 8.18. Same as Fig.8.13 except that the symbols are now the same as in Fig. 8.17 (top left panel).

around 8.3, the weakest submm excesses observed at 500 μm with a graphite grain model may be representative of the fact that a Galactic grain composition is not appropriate to model the dust emission of these galaxies.

Impact on the dust mass

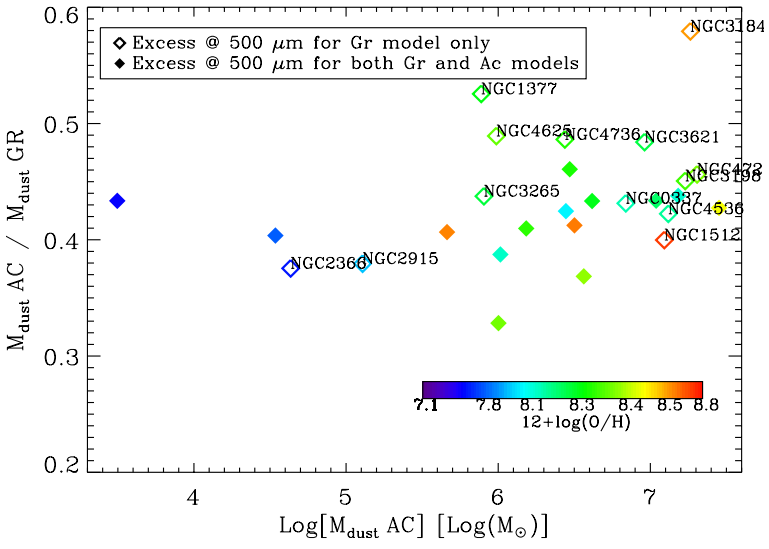

Fig. 8.19. Comparison of the dust mass obtained with the Ac model, $M_{dust}AC$, and the dust mass obtained with the Gr model, $M_{dust}GR$. The colours code the metallicity. The symbols are the same as in Fig. 8.17 top left panel. Names are indicated for galaxies where the Ac model can account for the submm excess.

Because the dust emissivity index is lower for the AC SED model, the grains are more emissive, thus requiring less dust mass to account for the same luminosity. And indeed the dust masses derived with the new dust composition are lower by a factor of ~ 2.3 ($M_{dust}AC/M_{dust}GR \sim 0.43$,

see Fig. 8.19). The Ac model SEDs for the 37 galaxies with a submm excess with the Gr model, are presented in Fig. 8.20 between 200 μm and 1300 μm, together with the Gr model SEDs.

8.4 Summary

In this Chapter we saw that submm constraints combined to a realistic dust model is crucial to get an accurate estimate of the dust properties, and especially of the dust mass. Indeed a modified blackbody model tends to systematically underestimate the dust mass by a factor of 1.8 compared to a semi-empirical dust SED model. The temperature distribution in low-metallicity environments is broader and the dust is also globally warmer than in more metal-rich systems. The dust-to-stellar mass ratios is more or less constant over the metallicity range we are probing, but we found that, in this sample, dwarf galaxies are more efficient in forming stars than their metal-rich counterparts. We identified a number of galaxies presenting an excess at 500 μm and found that the submm excess appears preferentially in low-metallicity galaxies, but that the intensity of the excess does not depend on metallicity. An alternative dust composition with more emissive dust grains can fully explain the submm excess in about 1/3 or the sample.

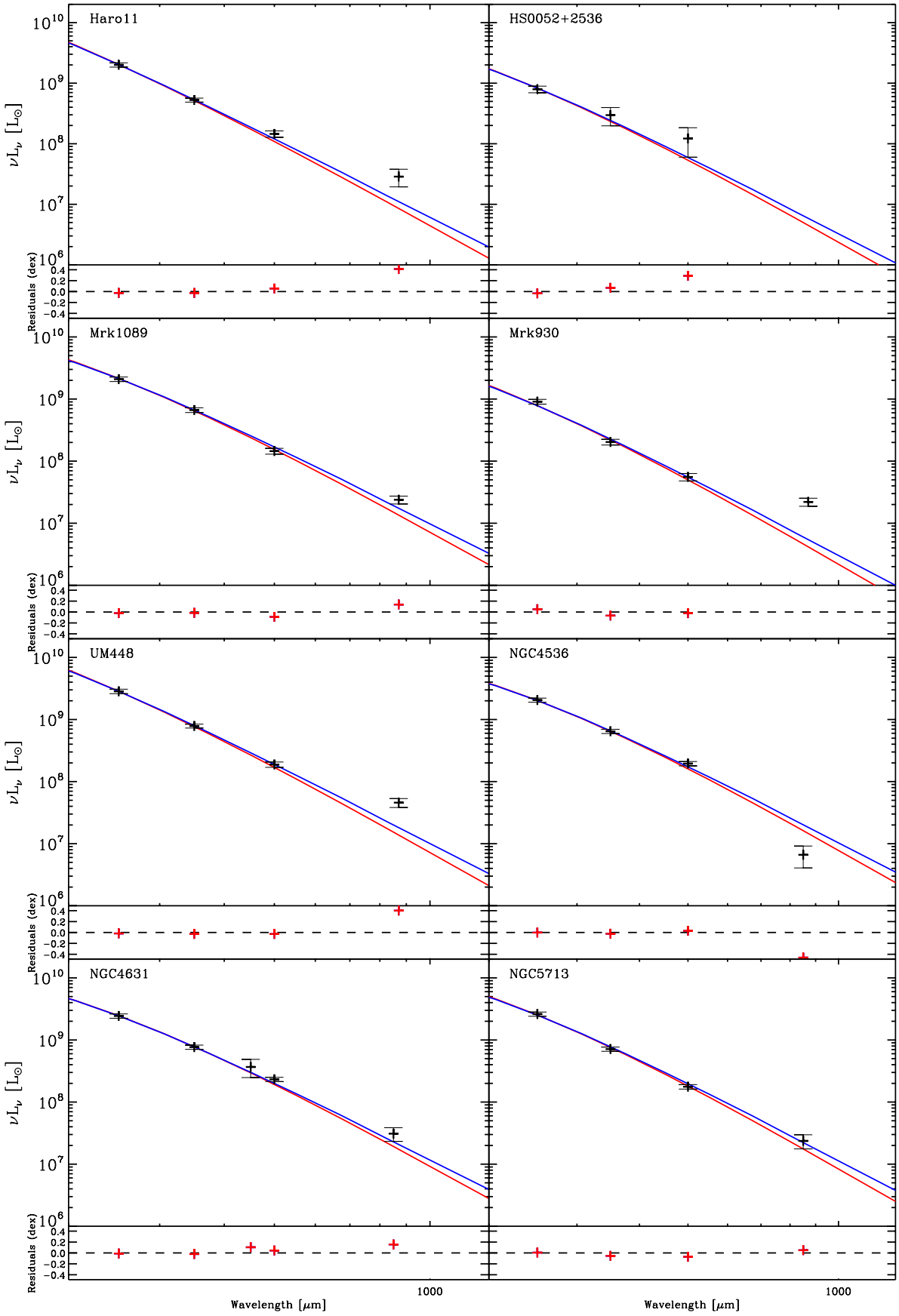

Fig. 8.20. SEDs modelled with the graphite grains model (red) and amorphous carbon grains (blue) for the galaxies showing a submm excess with the Gr model. To facilitate the comparison between the two modelled SEDs, we zoom into the [200,1300] μm range. The observed points are in black. The bottom panel of each plot indicates the residuals from the graphite grains model fit.

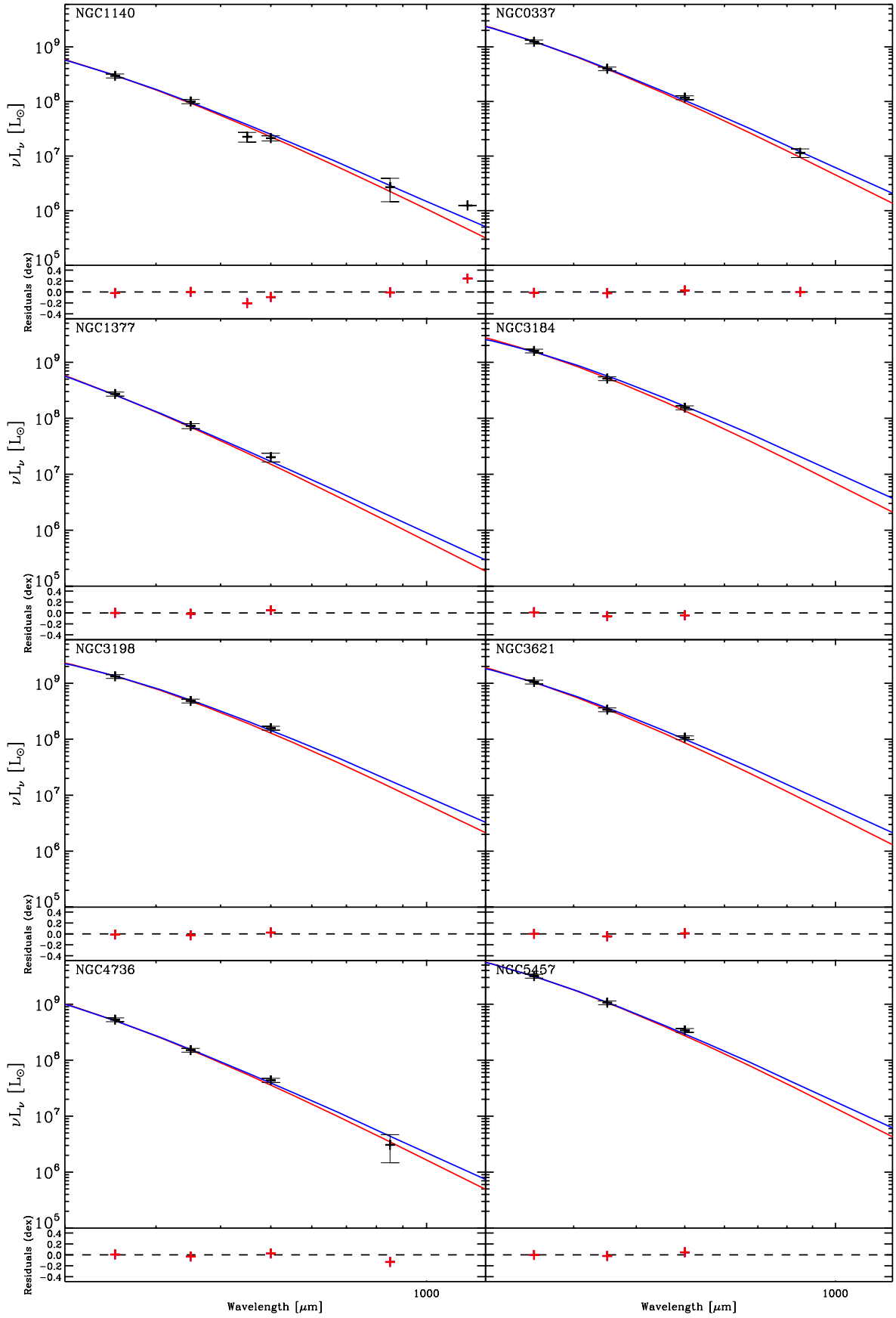

Fig. 8.20. Comparison of the Gr and Ac SEDs between 200 μm and 1300 μm *(continued)*.

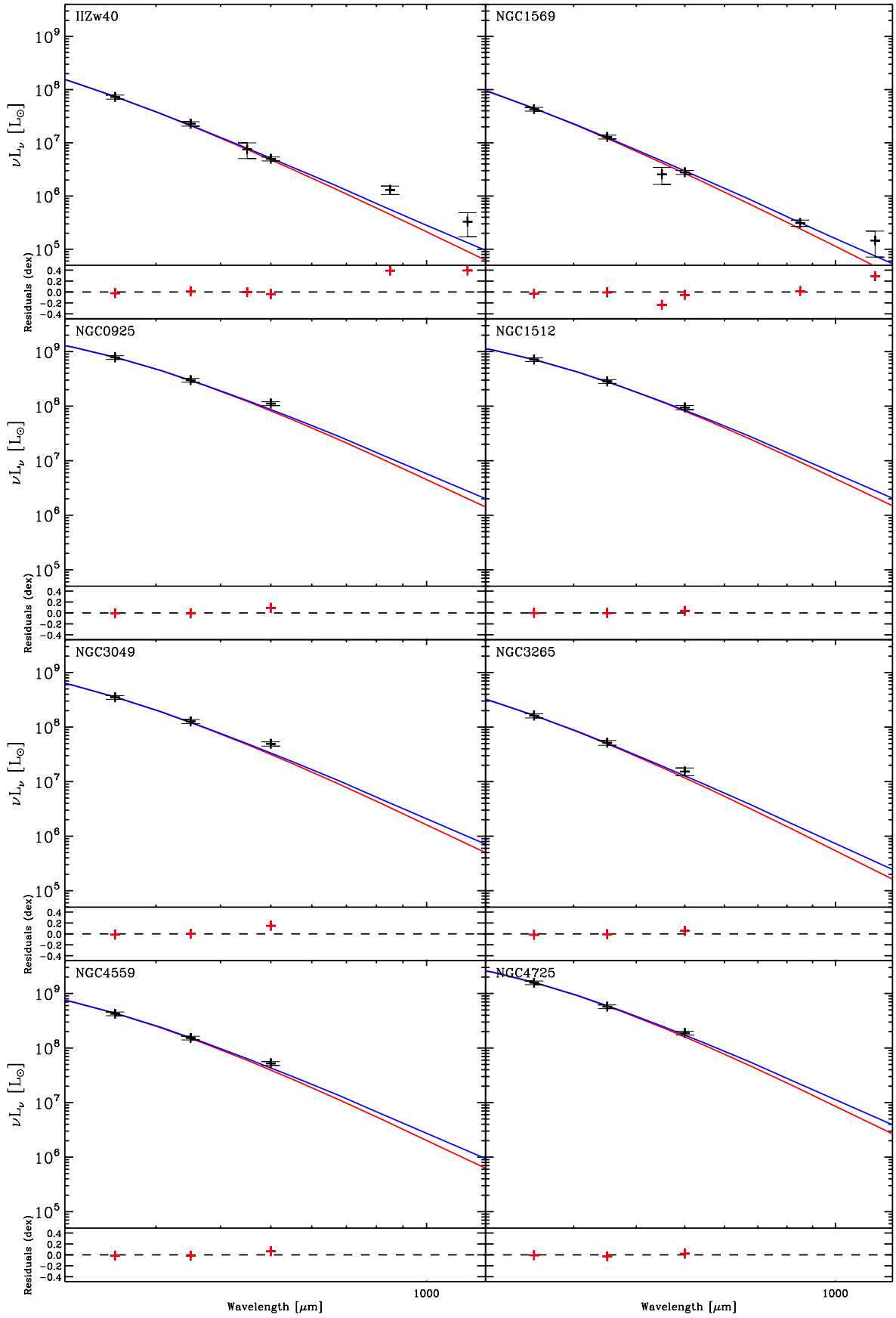

Fig. 8.20. Comparison of the Gr and Ac SEDs between 200 μm and 1300 μm *(continued)*.

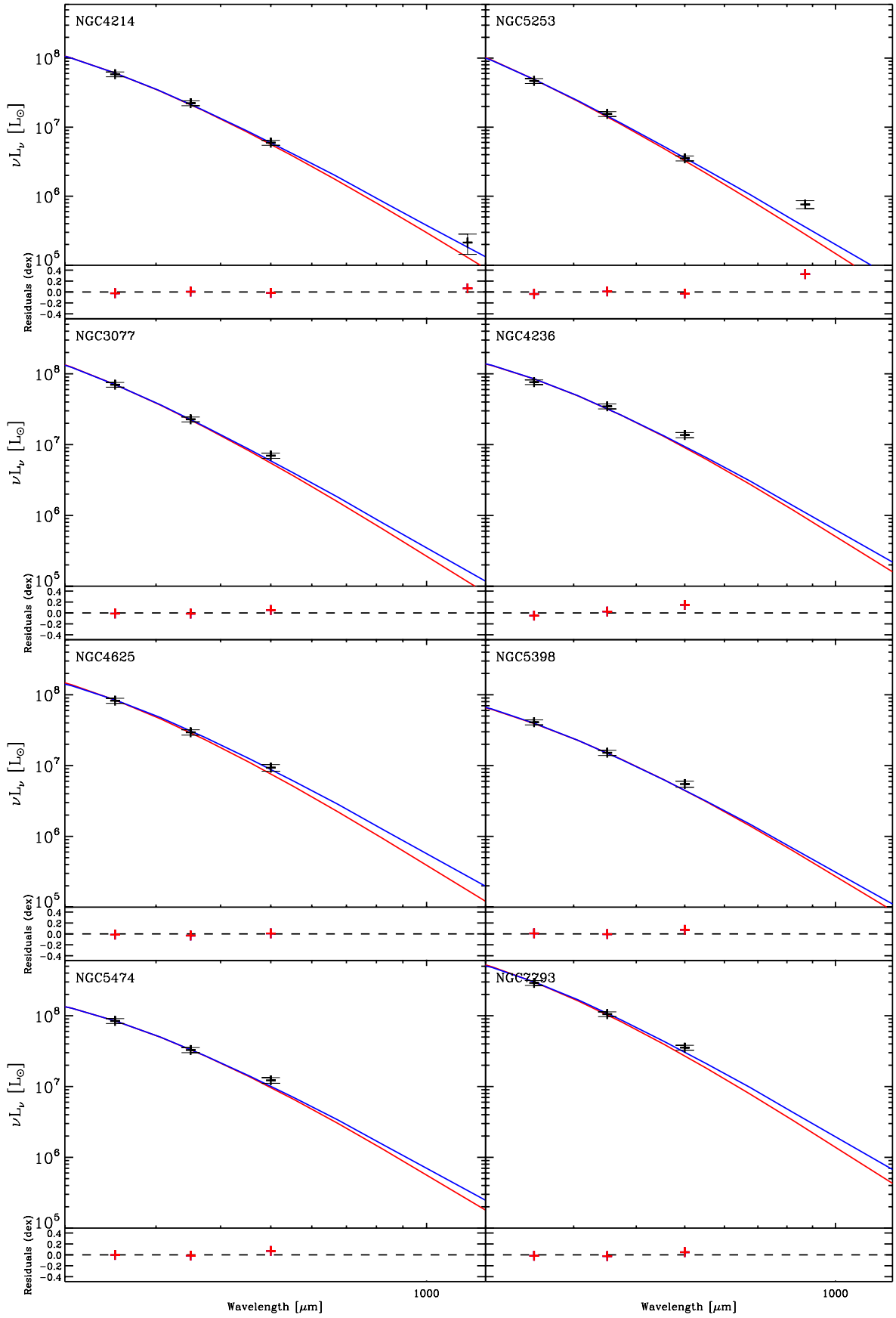

Fig. 8.20. Comparison of the Gr and Ac SEDs between 200 μm and 1300 μm *(continued)*.

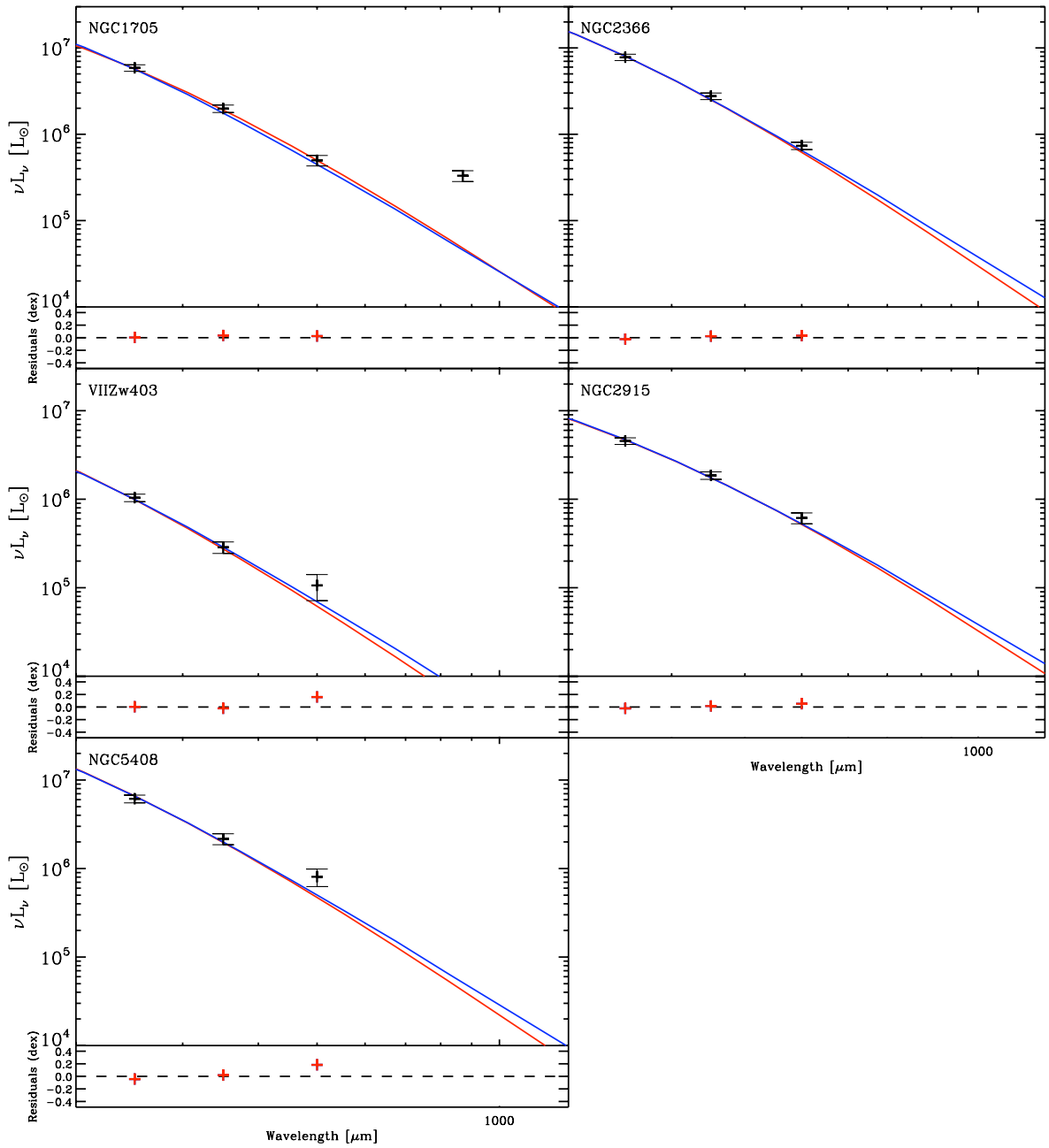

Fig. 8.20. Comparison of the Gr and Ac SEDs between 200 μm and 1300 μm *(continued)*.

Table 8.1. Submm residuals for the DGS and KINGFISH samples in %.

Name	Exc BB ?	R(500)±ΔR(500)	Exc ?	R(850/870)±ΔR(850/870)	Exc ?	R(1200)±ΔR(1200)	Exc ?
DGS							
Haro11	yes	24.0 ± 12.1	yes*	235.6 ± 32.4 ^{L}	yes*		
Haro2		-14.0 ± 9.7		9.3 ± 37.4 ^{S}			
Haro3		-12.2 ± 9.4					
He2-10		-13.3 ± 8.6		-16.8 ± 12.9 ^{S}		-11.3 ± 45.5	
HS0052+2536	yes	113.8 ± 50.8	yes*				
IC10		-8.2 ± 31.1					
IIZw40		-2.2 ± 8.5		206.6 ± 18.1 ^{S}	yes*	263.0 ± 47.8	yes*
Mrk1089		-11.1 ± 10.8		76.7 ± 14.5 ^{L}	yes*		
Mrk930		4.5 ± 13.6		428.5 ± 14.7 ^{L}	yes*		
NGC1140		-11.3 ± 10.8		27.0 ± 45.8 ^{S}			
NGC1569		-2.3 ± 8.6		35.9 ± 20.8 ^{S}	yes	202.4 ± 69.0	yes*
NGC1705	yes	-4.7 ± 13.8		589.9 ± 68.7 ^{L}	yes*		
NGC2366	yes	12.8 ± 9.7	yes				
NGC4214	yes	0.9 ± 8.2				64.4 ± 32.5	yes
NGC4449		-8.7 ± 8.1					
NGC4861	yes	-4.0 ± 12.4					
NGC5253		1.7 ± 8.2		171.2 ± 17.1 ^{L}	yes*		
NGC625	yes	3.3 ± 8.6					
NGC6822	yes	9.9 ± 31.1					
UM311		-10.5 ± 9.0					
UM448		3.8 ± 9.8		232.7 ± 16.4 ^{L}	yes*		
VIIZw403	yes	60.8 ± 32.7	yes*				
KINGFISH							
NGC0337	yes	16.4 ± 8.3	yes	28.1 ± 18.0 ^{S}	yes		
NGC0628		6.3 ± 8.4					
NGC0855		-16.6 ± 16.8					
NGC0925	yes	30.5 ± 8.0	yes*				
NGC1097		1.4 ± 8.0		-37.5 ± 71.5 ^{S}			
NGC1266		-4.4 ± 11.5					
NGC1291		5.4 ± 9.2					
NGC1316		6.3 ± 31.3					
NGC1377	yes	24.4 ± 17.9	yes				
IC0342		-3.4 ± 7.6					
NGC1482		-5.6 ± 8.6		-36.9 ± 27.5 ^{S}			
NGC1512	yes	12.8 ± 9.0	yes				
NGC2146		-10.5 ± 7.9					
HoII		8.1 ± 55.9					
NGC2798		3.1 ± 9.3		-6.7 ± 25.1 ^{S}			
NGC2841		1.3 ± 7.9					
NGC2915	yes	14.2 ± 14.0	yes				
HoI	yes	25.4 ± 33.8					
NGC2976		7.3 ± 8.1		-11.0 ± 43.1 ^{S}			
NGC3049	yes	48.7 ± 9.1	yes*				
NGC3077	yes	20.5 ± 8.5	yes*				
M81dwB		33.7 ± 55.7					
NGC3190		-8.1 ± 8.9		-23.7 ± 24.8 ^{S}			
NGC3184		8.3 ± 8.1	yes				
NGC3198	yes	17.0 ± 8.0	yes				
IC2574	yes	-0.3 ± 9.9					
NGC3265	yes	23.2 ± 16.4	yes				
NGC3351		-6.9 ± 8.2					
NGC3521		4.8 ± 8.0		-31.9 ± 47.4 ^{S}			
NGC3621	yes	17.1 ± 7.6	yes				
NGC3627		-6.6 ± 7.7		-38.7 ± 54.2 ^{S}			
NGC3773		6.0 ± 14.9					
NGC3938		5.2 ± 8.2					
NGC4236	yes	44.8 ± 8.5	yes*				
NGC4254		-10.5 ± 8.0		-56.0 ± 89.4 ^{S}			
NGC4321		-2.7 ± 8.3		-63.3 ± 87.0 ^{S}			
NGC4536	yes	15.0 ± 8.1	yes	-56.7 ± 38.6 ^{S}			
NGC4559	yes	26.6 ± 8.0	yes*				
NGC4569		-10.0 ± 8.2		-35.9 ± 21.2 ^{S}			
NGC4579		-3.2 ± 8.2		-29.1 ± 19.2 ^{S}			
NGC4594	yes	-0.6 ± 9.5		-66.8 ± 80.3 ^{S}			
NGC4625	yes	16.9 ± 10.7	yes				

Table 8.1. (continued) Submm residuals for the DGS and KINGFISH samples in %.

Name	Exc BB ?	R(500)±ΔR(500)	Exc ?	R(850/870)±ΔR(850/870)	Exc ?	R(1200)±ΔR(1200)	Exc ?
NGC4631	yes	14.6 ± 7.9	yes*	70.5 ± 24.8 ^{S}	yes*		
NGC4725		12.6 ± 8.0	yes				
NGC4736	yes	14.6 ± 8.5	yes	-6.1 ± 52.1 ^{S}			
NGC4826		-2.5 ± 8.1		11.5 ± 40.8 ^{S}			
NGC5055		0.8 ± 8.1					
NGC5398	yes	19.1 ± 9.9	yes*				
NGC5408	yes	61.2 ± 22.4	yes*				
NGC5457	yes	18.2 ± 7.9	yes*				
NGC5474	yes	22.1 ± 9.2	yes*				
NGC5713		-8.1 ± 8.2		42.7 ± 25.6 ^{S}	yes		
NGC5866		-5.5 ± 9.8		-28.3 ± 29.3 ^{S}			
NGC6946		-6.7 ± 7.8		-74.9 ± 28.5 ^{S}			
NGC7331		4.2 ± 8.1		-18.6 ± 21.4 ^{S}			
NGC7793	yes	24.9 ± 8.0	yes*				

^{L} LABOCA residual at 870 μm.

^{S} SCUBA residual at 850 μm.

* Excess remains if use amorphous carbon grains model.

Chapter 9

Gas-to-Dust mass ratios as a function of metallicity over a 2 dex metallicity range

Contents

In this last Chapter, we incorporate the gas into our dust picture, and look at the gas-to-dust mass ratios (G/D) as a function of metallicity. The G/D links the amount of metals locked up in dust and in the gas phase and is thus a powerful tracer of the evolutionary stage of a galaxy. Investigations of the relation between the observed G/D and metallicity can thus place important constraints on the physical processes governing galaxy evolution and more specifically on chemical evolution models.

9.1 Motivations

The observed G/D of integrated galaxies as a function of metallicity has been intensively studied over the past decades (e.g., Issa et al. 1990; Lisenfeld & Ferrara 1998; Hirashita et al. 2002; James et al. 2002; Hunt et al. 2005; Draine et al. 2007; Engelbracht et al. 2008; Galliano et al. 2008; Muñoz-Mateos et al. 2009; Bendo et al. 2010b; Galametz et al. 2011; Magrini et al. 2011). In the disk of our Galaxy the proportion of heavy elements in the gas and in the dust has been shown to scale with the metallicity (Dwek 1998) if one assumes that the time dependence of the dust formation timescale is the same as that of the dust destruction timescale. This results in a constant dust-to-metal mass ratio and gives a dependence of the G/D on metallicity as: $G/D \propto Z^{-1}$ (that we call hereafter the "reference" trend). This reference trend between G/D and metallicity seems consistent with the observations of galaxies with near-solar metallicities (e.g., James et al. 2002; Draine et al. 2007; Bendo et al. 2010b; Magrini et al. 2011). However some studies also show that the G/D of some low-metallicity dwarf galaxies deviate from this reference trend, with a higher G/D than expected for their metallicity (Lisenfeld & Ferrara 1998; Galliano et al. 2003; Hunt et al. 2005; Galliano et al. 2005, 2008; Bernard et al. 2008; Engelbracht et al. 2008; Galametz et al. 2011; Galliano et al. 2011).

The G/D is often used to empirically estimate the "CO-free" molecular gas. This molecular gas, not directly traced by CO measurements, was first proposed in low-metallicity galaxies using the 158 μm [CII] line (Poglitsch et al. 1995; Israel et al. 1996; Madden et al. 1997, 2012). Alternatively, using the dust mass determined from FIR measurements and assuming a G/D, given the metallicity of the galaxy, a gas mass can be estimated. This gas mass is then compared to the observed HI and CO gas masses to estimate the "CO-free" gas mass. This method is also used to estimate the CO-to-H2 conversion factor in local (e.g., Guelin et al. 1993, 1995; Neininger et al. 1996; Boselli et al. 2002; Sandstrom et al. 2013) and high-z galaxies (e.g., Magdis et al. 2012; Magnelli et al. 2012). However using these methods requires an accurate estimation of the G/D at a given metallicity.

A certain number of instrumental limitations and/or model caveats have limited former studies of the G/D. First, limits in wavelength coverage in the FIR have hampered the precise determination of the dust masses. For the earliest studies, the dust masses were derived from *IRAS* or *Spitzer* measurements, not extending further than 100-160 μm, therefore not tracing the cooler dust. As the bulk of the dust mass in galaxies often resides in the cold dust component, this has important consequences for the dust mass and therefore G/D determination. Before *Herschel*, using *Spitzer* and ground-based data, Galametz et al. (2011) indeed showed that a broad wavelength coverage of the FIR-to-submm part of the SED was critical to obtain accurate estimates of the dust masses. We confirmed these results in Chapter 8. Second, some of the studies presented previously used modified blackbody models to derive dust masses. Using *Herschel* data and a semi-empirical dust model, we showed in Chapter 8 that the dust mass modelled with a modified blackbody could be underestimated by a factor of ~ 2, consistent with the findings of Dale et al. (2012) on the KINGFISH sample. And finally, the limited sensitivities of the pre-*Herschel* era instruments only allowed the detection of dust for the brightest and highest-metallicity dwarf galaxies, limiting G/D studies to metallicities $\geq 1/5\ Z_{\odot}$ ($12+\log(O/H) = 8.0$).

In this work we investigate the relation between the G/D and metallicity avoiding the limitations

and caveats mentioned in the previous paragraph. Using our new *Herschel* data to constrain a semi-empirical dust model, we have a more accurate determination of the dust masses compared to *Spitzer*-only dust masses and/or modified blackbody dust masses. Our sample also covers a wide range in metallicity (2 dex, from 12+log(O/H) = 7.1 to 9.1), with a significant fraction of the sample below 12+log(O/H) = 8.0 ($\sim$ 30%, see Section 9.2), thanks to the increased sensitivity of *Herschel* which enables us to access the dust in the lowest metallicity galaxies. We are thus able to provide better constraints on the G/D at low-metallicities.

In Section 9.2, we describe the sample and the method used to estimate dust and total gas masses are described in Section 9.3 and Section 9.4 respectively. Then we investigate the relation of the observed G/D with metallicity in Section 9.5 and fit several empirical relations to the data. We then interpret our results with the aid of several chemical evolution models in Section 9.6. Throughout we consider $(G/D)_{\odot} = 162$[1] (Zubko et al. 2004).

9.2 Sample

We combine 3 different samples for our study of the G/D: the Dwarf Galaxy Survey (DGS, Madden et al. 2013), the KINGFISH survey (Kennicutt et al. 2011) and a subsample of the sample presented in Galametz et al. (2011) (called the "G11 sample" hereafter). The basic parameters for all of the galaxies such as positions and distances can be found in Madden et al. (2013) and Chapter 3 for the DGS, Kennicutt et al. (2011) for KINGFISH and Galametz et al. (2011) for the G11 sample.

The G11 sample consists of all of the galaxies in Galametz et al. (2011) that are neither already in the DGS nor in the KINGFISH samples, except those galaxies which show a submm excess (see Section 9.3). This gives 17 additional galaxies, mostly solar or super-solar environments (mostly spiral galaxies), with metallicities from 12+log(O/H) = 8.14 to 9.1. The metallicity distribution for each of the 3 samples is presented in Fig. 9.1.

All of these metallicities have been derived using empirical strong emission line methods (see Madden et al. 2013 for the DGS, Kennicutt et al. 2011 for KINGFISH and Galametz et al. 2011 for G11 metallicity determination). The DGS and KINGFISH metallicities have been obtained through the R_{23} ratio[2] with the Pilyugin & Thuan (2005) calibration (see Chapter 3). Galametz et al. (2011) do not indicate precisely which calibration they use to convert R_{23} into metallicity, thus several metallicities for the G11 galaxies were re-estimated from the original line intensities with the Pilyugin & Thuan (2005) calibration. We also assume a conservative 0.1 dex uncertainty for the G11 metallicities. On average for the total sample, the uncertainty on the metallicity measurements is $\sim$ 0.1 dex. The metallicities for the whole sample are listed in Table 9.3. Other methods exist to determine metallicities and can lead to very different values, but this will only introduce a systematic offset in the adopted values here (Kewley & Ellison 2008). Note that these metallicity values correspond to global estimates. On smaller scales within galaxies, differences can occur due to inhomogeneous mixing of metals: metallicity gradients have been observed in large spiral galaxies (Garnett et al. 2004; Bendo et al. 2010b; Moustakas et al. 2010). Dwarf galaxies, however, are smaller in size than metal-rich galaxies and we can presume, for this study, that metallicity is more homogeneous within these environments (Revaz & Jablonka 2012; Valcke et al. 2008) .

This gives us a total of 126 galaxies spanning a 2 dex range in metallicity (Fig. 9.1). We see that the low-metallicity end of the distribution is fairly well sampled as we have $\sim$ 30 % of the total sample with metallicities below 1/5 $Z_{\odot}$.

[1] This value is from Table 6 from Zubko et al. (2004) for the BARE-GR-S model, which corresponds to the dust composition used for our modelling (see Section 7.1).

[2] Remember: R_{23}=([OII]λ3727+[OIII]$\lambda\lambda$4959,5007)/Hβ.

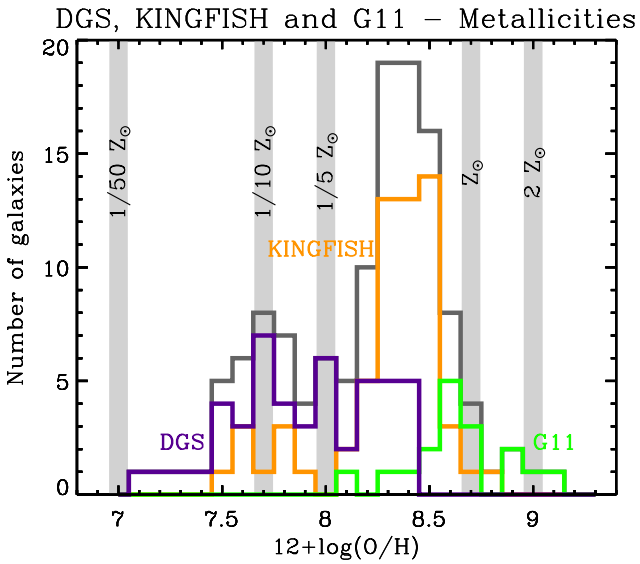

Fig. 9.1. Metallicity distribution of the DGS (purple), KINGFISH (orange) and G11 (green) samples from 12+log(O/H) = 7.14 to 9.1. The total distribution is indicated in grey. Solar metallicity is indicated here as a guide to the eye, as well as the 1/50, 1/10, 1/5 and 2 $Z_{\odot}$values.

9.3 Dust masses

To ensure a consistent determination of the dust masses throughout our sample, all of the galaxies are modelled with the dust SED model presented in Galliano et al. (2011). The dust masses for the DGS and KINGFISH samples can be found in Chapter 7. A submm excess is observed in some DGS and KINGFISH galaxies at 500 μm (Chapter 8, Dale et al. 2012). If present, the excess is rather small at 500 μm (the median S/N of the excess at 500 μm is $\sim$ 2.0) and can increase as we go to longer wavelengths (see Chapter 8). However, because of the unknown origin of this excess and because of the uncertainties it can bring in the dust mass estimation, we do not attempt to model this excess with additional modifications to the model. We discuss this choice in Section 9.5.3.

We also model galaxies from the G11 sample, as some model assumptions were different in Galametz et al. (2011). *Herschel* constraints are not present but other submm constraints are taken into account such as JCMT/SCUBA at 850 μm and/or APEX/LABOCA at 870 μm, allowing a precise determination of the dust masses (given in Table 9.1). Galametz et al. (2011) also observed a submm excess in 9 galaxies of their original sample and modelled it with a Very Cold Dust (VCD) component. However the submm excess is not fully understood yet and this extra VCD component may lead to an overestimation of the dust mass. Because we do not have constraints between 160 μm and the available ground-based submm fluxes to see where the submm excess starts, we do not consider nor model these galaxies here.

The wavelength coverage is not exactly the same from galaxy to galaxy. The most important constraints for the determination of the dust mass are constraints sampling the peak of the dust SED. *Herschel* provides such constraints for all of the DGS and KINGFISH galaxies. Some dwarf galaxies are not detected with *Herschel* at submm wavelengths (beyond 250 μm) and are noted in Fig. 9.4 (see Section 9.4). These galaxies harbour particularly warm dust (see Chapter 8, Rémy-Ruyer et al. 2013); the peak of their SED is thus shifted towards shorter wavelengths and is then well sampled by constraints until 160 μm where the galaxy is still detected. For galaxies in the G11 sample, the peak of the dust SED is probed by *Spitzer* observations and the Rayleigh Jeans slope of the SED by longer submm wavelength observations. Thus we are confident in the dust masses

we derive with these sets of constraints.

The errors on the dust masses for the G11 sample are estimated following the same procedure as for the DGS and KINGFISH galaxies in Chapter 7, by generating 300 random realisations of the SED, perturbed according to the random and systematic noise, in order to get a distribution for the dust mass. The error bars on the dust mass are taken to be the 66.67 % confidence interval of the distribution (i.e., the range of the parameter values between 0.1667 and 0.8333 of the repartition function). The dust masses and uncertainties for the G11 sample are presented in Table 9.1.

Table 9.1. Dust masses for the G11 sample.

Name	M_{dust} [$M_\odot$]	Uncertainty (%)
M83	1.10×10^{7}	8.14
NGC1808	2.54×10^{7}	34.24
NGC7552	7.24×10^{7}	16.10
M82	6.85×10^{6}	33.02
NGC1068	2.77×10^{8}	36.05
NGC0891	5.84×10^{7}	11.84
MGC+02-04-025	1.01×10^{8}	47.08
NGC7469	1.55×10^{8}	19.16
NGC5256	2.01×10^{8}	62.93
NGC5953	2.25×10^{7}	18.90
M51	3.74×10^{8}	21.82
NGC3995	5.75×10^{7}	23.47
NGC3994	5.27×10^{7}	34.81
NGC6052	5.84×10^{7}	32.58
NGC1222	1.33×10^{7}	26.71
NGC7674	9.83×10^{7}	29.69
NGC4670	1.13×10^{6}	21.12

9.4 Gas masses from the literature

9.4.1 Atomic gas masses

The HI masses and their errors are compiled from the literature, and rescaled to the distances used here. Most of the atomic gas masses are given in Galametz et al. (2011) for the G11 sample, and in Draine & Li (2007) for the KINGFISH survey. They are presented in Madden et al. (2013) and Chapter 3 for the DGS. The errors were not available for all of the HI measurements. When no error was available for the HI mass, we adopted the mean value of all of the relative errors on the HI masses compiled from the literature: $\sim 16\%$.

Correcting the HI masses

However the HI extent of a galaxy is not necessarily the same as the aperture used to probe the dust SED, as the HI often extends beyond the optical radius of a galaxy (Hunter 1997). This can be particularly true for dwarf galaxies where the HI halo can be very extended: some irregular galaxies present unusually extended HI gas (up to seven times the optical radius, Huchtmeier 1979; Huchtmeier et al. 1981; Carignan & Beaulieu 1989; Carignan et al. 1990; Thuan et al. 2004). We also note that in some galaxies (e.g., NGC 4449), gas morphology may be highly perturbed due to past interactions or mergers (e.g., Hunter et al. 1999). This may also lead to significant uncertainties in the HI mass and thus on the derived G/D (e.g., Karczewski et al. 2013). Thus we check the literature for the DGS sample for the size of the HI halo to compare it to the dust aperture. It was not possible to find this information for $\sim 38\%$ of the sample (HI not detected or no map available).

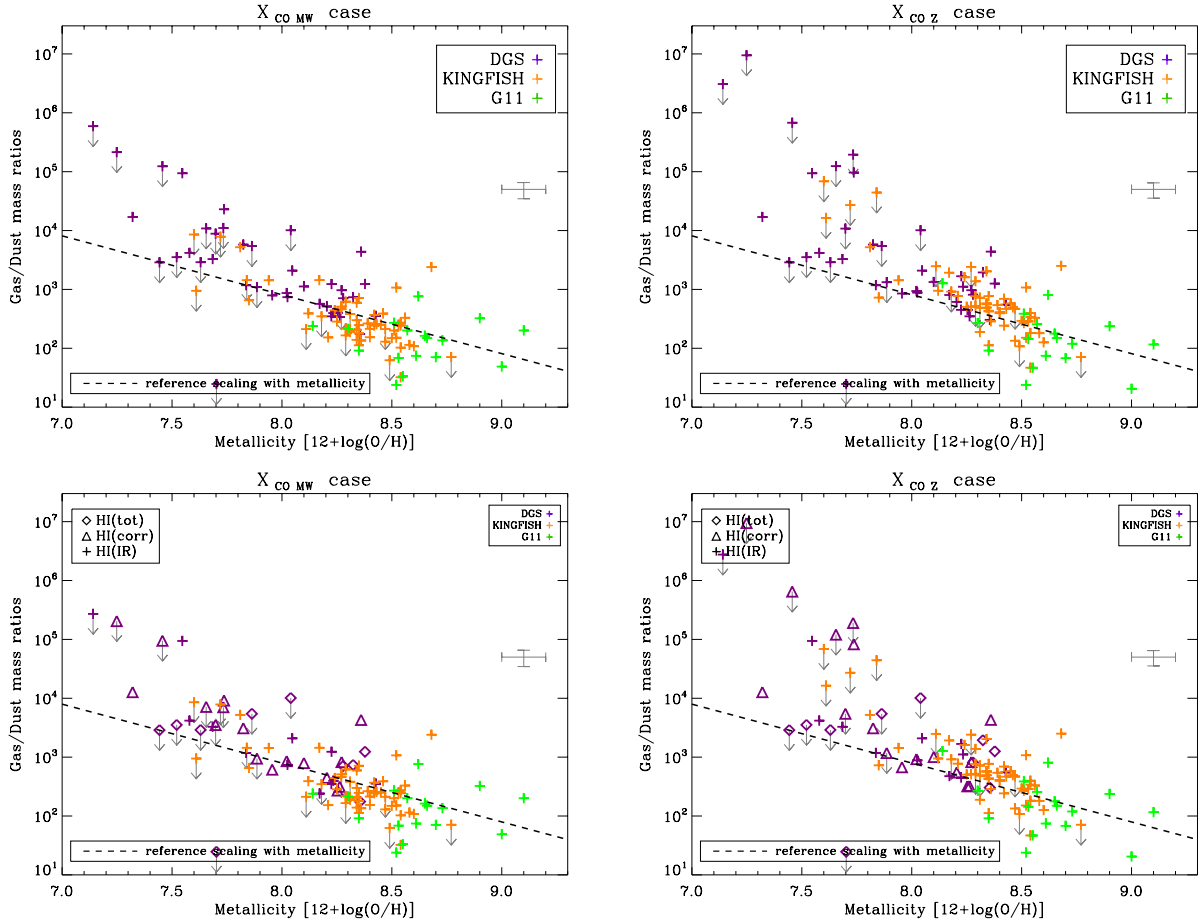

Fig. 9.2. G/D mass ratios as a function of metallicity for the 2 values of X_{CO} $X_{CO,MW}$ (*right*) and $X_{CO,Z}$ (*left*), before (*top*) and after (*bottom*) correcting the HI masses. The mean error for the datapoints is shown in grey. On both panels, the colours delineate the three samples: DGS in purple, KINGFISH in orange and G11 in green. On the bottom panels, the symbol traces the changes made in the HI masses (see text for details on the uncertainties and the changes on the atomic gas masses).

For the rest, 25% of the DGS galaxies have a HI extent that corresponds to the dust IR aperture, which has been chosen to be 1.5 times the optical radius (for most cases, see Chapter 4 and Rémy-Ruyer et al. 2013); and 35% have a HI halo that is more extended. If we assume that the HI mass distribution follows an exponential profile (based on the observed high central gas concentration seen in BCDs, e.g., van Zee et al. 1998, 2001; Simpson & Gottesman 2000), we can correct the total HI mass for these galaxies to find the HI mass corresponding to the dust aperture.

$$M_{HI}(IRcorr) = M_{HI} \times \frac{\int_0^{r_{dust}} \exp^{-r^2/(2\sigma^2)}\ \mathrm{d}r}{\int_0^{r_{HI}} \exp^{-r^2/(2\sigma^2)}\ \mathrm{d}r} \tag{9.1}$$

where r_{dust} and r_{HI} are the dust and HI radii respectively, and σ the standard deviation of the gaussian profile: $\sigma = r_{HI}/2.35$.

In reality, the HI profile can show a complicated structure with clumps and shells, rendering the profile more assymetric. Our correction corresponds to a factor of ~ 1.55 on average, for these galaxies. Several studies (Thuan & Martin 1981; Swaters et al. 2002; Lee et al. 2002; Begum & Chengalur 2005a; Pustilnik & Martin 2007) have tried to quantify the extent of the HI halo for dwarf galaxies and found that the ratio of HI size to the optical size is typically 2, which gives a

correction of ~ 1.4. This is similar to what we find here with our assumptions. The atomic gas masses for the sample, after correction if needed, are presented in Table 9.3. The G/D mass ratio before and after this correction is shown in Fig. 9.2.

9.4.2 Molecular gas masses

The H_2 masses have been compiled from the literature. They have been rescaled, when necessary, to the distance adopted here to derive the dust masses.

There are two main issues in determining the molecular gas masses. First, detection of CO in low-metallicity galaxies is challenging: sensitivity has limited CO detections to galaxies with 12+log(O/H)$\gtrsim 8.0$ (e.g., Leroy et al. 2009; Schruba et al. 2012). The other issue in the H_2 mass determination is the choice of the conversion factor between CO intensities and molecular gas masses, X_{CO}. Indeed the variation of this factor with metallicity is poorly constrained, and a number of studies have been dedicated to quantifying the dependence of X_{CO} on metallicity (Wilson 1995; Israel 1997; Boselli et al. 2002; Israel et al. 2003; Strong et al. 2004; Leroy et al. 2011; Schruba et al. 2012; Bolatto et al. 2013). From a sample of 16 dwarf galaxies, and assuming a constant H_2 depletion timescale, Schruba et al. (2012) found a X_{CO} scaling with $(O/H)^{-2}$. This relation takes into account possible "CO-free" gas as the X_{CO} conversion factor is estimated from the total reservoir of molecular gas needed for star formation (Schruba et al. 2012). Following Cormier et al. (2014), we estimate the molecular gas masses from a constant X_{CO} factor using the Galactic value: $X_{CO,MW} = 2.0 \times 10^{20}$ cm^{-2} (K km s^{-1})$^{-1}$ (Ackermann et al. 2011), giving us $M_{H_2,MW}$, and from a X_{CO} factor depending on $(O/H)^{-2}$: $X_{CO,Z}$, giving us $M_{H_2,Z}$:

$$X_{CO,Z} = X_{CO,MW} \times \left(\frac{Z_\odot}{Z}\right)^2 \tag{9.2}$$

This provides a conservative range of molecular gas mass estimates that reflects how uncertain the molecular gas mass determination is. For this reason, we do not give any error bar on our molecular gas mass.

Correcting the H_2 masses

In order to go beyond the CO upper limits and to constrain the G/D behaviour at low metallicities we find a way to estimate the amount of molecular gas for the lowest metallicity galaxies. Figure 9.3 shows the ratio of M_{H_2}-to-M_{HI} as a function of metallicity for our sample and for both cases of X_{CO}. We note that around 12+log(O/H) ~ 8.1 the ratio M_{H_2}/M_{HI} drops suddenly for the detected galaxies for both X_{CO}. For these very low-metallicity galaxies with 12+log(O/H) ≤ 8.1, the mean ratio between the detected M_{H_2} and M_{HI} is 1.2%, for $X_{CO,MW}$. Using $X_{CO,Z}$, this ratio goes up to 68%, the molecular gas mass is not negligible anymore but is still more than a factor of 2 lower than the atomic gas mass. Thus for galaxies with non-detections in CO, or without any CO observations, and with 12+log(O/H) ≤ 8.1, we replace the upper limit values by $0.012 \times M_{HI}$ for $M_{H_2,MW}$ and $0.68 \times M_{HI}$ for $M_{H_2,Z}$. Given the low molecular gas fraction we find, this will not greatly affect our interpretation of G/D nor the conclusions. From now on, the galaxies for which we apply this correction will be treated as detections. This 12+log(O/H) value of ~ 8.1 has already been noted as being special for dwarf galaxies (e.g., for the strength of the PAH features: Engelbracht et al. 2005; Madden et al. 2006; Draine et al. 2007; Engelbracht et al. 2008; Galliano et al. 2008). The molecular gas masses we use in the following analysis are presented in Table 9.3. The difference between the G/D before and after the H_2 mass correction can be seen by comparing Fig. 9.2 *bottom* and Fig. 9.4.

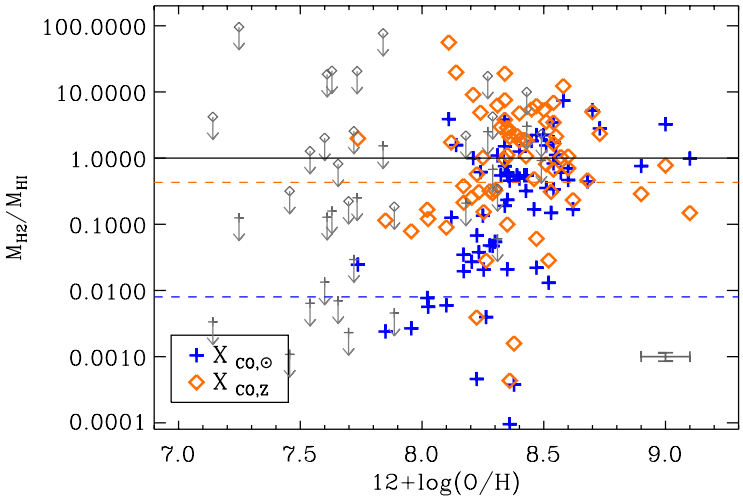

Fig. 9.3. M_{H_2}/M_{HI} as a function of metallicity for the whole sample. The blue crosses are for molecular gas masses computed with $X_{CO,MW}$ and the orange diamonds are for molecular gas masses computed with $X_{CO,Z}$. Upper limits in the molecular gas mass are indicated with grey arrows and smaller grey symbols. The mean error for the data points is shown in grey on the bottom right of the plot. The plain line shows the unity line. The dashed blue and orange lines show the 1.2% and 68% molecular-to-atomic gas mass fractions respectively and represent the mean H_2-to-HI ratio of the detected galaxies with 12+log(O/H) < 8.1 (see text).

9.4.3 Total gas masses

We get the total gas mass, M_{gas}, by adding all of the different gas contributions: the atomic gas mass, the molecular gas mass, the helium gas mass and the gaseous metal mass:

$$M_{gas} = M_{HI}(IRcorr) + M_{H_2} + M_{He} + Z \times M_{gas}, \tag{9.3}$$

where $M_{\rm He}$ is the helium mass and Z the mass fraction of metals in the galaxy. Assuming $M_{\rm He} = Y_{\odot}\, M_{\rm gas}$, where $Y_{\odot}$ is the Galactic mass fraction of Helium, $Y_{\odot} = 0.270$ (Asplund et al. 2009), we have:

$$M_{gas} = \mu_{gal}(M_{HI} + M_{H_2}), \tag{9.4}$$

with $\mu_{gal} = 1/(1\text{-}Y_{\odot}\text{- Z})$ the mean atomic weight. μ_{gal} has been computed for each galaxy and the mean value for our sample is 1.38±0.01 (see Table 9.3). We get Z assuming $(Z/Z_{\odot})$ =(O/H)/(O/H$_{\odot}$) and $Z_{\odot}$= 0.014 (Asplund et al. 2009).

We assume here that the ionised gas mass ($M_{\rm HII}$) is negligible compared to the HI mass. We perform the test for 67 galaxies of the sample, with $M_{\rm HII}$ derived from Hα measurements of Gil de Paz et al. (2003); Kennicutt et al. (2009); Skibba et al. (2011) and found $M_{\rm HII}/M_{HI}\sim$ 0.2%. However, we found two dwarf galaxies for which the ionised gas mass should be taken into account as it contributes equally or more than the atomic gas mass: Haro11 ($M_{\rm HII} \sim 1.2 \times M_{HI}$, Cormier et al. 2012) and Pox186 ($M_{\rm HII} \sim M_{HI}$, Gil de Paz et al. 2003). For these two galaxies, the total gas mass also includes $M_{\rm HII}$. For Haro11 the ionised gas mass is taken from Cormier et al. (2012). For Pox186, we assume that the mass of ionised gas M_{HII} is the mass coming from the Hα emission and is estimated from the Hα luminosity and the formula of Fathi et al. (2011):

$$M_{H\alpha} = m_H \times \frac{L_{H\alpha}}{3.56 \times 10^{-25} n_e} \tag{9.5}$$

where m_H is the mass of the hydrogen proton in $M_\odot$, $L_{H\alpha}$ is the total Hα luminosity in erg.s^{-1}, and n_e is the electron number density in cm^{-3}. $n_e = 70$ cm^{-3} in the HII region for Pox186 (Guseva et al. 2004). For these two galaxies, the total gas mass also includes $M_{\rm HII}$.

The G/D as a function of metallicity is presented in Fig. 9.4 a&b for the two cases: $X_{CO,MW}$ or $X_{CO,Z}$. The average error on the observed G/D is $\sim$ 27% in both X_{CO} cases ($\sim$ 10% for the total gas mass and $\sim$26% for the dust mass). The dashed line indicates the reference scaling of the G/D with metallicity. The colours of the symbols indicate the reliability of the data points by tracing if the gas or dust masses determinations are uncertain. Blue symbols refer to HI or H_2 non-detections or to the absence of H_2 observations for the galaxy. Red symbols indicate that the galaxy is not detected at wavelengths $\geq$ 160 μm. The combination of both indications for the gas and dust masses is shown with the purple symbols. Black symbols indicate that both gas and dust masses have reliable measurements (67% of the sample).

The type of symbols indicates whether or not the HI and/or H_2 masses have been corrected. For the HI masses we distinguish three cases for the DGS galaxies: the HI extent of the galaxy is unknown and we cannot correct the HI mass (diamonds), the HI extent is known and greater than the dust aperture and we correct the HI mass (triangles) and the HI extent is known and similar to the dust aperture, there is no need to correct the HI mass (crosses). The galaxies with 12+log(O/H) $<$ 8.1 for which the H_2 masses have been corrected (either from upper limit or lack of measurements) are indicated as filled symbols (see Section 9.4.2 on H_2 masses).

9.5 Analysis

9.5.1 Observed gas-to-dust mass ratio - metallicity relation and dispersion

To evaluate the general behaviour and scatter in the G/D values at different metallicities, we consider the error-weighted mean values of log(G/D) in metallicity bins (neglecting the upper/lower limits), with the bin sizes chosen to include at least two galaxies and to span at least 0.1 dex. The result is overlaid as pink filled circles in Fig. 9.4 c&d. We also look at the dispersion of the G/D values in each metallicity bin (see bottom panels of Fig. 9.4 c&d), by computing the standard deviation of the log(G/D) values in each bin (also neglecting the upper/lower limits). The dispersion is $\sim$ 0.37 dex (i.e., a factor of 2.3) on average for all bins and for both X_{CO} values. Additionally, in one bin the G/D vary on average by one order of magnitude. This confirms that the relation between G/D and metallicity is not trivial even at a given metallicity, over the whole metallicity range. We also see that the dispersion in the observed G/D values does not depend on metallicity. This indicates that the scatter within each bin may be intrinsic and does not reflect systematic observational or correction errors. This also means that the metallicity is not the only driver for the observed scatter in the G/D values: other processes operating in galaxies can lead to large variation in the G/D in a given metallicity range, throughout this range. However, there might be a selection bias in our sample. Indeed our sample is mainly composed of star-forming gas-rich dwarf galaxies at low metallicities and spiral galaxies at high metallicities. We could wonder if gas-poor dwarf galaxies would show different, possibly lower, G/D than that observed in gas-rich dwarfs, thus possibly increasing the observed scatter at low metallicities. On the high-metallicity side, Smith et al. (2012b) showed that the 30 elliptical galaxies detected with *Herschel* in the *Herschel* Reference Survey (HRS, Boselli et al. 2010b) had a mean G/D of $\sim$ 120, which is slightly lower than what we find for our elliptical and spiral galaxies at moderate metallicities. However, the dust masses were estimated via a modified blackbody model, thus we will not go deeper into any further comparison. Nonetheless, including more elliptical galaxies might also slightly increase the scatter at high metallicities.

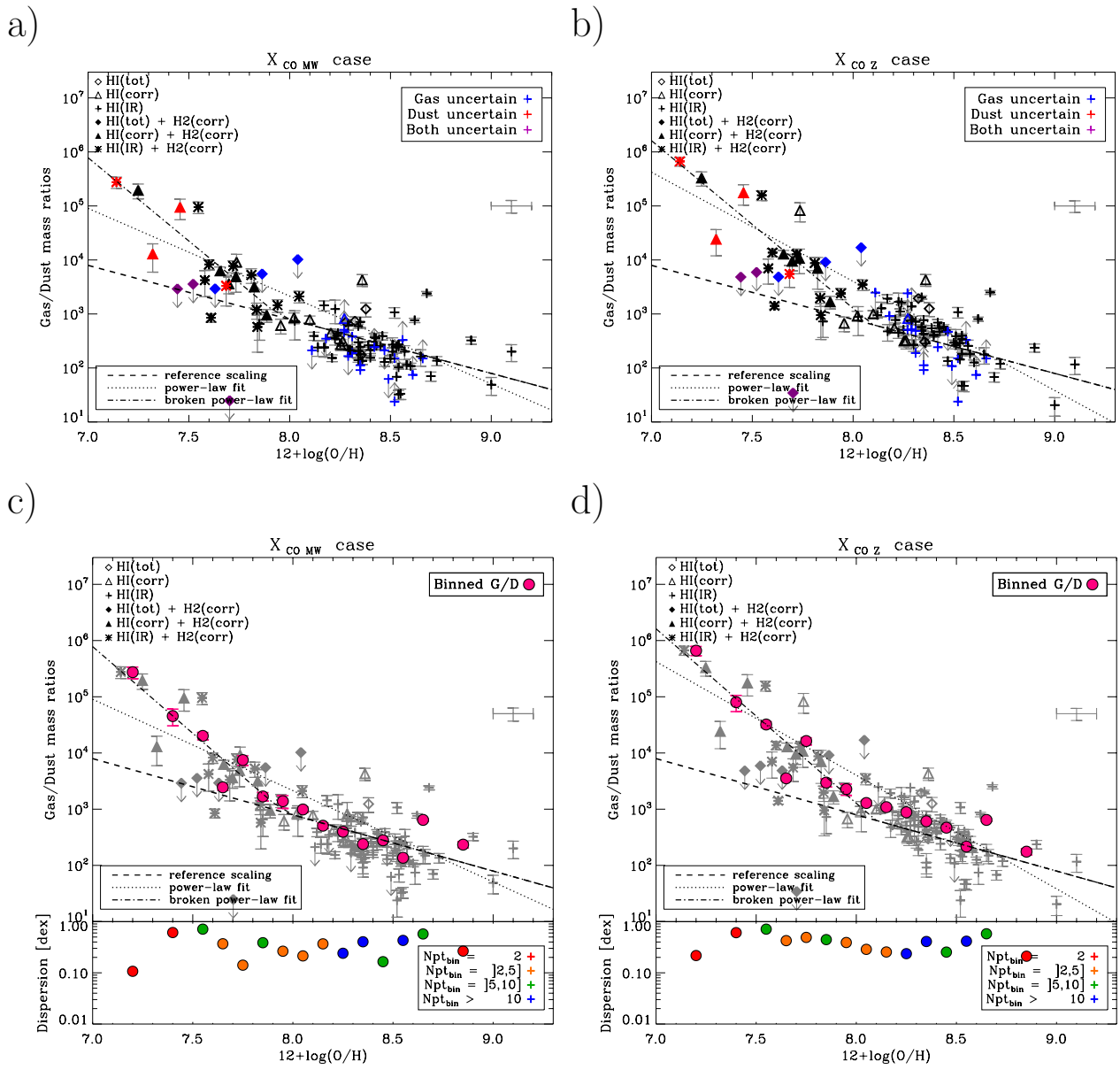

Fig. 9.4. *(Top row):* G/D as a function of metallicity for the 2 values of X_{CO}: $X_{CO,MW}$ (*a*) and $X_{CO,Z}$ (*b*). The mean error for the data points is shown in grey on the right of the plots. The colours code the reliability of the point depending if the gas mass is uncertain (in blue), the dust mass is uncertain (in red) or if both are uncertain (in purple). The symbol traces the changes made in the HI and H_2 masses (see text for details on the uncertainties and the changes on the gas masses). The dashed line represents the reference scaling of the G/D with metallicity (not fit to the data). The dotted and dash-dotted lines represent the best power-law and best broken power-law fits to the data. *(Bottom row):* Same as top row for $X_{CO,MW}$ (*c*) and $X_{CO,Z}$ (*d*), where the binned G/D values (see text) have been added as pink filled circles. For clarity, the observed G/D values are now shown in grey. On the bottom panels the relative dispersion in each bins, in terms of standard deviation, is shown and the colours show the number of galaxies in each bin.

9.5.2 Empirical relations and scatter

To investigate the variation of the G/D with metallicity, we first fit a power law (dotted line in Fig. 9.4) through the observed G/D values (excluding the limits): G/D $\propto (O/H)_0^{\alpha}$. The fit is performed with the IDL procedure MPFIT[3] and is shown in Fig. 9.4. The fit is weighted by the individual errors bars of the G/D values and the number density of points to avoid being dominated by the more numerous high-metallicity galaxies. We get a slope for the power law of α_0 = -1.6 ± 0.3 for $X_{CO,MW}$ and α_0 = -2.0 ± 0.3 for $X_{CO,Z}$. In both cases, α_0 is lower than -1, which corresponds to the slope of the reference relation.

We also fit a broken power law (dash-dotted line in Fig. 9.4), with two slopes α_L and α_H to describe the low- and high-metallicity slopes respectively, and with a transition metallicity, x_t, between the two regimes. Several studies (e.g., James et al. 2002; Draine et al. 2007; Galliano et al. 2008; Leroy et al. 2011) have shown that the G/D was well represented by a power law with a slope of -1 at high metallicities and down to 12+log(O/H) $\sim$ 8.0 - 8.2, and thus we fix α_H = -1. This gives us a low-metallicity slope, α_L, of -3.1 ± 1.8 with a transition metallicity of 7.96 ± 0.47 for $X_{CO,MW}$ and α_L = -3.1 ± 1.3 and a transition around a metallicity of 8.10 ± 0.43 for $X_{CO,Z}$. The low-metallicity slopes, α_L, are also for both cases lower than -1. The parameters for the different empirical relations are given in Table 9.2.

Table 9.2. Parameters for the three empirical relations between the G/D and metallicity: power law (slope of -1 and free) and broken power law for the two X_{CO} values.

Parameters	$X_{CO,MW}$ case	$X_{CO,Z}$ case
Power law, slope fixed: y = a + ($x_\odot$ - x) ("reference" scaling)		
a[1,2]	2.21	2.21
average logarithmic distance[3] [dex]	0.07	0.27
Power law, slope free: y = a + α_0 ($x_\odot - x$)		
a[1,2]	2.21	2.21
α_0	1.62±0.34	2.02±0.28
average logarithmic distance[3] [dex]	-0.21	-0.19
Broken power law: $y = a + \alpha_H (x_\odot - x)$ **for** $x > x_t$; $y = b + \alpha_L (x_\odot - x)$ **for** $x \leq x_t$		
a[1,2]	2.21	2.21
α_H	1.00	1.00
b	0.68	0.96
α_L	3.08±1.76	3.10±1.33
x_t	7.96±0.47	8.10±0.43
average logarithmic distance[3] [dex]	-0.06	0.06

Notes. y = log(G/D), x = 12+ log(O/H) and $x_\odot$ = 8.69.
[1]: Fixed parameters.
[2]: This correspond to the solar G/D: G/D$_\odot$ = 10^a = 162 (Zubko et al. 2004).
[3]: Derived for all of the individual galaxies, neglecting the upper/lower limits on the G/D.

If we let α_H free in the broken power-law fit, we get similar results within errors for α_L and x_t in both X_{CO} cases. We get α_H= -0.5 ± 0.9 and α_H= -1.6 ± 0.6, for $X_{CO,MW}$ and $X_{CO,Z}$ respectively, which is coherent with a slope of -1 within errors. Note that we have imposed here that our fits go through the solar G/D determined by Zubko et al. (2004). If we relax this condition (i.e., do not

[3]http://www.physics.wisc.edu/ craigm/idl/idl.html.

fix our "a" parameter in Table 9.2), we get values of the solar G/D ranging from $(G/D)_{\odot} = 90$ to 240 within $\sim 60\%$ of the value from Zubko et al. (2004).

Now we consider the deviation from each relation by looking at the logarithmic distance from the observed G/D values and the G/D values predicted by each of the three relations presented in Table 9.2. This is a way to look at the residuals from the two fits and the reference scaling, even though we did not actually fit the reference trend to the G/D values. These residuals are shown in Fig. 9.5. Average residuals in each metallicity bin defined previously are also computed. For a given point, the best relation is the one giving the residual closest to zero. From Fig. 9.5 we have another confirmation that a reference scaling of the G/D with metallicity does not provide reliable estimates of the G/D at low metallicities 12+log(O/H) $\lesssim 8.4$. We also note that, for the average residuals, the broken power law gives the residuals that are the closest to zero for nearly all the metallicity bins in both $X_{CO,MW}$ and $X_{CO,Z}$ cases, and that this corresponds to a predicted G/D uncertain to a factor of 1.6.

Even though 30% of our sample have metallicities below 1/5 $Z_{\odot}$, only seven galaxies have 12+log(O/H) ≤ 7.5 with two of them not detected in HI (SBS1159+545 and Tol1214-277). The remaining five galaxies (IZw18, HS0822+3542, SBS0335-052, SBS1415+437 and UGC4483) are important constraints for the broken power-law fit. These five galaxies all present broad dust SEDs peaking at very short wavelengths (~ 40 μm, and ~ 70 μm for HS0822+3542), indicating overall warmer dust with a wide range of dust grain temperatures, and subsequently very low dust masses; hence their high G/D. This peculiar SED shape had already been noted by Rémy-Ruyer et al. (2013).

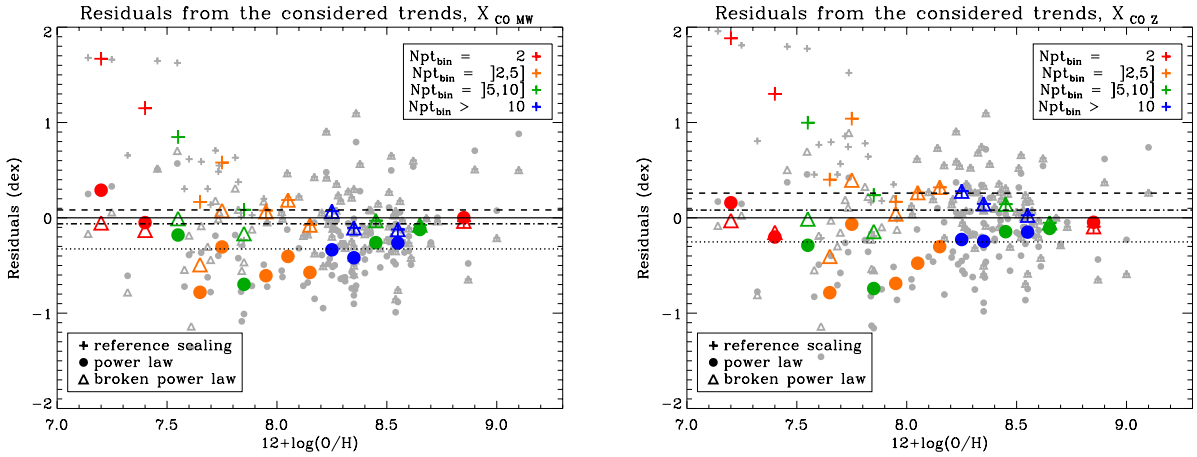

Fig. 9.5. Residuals (i.e., logarithmic distance) between the observed (and detected) G/D and predicted G/D for the three relations for $X_{CO,MW}$ (*left*) and $X_{CO,Z}$ (*right*): reference scaling of the G/D with metallicity (crosses), the best power-law fit (filled circles) and the best broken power-law fit (triangles). These residuals are shown in grey for the individual galaxies and in colour for the average residuals in each metallicity bin defined in Section 9.5.1. The colours show the number of galaxies in each bin. The mean residual for all of the observed G/D values is shown by the dashed (reference scaling), dotted (power-law fit) and dash-dotted (broken power-law fit) lines for the three relations and are reported in Table 9.2.

Using *Herschel* data and a semi-empirical SED model, Sandstrom et al. (2013) looked at the G/D in a sub-sample of 26 KINGFISH galaxies, mostly spirals. They simultaneously derive X_{CO} and G/D for their sample, taking advantage of the high spatial resolution of the KINGFISH gas and dust data. They found that the G/D for these galaxies follows the reference trend with the metallicity and shows small scatter. Their metallicity range is from 12+log(O/H) ~ 8.1 to 8.8 and thus these results are in agreement with our findings. Moreover the small scatter (less than a factor

of 2) observed by Sandstrom et al. (2013) can be due to the fact that they are probing very similar environments. In our case we have a wide variety of morphological types represented in our sample, that results in a larger scatter (a factor of ∼5 and 3 for $X_{CO,MW}$ and $X_{CO,Z}$ respectively for this metallicity range).

9.5.3 Discussion

In the previous section, we have shown that the reference scaling relation between metallicity and G/D derived for metallicities above 12+log(O/H) ∼ 8.0 does not apply to objects with lower metallicity. We empirically derived a new scaling relation better described by a broken power law with a transition metallicity around 12+log(O/H) ∼ 8.0, which confirms the importance of this value in low-metallicity dwarf galaxies. As mentioned in Section 9.1, this reference scaling relation arises from the hypothesis that the dust formation timescale and the dust destruction timescale behave similarly with time. Thus a possible interpretation of our results would be that the balance between formation and destruction of dust grains is altered at low metallicity, resulting in the observed steeper trend. Dwarf galaxies are subject to an overall harder ISRF than more metal-rich environments (Madden et al. 2006). The harder UV photons travel deeper into the ISM and photoprocess dust in much deeper regions in the clouds limiting the accretion and coagulation of the grains. The hard ISRF also affects the dust survivability in such extreme environments, especially carbonaceous dust: the dust destruction by hard UV photons is enhanced in low-metallicity galaxies for small carbon grains (e.g., Pilleri et al. 2012; Bocchio et al. 2012, 2013). In dwarf galaxies, dust destruction by SN shocks is enhanced too compared to larger scale galaxies, as most of the ISM can be affected by the shock due to the small physical size of the dwarfs and due to the globally lower density of the ISM.

In the following paragraphs we discuss the impact of several assumptions made to estimate the G/D on our results: the dust composition, the choice of the radiation field for the dust modelling, and the potential presence of a submm excess in some of our dwarf galaxies.

Dust composition - Galliano et al. (2011) demonstrated that a more emissive dust grain composition compared to that of the Galaxy, is more consistent for the low-metallicity Large Magellanic Cloud (LMC). This result has been confirmed by Galametz et al. (2013) in a star-forming complex of the LMC with an updated version of the SPIRE calibration[4], and by our study of the submm excess in Chapter 8. Changing accordingly the dust composition in our low-metallicity galaxies would give lower dust masses (by a factor of ∼ two) with more emissive dust grains and would also increase the G/D by the same factor, increasing the discrepancy at low metallicities between the observed G/D and the predicted G/D from the reference scaling relation.

Radiation field - In the dust modelling, we use an ISRF with the spectral shape of the Galactic ISRF for all of our galaxies for consistency. However, the ISRF in low-metallicity dwarf galaxies is harder, so we could wonder if this spectral shape is appropriate for the modelling of dwarf galaxies. As already mentioned in Chapter 7, the shape of the radiation field determines the emission of out-of-equilibrium small grains. Increasing the hardness of the radiation field increases the maximum temperature the small grains can reach when they undergo stochastic heating. However, these very small grains only have a minor contribution to the total dust mass, and thus the assumed shape of the ISRF does not bias our estimation of the total dust mass for dwarf galaxies.

[4]This updated SPIRE calibration from September 2012 had the effect of decreasing the SPIRE flux densities by about 10% compared to the Galliano et al. (2011) study.

Submm excess - A submm excess has been observed in the past in several low-metallicity galaxies that current dust SED models are unable to fully explain (Galliano et al. 2003, 2005; Dumke et al. 2004; Bendo et al. 2006; Zhu et al. 2009; Galametz et al. 2009; Bot et al. 2010; Grossi et al. 2010; Galametz et al. 2011). We confirmed the presence of such an excess in several DGS and KINGFISH galaxies (see Chapter 8). Several hypothesis have been made to explain this excess among which the addition of a VCD component in which most of the dust mass should reside. This VCD component would be in the form of very dense clumps in the ISM (Galliano et al. 2003, 2005). Taking this additional VCD component into account in the DGS and KINGFISH galaxies presenting a submm excess can result in a drastic increase of the dust mass and thus in a lower G/D. However, Galliano et al. (2011) showed that for a strip of the LMC, the submm excess is more important in the diffuse regions, possibly in contradiction with the hypothesis of very cold dust in dense clumps. Other studies have suggested an enhanced fraction of very small grains with high emissivity (Lisenfeld et al. 2002; Dumke et al. 2004; Bendo et al. 2006; Zhu et al. 2009), "spinning" dust emission (Ysard & Verstraete 2010) or emission from magnetic nano-particles (Draine & Hensley 2012) to explain the submm excess. Meny et al. (2007) proposed variations of the optical properties of the dust with the temperature which results in an enhanced emission of the dust at submm/mm wavelengths. We saw in Chapter 8 that a dust composition using amorphous carbon grains could explain the excess for some moderately metal-poor galaxies. Using dust masses estimated with amorphous carbon grains for the 37 galaxies presenting a submm excess would result in an increase of a factor of ~ 2 for the G/D of these galaxies, which is within the scatter of the G/D vs metallicity relation, and hence would not change our general conclusions.

9.6 Chemical evolution models

Chemical evolution models, under certain assumptions, can predict a possible evolution of the G/D as metallicity varies in a given galaxy. For example, in the disk of our Galaxy, chemical evolution models predict this "reference" scaling of the G/D with the metallicity (Dwek 1998). We consider three different models here, from Galliano et al. (2008), Asano et al. (2013) and Zhukovska (2014) to interpret our data. However, we have to keep in mind during this comparison that, since we do not know the ages of these galaxies and that the same metallicity can be reached at very different time by different galaxies, our sample cannot be considered as the evolution (snapshots) of one single galaxy.

9.6.1 A simple model to begin with

Galliano et al. (2008) developed a one-zone single-phase chemical evolution model, based on the model by Dwek (1998). They consider a closed-box model where the evolution of the dust content is regulated by balancing dust production by stars and dust destruction by star formation and SN blast waves. They assume the full condensation of the elements injected by Type II supernovae (SNII) into dust and instantaneous mixing of the elements in the ISM. The model is shown on Fig. 9.6 for various SN destruction efficiencies as the dark grey zone.

Two things can be noticed from Fig. 9.6. First, the model is consistent with the observed G/D at high metallicities within the scatter, and down to metallicities $\sim 0.5\ Z_{\odot}$. Second, the model does not work at low metallicities and systematically underestimates the G/D. This has already been noted by Galliano et al. (2008) for their test sample of galaxies and was attributed to the very crude assumptions made in the modelling, especially the instantaneous mixing of the SNII elements in the ISM. Another strong simplifying assumption made by Galliano et al. (2008) is that they did not take into account dust growth in the ISM as they assume full condensation of the grains. In

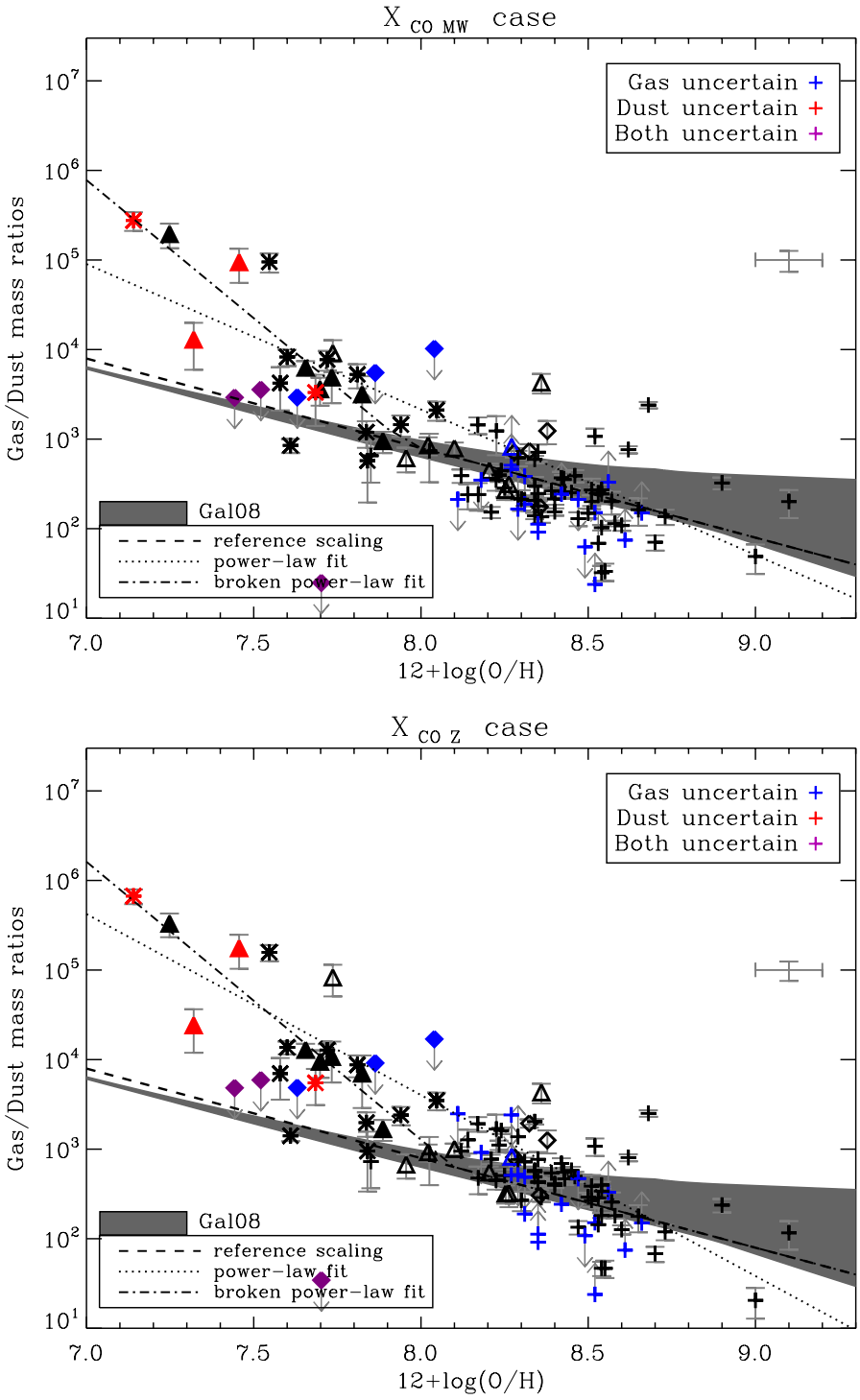

Fig. 9.6. G/D as a function of metallicity for the 2 values of X_{CO}: $X_{CO,MW}$ (*top*) and $X_{CO,Z}$ (*bottom*) with the chemical evolution model of Galliano et al. (2008). The colours and symbols are the same as for Fig.9.4. The dark grey stripes show the range of values from the Galliano et al. (2008) chemical evolution model. The black dashed line represents the reference scaling of the G/D with metallicity (not fit to the data). The black dotted and dash-dotted lines represent the best power-law and best broken power-law fits to the data.

the Galaxy, the typical timescale for dust formation by stars has been shown to be larger than the typical timescale for dust destruction (Jones & Tielens 1994; Jones et al. 1996). Because we still observe dust in the ISM, we need to reach equilibrium between formation and destruction of the dust grains, either via high SN yields or dust growth processes in the ISM. In the following sections we thus look at models including dust growth in the ISM.

9.6.2 Including dust growth in the ISM

Asano et al. (2013) propose a chemical evolution model, based on models from Hirashita (1999) and Inoue (2011), taking into account the evolution of the metal content in the dust phase in addition to the evolution of the total amount of metals. The dust formation is regulated by AGB stars, SNII and dust growth, via accretion, in the ISM. The dust is destroyed by SN shocks. Inflows and outflows are not considered (closed-box model) and the total mass of the galaxy is constant and set to 10^{10} $M_{\odot}$. Metallicity and age dependence of the various dust formation processes are taken into account. Asano et al. (2013) show that dust growth in the ISM becomes the main driver of the dust mass evolution, compared to the dust formation from metals produced and ejected into the ISM by stars, when the metallicity of the galaxy exceeds a certain "critical" metallicity. This critical metallicity increases with decreasing star-formation timescale. Asano et al. (2013) show that dust growth via accretion processes in the ISM is regulated by this critical metallicity over a large range of star-formation timescales (for $\tau_{\rm SF}$[5] = 0.5-5-50 Gyr). After reaching this critical metallicity the dust mass increases more rapidly, boosted by dust growth processes, before saturating when all of the metals available for dust formation are locked up in dust. The metallicity at which this saturation occurs thus also depends on the critical metallicity, which in turn depends on the star-formation history of the galaxy.

Figure 9.7 shows the models of Asano et al. (2013) (for $\tau_{\rm SF}$ = 0.5-5-50 Gyr) overlaid on the observed G/D values. The models were originally on an arbitrary scale and they are thus normalised at the $(\rm G/D)_{\odot}$ value. We assume an error on this value of $\sim$ 60%, from the range of values determined from the fits in Section 9.5.2, to have a tolerance range around the model (shown by the shaded grey area on Fig. 9.7). The three models show similar evolution with metallicity and indeed are homologous to each other when normalised by their respective critical metallicities (see Fig. 3 of Asano et al. 2013). We clearly see the influence of the critical metallicity on the dust mass evolution: at low metallicities the range of possible G/D values (illustrated by the grey area on Fig. 9.7) becomes wider around 12+log(O/H) $\sim$ 7.2 -7.3 before narrowing down around 12+log(O/H) $\sim$ 8.6. This broadening is due to the fact that in this range of metallicities, galaxies with high star-formation timescales have already reached their critical metallicity and have a rapidly increasing dust mass (and thus a low G/D at a given metallicity), compared to galaxies with lower star-formation timescales which have not yet reached this critical metallicity and with a dust mass still regulated by stars (thus with a higher G/D at the same metallicity). Galaxies with high star-formation timescales then reach saturation at moderate metallicities as they started their "active dust growth" phase at a lower critical metallicity (i.e., earlier in their evolution), while, at the same metallicity, galaxies with low star-formation timescales are still in the "active dust growth" phase. Then when these galaxies also reach saturation, because the dust growth in the ISM becomes ineffective, the range of possible G/D values narrows down.

From Fig. 9.7 we see that the models from Asano et al. (2013) are consistent with the G/D from *both* X_{CO} values.We note that below 12+log (O/H) $\sim$ 7.5, even the $\tau_{\rm SF}$ = 50 Gyr model does not agree anymore with the reference scaling of the G/D with metallicity (and below 12+log(O/H) $\sim$ 8.0 for $\tau_{\rm SF}$ = 5 Gyr). The other two empirical relations (our best power-law and broken power-law

[5]The star-formation timescale, $\tau_{\rm SF}$, is defined by the timescale during which star formation occurs: $\tau_{\rm SF}$=($M_{\rm ISM}$)/SFR, where SFR is the star-formation rate (see Eq. 5 of Asano et al. 2013).

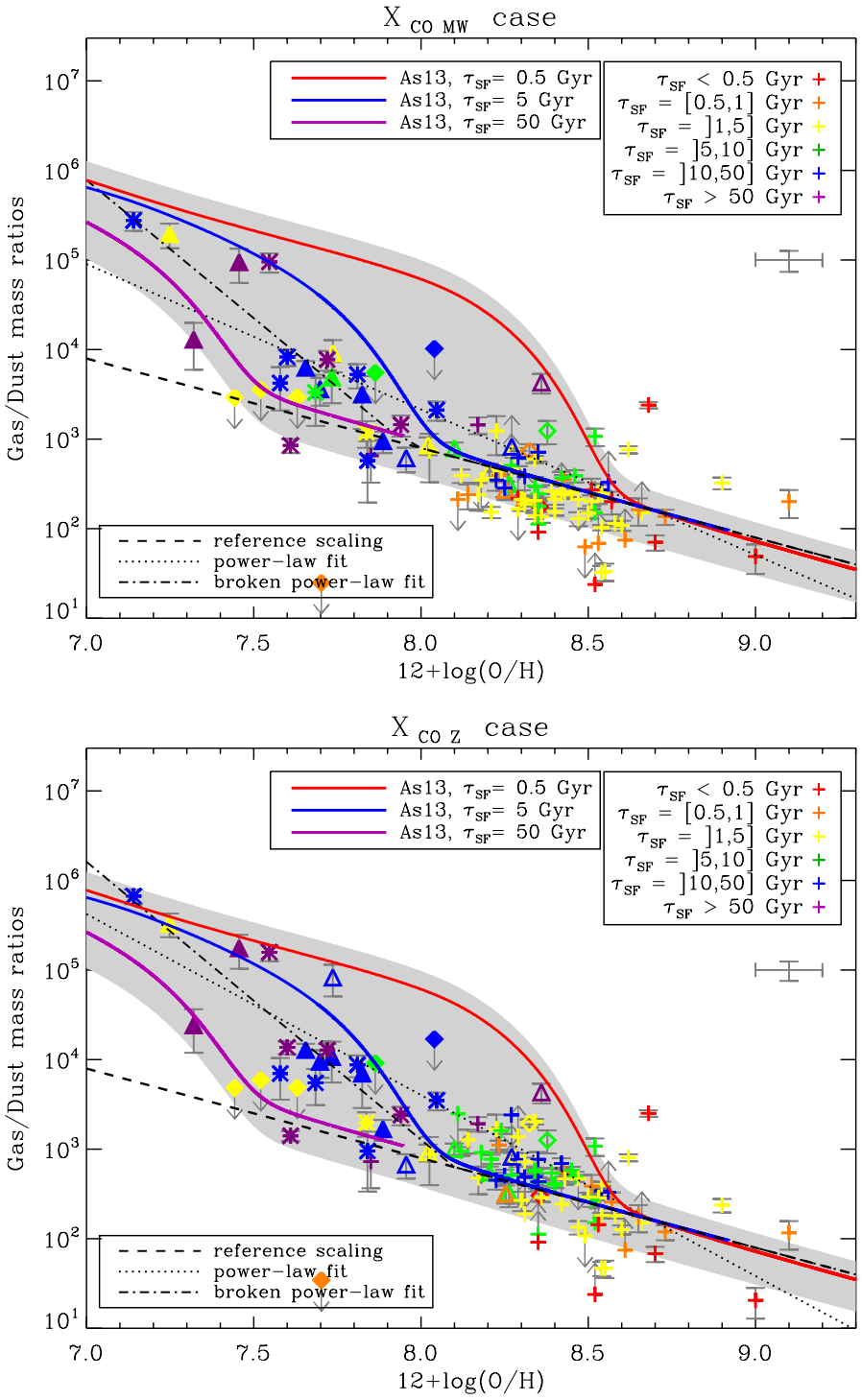

Fig. 9.7. G/D as a function of metallicity for the 2 values of X_{CO}: $X_{CO,MW}$ (*top*) and $X_{CO,Z}$ (*bottom*) with the chemical evolution model of Asano et al. (2013). The symbols are the same as for Fig. 9.4. The colours delineate ranges in star-formation timescales τ_{SF}. The model from Asano et al. (2013) is overlaid on the points for various τ_{SF} = 0.5 (red), 5 (blue), 50 (purple) Gyr. The black dashed line represents the reference scaling of the G/D with metallicity (not fit to the data). The black dotted and dash-dotted lines represent the best power-law and best broken power-law fits to the data.

fits) are consistent with the models of Asano et al. (2013) *within the considered metallicity range*: from 12+log(O/H) $\sim$ 7.0 to 9.1. Comparing with the shape of the Asano et al. (2013) models, our best broken power-law fit may overestimate the G/D for 12+log(O/H) $\leq$ 7.0. However, Izotov et al. (2012) recently suggested that there seems to be a metallicity floor around 12+log(O/H) $\sim$ 6.9, below which no galaxies are found in the local Universe, as already proposed by Kunth & Sargent (1986). Thus our metallicity range is close to being the largest achievable in the local Universe as far as low metallicities are concerned.

The galaxies from the DGS, KINGFISH and G11 samples are colour coded in Fig. 9.7 by an approximation of their star-formation timescale $\tau_{\rm SF}$, estimated from $\tau_{\rm SF} = (M_{gas} + M_{dust})/{\rm SFR}$, where the SFR have been estimated from L_{TIR} (see Chapter 7). The $\tau_{\rm SF}$ values are roughly consistent with the models from Asano et al. (2013). The median value of $\tau_{\rm SF}$ is $\sim$ 3.0 ($X_{CO,MW}$) and 5.5 ($X_{CO,Z}$) Gyr, but with a large dispersion of $\sim$ 20 Gyr around this value. As the models from Asano et al. (2013) encompass most of the observed G/D values, the dispersion seen in the G/D values can be due to the wide range of star-formation timescales in the considered galaxies. This is consistent with the large dispersion in the approximated star-formation timescales in our sample.

In Asano et al. (2013), the star formation is assumed to be continuous over the star-formation timescale. However, star-formation histories of many dwarf galaxies derived from colour-magnitude diagrams reconstruction show distinct episodes of star formation separated by more quiescent phases (e.g., Tolstoy et al. 2009and references therein). For example, Legrand et al. (2000) suggested for IZw18 a star-formation history made of bursts of star formation in between more quiescent phases, following the suggestion of Searle & Sargent (1972). Episodic star-formation histories have also been suggested in Nbody/Smoothed Particle Hydrodynamics simulations of dwarf galaxy evolution (e.g., Valcke et al. 2008; Revaz & Jablonka 2012). As we saw that the scatter in Fig. 9.7 seems to be due to the range of star-formation timescales probed by our sample, and assuming a continuous star formation, we thus need to consider the influence of the continuous vs. episodic star-formation modes.

9.6.3 Episodic versus continuous star formation

In the following we compare the observationally derived G/D with results of dust evolution models in dwarf galaxies with episodic star-formation history from Zhukovska (2014). These models were originally introduced to study the lifecycle of dust species from different origins in the Solar neighbourhood (Zhukovska et al. 2008). The model of Zhukovska (2014) is based on the Zhukovska et al. (2008) model that has been adapted to treat dwarf galaxies, specifically by considering episodic star formation. In Zhukovska (2014), the equations describing the evolution of the galaxy are now normalised to the total galactic masses M_{tot} (instead of surface densities) because dwarf galaxies are smaller in size and thus assumed to have a well mixed ISM. As in Zhukovska et al. (2008), the modelled dwarf galaxy is formed by gas infall starting from M_{tot}=0 and reach its total mass M_{tot} on the infall timescale. The assumed value of the infall timescale in Zhukovska (2014) is set to a much shorter value for dwarf galaxies than for the Solar neighbourhood. Since the G/D is the ratio of the gas and dust masses, it does not depend on the normalisation by the total mass M_{tot}, and is determined by the star-formation history and infall timescale. We refer the reader to Zhukovska (2014), for more details on the modelling.

Similarly to the models from Asano et al. (2013), Zhukovska (2014) include dust formation in AGB stars, SN II and dust growth by mantle accretion in the ISM. The main difference between these models is in the treatment of dust growth. Zhukovska (2014) assume a two-phase ISM consisting of clouds and an intercloud medium, where clouds are characterised by temperature, density, mass fraction, and lifetime. Dust growth by accretion in their model takes place only in the dense gas and also critically depends on the metallicity (see Zhukovska 2008).

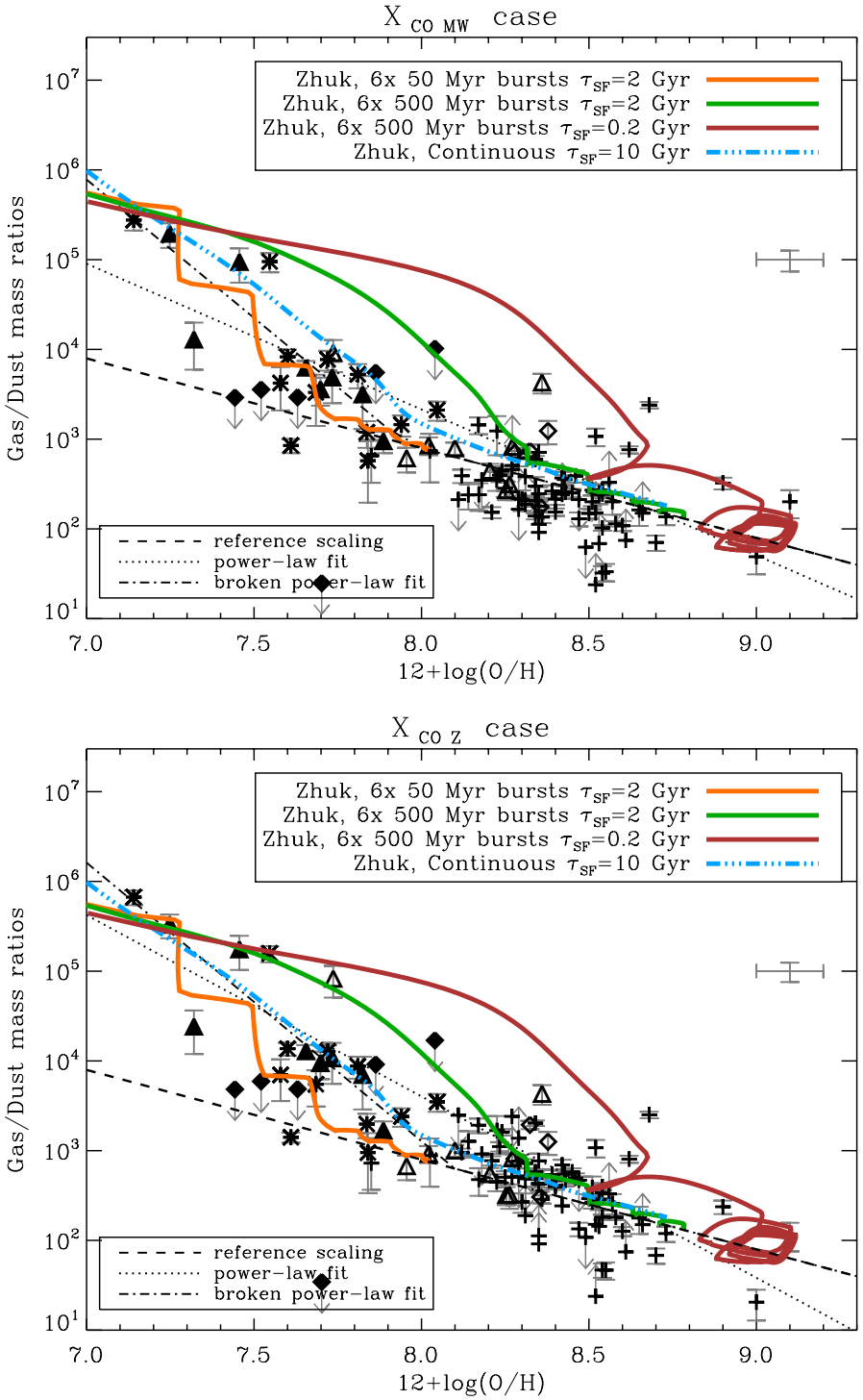

Fig. 9.8. G/D as a function of metallicity for the 2 values of X_{CO}: $X_{CO,MW}$ (*top*) and $X_{CO,Z}$ (*bottom*) with the chemical evolution model of Zhukovska (2014). The symbols are the same as for Fig. 9.4. The model from Zhukovska (2014) is shown for various star-formation histories: episodic with 6 bursts of 50 Myr and star-formation timescale of $\tau_{\rm SF}$ = 2 Gyr (orange), episodic with 6 bursts of 500 Myr and $\tau_{\rm SF}$ = 2 Gyr (green), episodic with 6 bursts of 500 Myr and $\tau_{\rm SF}$ = 0.2 Gyr (more intense star formation, brown) and continuous with a star-formation timescale $\tau_{\rm SF}$ = 10 Gyr (cyan dash-3 dots line). The black dashed line represents the reference scaling of the G/D with metallicity (not fit to the data). The black dotted and dash-dotted lines represent the best power-law and best broken power-law fits to the data.

In this paper we consider three models from Zhukovska (2014), which differ only in duration and intensity of the star formation bursts. All models consider six bursts of star formation starting at instants t = 0.5, 1, 2, 5, 7, and 11 Gyr. In the first and the second model, the burst duration is 50 Myr and 500 Myr, respectively, and the τ_{SF} during bursts is 2 Gyr. The first model is typical of a low-metallicity dwarf galaxy. In the third model, the burst duration is 500 Myr but the value of τ_{SF} is much shorter, 0.2 Gyr. During the quiescence phases τ_{SF} is set to be 200 Gyr. We also consider a model with continuous star formation on a 10 Gyr timescale, for comparison. In all models, the infall timescale is 0.3 Gyr and there are no galactic outflows. The initial metallicity Z of the infalling gas is set to be 10^{-4} with SNII like enhanced [α/Fe] ratio.

The models from Zhukovska (2014) are presented in Fig. 9.8 and reproduce the broadening of the observed G/D values at low metallicities (12+log(O/H) $\lesssim$ 8.3), and also converge around 12+log(O/H) $\sim$ 7.2, similar to the models of continuous star formation of Asano et al. (2013). Note how the star-formation history impacts the shape of the modelled G/D: the most extreme G/D values are obtained by the three models with episodic bursts of star formation. For the model with more intense star formation (brown curve on Fig. 9.8), 12+log(O/H) = 8.6 is reached during the first burst, and very high values of the G/D are quickly reached, up to two orders of magnitude above the reference scaling relation at moderate metallicities (12+log(O/H) $\sim$ 8.2 - 8.3). It also presents an interesting scatter of G/D values near 12+log(O/H) = 9.0 that is due to dust destruction during the SF bursts, and consistent with the scatter predicted by the Galliano et al. (2008) model (see Fig. 9.9). The fact that the low-metallicity slope of the broken power law is consistent with the continuous star formation model at low metallicities for the $X_{CO,Z}$ case indicates that this broken power law can provide a fairly good empirical way of estimating the G/D for a given metallicity.

9.6.4 Explaining the observed scatter in G/D values

Figure 9.9 shows the three models overlaid on the observed G/D values. The models from Asano et al. (2013) and Zhukovska (2014) provide trends that are consistent with each other and with the data and its scatter. More dust observations of extremely low-metallicity galaxies with 12+log(O/H) $<$ 7.5 are nonetheless needed to confirm this agreement between the models and the data at very low metallicities. The model of Galliano et al. (2008) fails to reproduce the observed G/D at low metallicities, but provides a good complement to explain the scatter seen at high metallicities, consistent with the predictions of the third bursty model by Zhukovska (2014). We thus conclude that the observed scatter at low metallicities in the G/D values is due to the wide variety of environments we are probing, and especially to the different star-formation histories. The observed scatter at higher metallicity seems to be due to different timescales for dust destruction by SN blast waves in the different environments and to the efficiency of dust shattering in the ISM.

We investigated here two different parameters to explain the scatter in the G/D values: star-formation histories and efficiency of dust destruction, but other processes could also give rise to the observed scatter. In our dust modelling we allow the mass fraction of small grains compared to big grains to vary from galaxy to galaxy (controlled by the f_{vsg} parameter), to account for potential variations in the grain size distribution. This had already been done in one low-metallicity galaxy by Lisenfeld et al. (2002). On the theoretical side, Hirashita & Kuo (2011) showed that the dust grain size distribution can have an important impact on the dust growth process in the ISM by regulating the grain growth rate. They also showed that the critical metallicity mentioned in Section 9.6.2, for which grain growth becomes dominant, also depends on the grain size distribution. Additionally the grain size distribution varies as the galaxy evolves and this evolution is controlled by different dust formation processes at different ages (Asano et al. 2013). Thus the observed scatter can also be due to variations of the grain size distribution between the galaxies, the effect of which can be related to the star-formation history.

Second, as discussed in Section 9.5.3 we use a dust model with the dust composition and optical

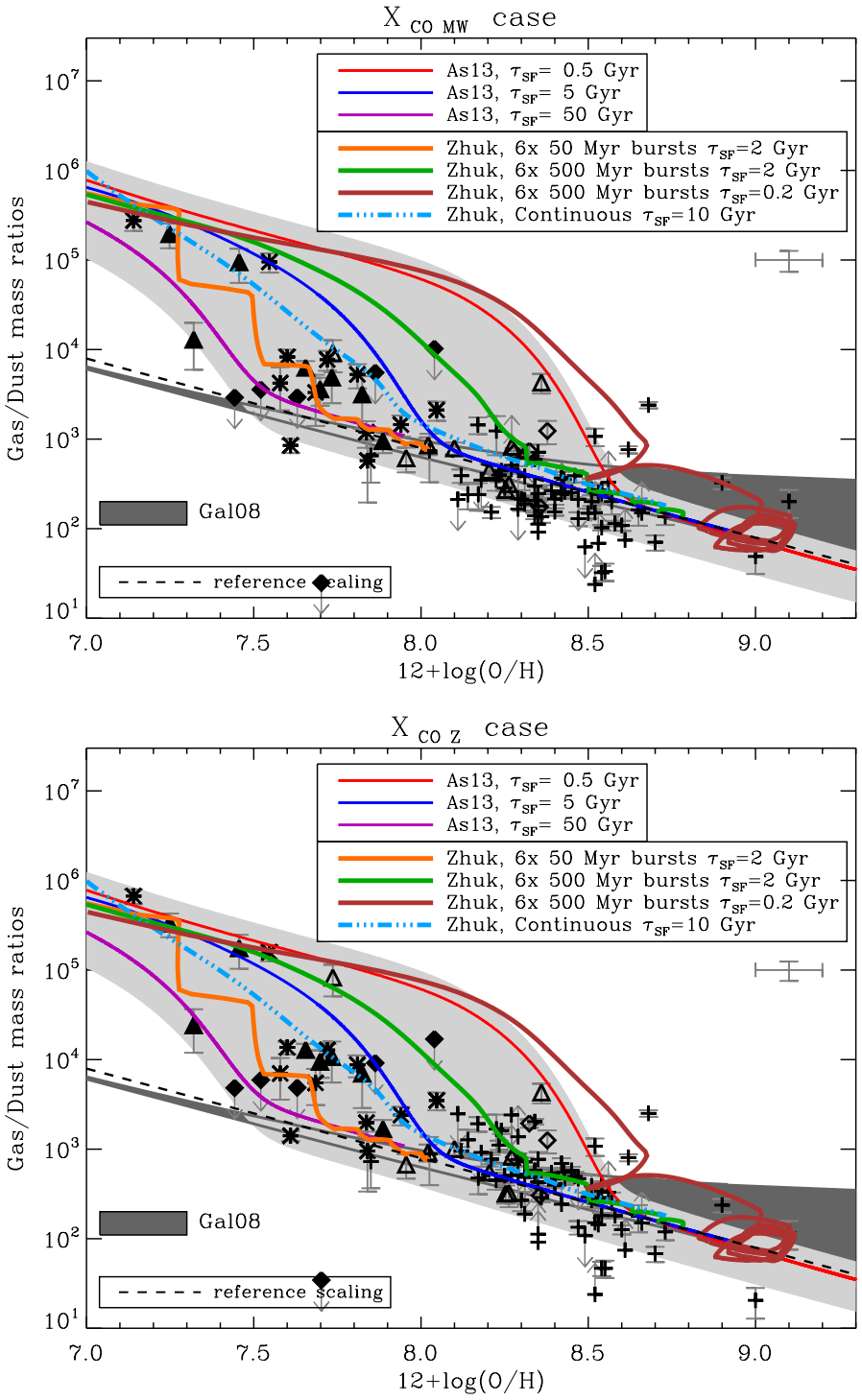

Fig. 9.9. G/D as a function of metallicity for the 2 values of X_{CO}: $X_{CO,MW}$ (*top*) and $X_{CO,Z}$ (*bottom*) with the three chemical evolution model considered in Section 9.6. The symbols are the same as for Fig. 9.4. The model ranges from Galliano et al. (2008) are delineated by the dark grey stripe. The models from Asano et al. (2013) are shown with the red, blue and purple lines. The models from Zhukovska (2014) are shown with the orange, green brown solid lines and cyan dash-3 dots line. The black dashed line represents the reference scaling of the G/D with metallicity (not fit to the data).

properties representative of dust in the Milky Way for all of the galaxies. Another explanation for the scatter seen at all metallicities could be that the dust composition in fact varies between the galaxies, leading to important variations in the emissivity of the dust grains (Jones 2012). This would then imply dust masses relatively similar at a given metallicity but large variations in the emissivity properties of dust from one galaxy to another. With our fixed emissivity (due to our fixed dust composition in our dust model) this effect would be seen through the variations in the derived dust masses (and then in the G/D values) seen at a given metallicity, thus giving rise to the observed scatter.

Another aspect not taken into account in the chemical models we use here is that the mass of the galaxy plays an important role in its chemical evolution. According to the chemical downsizing scenario, galaxies with different masses have different star-formation efficiencies (e.g., Brooks et al. 2007). The massive galaxies form stars before low-mass galaxies in the history of the Universe (Cowie et al. 1996). The exact reasons are not well known, some models would argue this is a feedback effect, with metals being lost in outflows in less massive galaxies (Frye et al. 2002), and others would argue that the local density and the ISM pressure is responsible (e.g., Cen & Ostriker 1999): if the ISM density is systematically lower in a dwarf galaxy, for instance, then the star-formation activity will be low on average, impacting the G/D value. A massive galaxy will not show the same behaviour, and this difference will also introduce some scatter in the observed G/D at a given metallicity.

Additionally external processes such as outflows or interactions and mergers, not considered here either in our models, can also be responsible for the scatter in the G/D values.

9.6.5 Implications for the observed G/D in galaxies

We saw in Sections 9.6.2 and 9.6.3 that the broken power-law relation in the $X_{CO,Z}$ case is consistent with the predictions from both chemical evolution models. Even though there are only five galaxies with 12+log(O/H) $\sim$ 7.5 to constrain the observed G/D at extremely low metallicities, this broken power-law relation is the best empirical estimate of the observed G/D for local galaxies we have at our disposal so far. Thus, we advise to use this empirical prescription to estimate the G/D based on a metallicity value for local galaxies, keeping in mind the large scatter and uncertainties on the broken power-law parameters: the estimated G/D would be accurate to a factor of $\sim$ 1.6. Note also that this empirical relation has been derived for metallicities estimated with a strong emission line method and the calibration from Pilyugin & Thuan (2005). Thus the estimation of the G/D with this empirical relation should be done from a metallicity derived *with the same method*. Additionally, more observations of the dust in extremely low-metallicity galaxies are needed in order to place more constraints on this empirical relation.

Table 9.3. Gas masses for the DGS, KINGFISH and G11 samples.

	M_{HI} $[M_\odot]$			M_{H_2} $[M_\odot]$			$\mathbf{M}_{gas}$ $[M_\odot]$				
Name	M_{HI} (Ref)	Unc (%)	HIarea (arcmin^2)	12+log(O/H) (Ref)	$M_{H_2,MW}$ (Ref)	$M_{H_2,Z}$	$M_{gas,MW}$	Unc (%)	$M_{gas,Z}$	Unc (%)	μ_{gal}
DGS											
Haro11	$5.01\times10^{8a,e}$ (1)	50.00	-	8.36 (1)	2.51×10^{8} (1)	1.17×10^{9}	1.74×10^{9}	19.94	3.01×10^{9}	11.50	1.38
Haro2	3.77×10^{8c} (2)	16.08	1.6	8.23 (1)	1.26×10^{8} (2)	1.03×10^{9}	6.93×10^{8}	12.06	1.94×10^{9}	4.31	1.38
Haro3	1.13×10^{9a} (3)	2.13	-	8.28 (1)	3.02×10^{7} (3)	2.01×10^{8}	1.60×10^{9}	2.08	1.84×10^{9}	1.81	1.38
He2-10	3.10×10^{8c} (4)	6.45	3.2	8.43 (1)	9.55×10^{7} (4)	3.21×10^{8}	5.61×10^{8}	4.93	8.73×10^{8}	3.17	1.39
HS0017+1055	$\leq1.74\times10^{8a}$ (5)	-	-	7.63 (1)	$\leq2.15\times10^{6d}$ (-)	$\leq1.18\times10^{8}$	$\leq2.42\times10^{8}$	-	$\leq4.01\times10^{8}$	-	1.37
HS0052+2536	$\leq4.82\times10^{10a}$ (6)	-	-	8.04 (1)	$\leq5.94\times10^{8d}$ (-)	$\leq3.26\times10^{10}$	$\leq6.72\times10^{10}$	-	$\leq1.11\times10^{11}$	-	1.38
HS0822+3542	5.75×10^{7b} (7)	22.22	0.6	7.32 (1)	9.48×10^{5d} (-)	5.21×10^{7}	8.02×10^{7}	21.86	1.50×10^{8}	11.66	1.37
HS1222+3741	-	-	-	7.79 (1)	-	-	-	-	-	-	1.37
HS1236+3937	-	-	-	7.72 (1)	-	-	-	-	-	-	1.37
HS1304+3529	-	-	-	7.93 (1)	-	-	-	-	-	-	1.38
HS1319+3224	-	-	-	7.81 (1)	-	-	-	-	-	-	1.37
HS1330+3651	-	-	-	7.98 (1)	-	-	-	-	-	-	1.38
HS1442+4250	3.10×10^{8a} (5)	2.27	-	7.60 (1)	3.82×10^{6d} (-)	2.10×10^{8}	4.30×10^{8}	2.24	7.13×10^{8}	1.35	1.37
HS2352+2733	$\leq2.30\times10^{10a}$ (6)	-	-	8.40 (1)	-	-	-	-	-	-	1.38
IZw18	1.00×10^{8c2} (8)	16.08	-	7.14 (1)	2.71×10^{6d} (5)	1.49×10^{8}	1.41×10^{8}	15.66	3.41×10^{8}	6.46	1.37
IC10	4.41×10^{7c2} (9)	4.52	-	8.17 (1)	4.84×10^{6} (6)	5.27×10^{7}	6.74×10^{7}	4.07	1.33×10^{8}	2.06	1.38
IIZw40	5.66×10^{8c} (10)	16.08	0.3	8.23 (1)	2.83×10^{7} (7)	2.41×10^{8}	8.20×10^{8}	15.32	1.11×10^{9}	11.29	1.38
Mrk1089	1.47×10^{10b} (11)	7.91	26.4	8.10 (1)	2.84×10^{8} (1)	4.31×10^{9}	2.07×10^{10}	7.76	2.62×10^{10}	6.12	1.38
Mrk1450	4.30×10^{7c} (12)	16.08	0.1	7.84 (1)	5.30×10^{5d} (-)	2.91×10^{7}	5.98×10^{7}	15.89	9.90×10^{7}	9.59	1.37
Mrk153	$\leq6.93\times10^{8a}$ (13)	-	-	7.86 (1)	$\leq8.39\times10^{6d}$ (-)	$\leq4.61\times10^{8}$	$\leq9.55\times10^{8}$	-	$\leq1.58\times10^{9}$	-	1.37
Mrk209	2.76×10^{7b} (13)	6.58	12.2	7.74 (1)	3.09×10^{6} (8)	2.50×10^{8}	4.21×10^{7}	5.92	3.81×10^{8}	0.66	1.37
Mrk930	3.19×10^{9c} (14)	11.06	0.1	8.03 (1)	3.07×10^{7} (1)	6.57×10^{8}	4.43×10^{9}	10.96	5.30×10^{9}	9.17	1.38
NGC1140	3.50×10^{9a} (15)	26.71	-	8.38 (1)	1.91×10^{7} (9)	8.02×10^{7}	4.87×10^{9}	26.57	4.95×10^{9}	26.11	1.38
NGC1569	1.77×10^{8b} (16)	16.08	24.0	8.02 (1)	7.08×10^{5} (10)	1.54×10^{7}	2.45×10^{8}	16.02	2.65×10^{8}	14.80	1.38
NGC1705	7.67×10^{7b} (17)	12.50	13.0	8.27 (1)	-	-	$\geq1.06\times10^{8}$	-	$\geq1.06\times10^{8}$	-	1.38
NGC2366	2.93×10^{8b} (18)	6.76	420.0	7.70 (1)	9.12×10^{6d} (11)	5.01×10^{8}	4.15×10^{8}	6.55	1.09×10^{9}	2.49	1.37
NGC4214	3.76×10^{8b} (16)	16.08	156.0	8.26 (1)	1.62×10^{6} (12)	1.16×10^{7}	5.22×10^{8}	16.02	5.36×10^{8}	15.61	1.38
NGC4449	9.55×10^{8b} (16)	16.08	144.0	8.20 (1)	2.67×10^{7} (13)	2.50×10^{8}	1.35×10^{9}	15.65	1.66×10^{9}	12.75	1.38
NGC4861	4.12×10^{8b} (19)	6.27	34.3	7.89 (1)	5.90×10^{6d} (1)	3.24×10^{8}	5.75×10^{8}	6.18	1.01×10^{9}	3.51	1.37
NGC5253	1.06×10^{8b} (20)	5.66	77.0	8.25 (1)	3.02×10^{6} (14)	2.26×10^{7}	1.51×10^{8}	5.50	1.78×10^{8}	4.67	1.38
NGC625	1.10×10^{8c} (21)	18.18	20.0	8.22 (1)	4.36×10^{6} (1)	3.72×10^{7}	1.58×10^{8}	17.49	2.03×10^{8}	13.59	1.38
NGC6822	1.04×10^{8b} (22)	10.45	676.0	7.96 (1)	3.58×10^{5} (15)	1.05×10^{7}	1.43×10^{8}	10.41	1.57×10^{8}	9.48	1.38
Pox186	$\leq2.00\times10^{6a,e}$ (23)	-	-	7.70 (1)	$\leq2.47\times10^{4d}$ (-)	$\leq1.35\times10^{6}$	$\leq4.74\times10^{6}$	-	$\leq6.57\times10^{6}$	-	1.37
SBS0335-052	4.37×10^{8b} (24)	10.27	0.2	7.25 (1)	5.67×10^{6d} (16)	3.12×10^{8}	6.07×10^{8}	10.14	1.03×10^{9}	5.99	1.37
SBS1159+545	$\leq6.30\times10^{7a}$ (5)	-	-	7.44 (1)	$\leq7.76\times10^{5d}$ (-)	$\leq4.26\times10^{7}$	$\leq8.74\times10^{7}$	-	$\leq1.45\times10^{8}$	-	1.37
SBS1211+540	5.60×10^{7c} (12)	16.08	0.1	7.58 (1)	6.90×10^{5d} (-)	3.79×10^{7}	7.78×10^{7}	15.89	1.29×10^{8}	9.59	1.37
SBS1249+493	1.00×10^{9c} (25)	48.15	0.06	7.68 (1)	1.23×10^{7d} (-)	6.77×10^{8}	1.39×10^{9}	47.56	2.30×10^{9}	28.71	1.37
SBS1415+437	4.37×10^{8c} (12)	16.08	0.4	7.55 (1)	5.38×10^{6d} (-)	2.96×10^{8}	6.06×10^{8}	15.89	1.00×10^{9}	9.59	1.37
SBS1533+574	3.00×10^{9c} (14)	11.29	0.2	8.05 (1)	3.70×10^{7d} (-)	2.03×10^{9}	4.18×10^{9}	11.15	6.92×10^{9}	6.73	1.38
Tol0618-402	-	-	-	8.09 (1)	-	-	-	-	-	-	1.38
Tol1214-277	$\leq3.22\times10^{8a}$ (5)	-	-	7.52 (1)	$\leq3.97\times10^{6d}$ (-)	$\leq2.18\times10^{8}$	$\leq4.47\times10^{8}$	-	$\leq7.41\times10^{8}$	-	1.37
UGC4483	2.52×10^{7b} (26)	5.00	14.4	7.46 (1)	4.06×10^{5d} (14)	2.23×10^{7}	3.51×10^{7}	4.92	6.52×10^{7}	2.65	1.37
UGCA20	6.92×10^{6b} (27)	13.82	9.8	7.50 (1)	2.46×10^{5d} (-)	1.35×10^{7}	9.83×10^{6}	13.34	2.80×10^{7}	4.68	1.37

Table 9.3. Gas masses for the DGS, KINGFISH and G11 samples (continued).

	M_{HI} [$M_\odot$]			M_{H_2} [$M_\odot$]			$\mathbf{M}_{gas}$ [$M_\odot$]				
Name	M_{HI} (Ref)	Unc (%)	HIarea (arcmin^2)	12+log(O/H) (Ref)	$M_{H_2,MW}$ (Ref)	$M_{H_2,Z}$	$M_{gas,MW}$	Unc (%)	$M_{gas,Z}$	Unc (%)	μ_{gal}
UM133	2.15×10^{8b} (28)	4.38	6.2	7.82 (1)	4.93×10^{6d} (-)	2.71×10^{8}	3.02×10^{8}	4.28	6.67×10^{8}	1.94	1.37
UM311	6.09×10^{10b} (29)	16.08	21.2	8.36 (1)	9.37×10^{7} (1)	4.28×10^{8}	8.44×10^{10}	16.06	8.48×10^{10}	15.97	1.38
UM448	6.00×10^{9a} (15)	27.63	-	8.32 (1)	3.55×10^{9} (3)	1.92×10^{10}	1.32×10^{10}	17.36	3.48×10^{10}	6.59	1.38
UM461	7.31×10^{7b} (26)	5.00	2.6	7.73 (1)	1.66×10^{6d} (3)	9.09×10^{7}	1.03×10^{8}	4.89	2.25×10^{8}	2.23	1.37
VIIZw403	3.25×10^{7b} (2)	8.28	10.4	7.66 (1)	6.41×10^{5d} (17)	3.52×10^{7}	4.54×10^{7}	8.12	9.29×10^{7}	3.97	1.37
KINGFISH											
NGC0337	3.34×10^{9} (27)	11.97	-	8.18 (2)	$\leq6.98\times10^{8}$ (18)	$\leq7.31\times10^{9}$	$\leq5.57\times10^{9}$	-	$\leq1.47\times10^{10}$	-	1.38
NGC0584	1.58×10^{8} (27)	35.92	-	8.43 (2)	$\leq4.78\times10^{8}$ (18)	$\leq1.58\times10^{9}$	$\leq8.82\times10^{8}$	-	$\leq2.41\times10^{9}$	-	1.39
NGC0628	3.72×10^{9} (30)	16.08	-	8.35 (2)	8.71×10^{8} (19)	4.17×10^{9}	6.35×10^{9}	13.04	1.09×10^{10}	7.59	1.38
NGC0855	1.32×10^{8} (27)	29.47	-	8.29 (2)	$\leq8.91\times10^{7}$ (18)	$\leq5.62\times10^{8}$	$\leq3.05\times10^{8}$	-	$\leq9.59\times10^{8}$	-	1.38
NGC0925	4.56×10^{9} (30)	16.08	-	8.25 (2)	6.14×10^{8} (19)	4.66×10^{9}	7.15×10^{9}	14.18	1.27×10^{10}	7.96	1.38
NGC1097	7.56×10^{9} (30)	16.08	-	8.47 (2)	1.67×10^{8} (20)	4.59×10^{8}	1.07×10^{10}	15.74	1.11×10^{10}	15.16	1.39
NGC1266	-	-	-	8.29 (2)	1.33×10^{9} (21)	8.39×10^{9}	$\geq1.84\times10^{9}$	-	$\geq1.16\times10^{10}$	-	1.38
NGC1291	1.78×10^{9} (30)	16.08	-	8.52 (2)	-	-	$\geq2.47\times10^{9}$	-	$\geq2.47\times10^{9}$	-	1.39
NGC1316	$\leq4.73\times10^{8}$ (30)	-	-	8.77 (2)	-	-	-	-	-	-	1.40
NGC1377	-	-	-	8.29 (2)	-	-	-	-	-	-	1.38
NGC1404	-	-	-	8.54 (2)	-	-	-	-	-	-	1.39
IC0342	9.49×10^{9} (31)	16.08	-	8.46 (3)	1.60×10^{9} (20)	4.60×10^{9}	1.54×10^{10}	13.77	1.95×10^{10}	10.83	1.39
NGC1482	$\leq8.01\times10^{8}$ (30)	-	-	8.11 (2)	3.11×10^{9} (19)	4.49×10^{10}	$\leq5.38\times10^{9}$	-	$\leq6.30\times10^{10}$	-	1.38
NGC1512	7.33×10^{9} (30)	16.08	-	8.56 (2)	-	-	$\geq1.02\times10^{10}$	-	$\geq1.02\times10^{10}$	-	1.39
NGC2146	3.89×10^{9} (27)	22.10	-	8.68 (2)	7.77×10^{10} (22)	8.13×10^{10}	1.14×10^{11}	1.05	1.19×10^{11}	1.01	1.40
HoII	4.21×10^{8} (27)	23.95	-	7.72 (2)	5.18×10^{6d} (18)	2.85×10^{8}	5.85×10^{8}	23.66	9.69×10^{8}	14.28	1.37
DDO053	6.16×10^{7} (30)	16.08	-	7.60 (2)	7.60×10^{5d} (11)	4.17×10^{7}	8.56×10^{7}	15.89	1.42×10^{8}	9.59	1.37
NGC2798	2.13×10^{9} (30)	16.08	-	8.34 (2)	3.21×10^{9} (19)	1.61×10^{10}	7.38×10^{9}	6.41	2.52×10^{10}	1.88	1.38
NGC2841	8.63×10^{9} (30)	16.08	-	8.54 (2)	2.92×10^{9} (19)	5.82×10^{9}	1.60×10^{10}	12.02	2.01×10^{10}	9.61	1.39
NGC2915	3.52×10^{8} (30)	16.08	-	7.94 (2)	4.34×10^{6d} (-)	2.39×10^{8}	4.90×10^{8}	15.89	8.12×10^{8}	9.59	1.38
HoI	1.45×10^{8} (16)	16.08	-	7.61 (2)	1.79×10^{6d} (18)	9.85×10^{7}	2.02×10^{8}	15.89	3.35×10^{8}	9.59	1.37
NGC2976	1.27×10^{8} (30)	16.08	-	8.36 (2)	5.81×10^{7} (19)	2.66×10^{8}	2.57×10^{8}	11.05	5.44×10^{8}	5.21	1.38
NGC3049	1.21×10^{9} (30)	16.08	-	8.53 (2)	1.80×10^{8} (18)	3.75×10^{8}	1.93×10^{9}	14.00	2.20×10^{9}	12.27	1.39
NGC3077	8.71×10^{8} (16)	16.08	-	8.52 (4)	3.80×10^{6} (9)	8.32×10^{6}	1.21×10^{9}	16.01	1.22×10^{9}	15.93	1.39
M81dwB	1.16×10^{7} (16)	16.08	-	7.84 (2)	1.43×10^{5d} (18)	7.85×10^{6}	1.61×10^{7}	15.89	2.67×10^{7}	9.59	1.37
NGC3190	4.27×10^{8} (27)	36.84	-	8.49 (2)	$\leq3.93\times10^{8}$ (18)	$\leq9.87\times10^{8}$	$\leq1.14\times10^{9}$	-	$\leq1.96\times10^{9}$	-	1.39
NGC3184	3.37×10^{9} (30)	16.08	-	8.51 (2)	1.19×10^{9} (19)	2.73×10^{9}	6.33×10^{9}	11.88	8.47×10^{9}	8.88	1.39
NGC3198	6.85×10^{9} (27)	26.71	-	8.34 (2)	1.30×10^{9} (18)	6.53×10^{9}	1.13×10^{10}	22.44	1.85×10^{10}	13.68	1.38
IC2574	1.32×10^{9} (30)	16.08	-	7.85 (2)	3.16×10^{6} (19)	1.51×10^{8}	1.82×10^{9}	16.05	2.02×10^{9}	14.43	1.37
NGC3265	1.75×10^{8} (27)	38.68	-	8.27 (2)	$\leq4.39\times10^{8}$ (18)	$\leq3.04\times10^{9}$	$\leq8.47\times10^{8}$	-	$\leq4.43\times10^{9}$	-	1.38
NGC3351	1.02×10^{9} (30)	16.08	-	8.60 (2)	4.77×10^{8} (19)	7.23×10^{8}	2.09×10^{9}	10.97	2.43×10^{9}	9.43	1.39
NGC3521	8.71×10^{9} (30)	16.08	-	8.39 (2)	4.77×10^{9} (19)	1.90×10^{10}	1.87×10^{10}	10.39	3.84×10^{10}	5.05	1.38
NGC3621	6.99×10^{9} (30)	16.08	-	8.27 (2)	-	-	$\geq9.65\times10^{9}$	-	$\geq9.65\times10^{9}$	-	1.38
NGC3627	8.46×10^{8} (30)	16.08	-	8.34 (2)	3.21×10^{9} (19)	1.61×10^{10}	5.61×10^{9}	3.36	2.34×10^{10}	0.80	1.38
NGC3773	9.03×10^{7} (30)	16.08	-	8.43 (2)	4.95×10^{7} (18)	1.64×10^{8}	1.94×10^{8}	10.39	3.52×10^{8}	5.71	1.39
NGC3938	8.00×10^{9} (30)	16.08	-	8.42 (2)	4.38×10^{9} (19)	1.52×10^{10}	1.71×10^{10}	10.39	3.21×10^{10}	5.54	1.38
NGC4236	2.69×10^{9} (30)	16.08	-	8.17 (2)	9.33×10^{7} (18)	1.02×10^{9}	3.84×10^{9}	15.55	5.12×10^{9}	11.65	1.38

Table 9.3. Gas masses for the DGS, KINGFISH and G11 samples (continued).

	M_{HI} $[M_\odot]$			M_{H_2} $[M_\odot]$			$\mathbf{M}_{gas}$ $[M_\odot]$				
Name	M_{HI} (Ref)	Unc (%)	HIarea (arcmin^2)	12+log(O/H) (Ref)	$M_{H_2,MW}$ (Ref)	$M_{H_2,Z}$	$M_{gas,MW}$	Unc (%)	$M_{gas,Z}$	Unc (%)	μ_{gal}
NGC4254	3.76×10^9 (30)	16.08	-	8.45 (2)	6.82×10^9 (19)	2.06×10^{10}	1.47×10^{10}	5.71	3.37×10^{10}	2.48	1.39
NGC4321	2.39×10^9 (30)	16.08	-	8.50 (2)	5.34×10^9 (19)	1.28×10^{10}	1.07×10^{10}	4.97	2.11×10^{10}	2.53	1.39
NGC4536	1.73×10^9 (30)	16.08	-	8.21 (2)	1.72×10^9 (19)	1.57×10^{10}	4.75×10^9	8.05	2.40×10^{10}	1.59	1.38
NGC4559	4.09×10^9 (30)	16.08	-	8.29 (2)	1.92×10^8 (18)	1.21×10^9	5.91×10^9	15.36	7.32×10^9	12.41	1.38
NGC4569	1.55×10^8 (30)	16.08	-	8.58 (2)	1.14×10^9 (19)	1.90×10^9	1.81×10^9	1.92	2.86×10^9	1.21	1.39
NGC4579	5.47×10^8 (30)	16.08	-	8.54 (2)	1.89×10^9 (19)	3.77×10^9	3.39×10^9	3.61	6.00×10^9	2.04	1.39
NGC4594	2.60×10^8 (30)	16.08	-	8.54 (2)	2.16×10^8 (19)	4.31×10^8	6.62×10^8	8.79	9.61×10^8	6.06	1.39
NGC4625	1.00×10^9 (30)	16.08	-	8.35 (2)	2.09×10^7 (18)	1.00×10^8	1.42×10^9	15.76	1.53×10^9	14.62	1.38
NGC4631	8.77×10^9 (30)	16.08	-	8.12 (2)	1.10×10^9 (19)	1.52×10^{10}	1.36×10^{10}	14.29	3.30×10^{10}	5.88	1.38
NGC4725	3.59×10^9 (30)	16.08	-	8.35 (2)	2.16×10^9 (19)	1.03×10^{10}	7.95×10^9	10.05	1.92×10^{10}	4.15	1.38
NGC4736	4.03×10^8 (30)	16.08	-	8.31 (2)	4.41×10^8 (19)	2.54×10^9	1.17×10^9	7.68	4.06×10^9	2.20	1.38
DDO154	3.55×10^8 (16)	16.08	-	7.54 (2)	4.37×10^{6d} (23)	2.40×10^8	4.93×10^8	15.89	8.17×10^8	9.59	1.37
NGC4826	2.77×10^8 (30)	16.08	-	8.54 (2)	4.80×10^8 (19)	9.58×10^8	1.05×10^9	5.88	1.72×10^9	3.61	1.39
DDO165	1.12×10^8 (27)	14.74	-	7.63 (2)	1.38×10^{6d} (18)	7.60×10^7	1.56×10^8	14.56	2.58×10^8	8.79	1.37
NGC5055	5.59×10^9 (30)	16.08	-	8.40 (2)	2.73×10^9 (19)	1.04×10^{10}	1.15×10^{10}	10.80	2.21×10^{10}	5.63	1.38
NGC5398	2.48×10^8 (27)	11.97	-	8.35 (2)	-	-	$\geq3.43\times10^8$	-	$\geq3.43\times10^8$	-	1.38
NGC5408	3.22×10^8 (30)	16.08	-	7.81 (2)	3.97×10^{6d} (-)	2.18×10^8	4.48×10^8	15.89	7.43×10^8	9.59	1.37
NGC5457	1.16×10^{10} (16)	16.08	-	8.42 (5)	-	-	$\geq1.60\times10^{10}$	-	$\geq1.60\times10^{10}$	-	1.38
NGC5474	9.71×10^8 (27)	24.87	-	8.31 (2)	$\leq5.88\times10^7$ (18)	$\leq3.38\times10^8$	$\leq1.42\times10^9$	-	$\leq1.81\times10^9$	-	1.38
NGC5713	5.51×10^9 (30)	16.08	-	8.24 (2)	3.39×10^9 (19)	2.69×10^{10}	1.23×10^{10}	9.96	4.47×10^{10}	2.73	1.38
NGC5866	$\leq2.85\times10^8$ (30)	-	-	8.47 (2)	6.38×10^8 (19)	1.76×10^9	$\leq1.28\times10^9$	-	$\leq2.83\times10^9$	-	1.39
NGC6946	3.58×10^9 (30)	16.08	-	8.40 (2)	4.50×10^9 (19)	1.71×10^{10}	1.12×10^{10}	7.13	2.86×10^{10}	2.79	1.38
NGC7331	8.85×10^9 (30)	16.08	-	8.34 (2)	6.70×10^9 (19)	3.36×10^{10}	2.15×10^{10}	9.16	5.86×10^{10}	3.36	1.38
NGC7793	8.75×10^8 (30)	16.08	-	8.31 (2)	-	-	$\geq1.21\times10^9$	-	$\geq1.21\times10^9$	-	1.38
G11											
M83	5.13×10^9 (31)	5.00	-	8.62 (6)	8.65×10^8 (20)	1.19×10^9	8.35×10^9	4.28	8.81×10^9	4.06	1.39
NGC1808	1.78×10^9 (31)	9.46	-	9.10 (7)	1.75×10^9 (20)	2.64×10^8	5.08×10^9	4.77	2.95×10^9	8.24	1.44
NGC7552	4.79×10^9 (31)	16.08	-	8.35 (8)	-	-	$\geq6.62\times10^9$	-	$\geq6.62\times10^9$	-	1.38
M82	8.91×10^8 (31)	10.29	-	8.51 (8)	4.43×10^8 (20)	1.01×10^9	1.85×10^9	6.87	2.65×10^9	4.81	1.39
NGC1068	2.24×10^9 (31)	18.35	-	9.00 (7)	7.26×10^9 (20)	1.74×10^9	1.36×10^{10}	4.32	5.68×10^9	10.32	1.43
NGC0891	7.59×10^9 (31)	16.08	-	8.90 (7)	5.75×10^9 (20)	2.19×10^9	1.89×10^{10}	9.15	1.38×10^{10}	12.48	1.42
MGC+02-04-025	1.74×10^9 (31)	16.08	-	8.52 (9)	-	-	$\geq2.41\times10^9$	-	$\geq2.41\times10^9$	-	1.39
NGC7469	1.51×10^9 (31)	16.08	-	8.70 (10)	6.28×10^9 (20)	6.00×10^9	1.09×10^{10}	3.12	1.05×10^{10}	3.24	1.40
NGC5256	-	-	-	8.53 (9)	9.92×10^9 (20)	2.07×10^{10}	$\geq1.38\times10^{10}$	-	$\geq2.88\times10^{10}$	-	1.39
NGC5953	5.75×10^8 (31)	16.08	-	8.73 (7)	1.62×10^9 (20)	1.34×10^9	3.07×10^9	4.22	2.69×10^9	4.82	1.40
M51	5.01×10^9 (31)	5.63	-	8.55 (8)	3.95×10^9 (20)	7.53×10^9	1.25×10^{10}	3.15	1.74×10^{10}	2.25	1.39
NGC3995	6.17×10^9 (31)	16.08	-	8.66 (7)	-	-	$\geq8.61\times10^9$	-	$\geq8.61\times10^9$	-	1.40
NGC3994	2.82×10^9 (31)	16.08	-	8.61 (7)	-	-	$\geq3.93\times10^9$	-	$\geq3.93\times10^9$	-	1.39
NGC6052	3.80×10^9 (31)	16.08	-	8.65 (7)	3.00×10^9 (20)	3.61×10^9	9.49×10^9	8.99	1.03×10^{10}	8.25	1.40
NGC1222	1.20×10^9 (31)	16.08	-	8.57 (7)	7.23×10^8 (21)	1.26×10^9	2.68×10^9	10.04	3.42×10^9	7.86	1.39
NGC7674	1.07×10^{10} (31)	16.08	-	8.14 (9)	6.34×10^9 (20)	7.99×10^{10}	2.35×10^{10}	10.10	1.25×10^{11}	1.90	1.38
NGC4670	1.66×10^8 (31)	16.08	-	8.30 (7)	9.00×10^6 (20)	5.42×10^7	2.42×10^8	15.26	3.04×10^8	12.12	1.38

References for metallicities (1) Madden et al. (2013) ; (2) Kennicutt et al. (2011) ; (3) McCall et al. (1985) ; (4) McQuade et al. (1995) ; (5) Kennicutt et al. (2003b) ; (6) Pilyugin et al. (2006) ; (7) Galametz et al. (2011) ; (8) Moustakas et al. (2010) ; (9) Veilleux et al. (1995) ; (10) Bonatto & Pastoriza (1990)

References for HI masses : (1) Cormier et al. (2014) ; (2) Thuan et al. (2004) ; (3) Gordon & Gottesman (1981) ; (4) Sauvage et al. (1997) ; (5) Pustilnik & Martin (2007) ; (6) MacHattie et al., in prep. ; (7) Chengalur et al. (2006) ; (8) Lelli et al. (2012) ; (9) Huchtmeier & Richter (1988) ; (10) Bettoni et al. (2003) ; (11) Williams et al. (1991) ; (12) Huchtmeier et al. (2005) ; (13) Thuan & Martin (1981) ; (14) Thuan et al. (1999a) ; (15) Davoust & Contini (2004) ; (16) Walter et al. (2008) ; (17) Meurer et al. (1998) ; (18) Hunter et al. (2011) ; (19) van Eymeren et al. (2009) ; (20) López-Sánchez et al. (2012) ; (21) Cannon et al. (2004) ; (22) de Blok & Walter (2006) ; (23) Begum & Chengalur (2005b) ; (24) Ekta et al. (2009) ; (25) Pustilnik et al. (2002) ; (26) van Zee et al. (1998) ; (27) Paturel et al. (2003) ; (28) Ekta & Chengalur (2010) ; (29) Moles et al. (1994) ; (30) Draine et al. (2007) ; (31) Galametz et al. (2011)

References for H_2 masses (1) Cormier et al. (2014) ; (2) Israel (2005) ; (3) Sage et al. (1992) ; (4) Kobulnicky et al. (1995) ; (5) Leroy et al. (2007) ; (6) Leroy et al. (2006) ; (7) Bettoni et al. (2003) ; (8) Young et al. (1995) ; (9) Albrecht et al. (2004) ; (10) Greve et al. (1996) ; (11) Schruba et al. (2012) ; (12) Walter et al. (2001) ; (13) Böttner et al. (2003) ; (14) Taylor et al. (1998) ; (15) Gratier et al. (2010) ; (16) Dale et al. (2001b) ; (17) Leroy et al. (2005) ; (18) Wilson et al. (2012) ; (19) Draine et al. (2007) ; (20) Galametz et al. (2011) ; (21) Young et al. (2011) ; (22) Young & Knezek (1989) ; (23) Leroy et al. (2009)

Note on mass references : The references given here are where the original measurement was found. If a correction was applied, the quoted masses are the corrected masses (see [b],[c],[d]) and not the original masses. If no correction was applied, the quoted masses are the original masses. Note that some galaxies have a molecular gas mass but no reference : this means that the molecular gas mass has been corrected (see [d]) but that no measurements of the molecular gas mass is available in the literature.

[a] For these galaxies, no information was available on the extent of the HI observations. The quoted HI mass is thus the total HI mass (diamonds in Fig. 9.4).

[b] For these galaxies, we were able to correct the HI mass and to rescale it to the HI mass contained in the IR aperture (triangles in Fig. 9.4).

[c] For these galaxies, the HI extent is similar to the IR aperture size and we consider that the total HI mass corresponds to the HI mass within the IR aperture (crosses in Fig. 9.4).

[c2] For these galaxies, the HI mass corresponding to the dust emitting region is given in the reference, and is the mass quoted here.

[d] For these galaxies, the H_2 mass correction was applied : i.e. non-detections or absence of data were replaced by $0.012 \times M_{HI}$ for $M_{H_2,MW}$ and $0.68 \times M_{HI}$ for $M_{H_2,Z}$ for galaxies with $12+\log(O/H) \leq 8.1$.

[e] For these 2 galaxies, the HII mass has a significant contribution to the total gas mass : $M_{\rm HII} \sim 1.2 \times M_{HI}$ for Haro 11 from Cormier et al. (2012) and $M_{\rm HII} \sim M_{HI}$ for Pox186 from Gil de Paz et al. (2003) in the $X_{CO,MW}$ case, and has to be taken into account to estimate the total gas mass.

Table 9.3. G/D for the DGS, KINGFISH and G11 samples.

Name	G/D($X_{CO,MW}$)	Uncertainty (%)	G/D($X_{CO,Z}$)	Uncertainty (%)	Comments[a]
DGS					
Haro11	1.75×10^{2}	21.77	3.04×10^{2}	14.43	-
Haro2	3.97×10^{2}	16.43	1.11×10^{3}	11.96	-
Haro3	7.08×10^{2}	12.27	8.12×10^{2}	12.22	-
He2-10	3.54×10^{2}	12.07	5.51×10^{2}	11.46	-
HS0017+1055	$\leq2.93\times10^{3}$	-	$\leq4.86\times10^{3}$	-	1+2
HS0052+2536	$\leq1.02\times10^{4}$	-	$\leq1.70\times10^{4}$	-	1+2
HS0822+3542	1.29×10^{4}	54.02	2.42×10^{4}	50.76	3
HS1222+3741	-	-	-	-	-
HS1236+3937	-	-	-	-	-
HS1304+3529	-	-	-	-	-
HS1319+3224	-	-	-	-	-
HS1330+3651	-	-	-	-	-
HS1442+4250	-	-	-	-	-
HS2352+2733	-	-	-	-	-
IZw18	2.76×10^{5}	23.57	6.69×10^{5}	18.77	3
IC10	2.40×10^{2}	34.26	4.76×10^{2}	34.08	-
IIZw40	1.23×10^{3}	46.42	1.67×10^{3}	45.25	-
Mrk1089	7.93×10^{2}	15.47	1.01×10^{3}	14.72	-
Mrk1450	1.19×10^{3}	208.33	1.97×10^{3}	207.94	-
Mrk153	$\leq5.62\times10^{3}$	-	$\leq9.25\times10^{3}$	-	1+2
Mrk209	9.15×10^{3}	39.03	8.26×10^{4}	38.58	-
Mrk930	7.38×10^{2}	55.41	8.82×10^{2}	55.08	-
NGC1140	1.23×10^{3}	29.20	1.26×10^{3}	28.79	-
NGC1569	8.55×10^{2}	22.39	9.25×10^{2}	21.53	-
NGC1705	$\geq8.24\times10^{2}$	-	$\geq8.24\times10^{2}$	-	2
NGC2366	3.60×10^{3}	34.47	9.47×10^{3}	33.93	-
NGC4214	3.14×10^{2}	30.52	3.22×10^{2}	30.30	-
NGC4449	4.46×10^{2}	18.79	5.48×10^{2}	16.45	-
NGC4861	9.52×10^{2}	26.80	1.68×10^{3}	26.31	-
NGC5253	2.71×10^{2}	23.11	3.19×10^{2}	22.93	-
NGC625	3.49×10^{2}	24.13	4.49×10^{2}	21.47	-
NGC6822	6.13×10^{2}	112.72	6.73×10^{2}	112.64	-
Pox186	$\leq2.49\times10^{1}$	-	$\leq3.45\times10^{1}$	-	1+2+3
SBS0335-052	1.95×10^{5}	143.38	3.30×10^{5}	143.15	-
SBS1159+545	$\leq2.91\times10^{3}$	-	$\leq4.83\times10^{3}$	-	1+2+3
SBS1211+540	4.22×10^{3}	50.54	6.99×10^{3}	48.93	-
SBS1249+493	3.31×10^{3}	57.66	5.49×10^{3}	43.44	3
SBS1415+437	9.52×10^{4}	24.11	1.58×10^{5}	20.51	3
SBS1533+574	2.11×10^{3}	24.14	3.49×10^{3}	22.44	-
Tol0618-402	-	-	-	-	-
Tol1214-277	$\leq3.57\times10^{3}$	-	$\leq5.92\times10^{3}$	-	1+2+3
UGC4483	9.45×10^{4}	41.33	1.75×10^{5}	41.13	3
UGCA20	-	-	-	-	3
UM133	3.16×10^{3}	58.97	6.99×10^{3}	58.85	-
UM311	4.28×10^{3}	24.78	4.31×10^{3}	24.72	-
UM448	7.36×10^{2}	19.27	1.94×10^{3}	10.64	-
UM461	4.88×10^{3}	48.49	1.07×10^{4}	48.29	-
VIIZw403	6.29×10^{3}	18.09	1.29×10^{4}	16.64	-
KINGFISH					
NGC0337	$\leq3.48\times10^{2}$	-	$\leq9.18\times10^{2}$	-	2
NGC0584	-	-	-	-	2+3
NGC0628	2.47×10^{2}	18.01	4.24×10^{2}	14.56	-
NGC0855	$\leq1.66\times10^{2}$	-	$\leq5.20\times10^{2}$	-	2
NGC0925	2.84×10^{2}	20.23	5.06×10^{2}	16.49	-
NGC1097	1.29×10^{2}	17.68	1.34×10^{2}	17.17	-
NGC1266	$\geq2.18\times10^{2}$	-	$\geq1.37\times10^{3}$	-	-
NGC1291	$\geq1.51\times10^{2}$	-	$\geq1.51\times10^{2}$	-	2

Table 9.3. G/D for the DGS, KINGFISH and G11 samples (continued).

Name	G/D($X_{CO,MW}$)	Uncertainty (%)	G/D($X_{CO,Z}$)	Uncertainty (%)	Comments[a]
NGC1316	-	-	-	-	-
NGC1377	-	-	-	-	-
NGC1404	-	-	-	-	-
IC0342	3.89×10^{2}	15.60	4.94×10^{2}	13.08	-
NGC1482	$\leq2.12\times10^{2}$	-	$\leq2.48\times10^{3}$	-	1
NGC1512	$\geq3.29\times10^{2}$	-	$\geq3.29\times10^{2}$	-	2
NGC2146	2.40×10^{3}	8.30	2.51×10^{3}	8.29	-
HoII	7.72×10^{3}	24.94	1.28×10^{4}	16.32	-
DDO053	8.25×10^{3}	20.77	1.37×10^{4}	16.46	-
NGC2798	5.94×10^{2}	9.39	2.03×10^{3}	7.11	-
NGC2841	2.71×10^{2}	15.08	3.40×10^{2}	13.24	-
NGC2915	1.45×10^{3}	26.39	2.40×10^{3}	23.15	-
HoI	8.50×10^{2}	17.91	1.41×10^{3}	12.66	-
NGC2976	1.35×10^{2}	14.29	2.87×10^{2}	10.46	-
NGC3049	2.51×10^{2}	24.91	2.86×10^{2}	23.98	-
NGC3077	1.07×10^{3}	22.18	1.08×10^{3}	22.12	-
M81dwB	5.75×10^{2}	65.93	9.52×10^{2}	64.70	-
NGC3190	$\leq6.26\times10^{1}$	-	$\leq1.08\times10^{2}$	-	2
NGC3184	2.00×10^{2}	17.48	2.68×10^{2}	15.60	-
NGC3198	3.00×10^{2}	26.10	4.92×10^{2}	19.09	-
IC2574	6.53×10^{2}	50.08	7.26×10^{2}	49.59	-
NGC3265	$\leq4.60\times10^{2}$	-	$\leq2.41\times10^{3}$	-	2
NGC3351	1.08×10^{2}	12.91	1.26×10^{2}	11.63	-
NGC3521	2.63×10^{2}	15.93	5.42×10^{2}	13.09	-
NGC3621	$\geq5.10\times10^{2}$	-	$\geq5.10\times10^{2}$	-	2
NGC3627	1.39×10^{2}	8.24	5.80×10^{2}	7.57	-
NGC3773	2.56×10^{2}	16.22	4.66×10^{2}	13.71	-
NGC3938	3.69×10^{2}	16.81	6.91×10^{2}	14.33	-
NGC4236	1.44×10^{3}	21.26	1.92×10^{3}	18.61	-
NGC4254	2.51×10^{2}	11.04	5.78×10^{2}	9.77	-
NGC4321	1.48×10^{2}	12.66	2.92×10^{2}	11.91	-
NGC4536	1.53×10^{2}	14.29	7.73×10^{2}	11.92	-
NGC4559	6.18×10^{2}	19.46	7.66×10^{2}	17.22	-
NGC4569	1.14×10^{2}	6.98	1.80×10^{2}	6.83	-
NGC4579	1.03×10^{2}	6.98	1.82×10^{2}	6.32	-
NGC4594	3.22×10^{1}	19.20	4.67×10^{1}	18.12	-
NGC4625	7.13×10^{2}	21.67	7.68×10^{2}	20.86	-
NGC4631	3.91×10^{2}	17.10	9.49×10^{2}	11.09	-
NGC4725	1.79×10^{2}	14.08	4.33×10^{2}	10.70	-
NGC4736	2.07×10^{2}	13.65	7.21×10^{2}	11.50	-
DDO154	-	-	-	-	3
NGC4826	2.44×10^{2}	9.99	3.98×10^{2}	8.85	-
DDO165	-	-	-	-	3
NGC5055	2.14×10^{2}	13.57	4.10×10^{2}	9.95	-
NGC5398	$\geq1.12\times10^{2}$	-	$\geq1.12\times10^{2}$	-	2
NGC5408	5.27×10^{3}	30.20	8.74×10^{3}	27.41	-
NGC5457	$\geq2.42\times10^{2}$	-	$\geq2.42\times10^{2}$	-	2
NGC5474	$\leq3.82\times10^{2}$	-	$\leq4.85\times10^{2}$	-	2
NGC5713	4.42×10^{2}	12.58	1.61×10^{3}	8.15	-
NGC5866	$\leq2.12\times10^{2}$	-	$\leq4.68\times10^{2}$	-	1
NGC6946	1.54×10^{2}	9.47	3.94×10^{2}	6.83	-
NGC7331	2.06×10^{2}	12.54	5.61×10^{2}	9.20	-
NGC7793	$\geq1.89\times10^{2}$	-	$\geq1.89\times10^{2}$	-	2
G11					
M83	7.62×10^{2}	9.19	8.04×10^{2}	9.09	-
NGC1808	2.01×10^{2}	34.57	1.16×10^{2}	35.21	-
NGC7552	$\geq9.14\times10^{1}$	-	$\geq9.14\times10^{1}$	-	2
M82	2.70×10^{2}	33.72	3.86×10^{2}	33.36	-
NGC1068	4.89×10^{1}	36.31	2.05×10^{1}	37.50	-

Table 9.3. G/D for the DGS, KINGFISH and G11 samples (continued).

Name	G/D($X_{CO,MW}$)	Uncertainty (%)	G/D($X_{CO,Z}$)	Uncertainty (%)	Comments[a]
NGC0891	3.23×10^{2}	14.96	2.37×10^{2}	17.21	-
MGC+02-04-025	$\geq2.38\times10^{1}$	-	$\geq2.38\times10^{1}$	-	2
NGC7469	7.05×10^{1}	19.41	6.79×10^{1}	19.43	-
NGC5256	$\geq6.86\times10^{1}$	-	$\geq1.43\times10^{2}$	-	-
NGC5953	1.36×10^{2}	19.37	1.19×10^{2}	19.51	-
M51	3.33×10^{1}	22.04	4.66×10^{1}	21.93	-
NGC3995	$\geq1.50\times10^{2}$	-	$\geq1.50\times10^{2}$	-	2
NGC3994	$\geq7.44\times10^{1}$	-	$\geq7.44\times10^{1}$	-	2
NGC6052	1.63×10^{2}	33.79	1.77×10^{2}	33.61	-
NGC1222	2.01×10^{2}	28.53	2.56×10^{2}	27.84	-
NGC7674	2.39×10^{2}	31.36	1.27×10^{3}	29.75	-
NGC4670	2.13×10^{2}	26.05	2.68×10^{2}	24.35	-

[a] : This column gives the reliability of the point, and works the same way as for the colors in Fig. 9.4.

1 - HI masses are non-detections (blue points in Fig. 9.4).

2 - H_2 is not detected or not observed for this galaxy (blue points in Fig. 9.4).

3 - The galaxy is not detected beyond 160 μm (red points in Fig. 9.4).

1+3 or 2+3 or 1+2+3 reflects a combinaison of the previous notes (purple points in Fig. 9.4).

A dash means that we are confident about the three quantities (black points in Fig. 9.4).

Conclusions

Summary of activities and results

The general goal of this work was to study the impact of metallicity on the observed ISM properties in galaxies and address the following questions:

- How do the dust properties in galaxies (such as mass, temperature, luminosity, etc.) vary with metallicity? And how do dust model choices influence the overall resulting dust properties?
- In which environments does the submm excess preferentially appear?
- How do the proportions of metals in the gas and dust phases relate to each other? How do the gas-to-dust mass ratios (G/D) evolve as a function of metallicity?

To conduct our study, a multi-wavelength approach has been followed over the whole IR-to-submm range. The data were interpreted first with a simple modified blackbody model, and second with a more complete semi-empirical dust model allowing a more realistic description of the dust properties.

Building up the database

I was lucky to start this work about a year after the launch of *Herschel* when the DGS data was already available for about half of the sample and when members of the PACS and SPIRE ICC had already overcome the major problems in the (complicated) *Herschel* data reduction. I was thus able to compare several methods for the data reduction and start the photometry on a few DGS galaxies for which the data were already available, before generalising for the whole sample once the observations were complete (in June 2011, nine months after the beginning of my PhD). The major drawback of analysing data from an instrument that is still operating, is the numerous and seemingly never-ending updates of the calibration. The PACS and SPIRE photometry are at the core of my analysis, (especially in the second part of this manuscript), and I did not count the numerous times where I had to redo the maps *and* photometry for the DGS galaxies to match the most recent update of the map-making technique and of the instrument calibration. It was important to keep track of the calibration: one of the most recent updates had the effect of decreasing the SPIRE flux densities by ~ 10 %, which could have had a non-negligible impact on the results we derive for the dust mass and the submm excess. The other perfect timing that I was very lucky to benefit from was the publication of the KINGFISH *Herschel* photometry by Dale et al. (2012) at the exact same moment where I was starting to analyse the DGS photometry with modified blackbodies. Including KINGFISH galaxies in my work was thus quite straightforward, and was essential to my work by greatly increasing the metallicity range I was using.

Performing a multi-wavelength approach as done in this work implies a considerable amount of literature searching and data homogenising. This was particularly true for the DGS galaxies, a bit less for the KINGFISH galaxies, as the KINGFISH sample is derived from the *Spitzer*-SINGS sample,

and most of the IR data for the KINGFISH sample had already been published and homogenised. For the DGS sample however, I searched the literature and databases to find and homogenise the data when available. It also involved treating *Spitzer* data for the DGS that had been taken in anticipation of the *Herschel* observations as a set of ancillary data for the DGS. MIPS data had already entirely been reprocessed and published by Bendo et al. (2012). I finalised the treatment of *Spitzer* data by performing photometry for the IRAC data and treating the IRS spectra to complete our wavelength coverage. In addition to the IR-to-submm data already existing, I wrote several successful proposals to complete our dataset in the submm. I was able to obtain new LABOCA data for three DGS galaxies and conduct the observations on *APEX* in Chile.

Metallicity, being our main test parameter in this study, required that I ensure that the metallicities were properly and homogeneously determined. Again this had already been done by Moustakas et al. (2010) for the SINGS/KINGFISH galaxies. For the DGS galaxies, I searched the literature to find the required optical line ratios and recomputed the metallicities using the same method and the same strong-line method calibration (Pilyugin & Thuan 2005) as for the KINGFISH galaxies.

And finally, I also gathered HI and CO data from the literature for the samples to derive the total gas masses and then G/D for the considered galaxies.

Study of the global dust properties

We showed that a good wavelength coverage of the peak and of the Rayleigh Jeans slope of the dust SED, as now possible with *Herschel*, is crucial if one wants to accurately determine the dust properties such as the dust mass and TIR luminosity. A realistic description of dust is also necessary to properly estimate the dust mass. Indeed we found that dust masses estimated using a modified blackbody model are *systematically underestimated* by a factor of ~ 1.8 compared to dust masses estimated with a full dust SED model. This can have important consequences for studies using modified blackbodies to derive dust masses, and for example, go further to estimate a G/D using this underestimated dust mass.

Combining FIR/submm colours with results from the full dust SED model and from the modified blackbody model, we showed that the dust SEDs in dwarf galaxies can have a very peculiar shape: they often have a broader peak of their dust SED, that is shifted to shorter wavelengths compared to the dust SED of more metal-rich environments. This reflects a higher average dust equilibrium temperature ($T_d \sim 30$ K) and a broader dust equilibrium temperature distribution ($\Delta T_d \sim 110$ K) in the low-metallicity galaxies compared to more metal-rich environments ($T_d \sim 20$ K and $\Delta T_d \sim 40$ K). This overall warmer dust is due to the harder ISRF interacting with the porous ISM of dwarf galaxies (e.g., Madden et al. 2006). This effect had already been observed for a handful of dwarf galaxies (e.g., Galliano et al. 2003, 2005; Walter et al. 2007; Engelbracht et al. 2008; Galametz et al. 2009) and is now confirmed on a larger sample of dwarf galaxies and quantified. As a consequence, we also found that low-metallicity dwarf galaxies emit more luminosity per unit dust mass over the whole IR range (about seven times more) than more-metal rich environments. This is directly linked to the harder ISRF observed in low-metallicity galaxies along with the low dust abundances.

We also explored dust-to-stellar mass ratios and specific star-formation rates and found that metallicity only has an impact of the second of these two parameters: the dust-to-stellar mass ratios is more or less constant over the metallicity range we are probing, but we found that dwarf galaxies are more efficient in forming stars than their metal-rich counterparts.

Study of the submm excess

We investigated the presence of an excess at submm wavelengths in our sample with a full dust model for a subsample of 78 galaxies detected at 500 μm. We found an excess at 500 μm in 35% of

the cases and not only in metal-poor galaxies. When including longer submm wavelengths (at 850, 870 or 1200 μm) we found that about half of the sample presents an excess in the submm. This shows that the submm excess is not uncommon and not only restricted to low-metallicity galaxies. We investigated the presence of the submm excess when using a modified blackbody model with a fixed emissivity, $\beta = 2.0$, and found coherent results compared to the submm excess from a full dust SED model. This enabled us to define a method to detect galaxies that have a strong chance of presenting a submm excess from a full dust model, by using *Herschel* data only and modified blackbodies. We also looked at the influence of metallicity on the excess. We showed that the submm excess appears preferentially in low-metallicity galaxies, but that the intensity of the excess does not depend on metallicity. At low metallicities (for 12+log(O/H) < 8.0), the mean starlight intensity, which is related to the dust average temperature, discriminates between the galaxies with or without excess: galaxies with low dust temperatures, given their low metallicity (~ 20 K), do not show an excess. FIR/submm colours also provide a good empirical tool to detect and predict the appearance of the submm excess. Galaxies showing an excess at 500 μm have high $\frac{F_{160}/F_{250}}{F_{250}/F_{500}}$ ratios ($\gtrsim 0.37$). Galaxies with $\frac{F_{160}/F_{250}}{F_{250}/F_{500}} \gtrsim 0.37$ that do not show an excess at 500 μm, either exhibit it at longer wavelength or are low-metallicity galaxies with low dust temperatures given their metallicity. At longer wavelengths, we find that the slope of the submm SED determines whether or not an excess is present: galaxies with $F_{500}/F_{850(870)} \lesssim 5.5$ present an excess for wavelengths ≥ 850 μm. We have thus highlighted in this study various observational and modelling criteria to identify galaxies that present an excess. This provides useful tools to determine if a galaxy has an excess when there is limiting data to model it with a full dust SED model.

Additionally we model the IR-to-submm SEDs of the excess galaxies with another dust model with an alternative dust composition: graphite grains are replaced by amorphous carbon grains. We were able to explain the excess in 12 galaxies out of the 37 presenting an excess at submm wavelength with the graphite grains model. These galaxies are mostly moderately metal-poor galaxies and had the weakest excesses with the graphite grains model. We thus believe that the submm excess in these galaxies may be due to the fact that a Galactic grain composition is not appropriate to model the dust emission in these galaxies. This confirms the results of Galliano et al. (2011); Galametz et al. (2013) who showed that a dust composition using amorphous carbon was also more appropriate for the moderately low-metallicity LMC. Nonetheless, a submm excess is still present in 25 galaxies of our sample when modelled with amorphous carbon grains, a sign that other mechanisms are needed to explain the excess in these galaxies.

Study of the variation of G/D and metallicity

We also studied the relation between G/D and metallicity using more accurate dust masses compared to previous studies of the G/D using *Spitzer*-only dust masses and/or modified blackbody dust masses. We also probed this parameter over an unprecedented metallicity range (2 dex) with a significant fraction of the sample below 12+log(O/H) = 8.0 ($\sim 30\%$), enabling us to better constrain the behaviour of the G/D at low metallicities. We model the observed trend of the G/D with metallicity using a simple power law (slope of -1 and free) and a broken power law. We found that the G/D does not follow the "reference" trend with metallicity (single power law with a slope of -1) over the whole metallicity range. The observed trend is steeper for metallicities lower than ~ 8.0. A large scatter is observed in the G/D values for a given metallicity: in metallicity bins of ~ 0.1 dex, the dispersion around the mean value is 0.37 dex on average. On average, the broken power law reproduces best the observed G/D compared to the two power laws (slope of -1 or free) and provides estimates of the G/D that are accurate to a factor of 1.6. Even though more data for galaxies with 12+log(O/H) ≤ 7.5 are necessary to better constrain the observed G/D at extremely low metallicities, this broken power law relation is the best empirical estimate of the observed G/D

for local galaxies we have at our disposal so far. This new empirical prescription can be used for local galaxies to estimate the G/D based on a metallicity value (where this metallicity value must be estimated with the same method than the one we used). Predictions from three chemical evolution models are also compared to the observed G/D values: a simple model from Galliano et al. (2008), a model from Asano et al. (2013) which includes dust growth in the ISM as a source of dust production and continuous star formation; and a model from Zhukovska (2014), more specific to dwarf galaxies, testing episodic star-formation histories and its effects on dust growth and the G/D. The good agreement of observed values of the G/D and its scatter with respect to metallicity with the predicted values of the three tested chemical evolution models, allows us to infer that the scatter in the relation is intrinsic to galactic properties, reflecting the different star-formation histories, dust destruction efficiencies, dust grain size distributions and chemical compositions across the sample.

Publications of the results

The main results of this work are published or in the process of being published. A first first-author paper has been published in Astronomy & Astrophysics (A&A 557, A95) presenting the photometry for the DGS sample and the first conclusions I derived on the dust properties with modified blackbodies (i.e., Chapters 4 and 5). A second first-author paper presenting the G/D versus metallicity results (Chapter 9) has been recently accepted by A&A (acceptance on the 9th of December 2013, arXiv 1312.3442). A third first-author paper is in preparation to present the results obtained on the dust properties and the submm excess with the full dust model, over the whole IR range (i.e., Chapters 6, 7 and 8). Additionally, I am also second author in Madden et al. (2013) where I was in charge of collecting all of the ancillary data for the presentation of the DGS sample. I am also a co-author in ten other papers from the *Herschel* SAG2 consortium. I was also lucky to have the opportunity of presenting my work at conferences through posters or oral presentations. I was also invited twice to give seminars about my work in other institutes.

Another major input of my work is the wide database of maps/photometry/parameters I put together for the DGS galaxies that should be made available for the community in the next few months.

Perspectives

This work opens a certain number of perspectives that I would like to explore in future works.

Zooming into the ISM

Galliano et al. (2011) recently modelled the LMC at different spatial resolutions and found that the lack of resolution could lead to an underestimation of the dust mass of about 50%. Modelling unresolved distant galaxies with the current available models can thus lead to large uncertainties on the dust properties, due to the mixing of the different ISM phases into a single beam: despite its small filling factor, the warm dust phase around the star forming regions can often dominate the emission. To interpret the observations correctly, spatial studies must zoom into the ISM structures to establish what processes drive the physics of these different regions. The wealth of available *Herschel* data on well resolved local galaxies, coupled with the existing *Spitzer* and ground-based data, makes it a perfect time to study the effect of varying spatial scales on the interpretation of SEDs of a wide variety of spatially resolved regions of galaxies from hot HII regions around young star clusters to cold dense molecular clouds. It is possible to relate the observed variations in the dust SEDs and gas properties to the actual physical phenomena (for example the heating of cold dust by the older, more evolved, stellar population), occurring within the ISM of the galaxy (e.g.,

Bendo et al. 2012; Parkin et al. 2012; Aniano et al. 2012; Galametz et al. 2012). The study of a variety of dust environments within the same galaxy (for example the LMC, SMC, M31 or M51, 4 galaxies extensively studied with *Herschel*) will unveil the dust physical conditions of these regions (intensity of the radiation field, temperature and grain size distributions, abundances, etc.). A few dwarf galaxies from the DGS also show resolved details with *Herschel* (SF regions, dust embedded young super star clusters...) out to submm wavelengths. With these few test cases we can study how the metallicity affects the impact of spatial resolution on the dust properties (such as the dust mass), allowing the construction of a rich interpretative framework for unresolved, more distant galaxies in the early Universe. These initial studies will undoubtedly be compelling cases to follow-up with ALMA, for example, to obtain the best spatial view of the structure of the ISM and to see how this affects dust mass determination in galaxies.

Follow-up on the submm excess

Our study has now, systematically identified galaxies harbouring a submm excess. An obvious follow-up on the submm excess project would be to extend the *Herschel* observations to longer wavelengths with more APEX/LABOCA or IRAM/GISMO (observing at 2 mm) observing campaigns, or by using the *Planck* database following the Early Release Compact Source Catalog and the *Planck* Catalog of Compact Sources; in cases where there is already a suggestion of submm excess at 500 μm but no observations at longer wavelengths. Using the criteria I defined to find the submm excess in galaxies could also be applied to other *Herschel* samples, for example the Herschel Reference Survey or the Herschel Virgo Cluster Survey, where there has already been evidence for submm excess (with modBB models, see Grossi et al. 2010) to make a more thorough selection of galaxies with potential submm excess in these samples. This would enrich the first systematic study we conducted on the submm excess at the end of Chapter 8 and see if our results are confirmed on an even larger number of galaxies. Such a study is now possible thanks to the wealth of existing *Herschel* data.

Application of various explanations proposed for the submm excess, such as spinning dust, and emissivity effects due to an inverse temperature-β correlation, on galaxies for which the excess remains after altering the dust composition, is a follow-up project that I would like to develop.

Galliano et al. (2011) found that the submm excess correlates with the diffuse ISM in the LMC. Thus zooming into smaller spatial scales, for example with ALMA in the submm, is a next step to better understand the origin of this excess and the local properties of the ISM that favour the manifestation of the excess. This will be an obvious follow-up to propose for some of the well-justified galaxies already showing a *global* submm excess. My work shows that the excess is not uncommon even in moderately metal-poor environments. Thus, one would expect the submm excess to also appear in the outer parts of large spiral galaxies where the metallicity can decrease by up to a factor of 10 between the centre and outer parts. *Globally* those galaxies do not show an excess but they may on *local* scales, hence highlighting the importance of zooming into the smaller scales of the ISM.

Constraining the G/D at extremely low metallicities

As a consequence of this work, the behaviour of the G/D is relatively well constrained at low metallicities. However, more extremely-low-metallicity galaxies (12+log(O/H) $\leq$ 7.5) are needed to strengthen our results. This study was based on a sample of rather gas-rich dwarf galaxies. To follow-up on this project we could look for more extremely metal-poor dwarf and/or gas-poor dwarf in other *Herschel* samples to see how their observed G/D compare with the derived trends and the considered chemical evolution models. There are a number of extremely low-metallicity galaxies that will soon become available in the *Herschel* archive. A similar treatement of the *Herschel* data

as presented here, along with the SED modelling, can be carried out to refine the low-metallicity behaviour of the G/D below 12+log(O/H) = 7.5. Dust and gas masses at this low-metallicity regime will be very important to chemical evolution models which are at the heart of understanding the process of evolution of galaxies.

Glossary

2MASS	2 Microns All-Sky Survey
Ac	Amorphous carbon
AdOpt	Advanced Optimal extraction (in CASSIS)
AGB	Asymptotic Giant Branch
AGN	Active Galactic Nuclei
ALMA	Atacama Large Millimetre/ submillimetre Array
APEX	Atacama Path finder EXperiment
BCD	Blue Compact Dwarf
BG	Big Grains
BoA	Bolometer Array analysis software (for LABOCA)
CASSIS	Cornell AtlaS of Spitzer Infrared spectrograph Sources
cm	centimetre
CMB	Cosmic Microwave Background
CNM	Cold Neutral Medium
COBE	COsmic Background Explorer
DCD	Disordered Charge Distribution
dE	dwarf Elliptical
DGS	Dwarf Galaxy Survey
DIRBE	Diffuse InfraRed Background Experiment
dIrr	dwarf Irregular
dS	dwarf Spiral
dSph	dwarf Spheroidal
eef	encircled energy fraction
ESO	European Southern Observatory
FIR	Far-InfraRed
FIRAS	Far InfraRed Absolute Spectrometer
FIRST	Far InfraRed and Submillimetre space Telescope
FOV	Field Of View
FUV	Far Ultra-Violet
FWHM	Full Width at Half Maximum
GALEX	GALaxy evolution EXplorer
G/D	Gas-to-Dust mass ratio
Gr	Graphite
HFI	High Frequency Instrument (on *Planck*)
HIFI	Heterodyne Instrument for the Far Infrared
HIM	Hot Ionised Medium
HIPE	*Herschel* Interactive Processing Environment
HRS	*Herschel* Reference Survey
ICC	Instrument Control Centre
ICF	Ionisation Correction Factors
IMF	Initial Mass Function
IR	InfraRed
IRAC	InfraRed Array Camera
IRAM	Institute for Radio Astronomy at Millimetre wavelengths
IRAS	InfraRed Astronomical Satellite
IRS	InfraRed Spectrograph
ISM	InterStellar Medium
ISO	Infrared Space Observatory
ISOCAM	ISO CAMera
ISRF	InterStellar Radiation Field
JCMT	James Cerk Maxwell Telescope
KINGFISH	Key Insights on Nearby Galaxies: a Far-Infrared Survey with *Herschel*
LABOCA	Large Apex BOlometer CAmera
LFI	Low Frequency Instrument (on *Planck*)
LH	Long-High (IRS module)
LINER	Low-Ionisation Nuclear Emission-line Regions
LIRG	Luminous InfraRed Galaxy
LL	Long-Low (IRS module)
LMC	Large Magellanic Cloud
LW	Long Wave - SCUBA
MAMBO	MAx-planck-Millimetre-BOlometer
MIPS	Multiband Imaging Photometer for *Spitzer*
MIR	Mid-InfraRed
mm	milimetre
modBB	modified BlackBody
NIR	Near-InfraRed

OSO	Onsala Space Observatory
PACS	Photodetector Array Camera and Spectrometer
PAH	Polycyclic Aromatic Hydrocarbon
PEGASE	Projet d'Étude des GAlaxies par Synthèse Évolutive
PDR	Photo-Dissociation Region
PSF	Point Spread Function
RSRF	Relative Spectral Response Function
SCUBA	Submillimetre Common-User Bolometer Array
SED	Spectral Energy Distribution
SEST	Swedish-ESO Submillimetre Telescope
SFR	Star-Formation Rate
SH	Short-High (IRS module)
SL	Short-Low (IRS module)
SMART	Spectroscopic Modeling Analysis and Reduction Tool (tool within CASSIS)
SMC	Small Magellanic Cloud
S/N	Signal-to-Noise ratio
SN	SuperNova
SNII	Type II Super-Nova
SPIRE	Spectral and Photometric Imaging REceiver
SSC	Super Star Cluster
submm	submillimetre
SW	Short Wave - SCUBA
TDA	Thermal Discrete Approximation
THINGS	The HI Nearby Galaxy Survey
TIR	Total InfraRed
TLS	Two Level System
UIB	Unidentified Infrared Bands
ULIRG	Ultra-Luminous InfraRed Galaxy
UV	Ultra-Violet
VCD	Very Cold Dust
VNGS	Very Nearby Galaxy Survey
VSG	Very Small Grain
WIM	Warm Ionised Medium
WISE	Wide-field Infrared Survey Explorer
WNM	Warm Neutral Medium
WR	Wolf-Rayet

Notations

a	dust grain radius
a_{max}	maximum dust grain radius
a_{min}	minimum dust grain radius
a_t	transition radius between small and big grains, fixed to 10 nm (Chap. 7)
$\mathcal{A}$	telescope area (Chap. 6)
$A(\lambda)$	extinction
A_{ul}	Einstein coefficient for spontaneous emission (Chap. 2)
A_V	V-band extinction
α	power-law index of the starlight intensity distribution
α_0	power-law index of the power-law fit to the observed G/D (Chap. 9)
α_H	high-metallicity slope of the broken power-law fit to the observed G/D(Chap. 9)
α_L	low-metallicity slope of the broken power-law fit to the observed G/D (Chap. 9)
α_S	spectral index (for colour correction)
α_{CO}	X-factor in terms of mass surface density
$\alpha_{CO,\odot}$	Galactic α_{CO} (3.8 $M_\odot$(K km s^{-1} pc^2)$^{-1}$)
α_{ij}	mass fraction of the jth element in the ith dust specie (Chap. 7)
$\alpha(\lambda)$	absorption coefficient
α_{sync}	spectral index of the synchrotron spectrum (Chap. 6)
b	background level (PACS photometry, Chap. 4)
$B_\nu(\lambda, T)$	Planck function
β	emissivity index
β_{obs}	effective emissivity index from a modified blackbody fit with free emissivity index
β_{theo}	theoretical emissivity index (from models)
c	speed of light
C	calibration factor for an instrument (Chap. 6)
$C_{abs}(a, \lambda)$	dust absorption cross-section
$C_{ext}(a, \lambda)$	dust extinction cross-section
C_{LL}	constant correction factor for Long-Low (Chap. 6)
$C_{sca}(a, \lambda)$	dust scattering cross-section
$C_{SL}(\lambda)$	wavelength-dependent correction factor for Short-Low (Chap. 6)
$C(T)$	specific heat per unit volume

D	distance
D_{25}	diameter corresponding to R_{25}
DEC	Declination
$\Delta R(\lambda)$	error on the relative residual at the wavelength λ
$\Delta\nu$	bandwidth of a filter
ΔU	difference between the maximum and minimum radiation field intensities
e_1	real part of the dielectric constant e_{diel} (Chap. 1)
e_2	complex part of the dielectric constant e_{diel} (Chap. 1)
e_{diel}	dielectric constant (Chap. 1)
eef_r	encircled energy fraction at radius r (PACS photometry, Chap. 4)
$E(\lambda-\lambda_0)$	colour excess between λ and λ_0
E_{ul}	energy difference between the upper and lower energy levels (Chap. 2)
ϵ_γ	energy of a photon (Chap. 1)
f_{ap}	measured flux density in source aperture (PACS photometry, Chap. 4)
f_{an}	measured flux density in background annulus (PACS photometry, Chap. 4)
f_{ion}	ionised-to-total PAH mass ratio
f_{PAH}	PAH mass fraction, normalised to the Galactic value
f_{tot}	total flux density of the source (PACS photometry, Chap. 4)
f_{sil}	silicate-to-(silicate+graphite) grains mass fraction
$f_{sil,\odot}$	Galactic silicate-to-(silicate+graphite) grains mass fraction (0.6912, Zubko et al. 2004)
f_{vsg}	very small grains mass fraction
$f_{VSG,gr,\odot}$	Galactic proportion of graphite VSG (0.1846, Zubko et al. 2004)
$f_{VSG,sil,\odot}$	Galactic proportion of silicate VSG (0.1655, Zubko et al. 2004)
f_i^m	mass fraction of the ith dust specie (Chap. 7)
$f_{gr,\odot}^m$	Galactic mass fraction of graphite (0.2947, Zubko et al. 2004)
$f_{PAH,\odot}^m$	Galactic PAH mass fraction (0.0457, Zubko et al. 2004)
$f_{sil,\odot}^m$	Galactic mass fraction of silicate (0.6596, Zubko et al. 2004)
F_0	zero-magnitude flux values (Chap 6)
F_{CO}	CO flux density
$F_i(a)$	size distribution of the ith dust specie per H atom (Chap. 7)
$F_{IRS}(band)$	synthetic photometry within a given band from IRS spectrum (Chap 6)
$F_{IRS,corr}(\lambda_{SL})$	final SL IRS spectrum (Chap 6)
$F_{IRS,corr}(\lambda_{LL})$	final LL IRS spectrum (Chap 6)
F_ν	flux density
$\bar{F}_S$	quantity observed by the *Herschel* bolometers (Chap. 3)
$F_S(\nu)$	source flux density
$F_S(\nu_0)$	monochromatic source flux density at the frequency ν_0 (output of the pipeline)
g_l	statistical weigth of the lower energy level (Chap. 2)
g_u	statistical weigth of the upper energy level (Chap. 2)
G_0	intensity of the radiation field (in Habing)
G/D	gas-to-dust mass ratio
$G/D_\odot$	Galactic gas-to-dust mass ratio (162, Zubko et al. 2004)
$G_i(a)$	size distribution of the ith dust specie (Chap. 7)
$\bar{G}_i(a)$	analytical function to approximate $G_i(a)$ (Chap. 7)
γ	ionisation parameter
γ_0	damping constant (Chap. 1)
γ_{lu}	collisional rate coefficient between the lower and upper energy levels (Chap. 2)
γ_{ul}	collisional rate coefficient between the upper and lower energy levels (Chap. 2)
Γ_{abs}	power absorbed by the dust
Γ_{em}	power emitted by the dust
h	Planck constant
H_0	Hubble constant, assumed to be 70 km s^{-1} Mpc^{-1}
$H(T)$	enthalpy
I_{CO}	CO intensity
I_λ	monochromatic specific intensity
j_λ	emission coefficient
J_λ	mean intensity
J_λ^{Gal}	mean intensity of the radiation field in the solar neighbourhood (Chap. 7)
J_λ^{UV}	UV component of J_λ^{Gal} (Chap. 7)
k	Boltzmann constant
K_4	conversion factor between the signal observed by the bolometers and the output of the pipeline
K_{4_E}	K_4 factor for extended sources in SPIRE
K_{4_P}	K_4 factor for point sources in SPIRE
$\kappa_{abs}(\lambda)$	dust opacity or mass absorption coefficient

l	length of a given line-of-sight (Chap. 1)
l_ν^{dust}	SED emitted by a single mass-element of the ISM (Chap. 7)
l_ν^i	monochromatic luminosities per unit dust mass of the ith dust specie, integrated over the size distribution (Chap. 7)
$l_\nu^\star$	monochromatic luminosities per unit stellar mass (Chap. 7)
L_{CO}	CO luminosity
L_{FIR}	far-infrared luminosity
$L_{H\alpha}$	Hα luminosity
$L_{H\beta}$	Hβ luminosity
L_ν	monochromatic luminosity
L_ν^{ff}	free-free monochromatic luminosity
L_ν^{model}	synthetic monochromatic luminosity from a given model
$L_\nu^{observed}$	observed monochromatic luminosity
L_ν^{radio}	radio monochromatic luminosity
$L_\nu^\star$	stellar monochromatic luminosity
L_ν^{sync}	synchrotron monochromatic luminosity
L_ν^{tot}	total monochromatic luminosity
$L_\nu^{tot,dust}$	total dust monochromatic luminosity
L_{TIR}	total infrared luminosity
$L_{TIR}(S)$	total infrared luminosity estimated only with *Spitzer* constraints (Chap. 8)
$L_{TIR}(S+H)$	total infrared luminosity estimated with *Spitzer* and *Herschel* constraints (Chap. 8)
L_{tot}	total luminosity of a galaxy
λ_0	designates a reference wavelength
Λ	cooling rate (Chap. 2)
$m(\lambda)$	complex refractory index (Chap. 1)
$mag(\lambda)$	apparent magnitude
m_e	mass of the electron
m_g	mass of a single dust grain (Chap. 1)
m_B	B-band apparent magnitude
m_H	mass of a hydrogen atom
m_{H_2}	mass of one H_2 molecule
m_j	atomic mass of the jth chemical element (Chap. 7)
$Mag(\lambda)$	absolute magnitude
M_B	B-band absolute magnitude
$M_d(S)$	dust mass estimated only with *Spitzer* constraints (Chap. 8)
$M_d(S+H)$	dust mass estimated with *Spitzer* and *Herschel* constraints (Chap. 8)
M_{dust}	dust mass from the full dust SED model
$M_{dust,BB}$	dust mass from a modified blackbody
M_g	total mass of the grains (Chap. 1)
M_{He}	helium mass
M_i	total mass of the grains of the ith dust specie (Chap. 7)
M_{gas}	total gas mass
$M_{gas,\odot}$	total gas mass estimated with $X_{CO,MW}$ (Chap 9)
$M_{gas,Z}$	total gas mass estimated with $X_{CO,Z}$ (Chap 9)
M_{HI}	atomic gas mass
M_{HI}(IRcorr)	atomic gas mass within the dust IR aperture (Chap 9)
$M_{\rm HII}$	ionised gas mass
M_{H_2}	molecular gas mass
$M_{H_2,MW}$	molecular gas mass estimated with $X_{CO,MW}$ (Chap 9)
$M_{H_2,Z}$	molecular gas mass estimated with $X_{CO,Z}$ (Chap 9)
$M_\star$	stellar mass
M_{tot}	total mass of a galaxy
M_V	V-band absolute magnitude
μ_{gal}	mean atomic weight
μ_V	V-band surface brightness
$n(a)$	dust grain size distribution (Chap. 1)
n_c	critical density of a two-level system (Chap. 2)
n_d	dust number density (Chap. 1)
n_e	electron density
n_l	population density of the lower energy level of a two-level system (Chap. 2)
n_u	population density of the upper energy level of a two-level system (Chap. 2)
N_{ap}	number of pixels within the source aperture (Chap. 4, 6)
N_{bg}	number of pixels within the background aperture (Chap. 4, 6)
N_d	dust column density (Chap. 1)
N_e^S	number of electrons collected by the instrument from the source (Chap. 6)
N_g	number of dust grains along the line-of-sight (Chap. 1)
N_H	line-of-sight column density of hydrogen (Chap. 7)
$N(H_2)$	molecular gas column density
N_j	column density of the jth chemical element of a dust specie (Chap. 7)
ν_0	designates a reference frequency

(O/H)	oxygen abundance (or 12+log(O/H))
$(O/H)_\odot$	solar neighbourhood oxygen abundance (4.90×10^{-4} (or 8.69), Asplund et al. 2009)
ω	pulsation (Chap. 1)
ω_0	resonant frequency (Chap. 1)
ω_p	plasma pulsation (Chap. 1)
Ω	solid angle
Ω_{mb}	main beam solid angle for radio astronomy (Chap. 6)
$\Omega(u,l)$	collision strength for upward collisions (Chap. 2)
$P(a,T)$	grain temperature probability distribution
$Q_{abs}(a,\lambda)$	absorption efficiency
$Q_{ext}(a,\lambda)$	extinction efficiency
$Q_{sca}(a,\lambda)$	scattering efficiency
r_0	source aperture radius (PACS photometry, Chap. 4)
r_1	inner background annulus radius (PACS photometry, Chap. 4)
r_2	outer background annulus radius (PACS photometry, Chap. 4)
r_{dust}	IR aperture dust radius (Chap 9)
r_{HI}	HI radius (Chap 9)
R_{25}	radius at which the surface brightness falls to a level of 25 mag/arcsec^2
$R(500)$	residual at 500 μm relative to the model
$R(850)$	residual at 850 μm relative to the model
$R(870)$	residual at 870 μm relative to the model
$R(1200)$	residual at 1200 μm relative to the model
RA	Right Ascension
$R(\nu)$	response function of a given band
R_V	extinction curve coefficient, ratio of the total-to-selective extinction
ρ	dust material mass density (Chap. 1)
ρ_i	mass density of the ith dust component (Chap. 7)
ρ_{ISM}	cloud mass density (Chap. 1)
SFR	star-formation rate
S^i_λ	source function for the ith dust component (Chap. 7)
$S/N(\lambda)$	signal-to-noise ratio of the excess at a given wavelength (or intensity of the excess)
$SSFR$	specific star-formation rate
σ_{F_0}	uncertainty on the zero-magnitude flux value (Chap. 6)
$\sigma_{int,i}$	intrinsic uncertainty coming from the data reduction for one pixel (Chap. 4)
σ_λ	final uncertainty on the flux density at the wavelength λ
σ_{mag}	error on the magnitude (Chap. 6)
σ_{sky}	standard deviation of all pixels in the background aperture (Chap. 4, 6)
t	integration time (Chap. 6)
T	temperature of the dust from a modified blackbody
T_{CMB}	temperature of the CMB radiation (2.73 K, Mather et al. 1994)
T_d	dust equilibrium temperature
$T_{d,\odot}$	dust equilibrium temperature of the diffuse Galactic dust (17.5 K, Boulanger et al. 1996)
T_e	electron temperature
$T_e(OIII)$	electron temperature determined from the [OIII]λ4363 line (Chap. 3)
T_{mb}	main beam temperature (Chap. 6)
T_{sub}	sublimation temperature for the grain (Chap. 7)
$\tau(\lambda)$	optical depth
$\tau_H(\lambda)$	extinction per H column density (Chap. 7)
τ_{SF}	star formation timescale (Chap. 9)
θ	FWHM of the main beam for radio astronomy (CO) (Chap. 6)
u_λ	energy density
unc_{ap}	uncertainty on the measured flux in the source aperture (PACS photometry, Chap. 4)
unc_{an}	uncertainty on the measured flux in the background annulus (PACS photometry, Chap. 4)
unc_b	uncertainty on the background level (PACS photometry, Chap. 4)
unc_{beam}	uncertainty from the SPIRE beam area (SPIRE photometry, Chap. 4)
unc_{bg}	uncertainty from the background determination (SPIRE photometry, Chap. 4)
unc_{calib}	systematic calibration uncertainty on the measured total flux density (Chap. 4)
unc_{flux}	non-systematic uncertainty on the measured total flux density (SPIRE photometry, Chap. 4)
$unc_{f_{tot}}$	non-systematic uncertainty on the measured total flux density (PACS photometry, Chap. 4)
unc_{int}	intrinsic uncertainty coming from the data reduction for the total flux density (Chap. 4)
unc_{source}	uncertainty on the measured flux in the source aperture (SPIRE photometry, Chap. 4)
unc_{sum}	uncertainty coming from summing pixels (PACS photometry, Chap. 4)
U	intensity of the stellar radiation field
$< U >$	mass-averaged starlight intensity
U_{min}	minimum intensity of the stellar radiation field
$U_{min}(S)$	minimum intensity of the stellar radiation field estimated only with *Spitzer* constraints
$U_{min}(S+H)$	minimum intensity of the stellar radiation field estimated with *Spitzer* and *Herschel* constraints
U_{max}	maximum intensity of the stellar radiation field

W_i	dilution factors for the optical components of J_λ^{Gal} (Chap. 7)
$x = 2\pi a/\lambda$	size parameter (Chap. 1)
X	mass fraction of hydrogen
$X_\odot$	mass fraction of hydrogen in the solar neighbourhood (0.7154, Asplund et al. 2009)
X_{CO}	conversion factor between CO and H_2, so called "X-factor"
$X_{CO,MW}$	Galactic conversion factor between CO and H_2 (2.0×10^{20} cm^{-2} (K km s^{-1})$^{-1}$, Ackermann et al. 2011)
$X_{CO,Z}$	metallicity-dependent X_{CO} factor, as in Schruba et al. (2012)
X_P	primordial mass fraction of hydrogen (0.76, Pagel 1997)
Y	mass fraction of helium
$Y_\odot$	mass fraction of helium in the solar neighbourhood (0.2703, Asplund et al. 2009)
Y_P	primordial mass fraction of helium (0.24, Pagel 1997)
Z	metallicity (mass fraction of metals)
$Z_\odot$	solar neighbourhood metallicity (0.0142, Asplund et al. 2009)
Z_P	primordial metallicity (0 by definition)

Appendix A

Observing Logs

Table A.1. DGS *Herschel* Observing Log.

Source	Obs ID	Description	Mapping mode	Duration (sec)	Date of observation
Haro 11	1342210636	PACS 70-1	Scan map	141	December 2010
	1342210637	PACS 70-2	Scan map	153	December 2010
	1342197713	PACS 100-1	Scan map	65	June 2010
	1342197714	PACS 100-2	Scan map	65	June 2010
	1342199386	SPIRE	Small map	307	June 2010
Haro 2	1342196745	PACS 70-1	Scan map	262	May 2010
	1342196746	PACS 70-2	Scan map	262	May 2010
	1342198283	PACS 100-1	Scan map	262	June 2010
	1342198284	PACS 100-2	Scan map	262	June 2010
	1342195686	SPIRE	Large map	639	April 2010
Haro 3	1342195618	PACS 70-1	Scan map	71	April 2010
	1342195619	PACS 70-2	Scan map	71	April 2010
	1342195616	PACS 100-1	Scan map	71	April 2010
	1342195617	PACS 100-2	Scan map	71	April 2010
	1342207035	SPIRE	Small map	307	October 2010
He 2-10	1342196121	PACS 70-1	Scan map	71	May 2010
	1342196122	PACS 70-2	Scan map	71	May 2010
	1342196119	PACS 100-1	Scan map	71	May 2010
	1342196120	PACS 100-2	Scan map	71	May 2010
	1342196888	SPIRE	Large map	241	May 2010
HS 0017+1055	1342199634	PACS 70-1	Scan map	220	July 2010
	1342199635	PACS 70-2	Scan map	220	July 2010
	1342199636	PACS 100-1	Scan map	220	July 2010
	1342199637	PACS 100-2	Scan map	220	July 2010
	1342201378	SPIRE	Small map	583	July 2010
HS 0052+2536	1342213514	PACS 70-1	Scan map	220	January 2011
	1342213515	PACS 70-2	Scan map	220	January 2011
	1342213516	PACS 100-1	Scan map	220	January 2011
	1342213517	PACS 100-2	Scan map	220	January 2011
	1342201326	SPIRE	Small map	583	July 2010
HS 0822+3542	1342209081	PACS 70-1	Scan map	212	November 2010
	1342209082	PACS 70-2	Scan map	212	November 2010
	1342209083	PACS 100-1	Scan map	212	November 2010
	1342209084	PACS 100-2	Scan map	212	November 2010
HS 1222+3741	1342211380	PACS 70-1	Scan map	276	December 2010
	1342211381	PACS 70-2	Scan map	276	December 2010
	1342211382	PACS 100-1	Scan map	276	December 2010
	1342211383	PACS 100-2	Scan map	276	December 2010
HS 1236+3937	1342211434	PACS 70-1	Scan map	220	December 2010
	1342211435	PACS 70-2	Scan map	220	December 2010
	1342197779	PACS 100-1	Scan map	220	June 2010
	1342197780	PACS 100-2	Scan map	220	June 2010
	1342199341	SPIRE	Small map	307	June 2010
HS 1304+3529	1342211289	PACS 70-1	Scan map	220	December 2010
	1342211290	PACS 70-2	Scan map	220	December 2010
	1342198475	PACS 100-1	Scan map	164	June 2010
	1342198476	PACS 100-2	Scan map	164	June 2010
	1342201224	SPIRE	Small map	307	July 2010
HS 1319+3224	1342211392	PACS 70-1	Scan map	276	December 2010
	1342211393	PACS 70-2	Scan map	276	December 2010
	1342211394	PACS 100-1	Scan map	276	December 2010
	1342211395	PACS 100-2	Scan map	276	December 2010
HS 1330+3651	1342211388	PACS 70-1	Scan map	276	December 2010
	1342211389	PACS 70-2	Scan map	276	December 2010
	1342211390	PACS 100-1	Scan map	276	December 2010
	1342211391	PACS 100-2	Scan map	276	December 2010

Table A.1. DGS *Herschel* Observing Log.

Source	Obs ID	Description	Mapping mode	Duration (sec)	Date of observation
HS 1442+4250	1342210958	PACS 70-1	Scan map	317	December 2010
	1342210959	PACS 70-2	Scan map	317	December 2010
	1342210960	PACS 100-1	Scan map	317	December 2010
	1342210961	PACS 100-2	Scan map	317	December 2010
	1342203597	SPIRE	Small map	307	August 2010
HS 2352+2733	1342212062	PACS 70-1	Scan map	276	December 2010
	1342212063	PACS 70-2	Scan map	276	December 2010
	1342212064	PACS 100-1	Scan map	276	December 2010
	1342212065	PACS 100-2	Scan map	276	December 2010
	1342201375	SPIRE	Small map	307	July 2010
I Zw 18	1342209354	PACS 70-1	Scan map	276	November 2010
	1342209355	PACS 70-2	Scan map	276	November 2010
	1342209356	PACS 100-1	Scan map	276	November 2010
	1342209357	PACS 100-2	Scan map	276	November 2010
	1342187175	SPIRE	Small map	2676	November 2009
IC 10	1342216141	PACS 70-1	Scan map	3061	March 2011
	1342216142	PACS 70-2	Scan map	3061	March 2011
	1342216143	PACS 100-1	Scan map	3061	March 2011
	1342216144	PACS 100-2	Scan map	3061	March 2011
	1342201446	SPIRE	Large map	2286	July 2010
II Zw 40	1342204313	PACS 70-1	Scan map	153	September 2010
	1342204314	PACS 70-2	Scan map	153	September 2010
	1342204315	PACS 100-1	Scan map	153	September 2010
	1342204316	PACS 100-2	Scan map	153	September 2010
	1342186116	SPIRE	Large map	1055	October 2009
Mrk 1089	1342193121	PACS 70-1	Scan map	65	March 2010
	1342193122	PACS 70-2	Scan map	65	March 2010
	1342193172	PACS 100-1	Scan map	65	April 2010
	1342193173	PACS 100-2	Scan map	65	April 2010
	1342192102	SPIRE	Small map	193	March 2010
Mrk 1450	1342195596	PACS 70-1	Scan map	182	April 2010
	1342195597	PACS 70-2	Scan map	182	April 2010
	1342195620	PACS 100-1	Scan map	182	April 2010
	1342195621	PACS 100-2	Scan map	182	April 2010
	1342199347	SPIRE	Small map	583	June 2010
Mrk 153	1342195827	PACS 70-1	Scan map	108	May 2010
	1342195828	PACS 70-2	Scan map	108	May 2010
	1342197018	PACS 100-1	Scan map	108	May 2010
	1342197019	PACS 100-2	Scan map	108	May 2010
	1342206187	SPIRE	Small map	583	October 2010
Mrk 209	1342195850	PACS 70-1	Scan map	65	May 2010
	1342195851	PACS 70-2	Scan map	65	May 2010
	1342197707	PACS 100-1	Scan map	65	May 2010
	1342197708	PACS 100-2	Scan map	65	May 2010
	1342199350	SPIRE	Small map	583	June 2010
Mrk 930	1342212066	PACS 70-1	Scan map	317	December 2010
	1342212067	PACS 70-2	Scan map	317	December 2010
	1342212068	PACS 100-1	Scan map	317	December 2010
	1342212069	PACS 100-2	Scan map	317	December 2010
	1342201374	SPIRE	Small map	583	July 2010
NGC 1140	1342212756	PACS 70-1	Scan map	909	January 2011
	1342212757	PACS 70-2	Scan map	909	January 2011
	1342212758	PACS 100-1	Scan map	909	January 2011
	1342212759	PACS 100-2	Scan map	909	January 2011
	1342201415	SPIRE	Large map	2047	July 2010

Table A.1. DGS *Herschel* Observing Log.

Source	Obs ID	Description	Mapping mode	Duration (sec)	Date of observation
NGC 1569	1342206046	PACS 70-1	Scan map	1280	October 2010
	1342206047	PACS 70-2	Scan map	1280	October 2010
	1342206048	PACS 100-1	Scan map	1280	October 2010
	1342206049	PACS 100-2	Scan map	1732	October 2010
	1342193013	SPIRE	Large map	529	March 2010
NGC 1705	1342186270	PACS 70-1	Scan map	376	October 2009
	1342186271	PACS 70-2	Scan map	376	October 2009
	1342186300	PACS 100-1	Scan map	376	October 2009
	1342186301	PACS 100-2	Scan map	376	October 2009
	1342186114	SPIRE	Large map	2579	October 2009
NGC 2366	1342220565	PACS 70-1	Scan map	1141	May 2011
	1342220566	PACS 70-2	Scan map	1141	May 2011
	1342220567	PACS 100-1	Scan map	1141	May 2011
	1342220568	PACS 100-2	Scan map	1141	May 2011
	1342193014	SPIRE	Large map	2047	March 2010
NGC 4214	1342211803	PACS 70-1	Scan map	2792	December 2010
	1342211804	PACS 70-2	Scan map	2792	December 2010
	1342211805	PACS 100-1	Scan map	2792	December 2010
	1342211806	PACS 100-2	Scan map	2792	December 2010
	1342199342	SPIRE	Large map	1661	June 2010
NGC 4449	1342221125	PACS 70-1	Scan map	3497	May 2011
	1342221126	PACS 70-2	Scan map	3497	May 2011
	1342221127	PACS 100-1	Scan map	3497	May 2011
	1342221128	PACS 100-2	Scan map	3497	May 2011
	1342198243	SPIRE	Large map	1035	June 2010
NGC 4861	1342211384	PACS 70-1	Scan map	685	December 2010
	1342211385	PACS 70-2	Scan map	685	December 2010
	1342211386	PACS 100-1	Scan map	685	December 2010
	1342211387	PACS 100-2	Scan map	685	December 2010
	1342199340	SPIRE	Large map	639	June 2010
NGC 5253	1342202376	PACS 70-1	Scan map	1141	August 2010
	1342202377	PACS 70-2	Scan map	1141	August 2010
	1342202378	PACS 100-1	Scan map	1141	August 2010
	1342202379	PACS 100-2	Scan map	1141	August 2010
	1342203078	SPIRE	Large map	1035	August 2010
NGC 625	1342213260	PACS 70-1	Scan map	1280	January 2011
	1342213261	PACS 70-2	Scan map	1280	January 2011
	1342213262	PACS 100-1	Scan map	1280	January 2011
	1342213263	PACS 100-2	Scan map	1280	January 2011
	1342195943	SPIRE	Large map	1618	May 2010
NGC 6822	1342186167	PACS 70-1	Scan map	2554	October 2009
	1342186168	PACS 70-2	Scan map	2554	October 2009
	1342186169	PACS 100-1	Scan map	2554	October 2009
	1342186170	PACS 100-2	Scan map	2554	October 2009
	1342185533	SPIRE	Large map	2579	October 2009
Pox 186	1342213618	PACS 70-1	Scan map	276	February 2011
	1342213619	PACS 70-2	Scan map	276	February 2011
	1342213620	PACS 100-1	Scan map	276	February 2011
	1342213621	PACS 100-2	Scan map	276	February 2011
	1342201238	SPIRE	Small map	583	July 2010
SBS 0335-052	1342202302	PACS 70-1	Scan map	276	August 2010
	1342202303	PACS 70-2	Scan map	276	August 2010
	1342202304	PACS 100-1	Scan map	276	August 2010
	1342202305	PACS 100-2	Scan map	276	August 2010
	1342203627	SPIRE	Small map	583	August 2010

Table A.1. DGS *Herschel* Observing Log.

Source	Obs ID	Description	Mapping mode	Duration (sec)	Date of observation
SBS 1159+545	1342209445	PACS 70-1	Scan map	220	November 2010
	1342209446	PACS 70-2	Scan map	220	November 2010
	1342196852	PACS 100-1	Scan map	276	May 2010
	1342196853	PACS 100-2	Scan map	276	May 2010
	1342199348	SPIRE	Small map	583	June 2010
SBS 1211+540	1342197777	PACS 70-1	Scan map	900	June 2010
	1342197778	PACS 70-2	Scan map	900	June 2010
	1342198182	PACS 100-1	Scan map	900	June 2010
	1342199349	PACS 100-2	Scan map	900	June 2010
	1342198181	SPIRE	Small map	583	June 2010
SBS 1249+493	1342199123	PACS 70-1	Scan map	220	June 2010
	1342199124	PACS 70-2	Scan map	220	June 2010
	1342199125	PACS 100-1	Scan map	220	June 2010
	1342199126	PACS 100-2	Scan map	220	June 2010
	1342199351	SPIRE	Small map	583	June 2010
SBS 1415+437	1342210592	PACS 70-1	Scan map	317	November 2010
	1342210593	PACS 70-2	Scan map	317	November 2010
	1342210594	PACS 100-1	Scan map	317	November 2010
	1342210595	PACS 100-2	Scan map	317	November 2010
SBS 1533+574	1342193505	PACS 70-1	Scan map	153	April 2010
	1342193506	PACS 70-2	Scan map	153	April 2010
	1342193066	PACS 100-1	Scan map	153	April 2010
	1342193067	PACS 100-2	Scan map	153	April 2010
	1342203600	SPIRE	Small map	583	April 2010
Tol 0618-402	1342196111	PACS 70-1	Scan map	558	May 2010
	1342196112	PACS 70-2	Scan map	558	May 2010
	1342196113	PACS 100-1	Scan map	558	May 2010
	1342196114	PACS 100-2	Scan map	558	May 2010
Tol 1214-277	1342222748	PACS 70-1	Scan map	671	June 2011
	1342222749	PACS 70-2	Scan map	671	June 2011
	1342222750	PACS 100-1	Scan map	671	June 2011
	1342222751	PACS 100-2	Scan map	671	June 2011
	1342201264	SPIRE	Small map	583	July 2010
UGC 4483	1342196016	PACS 70-1	Scan map	141	May 2010
	1342196017	PACS 70-2	Scan map	141	May 2010
	1342196018	PACS 100-1	Scan map	141	May 2010
	1342196019	PACS 100-2	Scan map	141	May 2010
	1342206192	SPIRE	Small map	583	October 2010
UGCA 20	1342213565	PACS 70-1	Scan map	293	January 2011
	1342213566	PACS 70-2	Scan map	293	January 2011
	1342213567	PACS 100-1	Scan map	300	January 2011
	1342213568	PACS 100-2	Scan map	293	January 2011
UM 133	1342213553	PACS 70-1	Scan map	293	January 2011
	1342213554	PACS 70-2	Scan map	293	January 2011
	1342213555	PACS 100-1	Scan map	293	January 2011
	1342213556	PACS 100-2	Scan map	293	January 2011
	1342201323	SPIRE	Small map	445	July 2010
UM 311	1342213237	PACS 70-1	Scan map	583	January 2011
	1342213238	PACS 70-2	Scan map	583	January 2011
	1342213239	PACS 100-1	Scan map	583	January 2011
	1342213240	PACS 100-2	Scan map	583	January 2011
	1342201321	SPIRE	Large map	658	July 2010
UM 448	1342198595	PACS 70-1	Scan map	71	June 2010
	1342198596	PACS 70-2	Scan map	71	June 2010
	1342199769	SPIRE	Small map	307	July 2010

Table A.1. DGS *Herschel* Observing Log.

Source	Obs ID	Description	Mapping mode	Duration (sec)	Date of observation
UM 461	1342211793	PACS 70-1	Scan map	317	December 2010
	1342211794	PACS 70-2	Scan map	317	December 2010
	1342211795	PACS 100-1	Scan map	317	December 2010
	1342211796	PACS 100-2	Scan map	317	December 2010
	1342200110	SPIRE	Small map	307	July 2010
VII Zw 403	1342195400	PACS 70-1	Scan map	71	April 2010
	1342195401	PACS 70-2	Scan map	71	April 2010
	1342195478	PACS 100-1	Scan map	71	April 2010
	1342195479	PACS 100-2	Scan map	71	April 2010
	1342199363	SPIRE	Small map	583	July 2010

Table A.2. DGS *Spitzer*/IRAC and IRS Observing Log.

	IRAC	**IRS**	
Sources	AOR key	AOR key	Extraction
Haro 11	4326400	9007104	Optimal
Haro 2	5539840	9489920	Map
Haro 3	11180288	12556288	Tapered
He 2-10	4329472	4340480	Tapered
HS 0017+1055	26387200	26393344	Optimal
HS 0052+2536	26387456	17463040	Optimal
HS 0822+3542	4328960	1763808	Optimal
HS 1222+3741	17564928	26393600	Optimal
HS 1236+3937	26387712	26393856	Optimal
HS 1304+3529	26387968	26394112	Optimal
HS 1319+3224	26388480	26394624	Optimal
HS 1330+3651	26388736	26394880	Optimal
HS 1442+4250	10388480	12562944	Optimal
HS 2352+2733[a]	26388992	26395136	-
I Zw 18	4330752	16205568	Optimal
IC 10	4424960	26396672	Map
II Zw 40	4327936	9007616	Optimal
Mrk 1089	11250432	26395392	Tapered
Mrk 1450	4334336	16206080 (SL), 9011712 (LL)	Optimal
Mrk 153	4333056	4342272	Optimal
Mrk 209	22556672	12557568	Optimal
Mrk 930	4338944	4344320	Tapered
NGC 1140	4327168	4830976	Tapered
NGC 1569	4434944	3856640	Tapered
NGC 1705	5535744	9513216	Map
NGC 2366	4436480	21920768	Map
NGC 4214[b]	4457984	-	-
NGC 4449	4467456	26396928	Map
NGC 4861[c]	4337408	-	-
NGC 5253	4386048	4386304	Map
NGC 625[c]	22520064	-	-
NGC 6822[b,c]	5507072	-	-
Pox 186	26389248	12629760	Optimal
SBS 0335-052	4327424	8986880	Optimal
SBS 1159+545	26389504	9008896	Optimal
SBS 1211+540	26389760	26395392	Optimal
SBS 1249+493	26390016	26395904	Optimal
SBS 1415+437	10392832	12562432 (SL), 8990464 (LL)	Optimal
SBS 1533+574	17563904	8996352	Optimal
Tol 0618-402	4328448	8090624	Optimal
Tol 1214-277	4336384	9008128	Optimal
UGC 4483	4329728	26396160	Optimal
UGCA 20[a]	26390272	26396416	-
UM 133	26390528	21922304	Map
UM 311[b]	10392576	-	-
UM 448	4334592	4342784	Tapered
UM 461	4335104	16204032 (SL), 9006336 (LL)	Optimal
VII Zw 403	4334080	9005824	Tapered

Notes :
[a] : For these galaxies, the IRS slits are not centered on the source position and thus we do not present any IRS spectrum.
[b] : For these galaxies, only local pointings have been done and we cannot present an IRS spectrum for the total galaxy.
[c] : Only high resolution IRS spectrum (SH and/or LH) is available.

Appendix B

The DGS galaxies

Haro 11

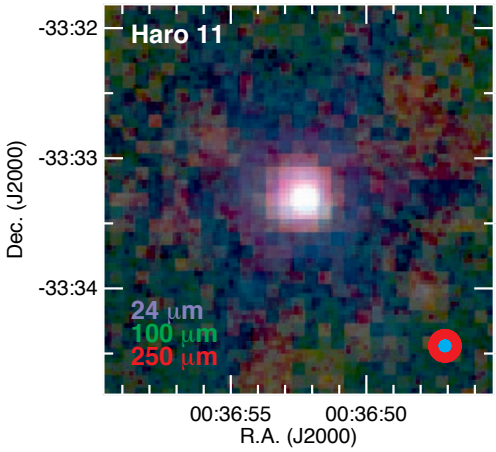

RA : 00h36m52.7s DEC : −33d33m17s

D = 92.1 Mpc 12+log(O/H) = 8.36

Morph Type : HIIgalaxy

Other names : ESO350, IG038

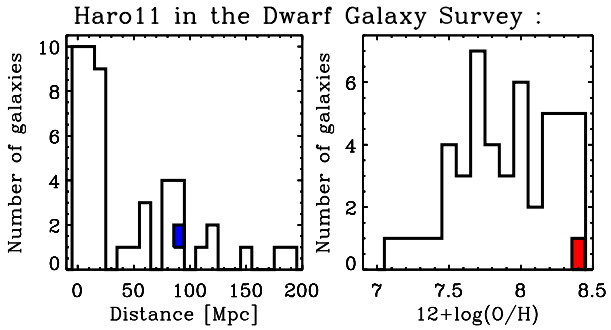

Haro 2

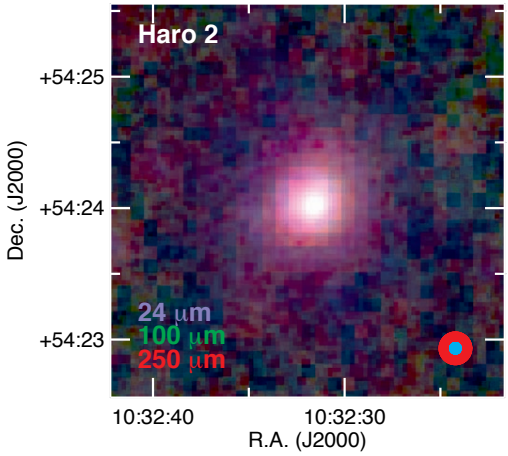

RA : 10h32m32.0s DEC : 54d24m02s

D = 21.7 Mpc 12+log(O/H) = 8.23

Morph Type : Im−pec, WR, HIIgalaxy

Other names : Mrk33, SBS1029+546, UGC05720

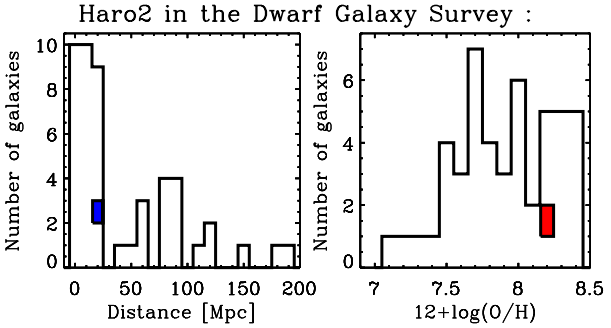

Haro 3

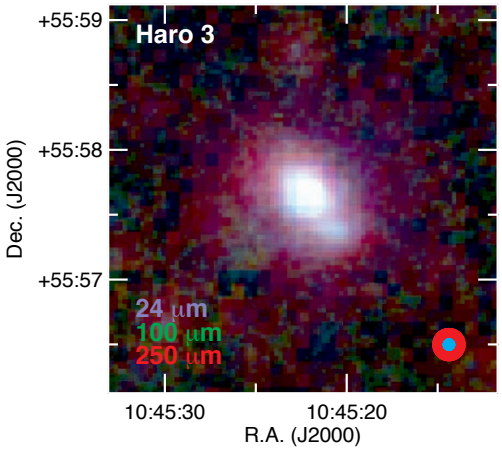

RA : 10h45m22.4s DEC : 57d57m37s

D = 19.3 Mpc 12+log(O/H) = 8.28

Morph Type : BCD, HIIgalaxy

Other names : Mrk35, NGC3353, SBS1042+562, UGC05860

Haro3 in the Dwarf Galaxy Survey :

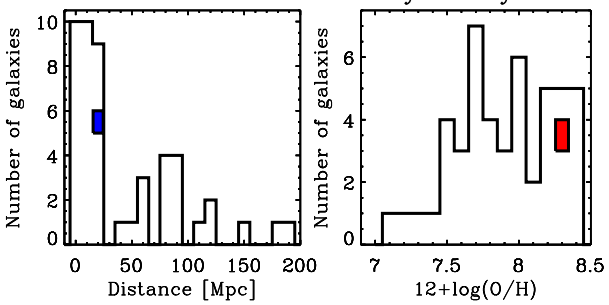

He 2-10

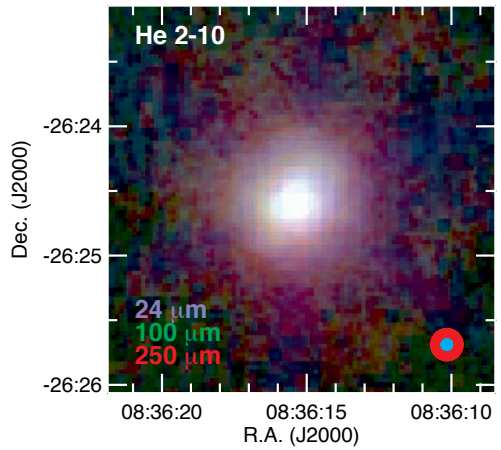

RA : 08h36m15.1s DEC : −26d24m34s

D = 8.7 Mpc 12+log(O/H) = 8.43

Morph Type : I0−pec, starburst

Other names : N/A

He2−10 in the Dwarf Galaxy Survey :

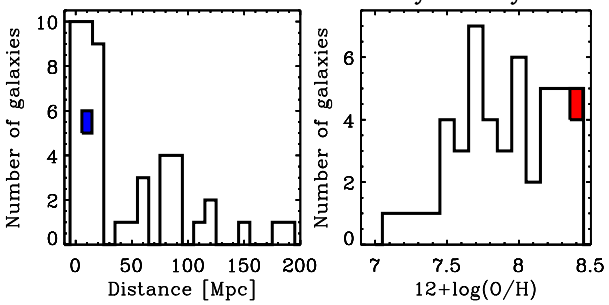

HS 0017+1055

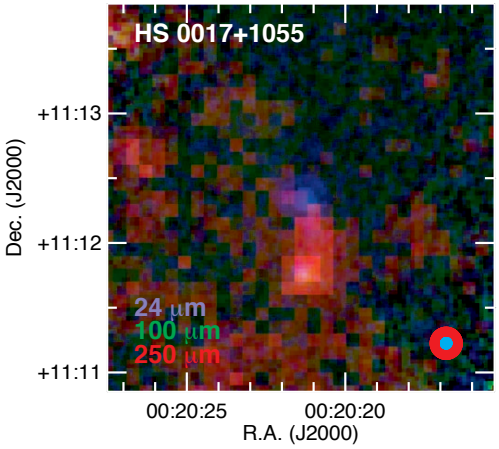

RA : 00h20m21.4s DEC : 11d12m21s

D = 79.1 Mpc 12+log(O/H) = 7.63

Morph Type : BCG

Other names : N/A

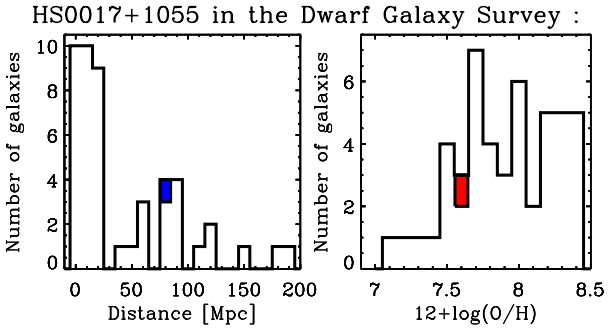

HS 0052+2536

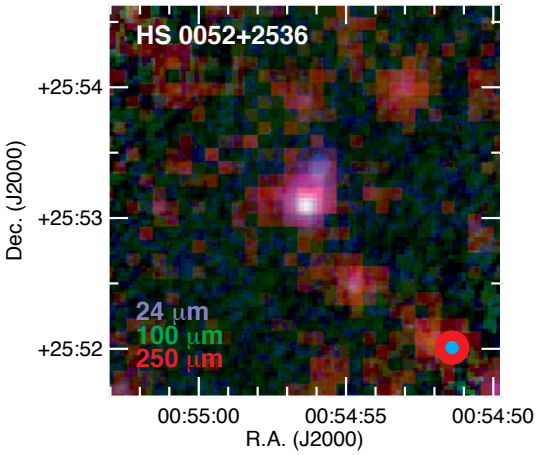

RA : 00h54m56.4s DEC : 25d53m08s

D = 191.0 Mpc 12+log(O/H) = 8.04

Morph Type : N/A

Other names : N/A

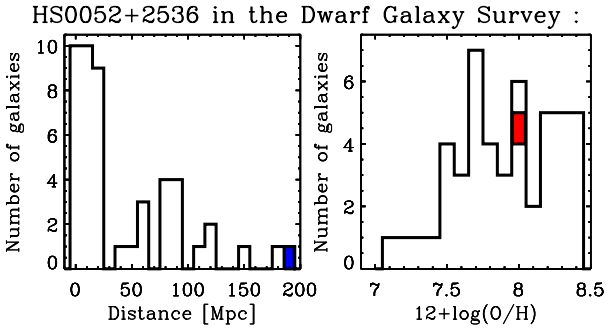

HS 0822+3542

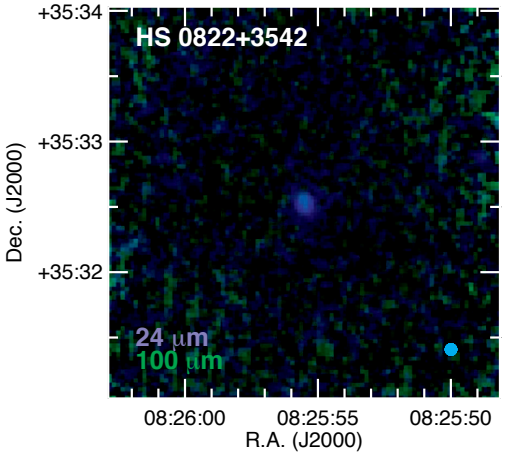

RA : 08h25m55.5s DEC : 35d32m32s

D = 11.0 Mpc 12+log(O/H) = 7.32

Morph Type : BCG, iL,C, BCD

Other names : SDSSJ0825+3542

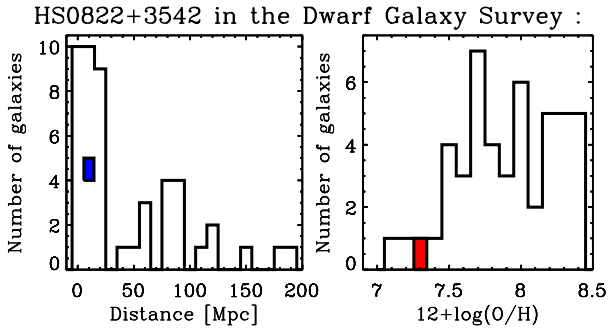

HS 1222+3741

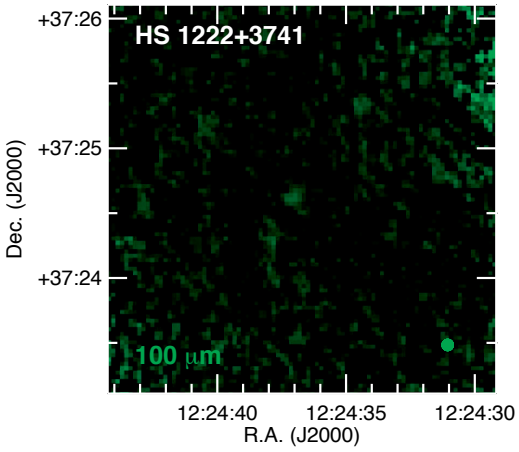

RA : 12h24m36.7s DEC : 37d24m37s

D = 181.7 Mpc 12+log(O/H) = 7.79

Morph Type : Im, BCD

Other names : SDSSJ122436.71+372436.5

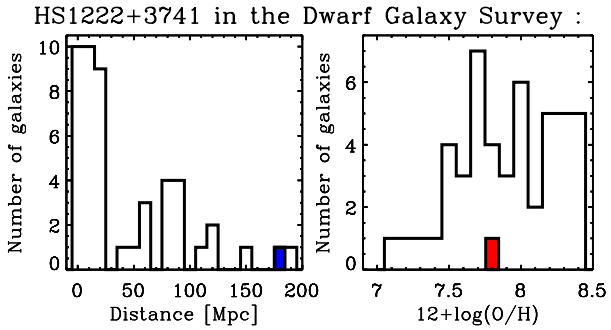

HS 1236+3937

RA : 12h39m20.2s DEC : 39d21m05s

D = 86.3 Mpc 12+log(O/H) = 7.72

Morph Type : HIIgalaxy

Other names : SDSSJ123920.18+392104.5

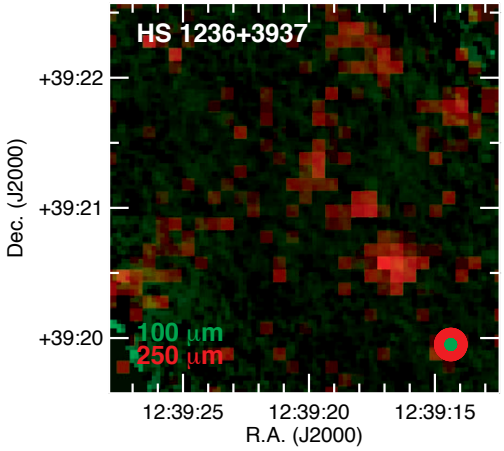

HS1236+3937 in the Dwarf Galaxy Survey :

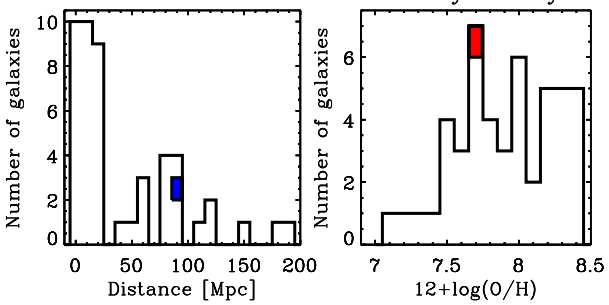

HS 1304+3529

RA : 13h06m24.2s DEC : 35d13m43s

D = 78.7 Mpc 12+log(O/H) = 7.93

Morph Type : N/A

Other names : SDSSJ130624.19+351343.0

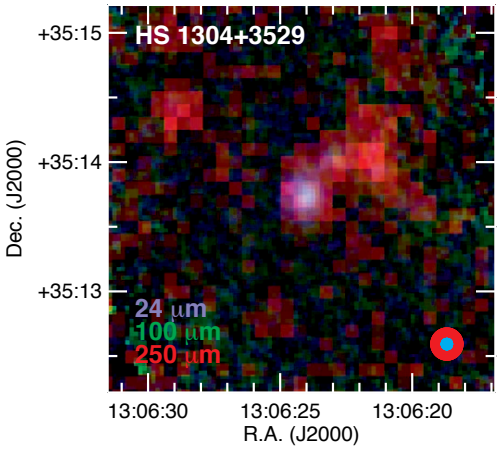

HS1304+3529 in the Dwarf Galaxy Survey :

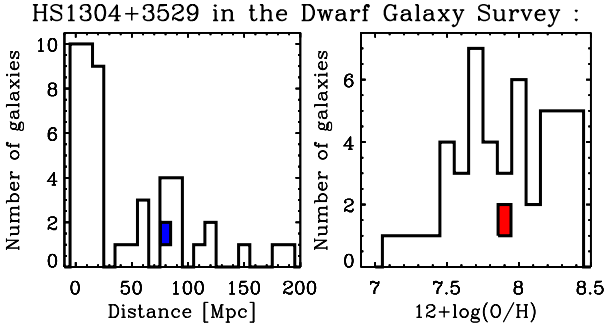

HS 1319+3224

RA : 13h21m19.7s DEC : 32d08m25s

D = 86.3 Mpc 12+log(O/H) = 7.81

Morph Type : HIIgalaxy

Other names : SDSSJ132119.70+320825.1

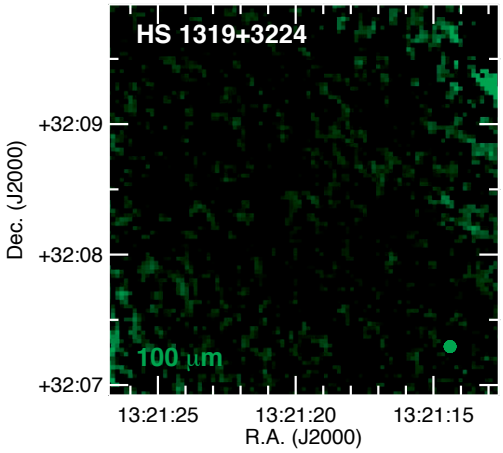

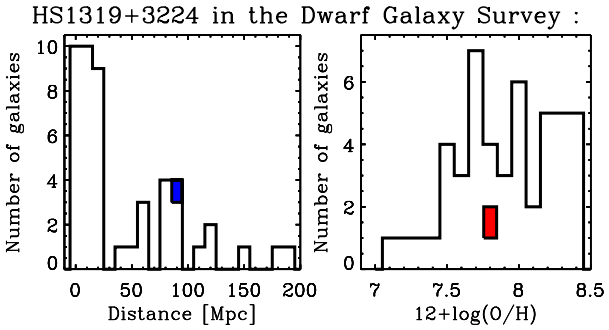

HS 1330+3651

RA : 13h33m08.3s DEC : 36d36m33s

D = 79.7 Mpc 12+log(O/H) = 7.98

Morph Type : HIIgalaxy

Other names : N/A

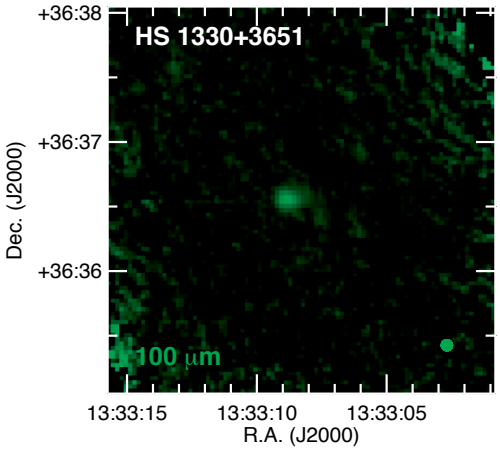

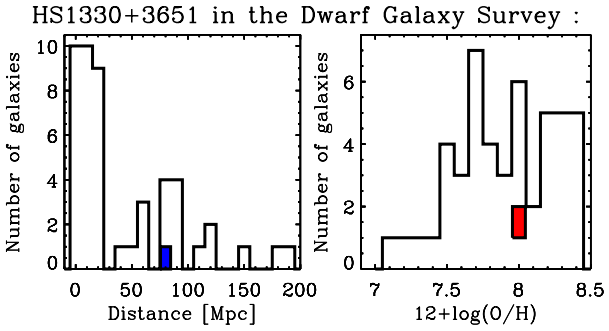

HS 1442+4250

RA : 14h44m12.8s DEC : 42d37m44s

D = 14.4 Mpc 12+log(O/H) = 7.60

Morph Type : Pec, BCG

Other names : UGC09497

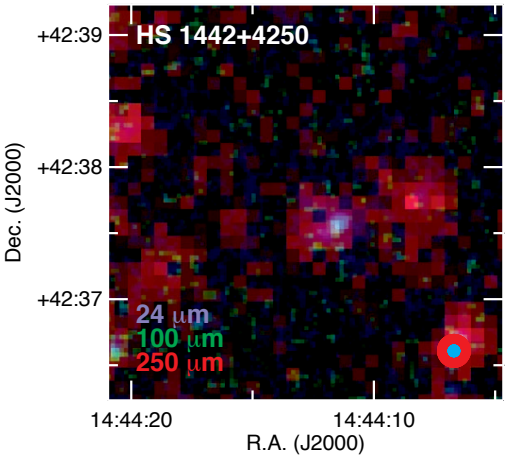

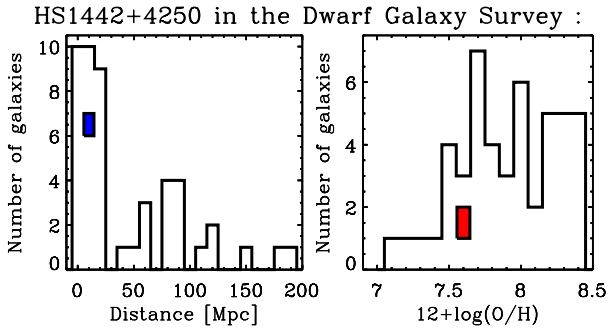

HS 2352+2733

RA : 23h54m56.7s DEC : 27d49m59s

D = 116.7 Mpc 12+log(O/H) = 8.40

Morph Type : N/A

Other names : N/A

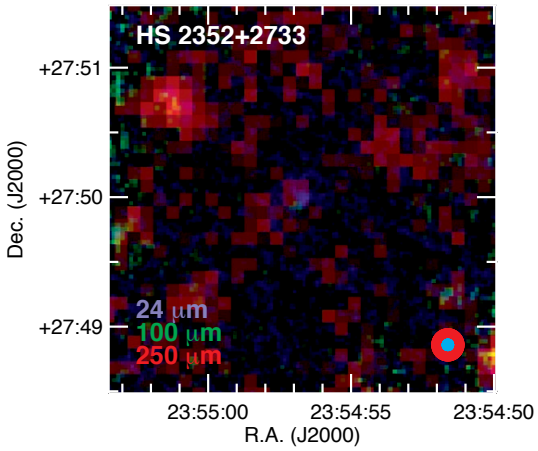

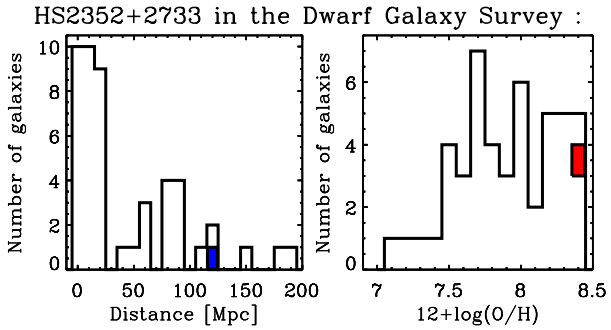

I Zw 18

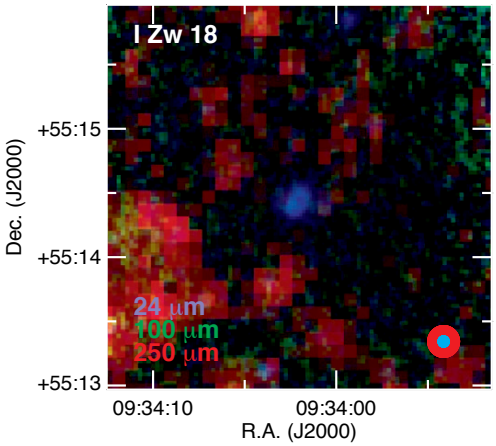

RA : 09h34m02.0s DEC : 55d14m28s

D = 18.2 Mpc 12+log(O/H) = 7.14

Morph Type : cI, BCG

Other names : HS0930+5527, Mrk116, SBS0930+554, UGC

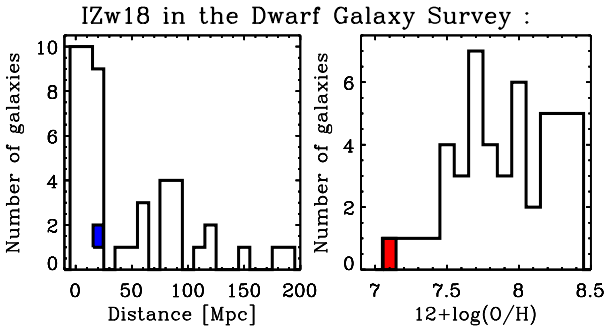

II Zw 40

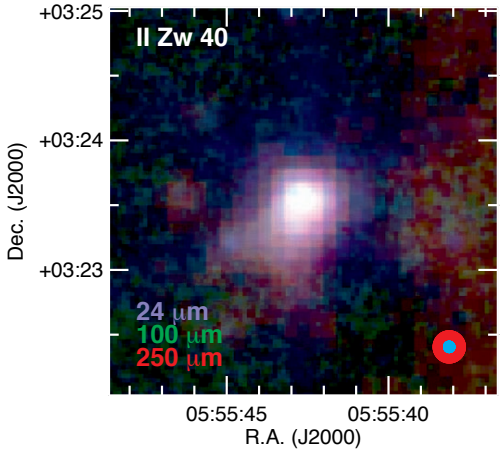

RA : 05h55m42.6s DEC : 3d23m32s

D = 12.1 Mpc 12+log(O/H) = 8.23

Morph Type : BCD, SBc, merger, HIIgalaxy

Other names : UGCA116

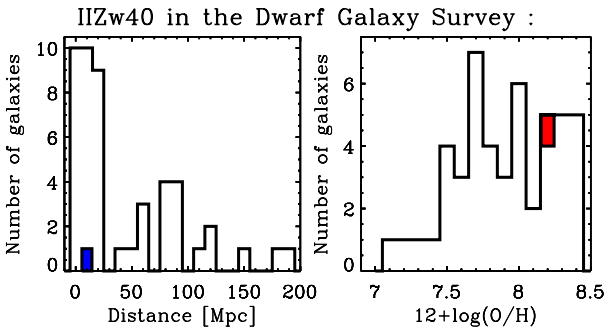

IC 10

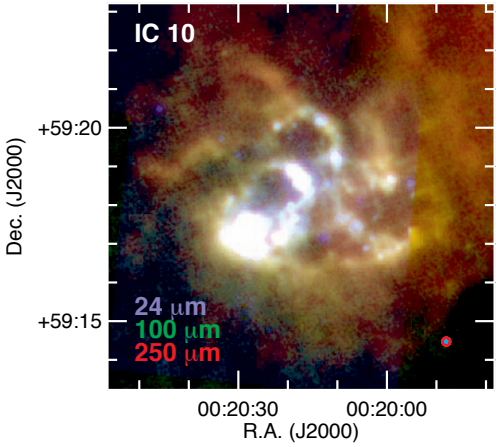

RA : 00h20m17.3s DEC : 59d18m14s

D = 0.7 Mpc 12+log(O/H) = 8.17

Morph Type : Ibm, dIrr, BCD

Other names : UGC00192

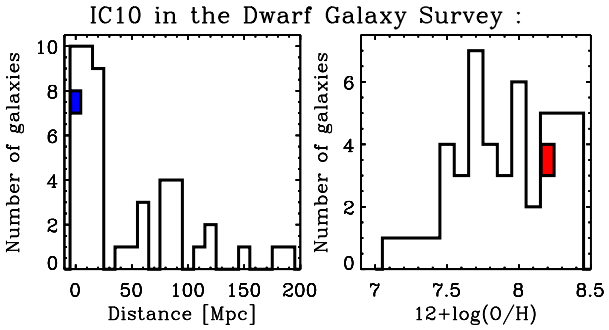

Mrk 1089

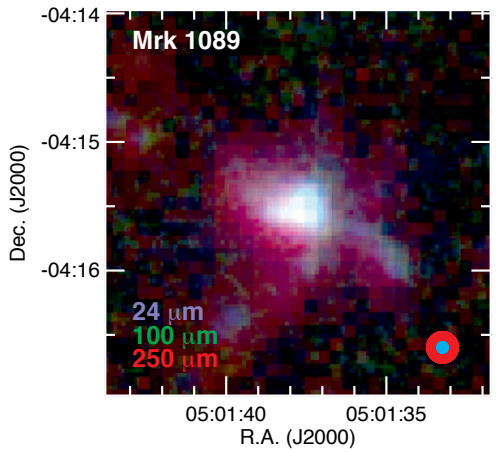

RA : 05h01m37.7s DEC : −4d15m28s

D = 56.6 Mpc 12+log(O/H) = 8.10

Morph Type : SB(s)m−pec, merger, HIIgalaxy

Other names : HCG31C, NGC1741

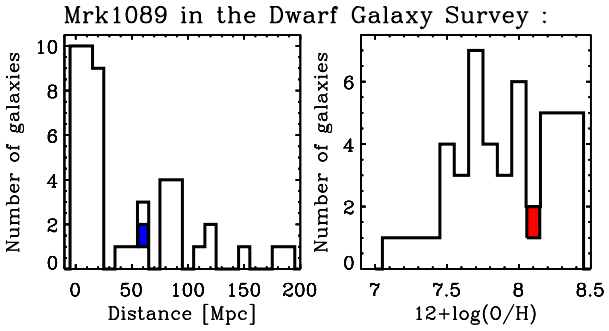

Mrk 1450

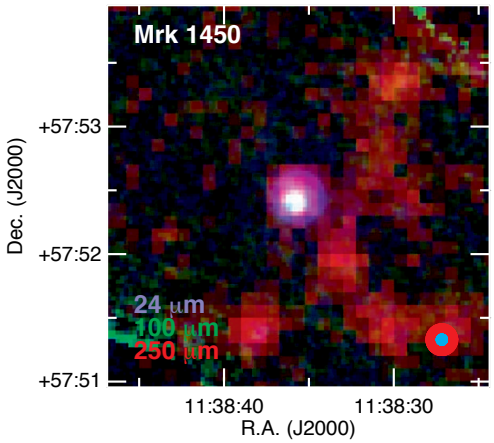

RA : 11h38m35.7s DEC : 57d52m27s

D = 19.8 Mpc 12+log(O/H) = 7.84

Morph Type : HIIgalaxy, WR, BCD, starburst

Other names : SBS1135+581, VIIZw415

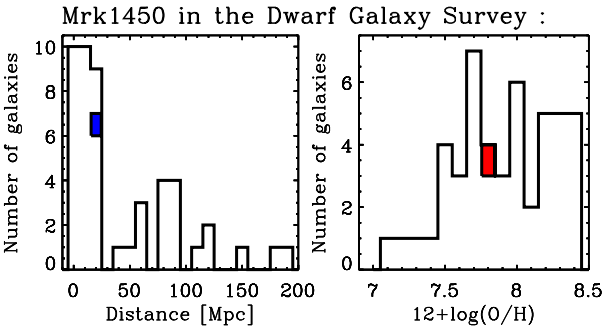

Mrk 153

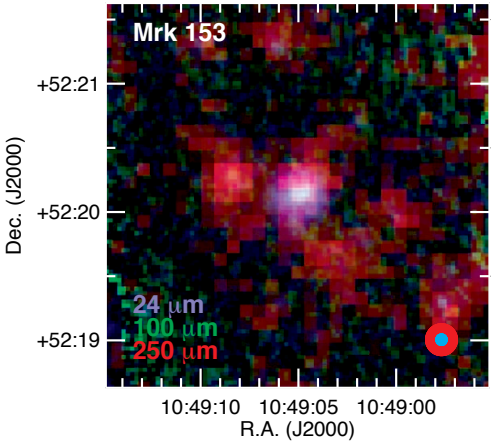

RA : 10h49m05.0s DEC : 52d20m08s

D = 40.3 Mpc 12+log(O/H) = 7.86

Morph Type : Scp

Other names : SBS1046+526, UGCA219

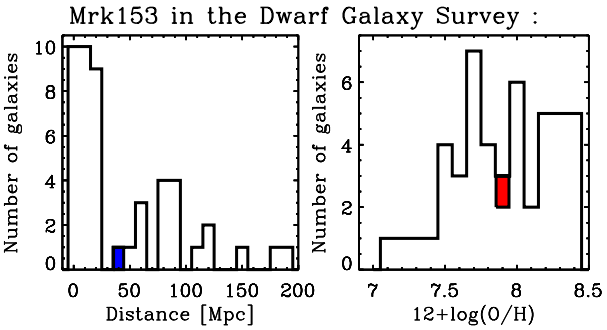

Mrk 209

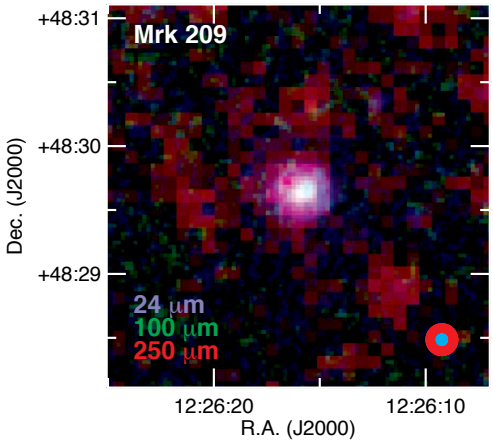

RA : 12h26m15.9s DEC : 48d29m37s

D = 5.8 Mpc 12+log(O/H) = 7.74

Morph Type : Sm−pec, BCDG, WR, HIIgalaxy

Other names : Haro29,

Mrk209 in the Dwarf Galaxy Survey :

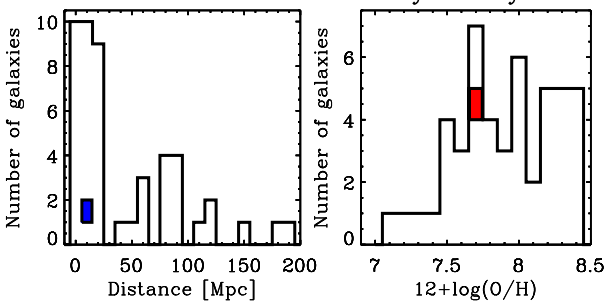

Mrk 930

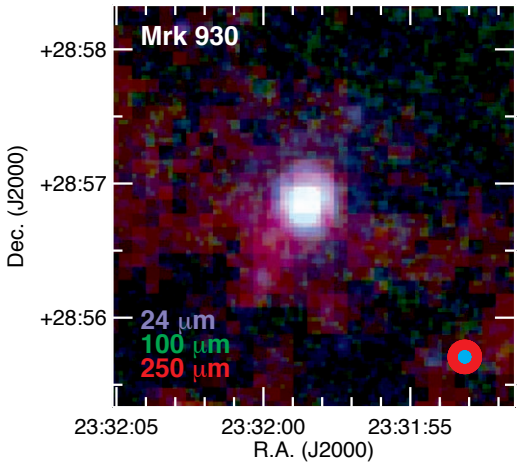

RA : 23h31m58.3s DEC : 28d56m50s

D = 77.8 Mpc 12+log(O/H) = 8.03

Morph Type : HIIgalaxy, merger,

Other names : N/A

Mrk930 in the Dwarf Galaxy Survey :

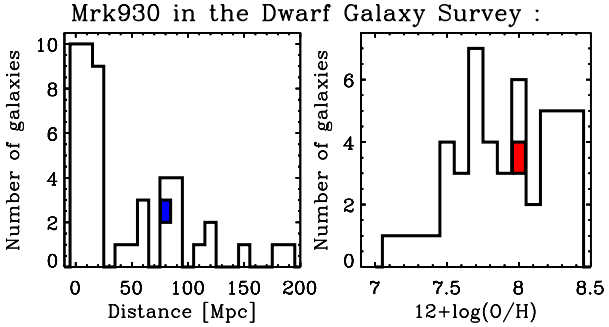

NGC 1140

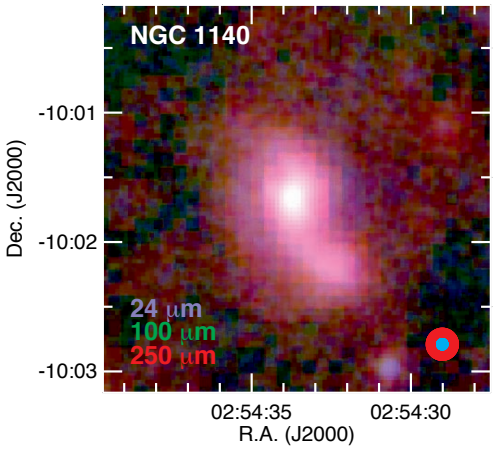

RA : 02h54m33.6s DEC : −10d01m40s

D = 20.0 Mpc 12+log(O/H) = 8.38

Morph Type : Ibm−pec, HIIgalaxy, Sy2

Other names : Mrk1083

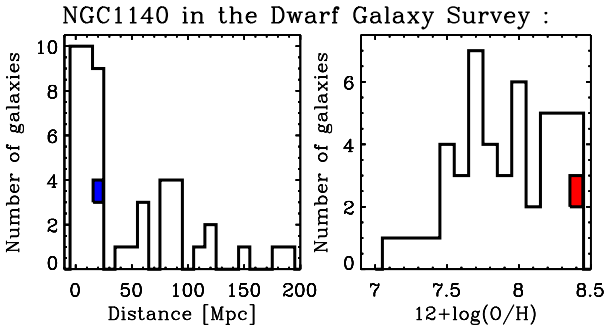

NGC 1569

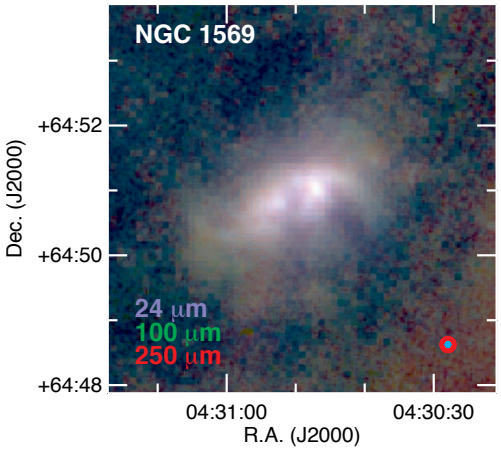

RA : 04h30m49.0s DEC : 64d50m53s

D = 3.1 Mpc 12+log(O/H) = 8.02

Morph Type : Ibm, starburst, Sy1

Other names : UGC03056, VIIZw016

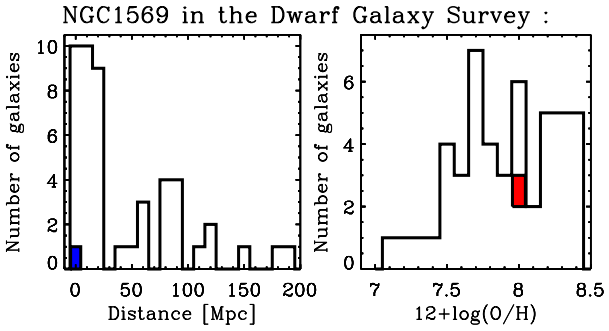

NGC 1705

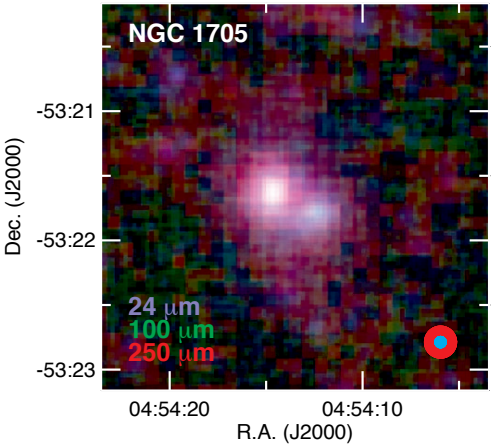

RA : 04h54m13.5s DEC : −53d21m40s

D = 5.1 Mpc 12+log(O/H) = 8.27

Morph Type : SA0−pec, HIIgalaxy, BCDG

Other names : ESO158, G013

NGC1705 in the Dwarf Galaxy Survey :

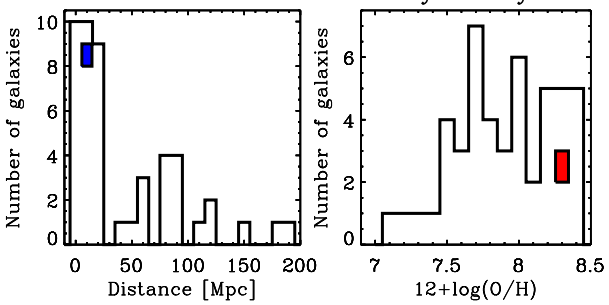

NGC 2366

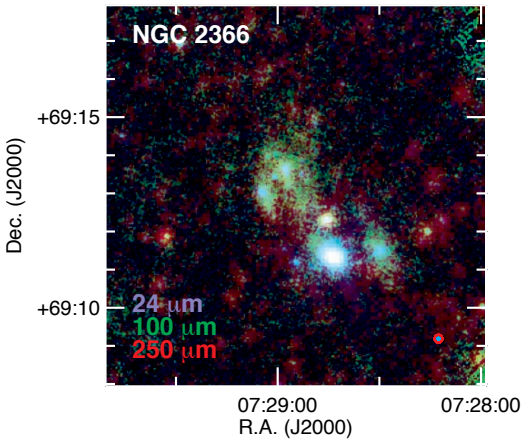

RA : 07h28m54.6s DEC : 69d12m57s

D = 3.2 Mpc 12+log(O/H) = 7.70

Morph Type : IB(s)m

Other names : DDO42, UGC03851

NGC2366 in the Dwarf Galaxy Survey :

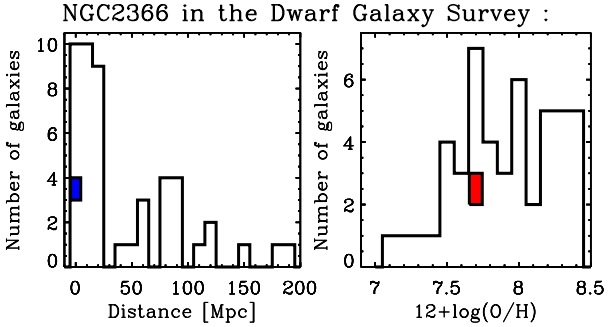

NGC 4214

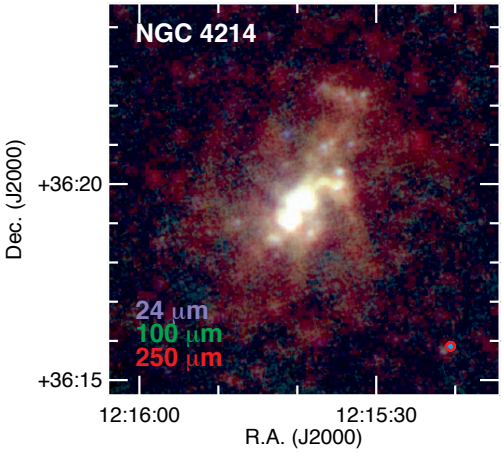

RA : 12h15m39.2s DEC : 36d19m37s

D = 2.9 Mpc 12+log(O/H) = 8.26

Morph Type : IAB(s)m, HIIgalaxy

Other names : NGC4228, UGC07278

NGC4214 in the Dwarf Galaxy Survey :

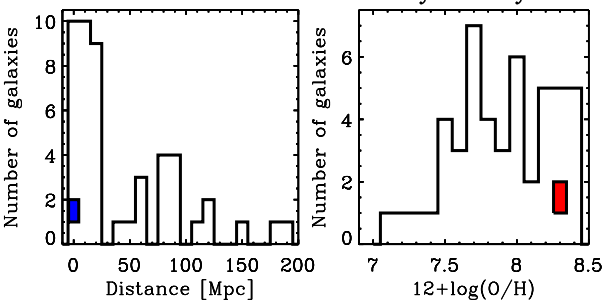

NGC 4449

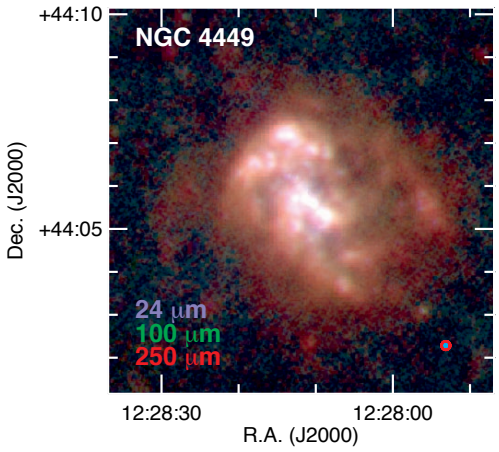

RA : 12h28m11.1s DEC : 44d05m37s

D = 4.2 Mpc 12+log(O/H) = 8.20

Morph Type : Ibm, HIIgalaxy, starburst

Other names : UGC07592

NGC4449 in the Dwarf Galaxy Survey :

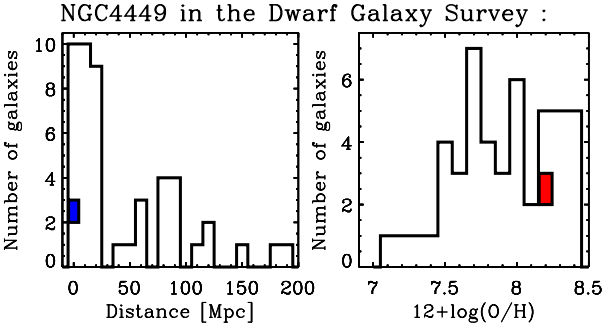

NGC 4861

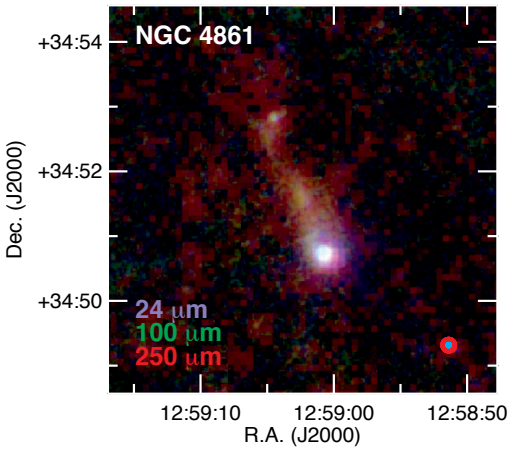

RA : 12h59m02.3s DEC : 34d51m34s

D = 7.5 Mpc 12+log(O/H) = 7.89

Morph Type : SB(s)m, HIIgalaxy, starburst

Other names : IC3961, IZw049, UGC08098

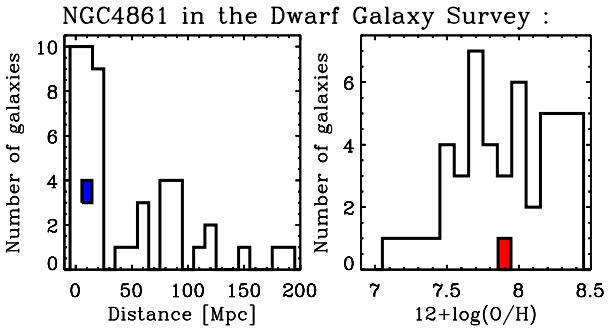

NGC 5253

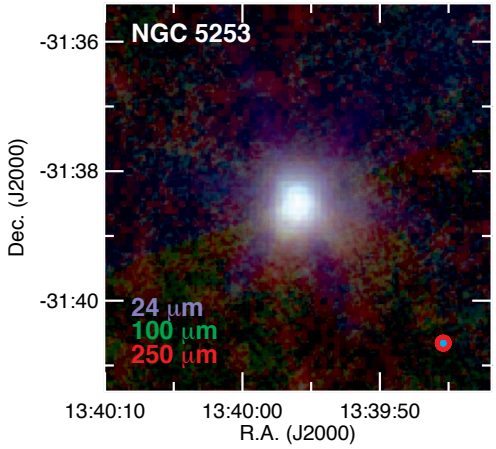

RA : 13h39m55.9s DEC : −31d38m24s

D = 4.0 Mpc 12+log(O/H) = 8.25

Morph Type : Im−pec, HIIgalaxy, starburst

Other names : ESO445, G004, Haro10, UGCA369

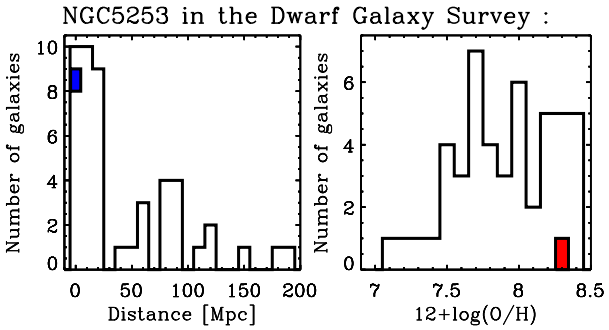

NGC 625

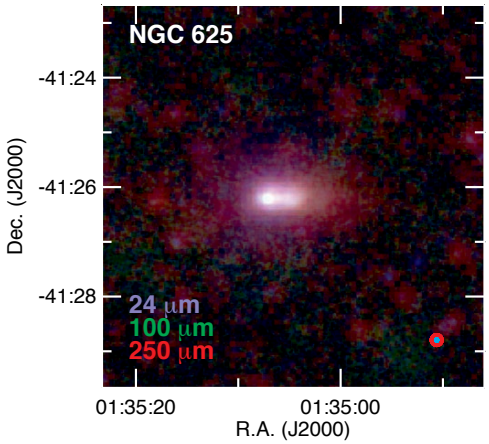

RA : 01h35m04.6s DEC : −41d26m10s

D = 3.9 Mpc 12+log(O/H) = 8.22

Morph Type : SB(s)m−sp, HIIgalaxy

Other names : ESO297, G005

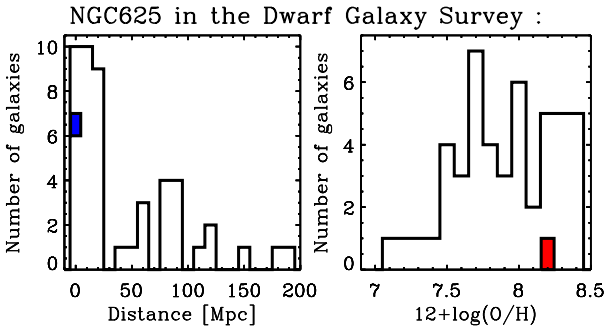

NGC 6822

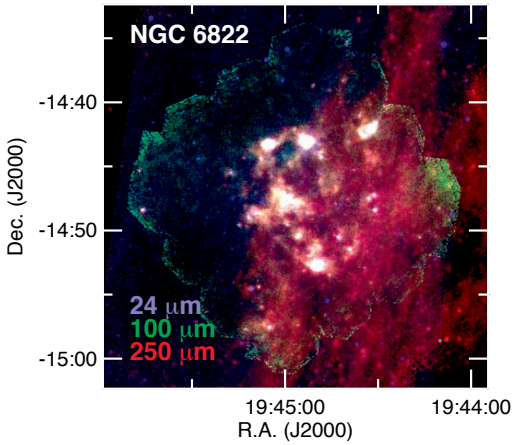

RA : 19h44m57.7s DEC : −14d48m12s

D = 0.5 Mpc 12+log(O/H) = 7.96

Morph Type : IB(s)m

Other names : DDO209, IC4895

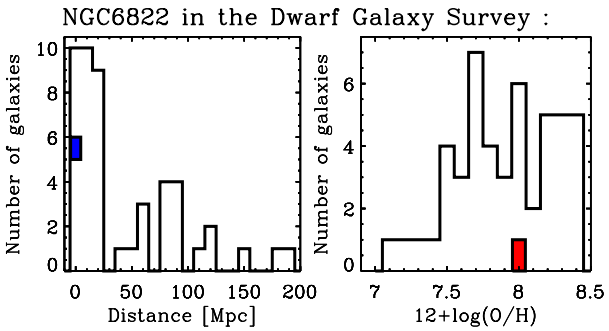

Pox 186

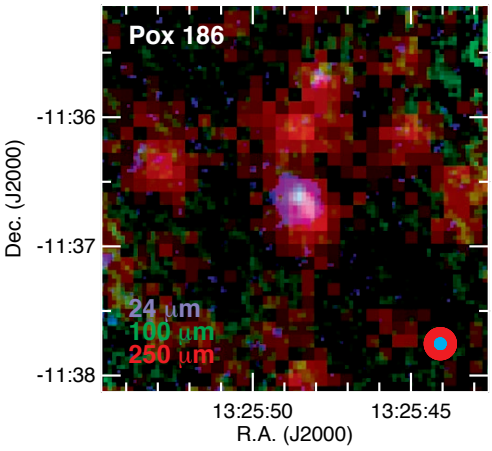

RA : 13h25m48.6s DEC : −11d36m38s

D = 18.3 Mpc 12+log(O/H) = 7.70

Morph Type : EmLineGalaxy

Other names : N/A

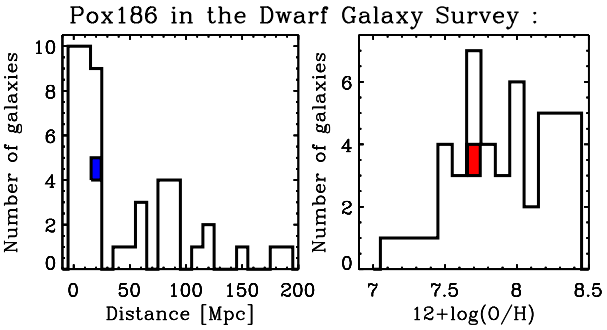

SBS 0335-052

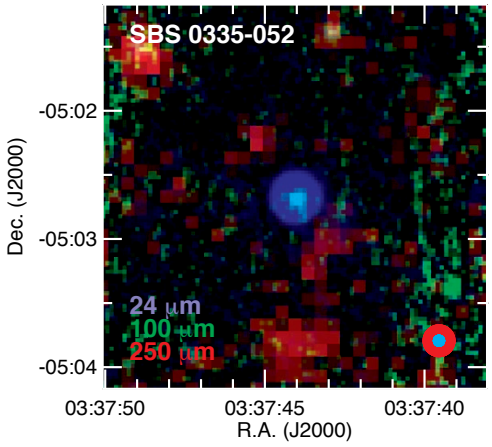

RA : 03h37m44.0s DEC : −5d02m40s

D = 56.0 Mpc 12+log(O/H) = 7.25

Morph Type : BCDG, HIIgalaxy, starburst

Other names : N/A

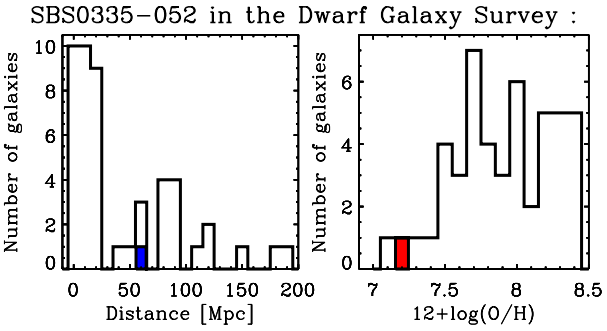

SBS 1159+545

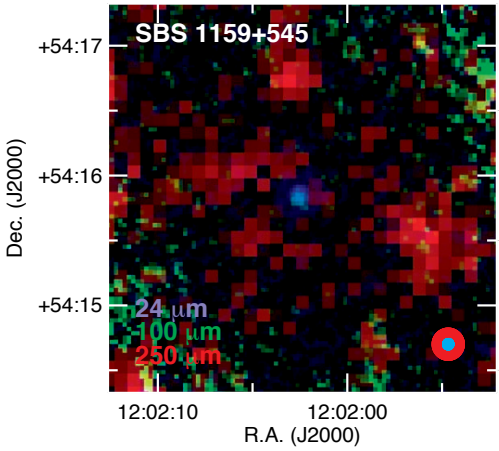

RA : 12h02m02.4s DEC : 54d15m50s

D = 57.0 Mpc 12+log(O/H) = 7.44

Morph Type : BCG

Other names : N/A

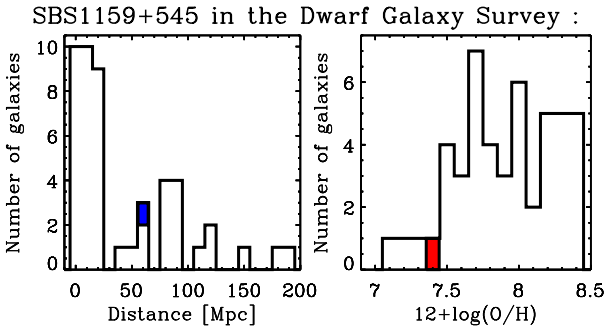

SBS 1211+540

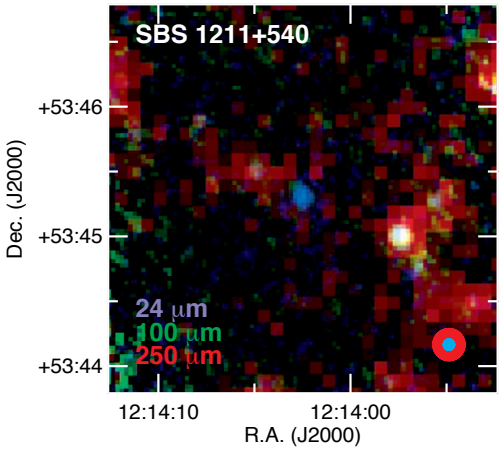

RA : 12h14m02.5s DEC : 53d45m17s

D = 19.3 Mpc 12+log(O/H) = 7.58

Morph Type : BCD, starburst

Other names : N/A

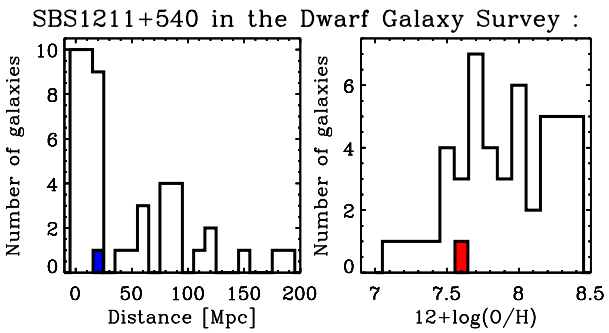

SBS 1249+493

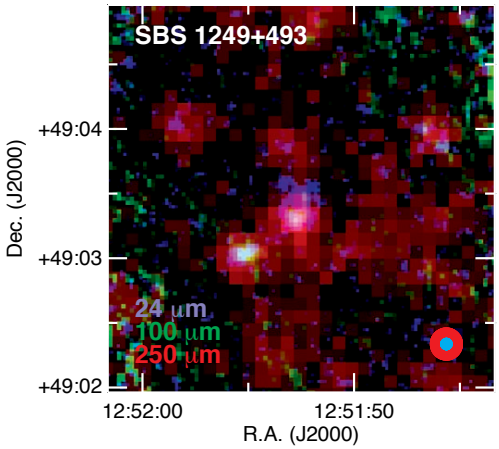

RA : 12h51m52.5s DEC : 49d03m28s

D = 110.8 Mpc 12+log(O/H) = 7.68

Morph Type : BCG

Other names : HS1249+4919

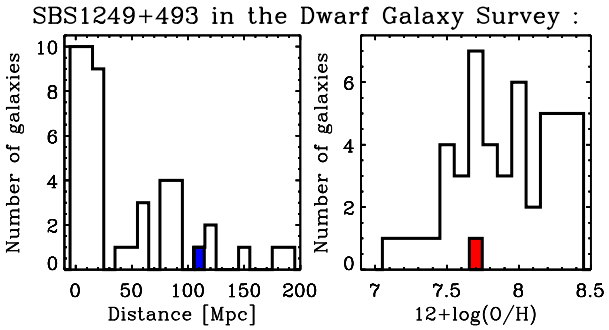

SBS 1415+437

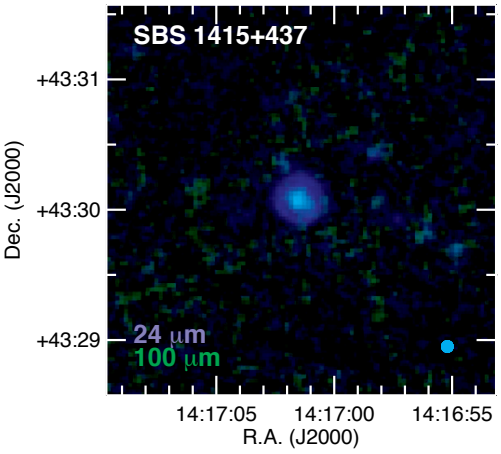

RA : 14h17m01.4s DEC : −43d30m05s

D = 13.6 Mpc 12+log(O/H) = 7.55

Morph Type : BCG, HIIgalaxy

Other names : N/A

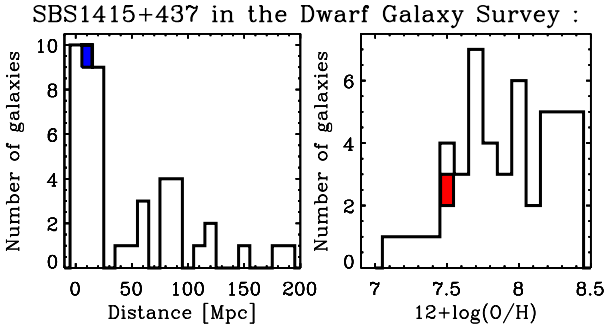

SBS 1533+574

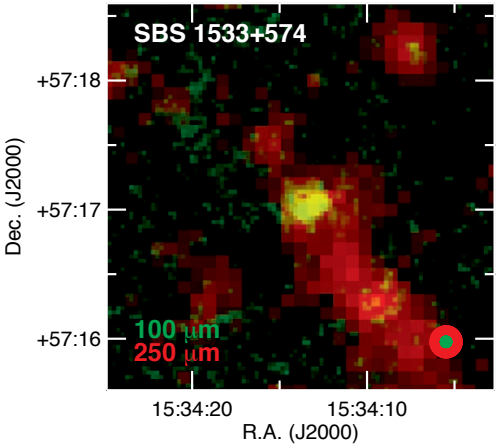

RA : 15h34m13.8s DEC : 57d17m06s

D = 54.2 Mpc 12+log(O/H) = 8.05

Morph Type : BCG

Other names : NGC5965, VIIZw611

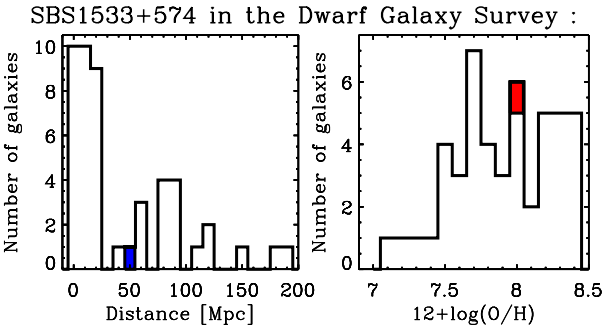

Tol 0618-402

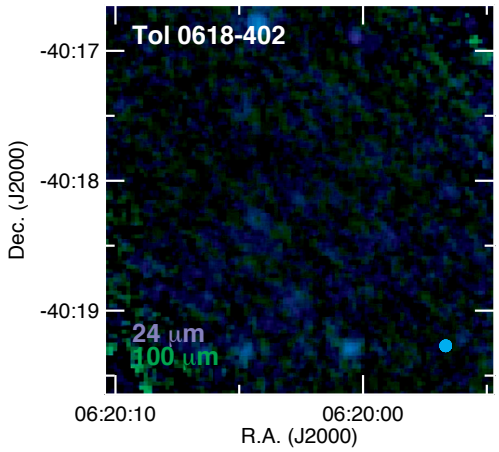

RA : 06h20m02.5s DEC : −40d18m09s

D = 150.8 Mpc 12+log(O/H) = 8.09

Morph Type : BCG

Other names : N/A

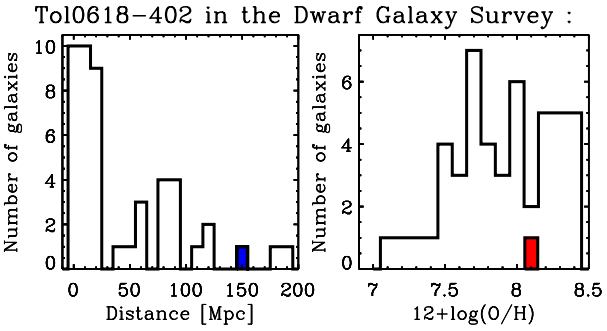

Tol 1214-277

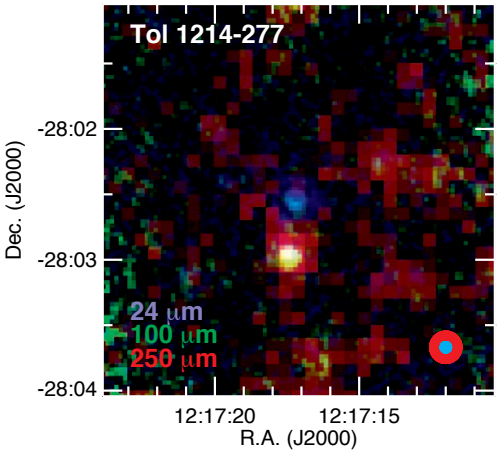

RA : 12h17m17.1s DEC : −28d02m33s

D = 120.5 Mpc 12+log(O/H) = 7.52

Morph Type : BCG, HIIgalaxy

Other names : Tol00021

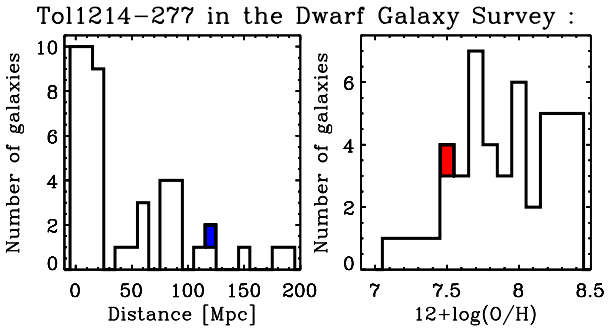

UGC 4483

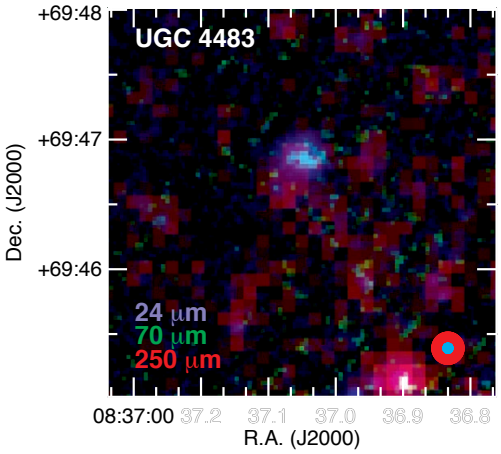

RA : 08h37m03.0s DEC : 69d46m31s

D = 3.2 Mpc 12+log(O/H) = 7.46

Morph Type : BCG, HIIgalaxy

Other names : N/A

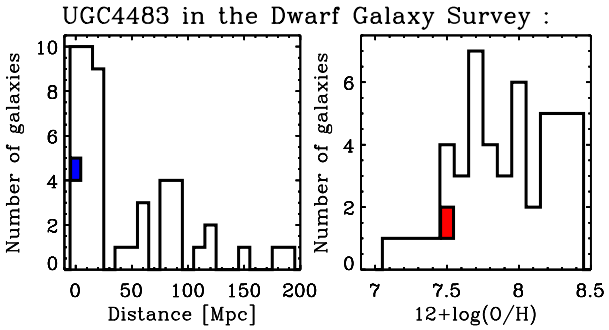

UGCA 20

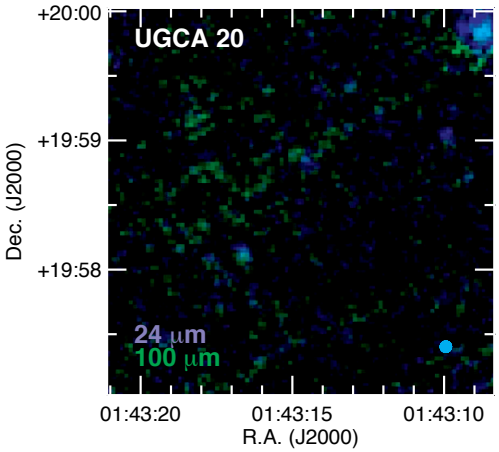

RA : 01h43m14.7s DEC : 19d58m32s

D = 11.0 Mpc 12+log(O/H) = 7.50

Morph Type : Im

Other names : HS0140+1943

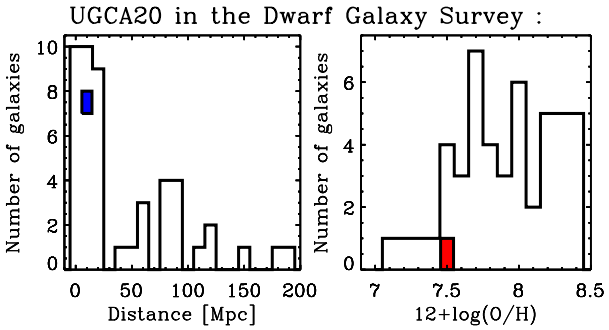

UM 133

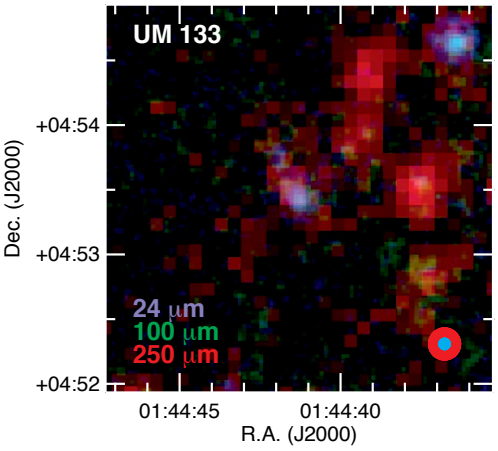

RA : 01h44m41.3s DEC : 4d53m26s

D = 22.7 Mpc 12+log(O/H) = 7.82

Morph Type : HIIgalaxy

Other names : N/A

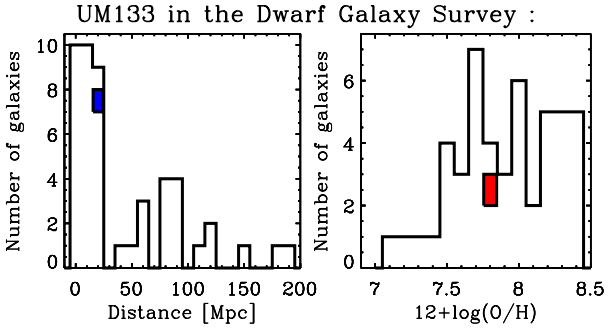

UM 311

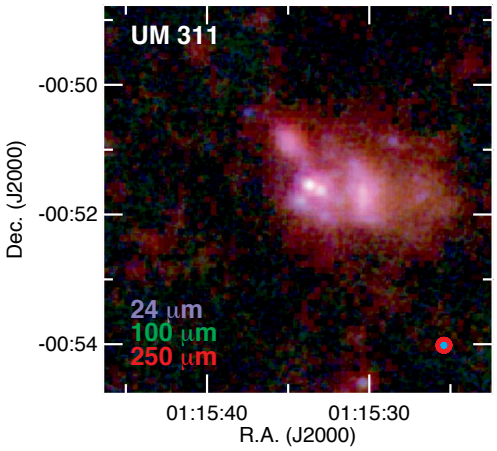

RA : 01h15m34.4s DEC : 0d51m46s

D = 23.5 Mpc 12+log(O/H) = 8.36

Morph Type : HIIgalaxy, WR

Other names : N/A

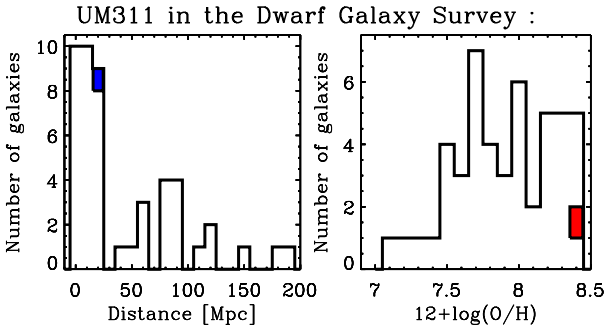

UM 448

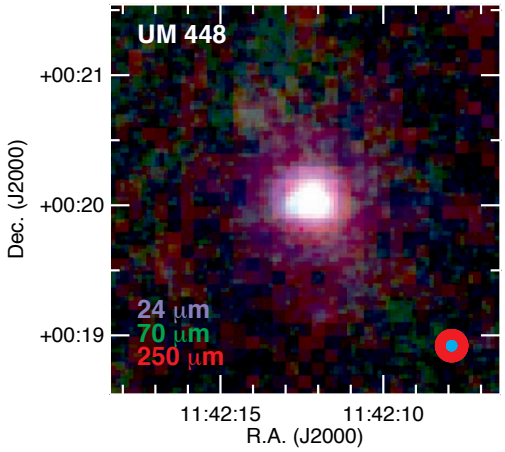

RA : 11h42m12.4s DEC : 0d20m03s

D = 87.8 Mpc 12+log(O/H) = 8.32

Morph Type : Sbpec, WR, HIIgalaxy, starburst

Other names : Mrk1304, UGC06665

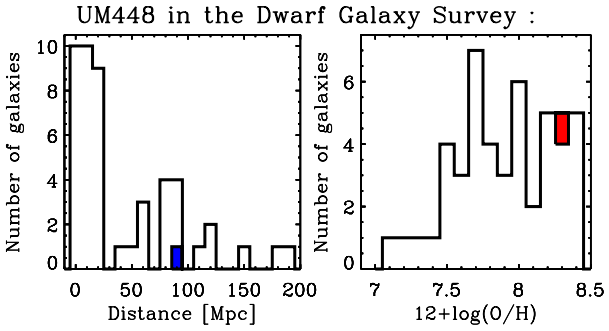

UM 461

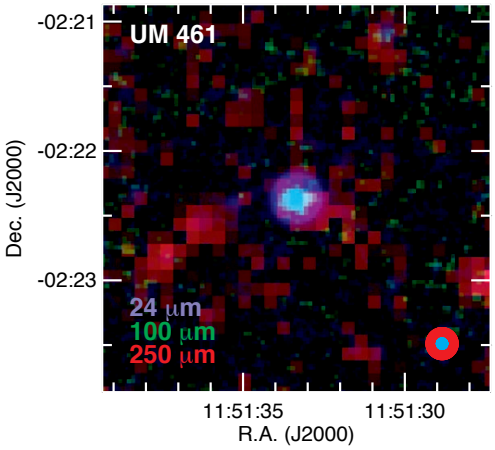

RA : 11h51m33.3s DEC : −2d22m22s

D = 13.2 Mpc 12+log(O/H) = 7.73

Morph Type : BCD

Other names : N/A

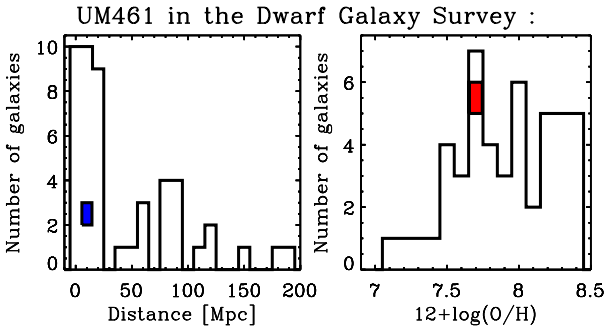

VII Zw 403

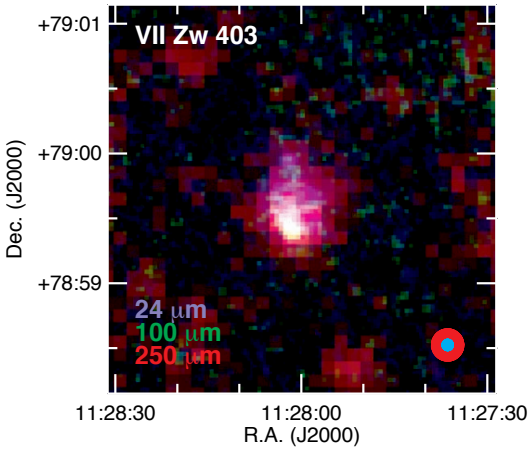

RA : 11h27m59.9s DEC : 78d59m39s

D = 4.5 Mpc 12+log(O/H) = 7.66

Morph Type : pec, HIIgalaxy

Other names : UGC06456

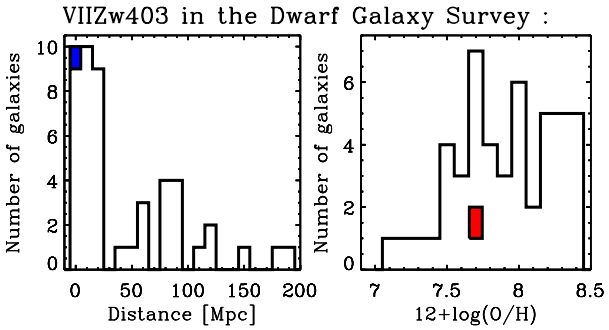

Appendix C

IRS data for the DGS galaxies

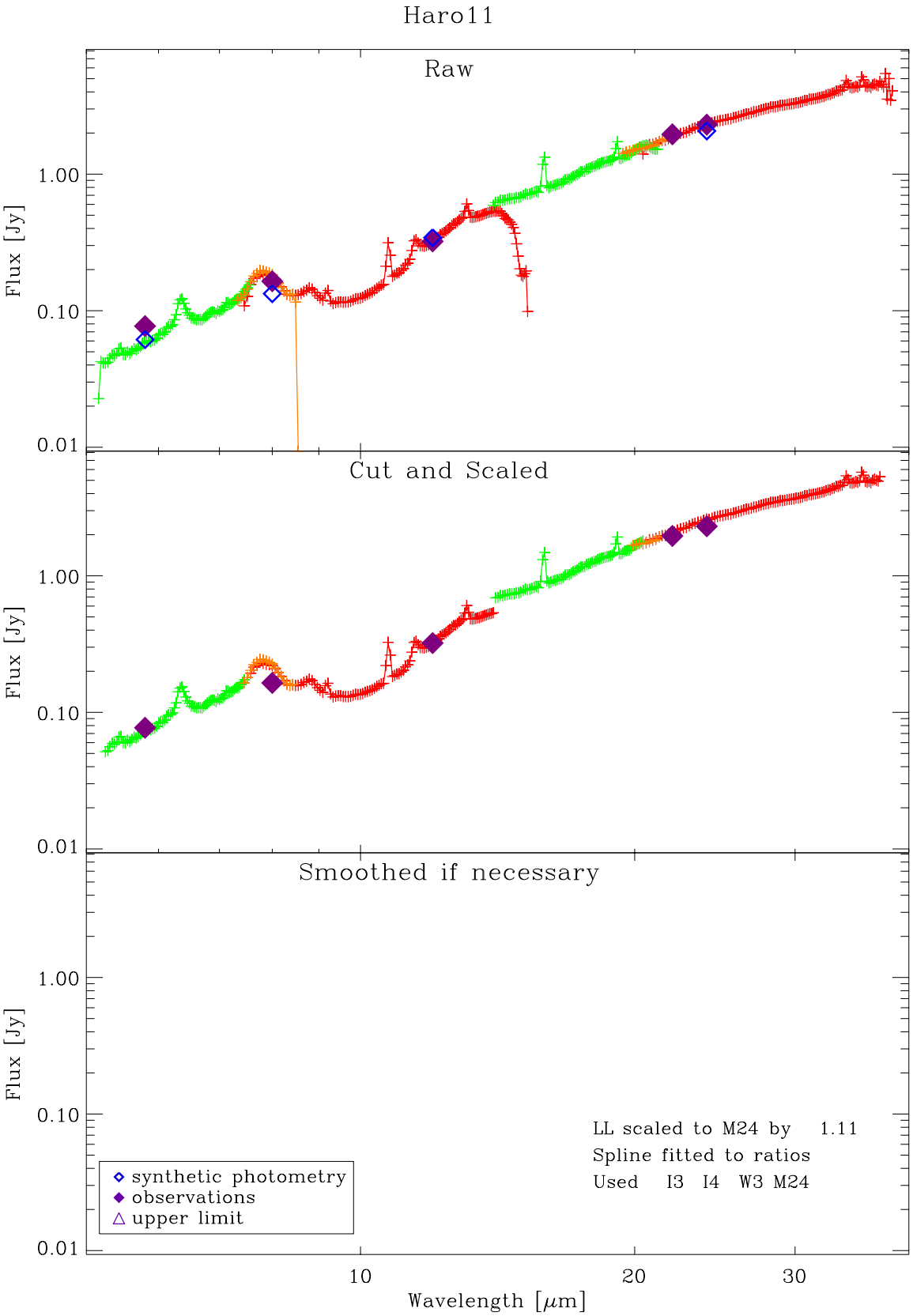

Fig. C.1. See Fig. 6.6

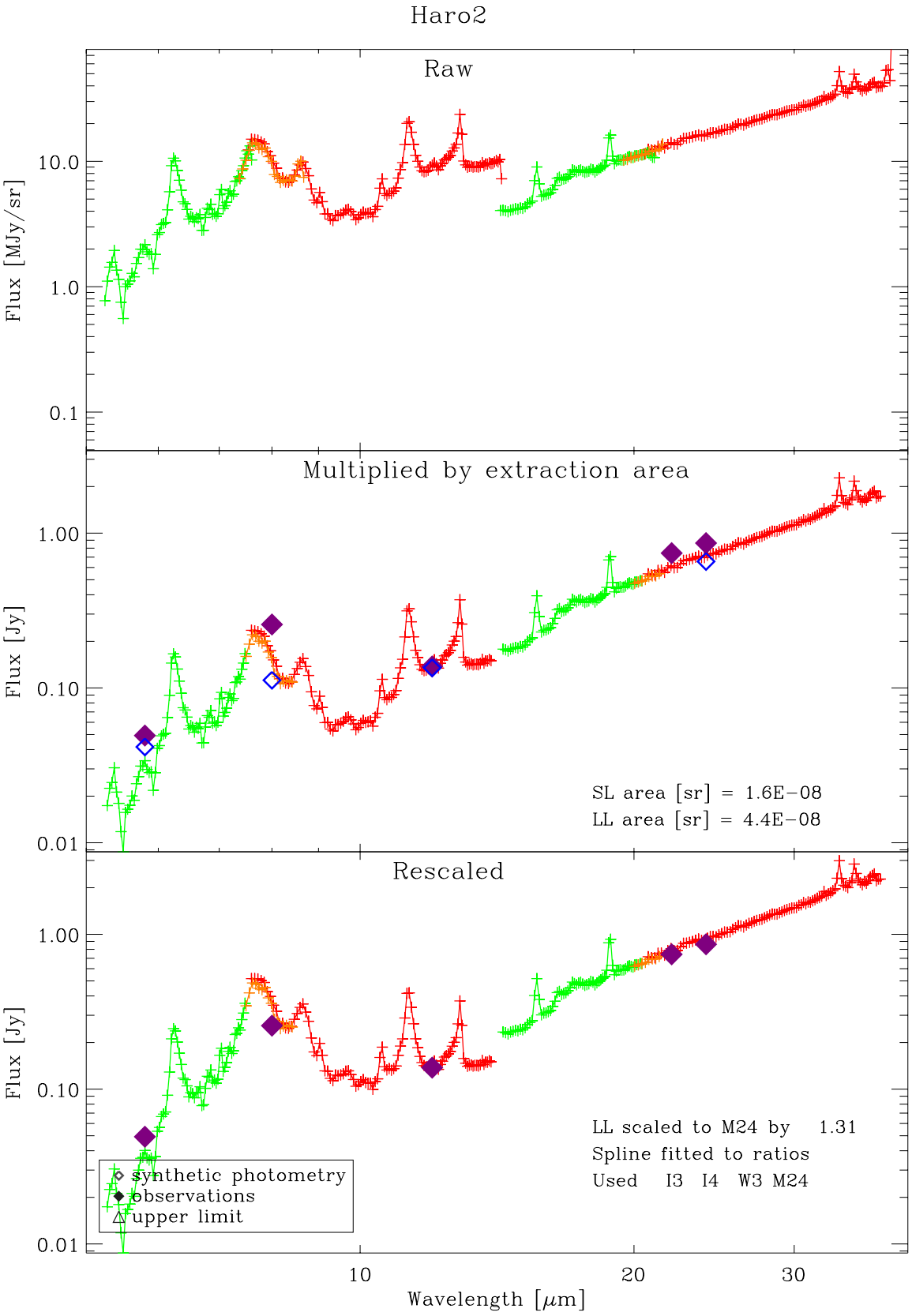
Haro2
Raw
Flux [MJy/sr]
10.0
1.0
0.1
Multiplied by extraction area
Flux [Jy]
1.00
0.10
0.01
SL area [sr] = 1.6E−08
LL area [sr] = 4.4E−08
Rescaled
Flux [Jy]
1.00
0.10
0.01
LL scaled to M24 by 1.31
Spline fitted to ratios
Used I3 I4 W3 M24
synthetic photometry
observations
upper limit
10
20
30
Wavelength [μm]

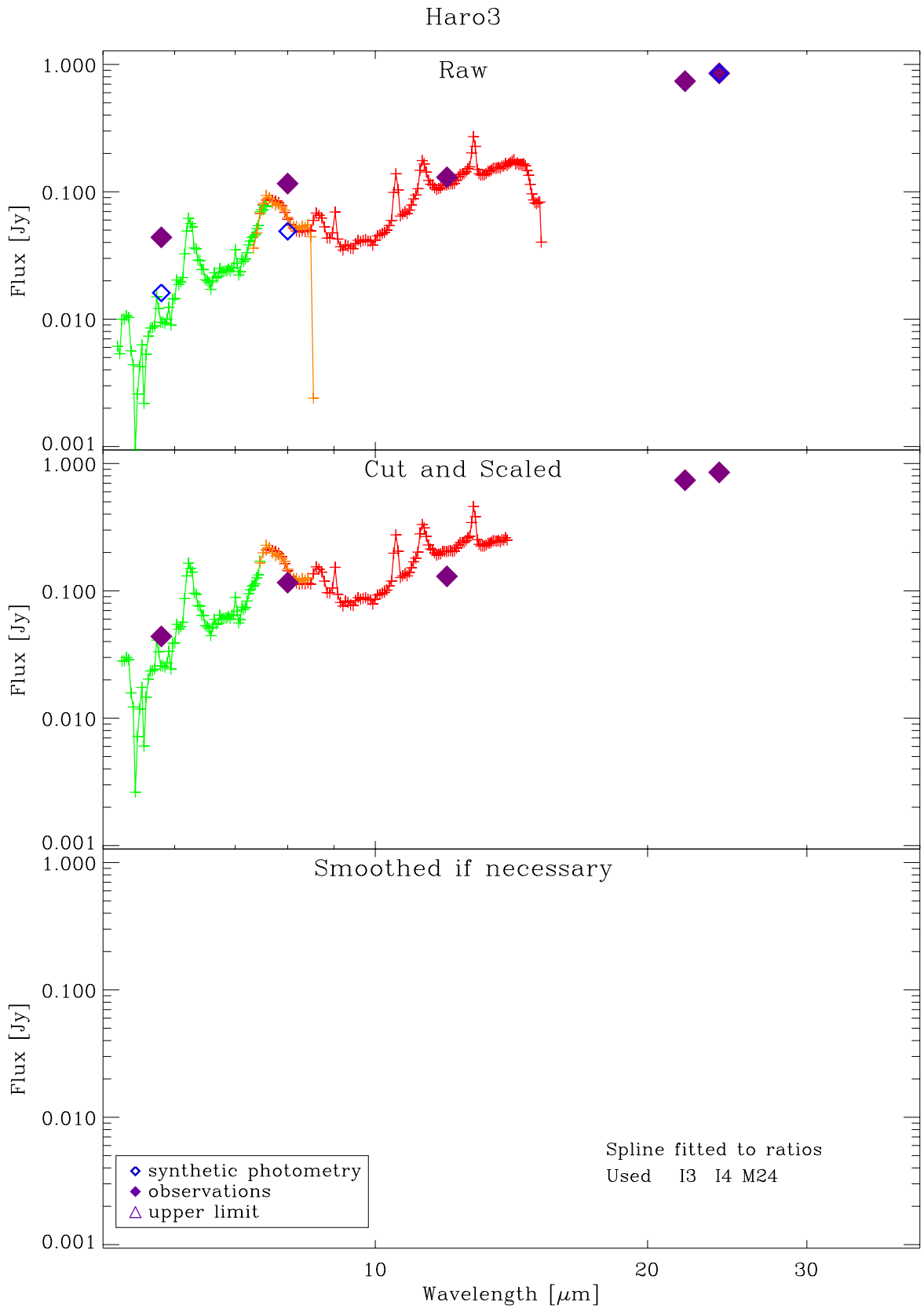
Haro3
Raw
Cut and Scaled
Smoothed if necessary
Flux [Jy]
1.000
0.100
0.010
0.001
10
20
30
Wavelength [μm]
synthetic photometry
observations
upper limit
Spline fitted to ratios
Used I3 I4 M24

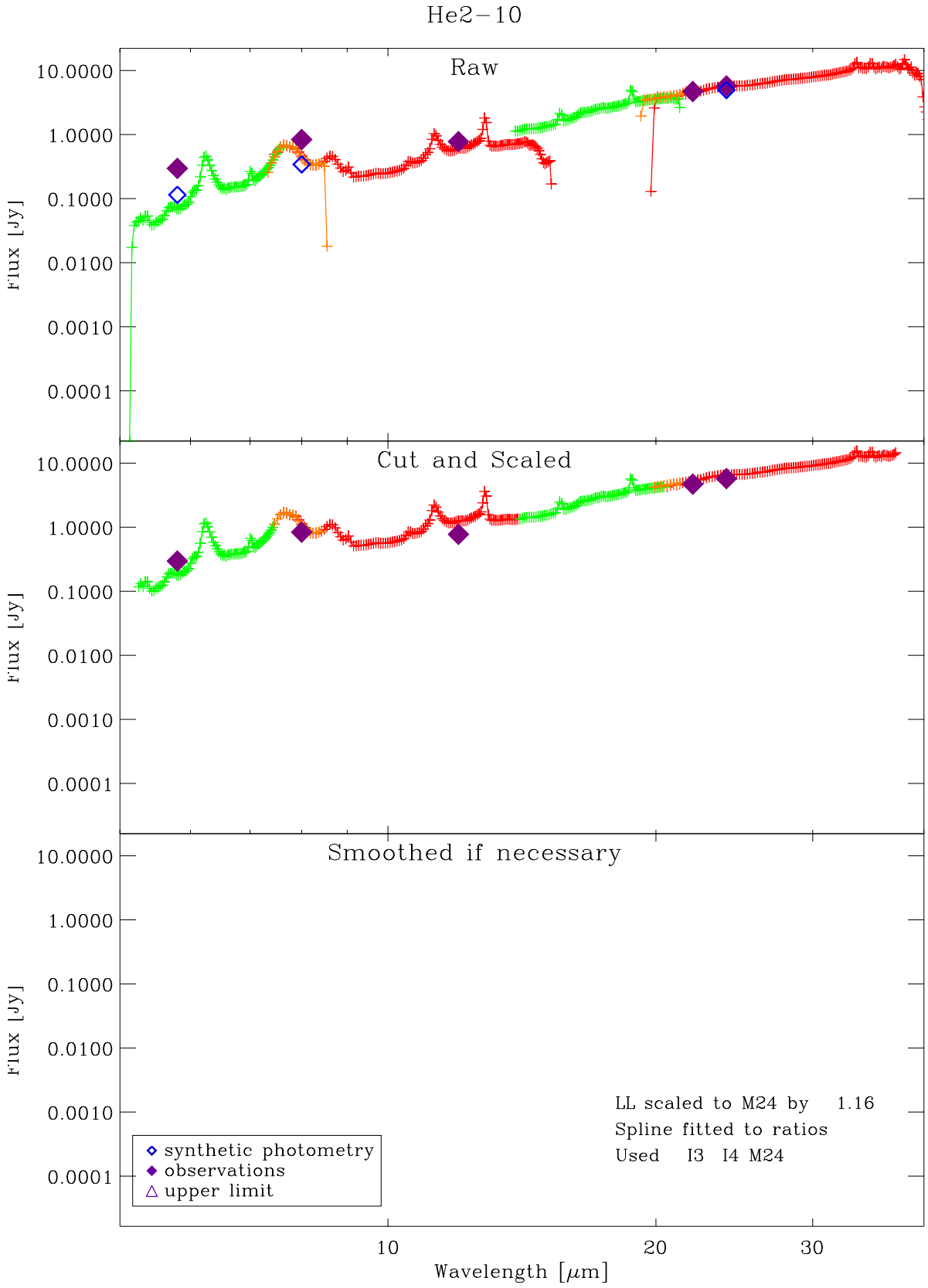
He2−10
Raw
Cut and Scaled
Smoothed if necessary
Flux [Jy]
10.0000
1.0000
0.1000
0.0100
0.0010
0.0001
10
20
30
Wavelength [μm]
LL scaled to M24 by 1.16
Spline fitted to ratios
Used I3 I4 M24
synthetic photometry
observations
upper limit

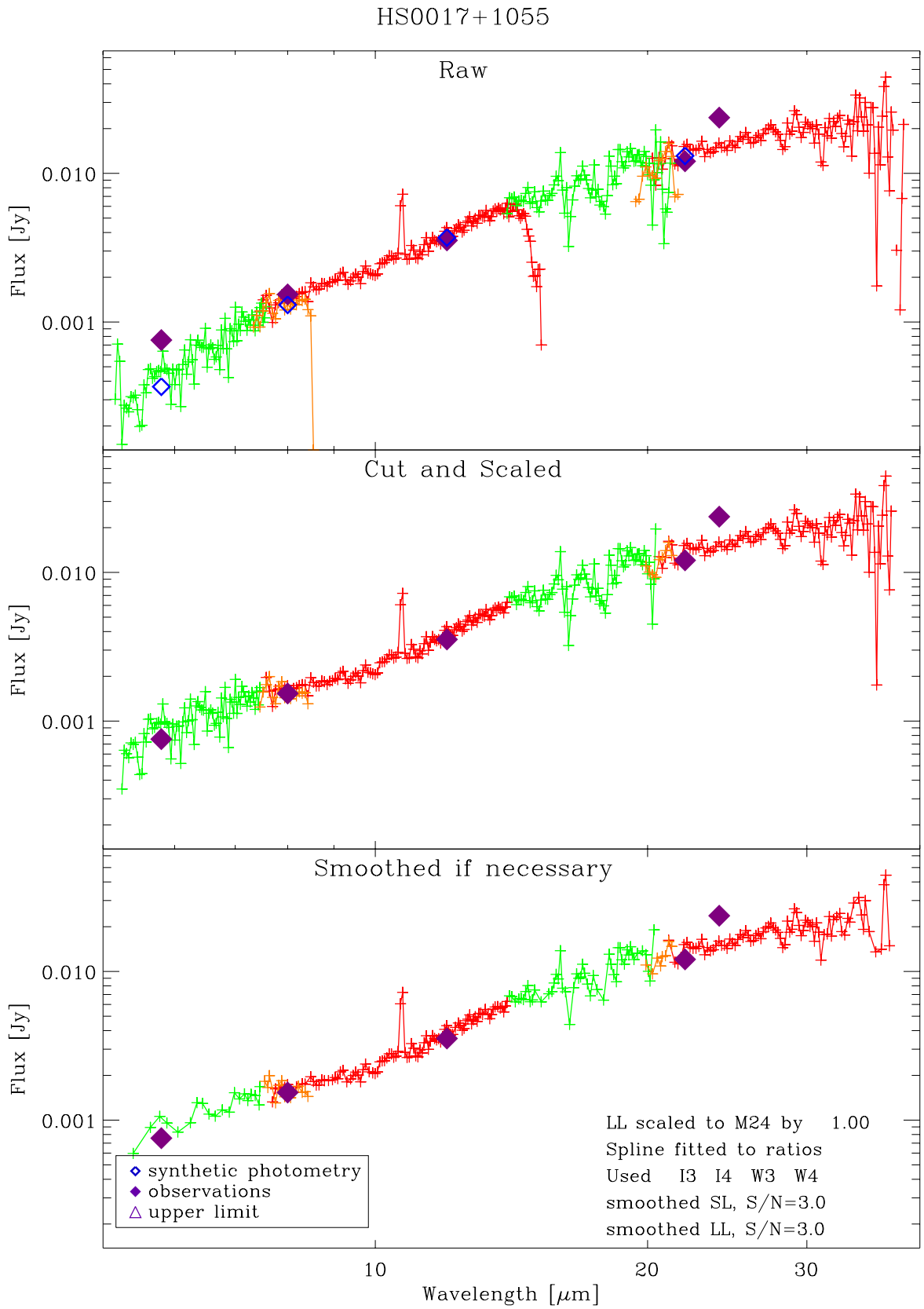
HS0017+1055
Raw
Cut and Scaled
Smoothed if necessary
Flux [Jy]
0.010
0.001
10
20
30
Wavelength [μm]
synthetic photometry
observations
upper limit
LL scaled to M24 by 1.00
Spline fitted to ratios
Used I3 I4 W3 W4
smoothed SL, S/N=3.0
smoothed LL, S/N=3.0

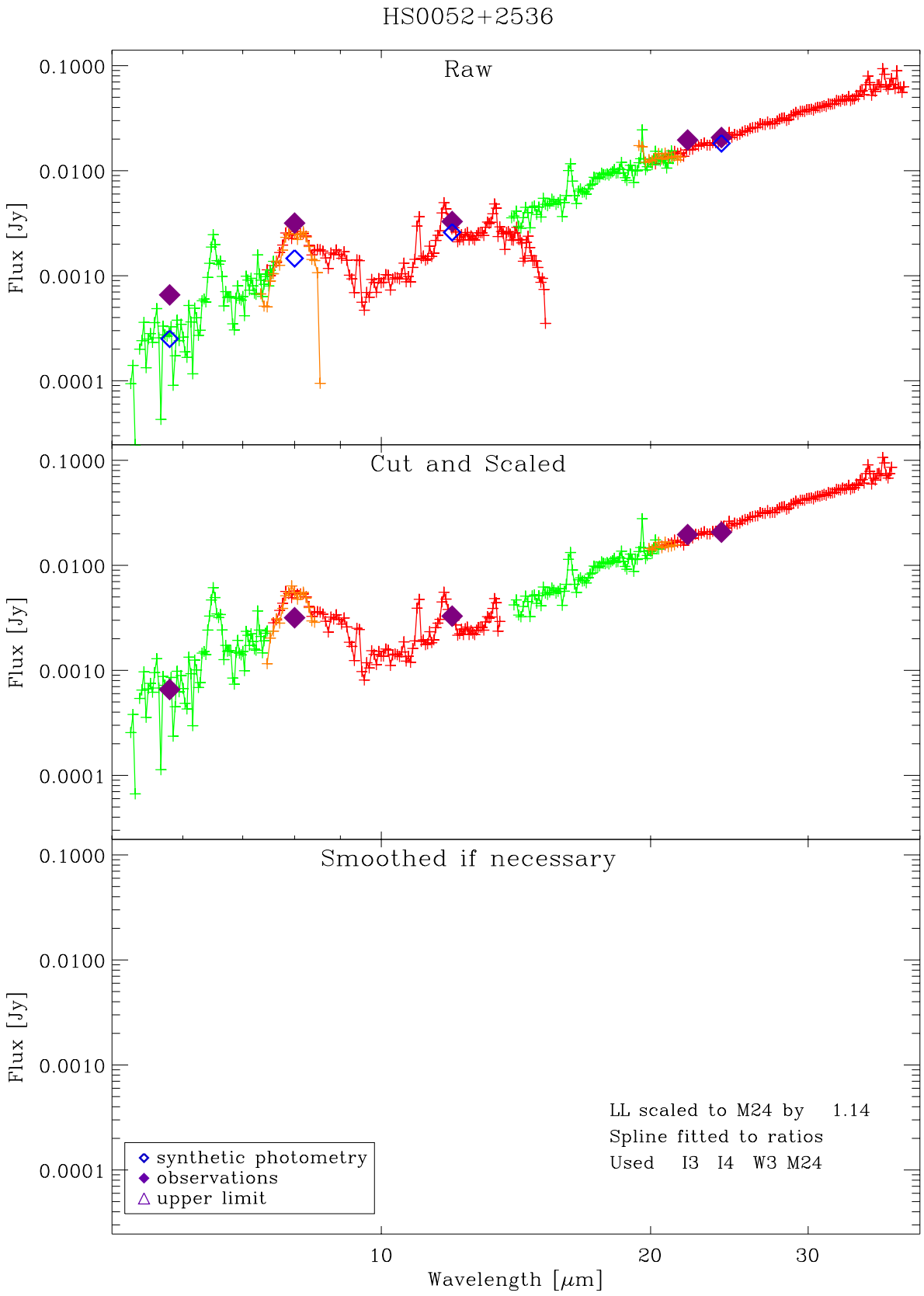
HS0052+2536
Raw
Cut and Scaled
Smoothed if necessary
Flux [Jy]
0.1000
0.0100
0.0010
0.0001
10
20
30
Wavelength [μm]
synthetic photometry
observations
upper limit
LL scaled to M24 by 1.14
Spline fitted to ratios
Used I3 I4 W3 M24

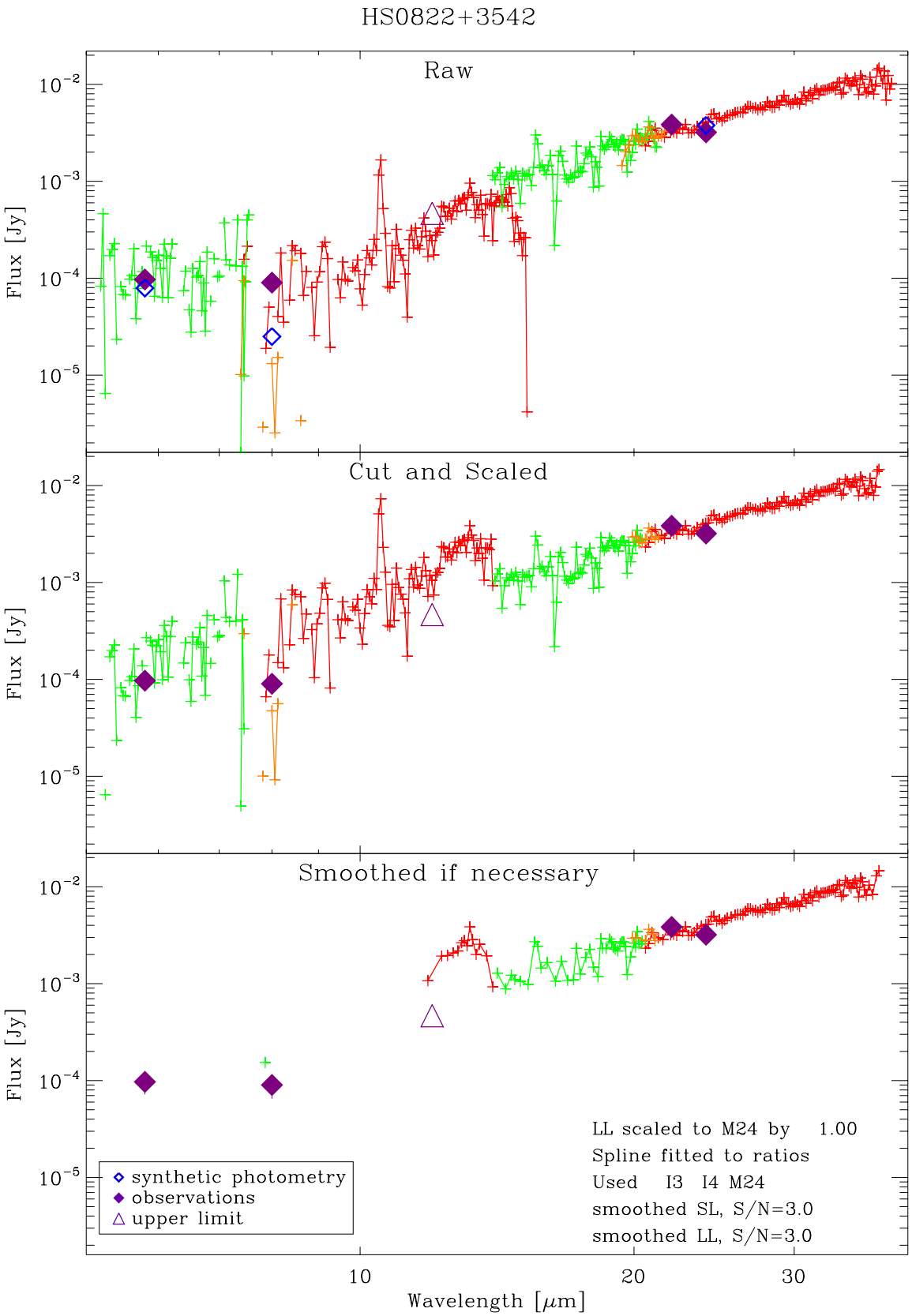
HS0822+3542
Raw
Cut and Scaled
Smoothed if necessary
Flux [Jy]
Wavelength [μm]
synthetic photometry
observations
upper limit
LL scaled to M24 by 1.00
Spline fitted to ratios
Used I3 I4 M24
smoothed SL, S/N=3.0
smoothed LL, S/N=3.0

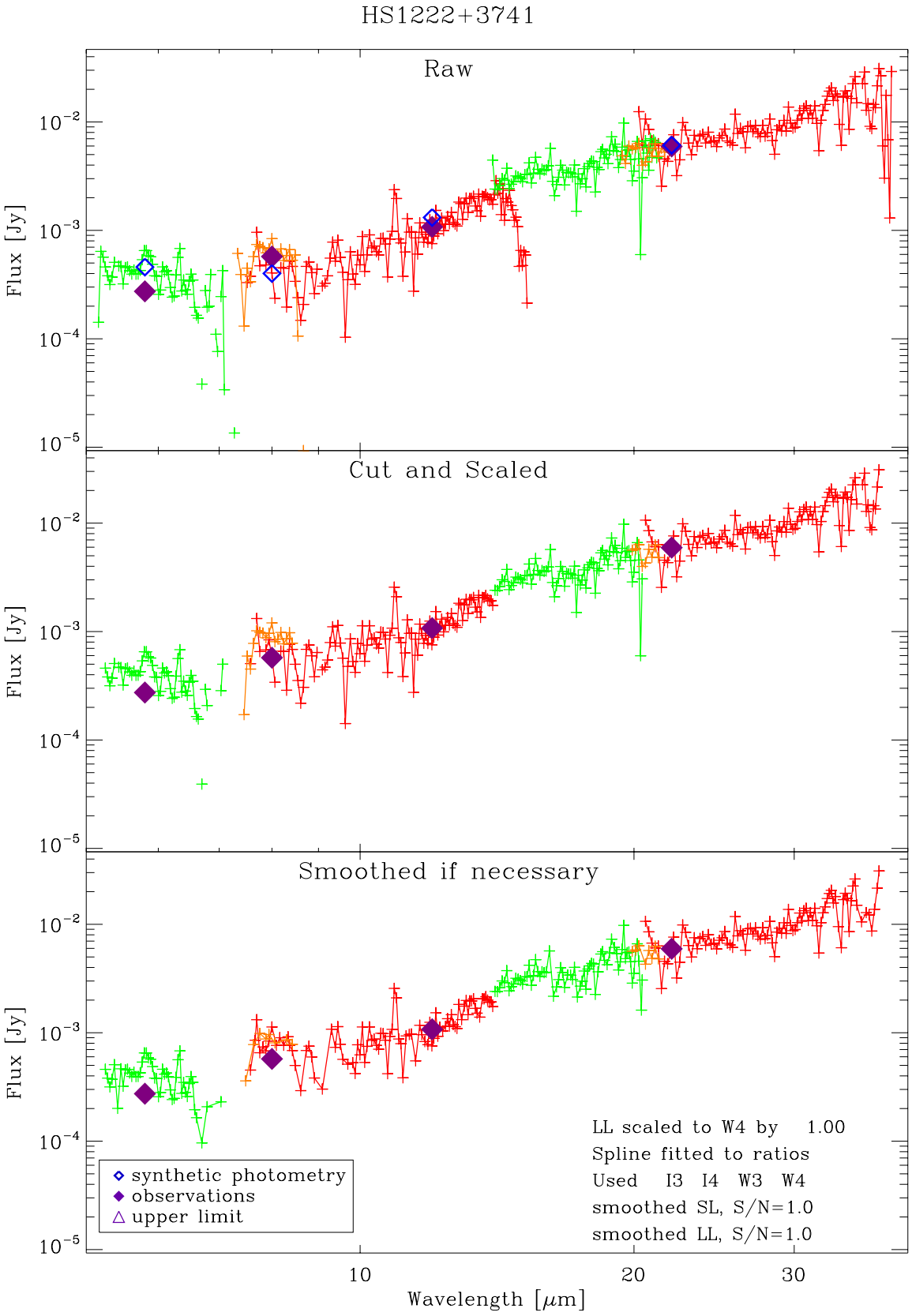
HS1222+3741
Raw
Cut and Scaled
Smoothed if necessary
Flux [Jy]
Wavelength [μm]
synthetic photometry
observations
upper limit
LL scaled to W4 by 1.00
Spline fitted to ratios
Used I3 I4 W3 W4
smoothed SL, S/N=1.0
smoothed LL, S/N=1.0

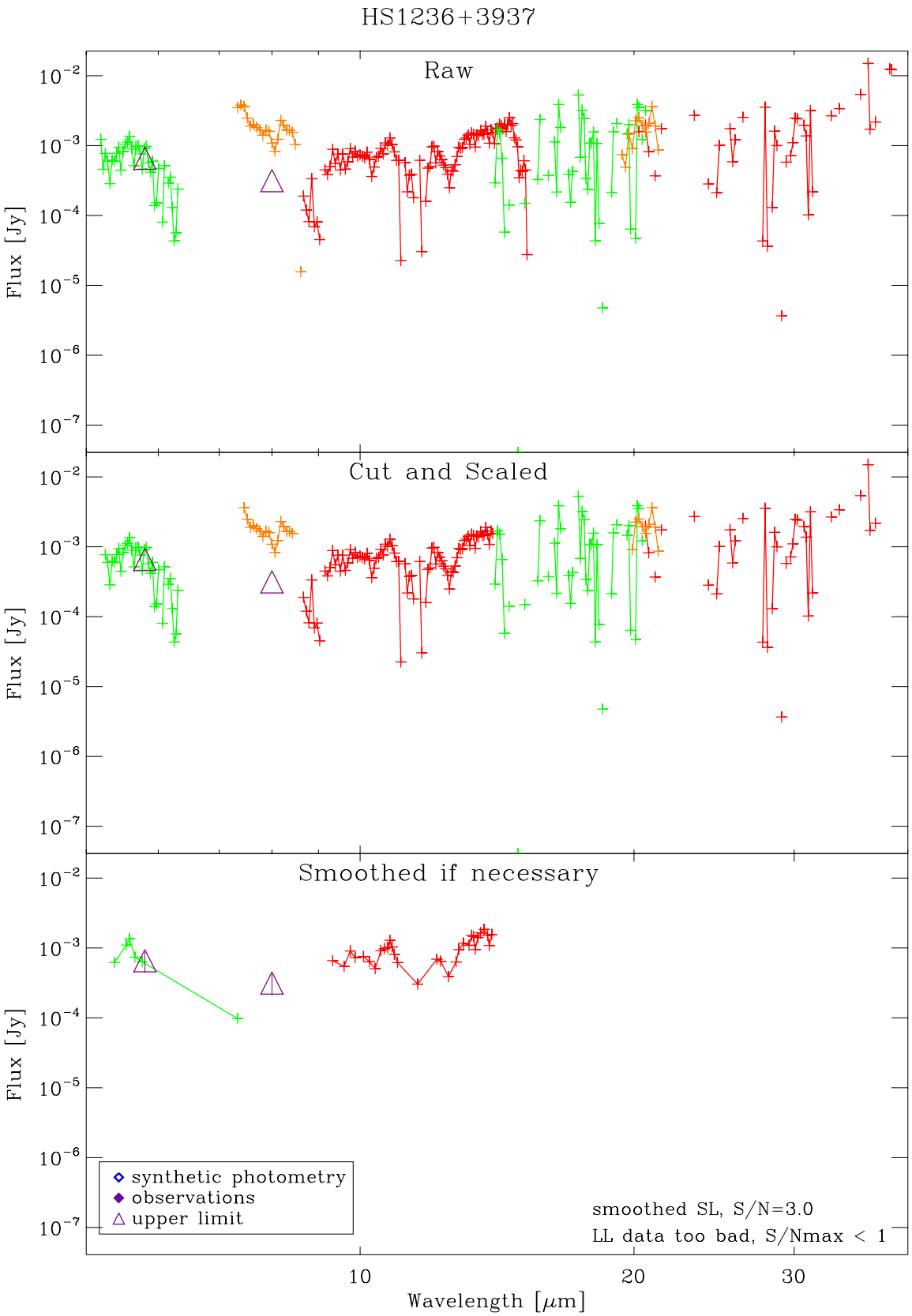
HS1236+3937
Raw
Cut and Scaled
Smoothed if necessary
Flux [Jy]
Wavelength [μm]
synthetic photometry
observations
upper limit
smoothed SL, S/N=3.0
LL data too bad, S/Nmax < 1

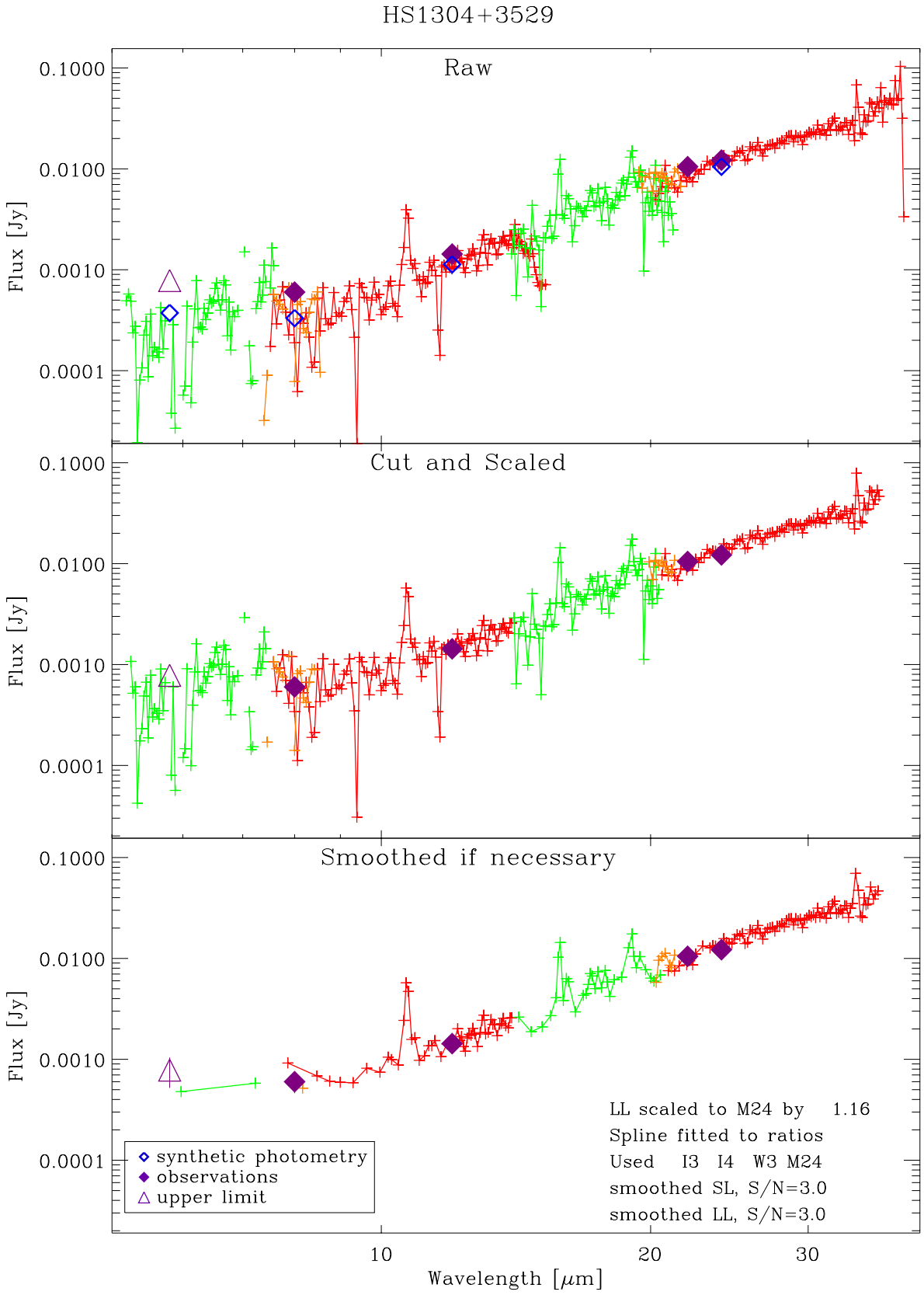
HS1304+3529
Raw
Cut and Scaled
Smoothed if necessary
Flux [Jy]
0.1000
0.0100
0.0010
0.0001
10
20
30
Wavelength [μm]
synthetic photometry
observations
upper limit
LL scaled to M24 by 1.16
Spline fitted to ratios
Used I3 I4 W3 M24
smoothed SL, S/N=3.0
smoothed LL, S/N=3.0

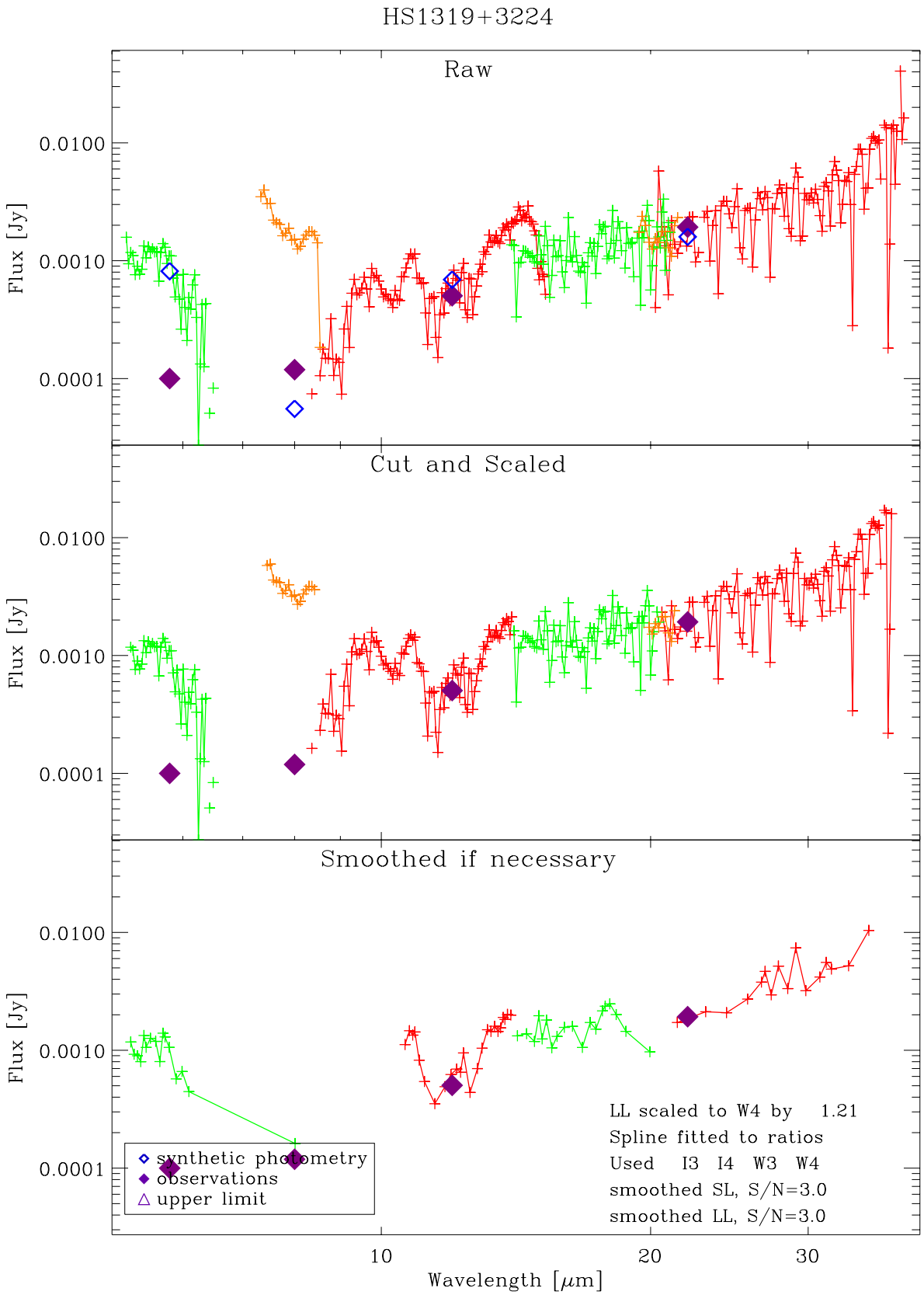
HS1319+3224
Raw
Cut and Scaled
Smoothed if necessary
Flux [Jy]
0.0100
0.0010
0.0001
10
20
30
Wavelength [μm]
synthetic photometry
observations
upper limit
LL scaled to W4 by 1.21
Spline fitted to ratios
Used I3 I4 W3 W4
smoothed SL, S/N=3.0
smoothed LL, S/N=3.0

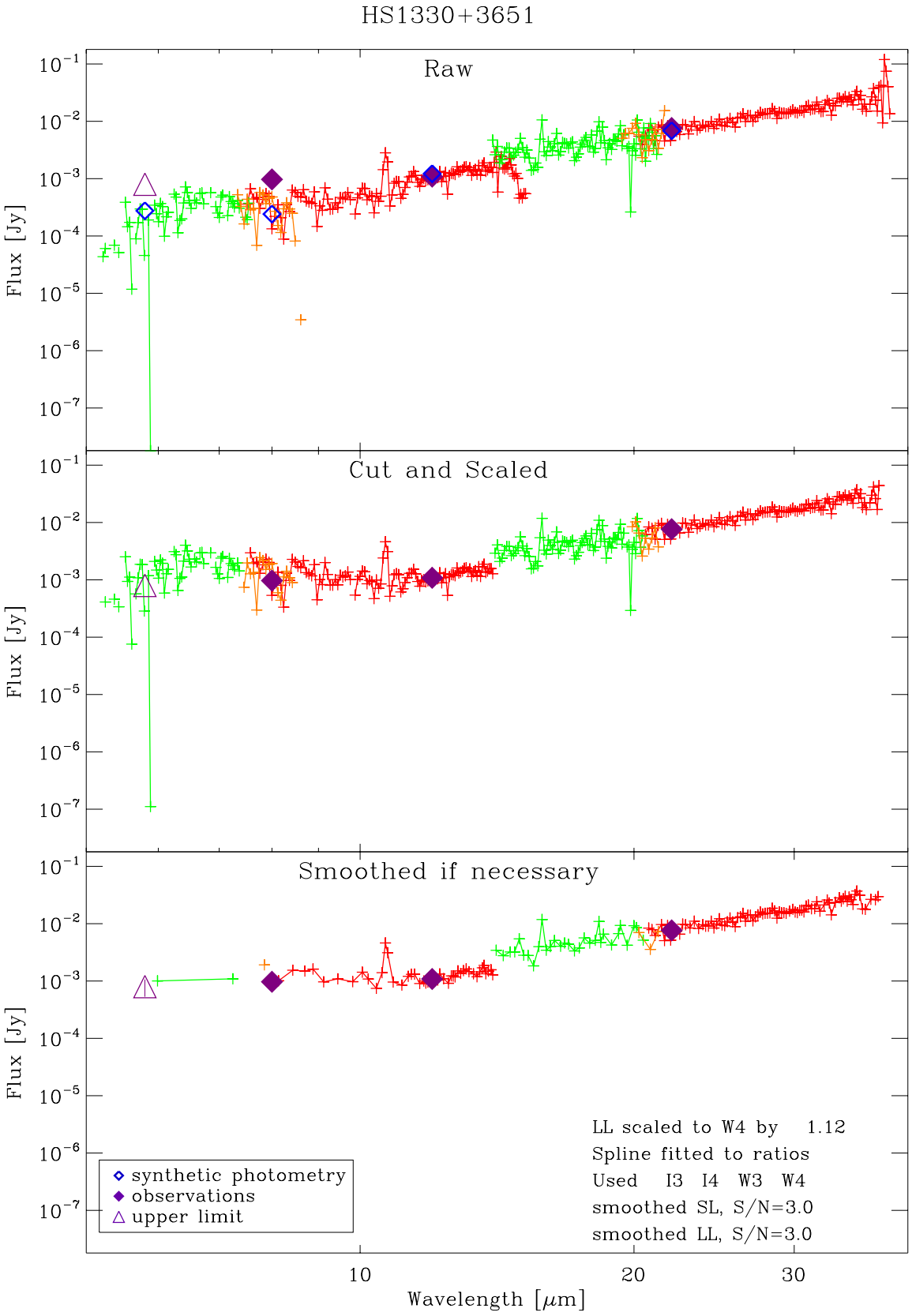
HS1330+3651
Raw
Cut and Scaled
Smoothed if necessary
Flux [Jy]
Wavelength [μm]
synthetic photometry
observations
upper limit
LL scaled to W4 by 1.12
Spline fitted to ratios
Used I3 I4 W3 W4
smoothed SL, S/N=3.0
smoothed LL, S/N=3.0

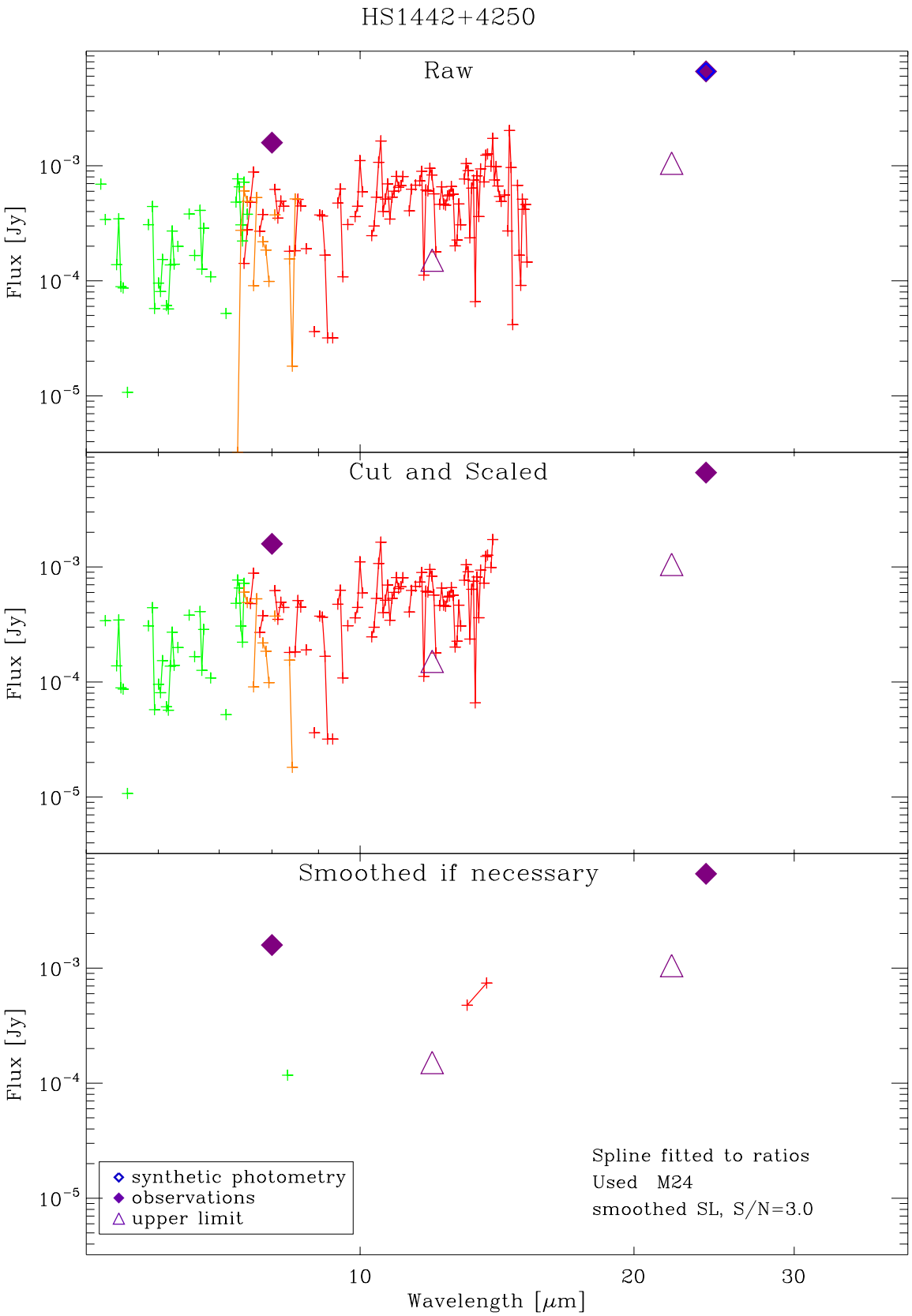
HS1442+4250
Raw
Cut and Scaled
Smoothed if necessary
Flux [Jy]
10^{-3}
10^{-4}
10^{-5}
synthetic photometry
observations
upper limit
Spline fitted to ratios
Used M24
smoothed SL, S/N=3.0
10
20
30
Wavelength [μm]

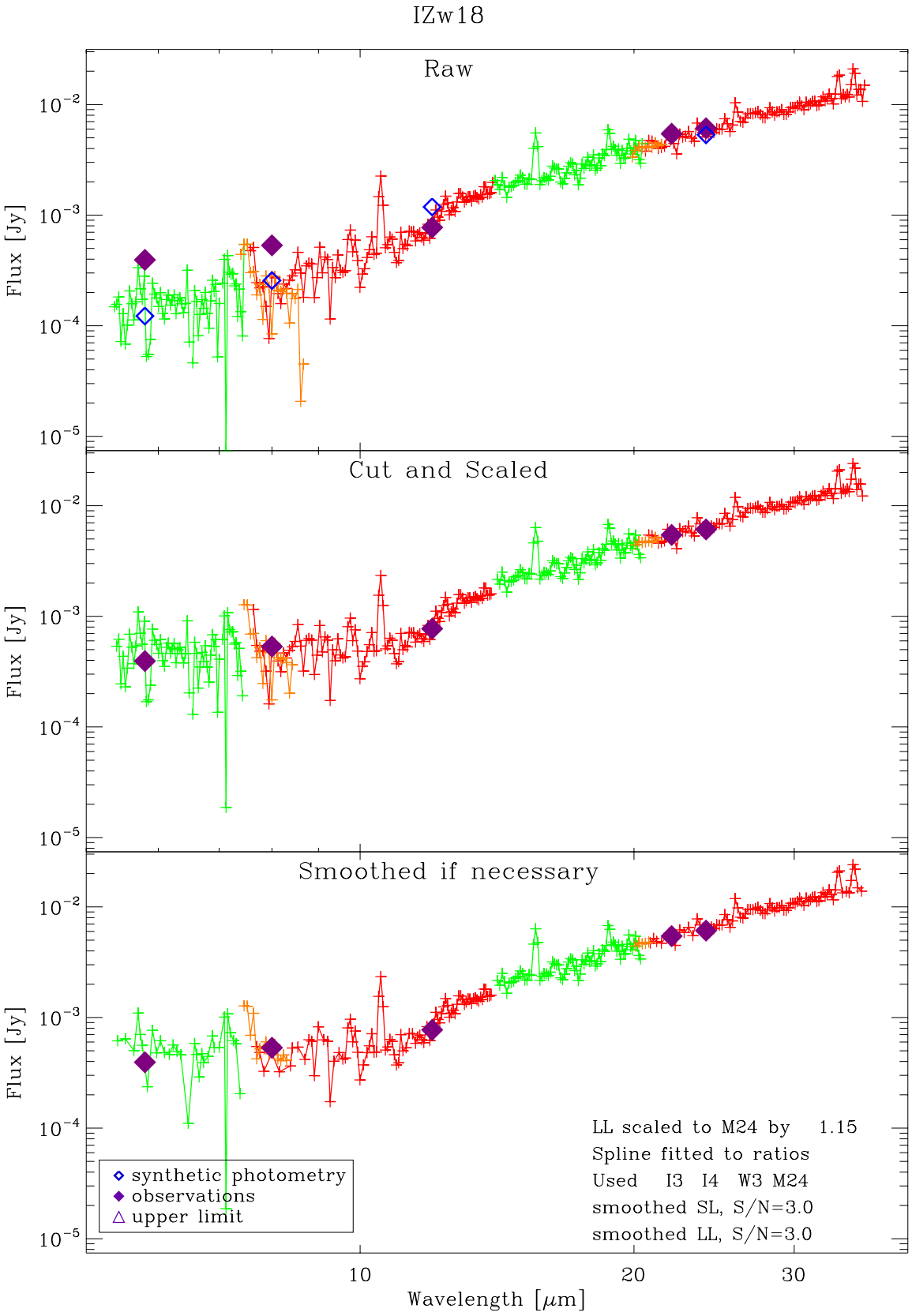
IZw18
Raw
Cut and Scaled
Smoothed if necessary
Flux [Jy]
Wavelength [μm]
synthetic photometry
observations
upper limit
LL scaled to M24 by 1.15
Spline fitted to ratios
Used I3 I4 W3 M24
smoothed SL, S/N=3.0
smoothed LL, S/N=3.0

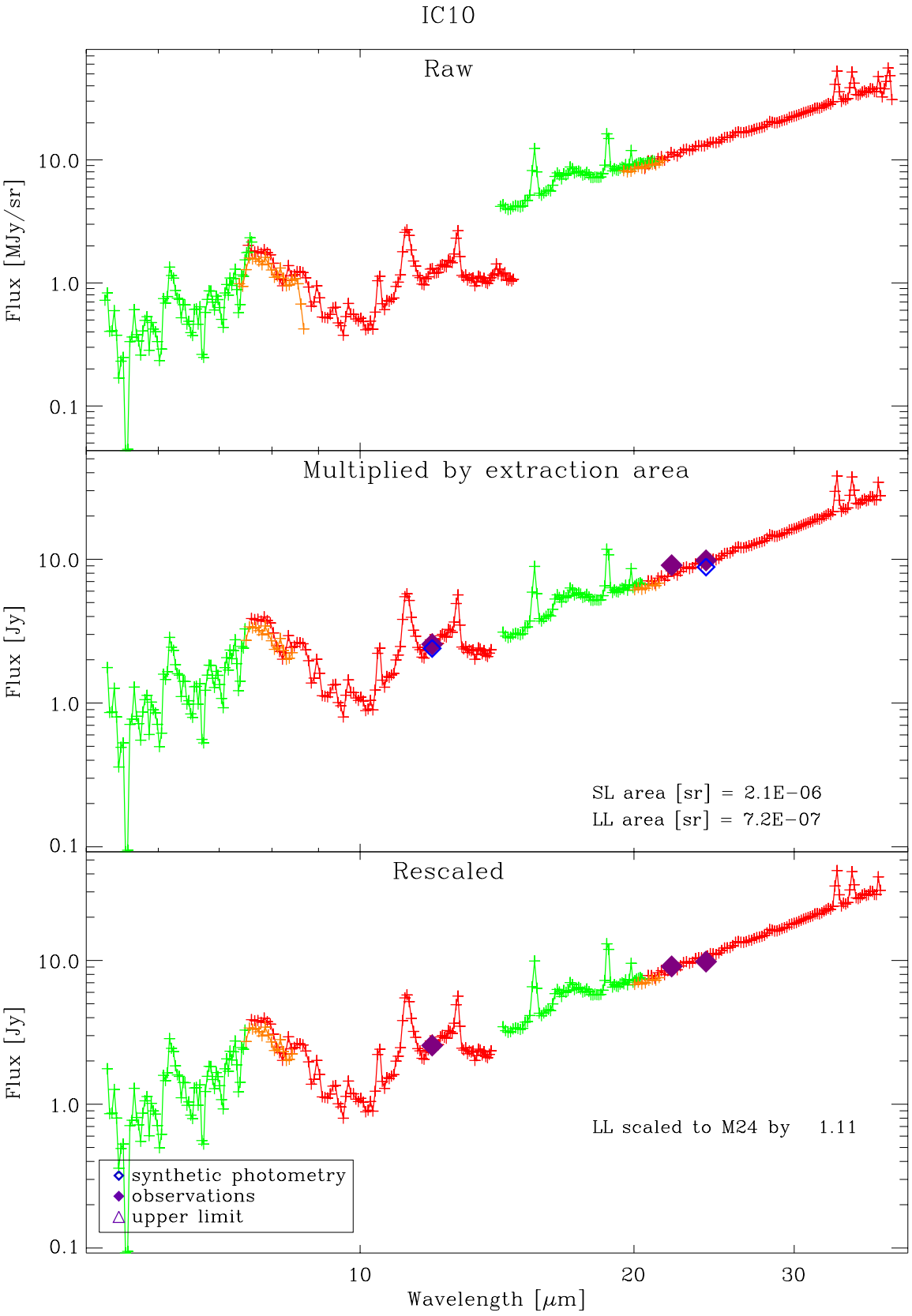
IC10
Raw
Flux [MJy/sr]
10.0
1.0
0.1
Multiplied by extraction area
Flux [Jy]
SL area [sr] = 2.1E−06
LL area [sr] = 7.2E−07
Rescaled
LL scaled to M24 by 1.11
synthetic photometry
observations
upper limit
10
20
30
Wavelength [μm]

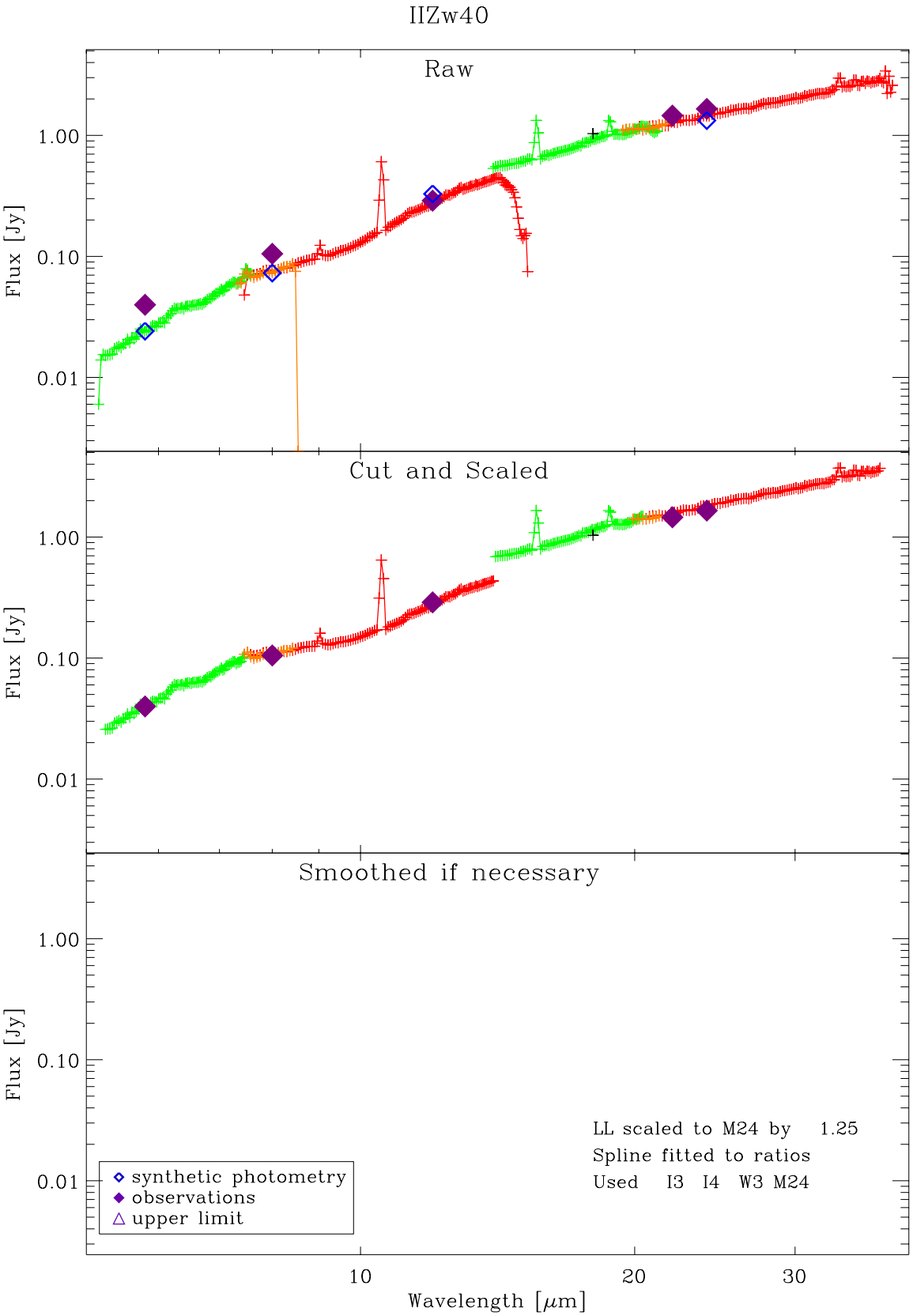
IIZw40
Raw
Cut and Scaled
Smoothed if necessary
Flux [Jy]
1.00
0.10
0.01
10
20
30
Wavelength [μm]
synthetic photometry
observations
upper limit
LL scaled to M24 by 1.25
Spline fitted to ratios
Used I3 I4 W3 M24

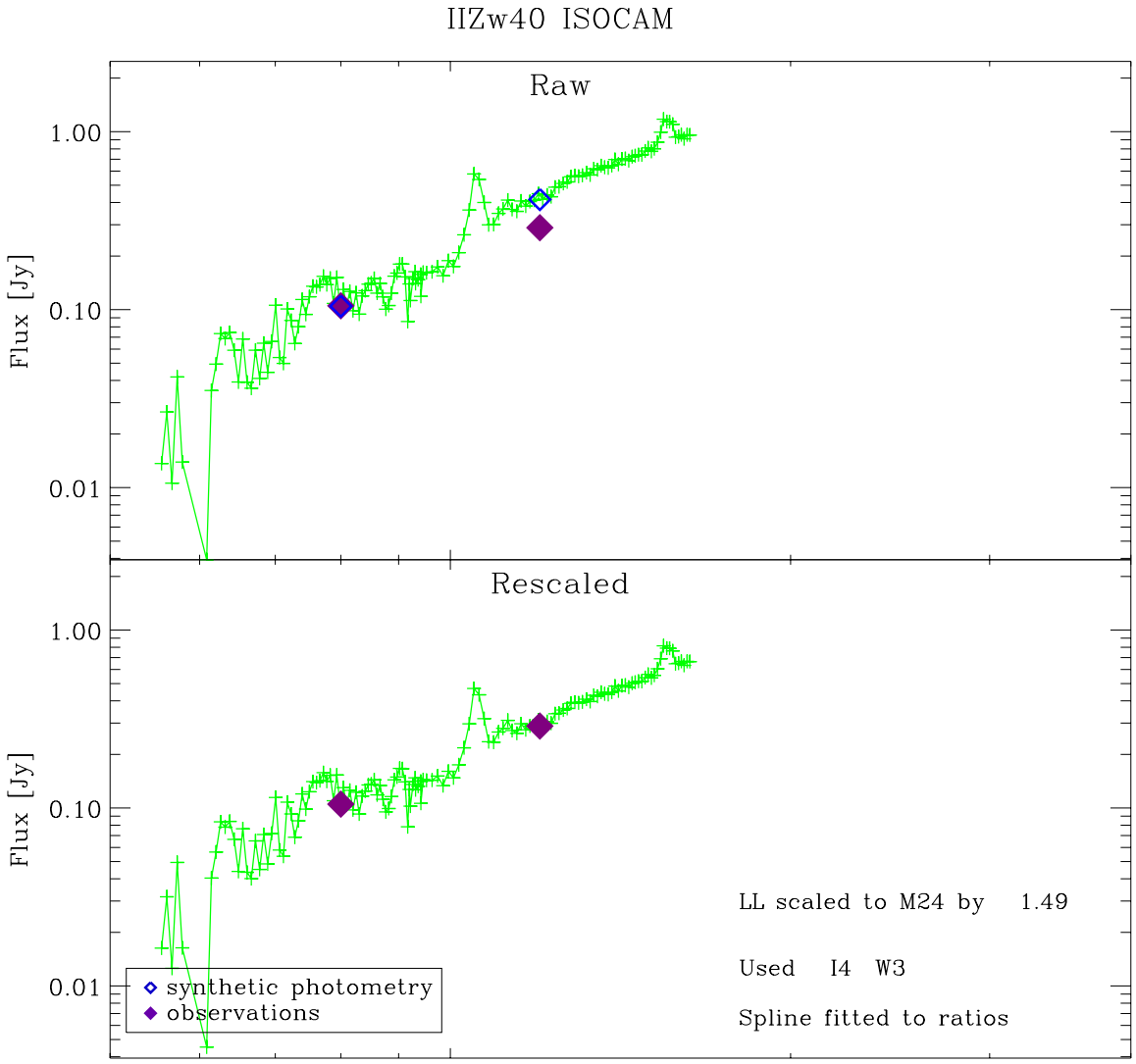
IIZw40 ISOCAM
Raw
Rescaled
Flux [Jy]
1.00
0.10
0.01
synthetic photometry
observations
LL scaled to M24 by 1.49
Used I4 W3
Spline fitted to ratios

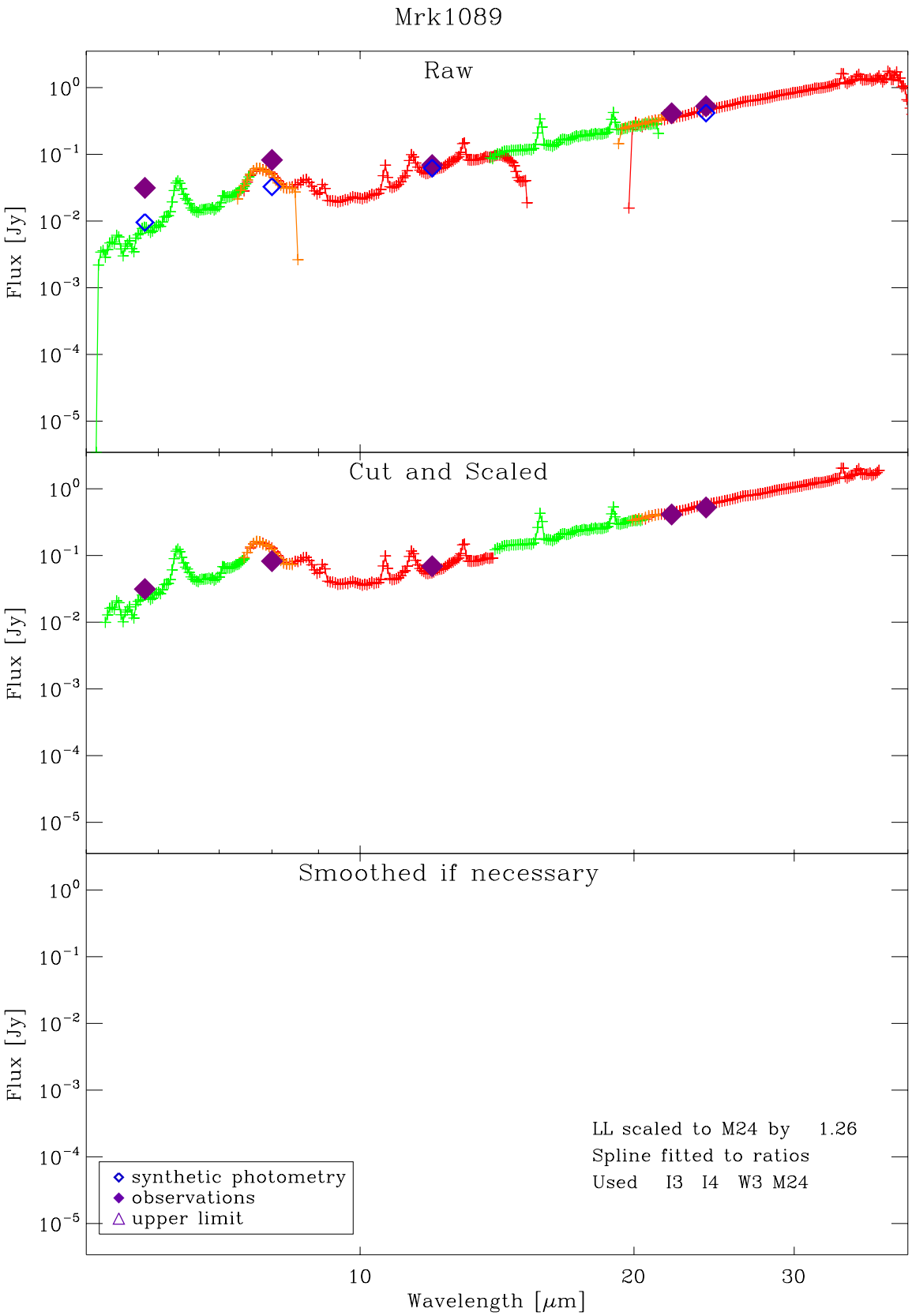
Mrk1089
Raw
Cut and Scaled
Smoothed if necessary
Flux [Jy]
Wavelength [μm]
LL scaled to M24 by 1.26
Spline fitted to ratios
Used I3 I4 W3 M24
synthetic photometry
observations
upper limit

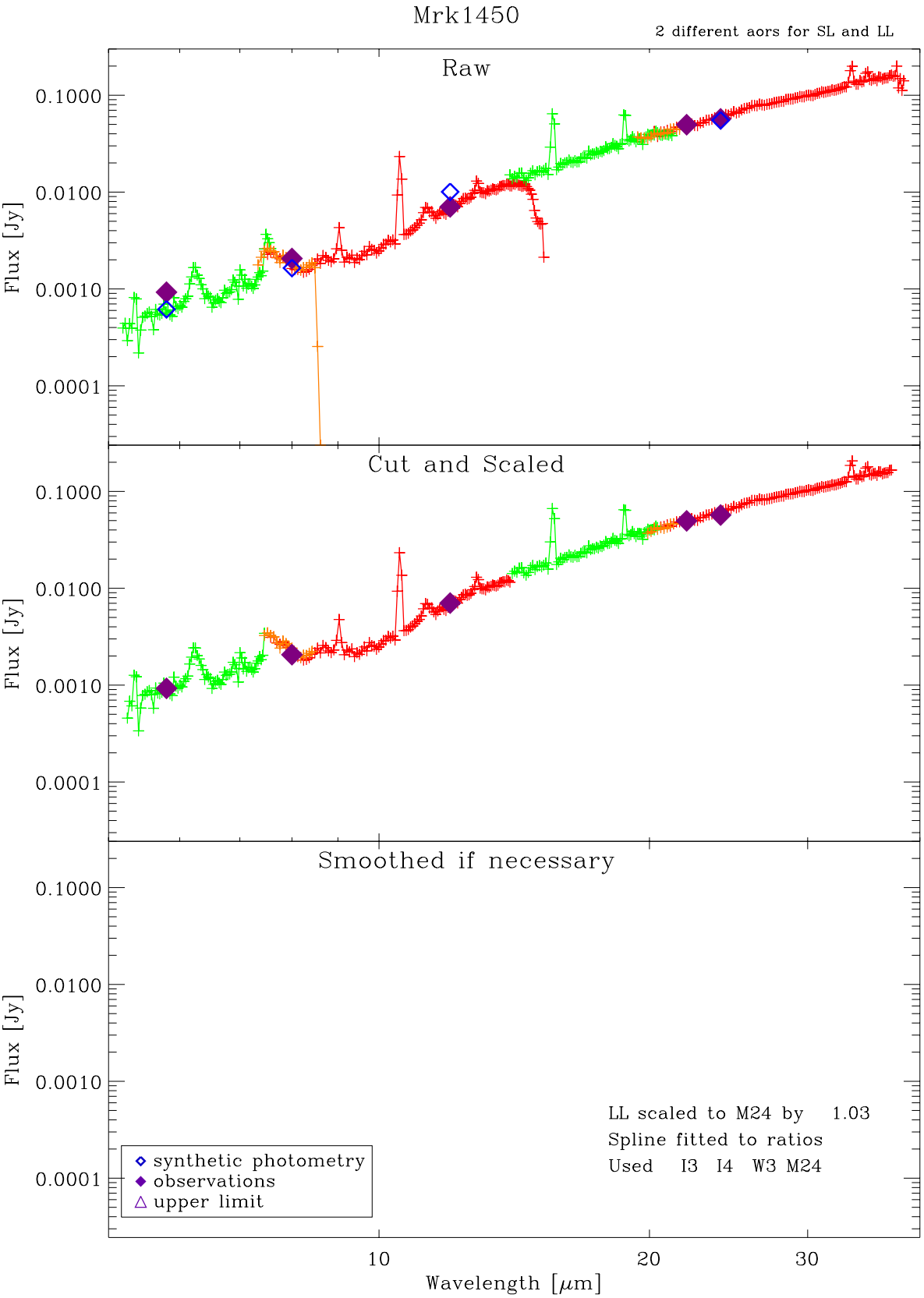
Mrk1450
2 different aors for SL and LL
Raw
Cut and Scaled
Smoothed if necessary
Flux [Jy]
0.1000
0.0100
0.0010
0.0001
10
20
30
Wavelength [μm]
synthetic photometry
observations
upper limit
LL scaled to M24 by 1.03
Spline fitted to ratios
Used I3 I4 W3 M24

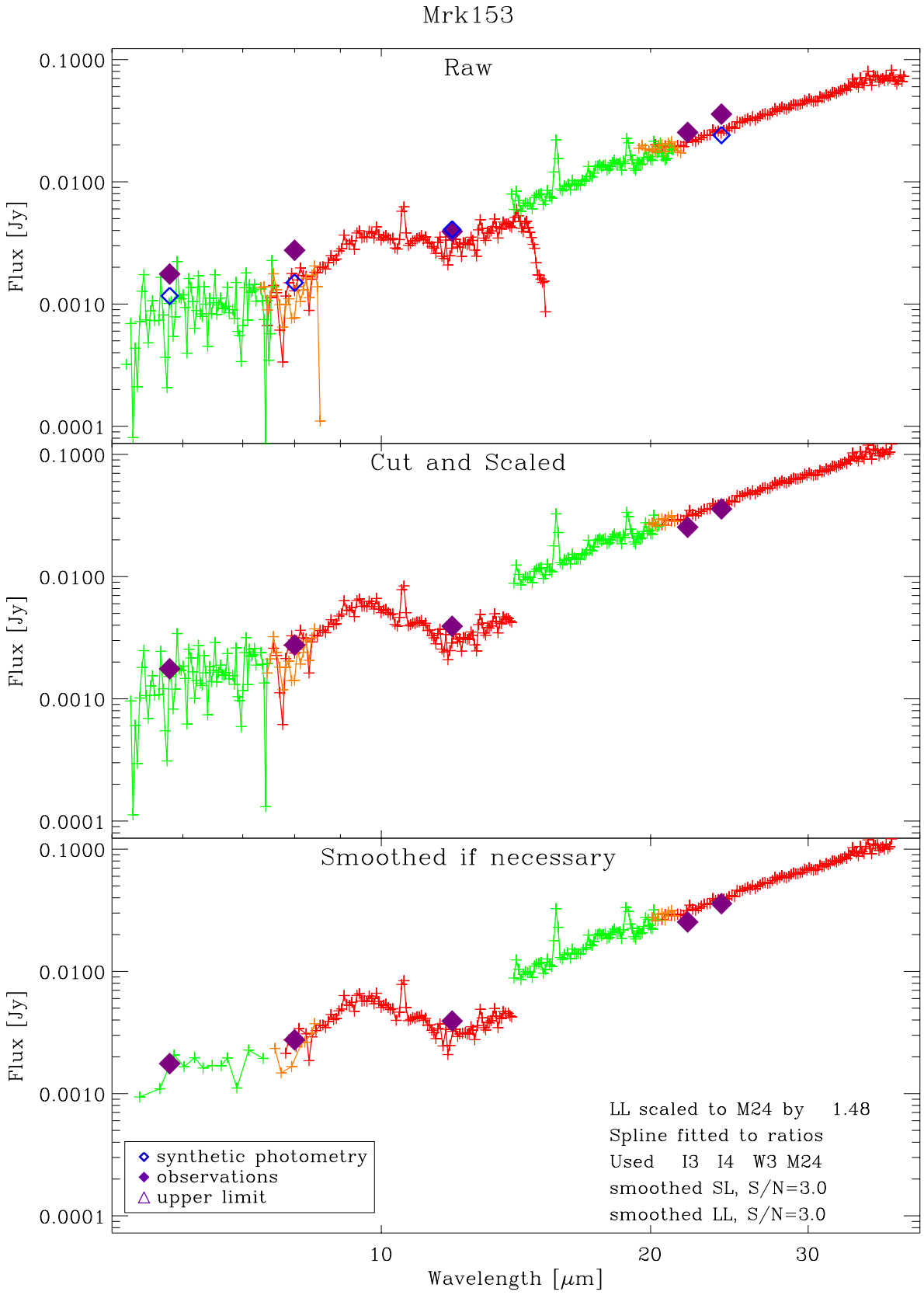
Mrk153
Raw
Cut and Scaled
Smoothed if necessary
Flux [Jy]
0.1000
0.0100
0.0010
0.0001
10
20
30
Wavelength [μm]
synthetic photometry
observations
upper limit
LL scaled to M24 by 1.48
Spline fitted to ratios
Used I3 I4 W3 M24
smoothed SL, S/N=3.0
smoothed LL, S/N=3.0

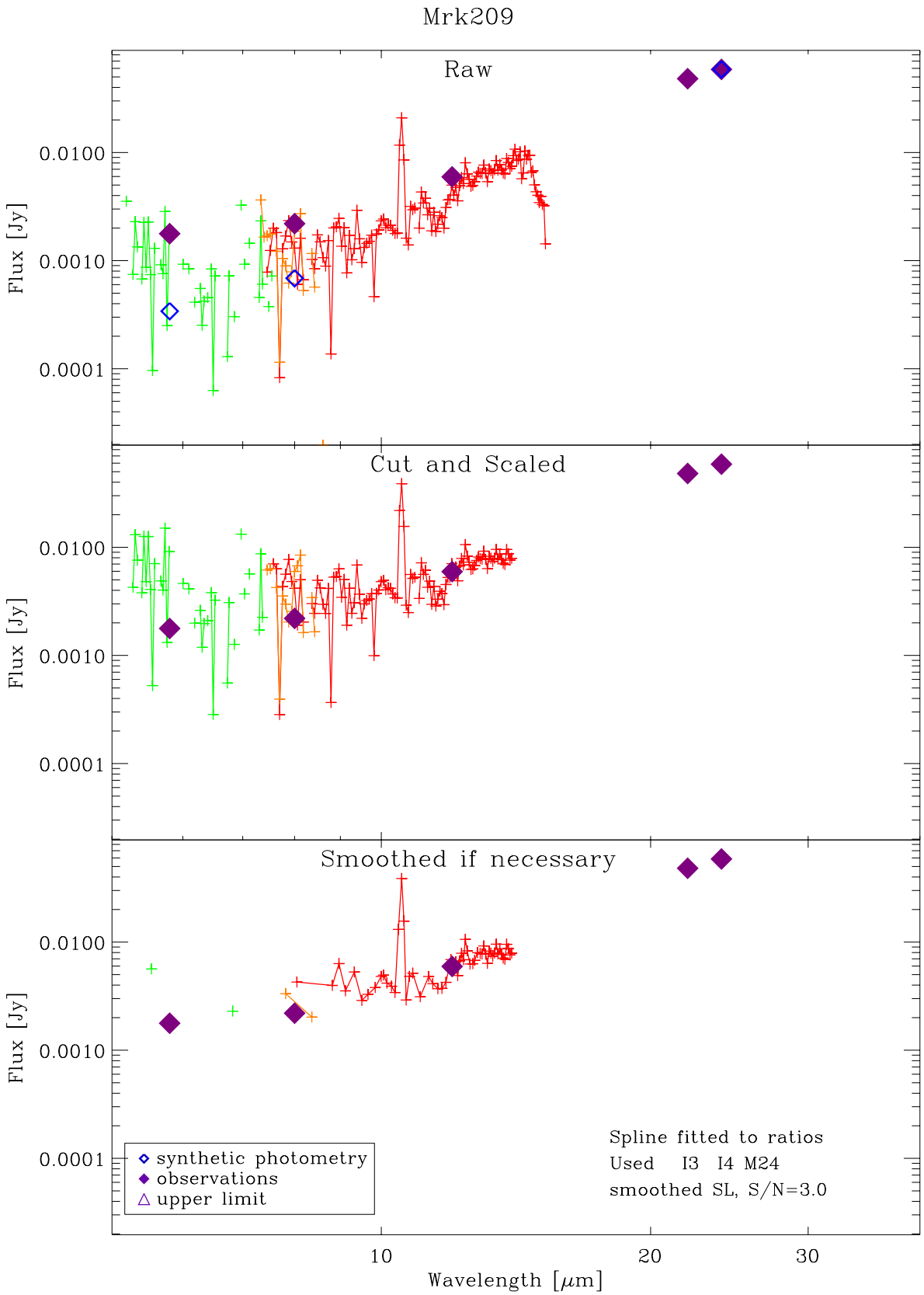
Mrk209
Raw
Cut and Scaled
Smoothed if necessary
Flux [Jy]
0.0100
0.0010
0.0001
10
20
30
Wavelength [μm]
synthetic photometry
observations
upper limit
Spline fitted to ratios
Used I3 I4 M24
smoothed SL, S/N=3.0

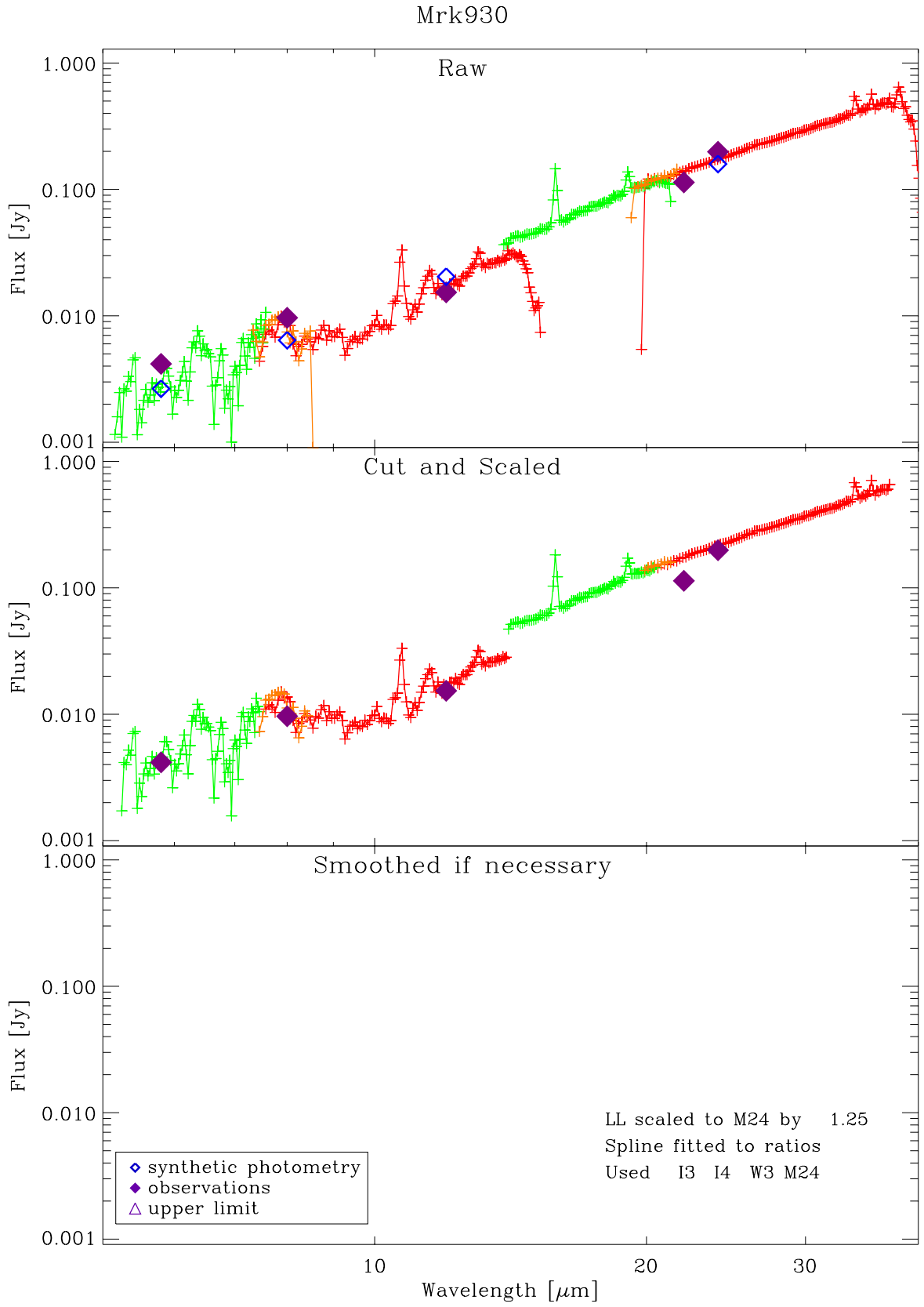
Mrk930
Raw
Cut and Scaled
Smoothed if necessary
Flux [Jy]
1.000
0.100
0.010
0.001
10
20
30
Wavelength [μm]
synthetic photometry
observations
upper limit
LL scaled to M24 by 1.25
Spline fitted to ratios
Used I3 I4 W3 M24

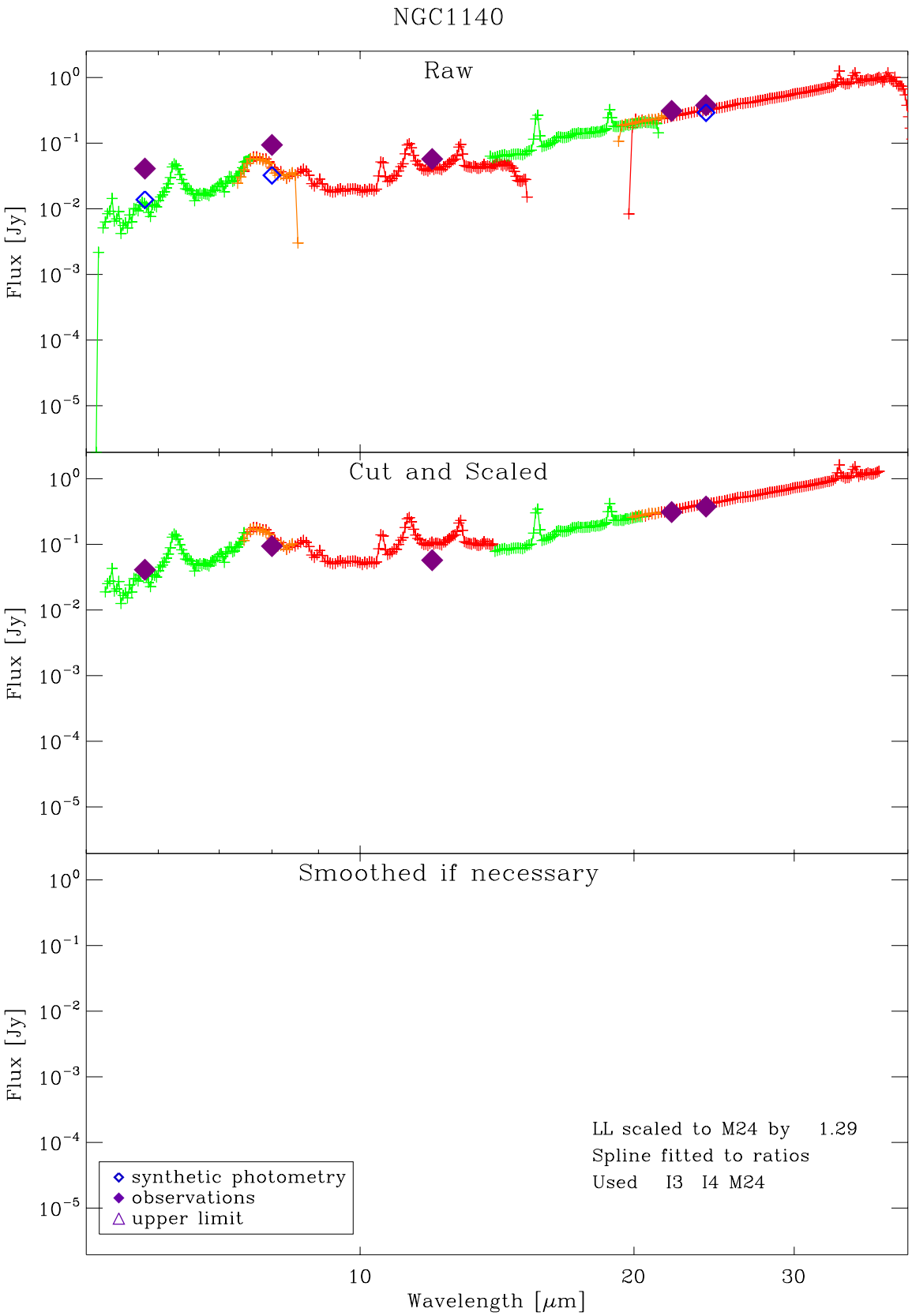
NGC1140
Raw
Cut and Scaled
Smoothed if necessary
Flux [Jy]
Wavelength [μm]
LL scaled to M24 by 1.29
Spline fitted to ratios
Used I3 I4 M24
synthetic photometry
observations
upper limit

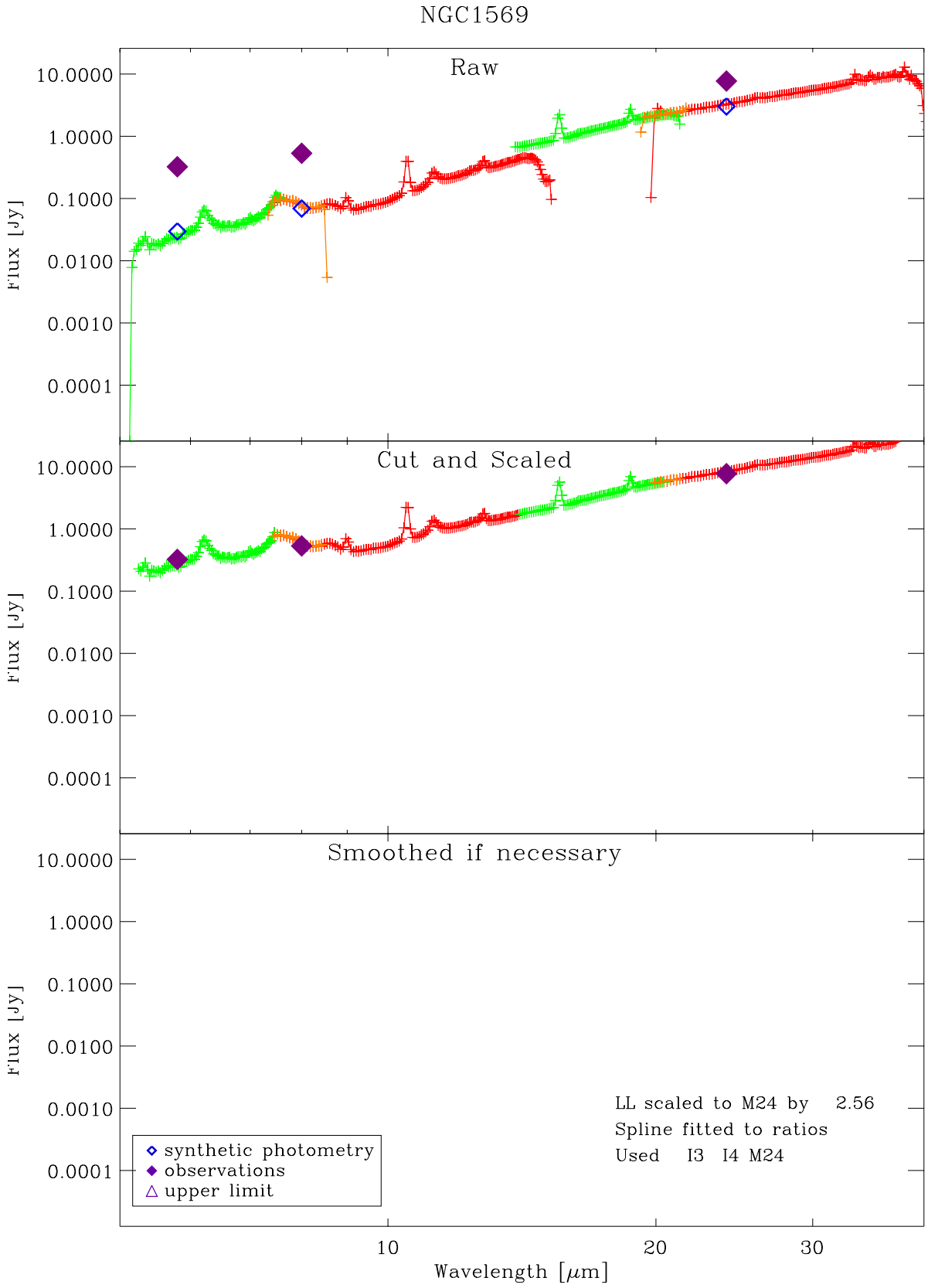
NGC1569
Raw
Cut and Scaled
Smoothed if necessary
Flux [Jy]
10.0000
1.0000
0.1000
0.0100
0.0010
0.0001
10
20
30
Wavelength [μm]
synthetic photometry
observations
upper limit
LL scaled to M24 by 2.56
Spline fitted to ratios
Used I3 I4 M24

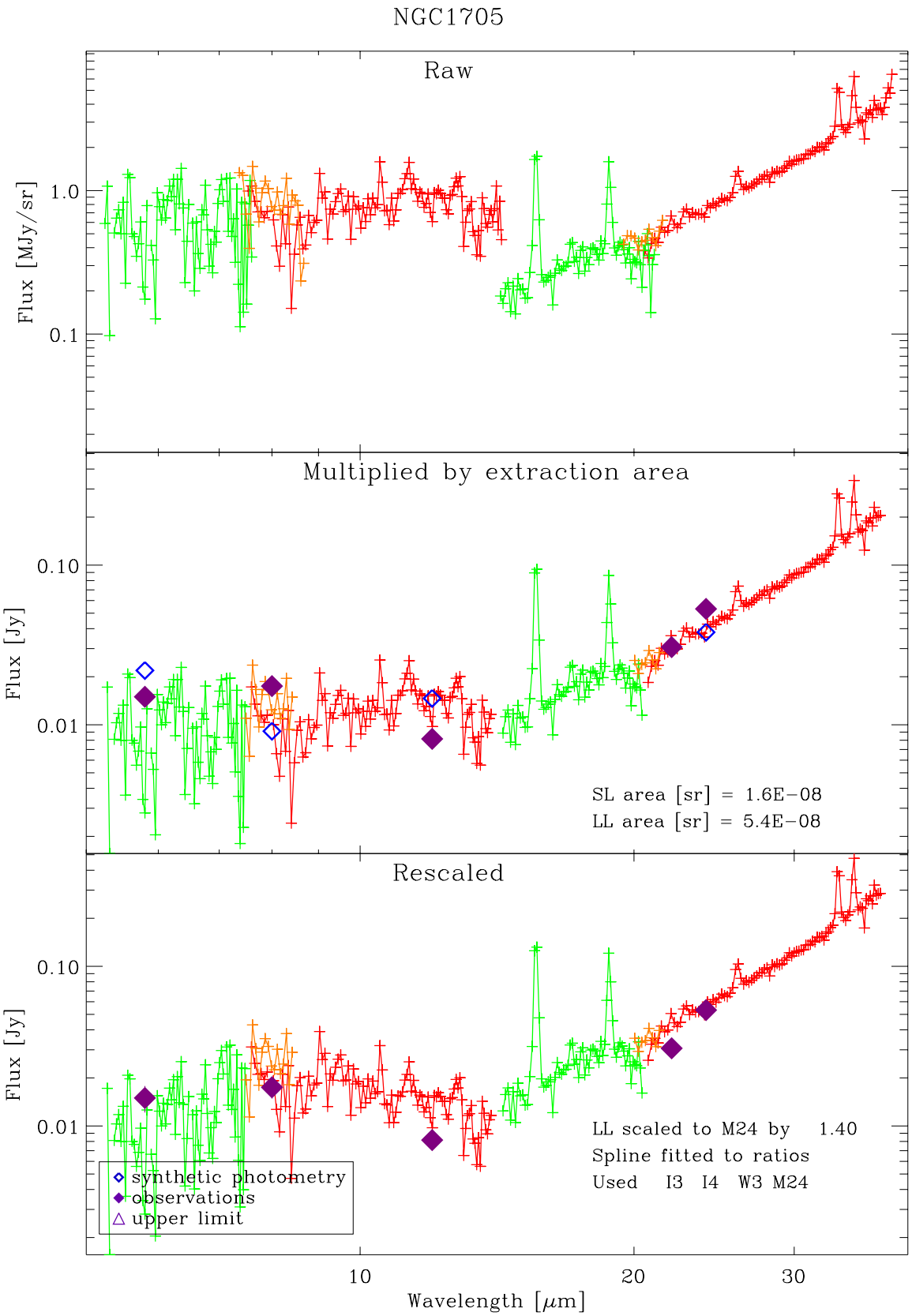
NGC1705
Raw
Flux [MJy/sr]
1.0
0.1
Multiplied by extraction area
Flux [Jy]
0.10
0.01
SL area [sr] = 1.6E−08
LL area [sr] = 5.4E−08
Rescaled
Flux [Jy]
0.10
0.01
LL scaled to M24 by 1.40
Spline fitted to ratios
Used I3 I4 W3 M24
synthetic photometry
observations
upper limit
10
20
30
Wavelength [μm]

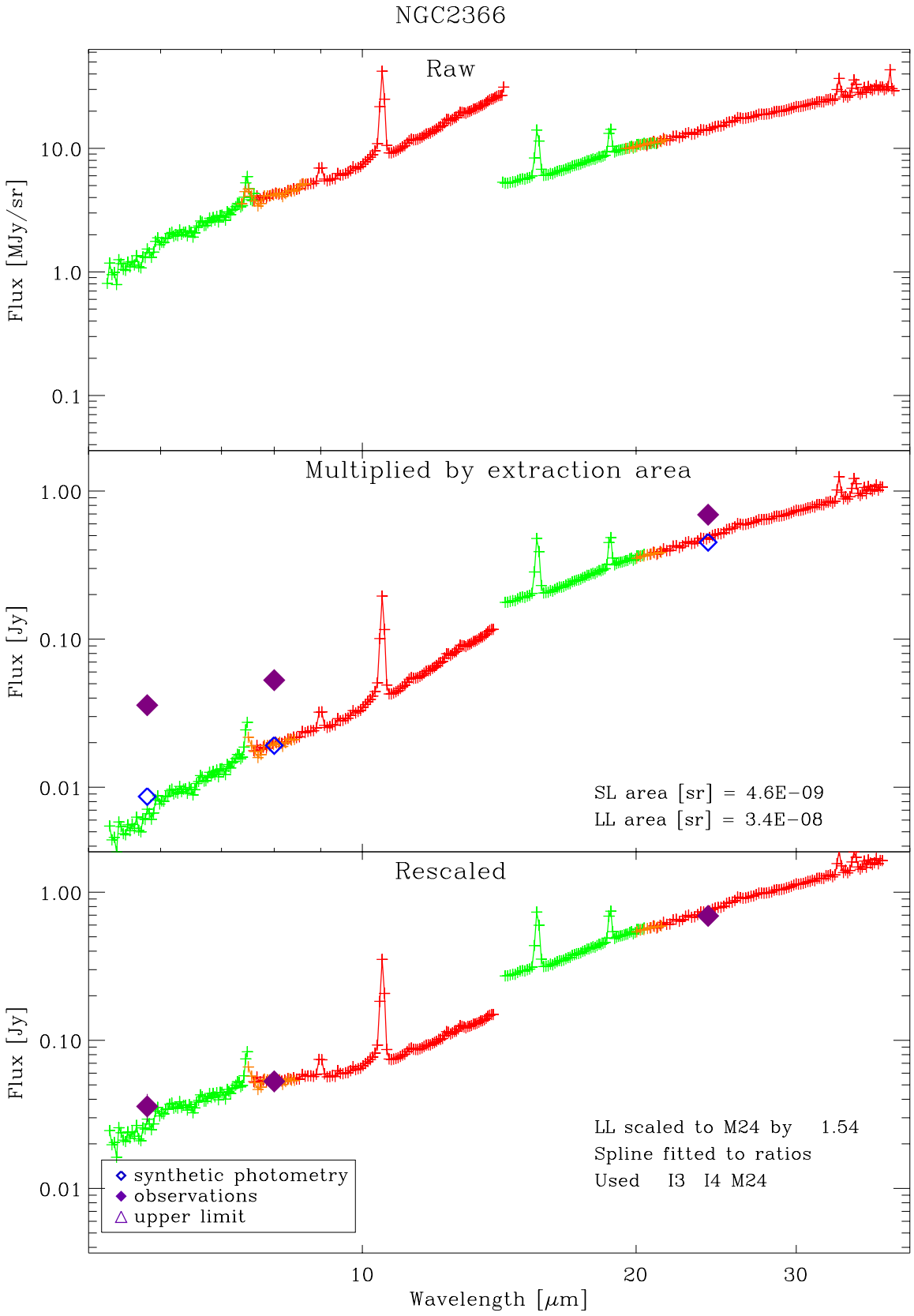
NGC2366
Raw
Flux [MJy/sr]
10.0
1.0
0.1
Multiplied by extraction area
Flux [Jy]
1.00
0.10
0.01
SL area [sr] = 4.6E−09
LL area [sr] = 3.4E−08
Rescaled
Flux [Jy]
1.00
0.10
0.01
LL scaled to M24 by 1.54
Spline fitted to ratios
Used I3 I4 M24
synthetic photometry
observations
upper limit
10
20
30
Wavelength [μm]

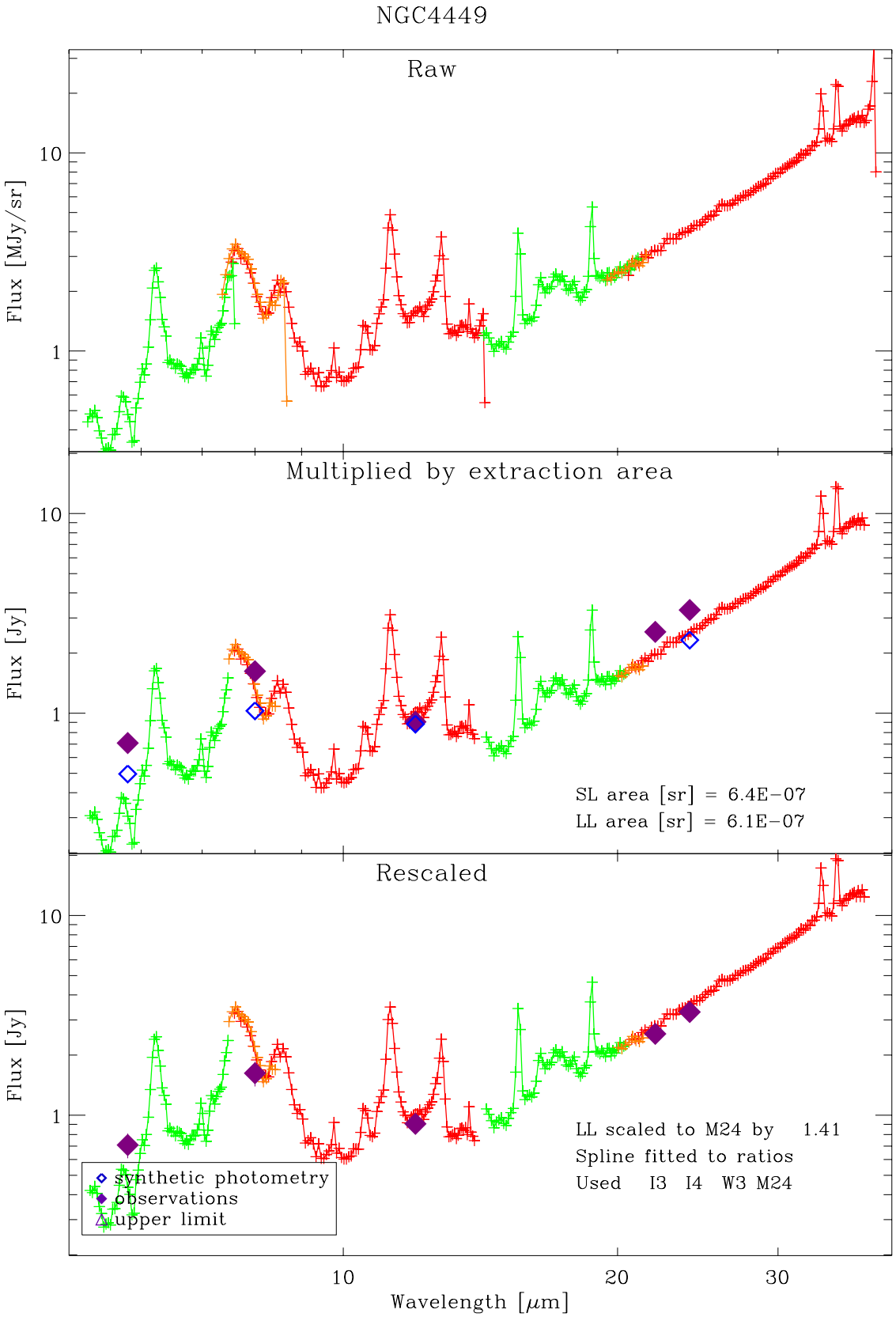
NGC4449
Raw
Flux [MJy/sr]
10
1
Multiplied by extraction area
Flux [Jy]
SL area [sr] = 6.4E−07
LL area [sr] = 6.1E−07
Rescaled
LL scaled to M24 by 1.41
Spline fitted to ratios
Used I3 I4 W3 M24
synthetic photometry
observations
upper limit
10
20
30
Wavelength [μm]

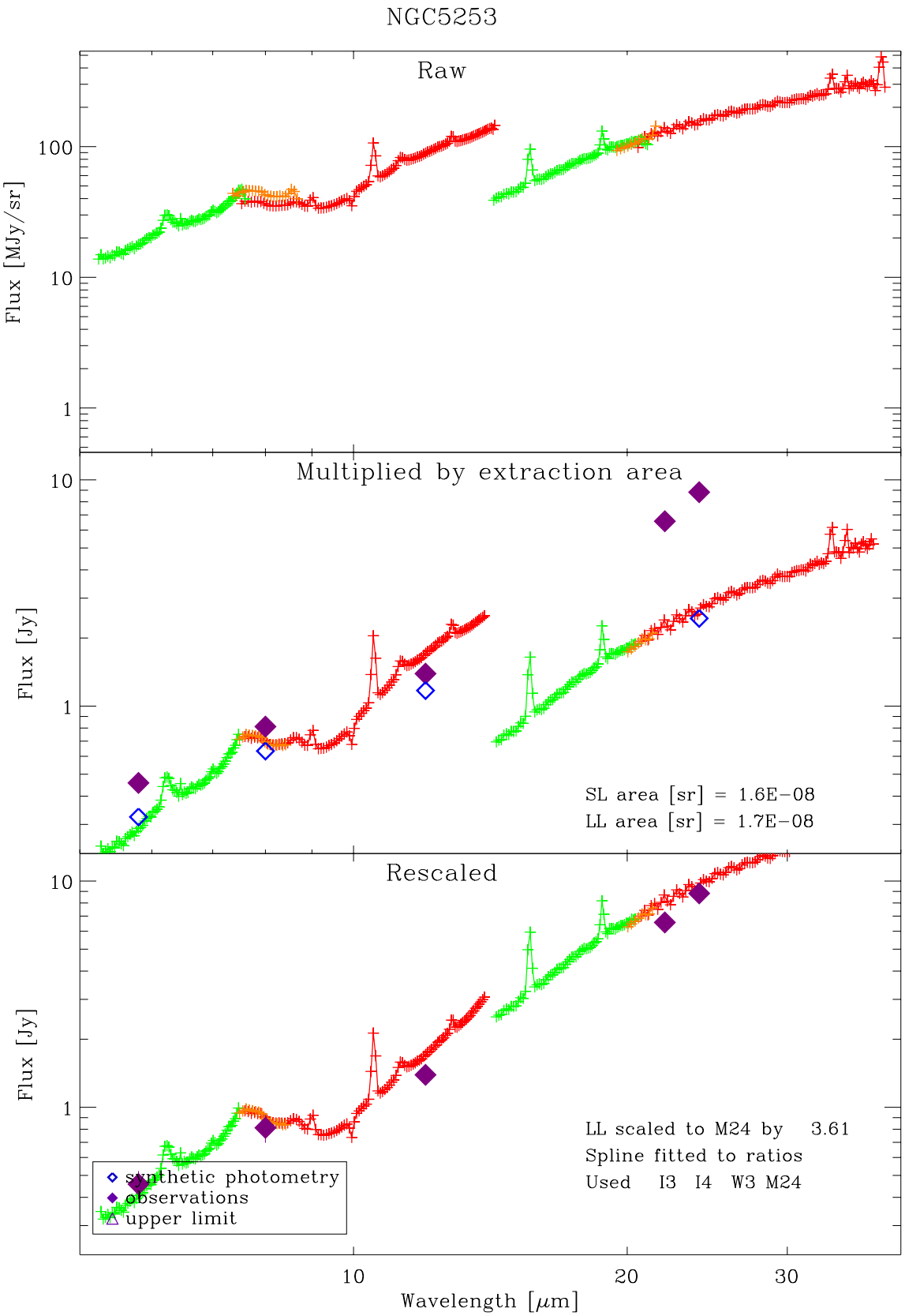
NGC5253
Raw
Flux [MJy/sr]
100
10
1
Multiplied by extraction area
Flux [Jy]
10
1
SL area [sr] = 1.6E−08
LL area [sr] = 1.7E−08
Rescaled
Flux [Jy]
10
1
LL scaled to M24 by 3.61
Spline fitted to ratios
Used I3 I4 W3 M24
synthetic photometry
observations
upper limit
10
20
30
Wavelength [μm]

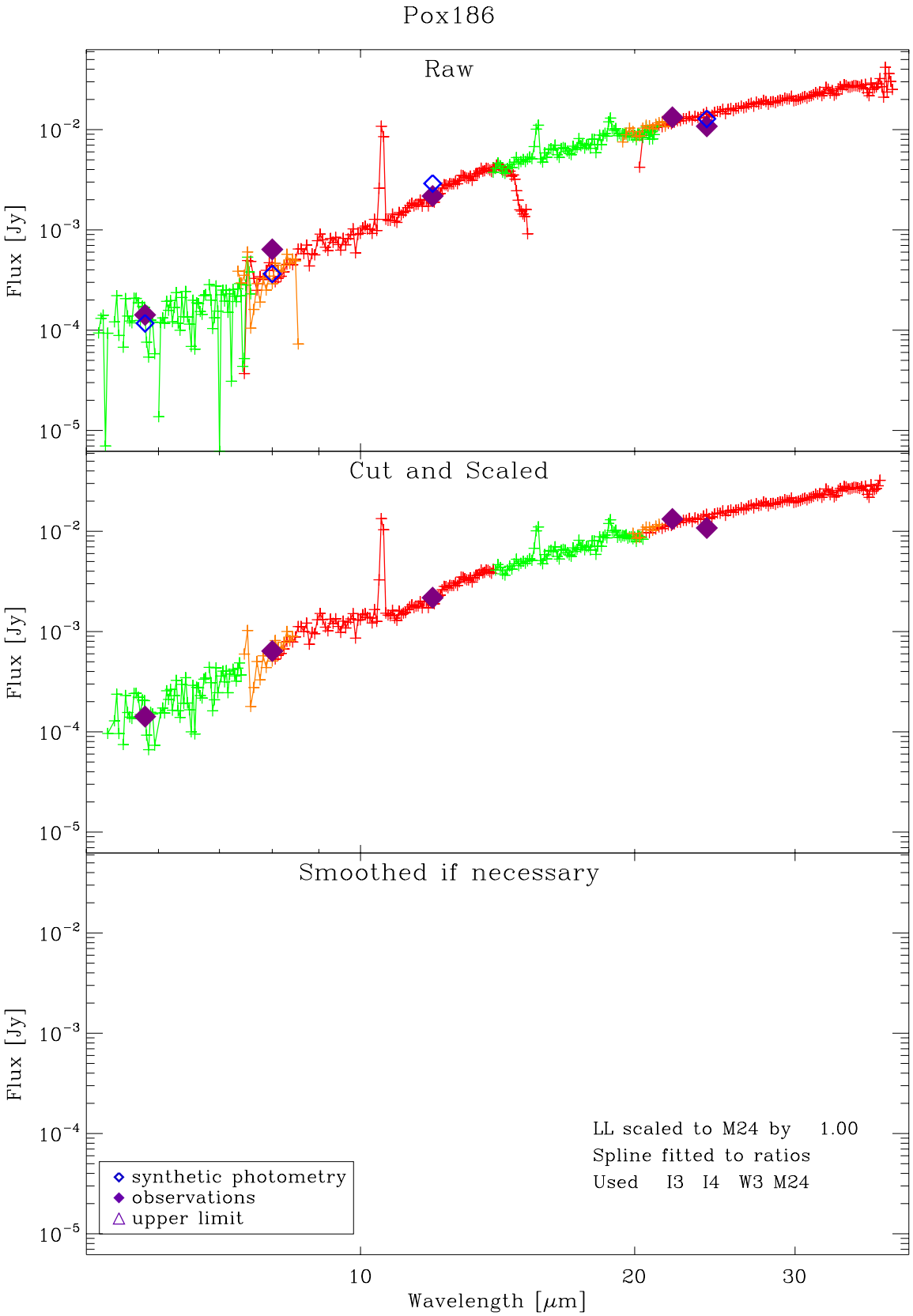
Pox186
Raw
Cut and Scaled
Smoothed if necessary
Flux [Jy]
Wavelength [μm]
LL scaled to M24 by 1.00
Spline fitted to ratios
Used I3 I4 W3 M24
synthetic photometry
observations
upper limit

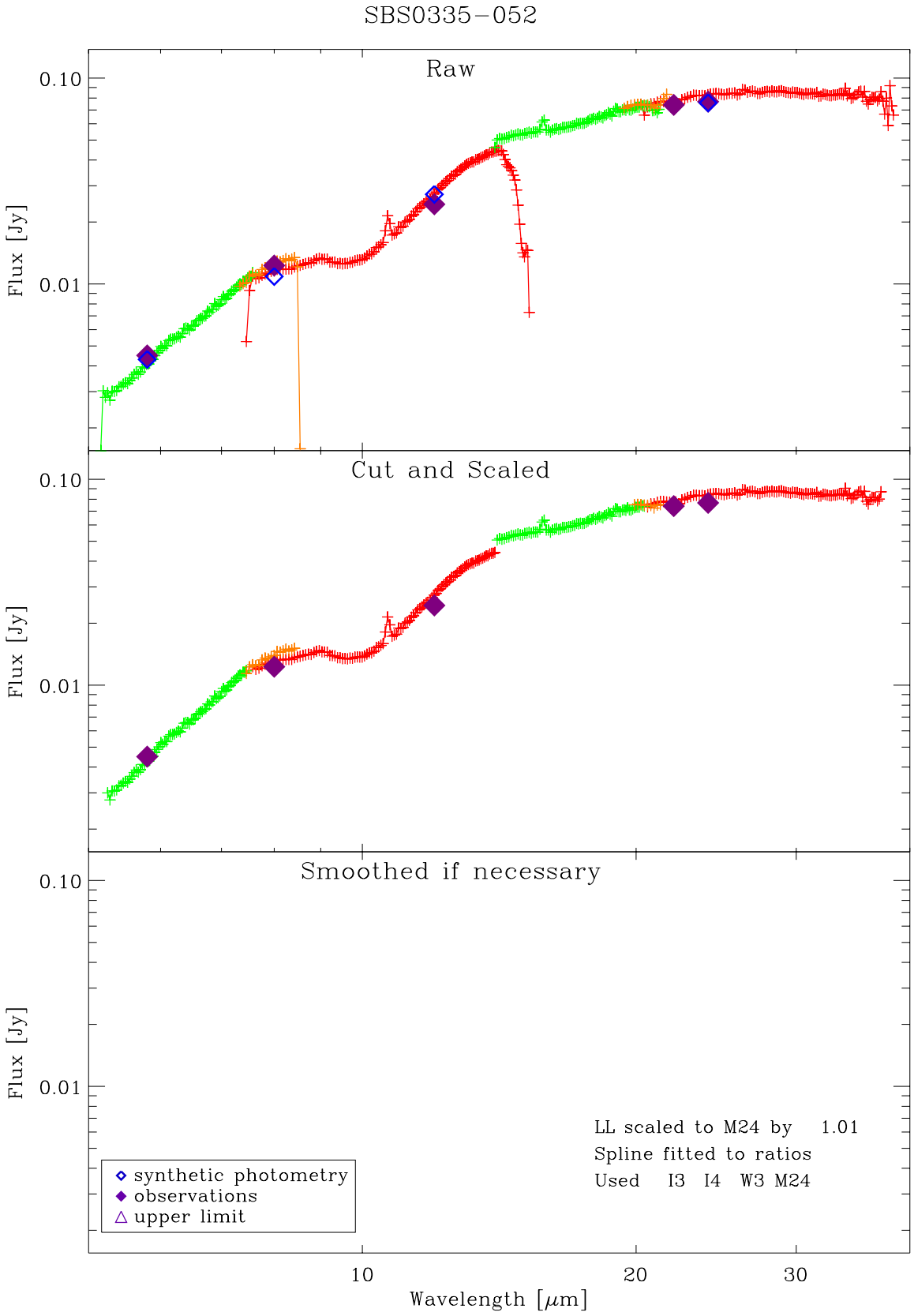
SBS0335−052
Raw
Cut and Scaled
Smoothed if necessary
Flux [Jy]
0.10
0.01
10
20
30
Wavelength [μm]
synthetic photometry
observations
upper limit
LL scaled to M24 by 1.01
Spline fitted to ratios
Used I3 I4 W3 M24

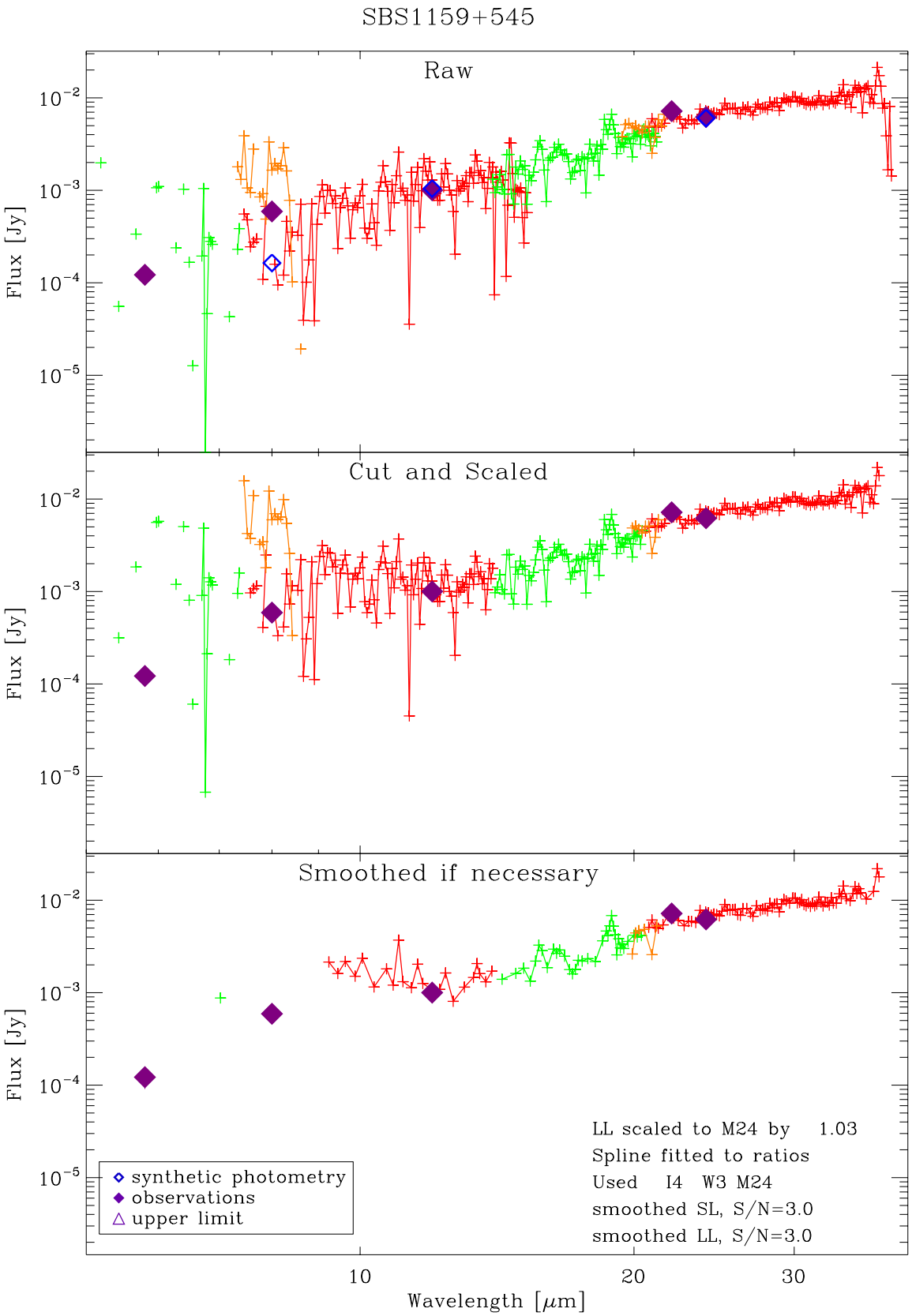
SBS1159+545
Raw
Cut and Scaled
Smoothed if necessary
Flux [Jy]
Wavelength [μm]
synthetic photometry
observations
upper limit
LL scaled to M24 by 1.03
Spline fitted to ratios
Used I4 W3 M24
smoothed SL, S/N=3.0
smoothed LL, S/N=3.0

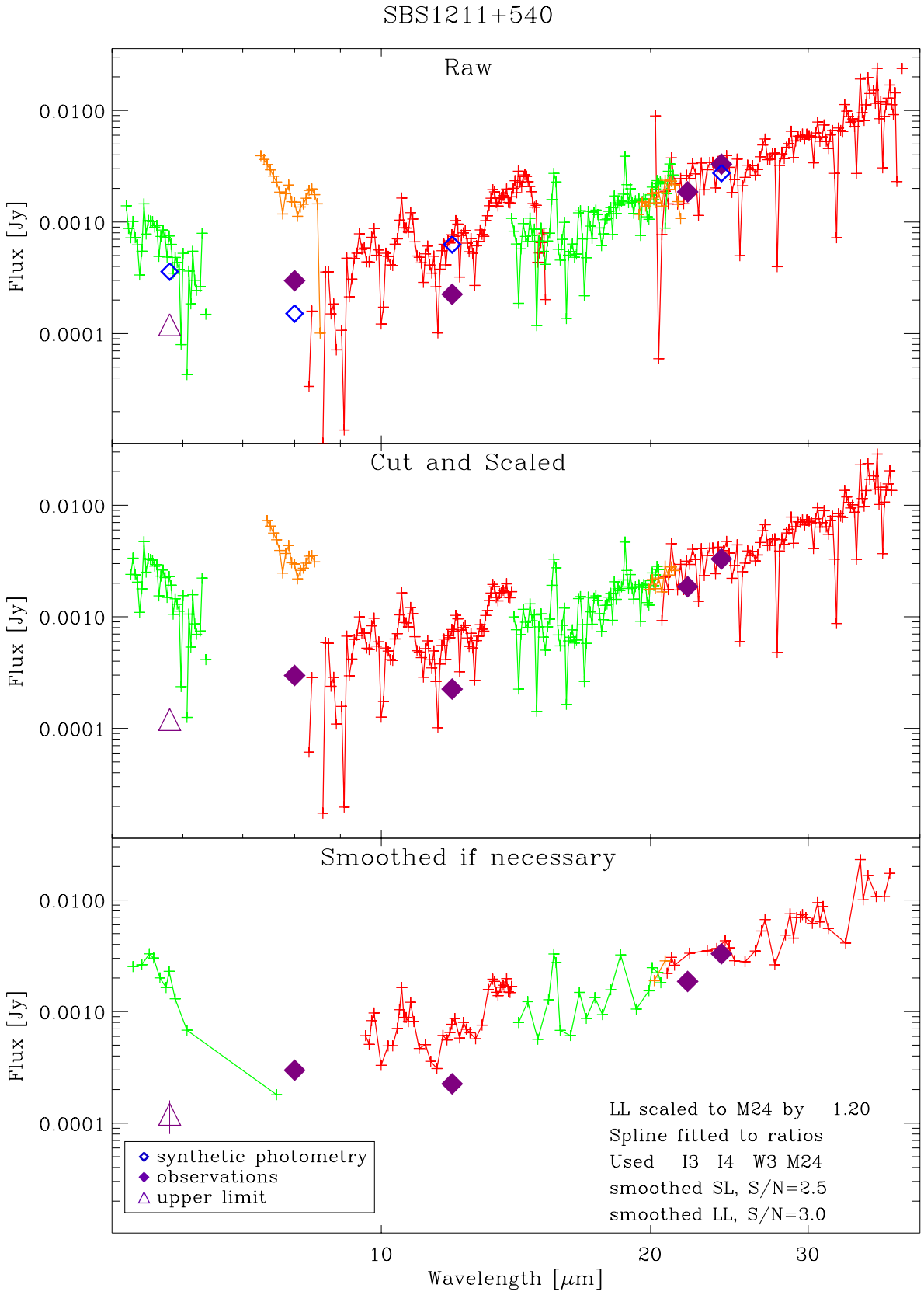
SBS1211+540
Raw
Cut and Scaled
Smoothed if necessary
Flux [Jy]
0.0100
0.0010
0.0001
10
20
30
Wavelength [μm]
synthetic photometry
observations
upper limit
LL scaled to M24 by 1.20
Spline fitted to ratios
Used I3 I4 W3 M24
smoothed SL, S/N=2.5
smoothed LL, S/N=3.0

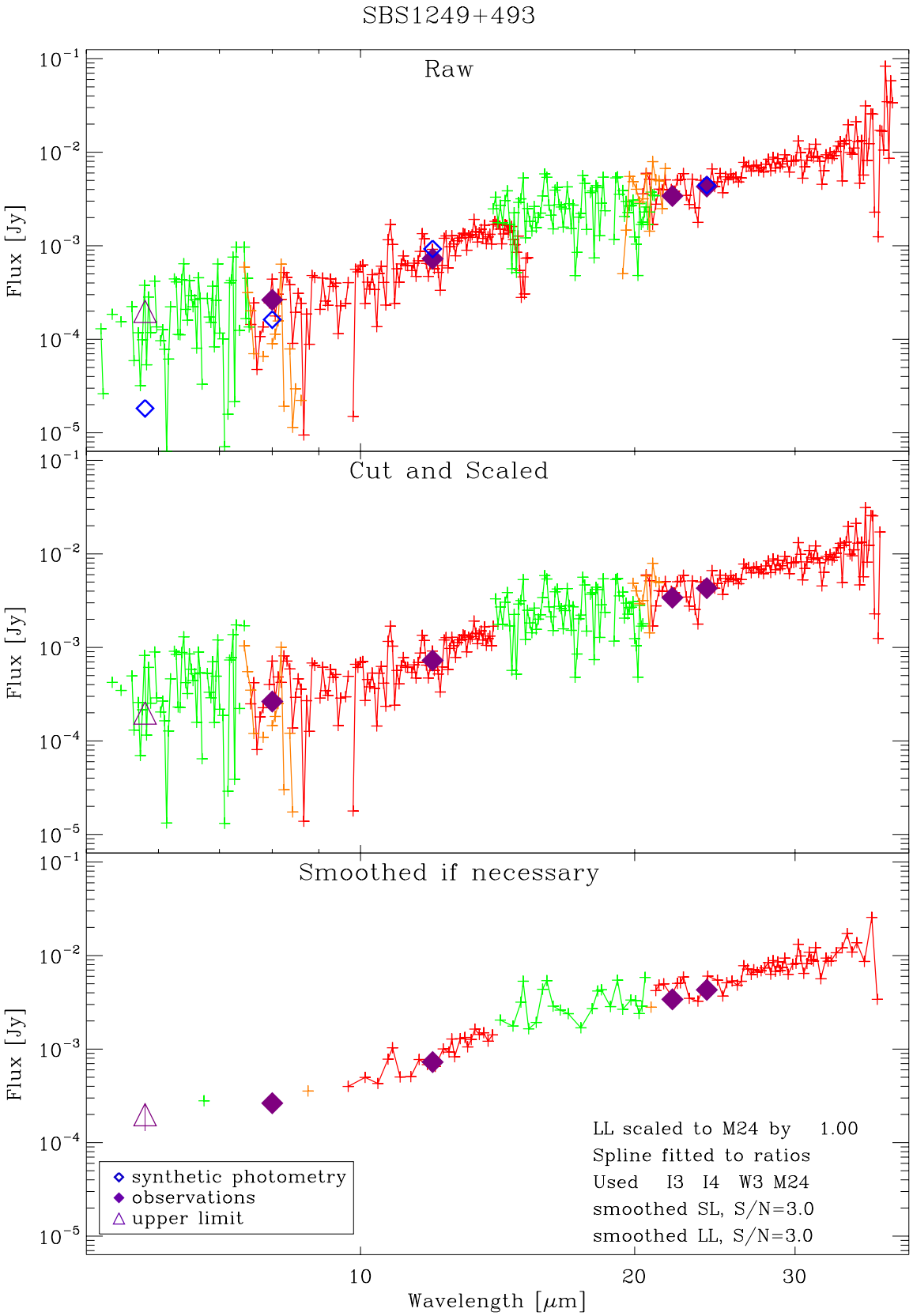
SBS1249+493
Raw
Cut and Scaled
Smoothed if necessary
Flux [Jy]
Wavelength [μm]
synthetic photometry
observations
upper limit
LL scaled to M24 by 1.00
Spline fitted to ratios
Used I3 I4 W3 M24
smoothed SL, S/N=3.0
smoothed LL, S/N=3.0

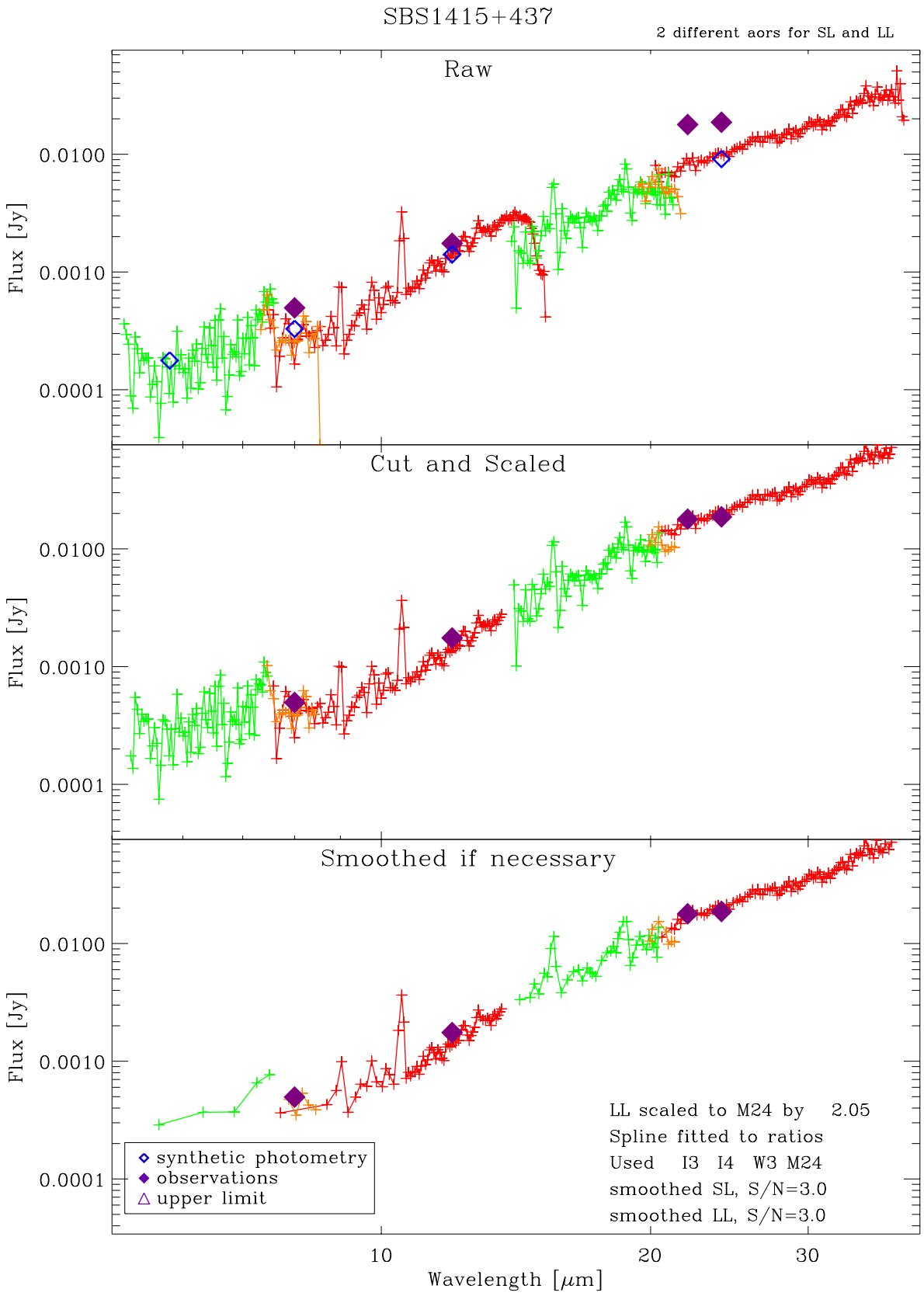
SBS1415+437
2 different aors for SL and LL
Raw
Cut and Scaled
Smoothed if necessary
Flux [Jy]
0.0100
0.0010
0.0001
10
20
30
Wavelength [μm]
synthetic photometry
observations
upper limit
LL scaled to M24 by 2.05
Spline fitted to ratios
Used I3 I4 W3 M24
smoothed SL, S/N=3.0
smoothed LL, S/N=3.0

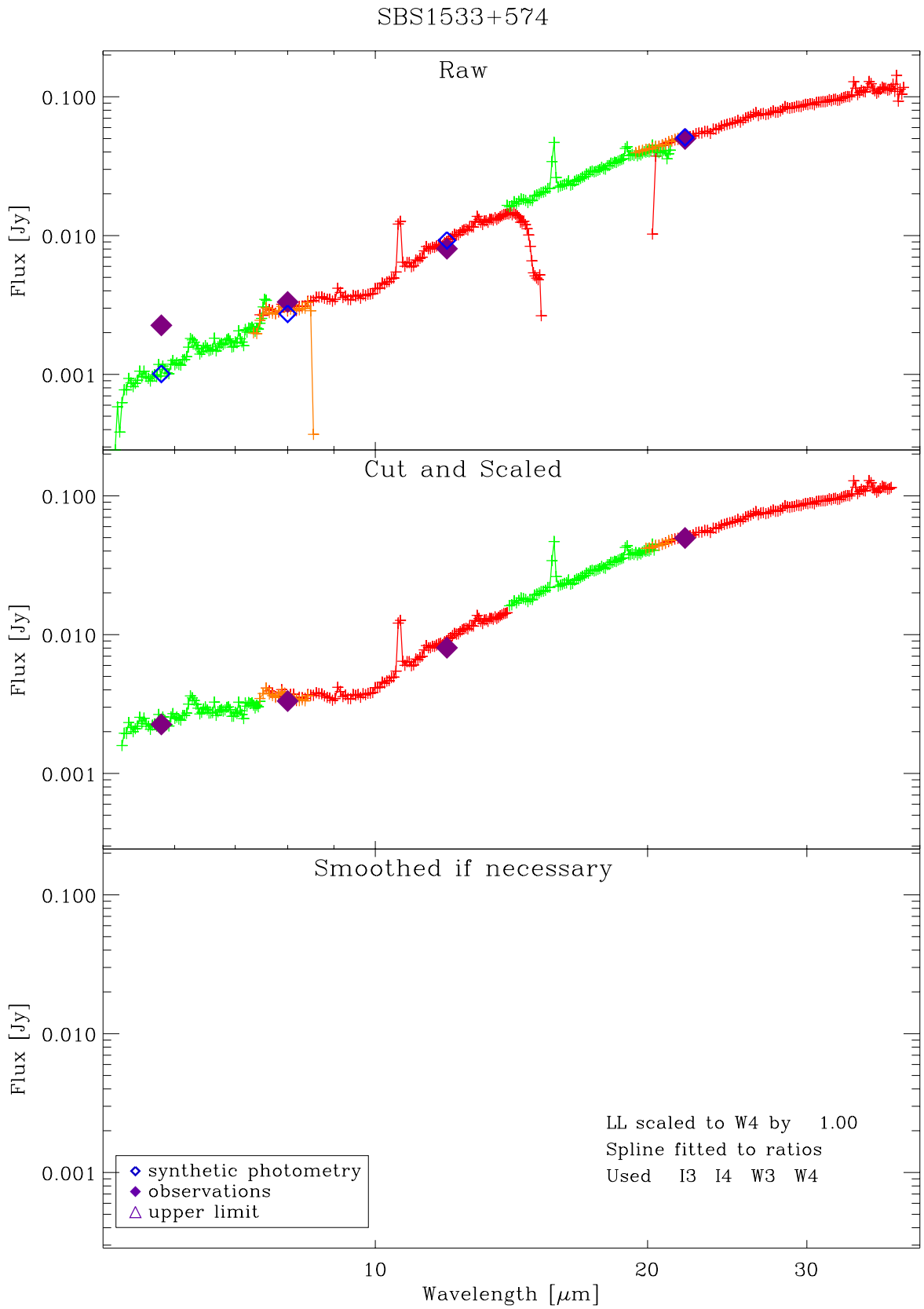
SBS1533+574
Raw
Cut and Scaled
Smoothed if necessary
Flux [Jy]
0.100
0.010
0.001
10
20
30
Wavelength [μm]
synthetic photometry
observations
upper limit
LL scaled to W4 by 1.00
Spline fitted to ratios
Used I3 I4 W3 W4

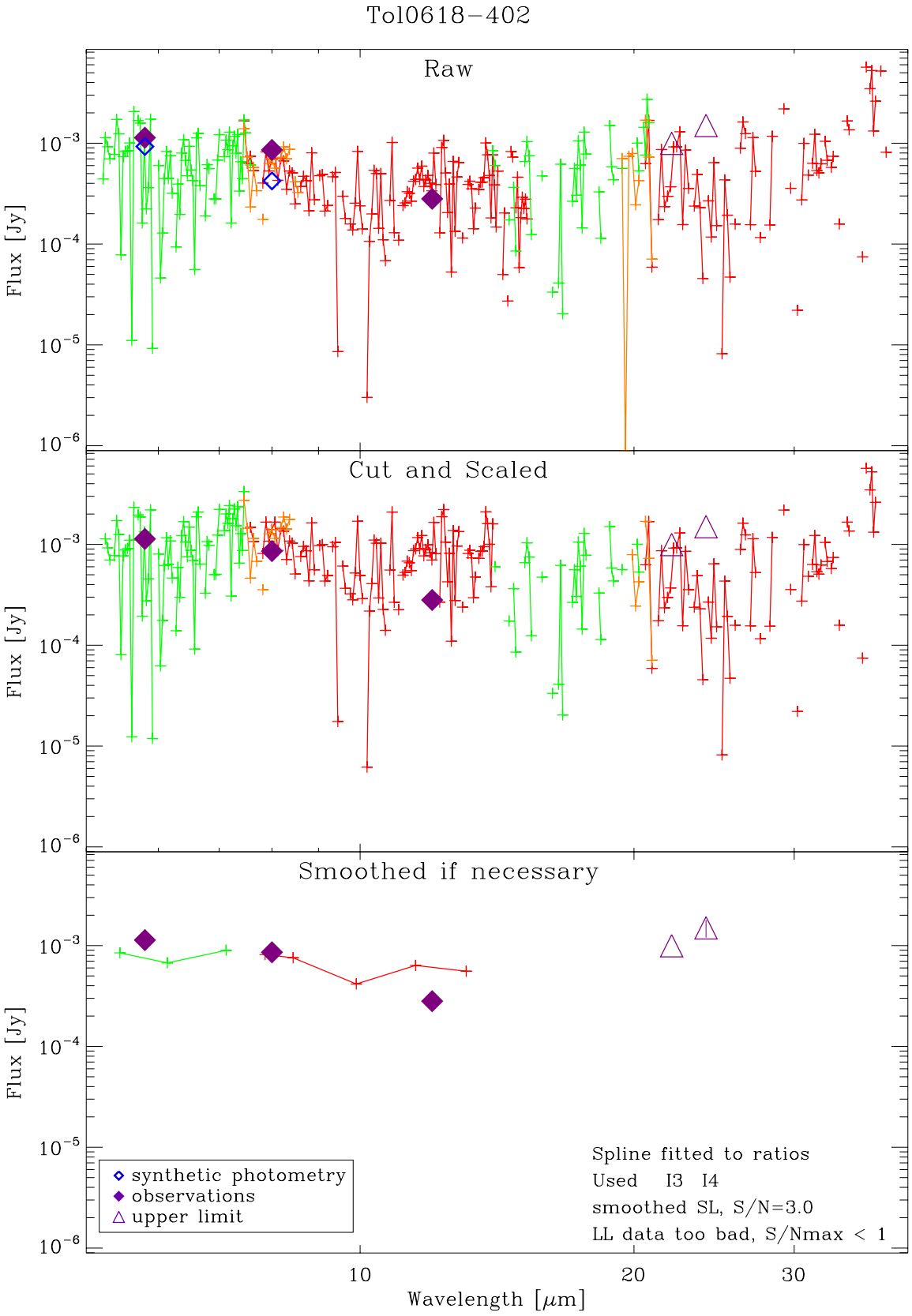
Tol0618−402
Raw
Cut and Scaled
Smoothed if necessary
Flux [Jy]
Wavelength [μm]
synthetic photometry
observations
upper limit
Spline fitted to ratios
Used I3 I4
smoothed SL, S/N=3.0
LL data too bad, S/Nmax < 1

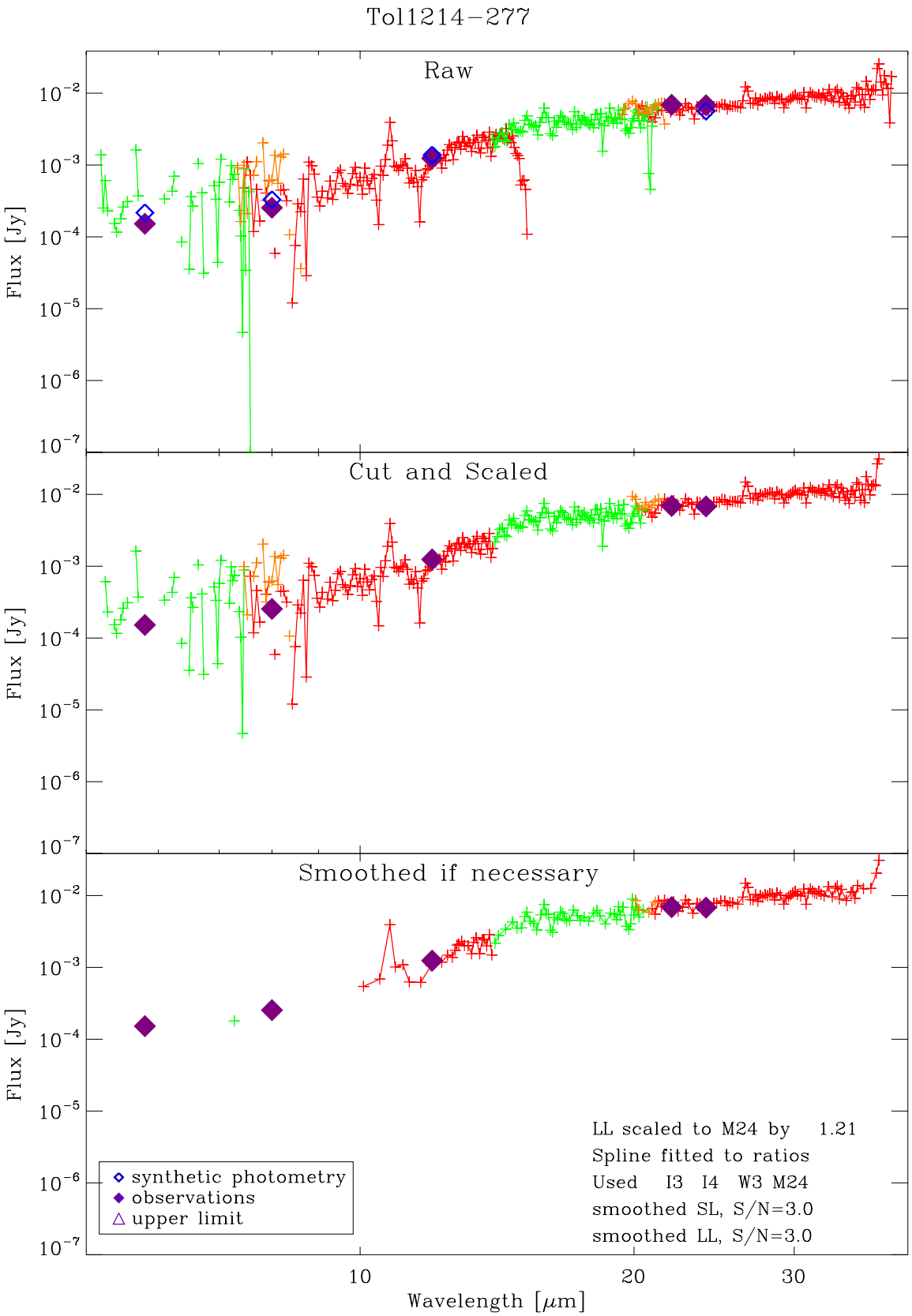
Tol1214−277
Raw
Cut and Scaled
Smoothed if necessary
Flux [Jy]
Wavelength [μm]
synthetic photometry
observations
upper limit
LL scaled to M24 by 1.21
Spline fitted to ratios
Used I3 I4 W3 M24
smoothed SL, S/N=3.0
smoothed LL, S/N=3.0

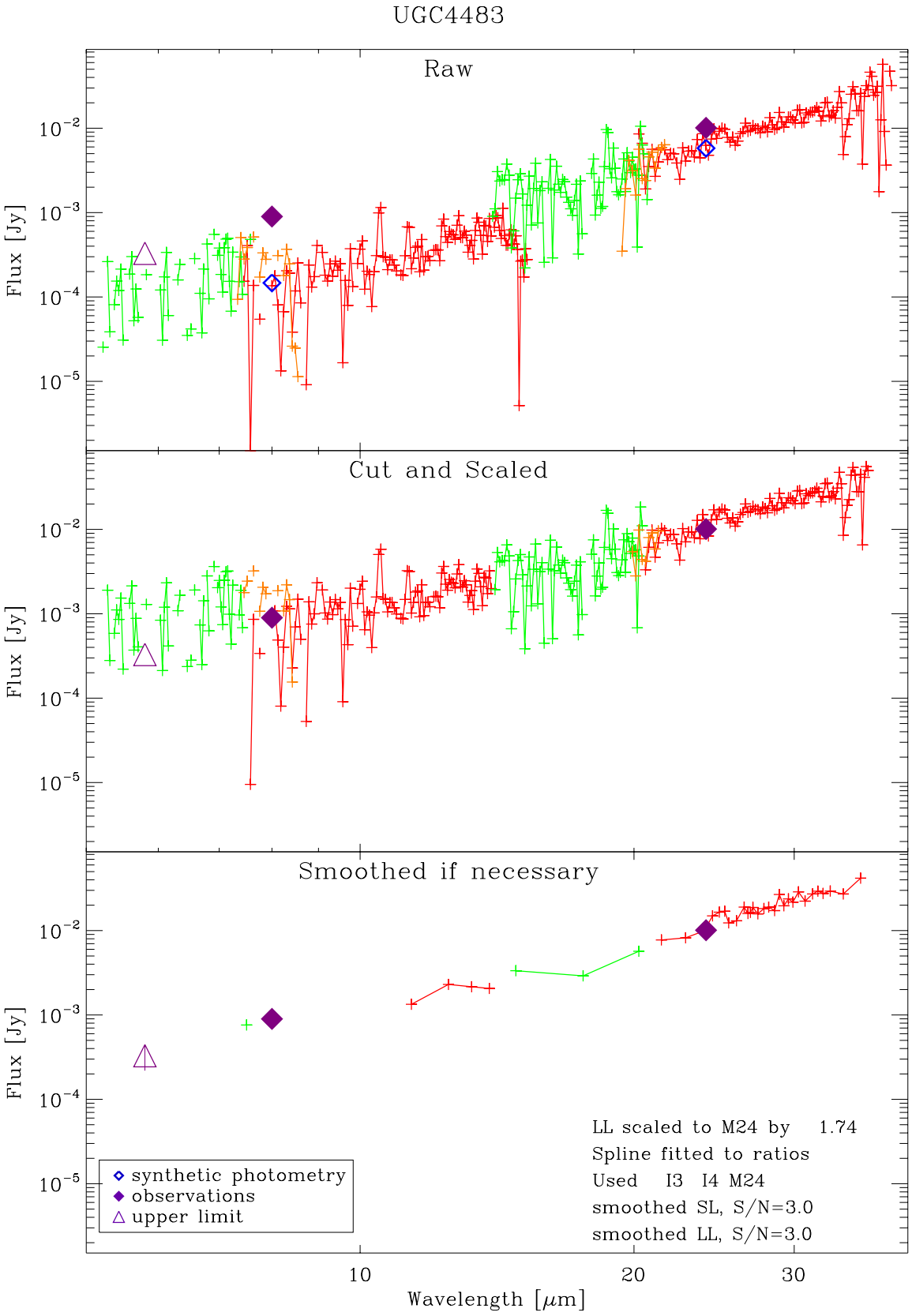
UGC4483
Raw
Cut and Scaled
Smoothed if necessary
Flux [Jy]
Wavelength [μm]
synthetic photometry
observations
upper limit
LL scaled to M24 by 1.74
Spline fitted to ratios
Used I3 I4 M24
smoothed SL, S/N=3.0
smoothed LL, S/N=3.0

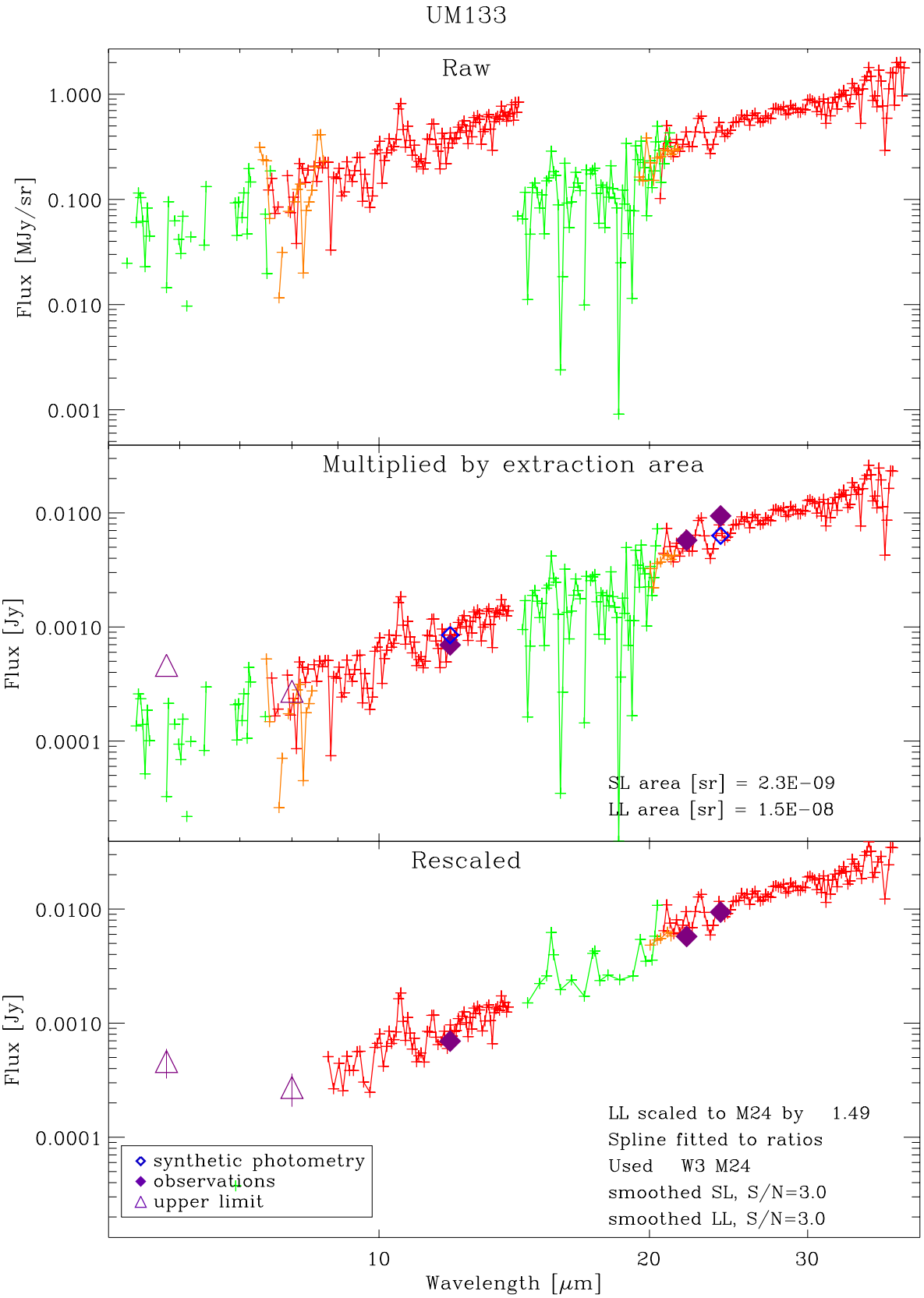
UM133
Raw
Flux [MJy/sr]
1.000
0.100
0.010
0.001
Multiplied by extraction area
Flux [Jy]
0.0100
0.0010
0.0001
SL area [sr] = 2.3E−09
LL area [sr] = 1.5E−08
Rescaled
Flux [Jy]
0.0100
0.0010
0.0001
LL scaled to M24 by 1.49
Spline fitted to ratios
Used W3 M24
smoothed SL, S/N=3.0
smoothed LL, S/N=3.0
synthetic photometry
observations
upper limit
10
20
30
Wavelength [μm]

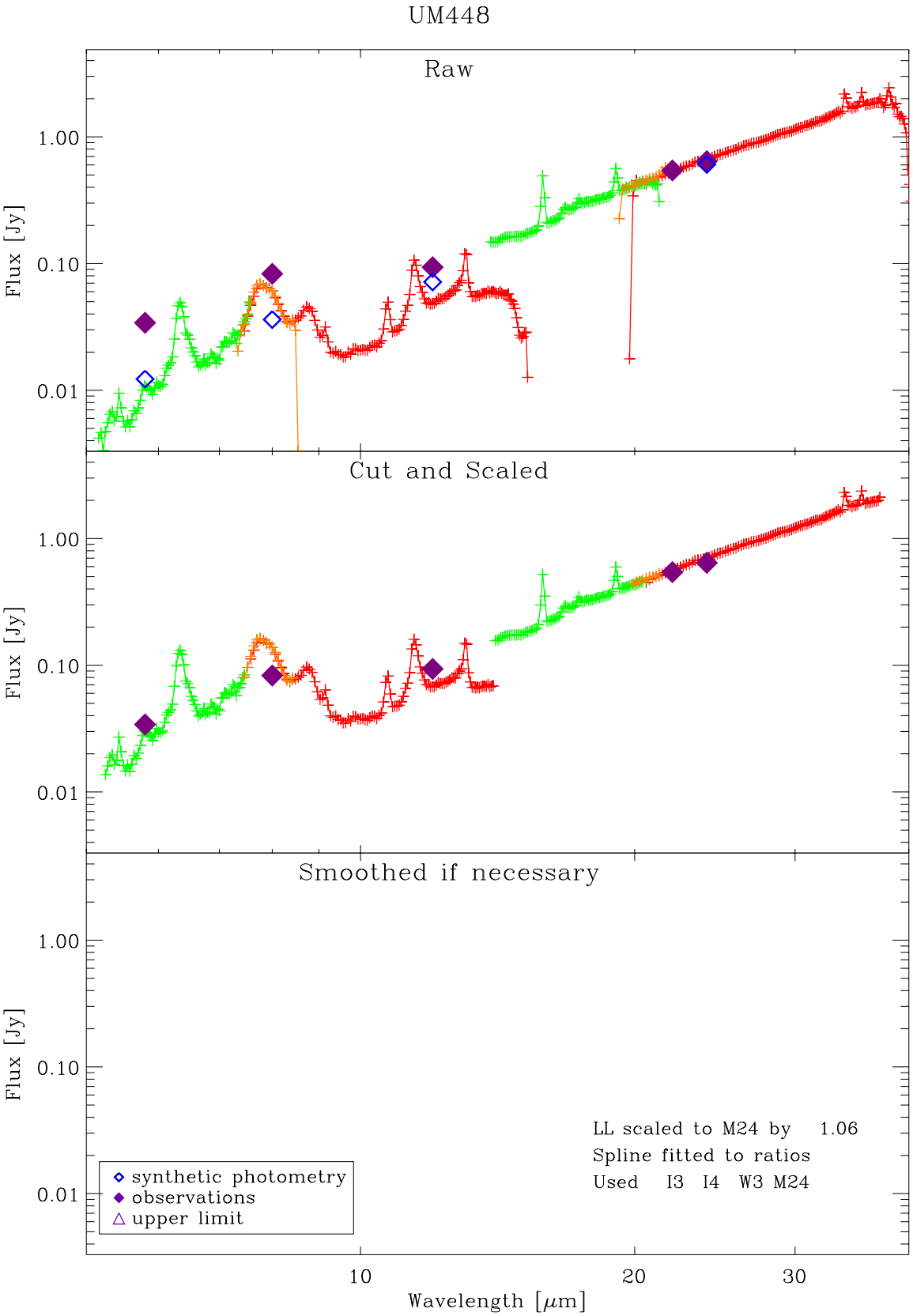
UM448
Raw
Cut and Scaled
Smoothed if necessary
Flux [Jy]
1.00
0.10
0.01
10
20
30
Wavelength [μm]
synthetic photometry
observations
upper limit
LL scaled to M24 by 1.06
Spline fitted to ratios
Used I3 I4 W3 M24

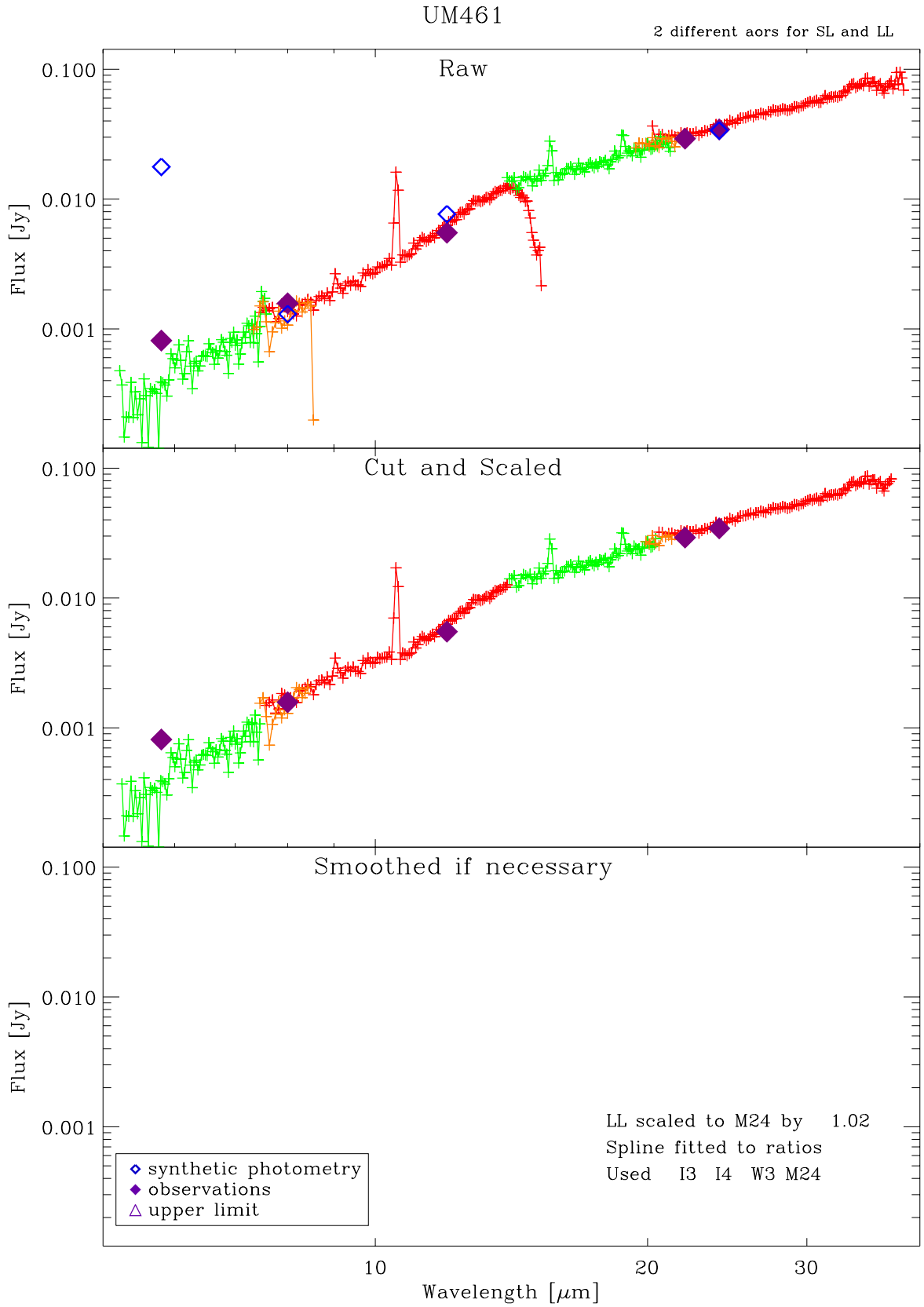
UM461
2 different aors for SL and LL
Raw
Cut and Scaled
Smoothed if necessary
Flux [Jy]
0.100
0.010
0.001
10
20
30
Wavelength [μm]
synthetic photometry
observations
upper limit
LL scaled to M24 by 1.02
Spline fitted to ratios
Used I3 I4 W3 M24

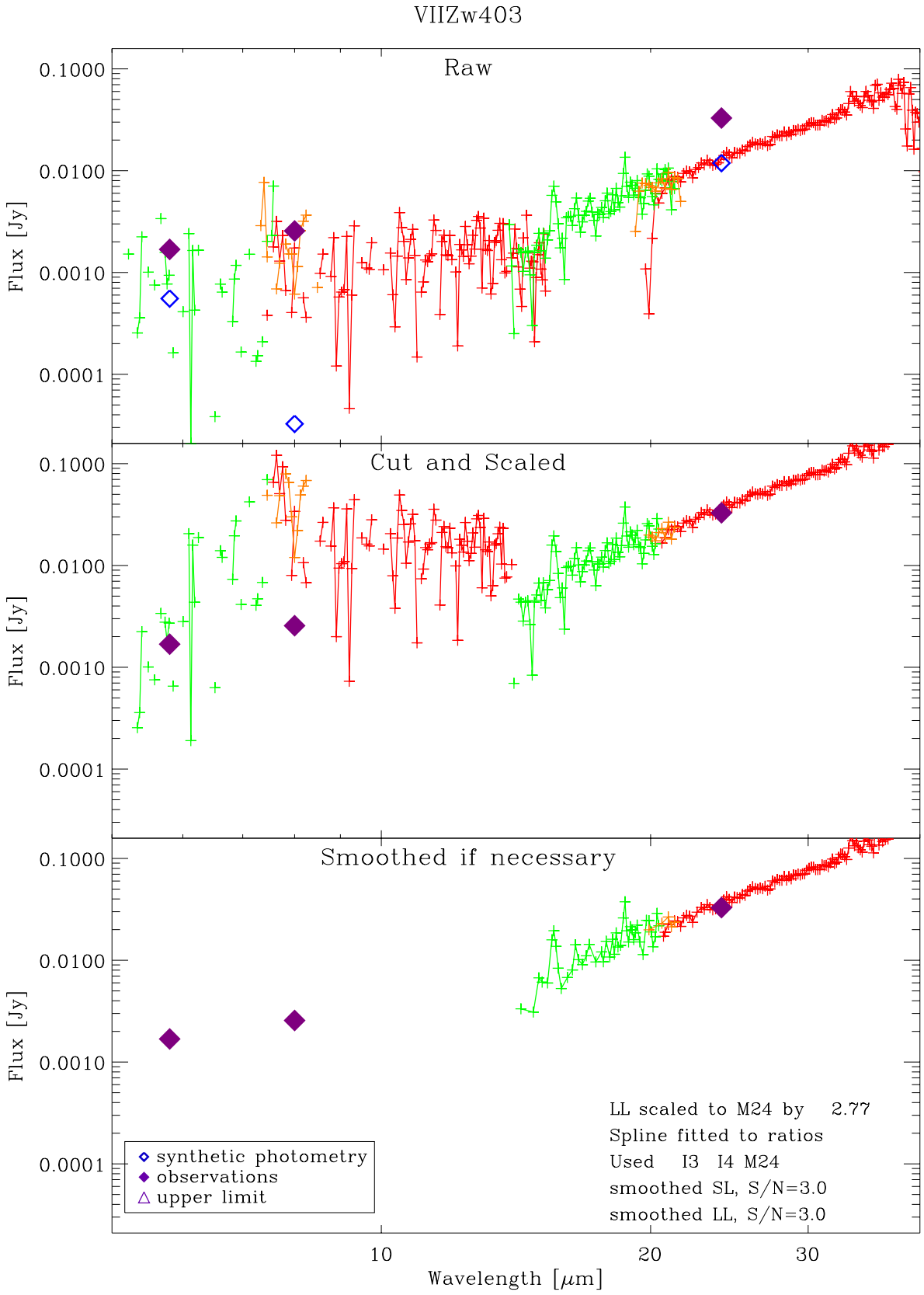
VIIZw403
Raw
Cut and Scaled
Smoothed if necessary
Flux [Jy]
0.1000
0.0100
0.0010
0.0001
10
20
30
Wavelength [μm]
synthetic photometry
observations
upper limit
LL scaled to M24 by 2.77
Spline fitted to ratios
Used I3 I4 M24
smoothed SL, S/N=3.0
smoothed LL, S/N=3.0

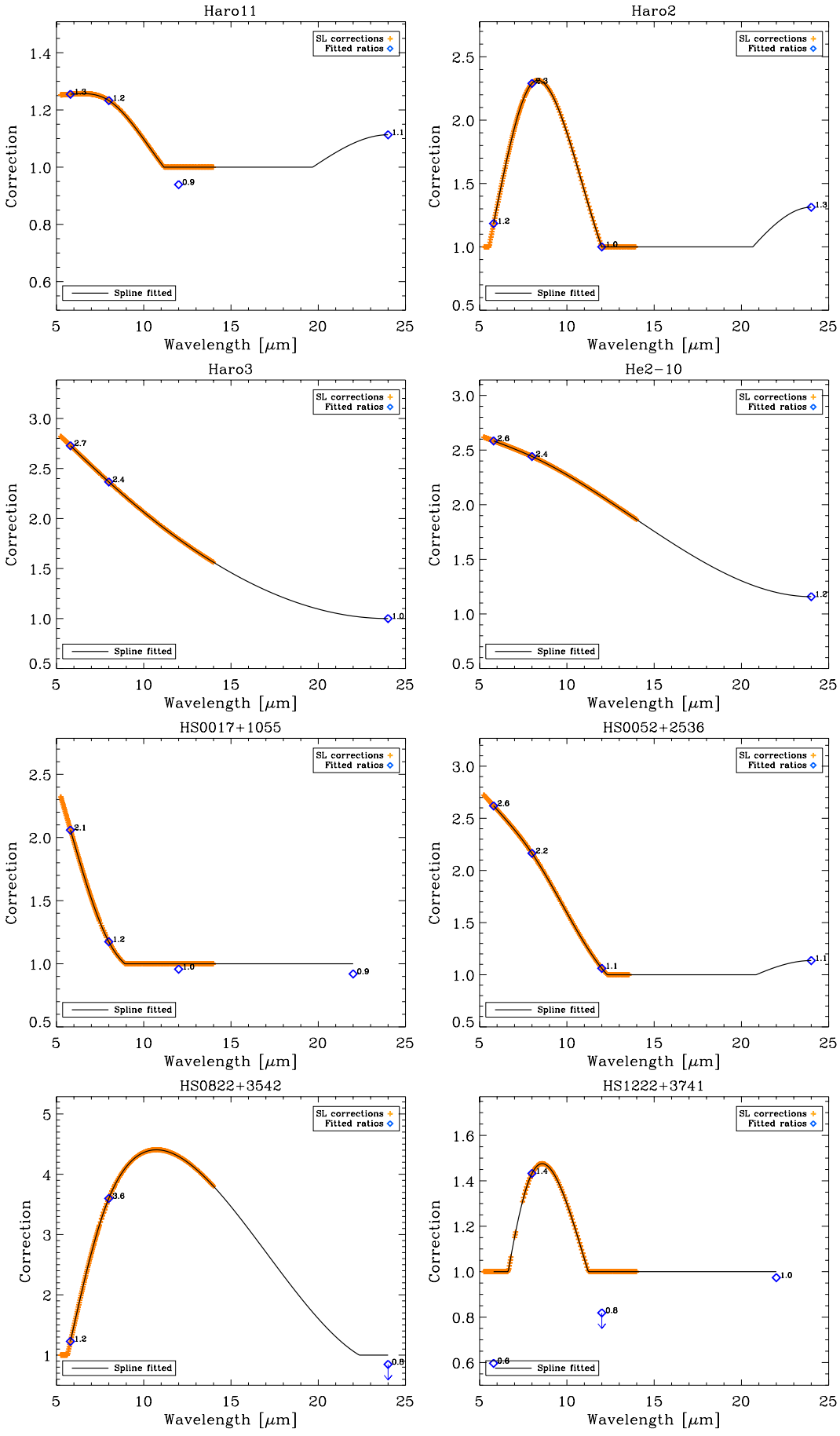

Fig. C.2. See Fig. 6.5 *(right)*

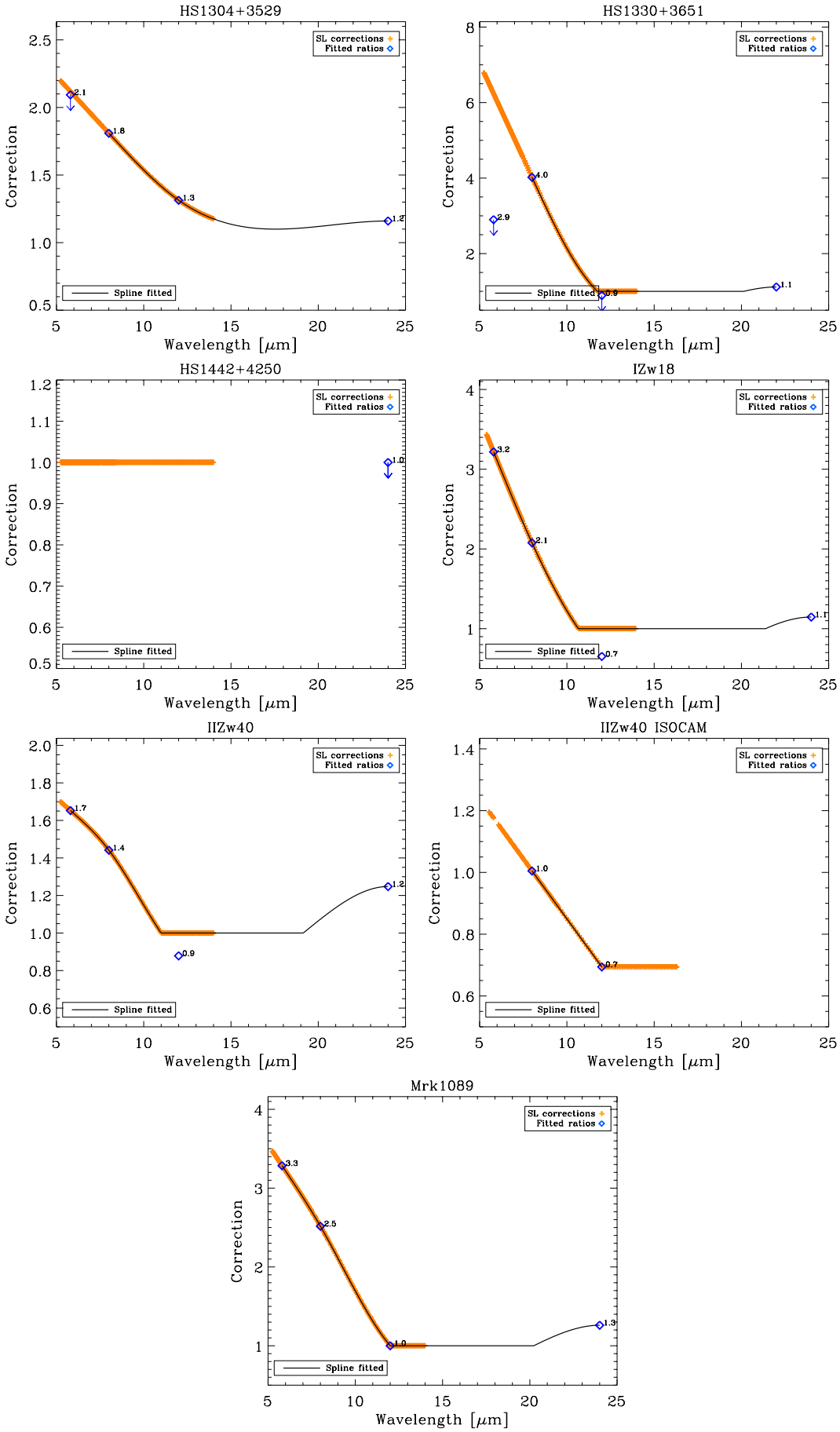
HS1304+3529
HS1330+3651
HS1442+4250
IZw18
IIZw40
IIZw40 ISOCAM
Mrk1089
SL corrections
Fitted ratios
Spline fitted
Correction
Wavelength [μm]

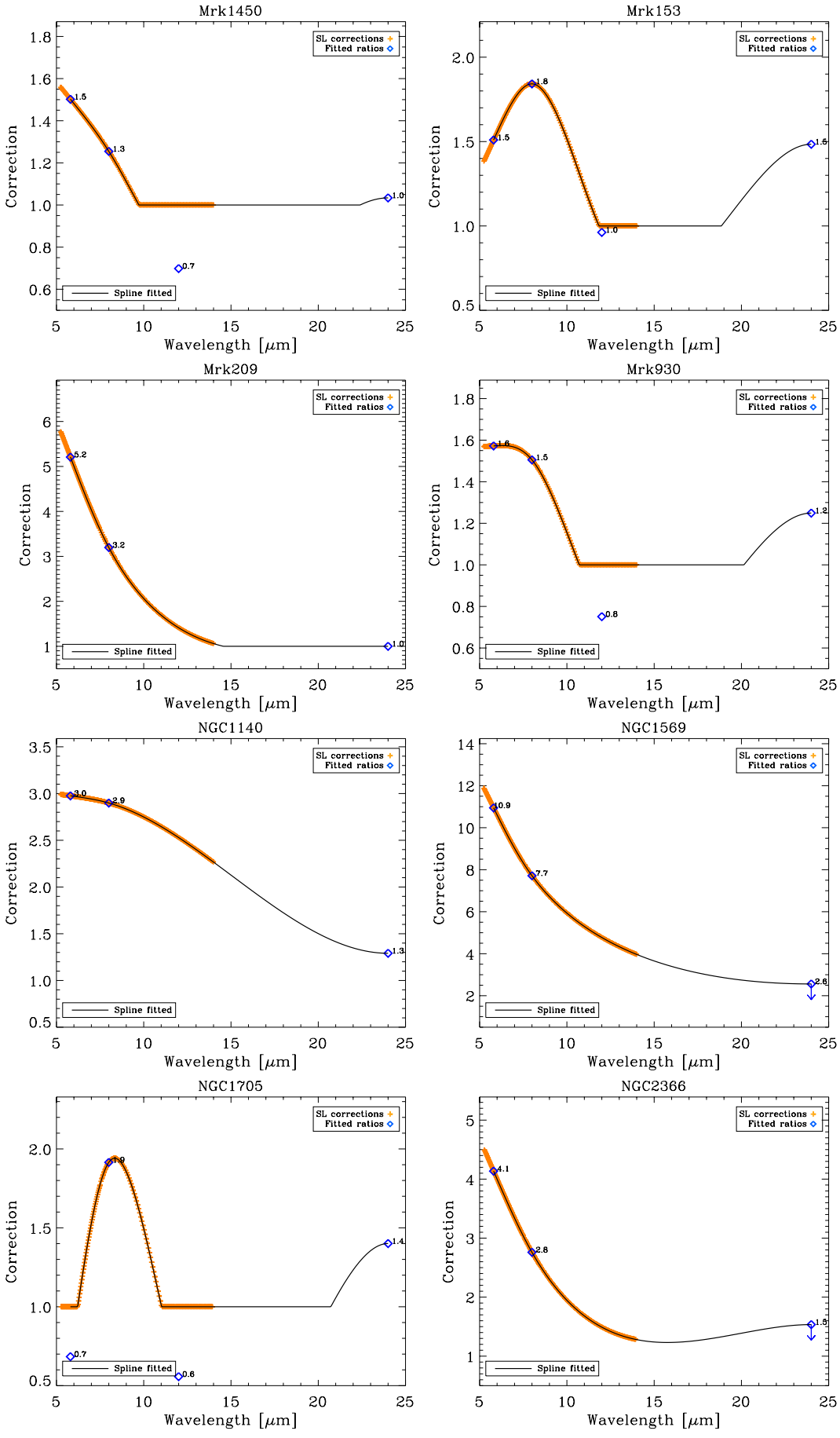
Mrk1450
Mrk153
Mrk209
Mrk930
NGC1140
NGC1569
NGC1705
NGC2366
SL corrections
Fitted ratios
Spline fitted
Correction
Wavelength [μm]

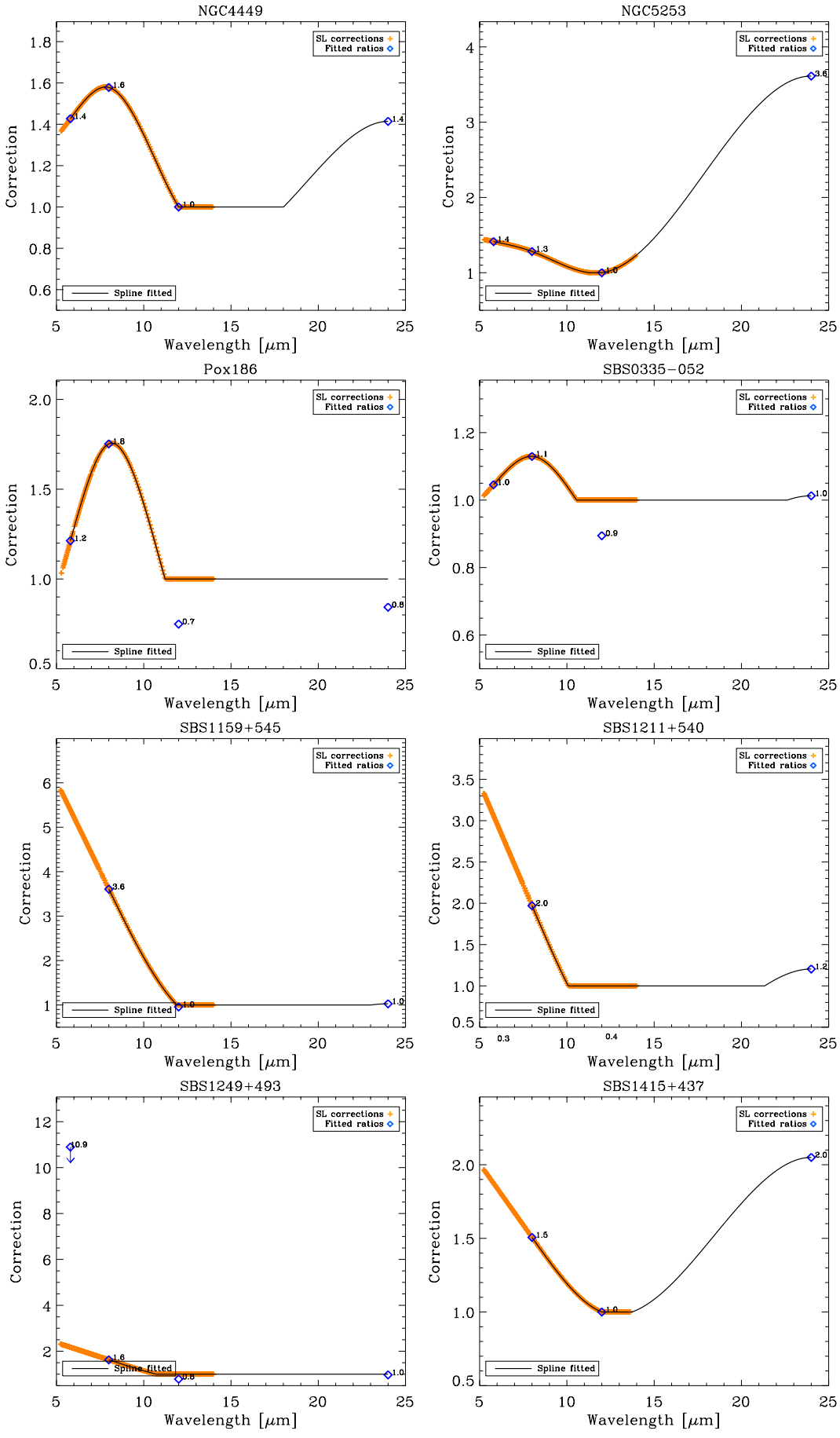
NGC4449
NGC5253
Pox186
SBS0335−052
SBS1159+545
SBS1211+540
SBS1249+493
SBS1415+437
SL corrections
Fitted ratios
Spline fitted
Correction
Wavelength [μm]

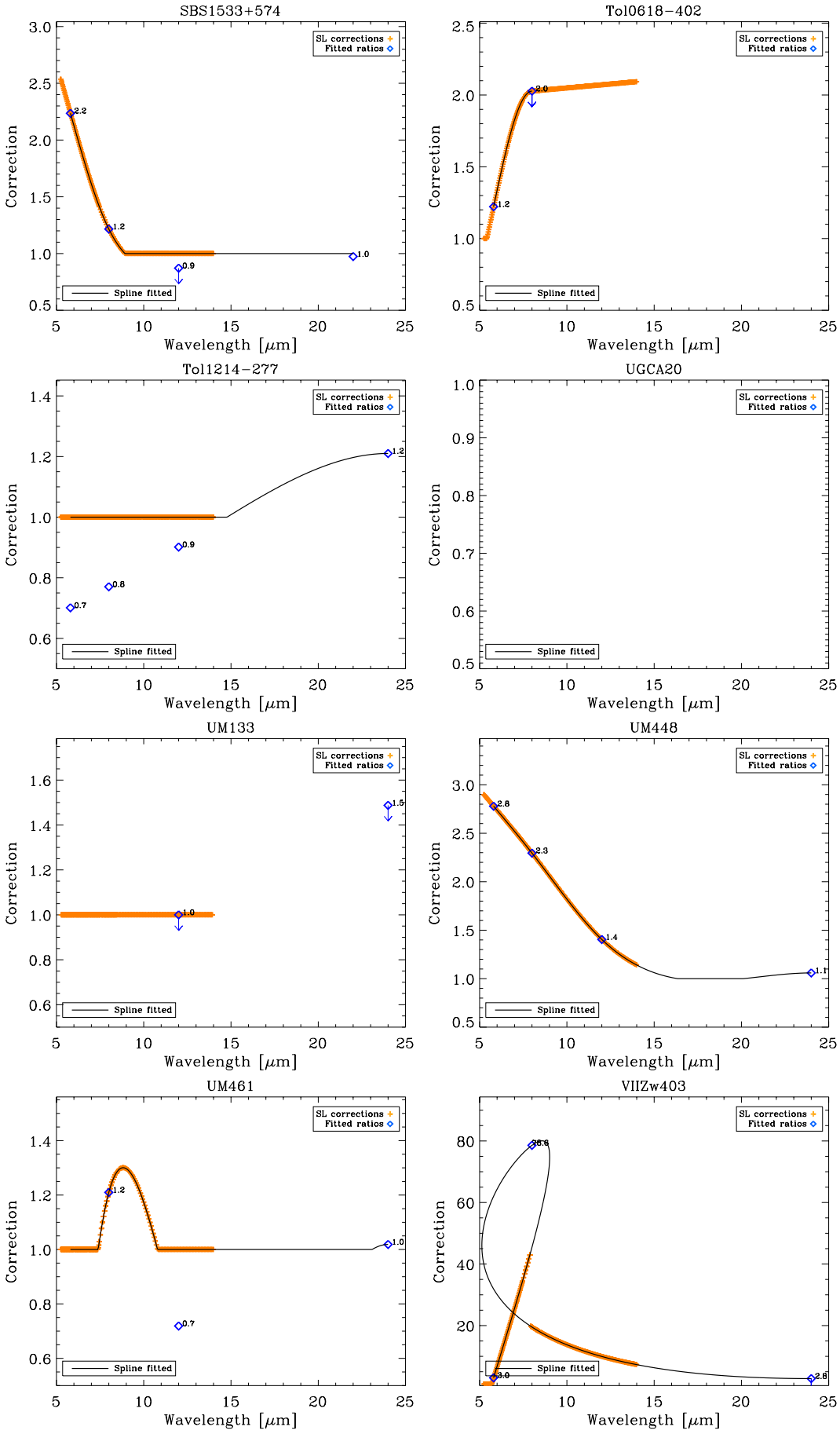
SBS1533+574
Tol0618−402
Tol1214−277
UGCA20
UM133
UM448
UM461
VIIZw403
SL corrections
Fitted ratios
Spline fitted
Correction
Wavelength [μm]

Bibliography

Ackermann, M., Ajello, M., Baldini, L., et al. 2011, ApJ, 726, 81

Adamo, A., Östlin, G., Zackrisson, E., et al. 2010, MNRAS, 407, 870

Albrecht, M., Chini, R., Krügel, E., Müller, S. A. H., & Lemke, R. 2004, A&A, 414, 141

Albrecht, M., Krügel, E., & Chini, R. 2007, A&A, 462, 575

Aller, L. H., ed. 1984, Astrophysics and Space Science Library, Vol. 112, Physics of thermal gaseous nebulae

Aloisi, A., Clementini, G., Tosi, M., et al. 2007, ApJ, 667, L151

Aloisi, A., van der Marel, R. P., Mack, J., et al. 2005, ApJ, 631, L45

Amblard, A., Cooray, A., Serra, P., et al. 2010, A&A, 518, L9

Anderson, L. D., Zavagno, A., Rodón, J. A., et al. 2010, A&A, 518, L99

Aniano, G., Draine, B. T., Calzetti, D., et al. 2012, ApJ, 756, 138

Arendt, R. G., Odegard, N., Weiland, J. L., et al. 1998, ApJ, 508, 74

Asano, R. S., Takeuchi, T. T., Hirashita, H., & Inoue, A. K. 2013, Earth, Planets, and Space, 65, 213

Asplund, M., Grevesse, N., Sauval, A. J., & Scott, P. 2009, ARA&A, 47, 481

Auld, R., Bianchi, S., Smith, M. W. L., et al. 2013, MNRAS, 428, 1880

Baas, F., Israel, F. P., & Koornneef, J. 1994, A&A, 284, 403

Bazell, D. & Dwek, E. 1990, ApJ, 360, 142

Begum, A. & Chengalur, J. N. 2005a, MNRAS, 362, 609

Begum, A. & Chengalur, J. N. 2005b, MNRAS, 362, 609

Bendo, G. J., Dale, D. A., Draine, B. T., et al. 2006, ApJ, 652, 283

Bendo, G. J., Galliano, F., & Madden, S. C. 2012, MNRAS, 423, 197

Bendo, G. J., Joseph, R. D., Wells, M., et al. 2003, AJ, 125, 2361

Bendo, G. J., Wilson, C. D., Pohlen, M., et al. 2010a, A&A, 518, L65

Bendo, G. J., Wilson, C. D., Warren, B. E., et al. 2010b, MNRAS, 402, 1409

Bergvall, N., Zackrisson, E., Andersson, B.-G., et al. 2006, A&A, 448, 513

Bernard, J.-P., Reach, W. T., Paradis, D., et al. 2008, AJ, 136, 919

Bettoni, D., Galletta, G., & García-Burillo, S. 2003, A&A, 405, 5

Bianchi, S. 2013, A&A, 552, A89

Bocchio, M., Jones, A. P., Verstraete, L., et al. 2013, A&A, 556, A6

Bocchio, M., Micelotta, E. R., Gautier, A.-L., & Jones, A. P. 2012, A&A, 545, A124

Bohren, C. F. & Huffman, D. R. 1983, Absorption and scattering of light by small particles

Bolatto, A. D., Jackson, J. M., Wilson, C. D., & Moriarty-Schieven, G. 2000, ApJ, 532, 909

Bolatto, A. D., Wolfire, M., & Leroy, A. K. 2013, ARA&A, 51, 207

Bonatto, C. J. & Pastoriza, M. G. 1990, ApJ, 353, 445

Boquien, M., Calzetti, D., Combes, F., et al. 2011, AJ, 142, 111

Bordalo, V., Plana, H., & Telles, E. 2009, ApJ, 696, 1668

Boselli, A., Ciesla, L., Buat, V., et al. 2010a, A&A, 518, L61

Boselli, A., Ciesla, L., Cortese, L., et al. 2012, A&A, 540, A54

Boselli, A., Eales, S., Cortese, L., et al. 2010b, PASP, 122, 261

Boselli, A., Lequeux, J., & Gavazzi, G. 2002, A&A, 384, 33

Bot, C., Ysard, N., Paradis, D., et al. 2010, A&A, 523, A20+

Böttner, C., Klein, U., & Heithausen, A. 2003, A&A, 408, 493

Boulanger, F., Abergel, A., Bernard, J.-P., et al. 1996, A&A, 312, 256

Braine, J., Duc, P.-A., Lisenfeld, U., et al. 2001, A&A, 378, 51

Bresolin, F. 2007, ApJ, 656, 186

Brinks, E. & Taylor, C. L. 1994, in European Southern Observatory Conference and Workshop Proceedings, Vol. 49, European Southern Observatory Conference and Workshop Proceedings, ed. G. Meylan & P. Prugniel, 263

Brooks, A. M., Governato, F., Booth, C. M., et al. 2007, ApJ, 655, L17

Campbell, A., Terlevich, R., & Melnick, J. 1986, MNRAS, 223, 811

Cannon, J. M., Dohm-Palmer, R. C., Skillman, E. D., et al. 2003, AJ, 126, 2806

Cannon, J. M., McClure-Griffiths, N. M., Skillman, E. D., & Côté, S. 2004, ApJ, 607, 274

Cannon, J. M., Walter, F., Armus, L., et al. 2006, ApJ, 652, 1170

Cantalupo, C. M., Borrill, J. D., Jaffe, A. H., Kisner, T. S., & Stompor, R. 2010, ApJS, 187, 212

Cardelli, J. A., Meyer, D. M., Jura, M., & Savage, B. D. 1996, ApJ, 467, 334

Carignan, C. & Beaulieu, S. 1989, ApJ, 347, 760

Carignan, C., Beaulieu, S., & Freeman, K. C. 1990, AJ, 99, 178

Cen, R. & Ostriker, J. P. 1999, ApJ, 519, L109

Chengalur, J. N., Pustilnik, S. A., Martin, J.-M., & Kniazev, A. Y. 2006, MNRAS, 371, 1849

Ciesla, L., Boselli, A., Smith, M. W. L., et al. 2012, A&A, 543, A161

Cohen, M., Wheaton, W. A., & Megeath, S. T. 2003, AJ, 126, 1090

Combes, F. 1991, Galaxies et cosmologie

Condon, J. J. 1992, ARA&A, 30, 575

Condon, J. J., Cotton, W. D., Greisen, E. W., et al. 1998, AJ, 115, 1693

Cormier, D., Lebouteiller, V., Madden, S. C., et al. 2012, A&A, 548, A20

Cormier, D., Madden, S. C., Lebouteiller, V., et al. 2014, ArXiv 1401.0563

Cowie, L. L., Songaila, A., Hu, E. M., & Cohen, J. G. 1996, AJ, 112, 839

Cresci, G., Mannucci, F., Sommariva, V., et al. 2012, MNRAS, 421, 262

Dale, D. A., Aniano, G., Engelbracht, C. W., et al. 2012, ApJ, 745, 95

Dale, D. A., Bendo, G. J., Engelbracht, C. W., et al. 2005, ApJ, 633, 857

Dale, D. A., Cohen, S. A., Johnson, L. C., et al. 2009, ApJ, 703, 517

Dale, D. A., Gil de Paz, A., Gordon, K. D., et al. 2007, ApJ, 655, 863

Dale, D. A. & Helou, G. 2002, ApJ, 576, 159

Dale, D. A., Helou, G., Contursi, A., Silbermann, N. A., & Kolhatkar, S. 2001a, ApJ, 549, 215

Dale, D. A., Helou, G., Neugebauer, G., et al. 2001b, AJ, 122, 1736

Davies, J. I., Bianchi, S., Cortese, L., et al. 2012, MNRAS, 419, 3505

Davoust, E. & Contini, T. 2004, A&A, 416, 515

de Blok, W. J. G. & Walter, F. 2006, AJ, 131, 343

de Graauw, T., Helmich, F. P., Phillips, T. G., et al. 2010, A&A, 518, L6

de Vaucouleurs, G., de Vaucouleurs, A., Corwin, Jr., H. G., et al. 1991, Third Reference Catalogue of Bright Galaxies, ed. de Vaucouleurs, G., de Vaucouleurs, A., Corwin, H. G., Jr., Buta, R. J., Paturel, G., & Fouque, P. (de Vaucouleurs, G.)

Dekel, A. & Silk, J. 1986, ApJ, 303, 39

Desert, F.-X., Boulanger, F., & Puget, J. L. 1990, A&A, 237, 215

Draine, B. T. 2003, ARA&A, 41, 241

Draine, B. T., Dale, D. A., Bendo, G., et al. 2007, ApJ, 663, 866

Draine, B. T. & Hensley, B. 2012, ApJ, 757, 103

Draine, B. T. & Lazarian, A. 1998, ApJ, 508, 157

Draine, B. T. & Lee, H. M. 1984, ApJ, 285, 89

Draine, B. T. & Li, A. 2001, ApJ, 551, 807

Draine, B. T. & Li, A. 2007, ApJ, 657, 810

Duc, P.-A. & Mirabel, I. F. 1998, A&A, 333, 813

Dudley, C. C. & Wynn-Williams, C. G. 1997, ApJ, 488, 720

Duley, W. W. & Williams, D. A. 1981, MNRAS, 196, 269

Dumke, M., Krause, M., & Wielebinski, R. 2004, A&A, 414, 475

Dunne, L., Gomez, H. L., da Cunha, E., et al. 2011, MNRAS, 417, 1510

Dupac, X., Bernard, J.-P., Boudet, N., et al. 2003, A&A, 404, L11

Dwek, E. 1998, ApJ, 501, 643

Dwek, E., Arendt, R. G., Fixsen, D. J., et al. 1997, ApJ, 475, 565

Ehle, M. 2005, in The Magnetized Plasma in Galaxy Evolution, ed. K. T. Chyzy, K. Otmianowska-Mazur, M. Soida, & R.-J. Dettmar, 31–38

Ekta, B. & Chengalur, J. N. 2010, MNRAS, 403, 295

Ekta, B., Pustilnik, S. A., & Chengalur, J. N. 2009, MNRAS, 397, 963

Engelbracht, C. W., Blaylock, M., Su, K. Y. L., et al. 2007, PASP, 119, 994

Engelbracht, C. W., Gordon, K. D., Rieke, G. H., et al. 2005, ApJ, 628, L29

Engelbracht, C. W., Rieke, G. H., Gordon, K. D., et al. 2008, ApJ, 678, 804

Erb, D. K., Shapley, A. E., Pettini, M., et al. 2006, ApJ, 644, 813

Eskew, M., Zaritsky, D., & Meidt, S. 2012, AJ, 143, 139

Fathi, K., Axon, D. J., Storchi-Bergmann, T., et al. 2011, ApJ, 736, 77

Feldmann, R., Gnedin, N. Y., & Kravtsov, A. V. 2012, ApJ, 747, 124

Ferrara, A. & Dettmar, R.-J. 1994, ApJ, 427, 155

Fioc, M. & Rocca-Volmerange, B. 1997, A&A, 326, 950

Fitzpatrick, E. L. 1999, PASP, 111, 63

Fricke, K. J., Izotov, Y. I., Papaderos, P., Guseva, N. G., & Thuan, T. X. 2001, AJ, 121, 169

Frye, B., Broadhurst, T., & Benítez, N. 2002, ApJ, 568, 558

Galametz, M., Hony, S., Galliano, F., et al. 2013, MNRAS, 431, 1596

Galametz, M., Kennicutt, R. C., Albrecht, M., et al. 2012, MNRAS, 425, 763

Galametz, M., Madden, S., Galliano, F., et al. 2009, A&A, 508, 645

Galametz, M., Madden, S. C., Galliano, F., et al. 2011, A&A, 532, A56

Galametz, M., Madden, S. C., Galliano, F., et al. 2010, A&A, 518, L55

Galliano, F., Dwek, E., & Chanial, P. 2008, ApJ, 672, 214

Galliano, F., Hony, S., Bernard, J.-P., et al. 2011, A&A, 536, A88

Galliano, F., Madden, S. C., Jones, A. P., Wilson, C. D., & Bernard, J.-P. 2005, A&A, 434, 867

Galliano, F., Madden, S. C., Jones, A. P., et al. 2003, A&A, 407, 159

Garnett, D. R., Kennicutt, Jr., R. C., & Bresolin, F. 2004, ApJ, 607, L21

Genzel, R., Tacconi, L. J., Rigopoulou, D., Lutz, D., & Tecza, M. 2001, ApJ, 563, 527

Gieren, W., Pietrzyński, G., Nalewajko, K., et al. 2006, ApJ, 647, 1056

Gil de Paz, A. & Madore, B. F. 2005, ApJS, 156, 345

Gil de Paz, A., Madore, B. F., & Pevunova, O. 2003, ApJS, 147, 29

Glover, S. C. O. & Clark, P. C. 2012, MNRAS, 421, 9

Gordon, D. & Gottesman, S. T. 1981, AJ, 86, 161

Gordon, K. D., Clayton, G. C., Misselt, K. A., Landolt, A. U., & Wolff, M. J. 2003, ApJ, 594, 279

Gordon, K. D., Engelbracht, C. W., Fadda, D., et al. 2007, PASP, 119, 1019

Gordon, K. D., Rieke, G. H., Engelbracht, C. W., et al. 2005, PASP, 117, 503

Gratier, P., Braine, J., Rodriguez-Fernandez, N. J., et al. 2010, A&A, 512, A68

Grebel, E. K. 2001, in Dwarf galaxies and their environment, ed. K. S. de Boer, R.-J. Dettmar, & U. Klein, 45

Grebel, E. K., Gallagher, III, J. S., & Harbeck, D. 2003, AJ, 125, 1926

Grenier, I. A., Casandjian, J.-M., & Terrier, R. 2005, Science, 307, 1292

Greve, A., Becker, R., Johansson, L. E. B., & McKeith, C. D. 1996, A&A, 312, 391

Griffin, M. J., Abergel, A., Abreu, A., et al. 2010, A&A, 518, L3

Grocholski, A. J., van der Marel, R. P., Aloisi, A., et al. 2012, AJ, 143, 117

Grossi, M., Hunt, L. K., Madden, S., et al. 2010, A&A, 518, L52

Groves, B., Dopita, M. A., Sutherland, R. S., et al. 2008, ApJS, 176, 438

Guelin, M., Zylka, R., Mezger, P. G., Haslam, C. G. T., & Kreysa, E. 1995, A&A, 298, L29

Guelin, M., Zylka, R., Mezger, P. G., et al. 1993, A&A, 279, L37

Guhathakurta, P. & Draine, B. T. 1989, ApJ, 345, 230

Guseva, N. G., Izotov, Y. I., Fricke, K. J., & Henkel, C. 2012, A&A, 541, A115

Guseva, N. G., Izotov, Y. I., Papaderos, P., & Fricke, K. J. 2007, A&A, 464, 885

Guseva, N. G., Izotov, Y. I., & Thuan, T. X. 2000, ApJ, 531, 776

Guseva, N. G., Papaderos, P., Izotov, Y. I., et al. 2003a, A&A, 407, 91

Guseva, N. G., Papaderos, P., Izotov, Y. I., et al. 2003b, A&A, 407, 105

Guseva, N. G., Papaderos, P., Izotov, Y. I., Noeske, K. G., & Fricke, K. J. 2004, A&A, 421, 519

Haser, S. M., Pauldrach, A. W. A., Lennon, D. J., et al. 1998, A&A, 330, 285

Helou, G. 1986, ApJ, 311, L33

Hermelo, I., Lisenfeld, U., Relaño, M., et al. 2013, A&A, 549, A70

Higdon, S. J. U., Devost, D., Higdon, J. L., et al. 2004, PASP, 116, 975

Hirashita, H. 1999, ApJ, 522, 220

Hirashita, H. 2013, MNRAS, 429, 3390

Hirashita, H. & Kuo, T.-M. 2011, MNRAS, 416, 1340

Hirashita, H., Tajiri, Y. Y., & Kamaya, H. 2002, A&A, 388, 439

Hodge, P., Smith, T., Eskridge, P., MacGillivray, H., & Beard, S. 1991, ApJ, 379, 621

Holland, W. S., Robson, E. I., Gear, W. K., et al. 1999, MNRAS, 303, 659

Holweger, H. 2001, in American Institute of Physics Conference Series, Vol. 598, Joint SOHO/ACE workshop "Solar and Galactic Composition", ed. R. F. Wimmer-Schweingruber, 23–30

Hony, S., Galliano, F., Madden, S. M., & SAGE Consortium. 2010, in Bulletin of the American Astronomical Society, Vol. 42, American Astronomical Society Meeting Abstracts 215, 459.14

Hopkins, A. M., Schulte-Ladbeck, R. E., & Drozdovsky, I. O. 2002, AJ, 124, 862

Huchtmeier, W. K. 1979, A&A, 75, 170

Huchtmeier, W. K., Krishna, G., & Petrosian, A. 2005, A&A, 434, 887

Huchtmeier, W. K. & Richter, O.-G. 1988, A&A, 203, 237

Huchtmeier, W. K., Seiradakis, J. H., & Materne, J. 1981, A&A, 102, 134

Hunt, L., Bianchi, S., & Maiolino, R. 2005, A&A, 434, 849

Hunt, L. K., Thuan, T. X., Sauvage, M., & Izotov, Y. I. 2006, ApJ, 653, 222

Hunter, D. 1997, PASP, 109, 937

Hunter, D. A., Elmegreen, B. G., & Ludka, B. C. 2010, AJ, 139, 447

Hunter, D. A., Gallagher, III, J. S., Rice, W. L., & Gillett, F. C. 1989, ApJ, 336, 152

Hunter, D. A. & Kaufman, M. 2007, AJ, 134, 721

Hunter, D. A. & Sage, L. 1993, PASP, 105, 374

Hunter, D. A., van Woerden, H., & Gallagher, J. S. 1999, AJ, 118, 2184

Hunter, D. A., Zahedy, F., Bowsher, E. C., et al. 2011, AJ, 142, 173

Inoue, A. K. 2011, Earth, Planets, and Space, 63, 1027

Israel, F. P. 1997, A&A, 328, 471

Israel, F. P. 2005, A&A, 438, 855

Israel, F. P., Baas, F., Rudy, R. J., Skillman, E. D., & Woodward, C. E. 2003, A&A, 397, 87

Israel, F. P. & de Bruyn, A. G. 1988, A&A, 198, 109

Israel, F. P., Maloney, P. R., Geis, N., et al. 1996, ApJ, 465, 738

Israel, F. P., Wall, W. F., Raban, D., et al. 2010, A&A, 519, A67

Issa, M. R., MacLaren, I., & Wolfendale, A. W. 1990, A&A, 236, 237

Izotov, I. I., Guseva, N. G., Lipovetskii, V. A., Kniazev, A. I., & Stepanian, J. A. 1991, A&A, 247, 303

Izotov, Y. I., Chaffee, F. H., Foltz, C. B., et al. 1999, ApJ, 527, 757

Izotov, Y. I., Papaderos, P., Guseva, N. G., Fricke, K. J., & Thuan, T. X. 2004, A&A, 421, 539

Izotov, Y. I., Stasińska, G., Meynet, G., Guseva, N. G., & Thuan, T. X. 2006, A&A, 448, 955

Izotov, Y. I. & Thuan, T. X. 1998, ApJ, 500, 188

Izotov, Y. I. & Thuan, T. X. 1999, ApJ, 511, 639

Izotov, Y. I., Thuan, T. X., & Guseva, N. G. 2012, A&A, 546, A122

Izotov, Y. I., Thuan, T. X., & Lipovetsky, V. A. 1994, ApJ, 435, 647

Izotov, Y. I., Thuan, T. X., & Lipovetsky, V. A. 1997, ApJS, 108, 1

Izotov, Y. I., Thuan, T. X., & Stasińska, G. 2007, ApJ, 662, 15

James, A., Dunne, L., Eales, S., & Edmunds, M. G. 2002, MNRAS, 335, 753

James, P. A. 1994, MNRAS, 269, 176

Jarrett, T. H., Chester, T., Cutri, R., Schneider, S. E., & Huchra, J. P. 2003, AJ, 125, 525

Jarrett, T. H., Cohen, M., Masci, F., et al. 2011, ApJ, 735, 112

Jones, A. & Tielens, A. 1994, in The Cold Universe, ed. T. Montmerle, C. J. Lada, I. F. Mirabel, & J. Tran Thanh Van, 35

Jones, A. P. 2004, in Astronomical Society of the Pacific Conference Series, Vol. 309, Astrophysics of Dust, ed. A. N. Witt, G. C. Clayton, & B. T. Draine, 347

Jones, A. P. 2012, A&A, 545, C3

Jones, A. P., Tielens, A. G. G. M., & Hollenbach, D. J. 1996, ApJ, 469, 740

Jones, A. P., Tielens, A. G. G. M., Hollenbach, D. J., & McKee, C. F. 1997, in American Institute of Physics Conference Series, Vol. 402, American Institute of Physics Conference Series, ed. T. J. Bernatowicz & E. Zinner, 595–613

Juvela, M. & Ysard, N. 2012a, A&A, 541, A33

Juvela, M. & Ysard, N. 2012b, A&A, 539, A71

Karachentsev, I. D., Dolphin, A. E., Geisler, D., et al. 2002, A&A, 383, 125

Karachentsev, I. D., Karachentseva, V. E., Huchtmeier, W. K., & Makarov, D. I. 2004, AJ, 127, 2031

Karachentsev, I. D., Sharina, M. E., Dolphin, A. E., et al. 2003, A&A, 398, 467

Karczewski, O. Ł., Barlow, M. J., Page, M. J., et al. 2013, MNRAS, 431, 2493

Kelly, B. C., Shetty, R., Stutz, A. M., et al. 2012, ApJ, 752, 55

Kemper, F., Vriend, W. J., & Tielens, A. G. G. M. 2004, ApJ, 609, 826

Kennicutt, R. C., Calzetti, D., Aniano, G., et al. 2011, PASP, 123, 1347

Kennicutt, Jr., R. C. 1989, ApJ, 344, 685

Kennicutt, Jr., R. C. 1998, ApJ, 498, 541

Kennicutt, Jr., R. C., Armus, L., Bendo, G., et al. 2003a, PASP, 115, 928

Kennicutt, Jr., R. C., Bresolin, F., & Garnett, D. R. 2003b, ApJ, 591, 801

Kennicutt, Jr., R. C., Hao, C.-N., Calzetti, D., et al. 2009, ApJ, 703, 1672

Kepley, A. A., Zweibel, E. G., Wilcots, E. M., Johnson, K. E., & Robishaw, T. 2011, ApJ, 736, 139

Kewley, L. J., Dopita, M. A., Sutherland, R. S., Heisler, C. A., & Trevena, J. 2001, ApJ, 556, 121

Kewley, L. J. & Ellison, S. L. 2008, ApJ, 681, 1183

Kim, M., Kim, E., Hwang, N., et al. 2009, ApJ, 703, 816

Kirkpatrick, A., Calzetti, D., Galametz, M., et al. 2013, ApJ, 778, 51

Kiuchi, G., Ohta, K., Sawicki, M., & Allen, M. 2004, AJ, 128, 2743

Klein, U., Graeve, R., & Wielebinski, R. 1983, A&A, 117, 332

Kobulnicky, H. A., Dickey, J. M., Sargent, A. I., Hogg, D. E., & Conti, P. S. 1995, AJ, 110, 116

Kobulnicky, H. A. & Johnson, K. E. 1999, ApJ, 527, 154

Kobulnicky, H. A., Kennicutt, Jr., R. C., & Pizagno, J. L. 1999, ApJ, 514, 544

Kobulnicky, H. A. & Kewley, L. J. 2004, ApJ, 617, 240

Kobulnicky, H. A. & Skillman, E. D. 1997, ApJ, 489, 636

Kong, X., Cheng, F. Z., Weiss, A., & Charlot, S. 2002, A&A, 396, 503

Köppen, J., Weidner, C., & Kroupa, P. 2007, MNRAS, 375, 673

Kormendy, J. & Sanders, D. B. 1992, ApJ, 390, L53

Krumholz, M. R. & Gnedin, N. Y. 2011, ApJ, 729, 36

Kunth, D., Lequeux, J., Sargent, W. L. W., & Viallefond, F. 1994, A&A, 282, 709

Kunth, D. & Östlin, G. 2000, A&A Rev., 10, 1

Kunth, D. & Sargent, W. L. W. 1986, ApJ, 300, 496

Laor, A. & Draine, B. T. 1993, ApJ, 402, 441

Lebouteiller, V., Barry, D. J., Spoon, H. W. W., et al. 2011, ApJS, 196, 8

Lebouteiller, V., Bernard-Salas, J., Sloan, G. C., & Barry, D. J. 2010, PASP, 122, 231

Lee, H. & Skillman, E. D. 2004a, ApJ, 614, 698

Lee, H. & Skillman, E. D. 2004b, ApJ, 614, 698

Lee, H., Skillman, E. D., & Venn, K. A. 2006, ApJ, 642, 813

Lee, J. C., Salzer, J. J., Impey, C., Thuan, T. X., & Gronwall, C. 2002, AJ, 124, 3088

Lee, M. G., Freedman, W., Mateo, M., et al. 1993, AJ, 106, 1420

Leger, A. & Puget, J. L. 1984, A&A, 137, L5

Legrand, F., Kunth, D., Roy, J.-R., Mas-Hesse, J. M., & Walsh, J. R. 2000, A&A, 355, 891

Lelli, F., Verheijen, M., Fraternali, F., & Sancisi, R. 2012, A&A, 537, A72

Lequeux, J., Peimbert, M., Rayo, J. F., Serrano, A., & Torres-Peimbert, S. 1979, A&A, 80, 155

Leroy, A., Bolatto, A., Walter, F., & Blitz, L. 2006, ApJ, 643, 825

Leroy, A., Bolatto, A. D., Simon, J. D., & Blitz, L. 2005, ApJ, 625, 763

Leroy, A., Cannon, J., Walter, F., Bolatto, A., & Weiss, A. 2007, ApJ, 663, 990

Leroy, A. K., Bolatto, A., Gordon, K., et al. 2011, ApJ, 737, 12

Leroy, A. K., Walter, F., Bigiel, F., et al. 2009, AJ, 137, 4670

Levesque, E. M., Kewley, L. J., & Larson, K. L. 2010, AJ, 139, 712

Li, A. & Draine, B. T. 2001, ApJ, 554, 778

Liang, Y. C., Hammer, F., Yin, S. Y., et al. 2007, A&A, 473, 411

Lisenfeld, U. & Ferrara, A. 1998, ApJ, 496, 145

Lisenfeld, U., Israel, F. P., Stil, J. M., & Sievers, A. 2002, A&A, 382, 860

López-Sánchez, Á. R. & Esteban, C. 2010, A&A, 517, A85

López-Sánchez, Á. R., Esteban, C., & Rodríguez, M. 2004, ApJS, 153, 243

López-Sánchez, Á. R., Koribalski, B. S., van Eymeren, J., et al. 2012, MNRAS, 419, 1051

Luridiana, V., Peimbert, A., Peimbert, M., & Cerviño, M. 2003, ApJ, 592, 846

Lynds, R., Tolstoy, E., O'Neil, Jr., E. J., & Hunter, D. A. 1998, AJ, 116, 146

Madden, S. C. 2000, New Astronomy Reviews, 44, 249

Madden, S. C., Galliano, F., Jones, A. P., & Sauvage, M. 2006, A&A, 446, 877

Madden, S. C., Poglitsch, A., Geis, N., Stacey, G. J., & Townes, C. H. 1997, ApJ, 483, 200

Madden, S. C., Rémy, A., Galliano, F., et al. 2012, in IAU Symposium, Vol. 284, IAU Symposium, ed. R. J. Tuffs & C. C. Popescu, 141–148

Madden, S. C., Rémy-Ruyer, A., Galametz, M., et al. 2013, PASP, 125, 600

Maddox, S. J., Efstathiou, G., Sutherland, W. J., & Loveday, J. 1990, MNRAS, 243, 692

Magdis, G. E., Daddi, E., Béthermin, M., et al. 2012, ApJ, 760, 6

Magnelli, B., Saintonge, A., Lutz, D., et al. 2012, A&A, 548, A22

Magrini, L., Bianchi, S., Corbelli, E., et al. 2011, A&A, 535, A13

Magrini, L. & Gonçalves, D. R. 2009, MNRAS, 398, 280

Maier, C., Meisenheimer, K., & Hippelein, H. 2004, A&A, 418, 475

Maiolino, R., Nagao, T., Grazian, A., et al. 2008, A&A, 488, 463

Mannucci, F., Cresci, G., Maiolino, R., et al. 2009, MNRAS, 398, 1915

Marble, A. R., Engelbracht, C. W., van Zee, L., et al. 2010, ApJ, 715, 506

Marzke, R. O. & da Costa, L. N. 1997, AJ, 113, 185

Masegosa, J., Moles, M., & Campos-Aguilar, A. 1994, ApJ, 420, 576

Mateo, M. L. 1998, ARA&A, 36, 435

Mather, J. C., Cheng, E. S., Cottingham, D. A., et al. 1994, ApJ, 420, 439

Mathis, J. S. 1990, in Astronomical Society of the Pacific Conference Series, Vol. 12, The Evolution of the Interstellar Medium, ed. L. Blitz, 63–77

Mathis, J. S., Mezger, P. G., & Panagia, N. 1983, A&A, 128, 212

Mathis, J. S., Rumpl, W., & Nordsieck, K. H. 1977, ApJ, 217, 425

Mauch, T., Murphy, T., Buttery, H. J., et al. 2008, VizieR Online Data Catalog, 8081, 0

McCall, M. L. 1984, MNRAS, 208, 253

McCall, M. L., Rybski, P. M., & Shields, G. A. 1985, ApJS, 57, 1

McConnachie, A. W. 2012, AJ, 144, 4

McGaugh, S. S. 1991, ApJ, 380, 140

McQuade, K., Calzetti, D., & Kinney, A. L. 1995, ApJS, 97, 331

Meier, D. S., Turner, J. L., Crosthwaite, L. P., & Beck, S. C. 2001, AJ, 121, 740

Meixner, M., Galliano, F., Hony, S., et al. 2010, A&A, 518, L71

Melisse, J. P. M. & Israel, F. P. 1994, A&A, 285, 51

Meny, C., Gromov, V., Boudet, N., et al. 2007, A&A, 468, 171

Meurer, G. R., Staveley-Smith, L., & Killeen, N. E. B. 1998, MNRAS, 300, 705

Meyer, D. M., Cardelli, J. A., & Sofia, U. J. 1997, ApJ, 490, L103

Meyer, D. M., Jura, M., & Cardelli, J. A. 1998, ApJ, 493, 222

Moles, M., Marquez, I., Masegosa, J., et al. 1994, ApJ, 432, 135

Moll, S. L., Mengel, S., de Grijs, R., Smith, L. J., & Crowther, P. A. 2007, MNRAS, 382, 1877

Moore, B., Ghigna, S., Governato, F., et al. 1999, ApJ, 524, L19

Mould, J. R., Huchra, J. P., Freedman, W. L., et al. 2000, ApJ, 529, 786

Moustakas, J., Kennicutt, Jr., R. C., Tremonti, C. A., et al. 2010, ApJS, 190, 233

Muñoz-Mateos, J. C., Gil de Paz, A., Boissier, S., et al. 2009, ApJ, 701, 1965

Murphy, E. J., Helou, G., Condon, J. J., et al. 2010, ApJ, 709, L108

Navarro, J. F., Frenk, C. S., & White, S. D. M. 1996, ApJ, 462, 563

Neininger, N., Guelin, M., Garcia-Burillo, S., Zylka, R., & Wielebinski, R. 1996, A&A, 310, 725

Oh, S.-H., de Blok, W. J. G., Brinks, E., Walter, F., & Kennicutt, Jr., R. C. 2011, AJ, 141, 193

O'Halloran, B., Galametz, M., Madden, S. C., et al. 2010, A&A, 518, L58

O'Halloran, B., Satyapal, S., & Dudik, R. P. 2006, ApJ, 641, 795

Olive, K. A., Steigman, G., & Skillman, E. D. 1997, ApJ, 483, 788

Ott, S. 2010, in Astronomical Society of the Pacific Conference Series, Vol. 434, Astronomical Data Analysis Software and Systems XIX, ed. Y. Mizumoto, K.-I. Morita, & M. Ohishi, 139

Pagel, B. E. J. 1997, Nucleosynthesis and Chemical Evolution of Galaxies

Pagel, B. E. J., Simonson, E. A., Terlevich, R. J., & Edmunds, M. G. 1992, MNRAS, 255, 325

Paradis, D., Bernard, J.-P., & Mény, C. 2009, A&A, 506, 745

Paradis, D., Veneziani, M., Noriega-Crespo, A., et al. 2010, A&A, 520, L8

Parkin, T. J., Wilson, C. D., Foyle, K., et al. 2012, MNRAS, 422, 2291

Paturel, G., Theureau, G., Bottinelli, L., et al. 2003, A&A, 412, 57

Peeters, E., Hony, S., Van Kerckhoven, C., et al. 2002, A&A, 390, 1089

Peimbert, A., Peimbert, M., & Luridiana, V. 2002, ApJ, 565, 668

Persic, M., Mariani, S., Cappi, M., et al. 1998, A&A, 339, L33

Petitpas, G. R. & Wilson, C. D. 2003, ApJ, 587, 649

Pettini, M. & Pagel, B. E. J. 2004, MNRAS, 348, L59

Pilbratt, G. L., Riedinger, J. R., Passvogel, T., et al. 2010, A&A, 518, L1

Pilleri, P., Montillaud, J., Berné, O., & Joblin, C. 2012, A&A, 542, A69

Pilyugin, L. S. 2001, A&A, 374, 412

Pilyugin, L. S. & Thuan, T. X. 2005, ApJ, 631, 231

Pilyugin, L. S. & Thuan, T. X. 2007, ApJ, 669, 299

Pilyugin, L. S., Thuan, T. X., & Vílchez, J. M. 2006, MNRAS, 367, 1139

Planck Collaboration, Ade, P. A. R., Aghanim, N., et al. 2011a, A&A, 536, A19

Planck Collaboration, Ade, P. A. R., Aghanim, N., et al. 2011b, A&A, 536, A20

Poglitsch, A., Krabbe, A., Madden, S. C., et al. 1995, ApJ, 454, 293

Poglitsch, A., Waelkens, C., Geis, N., et al. 2010, A&A, 518, L2

Popescu, C. C. & Hopp, U. 2000, A&AS, 142, 247

Pustilnik, S. A., Kniazev, A. Y., Pramskij, A. G., Ugryumov, A. V., & Masegosa, J. 2003, A&A, 409, 917

Pustilnik, S. A. & Martin, J.-M. 2007, A&A, 464, 859

Pustilnik, S. A., Martin, J.-M., Huchtmeier, W. K., et al. 2002, A&A, 389, 405

Reach, W. T., Dwek, E., Fixsen, D. J., et al. 1995, ApJ, 451, 188

Reach, W. T., Megeath, S. T., Cohen, M., et al. 2005, PASP, 117, 978

Rémy-Ruyer, A., Madden, S. C., Galliano, F., et al. 2013, A&A, 557, A95

Revaz, Y. & Jablonka, P. 2012, A&A, 538, A82

Rice, W., Lonsdale, C. J., Soifer, B. T., et al. 1988, ApJS, 68, 91

Rieke, G., Lada, C., Lebofsky, M., et al. 1984, in Bulletin of the American Astronomical Society, Vol. 16, Bulletin of the American Astronomical Society, 906

Roman-Duval, J., Israel, F. P., Bolatto, A., et al. 2010, A&A, 518, L74+

Rosenberg, J. L., Ashby, M. L. N., Salzer, J. J., & Huang, J.-S. 2006, ApJ, 636, 742

Roussel, H. 2013, PASP, 125, 1126

Sage, L. J., Salzer, J. J., Loose, H.-H., & Henkel, C. 1992, A&A, 265, 19

Sage, L. J., Welch, G. A., & Young, L. M. 2007, ApJ, 657, 232

Sanders, D. B., Mazzarella, J. M., Kim, D.-C., Surace, J. A., & Soifer, B. T. 2003, AJ, 126, 1607

Sandstrom, K. M., Leroy, A. K., Walter, F., et al. 2013, ApJ, 777, 5

Sauvage, M., Thuan, T. X., & Lagage, P. O. 1997, A&A, 325, 98

Sauvage, M., Vigroux, L., & Thuan, T. X. 1990, A&A, 237, 296

Savage, B. D. & Sembach, K. R. 1996, ARA&A, 34, 279

Savaglio, S., Glazebrook, K., Le Borgne, D., et al. 2005, ApJ, 635, 260

Saviane, I., Ivanov, V. D., Held, E. V., et al. 2008, A&A, 487, 901

Schruba, A., Leroy, A. K., Walter, F., et al. 2012, AJ, 143, 138

Schuller, F. 2012, in Society of Photo-Optical Instrumentation Engineers (SPIE) Conference Series, Vol. 8452, Society of Photo-Optical Instrumentation Engineers (SPIE) Conference Series

Schulte-Ladbeck, R. E., Hopp, U., Greggio, L., Crone, M. M., & Drozdovsky, I. O. 2001, AJ, 121, 3007

Searle, L. & Sargent, W. L. W. 1972, ApJ, 173, 25

Serra Díaz-Cano, L. & Jones, A. P. 2008, A&A, 492, 127

Sharina, M. E., Karachentsev, I. D., & Tikhonov, N. A. 1996, A&AS, 119, 499

Shetty, R., Glover, S. C., Dullemond, C. P., et al. 2011, MNRAS, 415, 3253

Shetty, R., Kauffmann, J., Schnee, S., & Goodman, A. A. 2009a, ApJ, 696, 676

Shetty, R., Kauffmann, J., Schnee, S., Goodman, A. A., & Ercolano, B. 2009b, ApJ, 696, 2234

Simon, J. D. & Geha, M. 2007, ApJ, 670, 313

Simpson, C. E. & Gottesman, S. T. 2000, AJ, 120, 2975

Skibba, R. A., Engelbracht, C. W., Dale, D., et al. 2011, ApJ, 738, 89

Skillman, E. D., Côté, S., & Miller, B. W. 2003, AJ, 125, 610

Smith, J. D. T., Draine, B. T., Dale, D. A., et al. 2007, ApJ, 656, 770

Smith, M. W. L., Eales, S. A., Gomez, H. L., et al. 2012a, ApJ, 756, 40

Smith, M. W. L., Gomez, H. L., Eales, S. A., et al. 2012b, ApJ, 748, 123

Smith, R. K. & Dwek, E. 1998, ApJ, 503, 831

Smoker, J. V., Davies, R. D., Axon, D. J., & Hummel, E. 2000, A&A, 361, 19

Snow, T. P. & Witt, A. N. 1996, ApJ, 468, L65

Sofia, U. J. & Meyer, D. M. 2001, ApJ, 554, L221

Sramek, R. A. & Weedman, D. W. 1986, ApJ, 302, 640

Stansberry, J. A., Gordon, K. D., Bhattacharya, B., et al. 2007, PASP, 119, 1038

Stasińska, G. 1990, A&AS, 83, 501

Stasińska, G. 2005, A&A, 434, 507

Stasińska, G. & Izotov, Y. 2003, A&A, 397, 71

Steigman, G. 2005, Physica Scripta Volume T, 121, 142

Stepnik, B., Abergel, A., Bernard, J., et al. 2003, A&A, 398, 551

Stepnik, B., Abergel, A., Bernard, J.-P., et al. 2001, in Astronomical Society of the Pacific Conference Series, Vol. 243, From Darkness to Light: Origin and Evolution of Young Stellar Clusters, ed. T. Montmerle & P. André, 47

Strong, A. W., Moskalenko, I. V., Reimer, O., Digel, S., & Diehl, R. 2004, A&A, 422, L47

Swaters, R. A., van Albada, T. S., van der Hulst, J. M., & Sancisi, R. 2002, A&A, 390, 829

Taylor, C. L., Kobulnicky, H. A., & Skillman, E. D. 1998, AJ, 116, 2746

Thuan, T. X. 1983, ApJ, 268, 667

Thuan, T. X. 1985, ApJ, 299, 881

Thuan, T. X., Hibbard, J. E., & Lévrier, F. 2004, AJ, 128, 617

Thuan, T. X., Izotov, Y. I., & Lipovetsky, V. A. 1995, ApJ, 445, 108

Thuan, T. X., Lipovetsky, V. A., Martin, J.-M., & Pustilnik, S. A. 1999a, A&AS, 139, 1

Thuan, T. X. & Martin, G. E. 1981, ApJ, 247, 823

Thuan, T. X., Sauvage, M., & Madden, S. 1999b, ApJ, 516, 783

Tielens, A. G. G. M. 2005, The Physics and Chemistry of the Interstellar Medium (Cambridge University Press)

Tielens, A. G. G. M., McKee, C. F., Seab, C. G., & Hollenbach, D. J. 1994, ApJ, 431, 321

Tolstoy, E., Hill, V., & Tosi, M. 2009, ARA&A, 47, 371

Tosi, M., Sabbi, E., Bellazzini, M., et al. 2001, AJ, 122, 1271

Tremonti, C. A., Heckman, T. M., Kauffmann, G., et al. 2004, ApJ, 613, 898

Tully, R. B. 1988, Nearby galaxies catalog (Cambridge University Press)

Tully, R. B., Bottinelli, L., Fisher, J. R., et al. 1978, A&A, 63, 37

Ugryumov, A. V., Engels, D., Kniazev, A. Y., et al. 2001, A&A, 374, 907

Ugryumov, A. V., Engels, D., Pustilnik, S. A., et al. 2003, A&A, 397, 463

Urry, C. M. & Padovani, P. 1995, PASP, 107, 803

Valcke, S., de Rijcke, S., & Dejonghe, H. 2008, MNRAS, 389, 1111

van den Bergh, S. 2009, ApJ, 694, L120

van Eymeren, J., Marcelin, M., Koribalski, B. S., et al. 2009, A&A, 505, 105

van Zee, L. & Haynes, M. P. 2006, ApJ, 636, 214

van Zee, L., Haynes, M. P., Salzer, J. J., & Broeils, A. H. 1996, AJ, 112, 129

van Zee, L., Salzer, J. J., & Skillman, E. D. 2001, AJ, 122, 121

van Zee, L., Westpfahl, D., Haynes, M. P., & Salzer, J. J. 1998, AJ, 115, 1000

Veilleux, S., Kim, D.-C., Sanders, D. B., Mazzarella, J. M., & Soifer, B. T. 1995, ApJS, 98, 171

Vennik, J., Hopp, U., & Popescu, C. C. 2000, A&AS, 142, 399

Walter, F., Brinks, E., de Blok, W. J. G., et al. 2008, AJ, 136, 2563

Walter, F., Cannon, J. M., Roussel, H., et al. 2007, ApJ, 661, 102

Walter, F., Taylor, C. L., Hüttemeister, S., Scoville, N., & McIntyre, V. 2001, AJ, 121, 727

Weingartner, J. C. & Draine, B. T. 2001, ApJ, 548, 296

Welch, G. A. & Sage, L. J. 2003, ApJ, 584, 260

Welty, D. E., Jenkins, E. B., Raymond, J. C., Mallouris, C., & York, D. G. 2002, ApJ, 579, 304

Whittet, D. C. B. 2003, Astronomy and Geophysics, 44, 35

Williams, B. A., McMahon, P. M., & van Gorkom, J. H. 1991, AJ, 101, 1957

Wilson, C. D. 1995, ApJ, 448, L97

Wilson, C. D., Warren, B. E., Israel, F. P., et al. 2012, MNRAS, 424, 3050

Wolfire, M. G., Hollenbach, D., & McKee, C. F. 2010, ApJ, 716, 1191

Worthey, G. 1994, ApJS, 95, 107

Wright, E. L., Eisenhardt, P. R. M., Mainzer, A. K., et al. 2010, AJ, 140, 1868

Wu, Y., Charmandaris, V., Hao, L., et al. 2006, ApJ, 639, 157

Yang, M. & Phillips, T. 2007, ApJ, 662, 284

Yin, S. Y., Liang, Y. C., & Zhang, B. 2007, in Astronomical Society of the Pacific Conference Series, Vol. 373, The Central Engine of Active Galactic Nuclei, ed. L. C. Ho & J.-W. Wang, 686

Young, J. S. & Knezek, P. M. 1989, ApJ, 347, L55

Young, J. S., Xie, S., Tacconi, L., et al. 1995, ApJS, 98, 219

Young, L. M., Bureau, M., Davis, T. A., et al. 2011, MNRAS, 414, 940

Young, L. M. & Lo, K. Y. 1997, ApJ, 490, 710

Ysard, N., Juvela, M., Demyk, K., et al. 2012, A&A, 542, A21

Ysard, N. & Verstraete, L. 2010, A&A, 509, A12

Zhao, Y., Gao, Y., & Gu, Q. 2013, ApJ, 764, 44

Zhu, M., Papadopoulos, P. P., Xilouris, E. M., Kuno, N., & Lisenfeld, U. 2009, ApJ, 706, 941

Zhukovska, S. 2008, PhD thesis, Ruperto-Carola-University

Zhukovska, S. 2014, ArXiv 1401.1675

Zhukovska, S., Gail, H.-P., & Trieloff, M. 2008, A&A, 479, 453

Zubko, V., Dwek, E., & Arendt, R. G. 2004, ApJS, 152, 211